Technische Universität München

Lehrstuhl für Anorganische und Metallorganische Chemie

Fundamental understanding of living cluster libraries in solution

Max Schütz

Vollständiger Abdruck der von der Fakultät für Chemie der Technischen Universität München zur Erlangung des akademischen Grades eines

Doktors der Naturwissenschaften (Dr. rer. nat.)

genehmigten Dissertation.

Vorsitzender: Prof. Dr. Thomas F. Fässler

Prüfende der Dissertation: 1. Prof. Dr. Roland A. Fischer

2. Prof. Dr. Martin Elsner

3. Prof. Dr. Andreas Schnepf

Die Dissertation wurde am 07.05.2021 bei der Technischen Universität München eingereicht und durch die Fakultät für Chemie am 20.07.2021 angenommen.

Die vorliegende Arbeit wurde am Lehrstuhl für Anorganische und Metallorganische Chemie der Technischen Universität München im Zeitraum von Dezember 2017 bis Mai 2021 erstellt.

„Man muss noch Chaos in sich haben, um einen tanzenden Stern gebären zu können.“

aus Friedrich Nietzsche, „Also sprach Zarathustra“, 1883-1885.

Abstract

"Living libraries" of intermetalloid, Cp*-ligated clusters (Cu/Zn, Cu/Al, Au/Al) in solution were systematically investigated using a novel approach based on *in situ* LIFDI-MS analysis and supported by *in situ* NMR and UV-Vis spectroscopy. In this context, the term *"living library"* denotes a highly sensitive mixture of species, the composition of which readily responds to external stimuli and reaction partners. Such cluster libraries are formed by "bottom-up", wet-chemical synthesis combining the low-valent ligands AlCp* and $[Zn_2](Cp^*)_2$ with suitable organometallic precursors of the transition metals. Specifically, cluster growth and reactivity pathways including radically mediated C-H and Si-H activation reactions, as well as CO_2 activation reactions, were investigated. Besides novel algorithms for the interpretation of LIFDI-MS spectra, the dissertation includes the extensive characterization (single crystal Xray analysis, bonding analysis) of specific isolated cluster species.

Zusammenfassung

Intermetalloide, ligandstabilisierte Cluster der Elementkombinationen Cu/Zn, Cu/Al und Au/Al wurden zum ersten Mal systematisch mit LIFDI-MS, *in situ* NMR und UV-Vis Spektroskopie in Lösung untersucht. Dabei wurde ein neuer Algorithmus zur Planung und Auswertung massenspektrometrischer Untersuchungen entwickelt. Die Clusterlösungen stellen hoch sensitive und dynamische Systeme dar, deren Zusammensetzung stark von Reaktionsbedingungen und -partnern abhängt. Sie werden daher als „lebende Bibliotheken" bezeichnet und können durch nasschemische Synthese ausgehend von den niedervalenten Spezies AlCp* und $[Zn_2](Cp^*)_2$ und geeigneten Präkursoren der Übergangsmetalle erhalten werden. Mittels der neuartigen LIFDI-MS basierten Methodik wurden sowohl Clusterwachstumsprozesse in derartigen Bibliotheken als auch die Aktivierung von C-H und Si-H Bindungen sowie von CO_2 durch spezifische Komponenten der Bibliotheken untersucht. Neben der Entwicklung neuer methodischer Ansätze erfolgte die Isolation und eingehende Charakterisierung (Einkristallstrukturanalyse und theoretische Bindungsanalyse) spezifischer Cluster.

I. Content

II List of Abbreviations

A	absorbance
Ar	aryl
ATR	attenuated total reflection
BAr_4^F	tetrakis[3,5-bis(trifluoromethyl)phenyl]borate
btsa	bis(trimethylsilyl)amide
Bu	butyl
CAAC	cyclic-alkyl-amino-carbene
CE	collision energy
Cp*	1,2,3,4,5 – pentamethylcyclopentadienyl
Cp	cyclopentadienyl
DFT	density functional theory
^{i}Dipp	1,3-bis(2,6-diisopropylphenyl)-2,3-dihydro-1H-imidazole
dmpm	bis(dimethylphosphino)methane
dppbz	1,2-bis(diphenylphosphino)-benzene
dppp	1,3-bis(diphenylphosphino)propane
ESD	euclidean similarity distance
ESI	electro-spray ionization
Et	ethyl
HCD	higher energy C-trap for dissociation
HOMO	highest occupied molecular orbital
HPLC	high pressure liquid chromatography
I	(peak) intensity
^{i}	*iso-*
IR	infrared
L	ligand
LC	liquid chromatography
LIFDI-MS	liquid injection field desorption mass spectrometry

LUMO	lowest occupied molecular orbital
M	metal atom
Me	methyl
m/z	mass-to-charge ratio
MALDI	matrix assisted laser desorption ionization
Mes	mesityl
MS	mass spectrometer
^{n}	*normal-*
NBO	natural bond orbital
NHC	N-heterocyclic carbene
NICS	nuclear independent chemical shift
NMR	nuclear magnetic resonance
PES	potential energy surface
PEt	2-phenylethanethiolate
p-MBA	para-mercaptobenzoicacid
Ph	phenyl
ppm	parts per million
Pr	propyl
PXRD	powder-Xray-diffraction
R	organic residue / organic ligand
RT	room temperature
SC-XRD	single crystal Xray diffraction
SOMO	single occupied molecular orbital
SQUID	superconducting quantum interference device
TG	tree-growth
STol	4-methylbenzene-thiolate
TOA	trioctylammonium
^{t}	*tert-*
TEM	transmission electron microscopy

THF	tetrahydrofuran
^tNCBu	*tert*-butylisocyanide
TOF	time of flight
Tol	toluene
UHV	ultra-high vacuum
UV-Vis	ultraviolett-visible
VE	valence electron
VEC	valence electron concentration
WBI	Wiberg bond index
XPS	X-ray photoelectron spectroscopy

III Numeration of new compounds

1 $[Cu_7Al_6](Cp^*)_6$

1$_H$ $[HCu_7Al_6](Cp^*)_6$

1$_D$ $[DCu_7Al_6](Cp^*)_6$

2 $[Cu_8Al_6](Cp^*)_6$

3 $[Cu_{10}Zn_2](Cp^*)_2(Mes)_6$

4 $[Cu_4Zn_9](Cp^*)_8$

5 $[Cu_4Zn_{10}](Cp^*)_8$

6 $[H_xAu_6Al_6](Cp^*)_6$

7 $[H_xAu_7Al_6](Cp^*)_6$

8 $[Au_2Al_5](Cp^*)_5$

9 $[Cu_2Al](Cp^*)_3$

10 $[CuZn_{10}](Cp^*)_7$

11 $[Cu_4Al_4](Cp^*)_5(Mes)$

12 mixture $[HCu_7Al_6](Cp^*)_6$, $[H_4Cu_6Al_6](Cp^*)_6$, $[Cu_7Al_7](Cp^*)_6$, $[Cu_6Al_7](Cp^*)_6$, $[Cu_8Al_6](Cp^*)_6$

13 $[Au_4CuAl_5](Cp^*)_6$
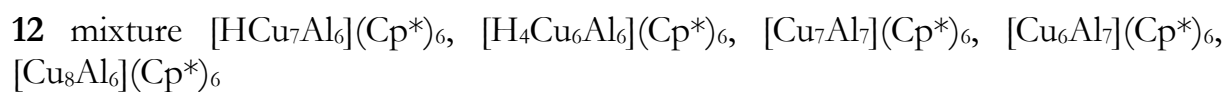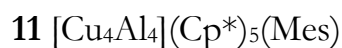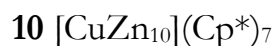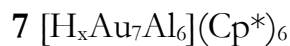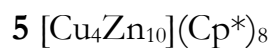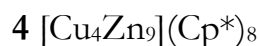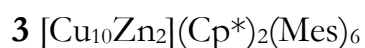
IV Notation on formula writing in this dissertation

Metal clusters are described in this dissertation with the general formula $[M_n](R)_m$ (n >> m; M = two or more different metal atoms; n = number of metal atoms aggregated in the cluster core; R = hydrocarbon ligand; square brackets denote the cluster core; round brackets denote the core protecting heteroatom-free, all-hydrocarbon ligand shell). It is noted that this nomenclature is different from the IUPAC nomenclature for coordination compounds. However, the chosen way of formula writing is considered to be more intriguing in terms of metal core compositions and valence electron count. [see also *M. Schütz, C. Gemel, M. Muhr, C. Jandl, S. Kahlal, J. Y. Saillard and R. A. Fischer, Exploring Cu/Al cluster growth and reactivity: From embryonic building blocks to intermetalloid, open-shell superatoms. Chem. Sci. 2021, 12, 6588-6599. Copyright 2021. Published by the Royal Society of Chemistry. Link: https://pubs.rsc.org/en/content/articlehtml/2021/sc/d1sc00268f.*]

1. Introduction

1.1 Cluster chemistry – what for?

Multi-atom metal clusters and their physicochemical properties as well as chemical reactivity have garnered increasing interest over recent decades. Besides a fundamental interest in structural and electronic features of metal rich molecules and particles, these systems in many cases show size-dependent, non-scalable properties differing from the corresponding bulk metal or alloy and rendering them interesting for catalysis and nanotechnology.[1-2] Besides the investigation of new, unexpected and intriguing reactivity, small-size molecular clusters might serve as a model system for technically significant heterogeneous catalysts. Even though heterogenous reaction processes consist of complex phenomena such as diffusion and transport processes with their corresponding kinetics, the catalytic chemical reaction is still a local event occurring at the active sites of the catalyst (see Figure 1).[3] In this context, isolated clusters of small size are able to mimic the local catalytically active center, which often is not a perfect surface plane but rather a defect site such as a vacancy, kink or step in the surface (see Figure 1).[3]

In basic terms, two different approaches exist for the generation and investigation of metal clusters and their reactivity, namely the study of naked metal clusters in the gas phase using (ultra)high vacuum techniques and the preparation of molecular clusters in solution by wet chemical methods as ligated and unligated derivatives. It should be noted that in both techniques, generation of one single cluster species is often not possible; rather a distribution of many clusters with different core sizes and atom arrangements is produced. This is due to a complicated potential energy surface with many local minima corresponding to a plethora of different cluster species. For example, 1467 local structural minima where identified only for a 13 atom cluster in a Lennard-Jones potential.[4] These clusters represent kinetic reaction products, as the formation of bulk metal is considered as the global thermodynamic minimum in any case. The composition of the cluster "libraries" produced is therefore strongly dependent on the reaction conditions applied.

1. Introduction

1.1 Cluster chemistry – what for?
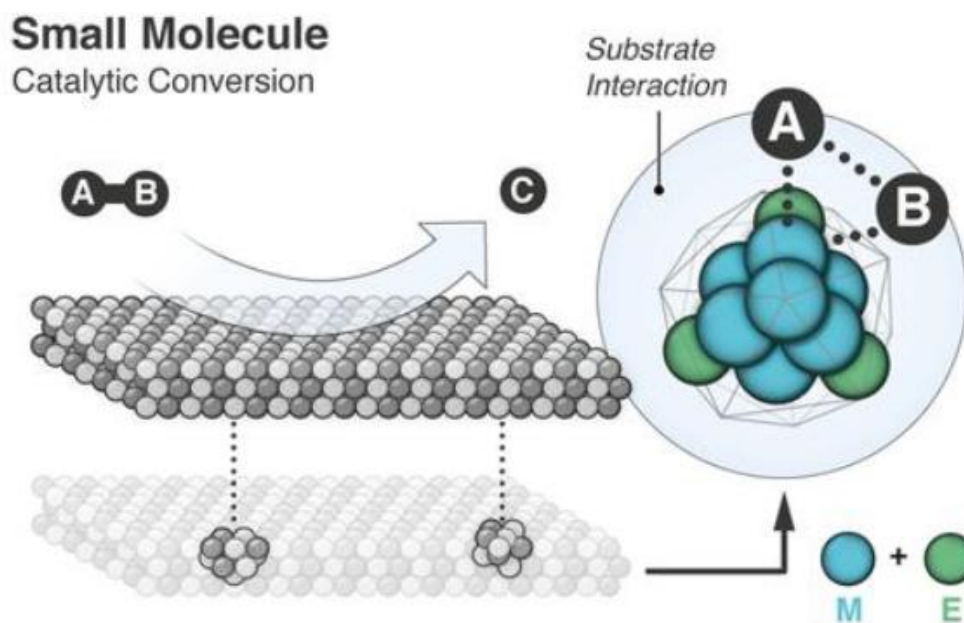
Figure 1
Conceptual visualization of the cluster approach mimicking elementary reaction steps on solid surfaces by molecular clusters. The example is for intermetallic systems as studied in this work (M = transition metal, E = Al, Zn) but the concept holds true for metal clusters in general. [Graphic by Dr. Johannes Richers.]

Compared to mononuclear coordination compounds, reactivity studies on molecular clusters in solution are scarce. This is partly due to stability *vs.* reactivity relationship: Stable – and thus isolable – clusters often present a rigid, ligand stabilized and coordinatively saturated geometry leading to a lack of reactive coordination sites accessible for surface reactions. Reactivity patterns are often difficult to assess, as also cluster fragmentation processes involving the rupture of metal-metal bonds must be considered. Nevertheless, the potential of multimetallic systems for catalysis should not be underestimated: Metal-metal bonds exhibit distinct electronic properties and in bimetallic systems also an intrinsic polarity, which might be the basis for a unique reactivity. Cooperative effects between metal centers in a cluster or small bimetallic molecule affording a specific catalytic activity are observed for many important organic transformations including polymerization, hydrogenation, hydroformylation and oxidation reactions.[5]

Coordination complexes and clusters of Hume-Rothery-phase elemental composition have had a long research tradition in the group of *R. A. Fischer*. However, progress in this field of chemistry is often slowed down by sophisticated and completely undiscovered reaction mechanisms, as well as by complicated work-up procedures including separation of highly sensitive product mixtures. This

1. Introduction
1.1 Cluster chemistry – what for?

dissertation will present new methods and perspectives to obtain a more fundamental understanding of intermetalloid, "Hume-Rothery inspired" cluster chemistry with the elemental combinations Cu/Al, Cu/Zn and Cu/Al as selected examples. Mass-spectrometry will be used as a powerful tool to monitor cluster formation reactions and to assess reactivity patterns of the so-obtained "living" cluster "libraries" (see Figure 2 for illustration). Even though working with libraries of species is well known from other disciplines and gas-phase cluster chemistry, it is unknown territory for highly air and moisture sensitive, organometallic cluster chemistry in solution. Therefore, this introduction consists of two complementary parts describing first the chemical background of cluster chemistry and second the related methodic strategies in other disciplines. Likewise, the results and discussion part of this thesis is divided into methodological and chemical results.
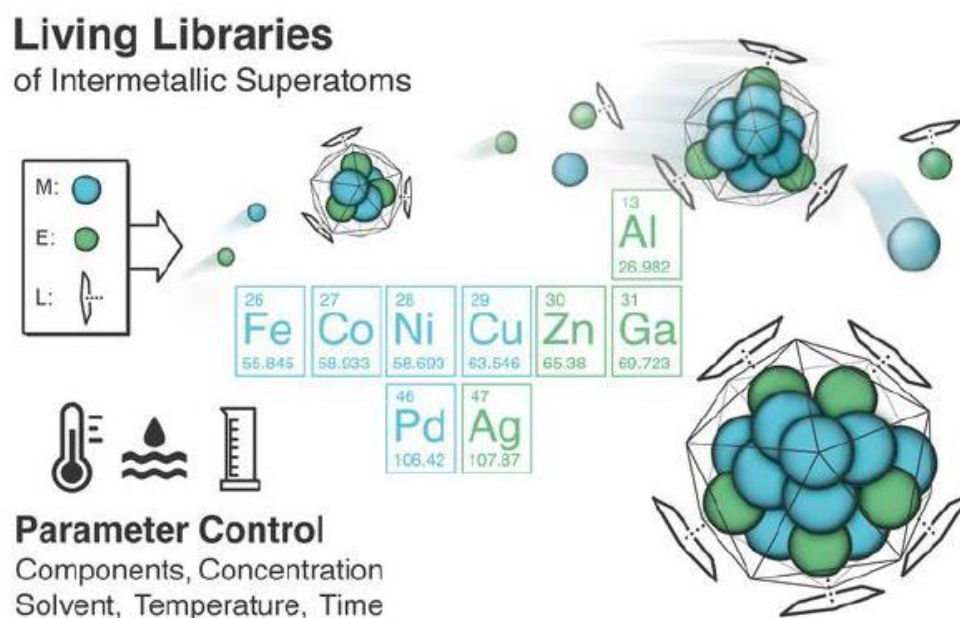
Figure 2
Living cluster libraries as highly dynamic and parameter dependent assemblies of intermetalloid Hume-Rothery superatoms (vide infra for a discussion of the superatom concept). [Graphic by Dr. Johannes Richers.]

The first part of the introduction will begin with an explanation of the chemistry of solid-state Hume-Rothery phases, as it forms the scientific basis as regards solid-state materials and the motivation for the research conception of this dissertation. In the second chapter, properties of molecular clusters will be reviewed regarding their bonding properties, structure, and reactivity. The focus of the chapter will lie on the elemental combinations used in this work (Cu, Zn, Al, Au). Despite being complex

and rather unpredictable, the synthesis of molecular clusters in solution often follows surprisingly simple concepts, like ligand replacement or co-reduction techniques. These common grounds of molecular cluster chemistry can even be extended to colloids and nanoparticles. The third chapter of the first part of the introduction will take a closer look at these correlations. Mass-spectrometric methods are widely used in biochemistry for the analysis of complex protein mixtures. In special cases, mass-spectrometry has also been used as a powerful tool in homogenous catalysis. The methodic chapter of the introduction will start with a discussion of these concepts. Working with libraries of species is also known from combinatorial chemistry, in which catalytically active complexes or enzymes are determined out of large mixtures of species by intricate testing procedures. These concepts are transferable to the reactivity assessment of cluster libraries in solution. The last chapter of the introduction will discuss methods to deal with complexity in theoretical (cluster) chemistry. Unsurprisingly, these methods will be a key strategy to make structure and reactivity proposals for organometallic cluster species detected in mass-spectrometric experiments.

1.2. The chemistry of Hume-Rothery phases

1.2.1 Structural and electronic aspects of Hume-Rothery phases CuZn/CuAl

In Hume-Rothery intermetallic phases, structural aspects are strongly determined by the so called valence electron concentration (*VEC*), leading to a rich diversity of β-, γ-, and ε-brass with VEC = 1.5 (CuZn), 1.615 (Cu_5Zn_8), and 1.75 ($CuZn_3$) (see Figure 3).[6]
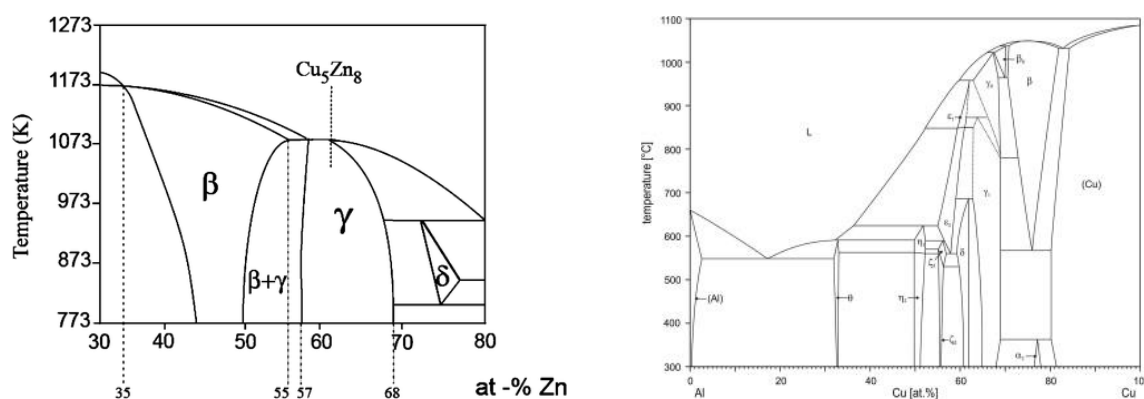
Figure 3
Left: Phase diagram of the Cu/Zn brass system.[7] Right: Rudimentary sketch of the phase diagram of the Cu/Al intermetallic system illustrating the rich structural variety of Hume-Rothery phases.[8] [Reprinted (adapted) with permission from O. Gourdon, D. Gout, D. J. Williams, et al. Inorg.

1. Introduction
1.2. The chemistry of Hume-Rothery phases

This structural diversity is only observed at Zn contents of > 40 at. %; at lower Zn contents an α-brass structure based on a regular fcc-Cu structure with incorporated Zn atoms is formed.[6] Even though the strong correlation between structure and VEC has been known for a long time, no simple intriguing chemical picture exists for their understanding.[9] The structural stabilization effect for a specific VEC stems simply spoken from an interaction between the Fermi surface (sphere with radius k_F in reciprocal space) with the first Brillouin zone. In the Jones and Mott model, a specific VEC is associated with the so called "Jones zone", a zone in reciprocal space with large structural factors for γ-brass and crossing the Fermi-surface.[7] The stabilization effect is therein achieved by interaction and distortion of the Fermi surface with the free valence electrons enclosed in the Jones zone.[7] Despite these principles being known for a long time, a detailed structural analysis including atomic positions of Cu and Zn remains challenging. Site occupancies in solid state phases are associated with specific site energies in the crystal lattice as well as with pairwise interatomic interactions (*e.g.* bond polarity between M-M´). Noteworthy, these underlying principles can well be transferred to intermetalloid clusters in terms of similar interatomic distances and geometric analogies. In the following, some structural aspects of CuZn and CuAl Hume-Rothery phases will be outlined.

The γ-brass structure consists of an inner tetrahedron of M2 = Cu atoms, embedded into a tetrahedron of M1 (= Zn) atoms, whereby M2 occupies face-capping positions (see Figure 4).[7] These two tetrahedra are surrounded by an octahedron of M3 = Zn atoms. Additionally, a distorted cuboctahedron of M4 = Cu atoms is placed above the edges of the octahedron.[7] These polyhedra adopt a bcc packing in the extended crystal structure. In an alternate description, the structure can be explained on the basis of four interpenetrated M1 = Zn centered icosahedra forming a "γ-brass" structural motif (see Figure 4, right).[7] These rather complicated features highlight the approximate "quasi-crystalline" character of the phase (five-fold symmetry axis as in icosahedral motifs is in a strict sense not compatible with a translational symmetry).[7]
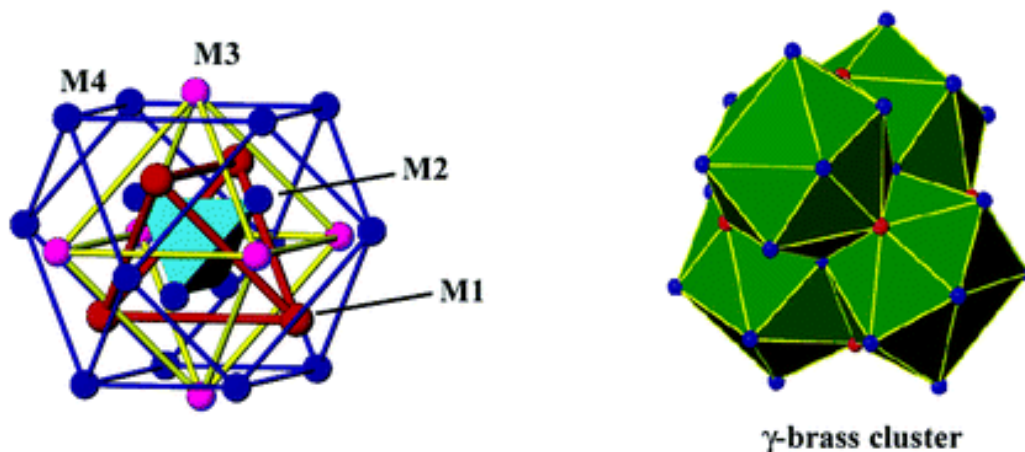
Figure 4

Left: Representation of the icosahedra occurring in the cubic γ-brass structure (Cu = red spheres, Zn = blue spheres).[7] Right: The 26-atom cluster in γ-brass forming a bcc-packing.[7] [Reprinted (adapted) with permission from O. Gourdon, D. Gout, D. J. Williams, et al. Inorg. Chem. 2007, 46, 1, 251–260. Copyright 2007 American Chemical Society.]

Likewise to the CuZn structure presented above, the CuAl system exhibits large structural variety between 27 at% and 82 at% Cu (see phase diagram, Figure 3).[8] Noteworthy, due to the complexity of the system, not all details of the phase diagram above have been uncertainly confirmed; the scetch has therefore rather to be seen as example for the immense structural variety in Hume-Rothery phases.[8] In $CuAl_2$ (θ-phase in phase diagram above), Cu atoms are incorporated into condensed, distorted square-antiprisms of Al ($[CuAl_{8/4}]$).[10] Cu_9Al_4 shows large structural analogies to the structure of γ-brass presented above including the same polyhedral units of $IT = M2$ (inner tetrahedron), $OT = M1$ (outer tetrahedron), $OH = M3$ (octahedron) and $CO = M4$ (cuboctahedron), albeit in a distorted fashion.[11] Two different element distributions within this cluster unit are found with $IT = Al / CO = Cu$ and $IT = Cu / CO = Al$. OT and OH are always occupied by Cu.[11]

1.2.2 Reactivity of Hume-Rothery phases

The generation of intermetalloid clusters composed of transition metals (TM) and group 12/13 metals (E) is a promising field of research, as the corresponding Hume-Rothery phases have been shown to be good heterogeneous catalysts, for example in the semihydrogenation of alkynes or in the production of methanol from CO/H_2 or CO_2/H_2. These two catalytic reactions occurring at solid-state Hume-Rothery phases will be exemplary discussed in the following.

1. Introduction

1.2. The chemistry of Hume-Rothery phases

The semihydrogenation of acetylene is an important industrial reaction in the production of polyethylene (removal of traces of acetylene in the ethylene feed)[12] and also a synthetic challenge in the synthesis of vitamins (*e.g.* vitamin A) and other complex organic molecules.[13-14] Currently, expensive PdAg alloys are used in an industrial scale for this reaction. However, less expensive alternatives based (partially) on non-noble metals have been identified as promising candidates. In this context, the solid state phases $Al_{13}Fe_4$ and PdGa as well as NiSn nanocrystals and intermetallic PdZn nanostructures turned out to be stable and highly selective (non-noble) metal catalyst.[12-13 15-16] The chemical properties of the catalytically active transition metal are tuned by embedding it into a framework structure of a maingroup element (see Figure 5). High catalytic selectivity is caused by geometric restraints for substrate binding resulting from the site isolation of the transition metal inside the Zn/Ga/Al matrix and by electronic effects stemming from the strongly polar TM-E bonds.[12-13]
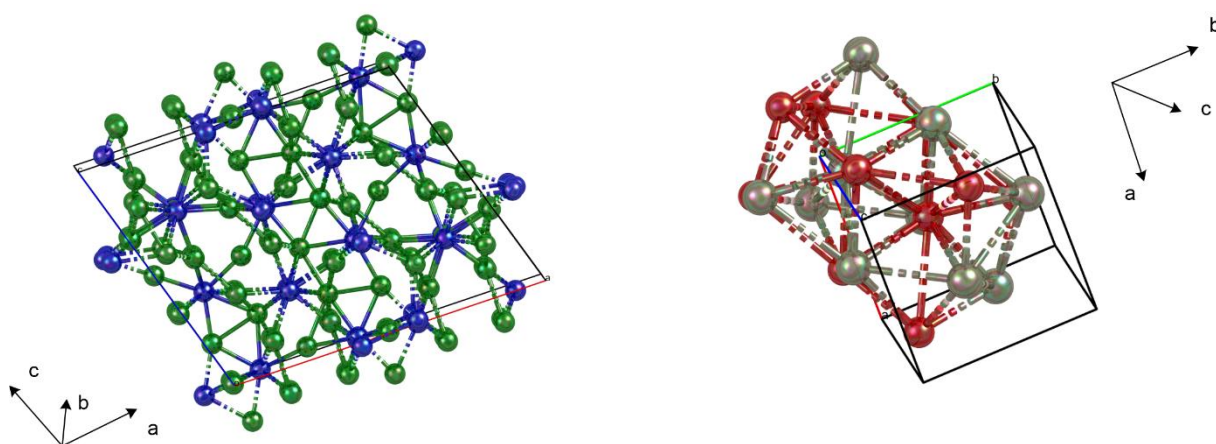
Figure 5
Crystal structures of Fe_4Al_{13} (left, Fe = blue, Al = green)[17] and PdGa (right, Pd = red, Ga = grey)[18] showing the site isolation of Fe / Pd atoms embedded into a matrix of Al / Ga. [Own graphic based on literature.[17-18]]

Intermetallic phases of Cu and Zn have not only been important metallurgic materials since ancient times but also their bimetallic chemistry has gained industrial and scientific interest in terms of medical, (opto-)electronic and catalytic purposes.[19-21] The latter ones include methanol production, water-gas shift reaction, methanol steam reforming and hydrogenation reactions.[21] Commercially, methanol production is performed from synthesis gas (H_2/CO) over Cu/ZnO/Al_2O_3 with a world production capacity of more than 28 million tons per year. Despite the enormous success of this process, mechanistic details of the catalyzed reaction are still hardly understood. Especially the role and nature of the catalytically active center(s) are heavily under debate in surface science. The "brass" alloy CuZn was also shown to be an active catalyst in this process, as it is oxidized to Cu/ZnO under catalytic conditions, reaching comparable activity to ZnO/Cu catalysts with the same Zn

coverage.[22] The catalytic efficiency is understood by a sophisticated interplay between Cu and Zn/ZnO centers. Whereas Cu easily adsorbs and cleaves hydrogen, O* species are stabilized by ZnO during the CO/CO_2 hydrogenation reaction.[22-23] In detail, active sites consist mainly of defect-like surface structures, *e.g.* Cu steps, kinks, edges and stacking faults (*vide supra*).[24] Further, the manner of decoration of Cu with ZnO seems important for catalytic activity, as enrichment of ZnO at the surface in terms of a core-shell system is profitable for catalytic activity.[24]

These findings from heterogenous surface science are encouraging for the conceptual idea of using molecular clusters (or nanoparticles) as precise models for the locally defined active centers of heterogenous catalyst surfaces. Several studies were made for Cu and CuZn nanoparticles and colloids in solution and in some cases their activity for methanol production was tested.[21, 25-27] For example, β-brass CuZn nanoparticles in ionic liquids were shown to be active catalysts in methanol production.[27] Most interestingly, Zn- free Cu nanoparticles were also proven to be active in methanol production by *Schüth. et. al.*[28]

1.3. Properties of molecular clusters

1.3.1 Electronic properties of molecular clusters

The investigation of the electronic structure of clusters in the gas phase or in solution has gained considerable interest in many theoretical groups and hence a comprehensive description will be out of the frame of this work. As the electronic structure of clusters however forms the basis for any *stability and reactivity* assessment, some theoretical concepts for understanding electronic building principles for (intermetallic) clusters will be given within this paragraph.

The most straight-forward concept for understanding of (inorganic) cluster compounds is applied in cases, in which every atom obeys the 8 valence electron rule (for main group clusters) or the 18 valence electron rule (for transition metal clusters). In these cases, the number of bonds E in the cluster is given by the following equations:[29]

$$E = \frac{8n - N_e}{2} \quad \textit{for main group clusters} \quad (1.1)$$

$$E = \frac{18n - N_e}{2} \quad \textit{for transition metal clusters} \quad (1.2)$$

with n being the number of vertices in the cluster and N_e being the number valence electrons. This concept can be applied for *Zintl* clusters such as NaSi, forming $[Si_4]^{4-}$ tetrahedra, in which every Si atom obeys the 8-electron rule.[30] Another example are carbonyl clusters such as $[Ir_4](CO)_{12}$, forming an Ir tetrahedron, in which every Ir atom obeys the 18 valence electron rule (see Figure 6).[31]

The underlying difficulty in assessing electronic structure of more complicated clusters arises from the fact that many clusters cannot be properly described by classical two-center, two-electron bonds, because the connectivity of the vertices exceeds the number of valence electrons available for bonding.[29] Several approaches exist for understanding of these – at a first sight – "electron deficient" clusters, such as $[B_6H_6]^{2-}$. In the *Wade-Mingos* concept, a B-H or a $M(CO)_3$ fragment is associated with three orbitals available for skeletal cluster bonding (see Figure 6). Thereby, a *closo*-deltahedral cluster (a cluster exhibiting entirely triangular faces) is found to necessarily have the following number of valence electrons N_e:[29]

$$N_e = 4n + 2 \text{ for main group clusters (1.3)}$$

$$N_e = 14n + 2 \text{ for transition metal clusters (1.4)}$$

In the *Wade-Mingos* concept, this number of required valence electrons does not change when removing successively vertices from the cluster resulting in *nido, arachno* or *hypho* clusters.[29] The *Wade-Mingos* rules have turned out to be a powerful tool for an empirical structure prediction based on relatively simple electron counting rules.

In a more detailed analysis of electronic structure, the n+1 bonding skeletal electron pairs in *closo*-clusters are obtained by *linear combination of atomic/frontier orbitals* (LCAO). The bonding orbitals can thereafter be identified as the S^σ (s-type cluster orbital obtained by combination of atomic σ-orbitals) and the three $P^{\sigma/\pi}$ cluster orbitals.[29] The $P^{\sigma/\pi}$ cluster orbitals are therein obtained by mixing of P^σ (p-type cluster orbital obtained by combination of σ-orbitals) and P^π (p-type cluster orbital obtained by combination of π-orbitals) orbitals. In rather simple systems, atomic orbitals can serve as a basis set for construction of the cluster orbitals. This is the case *e.g.* for alkali clusters such as Li_6, in which the Li 1s orbitals are used as basis functions.[29] In more complicated cases, the frontier orbitals of the cluster vertices are considered, such as sp_z hybrids of BH functionalities in $B_6H_6^{2-}$ (see Figure 6).[29]

1. Introduction
1.3. Properties of molecular clusters

a)

8 VE Zintl cluster

18 VE cluster

b)

closo-Wade cluster (14 VE)

closo-Wade cluster (2 VE) with d-electron contributions

c)

open-shell superatom (39 VE)

closed-shell superatom (40 VE)
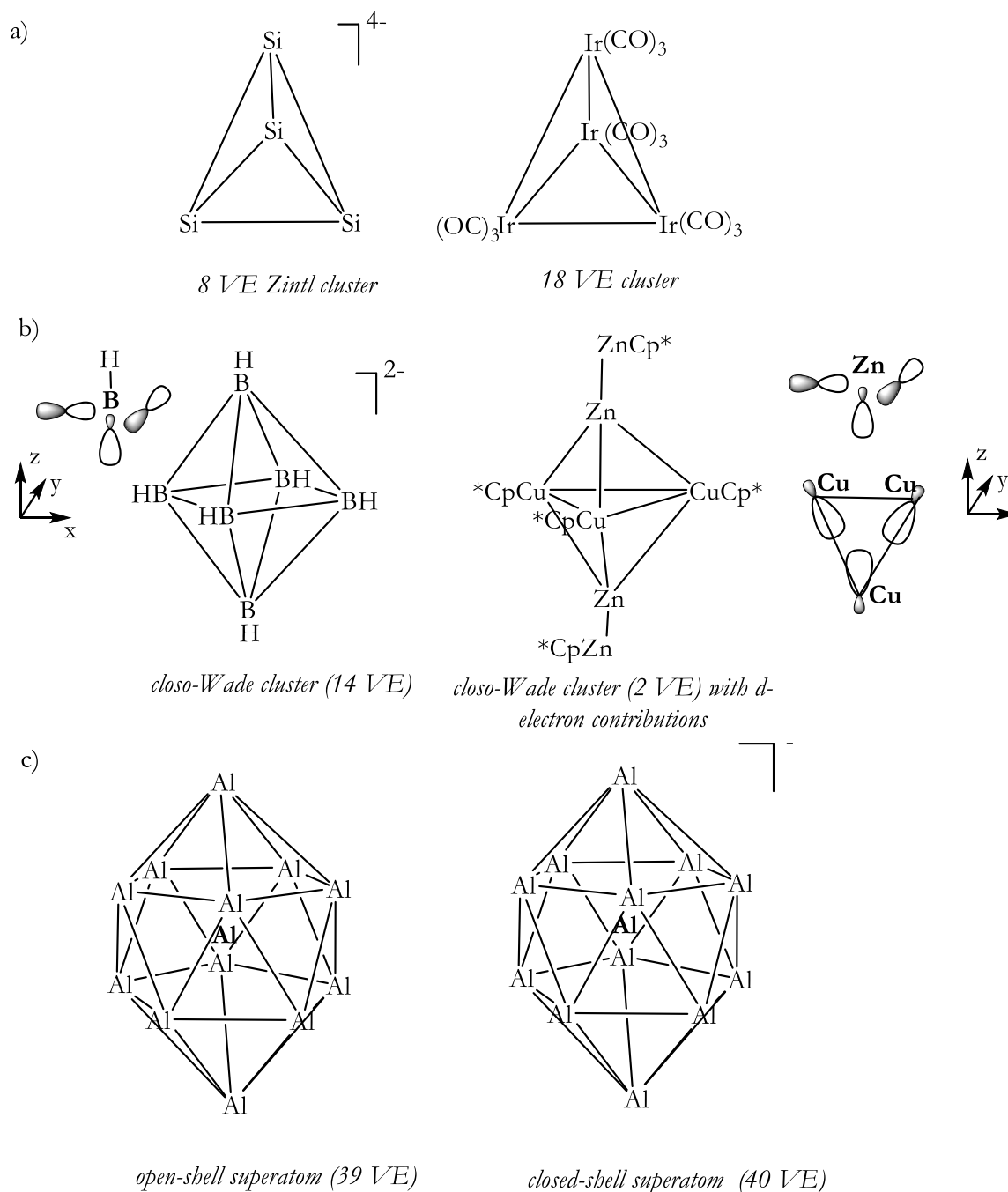
Figure 6

Different approaches for electronic structure rationalization in metal clusters. a) 8 / 18 valence electron clusters. Every bond is associated with two cluster electrons. b) "Electron-deficient" clusters and Wade-Mingos concept. In $[B_6H_6]^{2-}$ every atom contributes 3 skeletal orbitals to cluster bonding (see sketch on the left: One sp_z hybrid and two p orbitals). In $[Cu_3Zn_4](Cp^*)_5$, the Wade-electron count is fulfilled if Cu 3d / 4s / 4p orbitals are considered to contribute to cluster bonding (see right sight for an exemplary sketch of the skeletal orbitals of one Zn atom and of one skeletal orbital of the $[Cu_3Cp^*_3]$ fragment. c) The superatom concept allows for rationalization of reactivity patterns. Closed-shell systems are rather inert, whereas their open-shell analogues are considered to be highly reactive. [Own figure.]

1. Introduction
1.3. Properties of molecular clusters

Another model for rationalization of electronic properties of (spherical) metal clusters is the so-called *Jellium* model and *superatom* concept.[29, 32] Originally developed for the explanation of "magic numbers" (*i.e.* specific extraordinary stable and abundant cluster sizes) occurring in molecular beams of alkali metal clusters (UHV experiments), it allows for an heuristic and empirical estimation of stability and reactivity patterns also of ligated metallic clusters by comparing their chemistry with that of single atoms/elements.[32] In the Jellium model, the cluster is considered to be built in a simplified view from a *valence electron subsystem* and a *core electron subsystem*.[32] The smeared out electron density is treated in the potential energy function created by the overall positively charged core systems. For a spherical system, this leads to electronic wavefunctions written as a product of spherical harmonics with energy levels depending only on the distance from a fixed origin.[32] As a result, the same degeneracies result as for an atom and the stabilities of specific cluster sizes can directly be related to the valence electron count. The order of the resulting electronic states in the *superatomic* description deviates however from the order observed for simple atoms and is described as follows (see Figure 7 for illustration of the Jellium model and the superatom concept):[33-34]

$$1S^2 \mid 1P^6 \mid 1D^{10} \mid 2S^2 \ 1F^{14} \mid 2P^6 \ 1G^{18} \mid 2D^{10} \ 3S^2 \ 1H^{22} \mid 2F^{14} \ 3P^6 \ 1I^{26} \mid \dots$$

This deviation can be explained by the fact that in the superatom, the positive (background) charge is distributed all over the cluster sphere, whereas in a single atom, the positive charge is centered at the nucleus.[33] The above described electronic configurations correspond to shell-closures and the stability of clusters with such an electron count is therefore analogous to the 8 valence electron or the 18 valence electron rule for main group and transition metal atoms, respectively.[33]
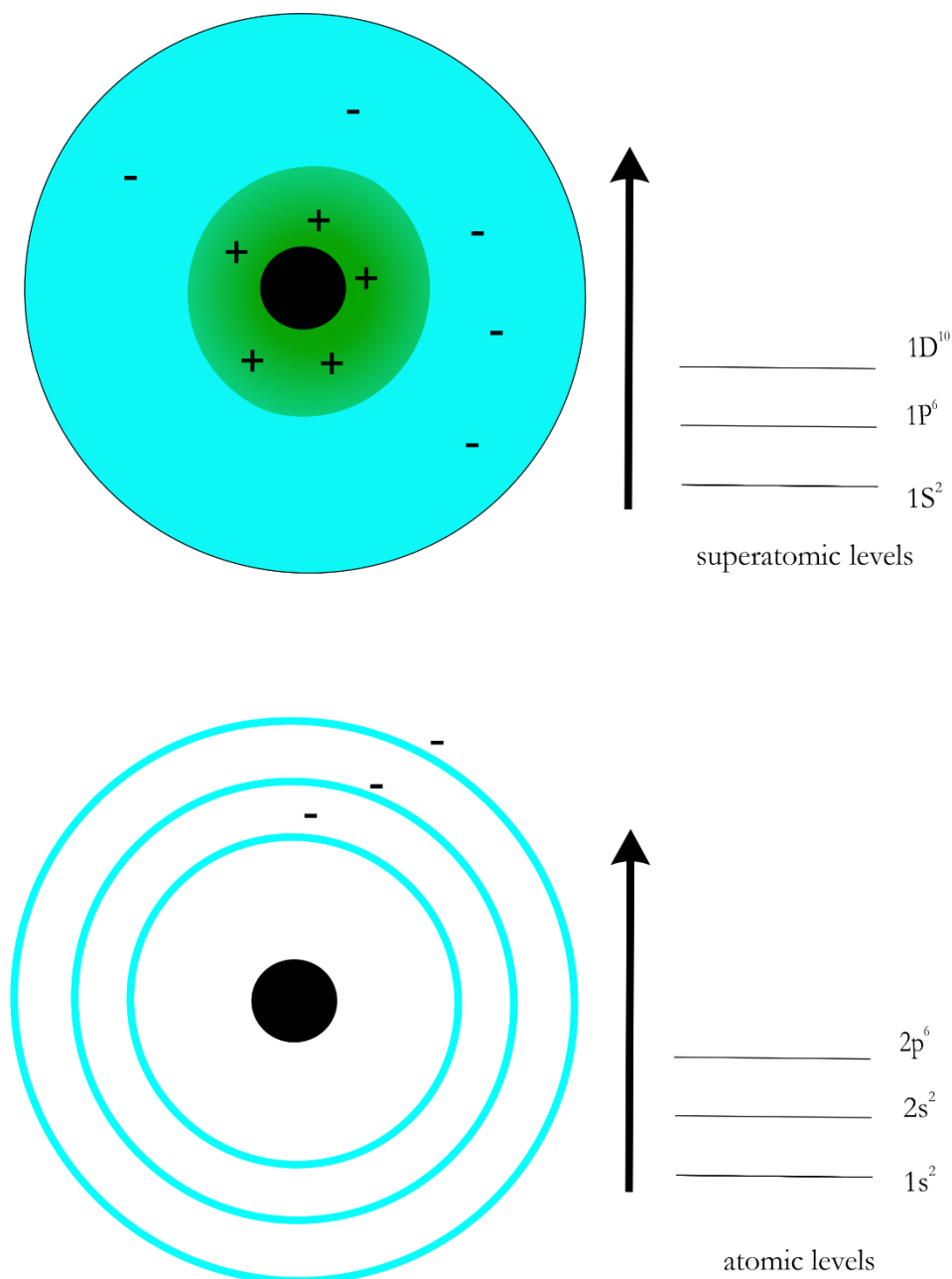
Figure 7
Simplified visualization of the superatom concept and the Jellium model. Bottom: Very simplified model of an atom and of atomic orbitals with the positive charge fixed at the atomic nucleus (dark point). Top: Jellium model of a cluster with a "frozen core" of overall positive charge consisting of core electrons (green) and atomic nuclei (dark). The valence electrons are considered as free electrons and treated in the potential of the positive core leading to superatomic orbitals very similar to those of a single atom. [Own figure based on literature.[32]]

Noteworthy, for small and spherical clusters (*e.g.* alkali metal clusters), the superatomic description is mostly consistent with molecular orbital / *LCAO* considerations. This is due to fact that in these systems treatment of the s-electrons as free electrons works well. In clusters containing p- or d-block elements, the *Jellium*

model has to be applied with care due to a) deviations from spherical symmetry leading to splitting of energy levels and b) the involvement of "non-spherical" (tensor-like) p- and d-orbitals contributing to skeletal bonding.[29, 32] However, even for these complicated systems and those discussed in this work, the superatom concept may present a fruitful and understandable model for stability and reactivity assessment. Even though the bonding situation in large intermetalloid clusters has to be analyzed case-to-case by frontier orbital analysis and DFT calculations, the results obtained thereafter might still be interpreted by the superatom concept.

An idea arising from the superatom concept is the construction of "third dimension of the periodic table", in which clusters represent a 3D-counterpart of the corresponding elements in the classical 2D periodic table.[32] By this "projection" of cluster chemistry to the chemistry of the elements, reactivity patterns would be easier to assess and at least partial rationalization of the complex world of cluster (growth) reactions might be achievable. However, due to the restrictions of the model pointed out above, this idea seems rather visionary and idealistic. Nevertheless, some concepts have well been applied. For example, the open-shell cluster Al_{13} (mimicking a halogen atom) exhibits a strong reactivity to oxygen and iodine; its closed-shell, "magic-number" congener Al_{13}^- proved to be inert.[32-33]

1.3.2 Structural aspects of molecular clusters in solution

Parts of the following discussion were submitted as a review article in the journal Chemical Society Reviews. [Reproduced (adapted) from M. Schütz, C. Gemel, W. Klein, R. A. Fischer, T. F. Fässler, Intermetallic phases meet intermetalloid clusters. Chem. Soc. Rev., 2021, 50, 8496-8510 with permission from the Royal Society of Chemistry. Copyright 2021. Published by the Royal Society of Chemistry. Link: https://pubs.rsc.org/en/content/articlelanding/2021/cs/d1cs00286d.]

1.3.2.1 Ligand stabilized clusters of Cu

With regard to ligand stabilized Cu clusters one has to differentiate between clusters with partial Cu(0) character and those featuring only Cu(I) or Cu(II) centers. Whereas for the latter many examples exist, preparation of the former remains a challenging task due to the relatively low Cu(I)/Cu(0) reduction potential (0.52 V).[35] For Cu nanoclusters with metallic Cu(0) character, only a limited number of well-characterized species have been reported. These include alkyne stabilized species such as $[Cu_{20}](CCPh)_{12}(OAc)_6$[36], $\{[Cu_{13}](S_2CN^nBu_2)_6(acetylide)_4\}[PF_6]$[37] or the large $[Cu_{53}]$ clusters $\{[H_{18}Cu_{53}](RCOO)_{10}(C{\equiv}C^tBu)_{20}Cl_2\}^+$[38] and $\{[Cu_{53}](C{\equiv}CPhPh)_9(dppp)_6Cl_3(NO_3)_9\}$[39] as well as its derivatives (dppp = 1,3-

bis(diphenylphosphino)propane). The latter feature an unusual structure with ABABC stacking motifs, which can be interpreted as a hybrid of fcc (face centered cubic) and hcp (hexagonal close packing) packing. Notably, non-fcc structures of Cu are otherwise only known from metal-vapor deposition techniques, electrodeposition or high-pressure induced phase transformations.[39]

A plethora of well-defined Cu(I) hydride clusters are known, usually stabilized by phosphane or thiolate ligands. They are typically accessible by wet-chemical reduction of Cu(I) salts with silanes, thiols, or boron hydrides. Besides Cu hydride clusters with pure Cu(I) character, there exist several species with mixed Cu(I) / Cu(0) valencies, such as $[H_{22}Cu_{25}](PPh_3)_{12}Cl$[40], $[H_{18}Cu_{30}]\{S_2P(OnPr)_2\}_{12}$[41] or $[H_{20}Cu_{32}](S_2P(O^iPr)_2)_{12}$[42], whereby the latter exhibits the largest number of hydrides in a molecular cluster as determined by neutron diffraction. Notably, also the highest-nuclearity Cu nanocluster reported so far, namely the large $\{[H_{32}Cu_{81}](PhS)_{46}(^tBuNH_2)^{10}\}^{3+}$ cluster also falls in this class (see Figure 9 for its structure).[43] Structural motifs in Cu hydride clusters include icosahedral cores capped by $[Cu_3]$ triangles, as illustrated in Figure 8 a) for $[H_{18}Cu_{30}]\{S_2P(OnPr)_2\}_{12}$[41]. Whereas such icosahedral motifs are common for coinage metal clusters, a unique situation was found in $[H_8Cu_{32}](PEt)_{24}(Cl)_2(PPh_4)_2$[44] (PEt = 2-phenylethanethiolate). The cluster consists of a $[Cu_{14}H_8]$ central core assembled from two square $[Cu_8]$ antiprisms (see Figure 8 b)). Hydrides occupy μ^4 and μ^3 bridging positions inside the core. The core is surrounded by two triangular $[Cu_2(PEt)]$ motifs, as well as two crown-like $[Cu_7(PEt)_{11}Cl]$ motifs. Inside these ligand motifs, no direct Cu-Cu bond is found, rather PEt ligands occupy bridging positions between two Cu centers. The ligand motifs are linked with the core by thiolate bridges, bridging hydrides, as well as direct Cu-Cu bonds.

Splitting up cluster structures into a central core unit surrounded by cuprate or aurate ligand shells is a general helpful tool for structural analysis of large Cu and Au clusters. The large $[H_{32}Cu_{81}](PhS)_{46}(^tBuNH_2)_{10}^{3+}$ cluster for example exhibits a planar $[Cu_{17}]$ unit embedded into a shell structure with $[Cu(SPh)_2]$ staple motifs (see Figure 9). This structural building principle is also known for large, ligand protected Au clusters (*vide infra*).[43]

Recently, a hydride and halogen free cluster $[Cu_{14}](C_2B_{10}H_{10}S_2)_6(CH_3CN)_8$ was synthesized by reaction of Cu triflate with carboranedithiole.[45] As side product, a disulfide coupling product was identified. In any case, isolation and characterization of specific species is a complicated task and suitable reaction conditions are hardly to predict.[40] The choice and dosage of reducing agent is therein of crucial importance: Whereas too low amounts of reducing agent decrease the chance of obtaining clusters with Cu(0) character, high excess of reducing agents often results in ill-

defined mixtures of cluster species.[45-46] Use of hydride containing reducing agents such as silanes or $NaBH_4$ also usually leads to generation of Cu clusters bearing different amounts of hydride ligands with the difficulty to localize them by standard crystallographic techniques.[45]

a)   b)
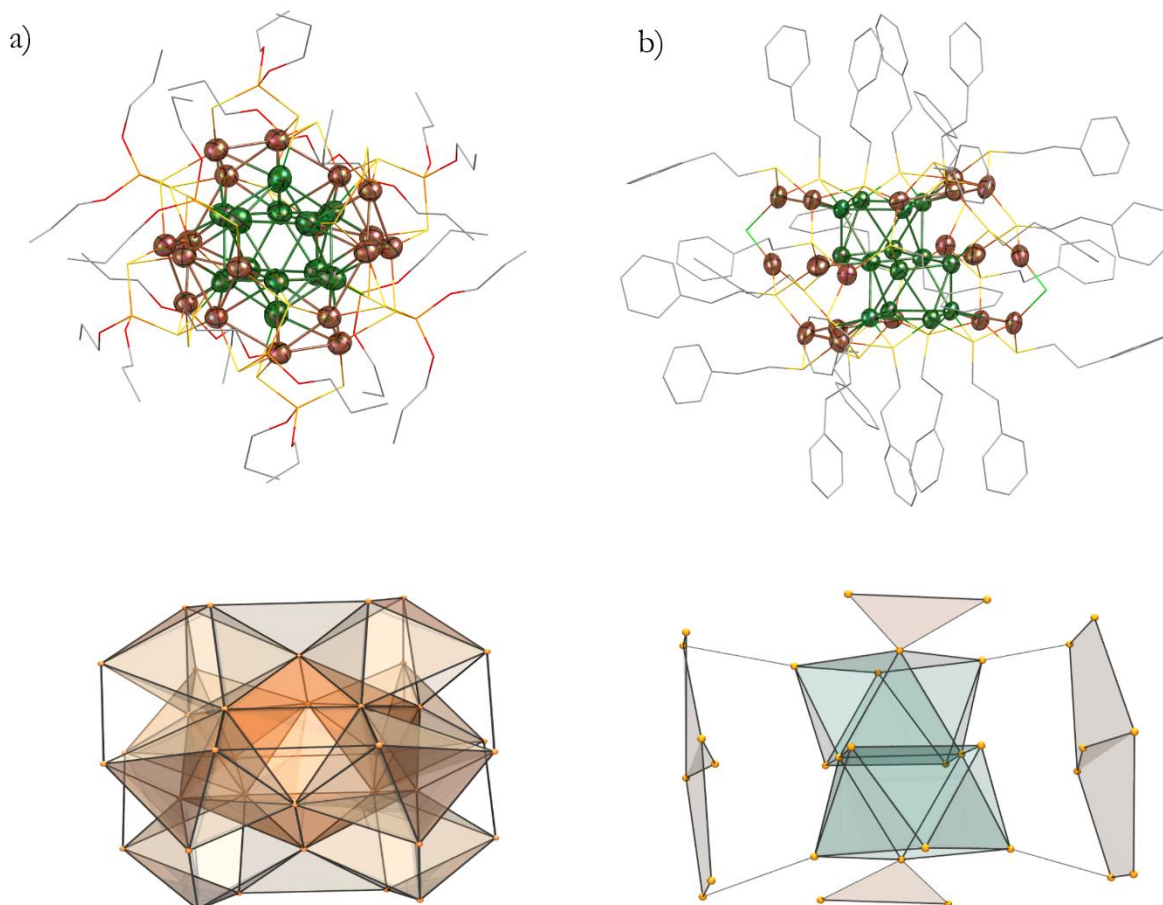
Figure 8

Top: Molecular structures as determined by SC-XRD of two ligand-protected, medium-size Cu clusters with partial Cu(0) character . Organic ligands are drawn as wireframes. Hydrogen atoms and counterions are omitted for clarity. Color code: Cu = orange, green, S = yellow, P = light orange, Cl = light green, O = red, C = grey. Hydrogen atoms and counterions are omitted for clarity. Bottom: Schematic visualization of polyhedral motifs in both clusters. a) $[H_{18}Cu_{30}]\{S_2P(OnPr)_2\}_{12}$[41] with icosahedral core motif. b) $[H_8Cu_{32}](PEt)_{24}Cl_2(PPh_4)_2$[44] with antiprismatic, box-light $[Cu_{14}]$ core. Notably, no direct Cu-Cu bonding is present in the ligand motifs. [Own figure based on literature.[41, 44]]

Due to the difficulties in isolation and characterization of well-defined products, the physicochemical properties of polydisperse assemblies of mixed-valent Cu clusters has been a topic of research in several groups. Electrochemical reduction of Cu ions

in the presence of *tert*-butyl ammonium nitrate led to a plethora of species [Cu$_N$] with N = 2-5 and 11-14, respectively, as identified by LDA-TOF mass spectrometry.[47] The clusters consisting of Cu(I), Cu(0) and surface bound Cu(II) are usable as building blocks with potential applications in sensors or biomedicine.[47] In contrast to the heavier congeners Ag and Au, even the preparation of small, multi-disperse [Cu$_N$] clusters is often difficult due to unwanted agglomeration. Using 2-mercapto-5-n-propylpyrimidine as protecting agent, [Cu$_N$] clusters with N<8 were synthesized by a wet-chemical reduction method in protic solvent.[48] It is of note that for such small Cu clusters, mass spectrometry (ESI-MS in particular) turned out to be a valuable method for analysis of cluster size distribution.[48] Thus obtained sub-nanometer sized Cu clusters were shown to exhibit interesting luminescent and catalytic properties.[48] Similar small-size cluster distributions were obtained by conducting the wet-chemical reduction in microemulsions.[46]
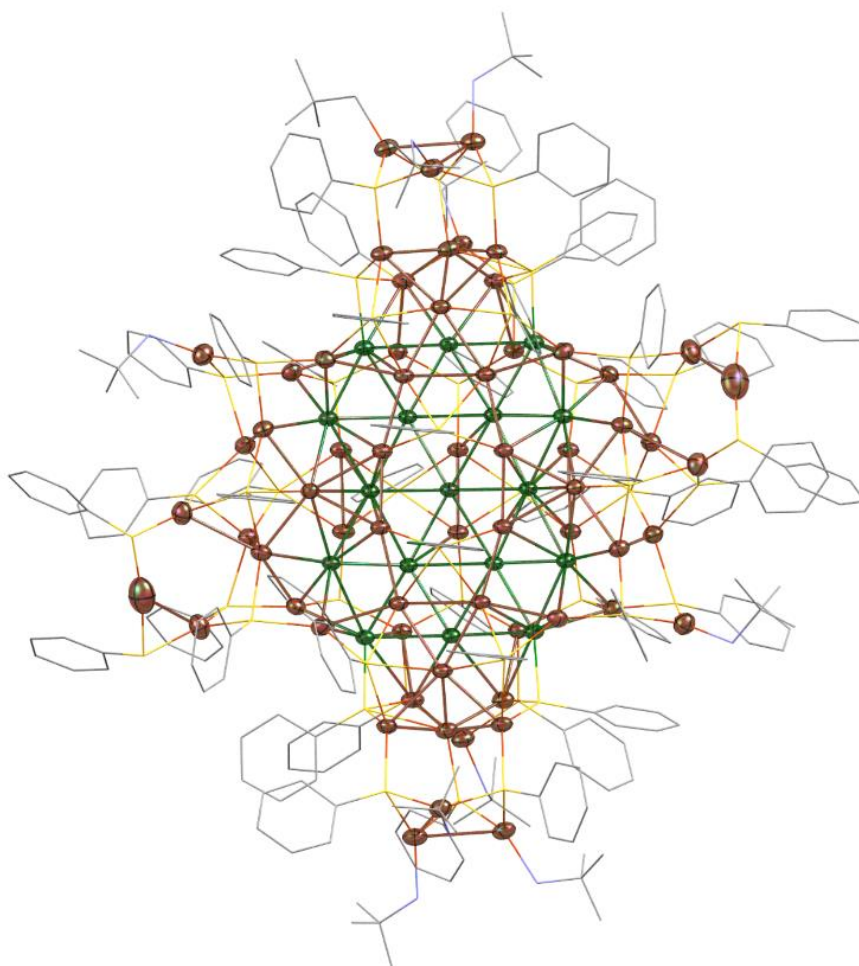
Figure 9
Molecular structure of $\{[H_{32}Cu_{81}](PhS)_{46}(^tBuNH_2)_{10}\}^{3+}$ as determined by SC-XRD highlighting the planar [Cu$_{17}$] core in green.[43] Organic ligands are drawn as wireframes. Hydrogen atoms and counterions are omitted for clarity. Color code: Cu = orange, green, S = yellow, N = light blue, C = grey. Hydrogen atoms and counterions are omitted for clarity. [Own figure based on literature.[43]]

1.3.2.2 Ligand stabilized clusters of Au

Larger Au nanoparticles are known since ancient times and have been used for example to color glass (ruby glass).[49] Au colloids were for the first time systematically investigated by Michael Faraday in the 19th century. However, all these nanoparticles (> 1nm) lacked a defined and precise structure, rather a broad size distribution was observed. The discovery of the famous $[Au_{55}](PPh_3)_{12}Cl_6$ cluster by *Schmidt. et al.* was therefore clearly a research highlight in cluster science in terms of its size (1.4 nm), its monodispersity and its geometric and electronic shell-closure.[49-50] Besides this prominent example, a plethora of ligand (thiolates, phosphines) protected Au clusters has been discovered over the years and only an exemplary selection will be presented in the following. The synthesis of molecular Au clusters mainly involves partial reduction of Au(I)-L (L= thiolate, phosphine) complexes (simply available by mixing $HAuCl_4$ and thiol ligands) with $NaBH_4$, B_2H_6 or related boranes/boronhydrides (*Brust-Schiffrin* method).[49, 51]

In these reactions, cluster sizes are determined by a complicated interplay of *fast reduction reactions* (leading to agglomeration and cluster growth) and *core-etching reactions* by residual Au(I)-SR or thiolate ligands.[51] Size-focusing towards $[Au_{25}]$ nanoclusters was possible by balancing cluster growth and etching reaction by addition of NaOH to the reaction mixture and therefore increasing the amount of free thiolate.[52] Understanding of the growth mechanism was possible by using CO as a soft reducing agent and monitoring the time-course of the reaction by ESI-MS and UV-Vis analysis.[53] The reaction products were classified into 0e- complex precursors (homoleptic and heteroleptic $[Au_n](SR)_n$ and $\{[Au_n](SR)_{n-p}Cl_{n+p}\}^-$, respectively), the 8e- $\{[Au_{25}](SR)_{18}\}^-$ product, as well as into 2e- (*e.g.* $[Au_{11}](SR)_9$), 4e- (*e.g.* $\{[Au_{15}](SR)_{12}\}^-$) and 6e- (*e.g.* $[Au_{19}](SR)_{13}$) intermediate clusters. This order implies a stepwise 2e- reduction mechanism for cluster growth. In the final size-focusing process, a series of $[Au_n]$ clusters with various sizes n evolve into monodisperse $\{[Au_{25}](SR)_{18}\}^-$ by a sequence of isoelectronic addition, disproportionation and comproportionation reactions.[53] The example highlights the complexity of cluster formation processes occurring even in relatively simple synthetic protocols. However, mechanistic aspects can be revealed by complementary analytical techniques (UV-Vis, ESI-MS) and the extension of this concept to more sensitive systems (air, moisture) seems to be very prospective.

Isolation of several $[Au_N]$ nanoclusters with N<39 protected by glutathione was possible by sophisticated separation techniques (gel-electrophoresis, liquid chromatography) from complex reaction solutions.[54] It is of note that for many of the ligand protected Au clusters, structural information of SC-XRD is not readily

available, but fragmentation pattern in mass-spectrometry, DFT calculations and microscopic techniques (TEM) are used to provide structural insights.

a)

b)
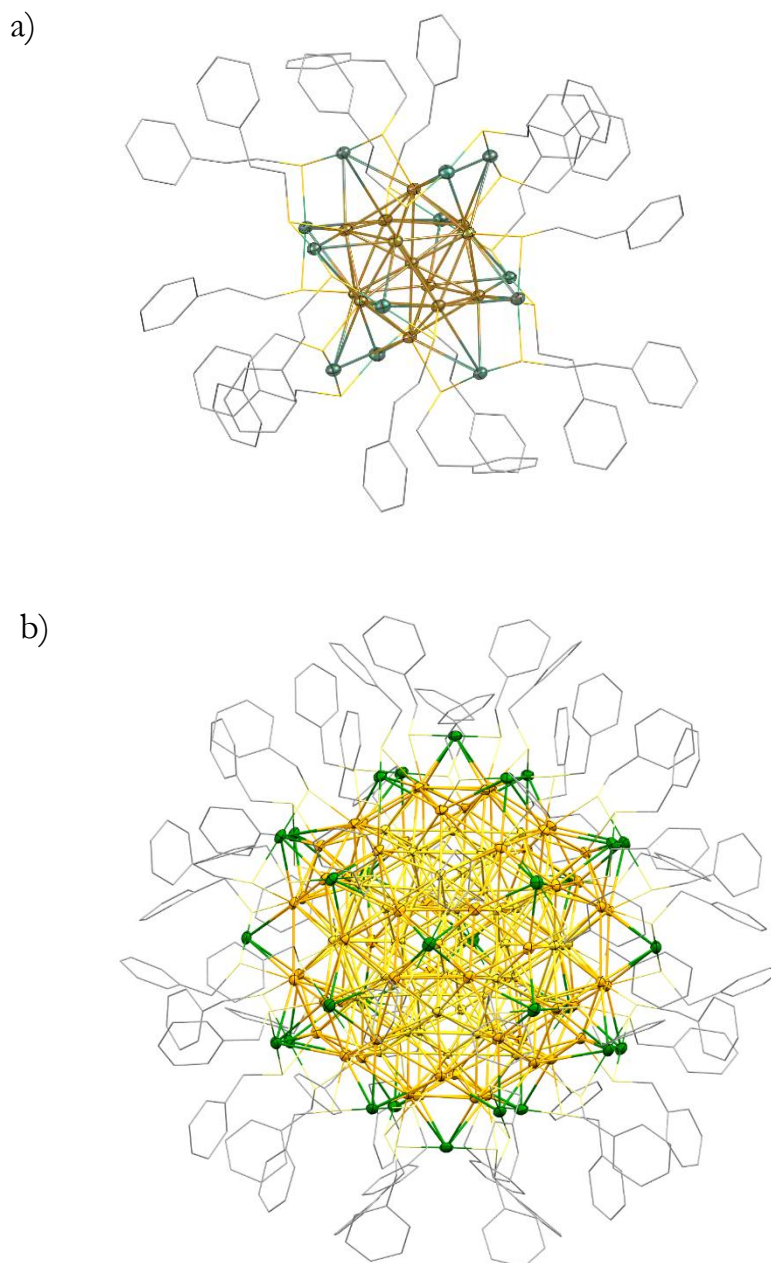
Figure 10
a) Molecular structure of {[Au₂₅](SCH₂CH₂Ph)₁₈}⁻ in the solid state as determined by SC-XRD.[55] Organic ligands are drawn as wireframes. Hydrogen atoms and counterions are omitted for clarity. Color code: Au = orange, green, S = yellow, C = grey. Hydrogen atoms and counterions are omitted for clarity. The picture illustrates the body-centered icosahedral [Au₁₃] core (orange) surrounded by 12 [Au(PEt₂)] staple motifs (green color for Au). b) Molecular structure of [Au₁₄₄](SCH₂Ph)₆₀ in the solid-state as determined by SC-XRD. Organic ligands are drawn as wireframes. Hydrogen atoms are omitted for clarity. Color code: Au = green, orange, yellow. S = light yellow, C = grey. The picture illustrates the [Au₅₅] Mackay-type cluster core (yellow Au atoms), surrounded by a rhombicosidodecahedral shell of 60 Au atoms

(orange). The ball-like structure is additionally surrounded by 30 [Au(SCH₂Ph)₂] staple motifs.
[Own figure based on literature.[55-56]]

In $[Au_{18}](SR)_{14}$ (R = cyclohexyl), a $[Au_9]$ core consisting out of two fused Au_6 units is embedded into a shell of three monomeric $Au(SR)_2$, one dimeric $[Au_2(SR)_3]$ and one tetrameric $[Au_4(SR)_5]$ unit. The structure of $[TOA]^+\{[Au_{25}](SCH_2CH_2Ph)_{18}\}^-$ (TOA = trioctylammonium) consists of a body-centered Au_{12} icosahedron, which is embedded into six orthogonal $[Au_2(SCH_2CH_2Ph)_3]$ "staples" (see Figure 10 a)).[55] Similar $[Au_x(SR)_{x+1}]$ staple units were found in many other crystallographically investigated Au clusters.[57-59] For example, in $[Au_{30}]S(S'Bu)_{18}$, a rod-like Au_{22} core is surrounded by thiolate ligands, a μ_3-S^{2-} unit and monomeric and trimeric Au-thiolate staples.[60] The $[Au_{22}]$ core is best described as superposition of two fused $[Au_{13}]$ cuboctahedrons, highlighting the analogy of molecular Au clusters to the fcc packing of bulk Au and Cu. The crystal structure of the very large $[Au_{102}](p-MBA)_{44}$ (p-MBA= para-mercaptobenzoicacid) may be described as a 49 atom *Marks* decahedron core embedded into two Au_{20} caps at the "poles" of the cluster and a Au_{13} equatorial ring.[61] Again, the structure exhibits multiple analogies to fcc packing motifs. Likewise, the crystal structure of $[Au_{144}](SCH_2Ph)_{60}$ consists of a *Mackay* type $[Au_{55}]$ polyhedron (composed of a $[Au_{12}]$ icosahedron embedded into a $[Au_{42}]$ shell) enclosed into a rhombicosidodecahedron shell of 60 Au atoms. The resulting ball like structure is surrounded by 30 [RS-Au-SR] units.[56] The structure is shown in Figure 10 b).

1.3.2.3 Ligand stabilized clusters of Al

In contrast to clusters of the noble metals (*e.g.* Pd, Au), clusters and even compounds with direct metal-metal bonds consisting of main group metals were rather unknown until the end of the 20th century.[62-63] The first Al-Al bond was reported in 1988 in form of tetrakis[bis(trimethylsilyl)methyl]dialan $[Al_2](CH(SiMe_3)_2)_2$, followed by several other small molecules involving direct Al-Al bonding, usually prepared by rather simple reduction and dehalogenation protocols.[62, 64] A central point in the „renaissance of the main group chemistry"[65] was the discovery of the giant $[Al_{77}]$ cluster stabilized by 20 $N(SiMe_3)_2$ ligands by *Schöckel et al.*.[66] Despite the unique structure of this compound, its synthesis protocol underlines general principles and mechanisms for the growth of clusters as intermediates on the way to the bulk metal.[67] It starts with the generation of metastable Al-X solutions prepared by „preparative cocondensation" of Al metal with gaseous HCl:

1. Introduction
1.3. Properties of molecular clusters

$$Al_{(l)} + HCl_{(g)} \underset{10^{-1}\ \text{mbar}}{\overset{1000\ °C}{\rightleftharpoons}} 1/2\ H_2 + 3AlCl_{(g)}$$
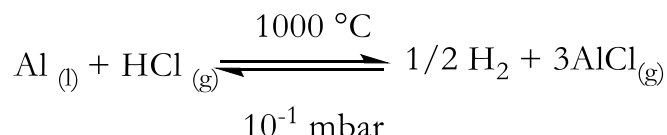
Scheme 1
Preparation of AlCl by cocondensation of Al metal with HCl.[63]

Al-Cl is isolated in a matrix of frozen solvent (*e.g.* toluene) at the cooled wall of the reaction vessel. These meta-stable solutions undergo disproportionation reactions upon warming to more than -78 °C according to the following equation:[66]

$$2\ Al_{(l)} + AlCl_{3\,(g)} \underset{10^{-2}\ \text{mbar}}{\overset{1000\ °C}{\rightleftharpoons}} 3\ AlCl_{(g)}$$
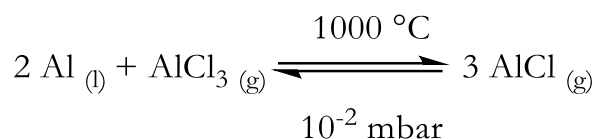
Scheme 2
Equilibrium between AlCl, Al and AlCl₃.[63] Metastable AlCl isolated in a frozen solvent matrix undergoes disproportionation upon warming to room-temperature.

On the way to the bulk metal Al, cluster species may be obtained as intermediates by addition of donor components or ligands (NEt₃, N(SiMe₃)₂, MgCp*₂, Et₂O, THF). Interestingly, the reaction sequence can be understood by the general concept illustrated in Scheme 5, page 41 (disproportionation of M^2-R^2 (AlCl) leading to cluster species $[M^2_n](R1)_x$ (R1 = donor molecule; n > x for intermetalloid clusters) and AlCl₃). The direct outcome of such reactions, however, usually remains unpredictable and isolation of any product requires sophisticated parameter control and intricate work-up procedures such as fractional crystallization. Also, the choice of the stabilizing ligand is crucial: During the warm-up process, substitution reactions (AlCl + LiL -> Al-L + LiX) compete with the disproportionation reaction (AlCl -> AlCl₃ + Al). In this regard, basically two different ligands turned out to be appropriate, namely Cp* (C₁₀H₁₅) and btsa (= N(SiMe₃)₂) and the obtained reaction outcomes will be discussed in the following.

Substitution of halogen with Cp* is thermodynamically favored over disproportionation at low temperatures (-78 °C). This led to isolation of the textbook Al(I) molecule [Al₄](Cp*)₄, which remarked a starting point for a rich transition metal – Al coordination and cluster chemistry, which forms also the basis for this work (for simplicity, AlCp* will be written instead of [Al₄](Cp*)₄ in the following).[68-69] However, when solutions of MgCp*₂ and AlBr are shortly warmed to room-temperature, the large cluster [Al₅₀](Cp*)₁₂ is isolated after complicated separation from side-products.[70] The structure of [Al₅₀](Cp*)₁₂ can be described in three shells

(see Figure 11 b)).[70] The outer shell consists of 12 AlCp* units in an icosahedral arrangement. The innermost shell is formed by an $[Al_8]$ square-based anti-prism. Between the inner and the outer shell, 30 Al atoms are found in an icosidodecahedral arrangement.

It is noted that by laser desorption techniques (MALDI-TOF) or by reaction between AlCp* and AlBr at elevated temperatures, further larger $[Al_N](Cp^*)_x$ and $[Al_N](Cp^*)_x(Br)_y$ clusters could be identified.[63, 71]

Disproportionation reactions of metastable Al-X (X = Br, Cl) solutions are less hindered in the presence of the btsa ligand, typically introduced by Li(btsa), leading to successful isolation of large metalloid aluminum clusters. Again, temperature control allows for isolation of specific clusters with the general trend of increasing cluster size with increasing temperature. For AlCl solutions, the clusters $\{[Al_7](R)_6\}^-$, $\{[Al_{12}](R)_6\}^-$ and $\{[Al_{69}](R)_{18}\}^{3-}$ (R = btsa) were obtained after mixing with Li(btsa) and warming to -7 °C, room temperature and 60 °C, respectively. Changing the halide also effects the reaction outcome, as for AlI, the above mentioned $\{[Al_{77}](R)_{20}\}^{2-}$ cluster was isolated after short warming to 60 °C. The cluster cores in these species form an $[Al_N]$ network displaying strong relationships to the structure of metallic aluminum. This especially holds true for the $[Al_{12}](btsa)_8$ anion depicted in Figure 11 a). It is best described as cut-out of the fcc-packing of bulk aluminum with an **A**(single Al atom) **B**($[Al_4]$ plane) **A**($[A_4]$plane) **B**($[Al_3]$triangle) stapling.[72]

The "every atom counts" principle is reflected when comparing the cluster cores of $\{[Al_{69}](R)_{18}\}^{3-}$ and $\{[Al_{77}](R)_{20}\}^{2-}$. Whereas the former exhibits an $[Al_{13}]$ cluster core with deltahedral geometry, the latter shows a $[Al_{13}]$ center with distorted icosahedral (cuboctahedral) geometry. This geometric difference is likely to be associated with differences in electronic structure and possibly also with physicochemical properties.

All these results impressively demonstrate the tremendous efforts that are necessary to obtain any information about the chemistry of cluster formation and to obtain control over the product distribution. Not only the high sensitivity of the compounds but also the fact that almost all information relies on X-Ray single crystal analysis renders the systematic study of reaction conditions to be a time taking endeavor, which is often based on trial - and error experiments.

a)

b)
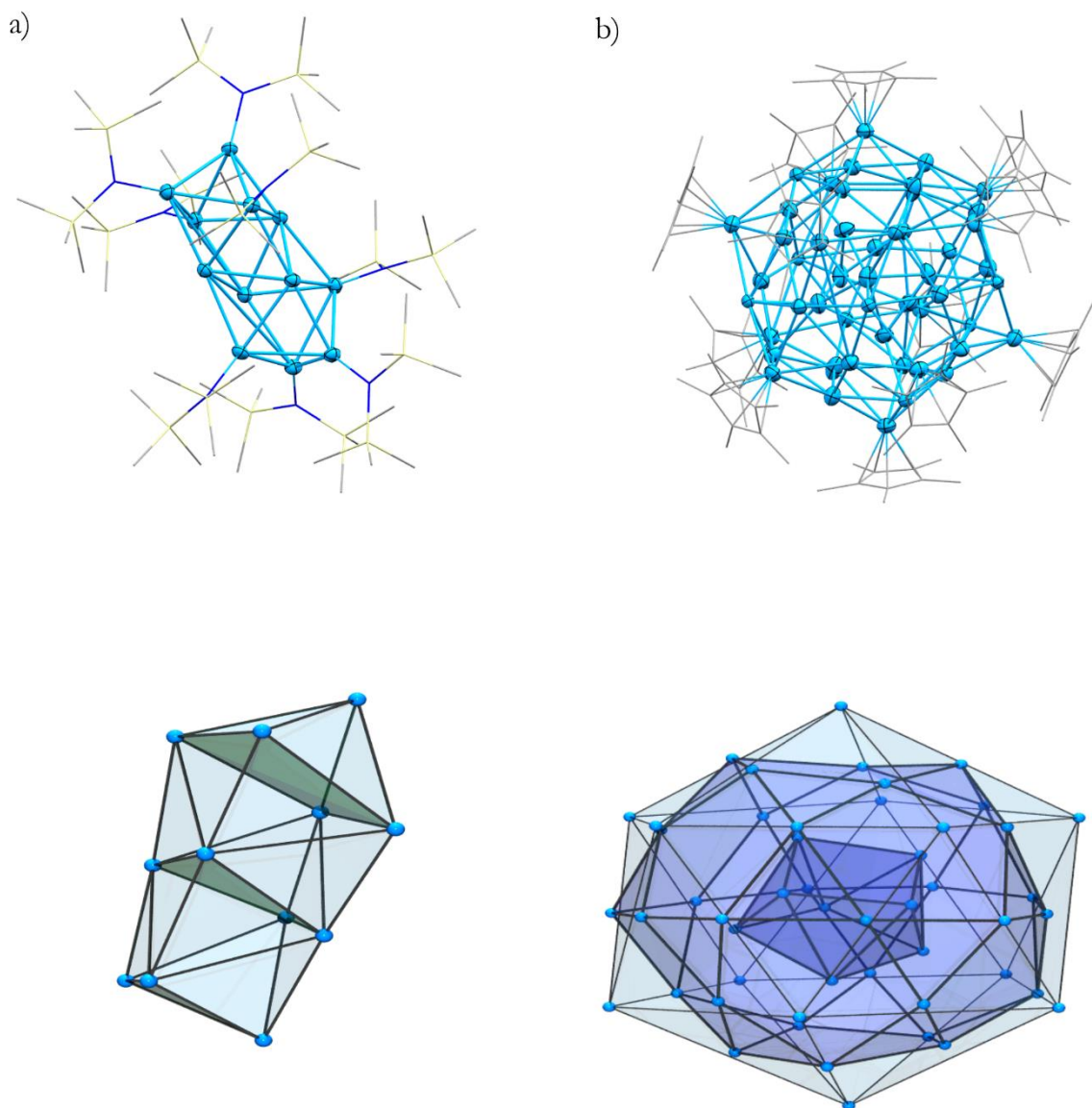
Figure 11
Top: Structures of the molecular Al clusters {[Al₁₂](btsa)₈}⁻ and [Al₅₀](Cp*)₁₂ as determined by SC-XRD. Color code: Al = blue, C = grey, N = dark blue, Si = yellow. Organic ligands are drawn as wireframes; hydrogen atoms and counterions are omitted for clarity. Bottom: Metal-core polyhedra of the clusters. a) {[Al₁₂](btsa)₈}⁻: A cut-out of the fcc packing of bulk Al.[72] b) [Al₅₀](Cp*)₁₂: An icosahedral [Al₅₀] core embedded into a pseudofullerene carbon shell.[70] [Own figure based on literature.[70, 72]]

1.3.2.4 Ligand stabilized clusters of Zn

In sharp contrast to the rich metalloid cluster chemistry of Al (and also Ga) as outlined above, ligand protected metal clusters composed solely of Zn have remained rather exceptional and exotic. This is due to the closed shell electronic configuration of both Zn(0) ($3d^{10}$ $4s^2$) and Zn (II) ($3d^{10}$ configuration) leading to predominant *van der Waals* but low covalent interactions in small cluster molecules.[73] With increasing cluster size, the bonding turns into metallic by mixing of 4s with 4p orbitals; however this mixing energy is rather low and the stabilizing effect small until large cluster sizes are reached.[74] Small Zn clusters are known as a guest in Zeolithe X (tetrahedral [Zn_4] units).[75] In the solid state phases V_8Ga_{41} and Mn_8Ga_{41}, Ga can be partially replaced by Zn atoms and Zn atoms were found to form distinct cluster units within the V-Ga / Mn-Ga framework, culminating in the occurence of a [Zn_{13}] cuboctahedron in $Mn_8Ga_{27.4}Zn_{13.6}$.[74, 76] The reason for that unusual formation of Zn clusters is associated with the stronger tendency of V/Mn to from bonds to Ga than to Zn leading to a separation of Zn units within a strongly bound VGa/MnGa matrix.[74] As mentioned above, several studies on naked zinc clusters in the gas phase (generated in a magnetron sputter gas aggregation source) also revealed very interesting electronic properties combining metallic and insulating properties in one molecule.[77-78] Due to the lack of stabilizing matrix effects (such as in zeolithes or solid state phases) and of defined low-pressure conditions in UHV experiments, all these presented results remain hardly transferable to molecular cluster chemistry in solution.

The discovery of the Zn(I)-Zn(I) bond in *Carmona´s* reagent [Zn_2](Cp*)$_2$ in 2004 therefore clearly was a milestone for the development of contemporary, low-valent Zn (cluster) chemistry.[79] Several small building blocks such as the triangular {[Zn_3](Cp*)$_3$}$^+$ and the mixed -valent "chain" molecule L-Zn-Zn-Zn-L (L= bulky amide) demonstrated that the generation of ligand stabilized [Zn_N] clusters with N > 2 is in principle possible.[80-81] Interestingly, controlled disproportionation reactions of [Zn_2]Cp*$_2$, induced by addition of ZnMe$_2$ (Me = methyl) and [FeCp$_2$][BAr^F] (BAr^F = tetrakis[3,5-bis(trifluoromethyl)phenyl]borate) led to isolation and characterization of the extremely sensitive ionic cluster {[Zn_{10}](Cp*)$_6$(Me)][BAr^F].[82] In analogy to the controlled disproportionation reactions in the formation of Al clusters, the reaction is accompanied by formation of Zn (II) byproducts and fulvene as a product of Cp* reductive coupling. The cluster {[Zn_{10}](Cp*)$_6$(Me)]}[BAr^F] can be transferred into the neutral species [Zn_9](Cp*)$_6$ upon dissolution in THF and to {[Zn_8](Cp*)$_5$(^{t}BuNC)$_3$}[BAr^F] upon reaction with *tert*-butylisonitrile (^{t}BuNC).[82] The structures of these three Zn clusters are shown in Figure 12. These transformations show that careful addition of external ligands causes substitution, ligand or even metal fragment (Zn-Me) removal reactions suggesting a rich cluster chemistry for molecular Zn clusters in general, similar to the Al cluster chemistry outlined above.

Notably, these perspectives rely on the rather weak skeletal bonding between the Zn cluster atoms rendering the species metastable and labile.

The structure of $\{[Zn_{10}](Cp^*)_6(Me)\}[BAr^F]$ (see Figure 12 a)) consists of an almost perfect $[Zn_6]$ octahedron with three edge-bridging $ZnCp^*$ units, one terminal $ZnCp^*$ and one $-CH_3$ group. $[Zn_9](Cp^*)_6$ (see Figure 12 b)) is structurally closely related featuring a slightly distorted bipyramidal $[Zn_5]$ core whose equatorial plane is capped by two edge-bridging and two terminal $ZnCp^*$ units. In $\{[Zn_8](Cp^*)_5(^tBuNC)_3\}[BAr^F]$, two $[Zn_4]$ rhombi are connected by one shared corner with one additional terminal $ZnCp^*$ unit (see Figure 12 c)). All these species are consisting with the *Wade-Mingos* rules with the important specialty that Zn-R fragments behave flexible - depending on the nature of the substituent R - in providing 2 or only 1 frontier orbital for stabilization of the skeletal cluster orbitals.[82]

a)

b)

c)
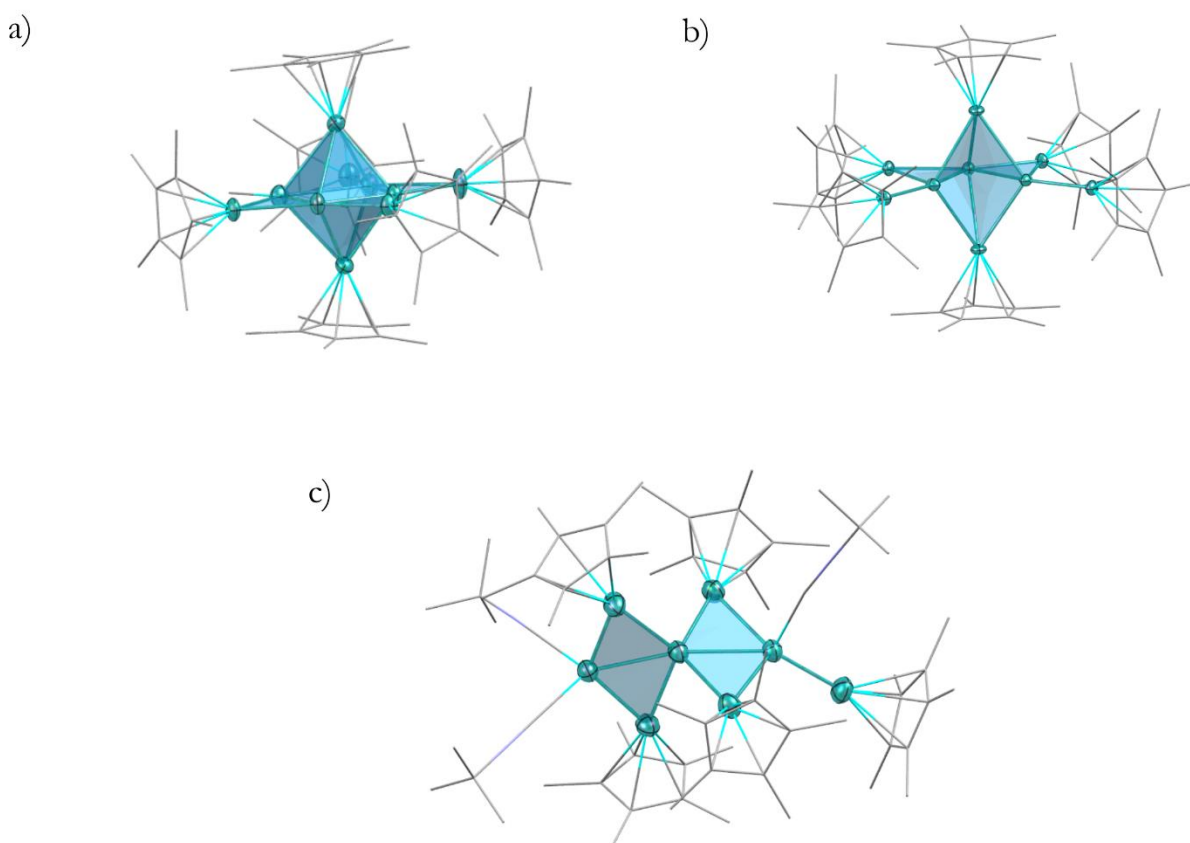
Figure 12
Molecular, ligand protected Zn clusters. Structures in the solid state as determined by SC-XRD.[82]
Color code: Zn = blue, C = grey. Hydrogen atoms and counter ions are omitted for clarity. a)
$\{[Zn_{10}](Cp^*)_6(Me)\}^+$. b) $[Zn_9](Cp^*)_6$. c) $\{[Zn_8](Cp^*)_5(^tBuNC)_3\}^+$. [Own figure based on
literature.[82]]

A remarkable electronic situation was also found in the extraordinarily stable (air!) Zn(I) cluster $\{[Zn_8](HL)_4(L)_8\}^{12-}$ (L = tetrazole dianion), synthesized from $Zn(ClO_4)_2$, NaN_3, NH_4F and $K[C(CN)_3]$ in DMF.[83] Its structure exhibits an Zn(I) cube with "cubic aromaticity", which is traced back to the electron count $8 \times 4s^1$ leading (with some mixing of Zn 4p and Zn 3d orbitals) to the closed-shell electronic situation $(a_{1g})^2 (t_{1u})^6$. Very recently, a metalloid $\{Zn_{12}\}$ unit stabilized in a polymetalloid environment was discovered in the cluster anion $[K_2Zn_{20}Bi_{16}]^{6-}$.[84] The species is gained by the reaction of strongly reducing $K_5Ga_2Bi_5$ with $ZnPh_2$ in ethylenediamine/[2.2.2]-cryptand. The $\{Zn_{12}\}$ unit consists of four edge-sharing $[Zn_4]$ tetrahedra and forms a stable cluster unit on its own, held together by 4-center bonding.[84] It is noted that due to its purely inorganic character (absence of any ligands), its synthesis in solution and its outstanding electronic situation being comparable to that of porphyrin, this cluster can be seen as an outstanding example closing the gap between clusters in solid-state phases and molecular clusters in solution.[85]

1.3.2.5 Intermetalloid clusters of Cu/Zn and Cu/Al

Despite the common use of brass alloys in a plethora of metallurgic and chemical applications (*vide supra*), the chemistry of molecular clusters of Cu/Zn has only emerged in the last few years. There exist several protocols for the wet-chemical, bottom-up synthesis of CuZn nanoparticles, *e.g.* by co-hydrogenolysis of $[CpCu(PMe_3)]$ and $[ZnCp^*_2]$, but synthesis and characterization of defined species remains challenging and often requires tedious separation steps such as fractional crystallization or "crystal picking".[26] Reaction of *Carmonas* reagent $[Zn_2](Cp^*)_2$ with $[CpCuCN\textit{i}Bu]$ leads to the two closely related species $[Cu_4Zn_4](\textit{t}BuNC)_4(Cp^*)_4$ and $[Cu_4Zn_4](\textit{t}BuNC)_4(Cp^*)_3(Cp)$.[86] Both clusters, which are crystallizing as inseparable mixture, consist of a $[Cu_4](\textit{t}BuNC)_4$ tetrahedron, tetracapped by a $[Zn_4](Cp^*)_4$, a $[Zn_4](Cp^*)_3(Cp)$ tetrahedron, respectively (see Figure 13 for illustration).[86] This superposition of $[Cu_4]$ and $[Zn_4]$ tetrahedra is known from the corresponding solid state alloy γ-brass (Cu_5Zn_8), although in an inversed manner.[7] The electronic situation of the compound is that of a $1S^2 1P^6$ closed-shell superatom with 8 valence electrons ("magic number").[86] The reduction of CpCu(I) centers in the course of the reaction is accomplished by oxidation of part of Zn(I)Cp* and the corresponding Zn(II) oxidation products $[ZnCp^*_2]$ and $[ZnCp^*Cp]$ were isolated as side-products.

Interestingly, the choice of the isonitrile ligand stabilizing the "CpCu" fragment is thereby of crucial importance, as from the closely related reaction between *in situ* generated $[Cp^*Cu]$ and $[Zn_2](Cp^*)_2$, the triangular embryonic building block $[CuZn_2](Cp^*)_3$ was obtained (see Figure 14 a)).[81] The reaction can be understood as "oxidative addition" of $[Zn_2](Cp^*)_2$, which is isolobal to H_2, to the unsaturated, electron deficient Cp*Cu(I) center. The Zn-Zn bond elongation in $[CuZn_2](Cp^*)_3$ as

determined by DFT geometry optimizations, as well as SC-XRD data with respect to $[Zn_2](Cp^*)_2$ is indicative of electron donation of the side-on coordinated Cp*Zn-ZnCp* fragment to Cp*Cu(I).[81] More detailed spoken, the bonding can be described as a 6-donation of Cp*Zn-ZnCp* to Cp*Cu in combination with a π-back-donation from Cu(I) to Cp*Zn-ZnCp*. Due to is delocalized 2e-3c bond, the [CuZn₂] triangle integrates itself to the class of sigma-aromatic systems such as $[H_3]^+$, the all Zn congener $[Zn_3](Cp^*)_3^+$ or $[Au_3](L)_3^+$ (L=1,3-bis(2,6-diisopropylphenyl)imidazol-2-ylidene).[87] In all these systems, only s-electron contribute to the delocalized bond.
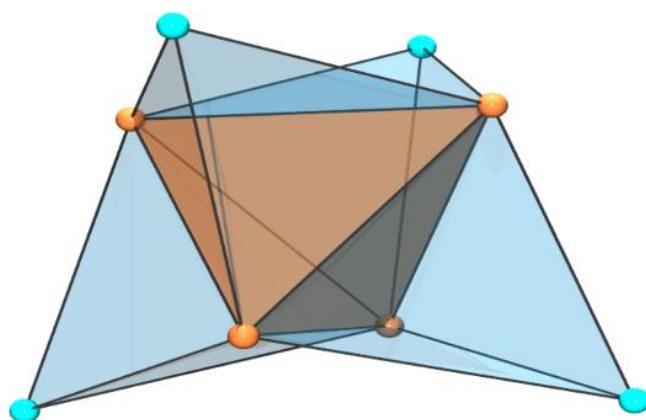
Figure 13
Schematic representation of the metal core of $[Cu_4Zn_4]('BuNC)_4(Cp^*)_4$ and $[Cu_4Zn_4]('BuNC)_4(Cp^*)_3(Cp).$[86] A Cu (orange) tetrahedron is tetracapped by four Zn (light blue) atoms. The structural motif ("stella quadrangula") is known in an inversed manner from bulk γ-brass. [Own figure based on literature.[86]]

$[CuZn_2](Cp^*)_3$ also was identified as a product species in the reaction between [Cu(OAc)] and $[Zn_2](Cp^*)_2$, besides the bipyramidal cluster $[Cu_3Zn_4](Cp^*)_5$.[88] The latter cluster consists of a central $[Cu_3](Cp^*)_3$ triangle, capped vertically by two [ZnZnCp*] units (see Figure 14 b)). The isoelectronic compound $[Cu_2Zn_5](Cp^*)_5$ with a central $[Cu_2Zn](Cp^*)_3$ triangle was obtained by reacting $[CuZn_2](Cp^*)_3$ with the "ZnZnCp*" transfer reagent $[Cp^*ZnZn(OEt)_3][BAr^F]$. Both reactions consist of rather complicated and not fully understood redox and ligand exchange processes involving the disproportionation of Zn(I) to Zn(0) and Zn(II) ($[Zn(OAc)_2]$ and $[ZnCp^*_2]$ were identified as side-products in small yield).[88] The cluster $[Cu_3Zn_4](Cp^*)_5$ is - at a first glance - highly electron deficient according to the *Wade-Mingos* rules exhibiting only one SEP (single electron pair) with one electron from each ·ZnZnCp* unit available for bonding. However, Cu $3d_\pi$ and $3d_{z2}$ orbitals, as well as a 4s/4p combination - containing the electron pair responsible for bonding withing the CuCp* triangle - significantly contribute to the bonding of the whole

cluster.[88] The Cu orbitals form in total three bonding orbitals with the four $4p_\pi$ (Zn) and 4sp (Zn) hybrids of the ZnZnCp* caps resulting in 6 bonding electron pairs as would also be required for stability by classical Wade-Mingos rules. In parallel to the pure Zn clusters described above, the bonding interaction is however of a rather weak nature due to small orbital overlaps.

Therefore, all these species have to be regarded as "dynamic" in the sense that they are prone to degradation, dissociation or cluster growth processes. Indeed, the limited thermal stability of $[Cu_3Zn_4](Cp^*)_5$, as well as of $[CuZn_2](Cp^*)_3$ give the perspective that there are more species to be discovered by systematic and careful adjustment of reaction conditions. Further, the results highlight the chance that for small system, synthesis according to a "building block" principle seems possible, such as in the generation of $[CuZn_2](Cp^*)_3$ or in controlled cluster growth by addition of $[Cp^*ZnZn(OEt)_3](BAr^F)$ to $[CuZn_2](Cp^*)_3$. However, even in these rather simple systems, ligand exchange and complicated redox processes occur and even subtle variations of ligands or starting materials can influence the reaction outcome in an unpredictable manner.
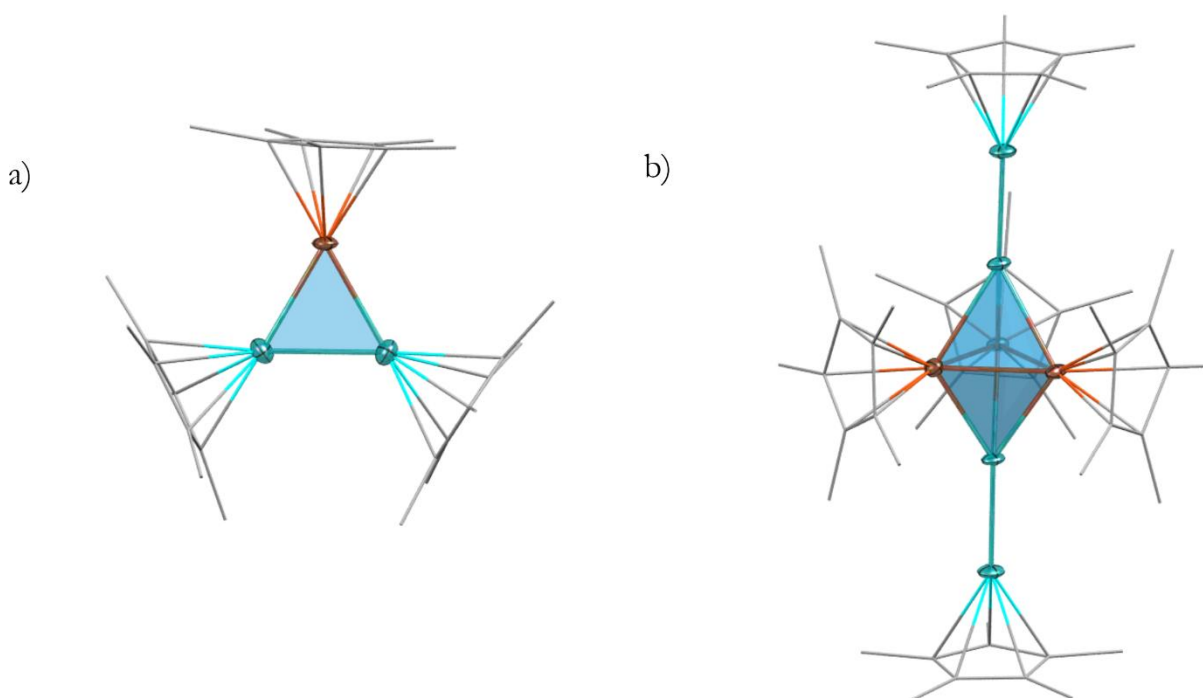
Figure 14
Molecular structures of ligand protected Cu/Zn clusters as determined by SC-XRD.[88] Hydrogen atoms are omitted for clarity and organic ligands are drawn as wireframes. Color code: Cu: orange, Zn: blue. a) $[CuZn_2](Cp^*)_3$, a 6-aromatic metal triangle. b) $[Cu_3Zn_4](Cp^*)_5$, a triangular bipyramid. [Own figure based on literature.[88]]

1. Introduction
1.3. Properties of molecular clusters

For the construction of intermetalloid Cu/Al clusters, the coordination chemistry of AlCp* represents a fruitful basis. On the one hand, many coordination complexes of AlCp* and the related GaCp* with transition metals have been discovered over the years, often obtained by ligand substitution reactions with transition metal olefin complexes, such as $[Pd_3Al_6](Cp^*)_6$[89], $[NiAl_4](Cp^*)_4$ or $[HNiAl_3](Cp^*)_3(C_6H_5)$.[69, 90] For Cu, such substitution reactions are hardly feasible due to the lack of precursor compounds containing Cu in the oxidation state 0 and only a cationic Cu(I) complex $\{[CuGa_4](Cp^*)_4\}[BAr^F]$ was accessed by reaction of $[Cu(MeCN)_4][BAr^F]$ with GaCp*.[91] However, such as in the synthesis of $[Al_{50}](Cp^*)_{12}$, which can also be written as $[Al_{38}](AlCp^*)_{12}$, redox processes involving the *in situ* generation of Cu(0) turned out to be a successful access to intermetalloid Cu/Al clusters. This principle can well be compared to the disproportionation of Al(I)Br in the work of *Schnöckel (vide supra)*. Basically, two different mechanisms have to be distinguished for the formation of molecular CuAl clusters in solution. The former includes the reductive elimination of H_2 from ligand stabilized "Cu-H" and the other the *in-situ* reduction of Cu(I) (Cu-R , R = *e.g.* alkyl, allyl) by part of the Al(I)Cp* in the system.

When *Stryker's* reagent $[H_6Cu_6](PPh_3)_6$ is reacted with AlCp* in a 1:6 molar ratio, the intermetalloid cluster $[H_4Cu_6Al_6](Cp^*)_6$ is obtained in good yield.[92] The structure consists of a dicapped Cu tetrahedron embedded into an octahedral shell of AlCp* ligands (see Figure 15 a)). From the six Cp* ligands, four are η^5 coordinated to Al, whereas two in the equatorial positions are η^2 coordinated. Noteworthy, the superposition of tetrahedral motifs (inner tetrahedron *IT* and outer tetrahedron *OT*) embedded into an octahedron (*OH*) is known as "stella quadrangula" from various solid state Hume-Rothery phases, such as Cu_5Zn_8 or Cu_9Al_4.[11] In the latter, the inner tetrahedron is occupied by Cu or Al atoms, whereas the *OT* as well as the *OH* are occupied by Cu. In the extended solid-state phase, the *OH* is additionally surrounded by a cuboctahedron consisting of Cu or Al atoms (*vide supra*). The location of the hydride ligands in $[H_4Cu_6Al_6](Cp^*)_6$ could not be determined by SC-XRay diffraction; however, their presence is clear from ^{1}H-NMR spectroscopy, as well as from deuteration experiments.[92] Due to its surface bound hydride ligands, $[H_4Cu_6Al_6](Cp^*)_6$ presents an ideal candidate for the investigation of its reactivity towards unsaturated functionalities.

An example for the second reaction type is the non-stoichiometric reaction of [CuMes] (in the following [CuMes] is used as an abbreviation for $[Cu_5](Mes)_5$) with AlCp* to yield $[Cu_{43}Al_{12}](Cp^*)_{12}$ in small yield being the first example of a heterometallic $[M_{55}]$ magic-number Mackay type cluster (see Figure 15 b)).[93] "Mackay-type" cluster therein declares a cluster with an "icosahedral shell structure consisting of concentric icosahedra" with fivefold symmetry axis.

a)

b)
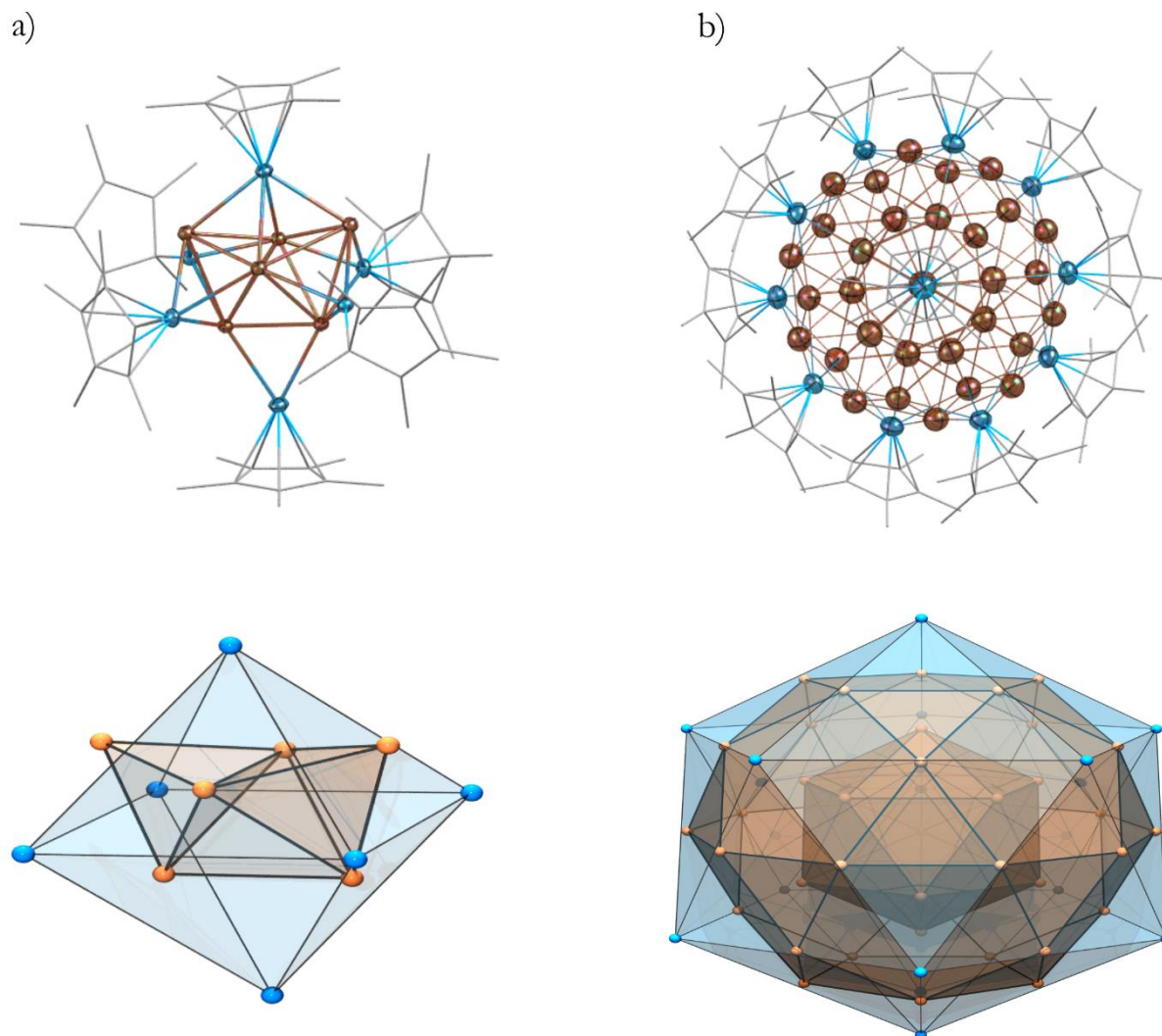
Figure 15

Intermetalloid, ligand protected Cu/Al clusters. Top: Molecular structures as determined by SC-XRD. Organic ligands are drawn as wireframes and hydrogen atoms are omitted for clarity. Color code: Cu = orange, Al = blue. Bottom: Schematic representation of the metal-core polyhedra. a) [H$_4$Cu$_6$Al$_6$](Cp*)$_6$.[92] b) [Cu$_{43}$Al$_{12}$](Cp*)$_{12}$.[93] [Own figure based on literature.[93, 92]]

Many monometallic examples of *Mackay* clusters have been reported including gas-phase clusters or [Pd$_{55}$](L)$_{12}$(μ_3-CO)$_{20}$ (L = P(^{iso}propyl)$_3$).[94-96] Likewise, this structural motif was found in several multi-shell large metal clusters, such as [Pd$_{145}$](CO)$_{72}$(PEt$_3$)$_{30}$[97] or [Au$_{133}$](S-C$_6$H$_4$-*p*-^{t}Bu)$_{52}$[98]. [Cu$_{43}$Al$_{12}$](Cp*)$_{12}$ consists of an internal, body-centered [Cu$_{13}$] icosahedron embedded into an [Cu$_{30}$Al$_{12}$] shell, which is itself composed of a [Cu$_{30}$] icosidodecahedron and an outer [Al$_{12}$] icosahedron bound to the Cp* ligands.[93] The electronic structure of [Cu$_{43}$Al$_{12}$](Cp*)$_{12}$ can be considered as an open-shell 67 electron superatom, in which the Al atoms are fully part of the cluster core, leading to a description of [Cu$_{43}$Al$_{12}$]$^{12+}$, stabilized by 12 anionic Cp* ligands. The three unpaired electrons occupy slightly antibonding jellium

states with low energy separation. This unique situation can be interpreted as the beginning of the evolution of a conduction band. It was confirmed by SQUID measurements exhibiting a temperature independent paramagnetism caused by coupling of low-lying (unoccupied) states with the ground state.[93]

The structural and electronic analogies to solid state phases described for the two clusters above clearly demonstrate the view on intermetalloid clusters as molecular models for solid state alloys. Clearly, the both synthetic approaches result in the formation of real Cu(0) cores, a situation which is rare for Cu (*vide supra*). Nevertheless, restrictions come up intrinsically from the synthetic approach: By using AlCp* as "ligand" for *in situ* generated Cu(0), Al can be found rather at external positions of the cluster, but not at internal core positions. Recent results from the analogous Ni-Ga chemistry however, show that mechanisms for Cp* transfer from the main group to the transition metal exist.[99] Nevertheless, the construction of real intermetalloid, mixed (TM/E) metal cores, remains a challenge so far. First and preliminary results support the hypothesis that by reaction of $[H_4Cu_6Al_6](Cp^*)_6$ with [CuMes], a congener of $[Cu_{43}Al_{12}](Cp^*)_{12}$, namely $[Cu_{43-x}Al_xAl_{12}](Cp^*)_{12}$ is formed with aluminum incorporated into the cluster core.[100]

1.3.3 Reactivity of molecular clusters

1.3.3.1 Naked metal clusters in the gas-phase

This paragraph will deal with fundamental principles of gas-phase cluster chemistry and shortly discuss relevant reactivity studies for clusters of elemental composition relevant for this work (Cu/Al, Au/Al, Cu/Zn). It is of note that gas-phase cluster chemistry does not only represent a conceptual link to this work in terms of physico-chemical cluster properties (electronic and geometric structures, reactivity), but also in terms of *methology* (*parallel assessment* of cluster assemblies *via* mass-spectrometric methods).

In the gas-phase approach, investigation of cluster reactivity with small (gaseous) molecules is accomplished by selecting specific species from the ion beam using an ion trap or a quadrupol mass spectrometer. Subsequently, the clusters can be reacted with (gaseous) small molecules and the reaction products analyzed by mass-spectrometric techniques.[3] Structural information about the cluster species is available by theoretical calculations in addition to spectroscopic techniques, such as infrared (photodissociation) spectroscopy (*vide infra*).[101] Noteworthy, structure-reactivity relationships obtained have to be regarded as conceptual findings; a direct transfer to real catalytic applications remains difficult due to the absence of solvation

and counterions in the gas-phase, and due to the large pressure gap between catalytic processes in general and UHV experiment.[102] Before discussing some relevant reactivity patterns of naked metal clusters in the gas-phase, the individual steps of gas-phase cluster experiments are shortly described in the following.

Experimental strategies in gas-phase cluster chemistry

Naked metal clusters in the gas-phase are generated by a heated oven-source (used *e.g.* for Alkali clusters), by bombardment of metal sheets with Ar or Xe atoms (sputtering) or by laser vaporization. Clusters are formed from evaporated metal by collisional cooling *e.g.* with inert He gas flow and subsequently expanded into high vacuum, whereby the sudden decrease in density causes the cluster growth to stop.[103] Cluster abundancies and identities are thereafter analyzed by mass-spectrometry, whereby ionization either takes place directly during cluster formation, is induced by additional laser pulses or simply by light (*e.g.* Hg-Xe lamp for Na clusters).[103-104] A typical laser-ablation set-up for the generation of transition metal clusters is shown in Figure 16.[103] It was used for the generation of bimetallic clusters, but the set-up can principally also be used for the generation of monometallic clusters.

Alternatively, naked metal clusters can be generated from ligand protected clusters in solution by electrospray ionization (ESI), whereby the ligands are stripped of by collision induced dissociation with carrier gas.[105]
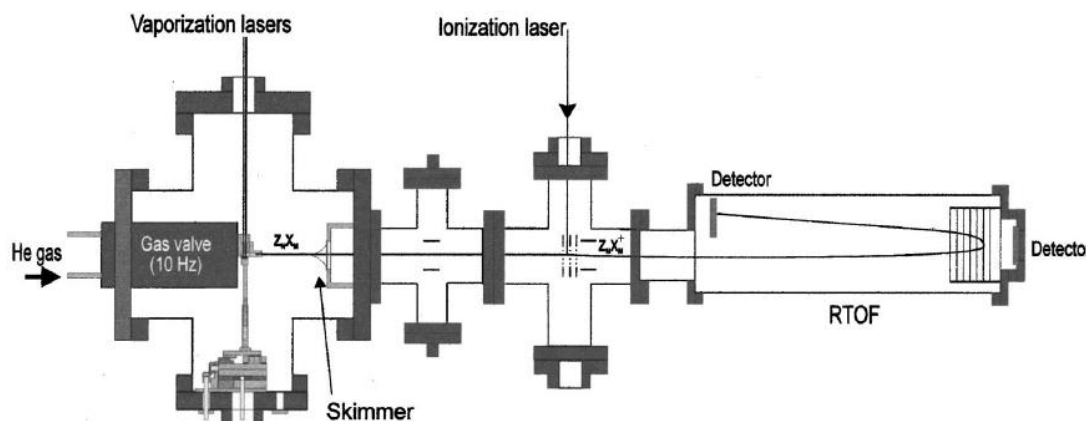
Figure 16
Apparative set-up for the generation and mass-spectrometric study of naked (bimetallic) metal clusters in the gas-phase.[103] [Reprinted with permission from W. Bouwen, P. Thoen, F. Vanhoutte, S. Bouckaert, F. Despa, H. Weidele, R.E. Silverand, P. Lievens, Rev. Sci. Instrum. 2000, 71, 1, 54-58. Copyright 2000, AIP Publishing.]

There exists a plethora of methods to investigate the physicochemical properties of clusters in the gas-phase. Electron affinity and electronic structure (HOMO-LUMO gaps) can be elucidated by photoelectron spectroscopy.[106] The structure of clusters can be investigated by trapped-ion electron diffraction, as it was done *e.g.* for anionic Au_{14}-Au_{19} clusters.[107] Further structural information is gained by fragmentation experiments, whereby fragmentation can be achieved by collision with inert gases or by absorption of UV-Vis/IR light.[106, 108] In the latter approaches, messenger fragment ions are formed by absorption of light at a specific (resonance) frequency. These fragment ions are subsequently detected by mass-spectrometry and the relation between their peak intensities and the wavelength of light produces an IR or UV-Vis spectrum.

Using ion traps, quadrupoles, or in ion mobility drift zones, clusters can be separated from each other.[106] Reactivity patterns are explored by exposing the clusters caught in an ion-trap to reactants and analyzing the products formed by MS. Alternatively, integer clusters are deposited on a support ("soft landing") and afterwards supposed to reactants or studied electrochemically.[109]

Reactivity patterns of gas-phase metal clusters

One of the earliest findings in gas-phase cluster chemistry was the discovery of discontinuous intensities in the MS spectra of pure $[Na_n]$ clusters, whereby clusters with the *magic numbers* n = 8, 20, 40, 58, 92 exhibit higher intensities and therefore higher stability.[104] The effect is traced back to closed-shell electronic configurations and can in the simplest case be explained by the Jellium model (*vide infra*). A similar trend is observed for clusters of Cu, Ag and Au in the gas-phase, as in a simplified picture these noble metals also contribute one *s*-electron to cluster bonding, such as Na. The magic numbers *n* are related with shell-closings according to the Jellium model and follow the relation n = $n_{shell\ closing}$ + 1 for cationic and n = $n_{shell\ closing}$ -1 for anionic clusters.[110]

Au clusters exhibit interesting reactivity patterns both in the gas-phase and on support. Whereas bulk Au is rather inert, Au clusters or highly dispersed Au films on metal oxides exhibit high reactivity to many small molecules such as H_2, CH_4 and O_2. On a molecular level, electronic properties and reactivity of (metal) particles and clusters might change drastically by addition or removal of single atoms.[111-112] For example, $[Au_7]$ clusters on a MgO surface are inactive in the oxidation of CO, whereas $[Au_{8-20}]$ clusters were shown to be active catalysts.[2] Small cationic Au clusters in the gas phase are reactive towards D_2 and CH_4, which is activated at room-temperature and bound as $-CH_3$ and -H. Anionic $[Au_n]^-$ (n = even number) clusters

are reactive towards O_2 forming superoxo and hydroperoxo complexes.[113] When reacted with CO in the gas-phase, the anionic Au clusters showed size-dependent reactivity patterns. Interestingly, when subjected to CO and O_2 in parallel, cooperative coadsorption effects were observed. In this context, $[Au_6]^-$ seems to exhibit a key role and high activity in catalytic CO oxidation.[113] Size dependent catalytic activity in CO combustion was also obtained for neutral Au clusters on a magnesia support, whereby neutral $[Au_8]$ turned out to be the smallest catalytically active size.[2] Reactivity differences were also reported for the oxygen activation on the closed shell cluster $[Au_8]$ and its H-doped congener $[HAu_7]$.[114] Whereas both clusters are closed-shell systems and expected to be relatively inert, $[HAu_7]$ shows enhanced reactivity towards O_2 and CO_2 as predicted by DFT calculations and experimental results. The effect is rationalized by the polarizing effect of the H-dopant leading to activation of the $[Au_7]$ metal core.[114] Gas-phase Cu clusters were shown to be only moderately reactive towards CO; no cluster CO adducts were observed in this case, rather CO cleavage and oxidation of the clusters was observed.[115] However, Cu clusters deposited on support were shown to exhibit interesting electrochemical behavior in electrochemical conversion of CO_2.[109]

Aluminium clusters in the gas phase have turned out to be a very instructive system for the exploration of electronic structure-reactivity relationships.[116] Especially the superatom concept is a valuable tool for rationalization of reactivity patterns of $[Al_n]^-$ clusters in the gas-phase (*vide supra*). Thereby, superatomic clusters are expected to exhibit reactivity patterns comparable to their atomic counterparts. In this context, closed-shell systems are expected to be of higher stability. When a stream of anionic Al clusters was reacted with gaseous CH_3I, $[Al_nI]^-$ clusters were detected by mass-spectrometry, but also the formation of neutral $[Al_nCH_3]$ clusters is propagated by the authors based on observed reaction rates.[116] Notably, in this experiment, the closed-shell, superatomic cluster $[Al_{13}]^-$ did not yield any reaction product, just as in the comparable reaction with oxygen. However, when reacted with HI, the adduct $[Al_{13}I]^-$ is observed. The reaction is interpreted by the "superhalogen" character of $[Al_{13}]^-$ and $[Al_{13}I]^-$ can be understood as an analogue to polyhalides.[116]

Interesting electronic properties were also discovered for naked Zn clusters: Not only were the abundancies in mass spectra explained in terms of electronic and geometric shell closings; for some sizes, metallic and insulating properties were found to be coexistent in one particle.[77] The insulating properties are associated with Zn "adatoms" bound on the cluster periphery. For other sizes, two distinct metallic domains were distinguished in one particle with only weak interactions.[77] These findings clearly illustrate the "every atom counts" principle and how subtle (atomic!) changes in cluster composition can have tremendous effects on electronic properties, as well as their reactivities.

1. Introduction
1.3. Properties of molecular clusters

The doping of Cu clusters with Al was shown to significantly enhance the reactivity towards NO, whereas the reactivity towards O_2 was not significantly affected.[111] The higher reactivity of the doped clusters is explained by enhanced adsorption energies and a larger number of favorable adsorption sites. Under multiple collision conditions, the cluster dioxides were detected as reaction products, clearly indicating the combustion of NO. Particular clusters, such as $[Cu_{18}Al]^+$ and $[Cu_6Al]^+$ were extraordinary stable, which is again explained by electronic shell-closures.[111] The CuAl oxide cluster system $[CuAl_4O_{7-9}]^-$ was shown to be a catalyst for CO oxidation as presented in Scheme 3 a).[117] Despite being a closed-shell system, $[CuAl_4O_7]^-$ can activate O_2 to regenerate the starting species $[CuAl_4O_9]^-$ in the catalytic cycle.[117-118] A similar catalytic cycle was proposed for the related system $[AuAl_3O_{3-5}]^+$ (Scheme 3 b)).[118]
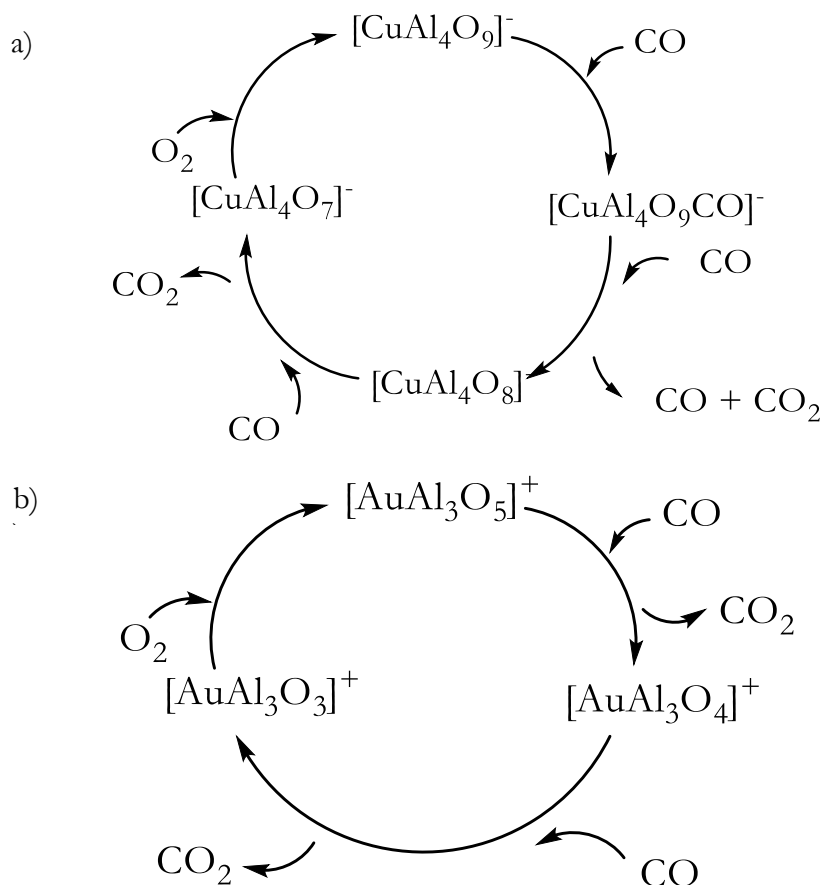
Scheme 3
Gas-phase intermetallic clusters as catalysts for CO oxidation. a) Cu/Al oxide clusters.[117] b) Au/Al oxide clusters.[118] [Own scheme based on literature.[117-118]]

In the examples presented in Scheme 3, (partial) oxidation of the intermetallic naked metal clusters has tremendous effect on their reactivity patterns. In other cases, the effect of the oxide on catalytic activity is still under debate, such as for methanol

synthesis over Cu/Zn and Cu/ZnO surfaces and nanoparticles.[23, 27] In any case, intermetallic clusters or nanoparticles might serve as "pre-catalysts", developing their full catalytic potential by careful oxidation, *e.g.* with NO_2, NO or O_2.[27, 111]

1.3.3.2. Reactivity of molecular clusters in solution

An early example of a catalytically active cluster is $[Ni_4](^tBuNC)_7$.[119] The compound was shown to catalyze trimerization of acetylenes and cyclodimerization of butadiene. In the presence of hydrogen, selective semihydrogenation of acetylenes takes place. As a catalytically active intermediate, $[Ni_4](^tBuNC)_4(C_6H_5C{\equiv}CC_6H_5)_3$ was crystallized with diphenylacetylene exhibiting an unsymmetrical bridging position. This highlights the chance that sterically rigid "protection groups" (such as the phenyl groups of diphenylacetylene) might present an opportunity in terms of enabling isolation and detailed characterization of stabilized intermediates.[119]

Two other examples in which metal clusters can be regarded as models for heterogenous surfaces are depicted in Figure 17. The Ru-carbonyl cluster (Figure 17 na)), having the acetylene bound to three metal centers in neighborhood to a bridging hydride, is an intermediate in the hydrogenation of diphenylacetylene.[120] The heterometallic "butterfly" cluster in Figure 17 b) can be seen as a model of an acetylene binding on a "surface-ridge".[120]
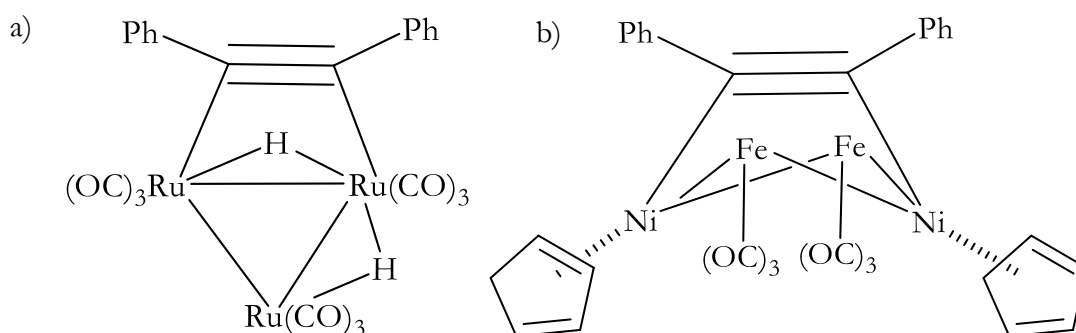
Figure 17
Clusters as molecular models for catalytically active surfaces. a) Binding of diphenylacetylene to three Ru centers.[120] b) Binding of diphenylacetylene at the "ridge" of a heterometallic Fe/Ni cluster.[120] [Own figure based on literature data.[120]]

A CO free Ru-arene cluster which turned out to be a hydrogen transferring reagent, was prepared by *Meister et al.* $\{[H_4Ru_4](\eta^6\text{-}C_6H_6)_4\}[BF_4]_2$ is able to perform catalytic hydrogenation of fumaric acid under hydrogen atmosphere.[121] More recently,

catalytic hydrogen/deuterium exchange with C_6D_6 was observed with the highly reactive cluster $[H_6Ni_5](P(^iPr)_3)_5$ (^iPr = -isopropyl).[122] Other examples of homometallic TM hydride clusters are the Cu (I) hydride cluster $[H_6Cu_6](PPh_3)_6$ and $[H_8Co_6](P(^iPr)_3)_6$, which were shown to afford conjugate reduction of 1,4-unsaturated ketones and catalytic hydrosilylation of ketones, respectively.[123-124] Following the active site isolation concept, the reactivity of $[H_4Cu_6Al_6](Cp^*)_6$ was investigated having in mind the high catalytic activity of some Hume-Rothery phases for semihyrogenation. Whereas with alkynes, an unspecific reaction behavior including polymerisation reactions was found, reaction of $[H_4Cu_6Al_6](Cp^*)_6$ with benzonitrile at room-temperature for 24 hours resulted cleanly in the 1:1 insertion product $[H_3Cu_6Al_6](Cp^*)_6(N=CHPh)$ (see Scheme 4).[92] Its crystal structure consists of an aldiminate functionality binding in a triangular manner to one Al atom of the octahedron and one Cu atom of the outer tetrahedron.
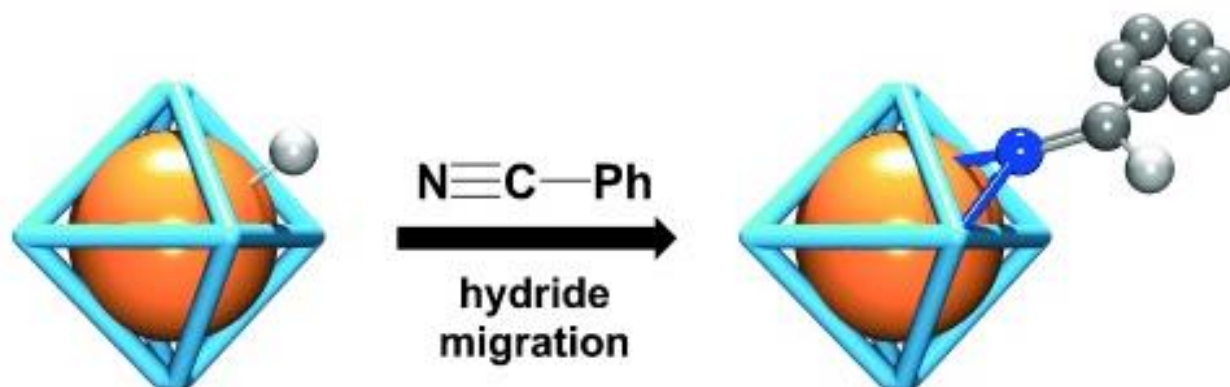
Scheme 4
Schematic representation of the surface reactivity of [H₄Cu₆Al₆](Cp)₆ undergoing hydride insertion into benzonitrile. [Reprinted with permission from C. Ganesamoorthy, J. Weßing, C. Kroll, R. W. Seidel, C. Gemel, R. A. Fischer, Angew. Chem. Int. Ed. 2014, 53, 30, 7943-7947. Copyright 2014, John Wiley and Sons.]*

1.3.4 Synthesis strategies for bimetallic clusters and colloids in solution

When it comes to the synthesis of metallic clusters in solution, basically two different routes exist: In the top-down method, pre-built cluster units are extruded from solid-state phases by wet-chemical methods with manifold options of subsequent functionalization.[85] In the bottom-up method, clusters are synthesized from molecular precursor compounds in solution.[85] The latter approach shows a fluid transition to the synthesis of nanoparticles and colloids, which can be interpreted as assemblies of large nanoclusters with a certain lack of molecular precision, stemming from an inhomogeneous size and structure distribution.

1.3.4.1 Multimetallic cluster growth in the top-down approach

Intermetallic phases with large property differences between the involved elements lead to a strong polarity of bonds in the solid-state structures inducing the formation of discrete polyanionic (in rare cases polycationic) cluster units.[85] Separation of discrete cluster units, dissolved in a counter-ion matrix, goes in hand with a charge transfer from the more electropositive to the more electronegative metal. From these *Zintl* phases, the ionic subunits can be extruded by soft wet-chemical methods, if the overall charge of the ionic subunits is not too high.[85] Nine atomic $[Tt_9]^{4-}$ or tetrahedral $[Tt_4]^{4-}$ clusters of the tetrel elements $Tt = Si\text{-}Pb$ can be extruded by liquid ammonia or ethylenediamine from the solid state alloys A_4Tt_9 or $A_{12}Tt_{17}$, whereby the addition of cation sequestering agents (*e.g.* crown ethers) enhances the solubility (A = counter cation, *e.g.* K). *Oxidation* of the anionic clusters is a valuable strategy for cluster growth or expansion reactions.[125] Reaction of $[Ge_9]^{4-}$ with $[Pd(PPh_3)_4]$ leads to one electron oxidation and $Pd(PPh_3)$ coordination forming the cluster $\{[Ge_9Pd](PPh_3)\}^{3-}$.[125-126] Reaction of the latter with $[Ni(PPh_3)_4]$ leads to incorporation of a naked Ni atom accompanied by a second one electron oxidation.[126] Similar reaction behavior was observed for the tin-analogue $[Sn_9]^{4-}$.[125] A complex reaction sequence was determined for the reaction of $[Ge_9]^{4-}$ with $[Ni(CO)_2(PPh_3)_2]$. The complex cluster $\{[Ni_2@Ge_{13}Ni_4](CO)_5\}^{4-}$ was identified as the initial reaction product at low-temperatures. Upon heating, it undergoes fragmentation, loss of CO ligands and coordination of free PPh_3 to form $\{[Ni@Ge_9Ni](PPh_3)\}^{2-}$.[127] Besides oxidation reaction, *ligand exchange reactions* are a valuable tool for the incorporation of a second metal. From the reaction of *Zintl* ions in solution with transition metal precursors, in some cases, intermediate complexes revealing stepwise release of organic ligands from the transition metal fragment have been isolated and structurally characterized.[128-129] For example, $[Sn_9]^{4-}$ was reported to coordinate to $[Ti(NH_3)_2Cp_2]^+$ upon release of one ammonia ligand.[128] Other examples include complexes of Zn and Cu with silylated $[Ge_9]$ clusters as ligands.[125, 130]

When it comes to bimetallic cluster units to be directly extruded from solid-state phases, complexity increases significantly, and reaction outcomes are often not predictable. Dissolution of the ternary phase $K_{4.79}Co_{0.79}Sn_9$ in ethylenediamine under the addition of [2.2.2]-cryptand leads to the formation of different Co-filled Sn clusters, namely $[Co_{0.68}@Sn_9]$, and two different conformers of $[Co_2@Sn_{17}]$.[131] Noteworthy, the reaction outcome is strongly dependent on reaction and crystallization conditions. Cluster rearrangement processes in solution were also observed upon dissolution of $K_2Ge_2P_2$, forming the anions $[Ge_2P_2]^{2-}$ and $[Ge_7P_2]^{2-}$ in solution.[132] Three different bimetallic cluster ions were isolated upon dissolution of $A_5E_2Bi_4$ ($A = Na, K, Rb, E = Ga, In$).[133] *Dehnen et al.* achieved to shed a light into cluster growth and rearrangement processes occurring upon solid-state synthesis and dissolution of a solid with nominal composition $K_8Ge_8As_8Ta$ by a combined experimental and quantum-chemical study.[134] The results are presented in Figure 18.

1. Introduction
1.3. Properties of molecular clusters

Two $[Ge_2As_2]^{2-}$ precursors react with one $[Ge_{10}]^{2-}$ unit to give two nine-atom cages $[Ge_7As_2]^{2-}$. Coordination of Ta atoms induces fragmentation and formation of $[Ta@Ge_6As_4]^{3-}$. The reactivity of this intermediate was extensively studied by a theoretical genetic algorithm study (*vide infra* for methodical details). $[Ta@Ge_6As_4]^{3-}$ easily undergoes low energy rearrangement processes to form topological fragments of known non-deltahedral cluster topologies. Addition of $[Ge_2As_2]^{2-}$ units to these fragments results in the final product clusters $[Ta@Ge_8As_4]^{3-}$ and $[Ta@Ge_8As_6]^{3-}$.

The examples clearly illustrate that the wet-chemical extrusion of cluster architectures out of solid-state phases is indeed a valuable starting point for a diverse (bimetallic) cluster chemistry in solution. However, due to isomerism, rearrangement and fragmentation processes, the integrity of the cluster units extruded is far from guaranteed.
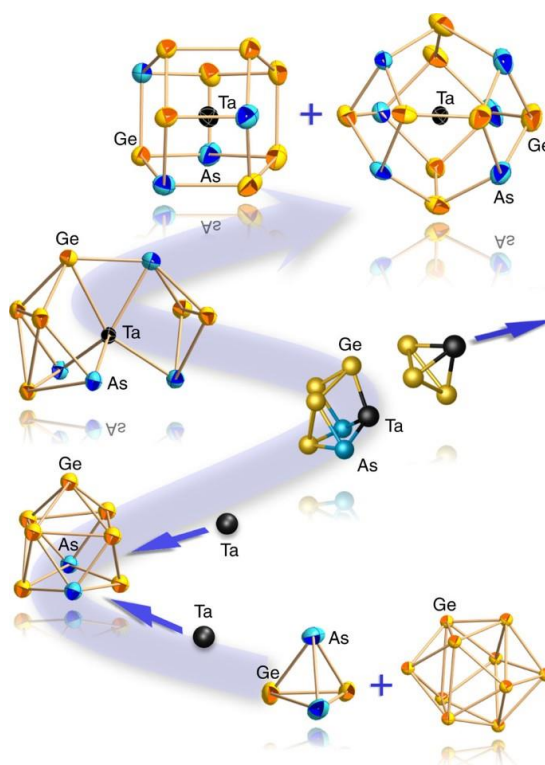

Figure 18
Stepwise formation of intermetalloid Ta/Ge/As clusters as determined by experimental and quantum-chemical investigations. [Reproduced with permission from S. Mitzinger, L. Broeckaert, W. Massa, F. Weigend, S. Dehnen, Nat. Commun. 2016, 7, 1, 1-10. Copyright 2016, Nature Publishing Group.]

1.3.4.2 Synthesis concepts for bimetallic nanoparticles and colloids

The synthesis of bimetallic nanoparticles can be regarded as opposite to the extrusion of defined and discrete cluster units from intermetallic phases in the top-down approach. However, general concepts for the construction of metal-metal bonds hold true not only for defined systems, but also for those with a distribution function of physicochemical properties.

Bimetallic nanoparticles and colloids are produced either by *coreduction* or *sucessive reduction* of suitable molecular precursor compounds or by sophisticated experimental techniques like *metal-vapor synthesis*.[135] The reduction of molecular precursors might be achieved either by addition of an external reducing agent (*e.g.* H_2, hydrogenolysis) or by one reaction partner acting as reductant and alloy component at once. In the reduction technique, it can be further distinguished between *dual-source* syntheses starting from separate metal precursors and *single-source* syntheses starting from one molecular, bimetallic precursor.

Coreduction of metal salts in the presence of a stabilizer was *e.g.* demonstrated for Au-Pt nanoparticles. Citrate reduction of tetrachloroauric acid and hexachloroplatinic acid leads to citrate stabilized metal Au-Pt bimetallic colloids as determined by UV-Vis spectroscopy.[135] Similar results have been achieved by successive reduction: Au particles were covered by Pd or Pt when $PdCl_2$ or H_2PtCl_6 were reduced in solutions of Au colloids in the presence of a stabilizer.[135] Nanoparticles of Hume-Rothery composition are obtained by co-hydrogenolysis of organometallic precursors in organic solvents or ionic liquids. Treatment of $[Ni(cod)_2]$, GaCp* and the surfactant hexadecylamine with H_2 at elevated temperatures in high-boiling solvents leads to NiGa nanoparticles with a diameter of ~ 5 nm.[136] Similar results were obtained in microwave-assisted pyrolysis of the precursors in ionic-liquids, but without the addition of surfactant. Notably, the synthesis can be seen as combination between ligand substitution and reduction. GaCp* is supposed to initially coordinate to Ni upon release of the COD ligand leading to smaller, Cp* decorated $[Ni_xGa_y]$ clusters. Cleavage of Cp* by hydrogen is likely to result in aggregation and nanoparticle formation. Hydrogenolysis of the single-source precursor $[Ni(PMe_3)_3GaCp*]$ did also lead to nanoparticle formation albeit in a very broad size distribution.[136] Poly(2,6-dimethyl-1,4-phenylene oxide) (PPO) capped $Cu_{1-x}Al_x$ (0.1<x<0.5) nanoparticles of 15±5 nm diameter were obtained upon co-hydrogenolysis of AlCp* with $[CpCuPMe_3]$ in mesitylene in the presence of PPO.[137] Likewise, $Cu_{1-x}Zn_x$ (0.09<x<0.5) colloids were prepared by reacting $[CpCuPMe_3]$ with $[ZnCp*_2]$ and PPO.[26] Unfortunately, the so obtained nanoparticles were inactive in methanol production. Microwave assisted thermal decomposition of Cu and Zn aldiminate precursors in ionic liquids was also shown

to result in the formation of β-CuZn and γ-Cu_3Zn alloy particles depending on the stoichiometry applied (1:1 and 3:1, respectively) without the need of any capping agent.[27] Most interestingly, the β-CuZn nanoparticles were shown to be active precatalysts for methanol products (*vide supra*).

Metal vapor synthesis is an alternate technique to prepare nanoparticles. Co-condensation of Cu with acetone leads to solvated metal atoms of Cu in an acetone matrix, which upon warming to room-temperature leads to Cu nanoparticles with a mean diameter of 3-4 nm.[138] Notably, modification of the solvated Cu atoms with ZnO nanoparticles is possible by directly reacting the solvated metal atoms with ZnO nanocrystals prepared by a sol-gel method.[139] Vaporization of brass in a SMAD set-up (SMAD = small atom dispersion) and co-condensation with solvent leads to dealloying into Cu and Zn atoms.[21] Subsequent nucleation upon warming leads to Cu/Zn@Cu nanostructures. The Cu/Zn core structure thereby consists of Cu(0) and Zn(0) with interfaces of Cu_5Zn_8. Thermal annealing of the samples produces a variety of CuZn brass phases. If the SMAD procedure is carried out in the presence of capping agents, a broad distribution of nanoparticles is produced.[21] Digestive ripening (refluxing overnight) of the particles significantly narrows down the size distribution of the particles and induces a phase-segregation of Cu and Zn and diffusion of the Zn atoms to the surface of the particles.

1.3.4.3 Multimetallic cluster growth by the bottom-up approach

In chapter 3.2.2, the synthesis of intermetalloid clusters of Cu/Al and Cu/Zn, as well as of molecular clusters of the pure elements Cu, Au and Zn, was described. These syntheses start from molecular (organometallic) precursors to build up larger cluster architectures by soft wet-chemical methods. Despite all differences and all experimental tricks and adaptions that are necessary for the isolation of any product, an overall synthetic concept for the bottom-up synthesis of molecular clusters seems to exist for the above-mentioned elements. Based on this knowledge, Scheme 5 proposes a generalized concept of how synthesis of (inter)metallic clusters in solution can be accomplished.

An obvious and simple approach of synthesizing low valent metal clusters is starting from precursor compounds in the oxidation state 0, followed by ligand substitution reactions. Such examples are widespread in literature and in the *R. A. Fischer* group this strategy was successfully used for the synthesis of many bimetallic coordination compounds and clusters by reacting Fe, Ni or Pd olefin complexes with the ECp* ligands AlCp*, GaCp* or $[Zn_2](Cp^*)_2$.[69, 89]

However, for the elements Cu, Au and also for the Al and Zn, such a synthesis concept based on simple ligand exchange processes is difficult to apply simply due to a lack of precursor compounds with formal oxidation state 0.[37] Rather, an inherent, intricate redox process is required. Scheme 5 illustrates different ways how metal M^1 can be reduced during the course of the reaction.[93] Either can the species M^2-R^2 serve as a reducing agent leading to the oxidized side product $M^2(R^{1/2})_3$ or can reductive elimination of ligands or ligand disproportionation lead to reduction of M^1. In this context, it is important to note that the distinct nature of M^1 and M^2 does not play a role as the two species might also be the same ($M^1 = M^2$) or M^2 might be a non-metal such as sulfur or boron (*vide supra* for the synthesis of Au nanoclusters by thiol reduction of Au(I) precursors).
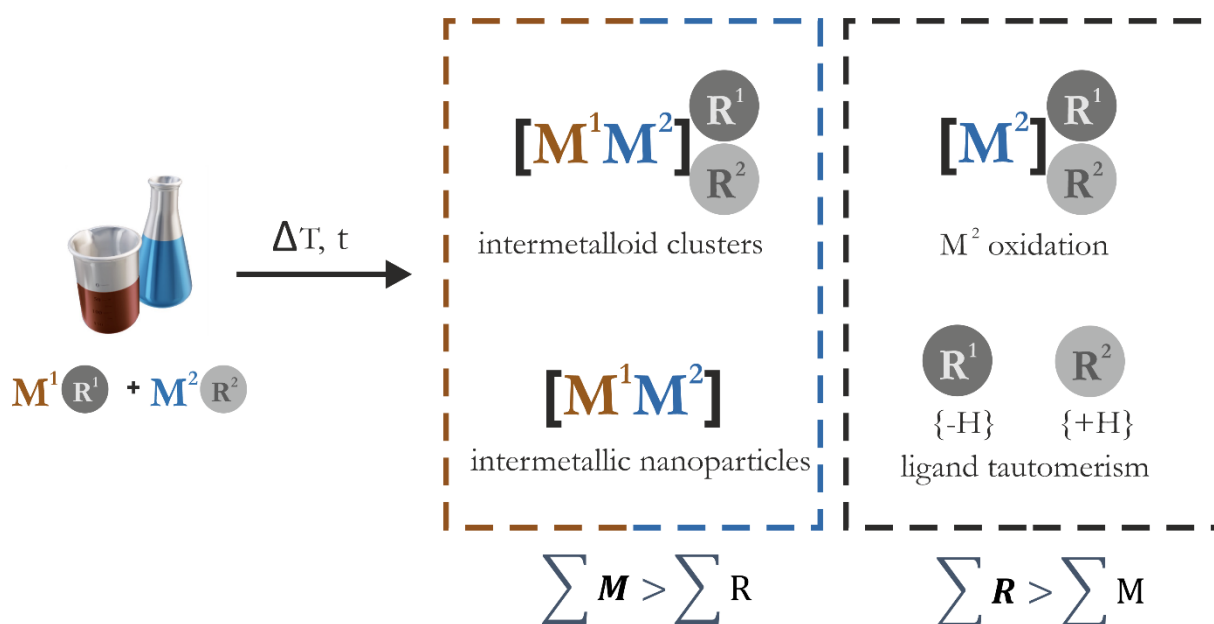
Scheme 5

General concept for the bottom-up synthesis of ligated metal clusters $[M_n](R)_m$ ($n \gg m$; M = two or more different metal atoms, e.g. M1 , M2 ; n = number of metal atoms aggregated in the cluster core; R = hydrocarbon ligand, e.g. R1 , R2 ; square brackets denote the cluster core; round brackets denote the core protecting ligand shell). Scheme 5 aims to conceptually catch a diversity of elementary reactions of the organometallic precursors M1R1 and M2R2 during cluster formation. More details and examples are described in the text. [Reprinted (adapted) with permission from M. Schütz, C. Gemel, M. Muhr, C. Jandl, S. Kahlal, J. Y. Saillard and R. A. Fischer, Exploring Cu/Al cluster growth and reactivity: From embryonic building blocks to intermetalloid, open-shell superatoms. Chem. Sci. 2021, 12, 6588-6599. Copyright 2021. Published by the Royal Society of Chemistry. Link: https://pubs.rsc.org/en/content/articlehtml/2021/sc/d1sc00268f.]

The flexibility of many metals in undergoing changes in coordination environment in addition to ligand exchange processes and equilibria often leads to broad product distributions, which are also strongly dependent on reaction parameters (*"living*

libraries").[134] As a consequence, and due to the poor structural analogies between precursor compounds and products obtained, cluster formation mechanisms, be it in the bottom-up or in the top-down approach, have largely remained unexplored up to now.[134] This is in striking contrast to organic or biochemical transformations, for which a large repertoire of well-studied reactions usually enables (more or less) controlled and rational construction of molecular architectures, *e.g.* by retrosynthetic approaches. To date, understanding of cluster growth mechanisms has mainly been based on single-crystal structure analysis of certain intermediates and products formed under specific reaction conditions and on quantum-chemical calculations.[134] An example is the reaction of [Cu(OAc)] with bis(trimethylsilyl)selenium in the presence of phosphines, producing a wide variety of Cu/Se clusters with high dependency on reaction conditions.[140] From some of these reaction solutions, cluster species have been isolated and structurally characterized. Also, the formation of Al clusters from Al(I) halide solutions is very much dependent on the conditions applied (*vide supra*).[70] In all these cases, any insight into the species formed is mainly gained by trial-and-error experiments with the aim to obtain single crystals for Xray diffraction. For clusters of the noble metals (Au, Ag or Pd), some alternate methods have been developed based on chromatographic separation of complex reaction mixtures and subsequent mass-spectrometric analysis, similar to approaches in organic or biochemistry (HPLC-MS).[141-143]

1.4 How to deal with multidimensional complexity

All the approaches in molecular cluster chemistry presented above seek to circumvent the complexity occurring in solution, either by complex separation or crystallization techniques or by the tedious search of conditions favoring only one product species. In striking contrast, strategies to work with complex "libraries" in solution is well known from biochemistry, where complex mixtures of proteins ("proteom analysis") are analyzed mainly by mass-spectrometric techniques accompanied by SC-Xray analysis of certain protein species (if possible).[144-145] Interestingly, also in material science, dealing with complex and dynamic (but not living!) systems is well known.[146] For a better conceptual overview of the methods and concepts relevant for this dissertation, strategies how to deal with multidimensional complexity from related disciplines will be explained in the following chapters. Due to their key importance for this dissertation, the focus will thereby lie on mass-spectrometric techniques.

1.4.1 Apparative aspects of mass-spectrometry

Mass spectrometric analysis is carried out in gas-phase, under UHV conditions and with charged analytes. A mass-spectrometer therefore consists of an ion-source, a mass-analyzer analyzing the m/z ratio and a detector registering the number of ions at a certain m/z value.

In biochemical research, the most common ion sources are ESI (electrospray ionization) and MALDI (matrix assisted laser desorption).[145] The ionization principles are illustrated in Figure 19. ESI ionizes the sample out of solution in a spray-chamber by application of a spray voltage, leading to highly charged droplets undergoing Coulomb explosions (see Figure 19 a)). Evaporation of solvent leads to charged analyte ions, which are introduced to the mass analyzer. However, in ESI, ionization is in principle only possible for analytes that are ionizable in solution, *e.g.* by protonation, which is hard for neutral molecules without any protonation sites, such as heteroatoms.[147] In MALDI, the analyte is sublimed and ionized out of a solid matrix by application of laser pulses. (see Figure 19 b)), [145] LIFDI ionization (liquid injection field desorption) is a very soft ionization technique, especially suited for organometallic analytes bearing weakly bound ligands such as olefins.[148] The ionization principle of LIFDI-MS is closely related to field desorption (FD), an ionization technique developed for low-polarity, non-ionic analytes. The analyte is deposed on a whisker-bearing metal wire ("activated emitter"), which is brought into high electric potentials of 10-12 kV against a counter electrode (~2 mm distance).[148] The analyte is thereafter ionized by electron tunneling into the emitter wire and immediately accelerated into the mass analyzer by the applied electric field.[148] In LIFDI, the emitter is placed under vacuum and the analyte is introduced under inert conditions by means of an injection capillary (see Figure 19 c) for illustration). LIFDI has several advantages over "normal" FD mass spectrometry: Not only can the analyte be transferred under inert conditions, but also enhanced reproducibility and faster measurement cycles are achieved.[148] There have been developed some modifications of LIFDI, *e.g.* continuous flow measurements, in which the analyte is applied continuously *via* capillary during application of the ionizing voltage. For example, analytes occurring in very small concentrations in crude oil fractions could be analyzed by this approach.[147]

As mass-analyzers, usually TOF (time of flight) analyzers, ion traps, quadrupoles, ion cyclotron resonance analyzers or orbitrap mass analyzers are used. Three of the most popular analyzers are schematically shown in Figure 20.

1. Introduction
1.4 How to deal with multidimensional complexity

In TOF instruments (see Figure 20 a)), the ions are accelerated to equal, high kinetic energy in an electric field and then separated according to their reached velocities in a flight tube (velocity is thereby indirectly proportional to m/z).[145] A quadrupole mass spectrometer selects ions of specific m/z ratio by varying an electric field between four rods leading to an unstable trajectory and to exclusion of ions with alternate m/z (see Figure 20 b)).[145] Similarly, ions of specific m/z are selected and stored in ion traps or ion cyclotron analyzers by application of electric or strong magnetic fields.

A rather new type of analyzer is the orbitrap analyzer, which has also been used in this dissertation. Ion packages are collected by a C-trap (ion trap) and are subsequently injected into the orbitrap. The orbitrap itself consists of an inner, spindle-like electrode embedded into an outer, barrel-like counter electrode.[149] Ions of specific m/z ratio are accelerated into helical trajectories around the inner electrode. The rotational frequency around the z-axis is thereby indicative of the m/z ratio of the ions and the image current can be read out and subjected to Fourier-transformation analysis, allowing for data analysis and mass spectrum generation.[149] The orbitrap analyzer is schematically shown in Figure 20 c).

1. Introduction
1.4 How to deal with multidimensional complexity
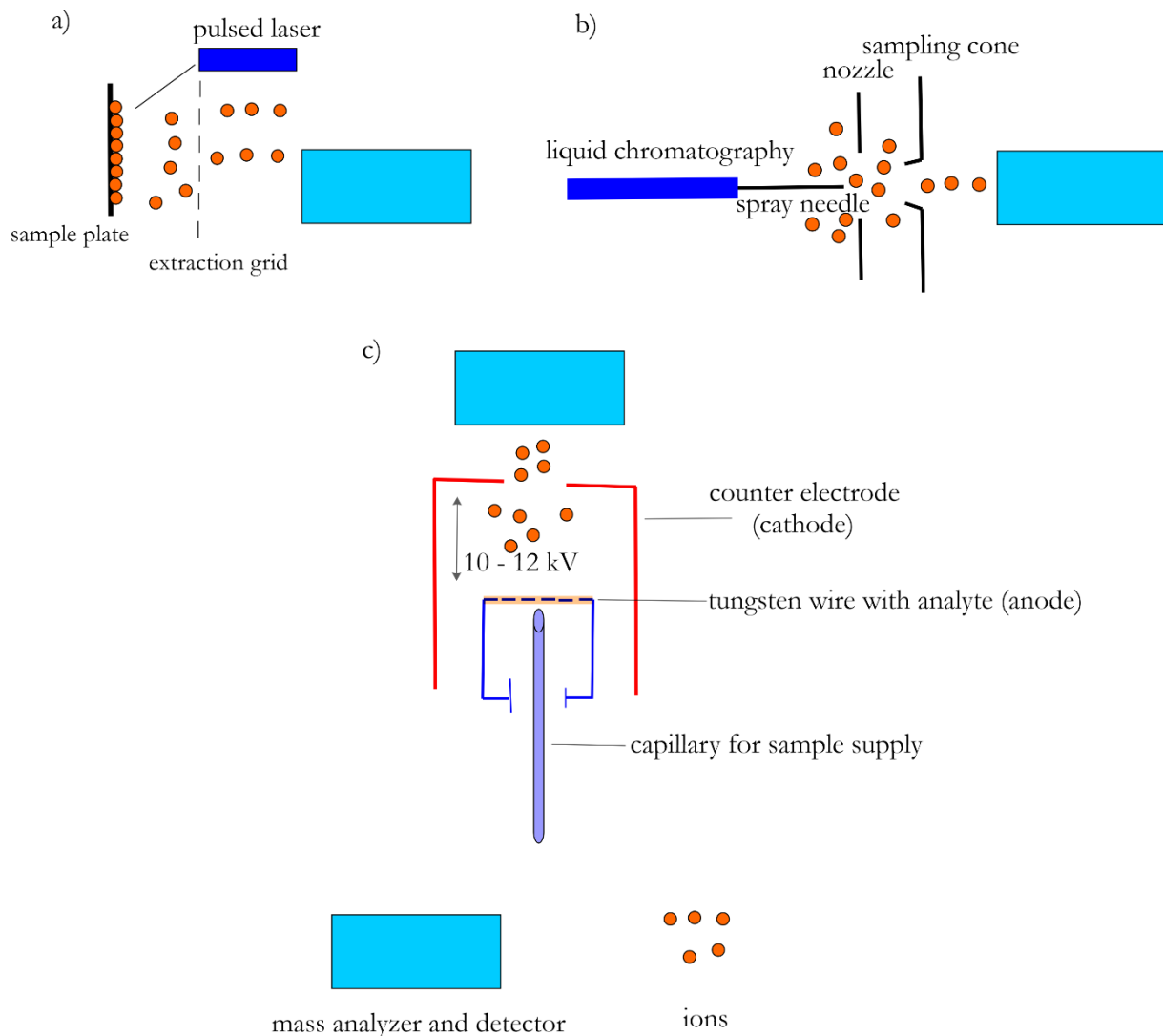
Figure 19
Schematic representation of different ion-sources in mass spectrometry. a) Matrix Assisted Laser Desorption (MALDI). b) Electro-Spray Ionization (ESI). c) Liquid Injection Field Desorption (LIFDI). [Own figure based on literature.[145]]

To obtain information not only about the overall m/z ratio in protein mixtures, but also about structural aspects (sequencing), MS/MS analysis is carried out. In these experiments, ions of interest with particular m/z are selected in an ion-trap, a TOF analyzer or a quadrupole, subsequently fragmentated by *collision induced fragmentation* (CID) and the fragments analyzed by the second mass analyzer (see Figure 21).[144] The peak pattern in the MS/MS spectra of proteins are not directly transferable to an amino-acid sequence but scanned against a protein sequence database using different "matching algorithms".[144]

1. Introduction

1.4 How to deal with multidimensional complexity

a)

defined inlet time

t

reflectron

b)

Q1   Q2

c)

outer electrode

inner electrode

ions   detector
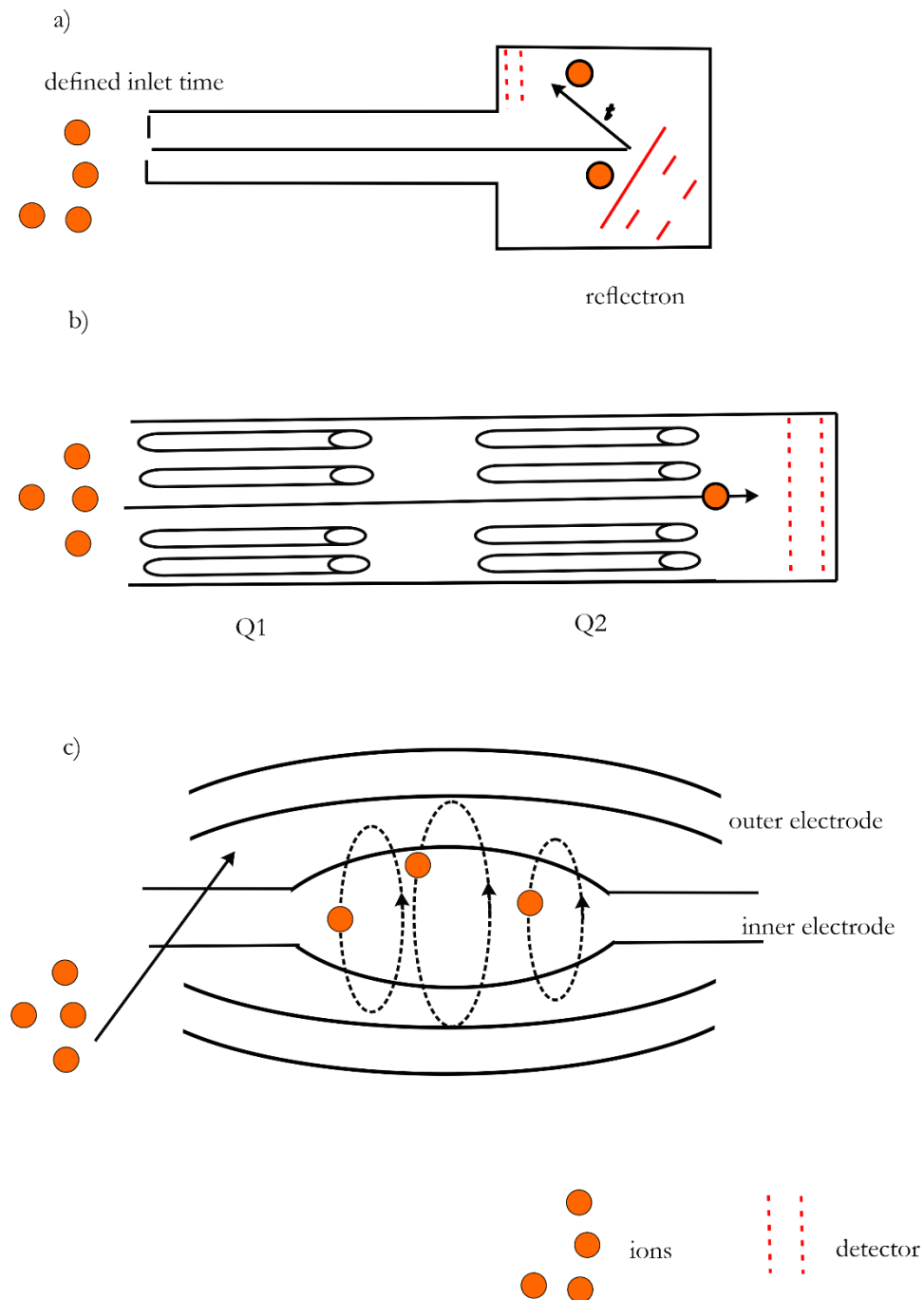
Figure 20

a) Schematic representation of a time-of-flight analyzer (TOF).[145] b) Schematic representation of a triple quadrupole (Q1 and Q2) mass spectrometer with ion trap/collision cell (Q2).[145] c) Schematic representation of an orbitrap mass analyzer consisting of outer an inner electrode. Ion packages collected in a C-trap are injected in the direction marked by the red arrow and spread into trajectories around the inner electrode according to their m/z ratio.[149] [Own Figure based on literature.[145, 149]]

There exist several strategies for protein identification and for the establishment of a protein/precursor-fragment relationship. MS2 can be fixed to a certain fragment and MS1 scanned for all precursor ions generating this fragment. Also, the mass

difference between ions in MS1 and MS2 can be kept constant, enabling search for a specific neutral fragment / a specific functional group in the analyte ("neutral loss scanning").[144] Searching for specific proteins with known fragmentation properties is possible by keeping MS1 and MS2 fixed at a certain precursor-fragment pair and recording the signal intensity against time (*e.g.* during chromatographic experiments).[144]
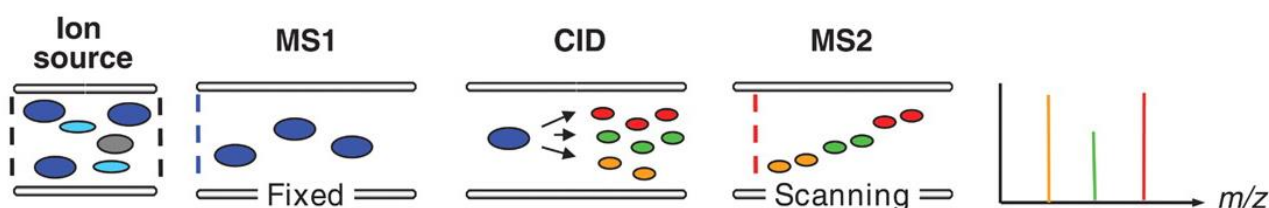

Figure 21

Schematic representation of a typical MS/MS experiment. [From B. Domon, R. Aebersold, Science, 2006, 312, 5771, 212-217. Reprinted with permission from AAAS.]

A more recent technology is the combination of an orbitrap analyzer with a higher energy C-trap for dissociation (HCD cell). Fragmentation is therein achieved by applying increased radiofrequency voltages to the ion packages in the C-trap, leading to higher collision energies with the collision gas in the chamber (usually <1 mbar N_2). [150] Applying these radiofrequency voltages, the ions oscillate around the poles of the octopole with higher amplitude and kinetic energy. Consequently, they *collide with higher kinetic energy* with the inert gas molecules. It can be assumed that despite the ions travelling a longer path in the collision cell at higher collision energies, the number of collisions is only marginally affected due to the low pressure in the HCD cell.

In principle, the procedure does not require an additional collision cell, as the C-trap inherent to orbitrap analyzers can be used for fragmentation. However, the ion trapping efficiency is increased by using an additional octopole as HCD-cell.[150] The alignment of components is shown schematically in Figure 22 a). The set-up can be used with or without an additional linear ion trap (LTQ) prior to the C-trap. LTQ enables selection of specific precursor ions for fragmentation experiments (MS/MS mode). If no LTQ is available, MS scans of precursor ions are performed by injection of accumulated ions from the C-trap to the orbitrap analyzer. *All ion fragmentation* in instruments without LTQ concerns the fragmentation of all accumulated ions in the HCD cell before the generated fragment ions are moved back to the C-trap and the orbitrap for analysis.[151]

1. Introduction

1.4 How to deal with multidimensional complexity

The HCD-cell/orbitrap system is able to detect certain marker fragments of proteins at medium fragmentation energies and in parallel to all other peptide-sequence related ions; a fact which was in certain cases hard to realize with alternate setups. [150]
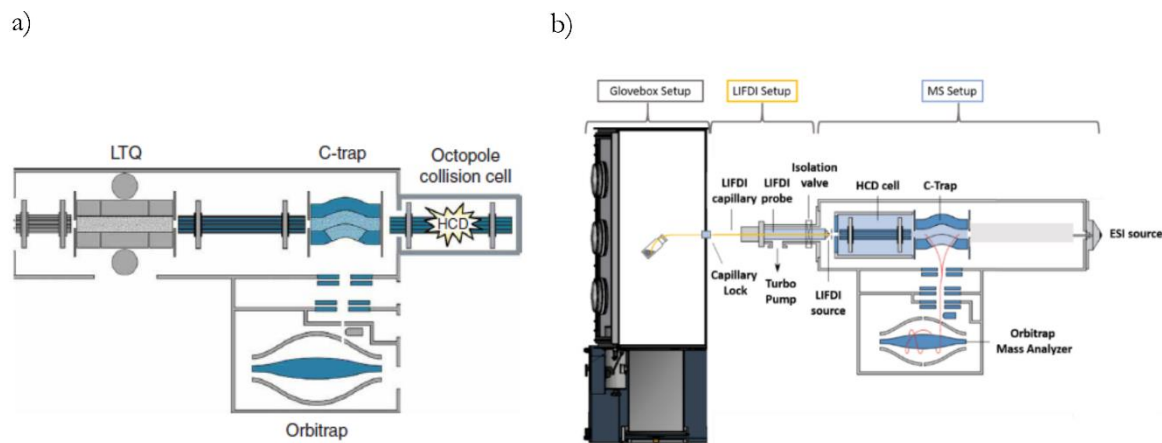

Figure 22

a) Schematic drawing of a hybrid linear-ion trap (LTQ) orbitrap system used for de novo protein sequencing. Precursor ions are selected in the linear ion trap, accelerated in the transport octupole and accumulated in the C-trap. Higher energy collision dissociation is either accomplished directly in the C-trap or in an additional octupole collision cell. [Reprinted with permission from J. V. Olsen, B. Macek, O. Lange, A. Makarov, S. Horning, M. Mann, Nature methods, 2007, 4, 9, 409-712. Copyright 2007, Springer Nature.] b) Set-up used in this work: Combination of an orbitrap mass-analyzer with an LIFDI and an ESI ions-source. The set-up does not include any ion-trap for mass-selection of specific precursor ions. [Reproduced (adapted) from M. Muhr, P. Heiss, M. Schütz, C. Gemel, M. H. Linden, H. B. Linden and R. A. Fischer, Dalton Trans. 2021, 50, 9031-9036 with permission from the Royal Society of Chemistry. Copyright 2021. Published by the Royal Society of Chemistry.]

In this work, a HCD-cell/orbitrap system equipped with a LIFDI ion source in an inert-gas glovebox will be used, which is depicted in Figure 22 b). There are two major differences to the set-up shown in Figure 22 a). First, the used set-up consists only of one single orbitrap analyzer without LTQ (MS mode); therefore, no isolation of precursor ions prior to fragmentation is possible. Second, ions generated by the LIFDI-source necessarily pass the HCD cell on their way to the C-trap. Noteworthy, the collision energy (CE) in the HCD cell cannot be set to zero, rather its lowest normalized value is 10.

1.4.2 Mass-spectrometric methods in proteome research

General approaches

There are basically two different objectives to be addressed in proteome/protein research, namely the identification of proteins in a complex sample, such as cell organelles or cell fractions, or the analysis of posttranslational modifications of a certain protein.[144] The underlying complexity in terms of mixtures of different proteins in a sample can be addressed in different ways.
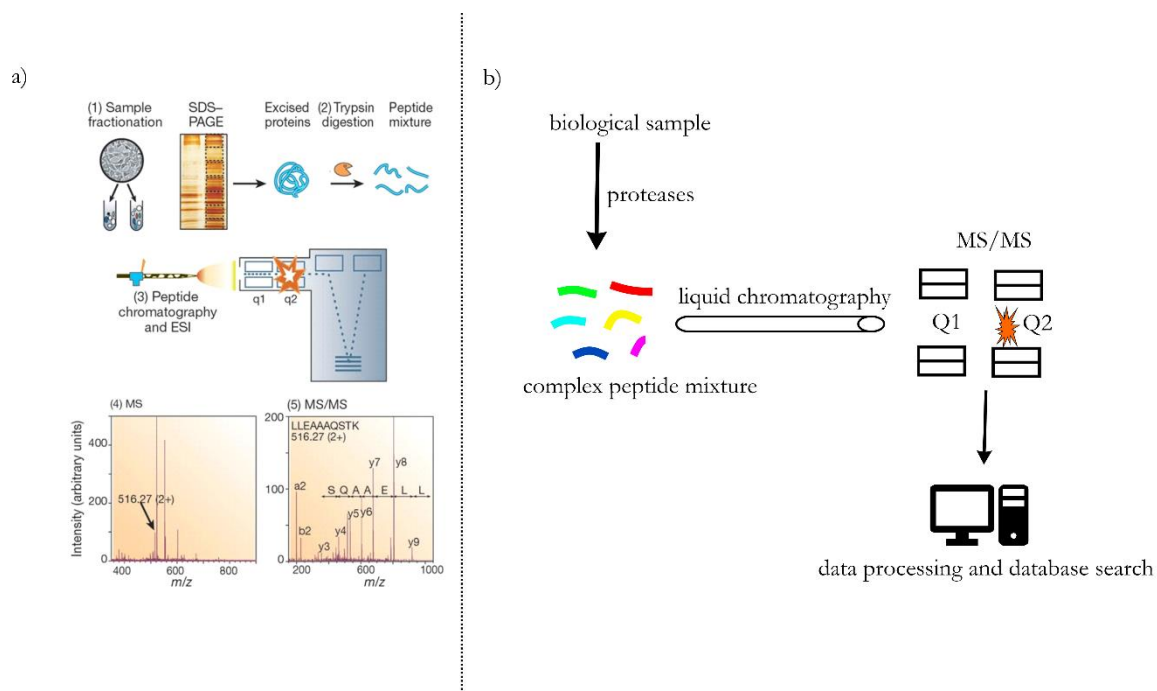

Figure 23
a) Original proteomics approach: Peptide fractionation by gel-electrophoresis MS/MS analysis of digested proteins.[145] [Reprinted with permission from R. Aebersold, M. Mann, Nature, 2003, 422, 6928, 198-207. Copyright 2003, Springer Nature.] b) Shotgun Proteomics approach: Direct digestion of complex biological samples and MS/MS analysis.[152] [Own Figure based on literature.[152]]

In the original proteomic approach, a mixture is initially separated by gel electrophoresis (SDS-page) and individual spots of the page – referring to a single, now "purified" protein – are subsequentially subjected to MS analysis after trypsin digestion (in this case normally MALDI-TOF).[144-145] The procedure is illustrated in Figure 23 a). The amino-acid sequence of each protein fragment after digestion is thereafter determined by the fragmentation behavior in MS/MS experiments. Due to the required protein separation and purification, however, sample throughput is

limited and the complexity of the systems to be analyzed is restricted to cases, in which sufficient separation by electrophoretic methods can be achieved.[144]

An alternate approach, referred to as "shotgun proteomics", allows for a direct and rapid analysis of proteins within a complex mixture with the possibility to monitor the system quantitatively and qualitatively (see Figure 23 b)).[144, 152-153] Complex protein assemblies are thereby digested by proteases and subjected to LC (liquid chromatography)-MS/MS. The digested peptide mixture is applied to a microcapillary column (*e.g.* consisting of a single cation exchange resin and a reverse-phase silica column).[152] The column outlet is directly connected to a micro-electrospray MS source. Peptide fractions eluted from the column are analyzed by MS/MS and the spectra are analyzed by a database to identify the proteins. Quantification of different proteins in separate samples is possible by different labeling strategies, outlined in the subsequent paragraph. By labeling with stable isotopes, signal intensities of native and labeled protein peaks in MS spectra can be analyzed for quantitative information. Alternatively, internal protein standards with isotope labels can be used for absolute quantification of a peptide in a sample. Drawbacks of the shotgun approach are the enormous complexity of the spectra and interference effects of different protein/peptide sequences.[144]

Some studies have been reported for shotgun protein analysis in MS instruments with higher collisional dissociation in Q-Exactive (orbitrap) instruments.[151, 154] In these approaches, the collisional energy is stepped to different values and the intensities of the ion peaks is determined for each collisional energy. From the resulting profiles (see Figure 24) it is easy to conclude how the fragmentation of the peptide is controlled by the energy applied. For example, further (additional) fragmentation of fragment ions at elevated collision energies can easily be concluded from maxima in the corresponding I (peak intensity) *vs.* CE plots at medium CE values.[154] If the procedure is applied to protein mixtures, the retention time from chromatographic separation is considered as additional parameter. Given the fact that fragment ions must possess an identical elution time as their parent ions, identification of mixture components is possible.[151]

Another approach in proteome analysis is the comparative pattern analysis, in which identification and quantification are decoupled. Peptides that quantitatively differ between samples are detected by their MS1 patterns after HPLC separation.[144] They are thereby characterized by their m/z ratio and their chromatographic retention time. Target proteins of quantitative interest are subsequently subjected to MS/MS analysis for sequencing. Specific, predetermined proteins of interest can also be searched for in MS1 spectra of a peptide mixture by searching for specific and characteristic peptide "profiles". Quantification of these proteins is possible by

addition of internal (isotopic labeled) standards. The latter approach is also called "hypothesis driven proteome analysis".[144]
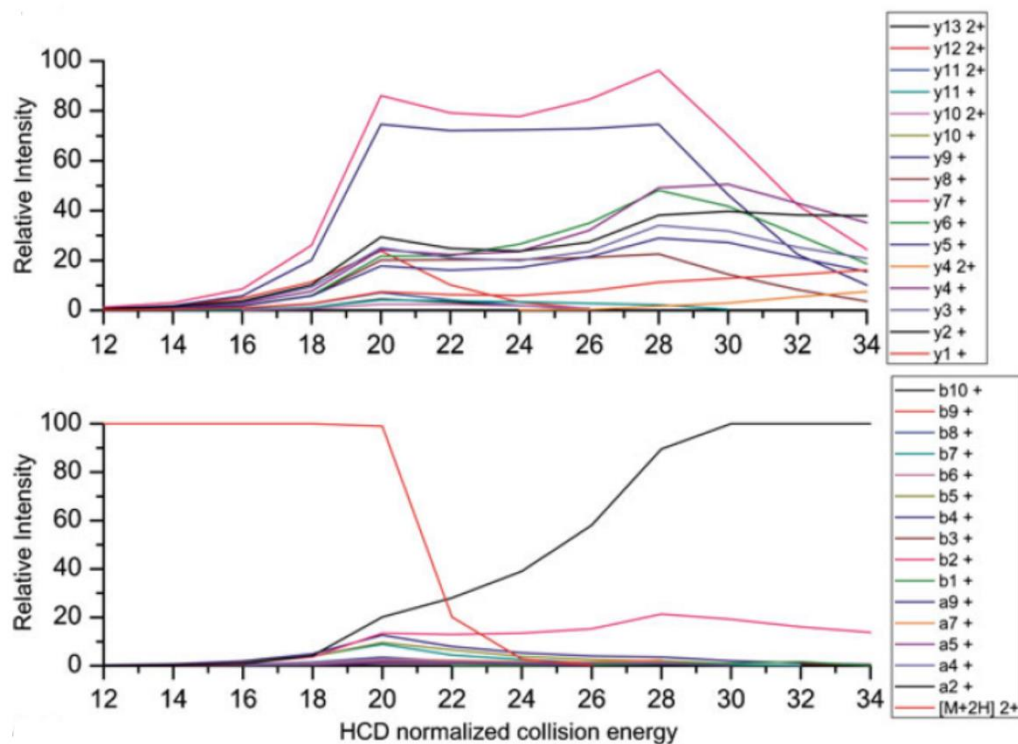

Figure 24

Fragment ions and molecular ion peak ([M+2H]$^{2+}$) of the peptide ELGQAGVDTYLQTK as determined by stepped collision energy experiments with a HCD-cell/orbitrap set-up. The intensity of [M+2H]$^{2+}$ is steadily decreasing at high collision energies (here: M = molecular parent ion). Initial fragment ions such as y_7 or y_9 show a plateau in intensity at CE 19-30 (upper graph) before they are themselves prone to fragmentation producing the smaller fragment ions y_6, y_5, y_4, and y_3. Some ions, such as a_2 and b_2 might be formed by multiple degradation pathways or be extraordinarily stable as they maintain high intensity even at elevated collision energies (lower graph). [Reprinted with permission from J. K. Diedrich, A. F. M. Pinto, J. R. Yates, Journal of the American Society for Mass Spectrometry, 2013, 24, 11, 1690-1699. Copyright 2013, American Society for Mass Spectrometry.]

Isotopic labeling in mass spectrometry

Isotopic labeling in mass spectrometry has mainly been used for quantification aspects. In general, mass spectrometry is a poor quantitative method.[145] The mass-spectrometric response and sensitivity is dependent on several physicochemical properties of the analyte, such as ionizability, size or charge.[155] However,

quantification is possible by comparing signal intensities of analyte peaks with and without stable isotope label, assuming that the isotopic label does not influence the physicochemical properties.[155]

In biochemistry, quantitative information about the abundancy of a specific peptide is therefore achieved by different labeling strategies. The isotopic label can be introduced to the peptides of interest metabolically, chemically or enzymatically.[144] The labeled samples are mixed with unlabeled ones in a known ratio and the mixture is subjected either to survey MS analysis (SILAC = stable isotope labelling by amino acids in cell culture) or to tandem MS/MS analysis (iTRAQ = isobaric tag for relative and absolute quantification).[155]

The SILAC procedure is illustrated in Figure 25. Enzymes are either labeled by growth of cells in isotopically enriched media, by tagging them chemically with isotopically enriched reagents or by proteolysis in ^{18}O enriched water.[145] The samples are subsequently combined and analyzed by MS or MS/MS for identification and quantification. The peaks can be arranged into two groups, stemming from labeled and unlabeled proteins, whereby the mass difference is dependent on the isotopic tag, the tagging method and the amino acid sequence of the protein.[145] It usually is multiple times the mass difference encoded in the isotopic tag, depending on how often the tag is incorporated into the fragment. Signal intensities of the peak pairs can be compared directly for quantification.

One drawback of the SILAC method is the fact that despite labeled and unlabeled proteins having similar physicochemical properties and ionizabilities, their retention times in chromatography might be slightly different, leading to problems in LC-MS/MS experiments.[156]

A method circumventing this problem is iTRAQ, in which isobaric tags (tags of the same mass) are introduced in the labelling process.[155-156] The tags consist of two isotopically enriched elements having in total the same overall mass in all tags used. Up to four different peptide samples are labeled with the isobaric, tandem mass tags and mixed. The mixture can be subjected to chromatographic separation and in MS1 spectra, the peaks of all samples coincide.[155] However, upon fragmentation, the tags are split up into their isotopically different fractions ("reporter ions") in MS2 spectra allowing for quantification.[144]
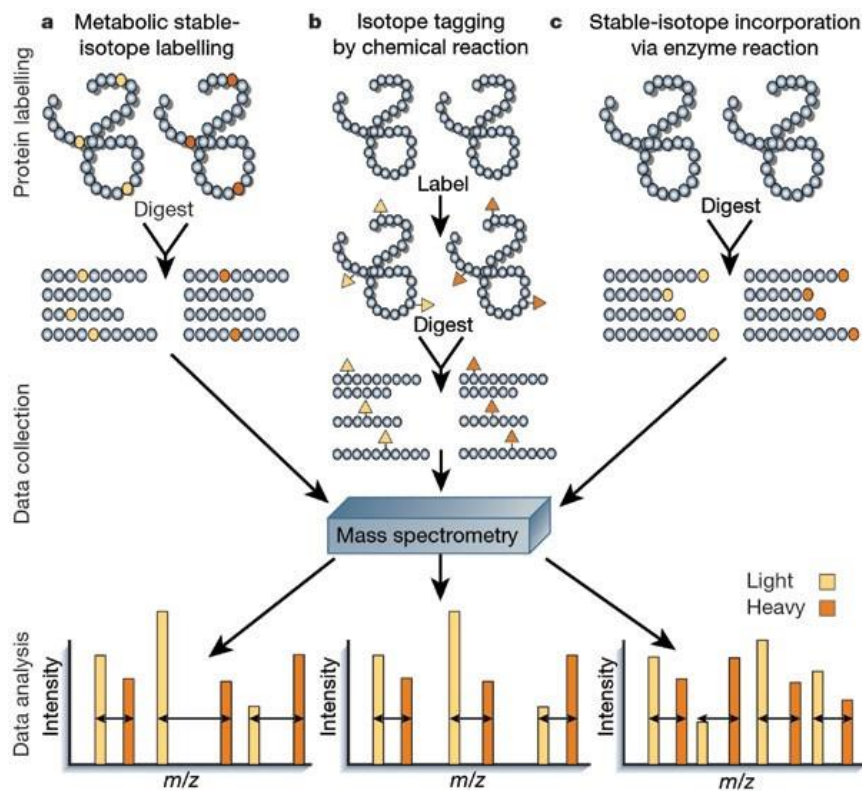
Figure 25
Stable-isotopes labeling for amino-acids (SILAC) for protein quantification. [Reprinted with permission from R. Aebersold, M. Mann Nature, 2003, 422, 6928, 198-207. Copyright 2003, Springer Nature.]

A third procedure for quantification in MS is addition of isotopically labeled standard solutions to otherwise unlabeled samples (internal standard).[144]

All the methods described result in very complicated spectra, especially for complex protein mixtures. Consequently, often only a small subfraction of proteins can be identified in one analysis and statistical tools are needed for data analysis.[155]

It should be noted that isotopic labelling in mass spectrometry for quantification is not restricted to biochemical research. *Isotope Dilution Mass Spectrometry for Elemental Analysis* is a technique in inorganic mass spectrometry based on ICP (inductively coupled plasma)- MS.[157] A known amount of a certain enriched isotope is added to a sample and MS is used to measure the altered isotopic ratios, allowing for quantification of the element of interest in the original sample.[157]

1.4.3 Mass spectrometry in organometallic chemistry

Not only when it comes to cluster species, organometallic chemistry is supposed to synthetic challenges: Ligand scrambling and exchange reaction often lead to several energetically close lying product isomers and even for rather simple structures no high-yield, general synthetic procedures exist. Classical separation techniques such as LC or HPLC are often only of limited applicability due to high air- and moisture sensitivity of many compounds. Research in homogenous catalysis, however, often requires a set of possible catalyst candidates for screening, the synthesis of which often represents a "bottle-neck" for the research progress.[158] Even for industrially relevant homogenous catalytic systems, the active catalyst species is not clearly known, rather the system is a formulation of components with a composition focused on high catalytic activity.[158]

Several studies have tried to circumvent these problems by "pool-testing" of catalyst libraries using ESI-MS as analytical technique or by reactivity assessment of mass-selected ions in the gas-phase (ion-molecule reactions). Even though ESI is normally better suited for polar compounds, such as peptides or biomolecules, organometallic compounds can be analyzed as dilute solutions in polar solvents such as THF, acetonitrile or chlorobenzene or mixtures of polar solvents with unpolar ones such as toluene.[158] Several alternate ionization techniques have been applied for transition metal carbonyl clusters. Beside field desorption (*vide supra*), MALDI or FAB (fast atom bombardment) have been used, but with some limitations such as redox- or cluster rearrangement reactions or ion-molecule reactions in the gas-phase.[159]

Reactivity studies on organometallic compounds with ESI-MS can either be accomplished by ion-molecular reactions in a reaction/collision cell inside the mass spectrometer after ionization or by tandem ESI-MS/MS analysis of complex reaction mixtures. A typical, exemplary set-up is shown in Figure 26, showing a Q1 (quadrupole 1), O1 (octopole 1 = collision cell), Q2 (quadrupole 2) arrangement.[158] An alternate system is O1, Q1, O2, Q2, often used for ion-molecule reactions described below (O = octopole, Q = quadrupole).[160]
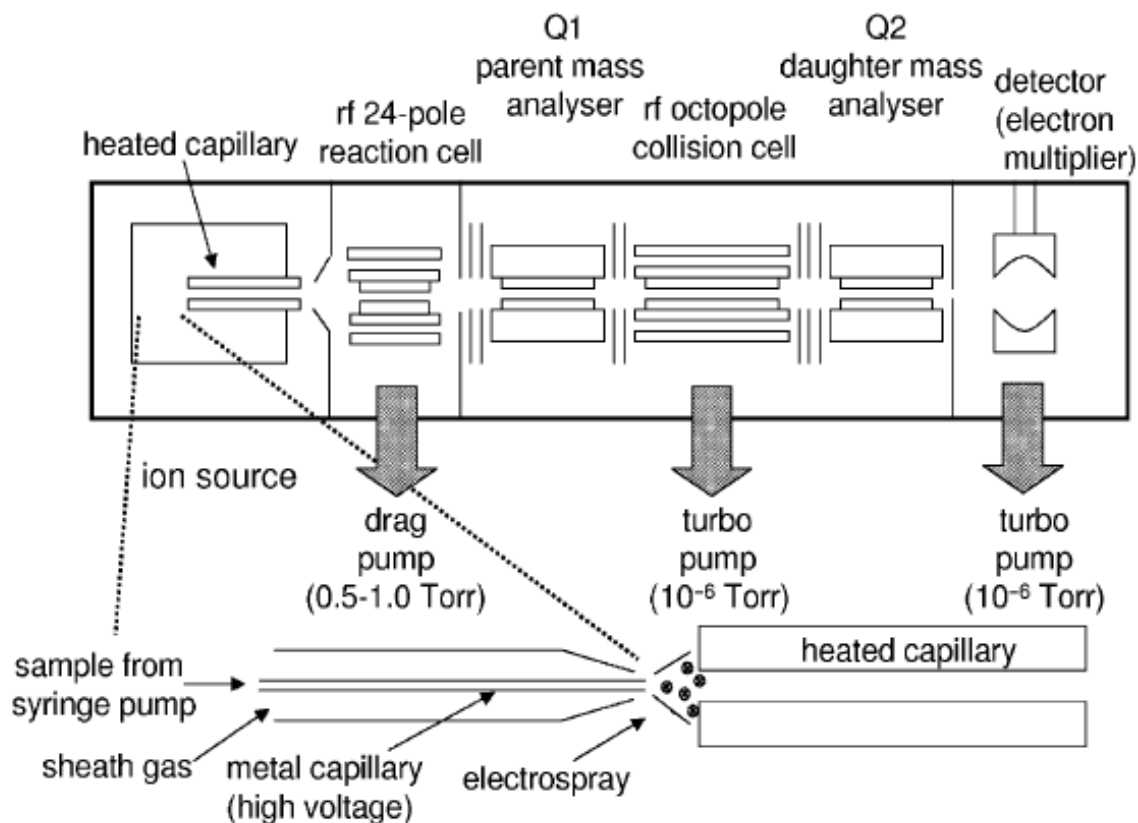
Figure 26
Typical set-up for ion-molecule reactions in an ESI-MS/MS experiment with an octupole collision cell. [Reprinted with permission from P. Chen, Angew. Chem. Int. Ed. 2003, 42, 25, 2832-2847. Copyright 2003, John Wiley and Sons.]

For ion-molecule reactions in the gas phase, the analyte is ionized by a typical electrospray procedure in a heated capillary and the solvent sphere is removed in part in the capillary and in part in the high-pressure region before the skimmer.[158] The resulting ions are analyzed in the first quadrupole mass analyzer (ESI-MS mode). For structural information, a daughter-ion spectrum is recorded (ESI-MS/MS mode), resulting in fragmentation by collision in O2. Specific fragments/ions of interest can also be produced selectively and can be induced to collide with reactant gas in O2.

For example, $[Fe(bpy)_3]^{2+}$ complexes were shown to form clusters with solvent molecules such as DMSO or DMF upon introduction of the respective solvents in the nitrogen purge during the ionization procedure.[161] The oxidation behavior of a mass-selected $[(salen)Mn(O_2)]^+$ (salen = N,N'-ethylenebis(salicylimine)) ion was investigated by collision with olefins and sulfides in O_2.[160] In another study, the C-H activation of cationic Ir(III) complexes was investigated.[162] The complex $[CpIr(PMe_3)CH_3]^+$ was shown to loose CH_4 upon high collision energies with N_2 and high tube lens potential to give $[CpIr(\eta^2\text{-}CH_2PMe_2)]^+$. When this ion was size-selected

and reacted with pentane or benzene residual pressure in the second octupole, oxidative addition to form $[CpIr(PMe_3)R]^+$ with R = C_6H_5 or C_5H_{11}) was observed. The study is of conceptual nature as it links results from the gas-phase with established reaction principles from solution - enabling a better understanding of complex and competing mechanistic processes in organometallic chemistry.[162] Ion-molecule reactions can be interpreted as a fundamental approach of dealing with "libraries" - yet in the gas-phase and not in solution - by size-selection of specific ions. It is therefore conceptually linked to the mass spectrometric investigation of naked metal clusters in the gas-phase.

"Pool-testing" of catalytic activity was accomplished by ESI-MS analysis of a library of Pd(II) catalysts for olefin metathesis. A library of 8 Pd(II) complexes with *Brookhart*-type diimine ligands was synthesized and pressurized with ethylene.[163] Analysis of the reaction product was accomplished with a ESI-MS/MS apparatus as depicted in Figure 26. The MS1 spectrum is complex, showing very broad mass envelopes due to polymer-chains of variable length bound to each Pd-complex. By mass selection of the heavier envelope and collision with Xe gas, however, the polymer was cleaved from Pd by β-hydride elimination resulting in (L)Pd-H complexes. Rapid identification of the best polymerization catalyst was possible by analysis of the MS2 spectra.[163]

In a similar experiment, a library of *Hofmann*-type Ru olefin metathesis catalyst was electro-sprayed, generating active, cationic catalyst species in the gas-phase *via* halide loss from the parent structure.[158] The ions were one after another mass-selected in Q1 and subjected to collision with vinyl ether or norbornene in the octupole with a finite and defined collision time. Analysis of the reaction products and relative intensities allows to define a figure-of-merit for catalytic activity for each of the catalyst candidates in the mixture.[158]

The analysis of intermetallic cluster mixtures in solution *via* mass-spectrometry has rarely been reported so far. The existent studies are mainly conducted on transition metal carbonyl clusters or thiolate protected clusters of the noble metals Ag and Au. A reaction mixture of four intermetallic RuCo carbonyl clusters was analyzed by ESI-MS, revealing the molecular ion peaks at low cone voltages.[164] It is noted that from these spectra, not only the molecular weight (m/z ratio), but also the cluster composition (isotopic pattern) can clearly be deduced, such as demonstrated in this dissertation (*vide infra*). Structural information was gained by applying the technique of EDESI-MS (*energy dependent* ESI-MS)[164-165]: By stepwise increasing the cone voltage, fragmentation of the ions is enhanced; creating a set of mass spectra (one for each cone voltage). The mass spectra obtained can be assembled into a map with the m/z ratio on the horizontal axis and the cone voltage on the vertical axis (see

Figure 27 for an example). [164-165] The dark ellipsoids in the 2D plot represent thereby the occurrence of a mass peak at the respective cone voltage. The peak intensities of all spectra measured can be merged by summation to result in a 1D overall mass spectrum. All the information obtained in the data sets are therefore shown in one picture. For the example presented in Figure 27, each diagonal line of peak intensities corresponds to one cluster species. Obviously, fragmentation behavior in this example is rather simple as it corresponds to the stepwise loss of carbonyl ligands.[164] The concept was conceptually transferred to the living cluster libraries investigated in this work to achieve fragment and parent ion identification (*vide infra*).
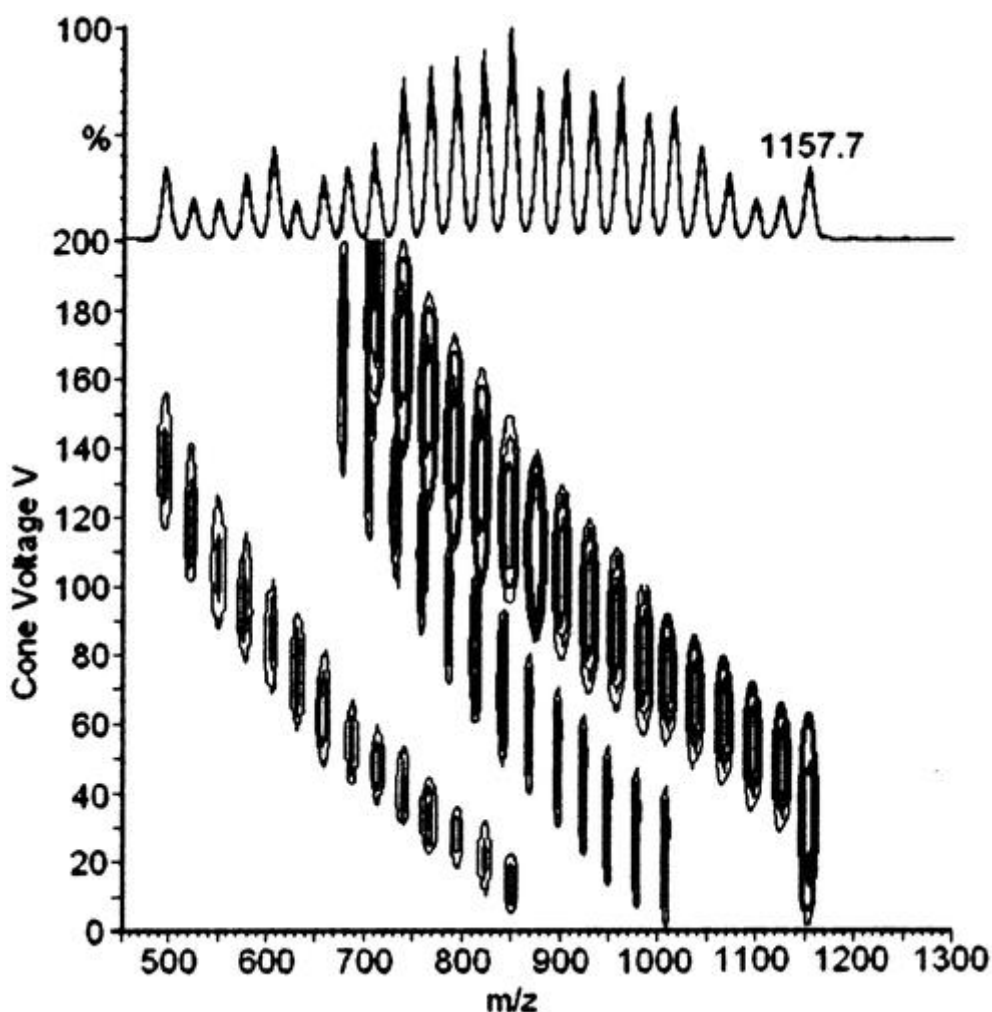

Figure 27
Data interpretation of energy-dependent ESI-MS experiments. Peak intensities at certain m/z are plotted against the respective applied cone-voltage. The upper spectrum results from summation of all measured spectra. [Reprinted with permission from P. J. Dyson, A. K. Hearley, B. FG. Johnson, T. Khimyak, J. S. McIndoe, P. RR. Langridge-Smith, Organometallics, 2001, 20, 19, 3970-3974. Copyright 2001, American Chemical Society.]

Time-dependent (ESI-)MS analysis of reaction solutions in combination with UV-Vis spectroscopy was also shown to be a powerful tool to shed a light into the "black box" of ligand protected Au cluster growth. More than 20 intermediates were detected by ESI-MS in the synthesis of Au_{25} clusters from simple Au thiolates and the observed changes in composition of the solution were shown to be in accordance with UV-Vis absorption data.[53] Likewise, cluster growth from $[Au_{25}]$ to $[Au_{44}]$ was elucidated by ESI-MS.[166] Very similar investigations were undertaken for the growth of Ag clusters[167] and for ligand exchange stimulated cluster conversion reactions from $[Ag_{44}]$ to $[Ag_{25}]$.[168]

It has to be noted that libraries of monometallic complexes and clusters are supposed to be less dynamic and less reactive to perturbations than libraries of intermetalloid clusters due to more defined coordination modes of the ligands, and the fact that only one metal is involved. Further, any reactivity observed in the gas-phase, *e.g.* by ion-molecule reactions, must be tested and verified in solution.

Nevertheless, the methods presented above illustrate a way how to deal and even benefit from the high complexity of organometallic reactions: Instead of synthesizing pure compounds prior to any reactivity assessment, libraries/mixtures of possible candidates can be analyzed in parallel by mass-spectrometric methods.[158] For noble metal clusters, chromatographic separation techniques[169] in combination with (time-dependent) mass spectrometry (MALDI and ESI) have already been shown to be valuable tools for identification of species[143], structure elucidation (isomerism)[142-143] and fundamental understanding of mechanistic principles[53]. Consequently, the question arises whether these methods can also be transferred to more sensitive and dynamic systems.

1.4.4 Libraries in combinatorial chemistry

As mentioned previously, the conceptual idea of working with libraries of species and with multidimensional complexity is generally not new but known from biochemistry, pharmaceutical research and from material science. Search for a new lead structure in pharmaceutics or of a novel catalyst candidate usually requires a tedious screening process, often based on serendipity, chemical intuition and empirical knowledge or hypotheses.[170-171] In pharmaceutical research, rational design of a novel drug is nowadays in principle possible by knowledge about the molecular background of many diseases. Nevertheless, a plethora of possible structures has to be tested for their usefulness and the synthesis rather than the testing often represent the bottle-neck of any research activity.[170] In catalysis, multidimensional complexity is defined by a complex interplay of parameter dependencies, such as solvent, additives, temperature and (electronic) structure of the ligand.[172] In this context,

combinatorial chemistry has developed as a tool to overcome the obstacles of repetitive and highly time-consuming test processes.

Instead of synthesizing *one compound after another*, many species of similar structure are generated *at once*, either in a mixture or in parallel (*e.g.* in a microtiter plate or by an automated system).[170, 172] It is noted that the background for this concept is given by nature itself: By only 20 amino-acids as building blocks, an immense "library" of peptide structures with different structures and physiological properties is accessible![170]

1.4.4.1 Combinatorial approaches in bio- and organic chemistry

General combinatorial strategies

In the so called *"split and mix"* approach, a mixture of species is produced by sequential reaction steps followed by splitting and mixing ending up with "libraries" containing every species in equimolar portions (see Figure 28 for illustration). The libraries are thereafter subjected to pharmaceutical or catalytic tests. However, the task is to identify the active species in the solution afterwards by "decoding" or "deconvolution" and by comparing the results of different libraries with similar composition. Deconvolution strategies ("backsearching") were presented by *Furka et al.* for libraries of peptides and oligonucleotides.[170, 173] If a peptide library consists for example out of a tetrapeptide in which every position can be occupied by 5 different aminoacids, there are 5^4 library members.[174] Finding the active one is accomplished by synthesizing 25 distinct libraries à 25 members, each with a defined combination A-B of the first two aminoacids. The most active of these libraries gives the "best" combination of A and B. Search for optimal aminoacid C is done by generating five libraries ABC^nD^{1-5} (n = 1-5). Each of them consists out of 5 members and each library has a fixed amino acid C. The most active one gives the optimal sequence ABC. The optimal residue D is found in the last round of deconvolution by generating again 5 libraries $ABCD^n$ (n = 1-5) and determination of the most active one.[174]

In an alternate procedure, called *recursive deconvolution*, an aliquot of each component is taken before mixing. These component libraries are used for the "backsearching" process saving the time and effort for new synthesis.[170] Another approach used for determination of the most active library member is called *"positional scanning"*. In this approach, n x m sub-libraries with fixed residues at the position m are generated for a peptide consisting of m aminoacids with n different amino acids used for each

position. Identification of active sub-libraries allows for determination of the most active amino-acid sequence by combinatorics.[170] Fast procedures for library generation and for testing have to be available in order to be the searching mechanisms efficient. Besides mass-spectrometric analysis of protein and catalyst mixtures, multiple strategies and methods dealing with such a high degree of complexity have been developed (*e.g.* high-throughput HPLC, UV-VIS, gel electrophoresis). Automation of synthetic procedures and of mixing (robotics) has also been and still is an important step in the development of combinatorial chemistry.[170, 172, 175]

Prerequisites for combinatorial synthesis and advanced methods

The methods presented above require several prerequisites for the libraries, their building blocks and the chemical reactions used in synthesis of the libraries.[170] The first and inherent prerequisite for any successful decoding is that the library members *do not affect each other* in terms of their catalytic activity or their pharmaceutical mode of action. The chemical reactions leading to the final product must be *sequential.* The library is designed by applying reaction sequences leading to the target molecule by *successive linkage of single building blocks.* The chemical transformations used in these reaction sequences must allow for a *high structural diversity* of the target molecules and one reaction must be *independent* of the subsequent one. These requirements are mostly met for peptides as a large structural variety is achievable simply by alternation of their amino-acid sequence. However, much work has been done to extend these principles to small organic molecules, be it in solution or on a solid support. Obviously, for metal clusters, such synthetic requirements represent a rather problematic issue due to the difficulties in their synthesis and their dynamic behavior in solution.

Different synthetic strategies might be used to fulfill the prerequisites mentioned above:[170] In the template mediated approach, the initial building block bears several sites of functionalization. Another approach is to generate new sites of modification by linkage of two building blocks. Anchoring the substrate on a solid support (beads) greatly facilitates mixing and separation procedures.[176] Further, the identity of the library member can be encoded on the bead by an independent chemical tag.

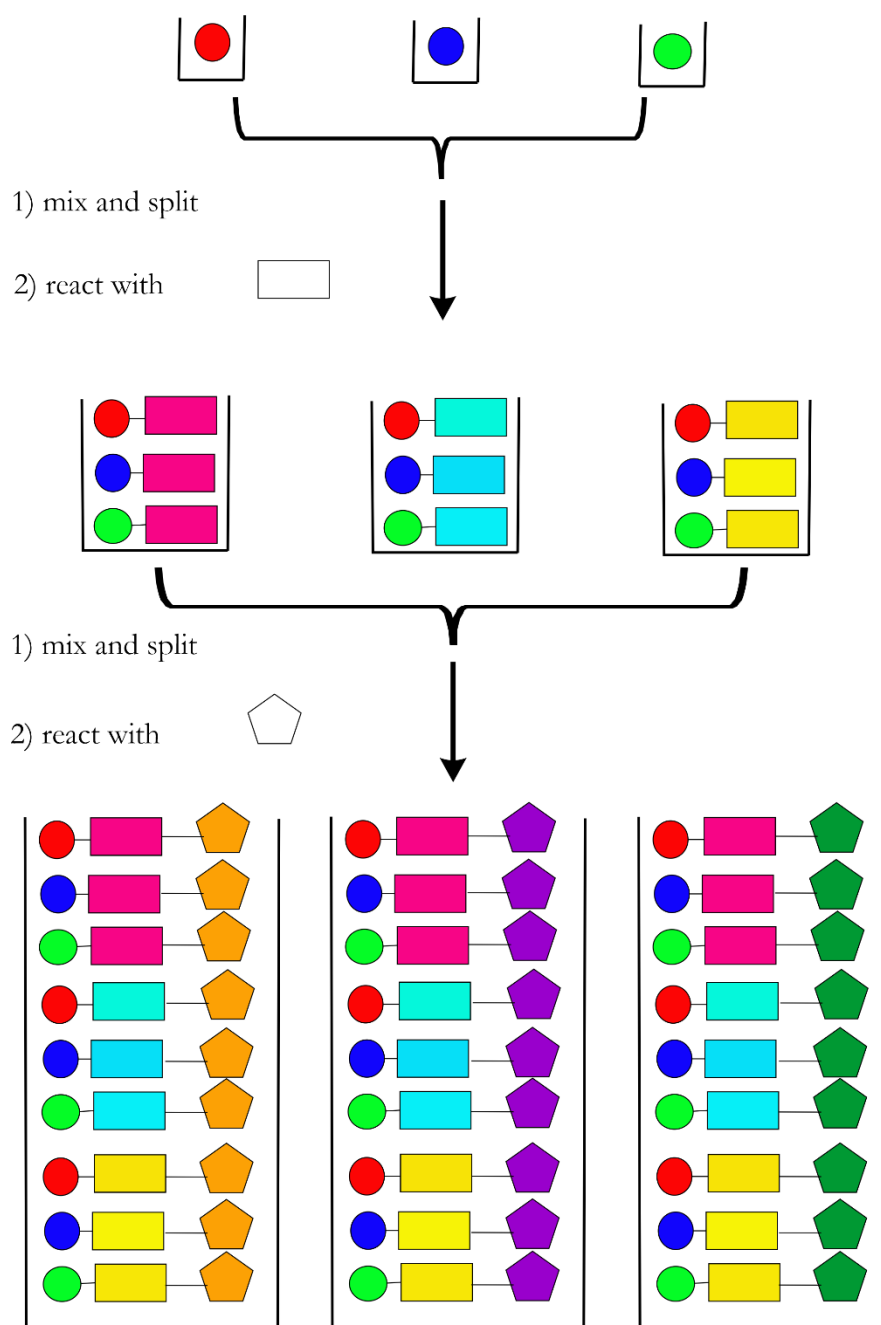# 1. Introduction

1.4 How to deal with multidimensional complexity

Figure 28

Schematic generation of libraries in combinatorial chemistry by the split and mix method.[170] In the final libraries, every compound occurs in equimolar portions. After test reactions, the active library member is identified by backsearching strategies (see text for details). [Own figure based on literature.[170]]

Similar tagging of library members for better identification can be done by linking them to a DNA fragment. These DNA fragments are easily multiplied by PCR (polymerase chain reaction) and selection of specific fragments is possible *e.g.* by introduction of streptavidin binding tags.[177] In this context, the directed evolution of catalytically active enzymes has gained considerable interest (see Scheme 6).[172, 175] A catalyst library of (modified) enzymes is generated by expression of a gene pool. The library is scanned for their warranted catalytic activity and the active enzyme species

is determined (*e.g.* by the "backsearching" process mentioned above). The corresponding gene is afterwards subjected to mutagenesis and the process repeated until a high catalytic activity is achieved. The procedure is different from purely synthetic protocols as it does not involve any "design" strategy but only natural "evolution" like processes.[172]
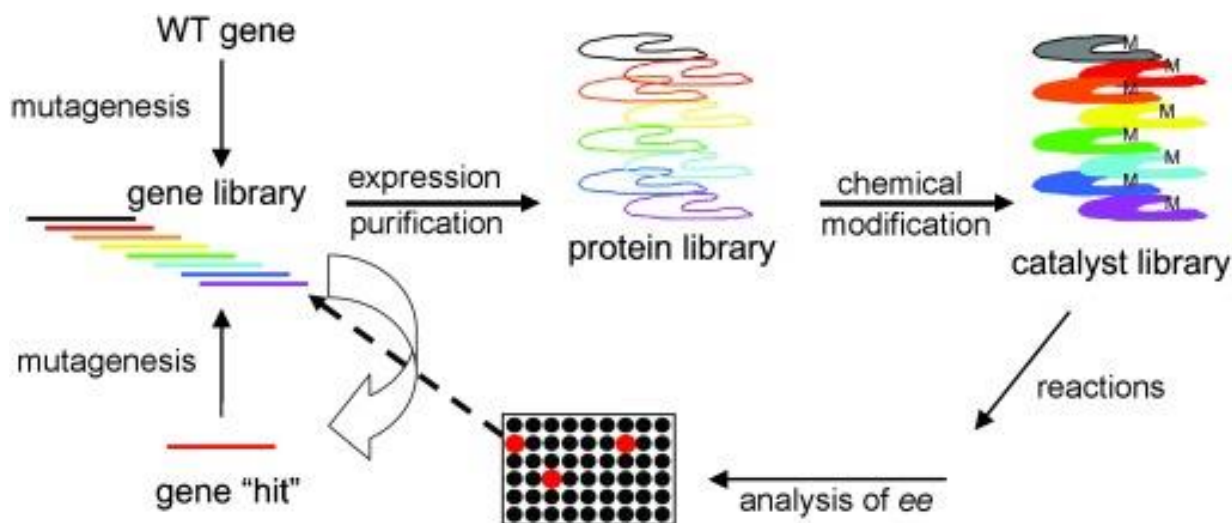
Scheme 6
Directed evolution of a catalytically active enzyme by combinatorial methods. [Reprinted with permission from M. T. Reetz, Angew. Chem. Int. Ed., 2008, 47, 14, 2556-2588. Copyright 2008, John Wiley and Sons.]

1.4.4.2 Combinatorial approaches in organometallic chemistry

In transition metal catalysis, combinatorial chemistry has mainly been employed for determination of highly active ligand structures and ligand combinations for asymmetric transformations.[171, 175] Exemplarily, two monodentate phosphine ligands are mixed together with a transition metal precursor. If the ligands are not identical, a library evolves resulting from the respective homo- and heterocombinations. The size of the resulting library/the number of possible catalyst candidates increases rapidly with increasing number of ligands tested. Instead of preparing one catalyst at a time, libraries of potential asymmetrical catalysts are prepared and tested for their catalytic activity.[175] In this approach, however, screening capacities represent the bottle-neck for exploration of the whole "chemical space" possible.[175]

1.4.4.3. Combinatorial approaches in material science and heterogenous catalysis

Several approaches have been undertaken to transfer principles of combinatorial chemistry to material science and heterogenous catalysis. Ternary inorganic materials are well suited candidates for combinatorial research.[178] In many cases, properties of a solid state material are hard to predict. Thin film libraries with up to 25000 different candidates have been prepared and tested for their luminescence properties.[178-180] The libraries were prepared on small substrates by automated deposition of the components, followed by thermal annealing process. For a promising candidate, a new library had to be constructed to explore the whole parameter space by varying the processing parameters. However, even under non-optimized conditions, considerably new knowledge can be acquired.[178] Alternatively, crystalline samples with a compositional gradient can be prepared, *e.g.* by melting or floating zone techniques, allowing for a rapid assessment of the variation of physicochemical properties with composition.[181]

In the field of heterogenous catalysis, combinatorial approaches are subject to some controversy.[182] On the one hand rapid screening of different catalyst materials in terms of their activity increases efficiency and accelerates the discovery of new materials. On the other hand, heterogenous, solid state catalysts are highly complex materials and in contrast to libraries of molecular compounds, the surface of a "pure" heterogenous catalyst has to be regarded as a library on its own: Catalytic activity is often determined not by a perfect surface (lattice plane) but rather by defects, vacancies, steps and kinks of the surface, of which the distinct nature is often unexplored. This fact hinders the generation of true "libraries" (mixtures of distinct compounds) as it would result in an inextricable and unmanageable degree of complexity.[182] Nevertheless, material databases have been constructed with the aim to enable a more conceptual catalyst design. For example, for electrocatalytic CO_2 conversion, a database was generated for Cu alloys considering phase diagrams (phase separation), surface strain effects and metal-metal oxide interfaces.[146]
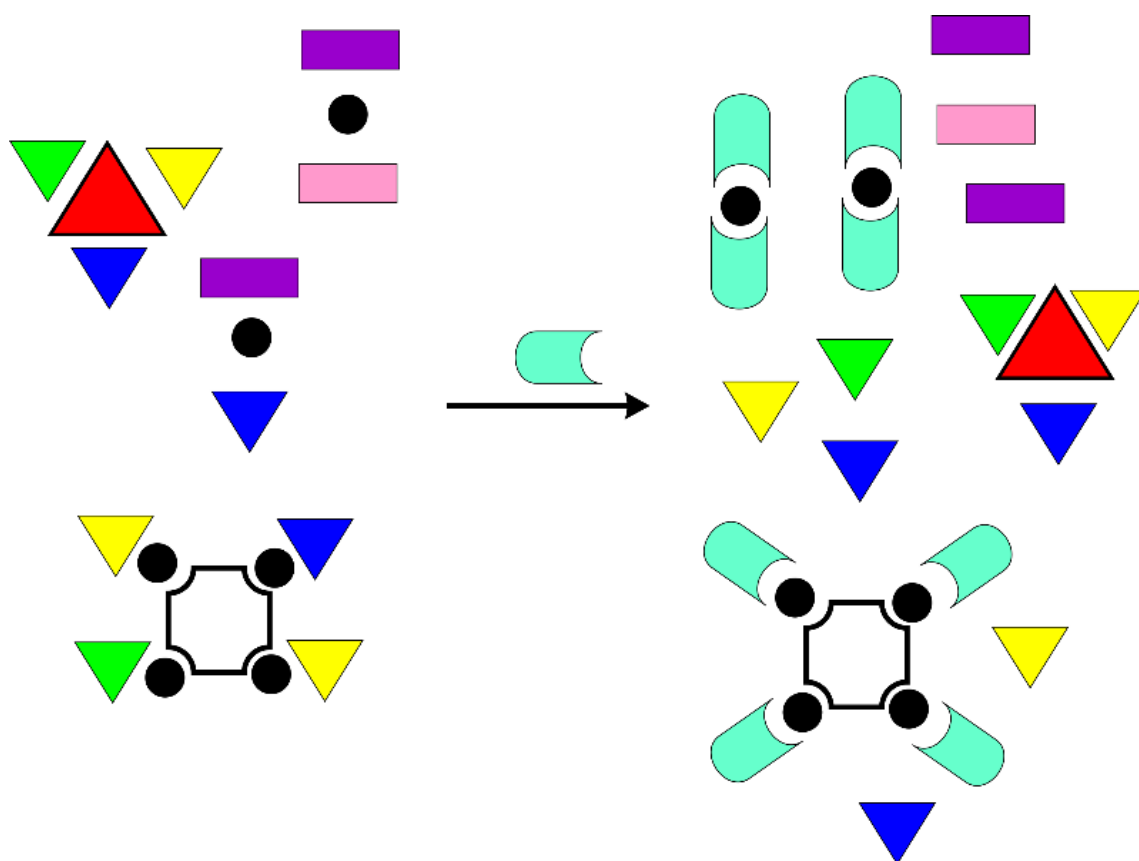
1.4.4.4 Dynamic combinatorial chemistry

A special area of combinatorial chemistry is *dynamic combinatorial chemistry*.[183-185] Dynamic combinatorial chemistry uses mixtures of compounds in thermodynamical equilibrium interconverting into each other. The species in solution are rather weakly bound assemblies connected through reversible interactions.[184] Addition of a molecular target binding to a specific component of the library causes the equilibrium to shift towards the good binder (see Scheme 7). This allows for applications in "molecular sensing", especially for biological targets.[184] Reactions leading to

generation of a dynamic library are for example disulfide exchange or alkene metathesis reactions. Co(II) terpyridine complexes $[Co(L)_2]^{2+}$ were shown to form a dynamic library upon exposure to a competing ligand L´ or a competing complex $Co(L´)_2^{2+}$.[186] In the study, the terpyridine ligand bore an aldehyde functionality at its backbone, which undergoes condensation reactions with amines. Imine exchange reactions therefore introduced a second dimension into the dynamic library. Both processes, ligand and imine exchange were shown to be independent from each other and the resulting dynamic library was therefore called an "orthogonal" library.[186] Notably, the libraries were mainly analyzed by ESI-MS and also by NMR spectroscopy. Another dynamic library was prepared from Pd(II) cage complexes with different pyridyl ligands.[187] Mixing of two cage structures $[Pd_3(L^1)_2]$ and $[Pd_3(L^2)_2]$ results in a library of homoleptic cages and heteroleptic cages ($[Pd_3(L^1L^2)_2]$). Cage formation and mixture identification was mainly conducted by NMR analysis. Addition of different receptor molecules results in changes in library composition, whereby the equilibrium is shifted towards the better acceptor cage for the respective molecule (the homo- and heteroleptic cages differ by the size of their cavity).[187]

Scheme 7
Schematic drawing of a dynamic combinatorial library consisting of different species (assemblies) in thermodynamic equilibrium. Addition of a target molecule causes a shift in equilibrium towards a good binder. [Own scheme based on literature.[185]]

1.4.5 Complexity in theoretical chemistry

As mentioned above, the evolution of physicochemical properties with size and shape of a cluster is a prominent field of research and subject to many theoretical investigations. Besides bonding analysis of isolated and crystallized cluster species, *ab initio* modeling has gained increasing importance. The theoretical modeling thereby enables a systematic study of a wide range of size and compositional distributions and is therefore comparable to combinatorial experimental approaches.

An example are metal oxide clusters (ZrO_2, CeO_2) of catalytic importance, transition metal chalcogenide clusters ($MoSe_2$), but also "nanobrass" CuZn clusters or pure Zn clusters with unique electronic properties (*vide supra*).[77, 188-190] This paragraph will give a short introduction into the methods used for *in silico* (*ab initio*) modeling of metal clusters.

In basic terms, the theoretical procedure is divided into three subsections: a) In first place, structures of energetically low-lying isomers have to be determined. As structure and shape crucially determine the chemical behavior of a cluster, profound knowledge about the atomic structure of the species must be gained.[191] b) Methods for assessment of the relative energies of the isomers must be chosen correctly. c) After identification of low-lying isomers, their physicochemical properties can be calculated and bonding analysis can be carried out. Step a) and b) are directly linked together as the search for relevant isomers implies a scanning of the whole potential energy surface for global and local minima and therefore requires an energetic evaluation of every isomeric structure.[191] Energy assessment is either accomplished by empirical potentials such as the *Sutton-Chen (SC)* or *Lennard-Jones (LJ)* potential, or by *density functional theory* (DFT). Strategies for steps a) and c) are described in the following. In step c) the degree of complexity has already been significantly reduced. Alternate theoretical procedures are applied at this stage, usually based on DFT calculations, which are not described in detail in this dissertation. However, results from such calculations are included in the results and discussion section for several novel cluster species.

Strategies for structure determination and evaluation

The task to determine the structure of a (nano)particle or cluster that minimizes its total energy is a global optimization problem and with increasing size of the particle/cluster, the complexity of the problem grows exponentially.[191] Except for very small sizes, gathering of all minima structures is unpractical and uneconomical

in terms of computational costs, as optimization of every possible isomer exceeds the computational capacities. The search for minimum structures therefore requires a tediously chosen optimization and search algorithm. Many different algorithms have been developed and only two exemplary algorithms will be considered here, which were also used for theoretical calculations in the frame of this work.

The *Basin Hoppin Monte Carlo* (BHMC) algorithm was initially used to assess many different possibilities of protein folding. With the use of LJ and SC potentials, as well as in combination with DFT methods it may well be used for metal clusters.[191] In the BHMC algorithm, every point of the three-dimensional PES is mapped/transformed to the nearest local minimum by local (gradient based) optimization algorithms, which drive the structural search in the direction of the steepest gradient of potential energy.[192] This transformation can be defined as (see Figure 29 for illustration):[191-192]

$$\widetilde{E}\left(\{R\}\right) = min\left(E_{tot}(\{R\})\right) \quad (1.5)$$

The transformation has the advantage to simplify the PES and facilitate the local minima search. The basins of the PES can now be explored by a Monte-Carlo algorithm.[192] Any trial structure is randomly modified leading to a jump/hopping in the PES. By conducting local (proximity to the parent structure) and non-local (distant) jumps, the whole PES can be explored.[191] The design and choice of these operators is thereby crucial for successful searching and a few of them will be described here.[191] The *atomic displacement operator* is a local operator, randomly displacing a set of atomic coordinates around their origin. In the *geometric center displacement operator*, the distance of an atom to the center of the particle is varied. The *surface angular operator* takes an atom from the inner particles and moves it to the surface helping to reduce the number of "empty" surface sites. The *exchange and geometric exchange operator* exchange the nature and/or the site of two atomic species (element distribution). The *occasional jump operator* allows for a subsequent number of modifications even if initially this leads to an increase in energy. It thereby helps to drive the system out of deep (funnel-like) minima of the PES.

The different operators can be cycled statically (defined sequence of operators) or dynamically.[191] In the dynamic scheme, each operator is used until the output structure reaches a certain number of rejections (too high energy). Afterwards, the system turns to the subsequent operator. The dynamic scheme allows efficient operators to act consecutively. The effectiveness of each operator might change during the whole optimization process, thereby rendering the dynamic scheme more efficient than the static one. During the optimization process, unphysical

conformations might occur. These are filtered out by use of a *filter operator* avoiding *e.g.* disconnected or too close lying atoms.
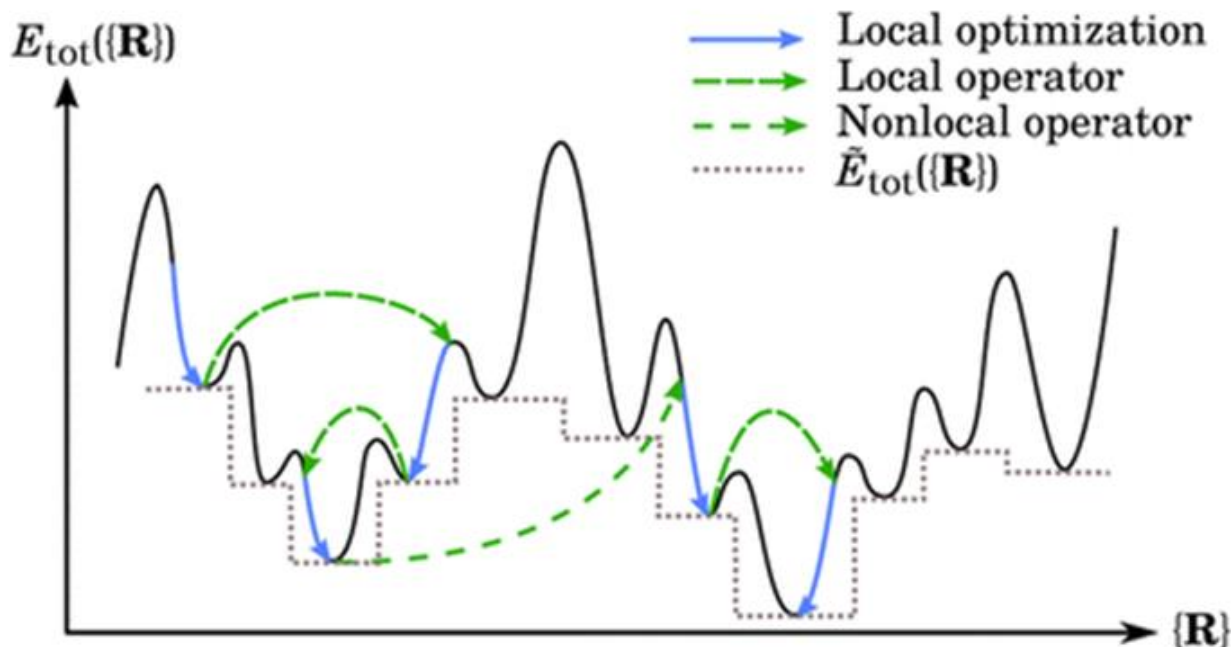

Figure 29
The Basin-Hoppin Monte-Carlo mechanism for exploration of the potential energy surface (PES). Mapping of the PES to local minima (basins) is illustrated by dashed lines. The PES is explored by local and nonlocal jump operators. [Reprinted with permission from G. G. Rondina, J. LF. Da Silva, J. Chem. Inf. Model., 2013, 53, 9, 2282-2298. Copyright 2013. American Chemical Society.]

An alternative approach for scanning the PES is a *tree-growth mechanism* combined with a *genetic algorithm*.[193] A genetic algorithm is thereby based on evaluation of the fitness of a structure (*i.e.* the energetic level). The initial structures for small clusters can be obtained by crystal structures or by force field calculations. In the hybrid-genetic algorithm, the initial structures are obtained by a tree-growth mechanism, which is illustrated in Figure 30 for the example of small molybdenum chalcogenide clusters.[188, 193] A set of parameters is defined as input for the tree growth, such as formula unit, maximum cluster size or maximum coordination number for an atom. In the mechanism, an initial fragment is grown by expansion using defined parameters for the expansion angle, the expansion bond lengths, the maximum number of new sites and the rotational angle. In a second step, the algorithm might search for possible bridging positions between the atoms. By an exclusion criterion, all structures with too close lying atoms or too high coordination numbers are excluded from the list. The algorithm might follow further restrictions to limit the

computational cost, *e.g.* active nodes might be considered inactive for the next growth step after expansion. From the resulting final expansion set, species with overlapping sites are deleted and the resulting structures are subjected to energetic evaluation. Energetic evaluation can be done by the use of defined potentials, by DFT calculations or by a combination of both methods (pre-selection of promising candidates before DFT calculations).[193]

The tree-growth mechanism can also be used in combination with an ESD (*euclidean similarity distance*) analysis.[188-189] ESD relies on the fact that <u>not</u> all of the structures generated in the tree-growth mechanism can be analyzed by time demanding DFT calculations. In the ESD algorithm every cluster unit containing atoms obtained from the tree-growth is converted into a vector. For a $[(MO_2)_{n+1}]$ cluster this results *e.g.* in a 3 x (n+1) dimensional vector. The vectors are analyzed by analysis of the atom distances x_i to the geometric center of the clusters defining a similarity parameter S comparing two configurations α and β:

$$S(\alpha, \beta) = \frac{\sum_{i=1}^{N} (x_{i,\alpha} - x_{i,\beta})^2}{\sum_{i=1}^{N} x_{i,\alpha}^2 - x_{i,\beta}^2} \quad (1.6)$$

A configuration β is thereby accepted if S is beyond a certain cutoff value, otherwise two structures α and β are assumed to be very similar. The ESD mechanism therefore reduces the number of structures to be submitted to DFT calculations. An advantage of the TG-ESD mechanism is that previous optimized structures can serve as an input whereas in BHMC random structural changes are generated; a fact that might elongate the search for minima. The TG-ESD mechanism is summarized in Figure 30 for molybdenum dichalcogenide clusters $[(MoQ_2)_n]$.[189]

It is of note that beside ESD, other clustering algorithms exist, determining similarity between different structural sets and reducing structural diversity (obtained *e.g.* by tree-growth mechanisms) to "identity sets".[194-195]

1. Introduction
1.4 How to deal with multidimensional complexity
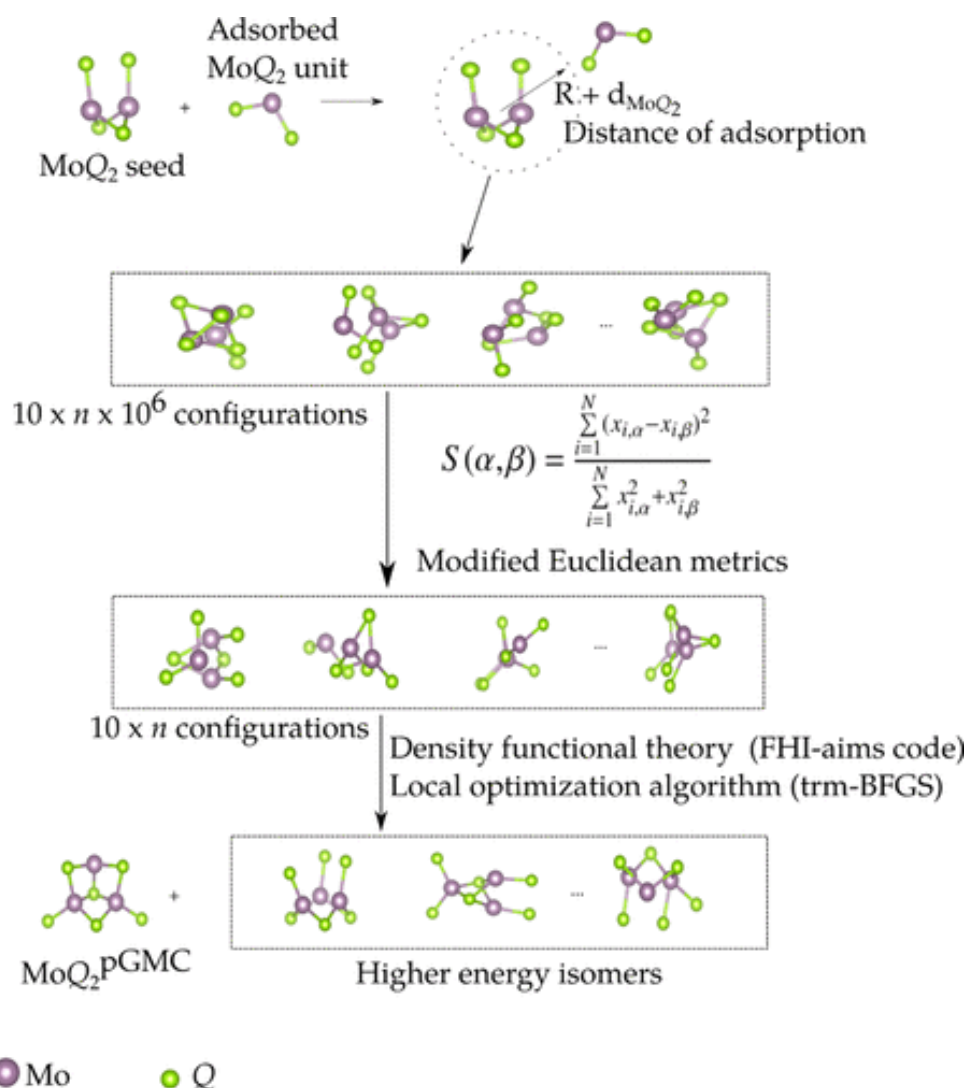
Figure 30

Sketch of the tree-growth algorithm combined with the Euclidean similarity distance (Q = chalcogenide). The structures generated by the tree-growth mechanism (up) are compared by the Euclidean similarity metrics. The energies of the reduced structural set are calculated leading to a structure of the putative global minimum (pGMC) and of higher lying isomers. [Reprinted with permission from A. M. S. Naidel, R. Besse, A. CH. Da Silva, D. Guedes-Sobrinho, M. P. Lima, J. LF. Da Silva, J. Phys. Chem. C., 2018, 122, 47, 27059-27069. Copyright 2018. American Chemical Society.]

2. Cluster chemistry – Inorganic chemistry at its dead end?

The known synthetic approaches for the generation of ligated, molecular "Hume-Rothery" inspired clusters result in formation of low-valent metal cores decorated with MCp* ligands. Figure 31 a) shows a model case, such as $[H_4Cu_6Al_6](Cp^*)_6$, in which a central core atom is exposed to the outside of the cluster and prone to reactivity. A situation with inverted core-shell composition is illustrated in Figure 31 b). It may result *e.g.* from Cp* transfer reactions. Controlled ligand removal from the outer transition metal is thought to result in reactive sites. $[Cu_{43}Al_{12}](Cp^*)_{12}$ represents a closed-shell, ligand protected system as shown in Figure 31 c). Clusters like this are thought to require activation to be reactive. Clusters with random element distribution and open coordination sites for surface reactivity (see Figure 31 d)) are thought to be highly reactive towards a variety of substrates (alkynes, nitriles, CO_2, N_2O etc.).

We strongly believe that comparison of different structural and electronic configurations at these active sites will significantly enhance our chemical knowledge. Due to their high reactivity, these species might however not be isolable in a classical manner and classical inorganic chemistry might run into a *dilemma*: Crystallizable, well-behaved species are often a thermodynamic "sink" of the system and not useful for reactivity studies, whereas the *highly reactive species tend to escape the researcher´s eye.*
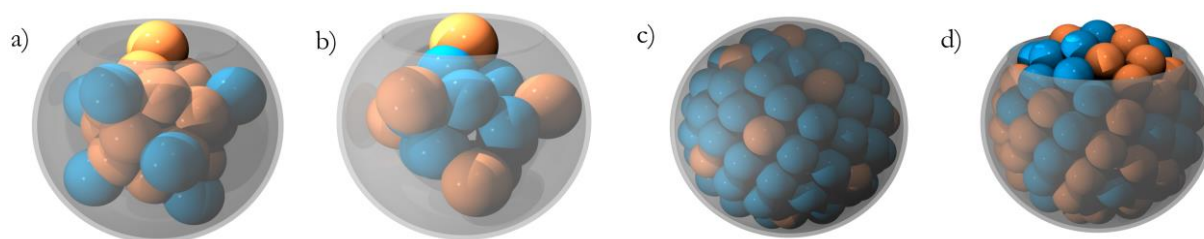
Figure 31
Different models for intermetalloid clusters of TM/E (TM = transition metal, orange, E = group 12/13 metal, blue) combination highlighting our research perspectives. a) Small core-shell cluster with reactive TM site. The [Cu₇Al₆](Cp)₆ cluster from this work falls in this class. b) Small core-shell cluster with inverted core composition. c) Large, ligand protected core-shell cluster. d) Large intermetalloid cluster with random elemental distribution and open coordination site. [Reprinted (adapted) with permission from M. Schütz, C. Gemel, M. Muhr, C. Jandl, S. Kahlal, J. Y. Saillard and R. A. Fischer, Exploring Cu/Al cluster growth and reactivity: From embryonic building blocks to intermetalloid, open-shell superatoms. Chem. Sci. 2021, 12, 6588-6599. Copyright 2021. Published by the Royal Society of Chemistry. Link: https://pubs.rsc.org/en/content/articlehtml/2021/sc/d1sc00268f.]*

2. Cluster chemistry – Inorganic chemistry at its dead end?

Investigation of these species in libraries without the need of isolation is thought to significantly enhance the research efficiency. This dissertation will deal with the fundamentally new idea of knowledge and method transfer concerning the work with complex library systems from life science, combinatorial chemistry and material chemistry to "living" libraries of intermetallic (TM/E, TM = Cu, Au; E = Al, Zn) clusters in solution, as illustrated in Figure 32. Parallel assessment of the product species by mass-spectrometry is the main method chosen here for analysis of reaction outcomes, similar to the approach in biochemistry and physical chemistry (gas-phase clusters). Specifically, the dissertation aims to gain a first fundamental understanding of these intermetallic cluster libraries. Besides the development of novel mass-spectrometry based work-flows for library identification, chemical questions regarding cluster growth mechanisms and reactivity patterns will be addressed.
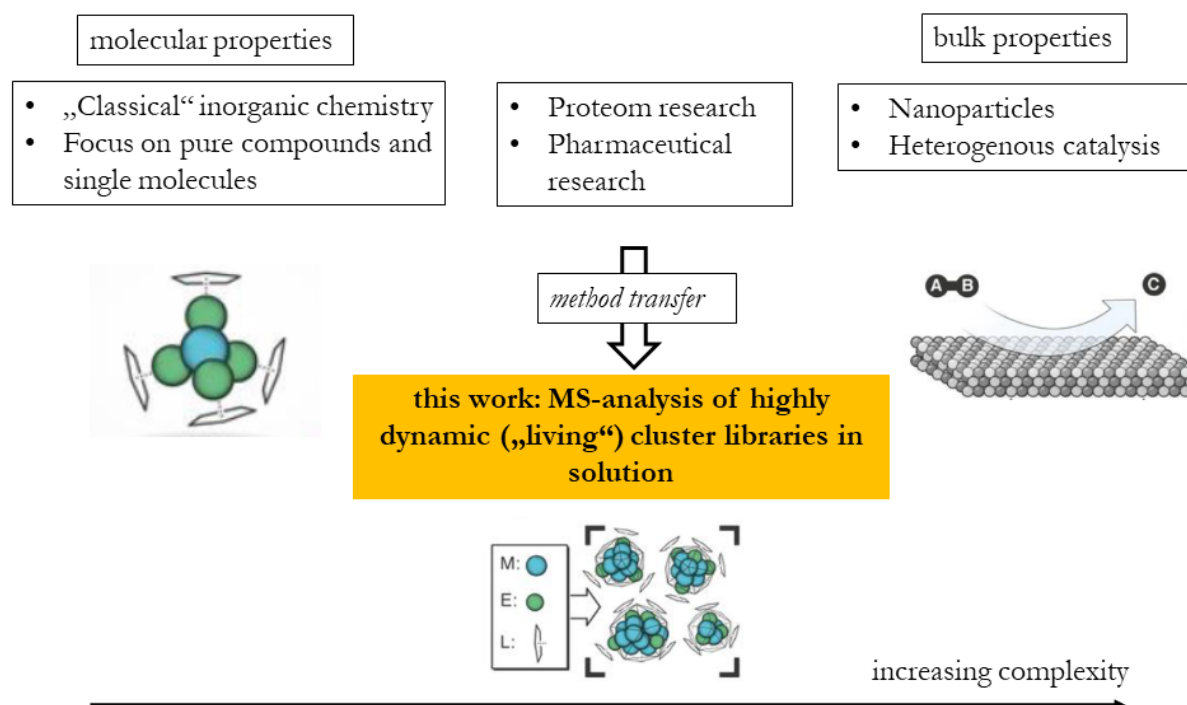
Figure 32
Intermetallic cluster libraries as linking element between molecular compounds and solid-state surfaces. Concepts of dealing with such a degree of complexity are known from biochemistry and combinatorial chemistry. [Own figure.]

3. Results and Discussion

The Results and Discussion part of this thesis will be divided into two main parts. The first part will explain the results obtained in the development of new concepts and new methodology for investigating living cluster libraries in solution. In this context, the term "living" is used to visually describe a highly dynamic and sensitive system of intermetalloid clusters, the composition of which strongly depends on external parameters (temperature, stoichiometry of reactants) and reaction partners. The concepts elaborated in this dissertation are mainly based on the use of LIFDI-MS for the analysis of cluster mixtures in solution. The general procedures and algorithms developed for the future design of experiments and for data processing are explained exemplary for an <u>isolated mixture ("micro-library") of two Cu/Al clusters</u>, as well as for a <u>more complex library of Cu/Zn clusters, which was studied in situ, directly from the reaction solutions</u>. A smaller chapter of the methodological part will explain concepts and strategies for "size-focusing" of cluster solutions, i.e. to selectively narrow down the product distribution into one or two cluster species.

The presented Cu/Al results were partly published as an article in the journal Chemical Science. [Reprinted (adapted) with permission from M. Schütz, C. Gemel, M. Muhr, C. Jandl, S. Kahlal, J. Y. Saillard and R. A. Fischer, Exploring Cu/Al cluster growth and reactivity: From embryonic building blocks to intermetalloid, open-shell superatoms. Chem. Sci. 2021, 12, 6588-6599. Copyright 2021. Published by the Royal Society of Chemistry. Link: https://pubs.rsc.org/en/content/articlehtml/2021/sc/d1sc00268f.]

The second part of the "Results and Discussion" section will focus on chemical interpretation of the results obtained by the methods presented in part 1, as well as by alternate techniques (SC-XRD, NMR, GC-MS, UV-Vis). Besides Cu/Zn, this will include detailed results on cluster growth processes and reactivity in the Cu/Al and Au/Al system. Further results from theoretical calculations are integrated in this part to support experimental findings.

3.1 Methodical part: Exploration of living cluster libraries by LIFDI-MS

3.1.1. The general workflow and choice of examples

Library generation

The reaction of AlCp* with 0.26 eq. of [CuMes] (the monomer notation [CuMes] is used instead of [Cu$_5$](Mes)$_5$ due to its simplicity; Mes = mesitylene) in toluene at 75 °C, followed by further addition of 0.54 eq. of [CuMes] and prolonged heating to 75 °C overnight leads to a dark brown reaction solution, from which a

3. Results and Discussion

3.1 Methodical part: Exploration of living cluster libraries by LIFDI-MS

microcrystalline cluster mixture can be isolated (see Scheme 8 a)). LIFDI-MS analysis of the isolated material reveals it to be a mixture of two Cu/Al clusters (see Figure 33 a)), namely $[Cu_7Al_6](Cp^*)_6$ (**1**) and $[Cu_8Al_6](Cp)_6$ (**2**).

Likewise, the reaction of [CuMes] with 0.75 eq. of $[Zn_2](Cp^*)_2$ in toluene at room-temperature yields a dark-red solution after 2 hours reaction time (see Scheme 8 b)).
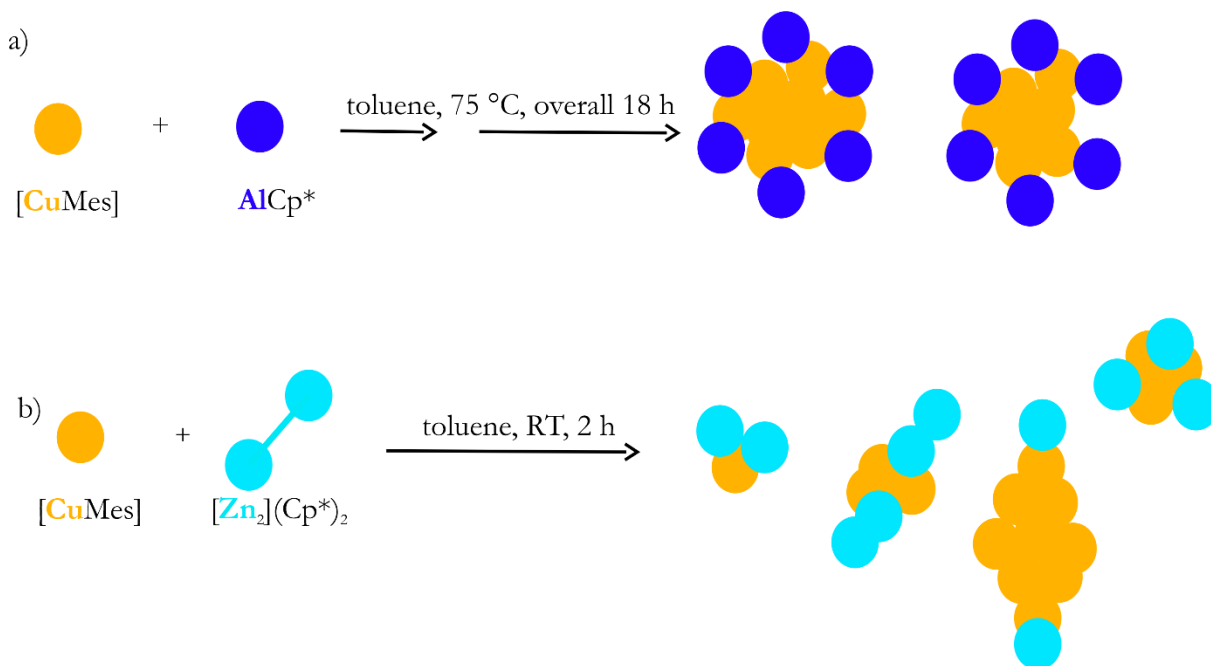
Scheme 8
Reaction conditions for the generation of Cu/Al (a)) and Cu/Zn (b)) cluster libraries. [Own figure.]

In situ LIFDI-MS analysis of the Cu/Zn reaction solution gives a complex spectrum with more than 100 peaks (see Figure 33 b)). Very similar spectra as in Figure 33 b) are obtained for other Cu:Zn stoichiometries applied. Noteworthy, isolation and structural characterization of the novel species $[Cu_{10}Zn_2](Cp^*)_2(Mes)_6$ (**3**), $[Cu_4Zn_{9/10}](Cp^*)_8$ (**4/5**), as well as of the reported clusters $[CuZn_2](Cp^*)_3$ and $[Cu_3Zn_4](Cp^*)_5$ is possible from this or closely related Cu/Zn libraries. However, $[Cu_4Zn_{9/10}](Cp^*)_8$, $[CuZn_2](Cp^*)_3$ and $[Cu_3Zn_4](Cp^*)_5$ are obtained as a co-crystallizing mixture and separation is only in part possible by extensive work-up procedures. This highlights the inefficiency of classical synthetic methods for the presented systems and demonstrates the need for an alternate methodology to fully understand and exploit the whole product range obtained.

3. Results and Discussion

3.1 Methodical part: Exploration of living cluster libraries by LIFDI-MS

a)
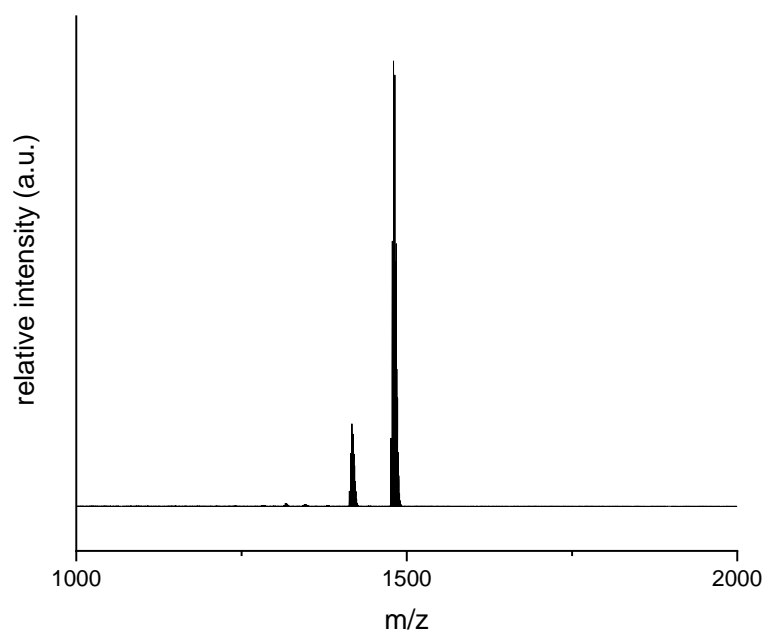
b)
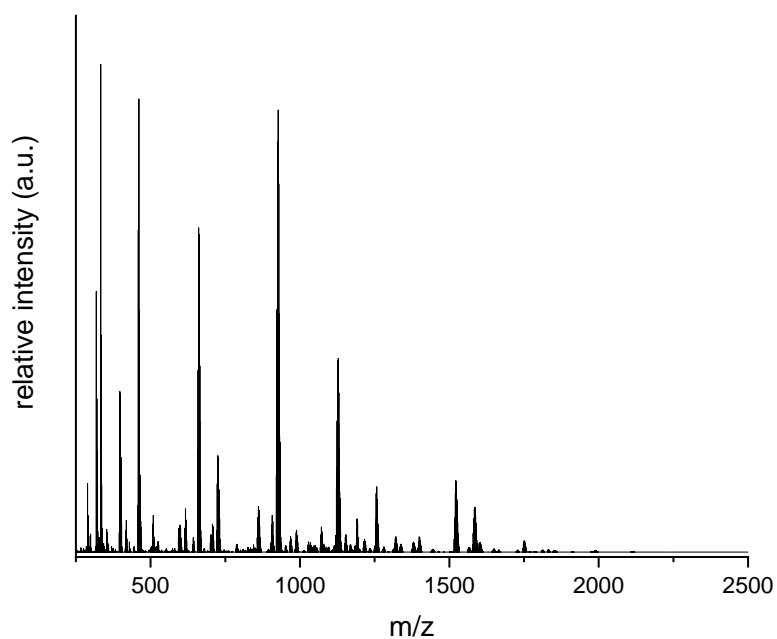
Figure 33

a) LIFDI-MS spectrum of the isolated cluster mixture stemming from the reaction between [CuMes] and AlCp* (0.8:1, 75 °C, 18 h). b) LIFDI-MS spectrum of the reaction solution [CuMes] + [Zn₂](Cp*)₂ (1: 0.75, toluene, RT, 2h). More details about assignment of cluster species to the peaks will be discussed later in the text.

General methodical algorithm

The presentation of the general workflow will thereafter focus on the presented cases. Spectra of the other stoichiometries were interpreted in the same manner and the results are compared in Table S1. Scheme 9 shows the general workflow and the methodology applied in this work for the analysis of cluster libraries in solution and for assessment of their reactivity.
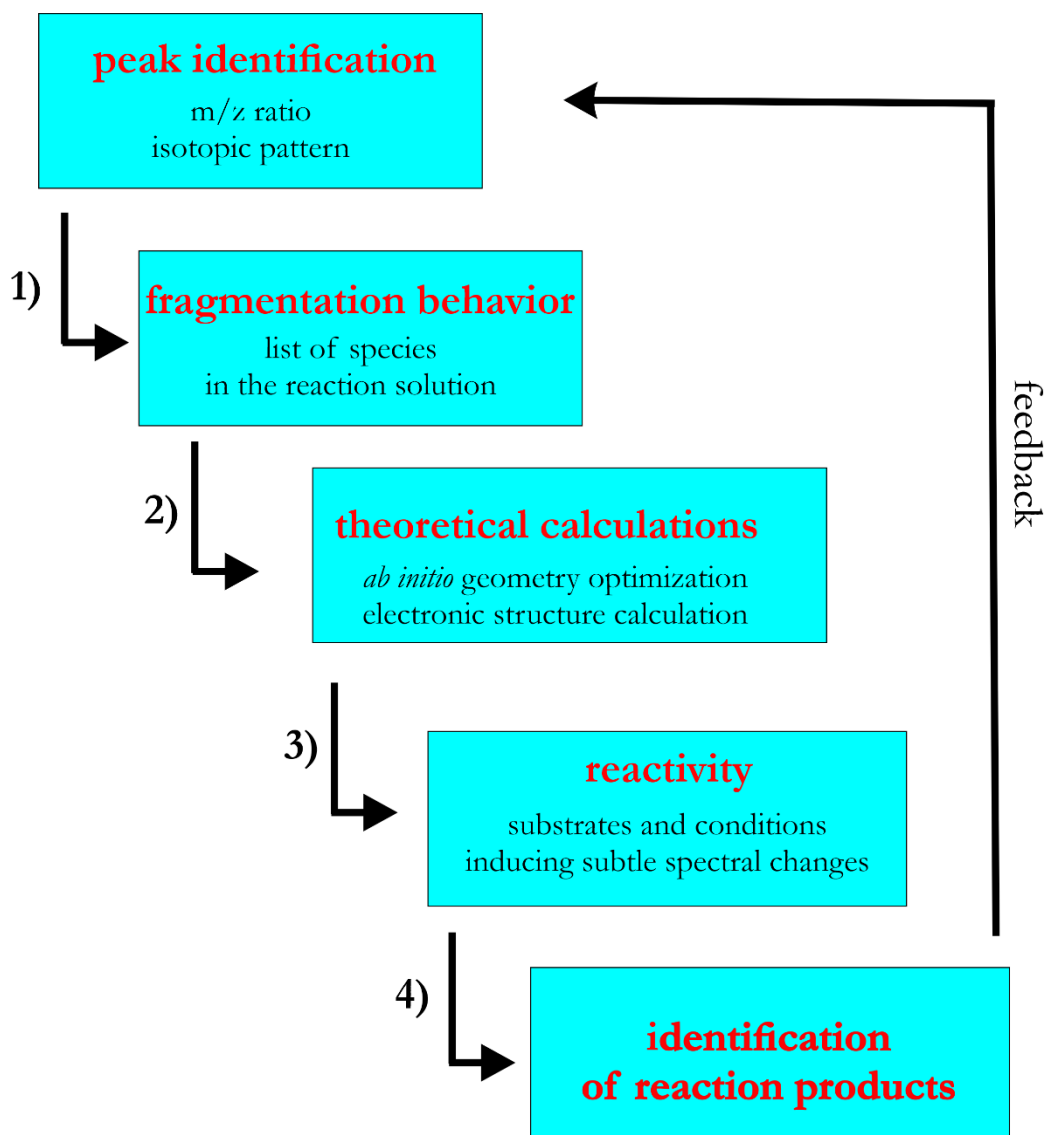
Scheme 9
General algorithm for the analysis of complex LIFDI-MS spectra of cluster libraries in solution as applied in this dissertation. [Own Scheme.]

Data interpretation starts with identification of the peaks in the spectrum obtained, *i.e.* assignment of sum formulas to the peaks (step 1) in Scheme 9). This is

accomplished by extraction of two sorts of information from each peak, namely the *m/z* ratio, as well as the isotopic pattern. As described later in the text, peak assignment might require sophisticated labelling strategies using isotopically enriched metals or ligand modifications in order to achieve unambiguous identification. This especially holds true for complicated isotopic patterns.

After identification of the peaks, a list of ions detected during the MS experiment can be generated (see Table S1). However, due to fragmentation, this list does not necessarily correspond to a list of species present in solution. This especially holds true for the used HCD-cell orbitrap system (see Figure 22), in which the ions generated by the LIFDI-source necessarily pass the HCD cell, in which the collision energy cannot be set to zero due to apparative aspects.

Once the fragmentation behavior has been addressed by additional experiments (step 2) in Scheme 9), a list of potential molecular species (potentially including remaining starting material) in solution is obtained. For these species, *ab initio* theoretical calculations based on the strategies presented in the introduction (see chapter 1.4.5) are conducted to obtain structure proposals for selected sum formulas (step 3) in Scheme 9). Optimized structural geometries can further be used to carry out a detailed bonding analysis.

The cluster libraries discussed herein are highly dynamic and sensitive systems that are supposed to react rapidly with organic substrates or small molecules including cluster growth, rearrangement or degradation phenomena. Finding the right choice of substrate and reaction conditions is therefore a delicate task. Once reaction conditions inducing subtle spectral changes are identified (step 4) in Scheme 9), the same workflow procedure is applied to enlighten the nature of the reaction products (step 5) in Scheme 9). The nature of the reaction products allows feedback into library design and composition. Combinatorial design of experiments using labeled (*e.g.* deuterated) reactants, solvents or libraries might lead to a more fundamental understanding of reaction scopes and mechanisms. In the following, the individual parts of the flow-chart in Scheme 9 will be discussed in detail for the examples of Cu/Al and Cu/Zn.

3.1.2 Peak identification

Basic considerations

The m/z ratio of the center of a detected mass peak itself is a rather unspecific value, as there exist many different possible fragment combinations for a given m/z ratio, even for low m/z values ("fragment" in this context means possible constituents of the ion detected, *e.g.* ligands, metal atoms). The isotopic pattern, *i.e.* the specific, relative intensities of the single peaks forming an isotopic envelope, is therefore a crucial tool for the determination of elemental composition. It has its origin in the natural isotopic abundancies of the elements leading by the rules of simple statistics to a defined number of different isotopologues for a given sum formula. However, a single peak inside the isotopic pattern does not necessarily correspond to one single isotopologue. Rather, the resolution of the instrument has to be taken into account. Different isotopologues might lie very close to each other in terms of their m/z ratio; if this m/z difference is smaller than the resolution R of the instrument, these single isotopologues will be detected as a single, Gaussian-type peak by the spectrometer. The situation is exemplary illustrated in Figure 34 for the small, triangular CuZn cluster $[CuZn_2](Cp^*)_3$.

These underlying principles lead to complicated situations for mixtures of compounds (overlapping peaks), as well as for large, metal rich molecules. For mixtures, mathematic deconvolution of the peak must be undertaken to determine the ratio of components. If the elemental isotopes of two different element have similar m/z ratios, unambiguous assignment of isotopic patterns might not be possible *a priori*. This is due to too many possible isotopologue combinations existing for a given experimental isotopic pattern. Strategies to solve both problems will be discussed in the following.

3. Results and Discussion

3.1 Methodical part: Exploration of living cluster libraries by LIFDI-MS

calculated isotopic pattern
for $[CuZn_2](Cp*)_3$

$R = 140000$

isotopic distributions
(natural abundancies):

^{63}Cu: 69.15 %
^{65}Cu: 30.85 %
^{64}Zn: 64.18 %
^{66}Zn: 27.74 %
^{67}Zn: 4.05 %
^{68}Zn: 18.46 %
^{70}Zn: 6.10 %
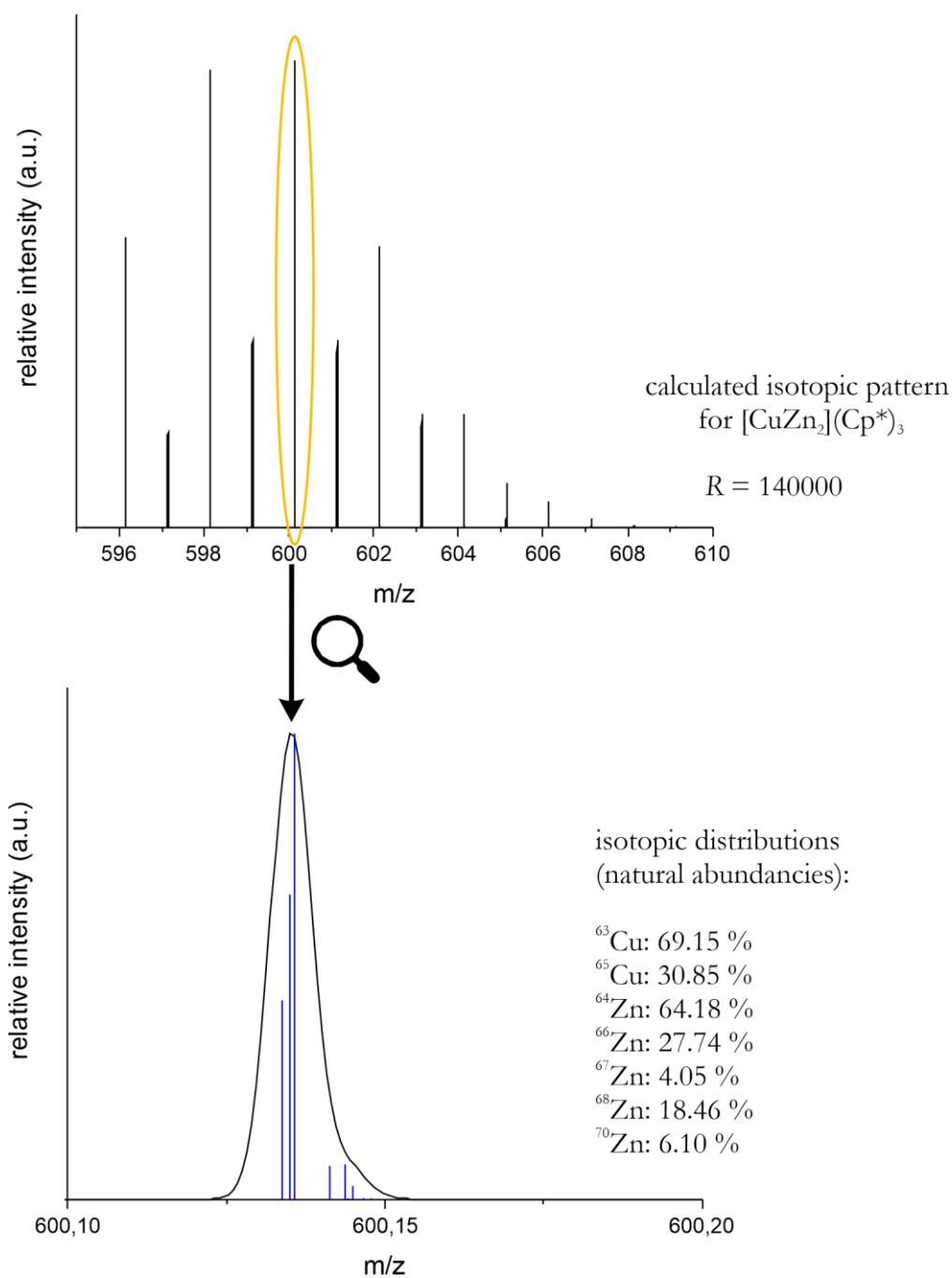
Figure 34
Top: Overall calculated isotopic pattern for the example $[CuZn_2](Cp*)_3$ at a given instrumental resolution R. Bottom: Every single peak of the isotopic envelope is composed of different, close-lying isotopologues (blue). [Own figure].

3. Results and Discussion
3.1 Methodical part: Exploration of living cluster libraries by LIFDI-MS

Example 1: The isolated Cu/Al micro-library

According to LIFDI-MS analysis, the "micro-library", which is isolable from the reaction between [CuMes] and AlCp* at certain conditions, consists of the open-shell, radical species $[Cu_7Al_6](Cp^*)_6$ (**1**) and its closed-shell congener $[Cu_8Al_6](Cp)_6$ (**2**). Both species differ by only one Cu atom in the core region of the cluster. Noteworthy, the amount of $[Cu_7Al_6](Cp^*)_6$ in the isolated mixture is < 5 mass % according to elemental analysis. Both species are unambiguously identified according to their isotopic envelopes and their m/z ratio (see Figure 35 a) and b)). Subtle differences of only one H atom, *e.g.* between $[Cu_7Al_6](Cp^*)_6$ and its hydride bearing congener $[HCu_7Al_6](Cp^*)_6$ (**1H**), which is accessed by different synthetical procedures, are well recognized by a shift of $\Delta m/z = 1$ in the LIFDI-MS spectra (see Figure 35 c)). This highlights the power of the method to precisely determine the nature not only of prominent species but also of small subfractions of the sample.

3. Results and Discussion
3.1 Methodical part: Exploration of living cluster libraries by LIFDI-MS

a)

b)

c)
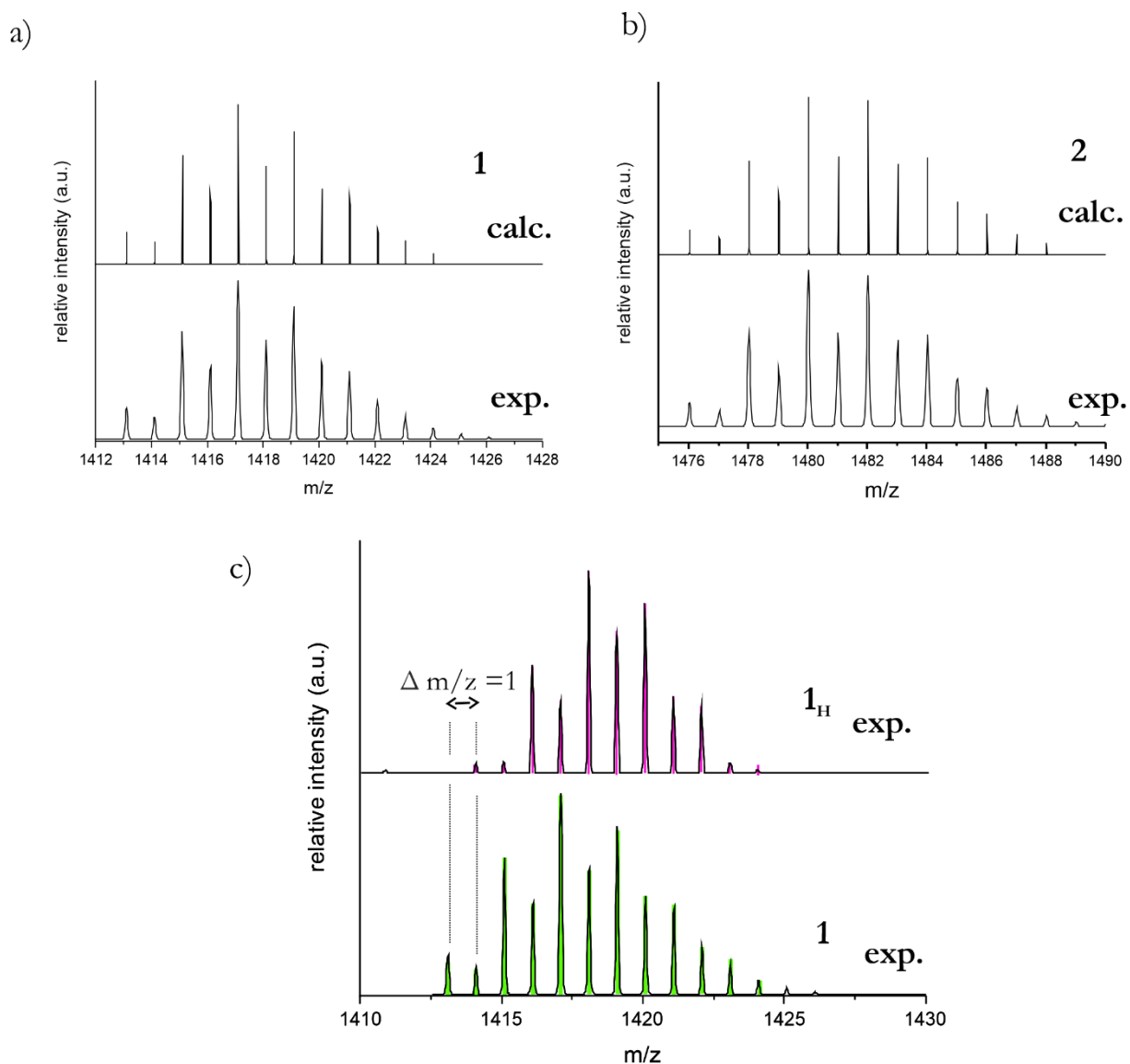
Figure 35
a) Comparison of calculated and experimental isotopic envelopes of [Cu₇Al₆](Cp)₆ (**1**). b) Comparison of calculated and experimental isotopic envelopes of [Cu₈Al₆](Cp*)₆ (**2**). c) Visualization of the hydride shift of one m/z unit by comparison of experimental mass spectra of **1** and its hydride bearing congener [HCu₇Al₆](Cp*)₆ (**1ₕ**).*

Example 2: The Cu/Zn library

For the Cu/Zn case, however, the situation is more complicated. The difference between the average atomic mass of Cu and that of Zn is only 1, leading to a much larger number of possible compositions for a given m/z, especially if the possibility of surface bound hydrides is considered. Additionally, the isotopic pattern also does not allow for unambiguous peak identification, even for medium size clusters. The situation is illustrated in Figure 36 for the prominent peak in the library mass

spectrum at m/z = 1521. Several computational matches with very similar goodness of fit (GoF) were identified for the experimental peak. Matches differ in the number of ligands (blue = 3 Cp* ligands, red = 6 Cp* ligands), as well as in the core composition.
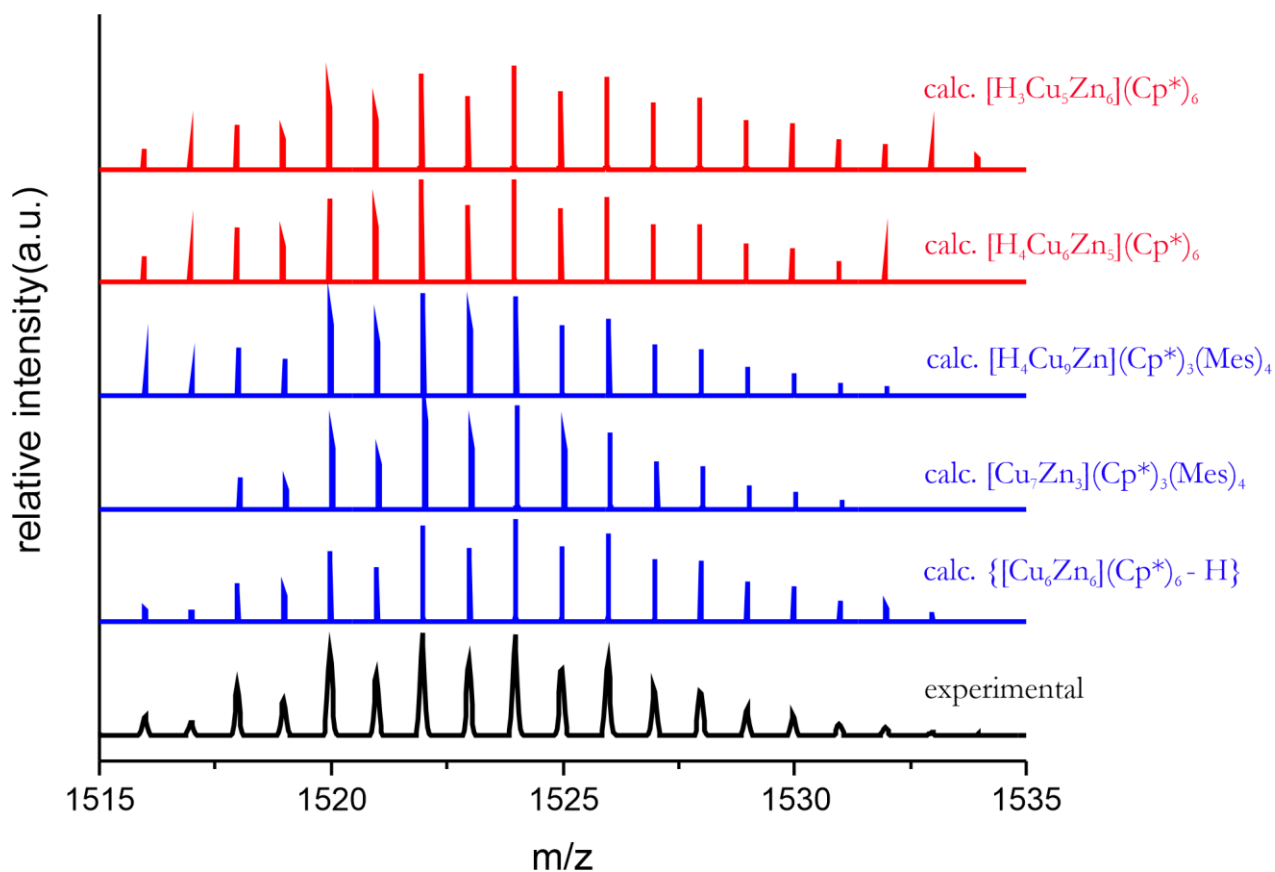
Figure 36
Several matching isotopic pattern with similar GoF for a given experimental peak from the spectrum presented in Figure 33 b). Blue = Matches with 3 Cp* ligands, red = Matches with 6 Cp* ligands. The "- H" description denotes that the match refers to the presented sum formula minus one hydrogen atom, which is e.g. explained by C-H activation of one Cp* ligand (either already in solution or during ionization).

To resolve this problem, a labeling strategy was designed, in which a) the Cp* ligands were replaced by Cp*Et and b) $[Zn_2](Cp^*)_2$ was replaced by isotopically enriched $[^{68}Zn]_2(Cp^*)_2$. The mass-spectrometric experiments were repeated with $[Zn_2](Cp^{*Et})_2$ and $[^{68}Zn]_2(Cp^*)_2$. The mass difference between Cp* and Cp*Et is 14 u.

$$\Delta\frac{m}{z}\left(Cp^{*Et} - Cp^*\right) = \frac{m}{z}\left(CH_2\right) = 14 \quad (1.7)$$

3. Results and Discussion
3.1 Methodical part: Exploration of living cluster libraries by LIFDI-MS

The number of Cp* ligands **n** of a species can thereafter be determined by scanning the Cp*Et labeled spectrum for peaks with a Δm/z shift of **n** x 14 with respect to the original peak in the unlabeled spectrum. The procedure is illustrated in Figure 37 and must be repeated for every peak in the spectrum. The number of matches for each peak is thereby reduced to species carrying the same number of Cp* ligands. Notably, the procedure did work for most of the peaks and corresponding, mass-shifted envelopes were identified in the Cp*Et labeled spectrum. Unambiguous peak identification was finally achieved by labeling experiments with [^{68}Zn]$_2$(Cp*)$_2$. The mass-difference between Zn(natural isotope abundancies) and ^{68}Zn is 2.62 u:

$$\Delta \frac{m}{z} \left[^{68}Zn - Zn(natural\ abundancy) \right] = 68\ u - 65.38\ u = 2.62\ u \quad (1.8)$$

Using the same procedure as for the Cp*Et labeling experiments, the number of Zn atoms and thereby the cluster core composition can be identified. The labeling with ^{68}Zn additionally changes (simplifies!) the isotopic patterns, leading to an easy and straightforward interpretation of most of the peaks. For many peaks, labeling with ^{68}Zn was sufficient to achieve unambiguous identification. Consequently, many of the cases, for which Cp*Et labeling did not yield clear results, could eventually be resolved by using the ^{68}Zn label.
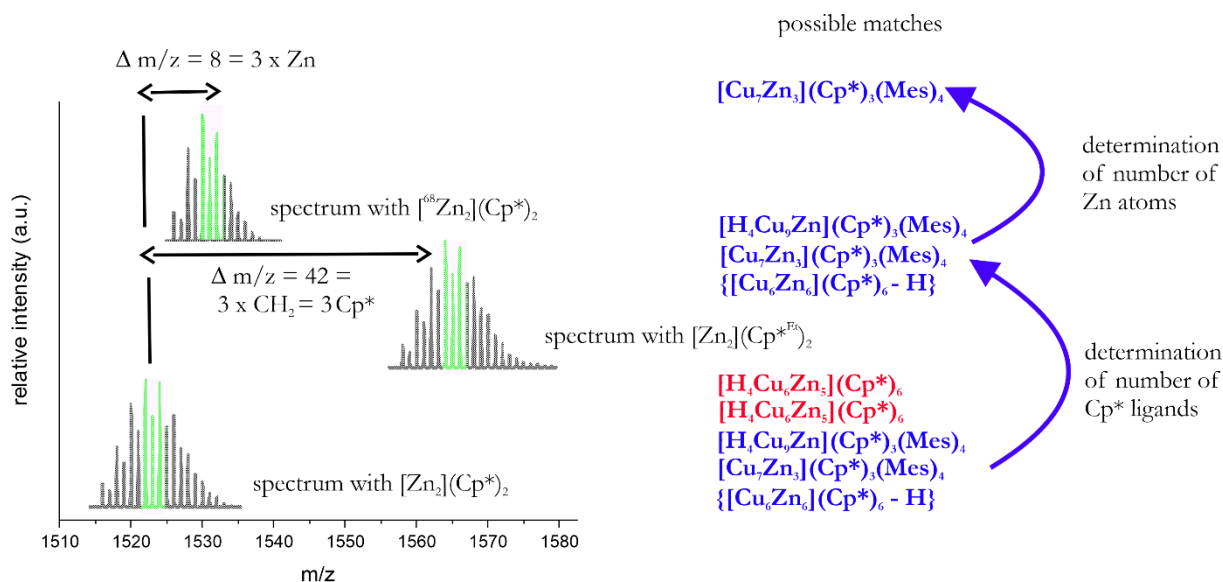
Figure 37
*Peak identification by labeling experiments with [Zn$_2$](Cp*Et)$_2$ and [^{68}Zn]$_2$(Cp*)$_2$. The procedure is shown exemplary for the peak at m/z = 1521 but is general for every peak of the spectrum. In some cases for which no corresponding peak in the [Zn$_2$](Cp*Et)$_2$ spectrum was found, information encoded in the ^{68}Zn spectrum was sufficient for unambiguous assignment.*

82

The procedure was repeated for all peaks of the spectrum and for three different Cu:Zn stoichiometries. A list of more than 50 species is produced, which is shown in Table S1 in the Appendix. It is also denoted in the table, whether a species was identified solely by its ^{68}Zn pattern or by combination of Cp*^{Et} and ^{68}Zn labeling experiments. The species in Table S1 can be grouped by chemical intuition into possible molecular ions and corresponding fragment species, formed by loss of ZnCp*, Cp* or mesityl units. However, an experimental approach to distinguish between fragment and parent ion species was designed as described in the following.

3.1.3. Fragmentation behavior

General considerations

Fragmentation behavior was assessed based on an approach similar to *energy dependent* ESI-MS[165] (*vide supra*) and *stepped collision energy* in orbitrap systems known from peptide fragmentation.[154] The collision energy in the HCD cell of the mass spectrometer was stepwise increased and for each collision energy, a spectrum of the original cluster library was recorded. The HCD cell set-up, as well as the underlying principles of HCD cell fragmentation are described in Figure 22 and chapter 1.4.1 in the introduction). The intensities of the peaks of interest were determined for the different collision energies by integration relative to the overall integral of the respective spectrum. Evaluation of the data is based on the following considerations illustrated in Figure 38. Molecular ion peaks are associated with a continuous decrease of peak intensity for increasing collision energies. This is due to enhanced fragmentation of parent ions at higher collision energies. Noteworthy, species with such a fragmentation behavior may still be fragment formed during the ionization procedure (*e.g.* due to thermal or discharge processes on the emitter). For fragment ions, an increase of peak intensity is expected for increasing collision energies due to their enhanced formation at higher collision energies. In some cases, no clear decision can be made either due to fluxional or continuous behavior of peak intensities at rising collision energies.

Spectra were recorded at normalized collision energies between 10 and 23. Note that 10 is the lowest possible collision energy using the given set-up and that use of normalized collision energies in arbitrary units is common for the given set-up (even though the values should bear the unit [eV] as communicated by the company Thermo-Scientific). [154] For collision energies higher than 23, an overall decrease of peak intensities for all peaks in the spectrum was observed. Obviously, all the sensitive cluster species in the gas phase, be it fragments or molecular ions, are unstable under these experimental conditions.

fragment ion   molecular ion

intermediate fragment/
extraordinary stable molecular ion
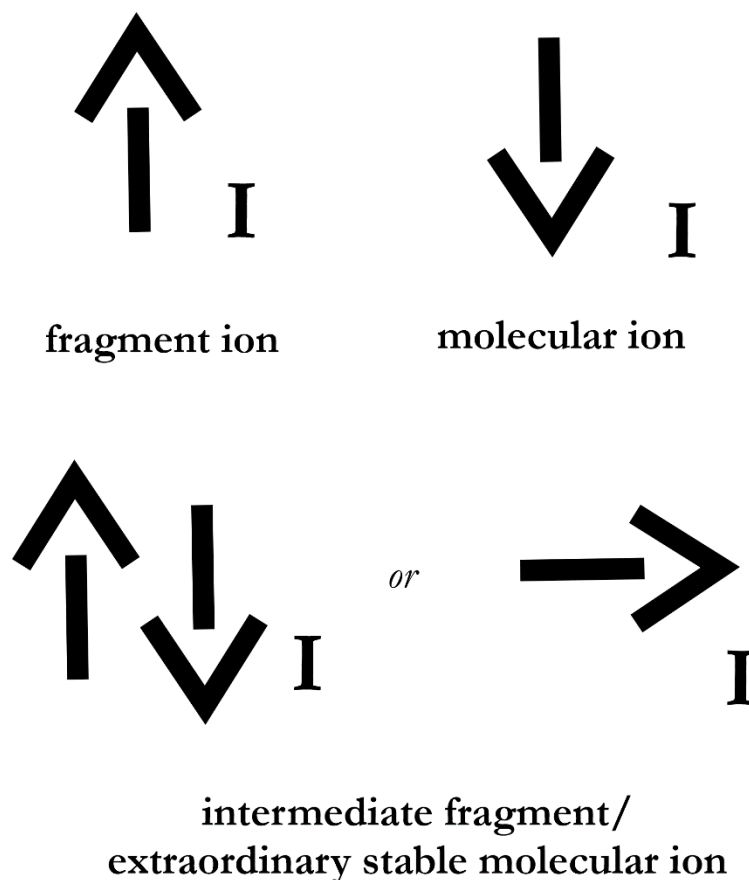
Figure 38
Different possible responses of peak intensities I at increasing collision energies. A rise of peak intensity is expected for fragment ions whereas for parent molecular ions, a decrease of peak intensity is anticipated.

Peak intensities of interest (*i.e.* for the peaks unambiguously identified by labeling experiments) were determined by computerized integration relative to the overall integral of the spectrum. To determine the influence of statistic fluctuations of peak intensities, which are not correlated to the collision energy applied, each experiment was repeated several times (5 – 10 times). The average value of peak intensity $\bar{I}$, as well as the corresponding *coefficient of variation* (*CV*) were calculated for every peak. Statistic fluctuations of peak intensities are supposed to occur during the ionization procedure. The analyte concentration on the LIFDI-emitter, which is hardly controllable during sample supply, chemical/physical modifications on the emitter´s surface (*e.g.* metal deposition, geometric rearrangements) or thermal decomposition of part of the analyte during ionization might be possible reasons for these fluctuations. The coefficient of variation of peak intensities at a standard heating rate of the emitter (30 mA/s) turned out to be much higher than at elevated heating rates of the emitter. 60 mA/s was determined as the optimum heating rate with respect to

a minimum variation coefficient of peak intensities under identical measurement conditions. The reason therefore is supposed to be the reduced thermal decomposition of sample at higher heating rates, as the overall exposition of the analyte to the hot surface of the emitter is reduced. Indeed, reduction of the heating rate to only 15 mA/s led to significant decrease of overall peak intensities due to thermal decomposition.

The fragmentation behavior was therefore assessed at heating rates of 60 mA/s. Data was thereafter analyzed as follows: Average peak intensities at elevated collision energies were compared with the average peak intensity at standard conditions. *Fragments* are associated with an *increase in peak intensity* with respect to the average peak intensity at standard conditions. Contrary, *parent ions* are associated with a *decrease in peak intensity*. In detail, the development of peak intensities with rising collision energy was analyzed by linear regression analysis. A positive slope of the regression line is thereafter indicative of a fragment, a negative one indicative of a parent ion. Only in cases, in which the absolute value of the slope was higher than the standard deviation of the slope, the results can be considered as significant.

The Cu/Zn library

Analysis of the fragmentation behavior of the Cu/Zn library was the topic of the Bachelor thesis of Moritz Lengl, which was supervised within the frame of this PhD project. The following results are therefore also part of the Bachelor thesis of Moritz Lengl.

The resulting *I vs. CE* plots for every ion from the Cu/Zn library are shown in the Appendix (Figures S1-S44) and exemplary in Figures 39 and 40. Obviously and as expected, the onset of fragmentation processes, as well as the extent of fragmentation with respect to collision energy, are different for different ions. Whereas for the molecular ion $[Cu_5Zn_2](Cp^*)_4(Mes)$ a continous decrease in peak intensity is detected, the situation is more complicated for $[Cu_7Zn_3](Cp^*)_3(Mes)_4$. Besides an outlier at CE = 14, a deviation from linearity is observed at higher collision energies (17 and 18). The latter effect is explained by significant production of light fragments with m/z < 200, escaping the overall integral and distorting therefore the determined relative peak intensities (which are calculated with respect to the overall integral of all peaks in the spectrum). Similar effects were observed for several peaks. Due to the intrinsically different onset of fragmentation and due to the bias in the data at higher collision energies, the linear region in the *CE vs. I* plots is slightly different for different ions. Noteworthy, the analysis by linear regression does therefore only allow for qualitative analysis (fragment *vs.* parent ion) but not for a quantitative analysis of

3. Results and Discussion
3.1 Methodical part: Exploration of living cluster libraries by LIFDI-MS

fragmentation processes. Figure 40 exemplary shows *I vs. CE* plots for the two fragment ions $[HCu_8Zn](Cp^*)_4$ and $[HCu_7](Cp^*)_3$, for which a continuous increase in peak intensity with rising CE is observed.
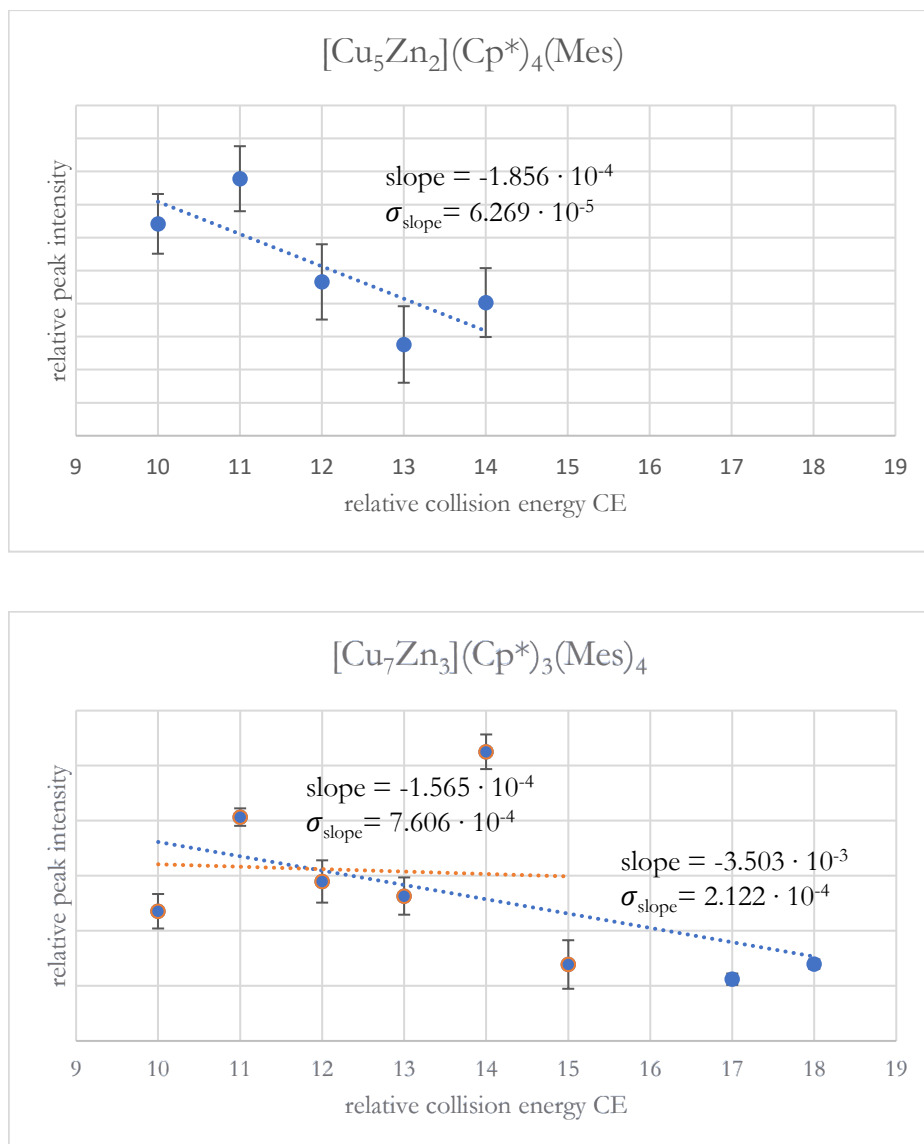
Figure 39

I vs. CE plots for two selected molecular ions, namely $[Cu_5Zn_2](Cp^*)_4(Mes)$ and $[Cu_7Zn_3](Cp^*)_3(Mes)_4$.

3. Results and Discussion
3.1 Methodical part: Exploration of living cluster libraries by LIFDI-MS
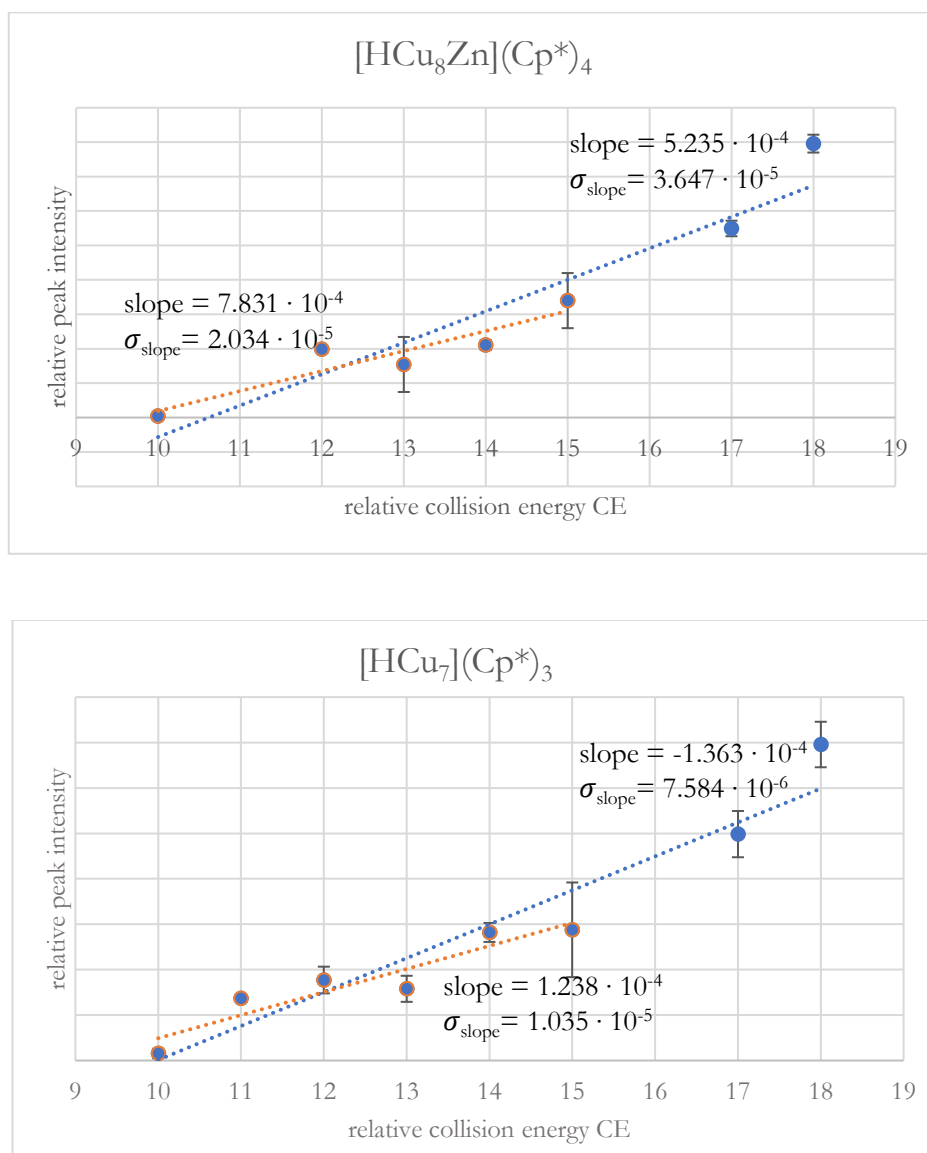
Figure 40
I vs. CE plots for two selected fragment ions, namely [HCu₈Zn](Cp*)₄ and [HCu₇](Cp*)₃.

The resulting list of all molecular ion species and fragments obtained by careful analysis of all *I vs. CE* plots are given in Table 1 and Table 2. Noteworthy, some of the molecular ions identified show striking similarities, such as $[Cu_7Zn_2](Cp^*)_4(Mes)$ and $[Cu_7Zn](Cp^*)_4(Mes)$. It may well be possible that these species have a fragment-parent ion relation with fragmentation occurring during ionization and not in the HCD cell. Other molecular ions, such as $[Cu_5](Cp^*)(Mes)_3$ and $[Cu_5](Cp^*)(Mes)_3$ seem to be the result of ligand exchange processes. For the ease of interpretation, such ions are grouped together in Table 1.

3. Results and Discussion
3.1 Methodical part: Exploration of living cluster libraries by LIFDI-MS

For some species, no significant variation in peak intensity was detected. Hence, no decision whether they are fragments or not is possible (see Figure 38, bottom). These species are also listed in Table 2. They might either be rather robust molecular ions that do not undergo fragmentation or fragment ions prone to further fragmentation reactions. The latter situation would lead to a "steady state" situation, in which formation and decay of the species is in equilibrium and therefore independent on the collision energy applied.

With the data and instrumentation at hand it is not possible to experimentally assign a fragment to a specific parent ion, which is due to the lack of an ion trap allowing for isolation of specific ions and study of their decay. However, the fragments can be tentatively assigned to a parent ion according to chemical considerations and according to fragmentation behavior observed for isolated species.

Fragmentation behavior of isolated species

The fragmentation behavior of four different and experimentally isolated pure clusters was determined, namely of $[CuZn_2](Cp^*)_3$, $[Cu_{10}Zn_2](Cp^*)_2(Mes)_6$ (**3**) and $[Cu_4Zn_{9/10}](Cp^*)_8$ (**4/5**) (the latter three compounds were discovered in the frame of this work and are described in the chemical section of Results and Discussion). The observed fragment peaks are summarized in Table S2 in the Appendix. For compound **3**, a rather simple fragmentation behavior was observed, mainly consisting of cleavage of -ZnCp*, -ZnMes, -Mes, -Cp*, -ZnCp*Mes or -ZnMes$_2$ units; a fact, which is closely related to its structure bearing -ZnCp* "capping" motifs (*vide infra*). For **4/5** and $[CuZn_2](Cp^*)_3$, however, a complicated fragmentation behavior including cluster rearrangement processes is observed. Besides cleavage of -ZnCp*, -ZnZnCp* or -CuCp* units, several (larger) clusters with new core compositions were detected. This fact is explained by the high temperature sensitivity of the compounds leading presumably to cluster growth, rearrangment or metal deposition processes during the LIFDI ionization process. As **3**, **4/5** and $[CuZn_2](Cp^*)_3$ also occur in the CuZn libraries, their fragment species can *directly be identified and assigned.*

It is noted that the molecular ion of $[CuZn_2](Cp^*)_3$ was not identified in the spectra of the CuZn library. However, its presence can be concluded from the characteristic fragmentation pattern observed (and is confirmed by *in situ* ^{1}H-NMR analysis, *vide infra*). Most of the other fragment species in the library spectra can be tentatively assigned to a parent ion assuming a similar fragmentation behavior as observed for the temperature stable, isolated species **3**. The results of the grouping process are included in Table 1.

3. Results and Discussion
3.1 Methodical part: Exploration of living cluster libraries by LIFDI-MS

Some of the species, for which no clear decision whether they are fragments or parent ions could be made, reveal striking similarities to molecular ion species. This is especially the case for those with $[Cu_7]$, $[Cu_7Zn]$, $[Cu_7Zn_2]$ and $[Cu_9]$ kernels. Based on chemical considerations concerning fragmentation procedures, these species are likely to result from $[Cu_7Zn_3](Cp^*)_3(Mes)_4$, $[Cu_7Zn_2](Cp^*)_4(Mes)$ / $[Cu_7Zn](Cp^*)_4(Mes)$ and $[Cu_9Zn_2](Cp^*)_3(Mes)_4$ / $[Cu_9Zn](Cp^*)_3(Mes)_4$ / $[Cu_9Zn_3](Cp^*)_4(Mes)_3$, respectively, by -Zn(L) or -Zn(L)$_2$ dissociation (L = mesityl, Cp*).

3. Results and Discussion

3.1 Methodical part: Exploration of living cluster libraries by LIFDI-MS

Table 1

*Molecular ion peaks (written in **bold** letters) identified in the LIFDI-MS spectra of Cu/Zn libraries (Cu:Zn 1:1.5) and fragment species (normal font) with tentative assignment to a parent ion. For the species in* **bold blue** *experimental isolation in pure form and study of fragmentation behavior is possible.*

Parent ion	
Fragments	
[Cu$_7$Zn$_3$](Cp*)$_3$(Mes)$_4$ / [Cu$_7$Zn](Cp*)$_2$(Mes)$_4$ / [Cu$_7$Zn](Cp*)$_3$(Mes)$_2$	**[Cu$_7$Zn$_2$](Cp*)$_4$(Mes) / [Cu$_7$Zn](Cp*)$_4$(Mes)**
[Cu$_9$Zn$_2$](Cp*)$_3$(Mes)$_4$ / [Cu$_9$Zn](Cp*)$_3$(Mes)$_3$	**[Cu$_{10}$Zn](Cp*)$_3$(Mes)$_3$**
	[Cu$_5$](Cp*)$_2$(Mes)$_2$ / [HCu$_5$](Cp*)$_2$(Mes) **[Cu$_5$](Cp*)(Mes)$_3$**
[Cu$_4$Zn$_{10}$](Cp*)$_8$ / [Cu$_4$Zn$_9$](Cp*)$_7$ [HCu$_3$Zn$_2$](Cp*)$_3$ [Cu$_3$Zn$_3$](Cp*)$_4$ [HCu$_5$Zn](Cp*)$_3$ / [Cu$_4$Zn$_2$](Cp*)$_3$ [HCu$_7$](Cp*)$_3$ [HCu$_4$](Cp*)$_2$	**[Cu$_4$](Cp*)(Mes)$_3$** **[Cu$_4$](Cp*)(Mes)$_2$**
[H$_3$Cu$_6$Zn$_5$](Cp*)$_5$(Mes)	**[CuZn$_2$](Cp*)$_3$** [CuZn](Cp*)$_2$ [Cu$_3$](Cp*)$_2$ [HCu$_7$](Cp*)$_3$ [H$_2$Cu$_7$Zn](Cp*)$_4$ [HCu$_4$](Cp*)$_2$
[HCu$_8$Zn$_3$](Cp*)$_4$(Mes)$_3$ [HCu$_8$Zn](Cp*)$_4$	**[Cu$_4$](Cp*)$_2$(Mes)**
[Cu$_9$Zn$_3$](Cp*)$_4$(Mes)$_3$	**[Cu$_3$Zn$_4$](Cp*)$_5$**
[HCu$_5$Zn$_2$](Cp*)$_4$(Mes) / [Cu$_5$Zn](Cp*)$_3$Mes [Cu$_5$Zn$_2$](Cp*)$_4$	**[Cu$_{10}$Zn$_2$](Cp*)$_2$(Mes)$_6$**

* the peak [H$_3$Cu$_6$Zn$_5$](Cp*)$_5$(Mes) has very low signal intensity rendering analysis of its fragmentation behavior difficult. Due to its supposed reactivity towards CO_2, however, it is listed as a molecular ion.

Note: The evaluation of the fragmentation behavior is still hampered by the mentioned bias in peak integration at CE > 15. The given assignment is therefore still prone to some uncertainty. Strategies

3. Results and Discussion

3.1 Methodical part: Exploration of living cluster libraries by LIFDI-MS

to overcome the bias in integration, e.g. by a correction factor accounting for the generation of light fragments with $m/z < 200$ are currently implemented into the integration program.

Table 2
Peaks for which no clear assignment molecular ion vs. fragment was possible.

peaks with unclear assignment	potential parent ion (see Table 1)
$[Cu_2Zn_3](Mes)_3$	
$[H_2Cu](Cp^*)_3$	
$[Cu_2Zn](Cp^*)_3$	
$[HCu_3Zn](Cp^*)_3$	
$[Cu_3Zn_2](Cp^*)_4$	$[Cu_3Zn_4](Cp^*)_5$
$[Cu_7](Cp^*)_2(Mes)_3$	$[Cu_7Zn_3](Cp^*)_3(Mes)_4$
$[Cu_7](Cp^*)_2(Mes)_4$	$[Cu_7Zn_3](Cp^*)_3(Mes)_4$
$[Cu_7](Cp^*)_3(Mes)$	$[Cu_7Zn_2](Cp^*)_4(Mes)$ / $[Cu_7Zn_3](Cp^*)_3(Mes)_4$
$[Cu_7](Cp^*)_2(Mes)_2$	$[Cu_7Zn_3](Cp^*)_3(Mes)_4$
$[HCu_7](Cp^*)_2(Mes)$	$[Cu_7Zn_2](Cp^*)_4(Mes)$ / $[Cu_7Zn_3](Cp^*)_3(Mes)_4$
$[Cu_7](Cp^*)_3(Mes)_2$	$[Cu_7Zn_3](Cp^*)_3(Mes)_4$
$[Cu_7Zn_2](Cp^*)_3(Mes)_3$	$[Cu_7Zn_3](Cp^*)_3(Mes)_4$
$[Cu_9](Cp^*)_2(Mes)_2$	$[Cu_9Zn_2](Cp^*)_3(Mes)_4$ / $[Cu_9Zn](Cp^*)_3(Mes)_3$ / $[Cu_9Zn_3](Cp^*)_4(Mes)_3$
$[Cu_9](Cp^*)_3(Mes)$	$[Cu_9Zn_2](Cp^*)_3(Mes)_4$ / $[Cu_9Zn](Cp^*)_3(Mes)_3$ / $[Cu_9Zn_3](Cp^*)_4(Mes)_3$
$[HCu_9](Cp^*)(Mes)_4$	$[Cu_9Zn_2](Cp^*)_3(Mes)_4$
$[H_3Cu_6Zn_5](Cp^*)_5(Mes)$	
$[Cu_{10}Zn_3](Cp^*)_3(Mes)_5$	
$[Cu_9](Cp^*)_3(Mes)_2$	$[Cu_9Zn_2](Cp^*)_3(Mes)_4$ / $[Cu_9Zn](Cp^*)_3(Mes)_3$ / $[Cu_9Zn_3](Cp^*)_4(Mes)_3$

91

3.1.4. Theoretical analysis

Remark: Theoretical analysis was conducted by the group of Prof. Juarez L.F. Da Silva (University of Sao Paulo, Brazil) and Prof. Jean-Yves Saillard (University of Rennes, France). The individual contributions are marked in the text.

Theoretical analysis of cluster species can be divided into different levels of complexity. In the simplest case, experimental structural information is available from SC-XRD (single crystal Xray diffraction) experiments with unambiguous assignment of the elements to the atom positions. For such cases, the Xray structure may serve as a direct input for theoretical calculations allowing for detailed bonding analysis. Such scenarios are supposed to be rather "classical" and will not be discussed further in this methodical part. However, it is referred to the theoretical treatment of the embryonic Cu/Al clusters $[Cu_4Al_4](Cp^*)_5(Mes)$ and $[Cu_2Al](Cp^*)_3$ in the chemical part, which may serve as illustrative examples for such a procedure.

The degree of information to be extracted from SC-XRD experiments might however be limited due to twinning effects, disorder or due to several co-crystallizing cluster species. Further, some elements are not be discernible by SC-XRD (hydrides) or not distinguishable (Cu and Zn). In these cases, the information obtained can serve as an input for theoretical calculations to deduce *e.g.* the position of hydrides or the elemental distribution. An example for the first scenario is location of the hydride in **1_H**, which was determined by DFT calculations. An example for the second scenario is the M_{13}/M_{14} cluster mixture $[Cu_4Zn_{9/10}](Cp^*)_8$ (**4/5**), which can be obtained in single crystalline form in very low yield from Cu/Zn library solutions (co-crystallization of **4** and **5** in the elementary cell). In this case, the elemental composition was determined by isotopic labelling experiments with ^{68}Zn and the location of the elements in the crystal structure was accomplished by DFT calculations based on the Euclidean similarity analysis (*vide supra*).

The most complex scenario concerns cases, in which no structural data at all is available. *Ab initio* modeling based on computational techniques like BHMC (basin hoppin Monte-Carlo) or genetic algorithms (tree-growth algorithm and Euclidean similarity analysis) is then the method of choice to propose a structure. The theoretical background of these methods is explained in the introduction. The procedure will shortly be discussed for $[Cu_7Zn_3](Cp^*)_3(Mes)_4$ observed as a parent ion and prominent peak in LIFDI-MS spectra of the Cu/Zn library.

3. Results and Discussion
3.1 Methodical part: Exploration of living cluster libraries by LIFDI-MS

In all cases, once a global minimum structure has been identified, detailed bonding analysis is the subsequent step in theoretical analysis. It serves as a benchmark for any reactivity assessment and might allow for predictions of reactivity patterns. This will be illustrated for the species **1** and **2**.

The Cu/Zn library

The following structure optimizations were carried out by Da Silva et al.

Single crystal analysis of the $M_{13/14}Cp*_8$ cluster mixture **4/5** reveals a structure of three distorted, interpenetrated tetrahedra surrounded by 8 Cp* ligands. In the case of the M_{14} cluster, one Cp* ligand is binding η^2-coordination mode to two metal atoms. Once the overall composition of the compound was addressed by isotopic labeling experiments (see Table 1 and Figure 61), the occupation of the metal sites was determined by total energy density functional theory (DFT) calculations. Several trial configurations were generated using the XRD framework structure, in which the Cu *vs.* Zn occupation of the metal sites were randomly fixed, keeping the chemical composition constant, in order to identify the lowest energy positional isomers. Although the number of sites is relatively small, the number of trial configurations is large due to the many possible combinations. Hence, it has a substantial computational cost. Thus, Euclidean similarity distance algorithm is applied to remove similar trial configurations, reducing the initial set to a smaller set of trial structures on which full geometry optimization were performed. The thus obtained lowest energy isomers of **4** and **5** are depicted in Figure 41.

These obtained low-energy isomers mark the starting point towards further theoretical analysis of the cluster mixture **4/5** including a detailed bonding analysis. Such work is currently in progress in the group of *Prof. Saillard.*

For *ab initio* modeling, the cluster $[Cu_7Zn_3](Cp*)_3(Mes)_4$ was chosen, as it represents a prominent species in the reaction solution. The theoretical procedure in such a case is organized in two steps. First, the cluster core without ligands is optimized based on genetic algorithms as presented in the introduction and as done in many theoretical works on small, naked metal clusters.[189] In a second step, the lowest-energy isomers of the clusters are introduced to the ligand environment. In this step, all Cp* protected clusters are much easier to handle, as Cp* behaves flexible to a certain degree in terms of its coordination mode to the metal centers. Therefore, in a simplified picture, the ligand environment can be regarded as spherical shell, in

which the cluster core can be rotated by the algorithm in order to determine new trial structures for energy optimization. However, such a procedure is tackled with difficulties upon treatment of the mesityl ligand, usually adopting a bridging μ^2-binding mode. Implementation of this chemical prerequisite into the theoretical algorithm is currently accomplished by the group of *Prof. Da Silva*.

[Cu₄Zn₉](Cp*)₈

4

[Cu₄Zn₁₀](Cp*)₈

5
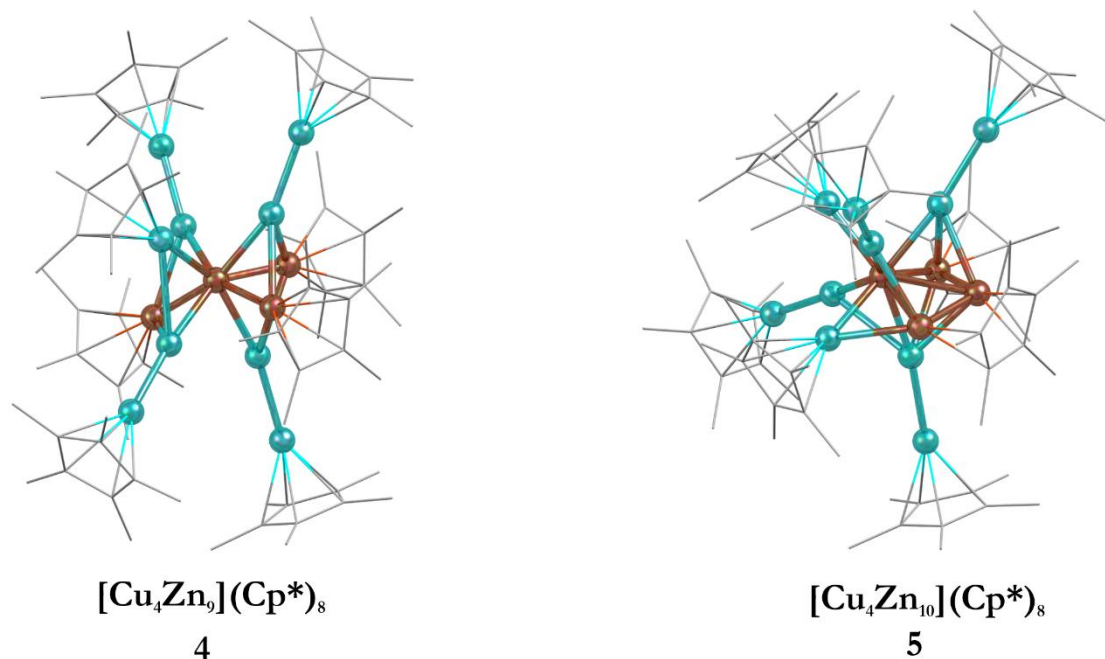
Figure 41
Lowest-energy isomers of [Cu₄Zn₉](Cp)₈ (**4**) and [Cu₄Zn₁₀](Cp*)₈ (**5**) based on the experimentally available single-crystal data with elemental composition obtained by isotopic labelling ⁶⁸Zn experiments and elemental distribution obtained by DFT calculations using the Euclidean similarity distance algorithm. Color code: Cu = dark orange, Zn = light blue.*

The Cu/Al microlibrary

SC-XRD of single crystals of the micro-library $1_H/2$ reveals detailed structural information. Both compounds 1_H and 2 consist of an octahedral shell of six AlCp* ligands embedding a [Cu₇], a [Cu₈] core, respectively (see Figure 42). The [Cu₇] and [Cu₈] kernels consist of a tricapped, a tetracapped, respectively, [Cu₄] tetrahedron and hence differ by only one external Cu atom. This information can be extracted from SC-XRD data in the form of one only partially occupied Cu atom (see chapter 3.2.3). Notably, the location of the hydride cannot be determined by means of SC-XRD.

3. Results and Discussion

3.1 Methodical part: Exploration of living cluster libraries by LIFDI-MS

The rather compact $Cu_4@Cu_4@Al_6$ shell arrangement of the inner core in **2** suggests looking it as a superatom[33, 196-197] with an electronic structure that can be rationalized within the spherical jellium model.[104] Indeed, its number of core bonding electrons (1 x 8 (Cu) + 2 x 6 (AlCp*) = 20) is one of the closed-shell stability "magic" numbers predicted by this model. It corresponds to the $1S^2\ 1P^6\ 1D^{10}\ 2S^2$ jellium electron configuration (the 3d(Cu) electrons are not supposed to be involved in this count[93]). This is confirmed by DFT calculations on **2** and on a simplified model in which the Cp* ligands were replaced by Cps. In the latter model, ten occupied Kohn-Sham orbitals can be easily identified as the jellium orbitals containing the 20 cluster electrons. The computed HOMO-LUMO gap of **2** is 1.17 eV and the HOMO, which is the weakly bonding 2S orbital (Figure 42 a), right side), lies 0.90 eV above the HOMO-1, which is of 1D nature.

Going from **2** to **1$_H$** also restores the closed-shell "magic" 20-electron configuration and provides an additional 1s(H) orbital that can participate to cluster bonding. Two low-energy isomers were found (see Figure 42 b), middle). In **1$_H$(a)** the hydride occupies the μ_3 capping position of the "missing" copper atom in **1**, In the isomer **1$_H$(b)**, which is the most stable by 5 kcal/mol, the hydride sits inside the copper cage ($H@Cu_4@Cu_3@Al_6$). Owing to the elongated shape of the inner Cu_4 tetrahedron, the hydride does not occupy its very center, but lies close to the smaller Cu_3 triangular face, in an μ_3 bonding mode. This configuration exhibits a large HOMO-LUMO gap of 1.81 eV. It is of note that, in both **1$_H$(a)** and **1$_H$(b)** isomers, the hydride caps the same Cu_3 face, but in an outer and inner position, respectively. In both isomers, the hydride NAO charge is substantially negative (-0.35 and -0.58, respectively).

Notably, the mixture **1$_H$/2** was analyzed by means of SC-XRD. However, according to DFT calculations and PXRD data, **1$_H$** and its radical congener **1** are supposed to be isostructural (see Figure S95). Removing one of the Cu2/Cu2a second-shell atoms in **2** generates the $[Cu_4@Cu_3@Al_6](Cp^*)_6$ odd-electron cluster **1**, with limited structural changes of the optimized geometry and a still rather spherical molecular shape. From the electronic structure point of view, when going from **2** to **1**, one loses one 4s(Cu) orbital (involved in cluster bonding) and the electron it contains. The result is a limited weakening of the bonding character in the occupied jellium orbitals. On the other hand, the electron loss generates a paramagnetic 19-electron superatom, with a singly occupied 2S HOMO (Figure 42 b), right side). This SOMO resembles somewhat the HOMO of **2** but is polarized on the capping Cu atom *trans*

to its "missing" congener. It also gets some contribution from three Al atoms (Figure 42 b).

a)

2   HOMO of **2**

b)

1$_H$

1$_H$(a)
ΔG = 4.9 kcal/mol

1$_H$(b)
ΔG = 0.0

SOMO of **1**
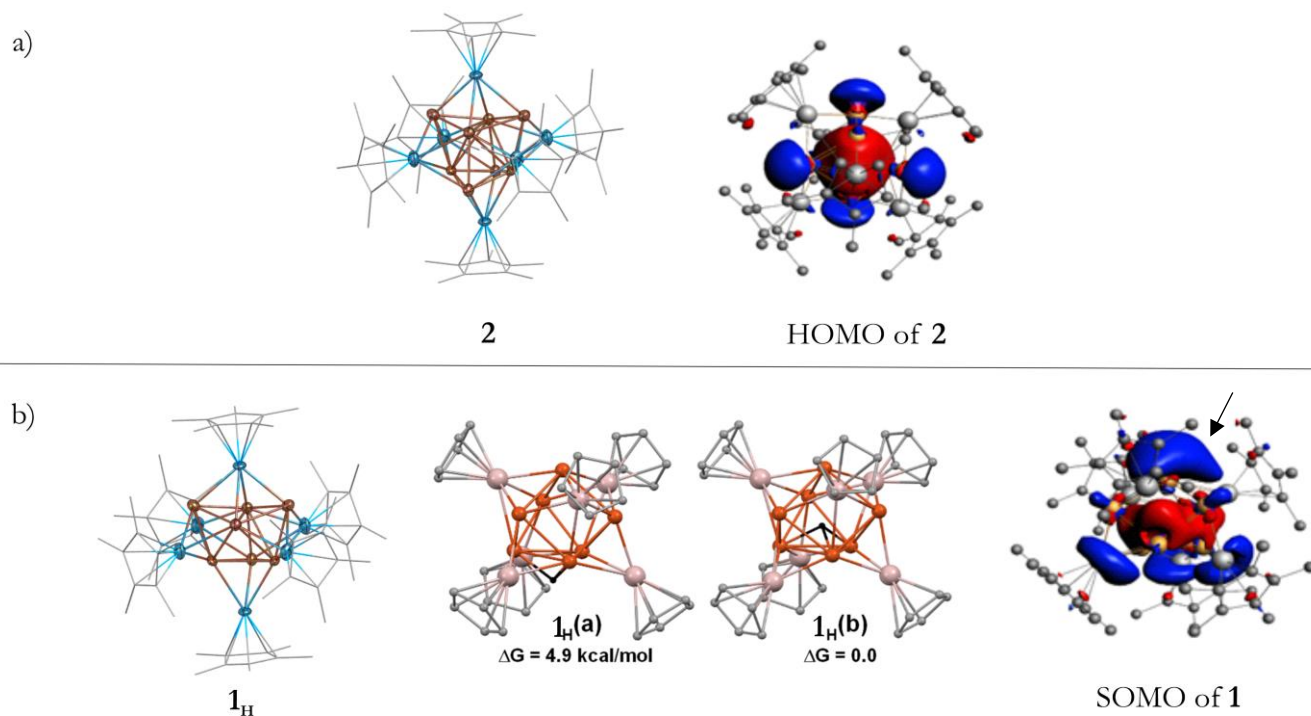
Figure 42
*a) Molecular structure of **2** in the solid state as determined by SC-XRD (left) and HOMO of **2** according to DFT calculations (right). b) Molecular structure of **1**$_H$ in the solid state as determined by SC-XRD (left); the two computed isomers of **1**$_H$ (methyl groups omitted for clarity) with the μ$_3$-hydride shown in black (middle) and SOMO of the radical species **1** according to DFT calculations (right). The SOMO of **1**, which is associated with the radical reactivity of this species is marked by an arrow. It is referred to Figure 72 and the associated text for a detailed crystallographic representation of **1**$_H$ and **2**.*

3.1.5. Reactivity studies

Reactivity assessment of cluster libraries is based on the motivation that species that are isolable and characterizable in a classical manner usually represent rather inert systems with a closed-shell electronic configuration and/or high steric protection. Both factors are considered to be unfavorable for catalytically interesting surface reactions (of course, the species might still be reactive). Further, during work-up procedures a lot of the original chemical "information" and diversity contained in the libraries is lost. For example, highly reactive species with open coordination sites or open-shell configurations might occur in small amounts in solution. In this dissertation project, LIFDI-MS analysis turned out to be a powerful tool to assess

reactivity patterns directly from reaction solutions. The procedure will again be presented on two different examples, namely the "micro-library" $[Cu_{7/8}Al_6](Cp^*)_6$ undergoing Cu-atom incorporation, C-H and Si-H activation reactions (see Scheme 10), as well as on the large CuZn library presented above undergoing CO_2 absorption.

The Cu/Al micro-library

The open-shell superatom $[Cu_7Al_6](Cp^*)_6$ (**1**) is anticipated to exhibit higher reactivity than its closed-shell congener $[Cu_8Al_6](Cp^*)_6$ (**2**). This reactivity difference is reflected by its ability to undergo Cu-atom incorporation upon exposure to Cu(I) sources (leading to the closed-shell species **2**), as well as by C-H and Si-H activation reactions of toluene and $(TMS)_3Si$, respectively (TMS = trimethylsilyl).

When the micro-library $[Cu_{7/8}Al_6](Cp^*)_6$ (**1/2**) is subjected to [CuMes] at elevated temperature (75 °C) in toluene, LIFDI-MS analysis of the reaction solution reveals complete disappearance of the molecular ion peak associated to $[Cu_7Al_6](Cp^*)_6$, whereas the one of $[Cu_8Al_6](Cp^*)_6$ remains unchanged (see Figure 43). It is assumed that, due to its radical nature, $[Cu_7Al_6(Cp^*)_6$ is more reactive towards [CuMes], while $[Cu_8Al_6](Cp^*)_6$ remains initially unreacted. The reaction was further elucidated by additional NMR experiments, as well as by TEM microscopy of evaporated reaction solutions (see chemical part). The results indicate that both **1** and **2** are prone to cluster growth reactions with external [CuMes]. However, **2** is formed as the initial reaction product from **1** + [CuMes]. Due to its closed-shell character, **2** is considered as an "island of stability" undergoing rather slow cluster growth processes. Noteworthy, these reactivity differences are directly evident from in-situ mass spectrometric experiments.

3. Results and Discussion
3.1 Methodical part: Exploration of living cluster libraries by LIFDI-MS
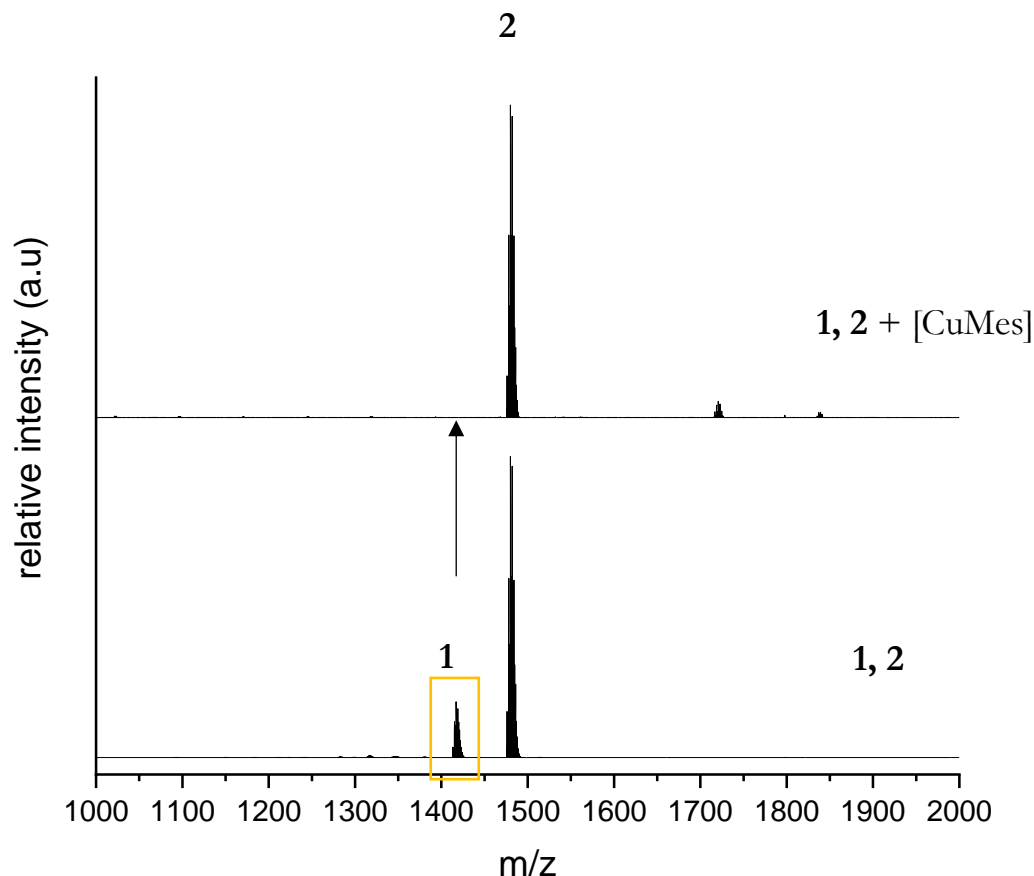
Figure 43
In situ LIFDI-MS analysis of the reaction of 1,2 with [CuMes] (5 eq., toluene, 75 °C, 5 h).

When $[Cu_{7/8}Al_6](Cp^*)_6$ (**1/2**) is heated in toluene to 110 °C for several days, LIFDI-MS analysis of the solution indicates partial transformation of $[Cu_7Al_6](Cp^*)_6$ to $[HCu_7Al_6](Cp^*)_6$. The maximum of the detected product peak in the mass spectrum coincides with the one of $[HCu_7Al_6](Cp^*)_6$. However, the relative intensities of the isotopologues do not match to the isotopic pattern of $[HCu_7Al_6](Cp^*)_6$, which requires the peak to be an overlap between a peak of $[Cu_7Al_6](Cp^*)_6$ and of $[HCu_7Al_6](Cp^*)_6$. Deconvolution of the peak is possible by a computerized numerical algorithm calculating a GoF (goodness of fit value) for all possible fractions of **1** and **1H**. The composition with the best GoF value corresponds best to the measured peak. For the example of the **1/1H** mixture, the peak was found to consist to 29 % out of **1H** and to 71 % out of **1** (see Figure 44 a) for illustration). Noteworthy, these values do <u>not</u> have a chemical meaning, as the relative ionizabilities of **1** and **1H** are unknown. In contrast, the closed-shell species **2** did not undergo any transformation during heating in toluene, such as it was expected from electronic structure considerations.

3. Results and Discussion

3.1 Methodical part: Exploration of living cluster libraries by LIFDI-MS
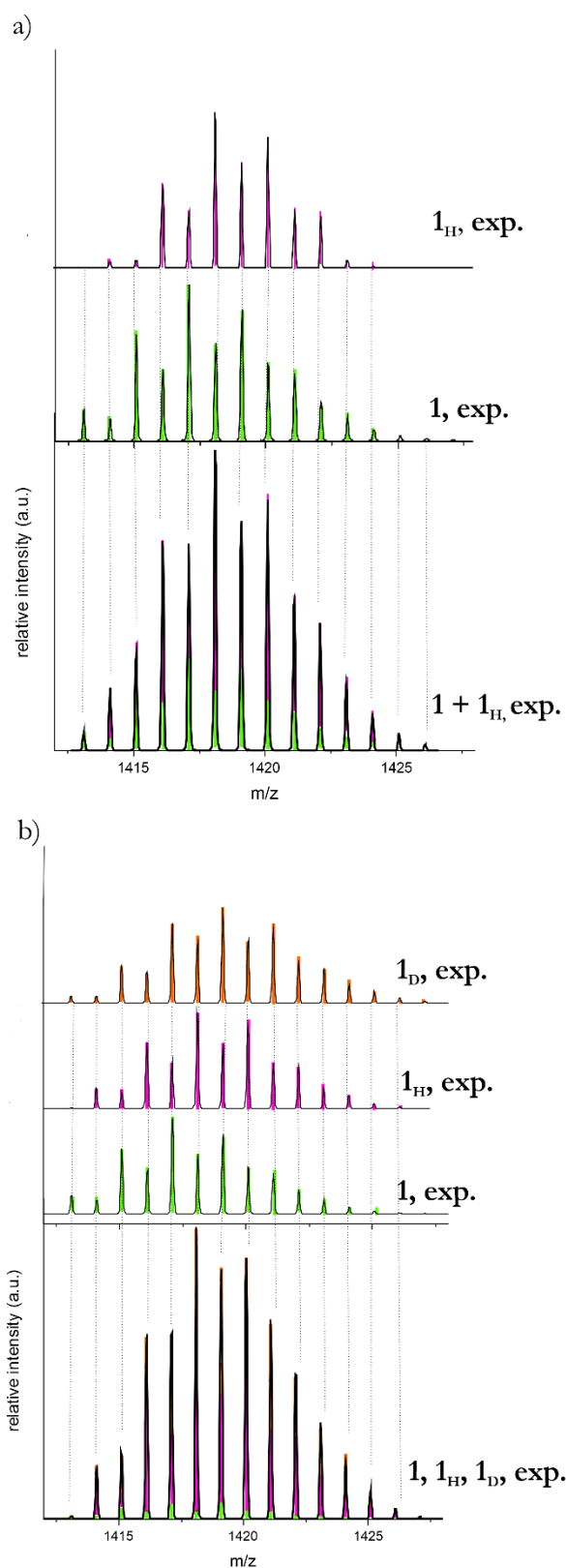
Figure 44

*Deconvolution of LIFDI-MS peaks. a) Isotopic pattern of a mixture of **1** and **1**$_H$ after heating **1** in toluene (110 °C, 7 days). b) Isotopic pattern of a mixture of **1**, **1**$_H$ and **1**$_D$ after reacting **1** with (TMS)₃SiD (110 °C, 5 days, toluene). Fractions of **1**, **1**$_H$ and **1**$_D$ are illustrated in green, purple and orange, respectively.*

3. Results and Discussion

3.1 Methodical part: Exploration of living cluster libraries by LIFDI-MS

GC-MS is a powerful tool for the detection of organic side products in such cluster reactivity studies. Whereas obviously no cluster products can be detected by this method due to the required aqueous work-up, organic products or ligands are well identified in their metal-cleaved and protonated (water-stable) form. For the above-mentioned experiment, no activation product of toluene was detected in GC-MS analysis of the reaction solutions. Instead, pentamethylfulvene was identified as the final organic reaction product. However, in toluene-d_8, no conversion from **1** to **1$_H$** was detected by LIFDI-MS at all. By simple combinatoric considerations, this leads to the conclusion that toluene-h_8 plays a crucial role in the reaction as the initial source of the hydride in **1$_H$**. Obviously, this toluene activation is much slower with toluene-d_8. The resulting toluene radicals are supposed to react further with Cp* ligands to result in formation of the C-H activation product of Cp*, pentamethylfulvene. A more detailed interpretation of the results can be found in the chemical part (chapter 3.2.3).

Partial transformation of **1** to **1$_H$** is also observed when **1/2** is reacted with (TMS)$_3$SiH. However, from this experiment alone, the origin of the hydride is not clear, as it might stem from a C-H or Si-H activation reaction or of a combination of both. Repeating the experiment with (TMS)$_3$SiD leads to a complicated isotopic pattern, as shown in Figure 44 b). Deconvolution of the peak considering **1**, **1$_H$** and **1$_D$** as constituents reveals it to be mixture of all three components (with **1$_H$** as the largest and **1** as the smallest fraction). Importantly, the detection of **1$_D$** in the reaction mixture unambiguously proves the ability of **1** not only to undergo C-H, but also Si-H/Si-D activation reactions. The results clearly demonstrate how a combinatorial design of experiments using *in-situ* LIFDI-MS analysis as major tool for the analysis of reaction solutions allows for the establishment of novel reactivity patterns (a more detailed discussion of the experiments and results is found in the chemical section). The reactivity of the open-shell cluster [Cu$_7$Al$_6$](Cp*)$_6$ (**1**) is summarized visually in Scheme 10.

3. Results and Discussion

3.1 Methodical part: Exploration of living cluster libraries by LIFDI-MS
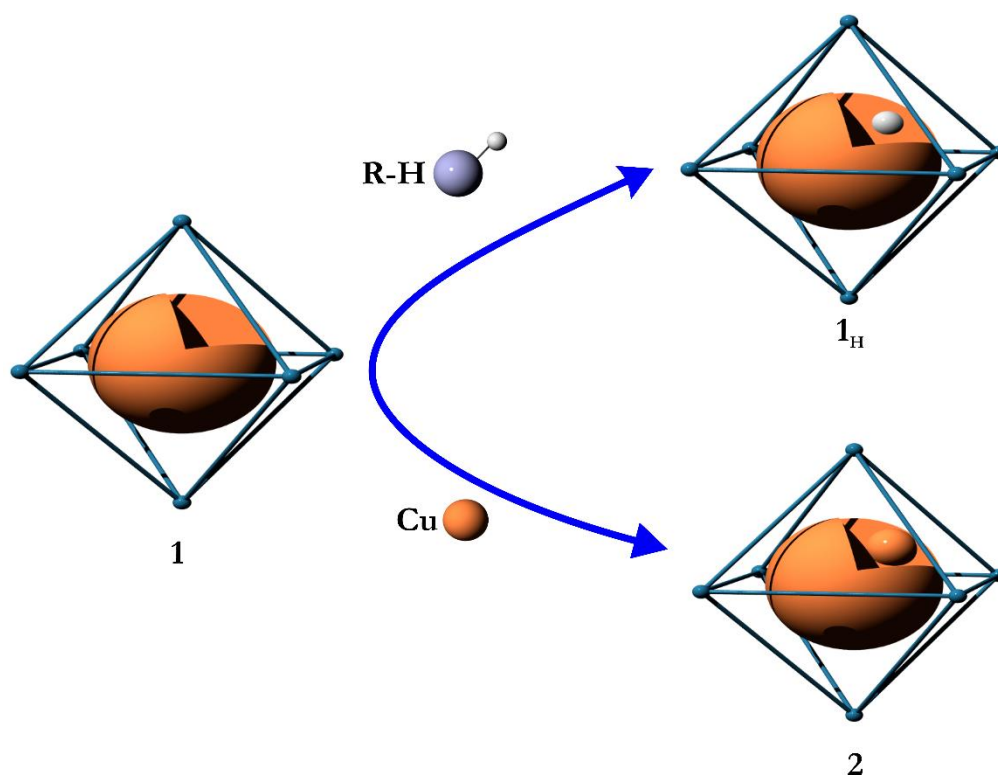
Scheme 10

*Illustration of the reactivity of the radical species $[Cu_7Al_6](Cp^*)_6$ (**1**) towards R-H (R = C, Si) and Cu-sources. $[Cu_7Al_6](Cp^*)_6$ undergoes C-H and Si-H activation of toluene, $(TMS)_3SiH$ and $(TMS)_4Si$ at elevated temperatures resulting in the hydride cluster $[HCu_7Al_6](Cp^*)_6$ (**1_H**). Reaction of $[Cu_7Al_6](Cp^*)_6$ with [CuMes] results in Cu atom incorporation and formation of $[Cu_8Al_6](Cp^*)_6$ (**2**). [Reprinted (adapted) with permission from M. Schütz, C. Gemel, M. Muhr, C. Jandl, S. Kahlal, J. Y. Saillard and R. A. Fischer, Exploring Cu/Al cluster growth and reactivity: From embryonic building blocks to intermetalloid, open-shell superatoms. Chem. Sci. 2021, 12, 6588-6599. Copyright 2021. Published by the Royal Society of Chemistry. Link: https://pubs.rsc.org/en/content/articlehtml/2021/sc/d1sc00268f.]*

The Cu/Zn library

As a more complicated example, reactivity of the CuZn cluster library was studied by *in-situ* LIFDI MS without prior isolation of any species. Reaction of the library solution with 1 bar CO_2 at room-temperature for 3-5 hours results in only subtle changes in library composition according to LIFDI-MS analysis. Two new peaks at $m/z = 1543$ and $m/z = 1630$ are the most prominent feature of the spectra of the reaction solutions (see Figure 45).

3. Results and Discussion
3.1 Methodical part: Exploration of living cluster libraries by LIFDI-MS
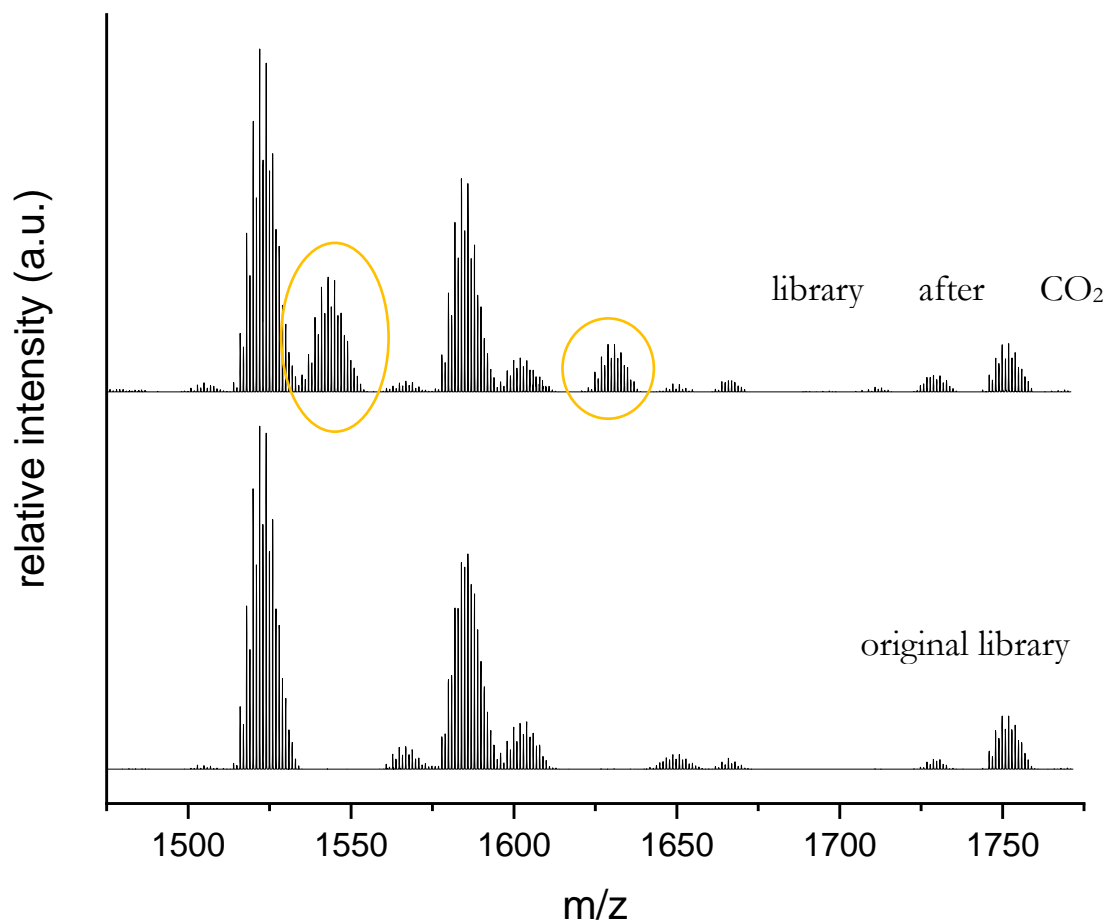
Figure 45
Cut-out of the in situ LIFDI-MS spectra of the Cu/Zn library before (bottom) and after (top) treatment with CO_2 (1 bar, RT, 5 h). Peaks corresponding to product species are marked in yellow.

The new peaks were analyzed by the same procedure as presented above for the original ones. Unambiguous assignment as $[Cu_5Zn_5](Cp^*)_6(CO_2)_2$ and $[Cu_8Zn_3](Cp^*)_3(Mes)_4(CO_2)$ was achieved by labeling experiments with $[^{68}Zn_2](Cp^*)_2$, whereas labeling with $[Zn_2](Cp^{*Et})_2$ led to inconclusive results due to strongly overlapping peaks. Noteworthy, the use of $^{13}CO_2$ leads to the expected $\Delta m/z$ shift of two for the ion peak of $[Cu_5Zn_5](Cp^*)_6(CO_2)_2$ and of one for the ion peak of $[Cu_8Zn_3](Cp^*)_3(Mes)_4(CO_2)$ in the LIFDI-MS spectrum (see Figure 46 for illustration) . Therefore, the number of bound CO_2 units in $[Cu_5Zn_5](Cp^*)_6(CO_2)_2$ and $[Cu_8Zn_3](Cp^*)_3(Mes)_4(CO_2)$ is unambiguously confirmed. It has to be noted that, in principle, the determined sum formulas would also be in line with a splitting of the CO_2 ligand into M-CO and M-O (M= Cu, Zn) units.[198] However, due to simplicity, the sum-formulas of the reaction products will be written as $[Cu_5Zn_5](Cp^*)_6(CO_2)_2$ and $[Cu_8Zn_3](Cp^*)_3(Mes)_4(CO_2)$ in the following.

3. Results and Discussion

3.1 Methodical part: Exploration of living cluster libraries by LIFDI-MS
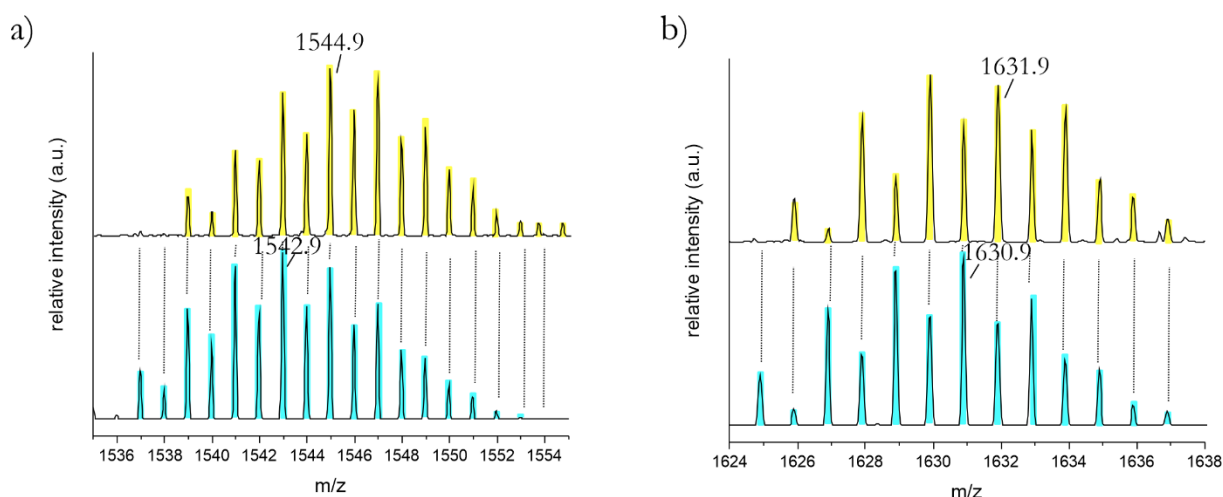
Figure 46

a) Visualization of the △m/z shift of 2 in the isotopic pattern of [Cu₅Zn₅](Cp*)₆(¹³CO₂)₂ (upper trace, yellow) in comparison to its unlabeled congener [Cu₅Zn₅](Cp*)₆(CO₂)₂ (lower trace, blue). b) Visualization of the △m/z shift of 1 in the isotopic pattern of [Cu₈Zn₃](Cp*)₃(Mes)₄(¹³CO₂) (upper trace, yellow) in comparison to its unlabeled congener [Cu₈Zn₃](Cp*)₃(Mes)₄(CO₂) (lower trace, blue). All patterns were experimentally determined by LIFDI-MS.

Inspection of the list of molecular ions (see Table 1) allows to propose possible precursors for the detected reaction products. The suggested reaction sequences are depicted in Scheme 11. It is noted that these reaction sequences are only suggestions based on related core compositions and metal:ligand ratios. They basically represent CO_2 incorporation accompanied by slight cluster rearrangement processes. For example, reaction sequence A is accompanied by release of three hydride ligands and replacement of one "CuMes" unit by Cp*. Reaction sequence B is likewise associated with loss of one hydride ligand and with a ligand exchange process (Cp*-> Mes). It is referred to the chemical part for a more detailed discussion of the underlying chemistry and for additional *in situ* NMR experiments.

$$\text{A:} \quad [H_3Cu_6Zn_5](Cp^*)_5(Mes) \xrightarrow{\quad CO_2 \quad} [Cu_5Zn_5](Cp^*)_6 (CO_2)_2$$

$$\text{B:} \quad [HCu_8Zn_3](Cp^*)_4(Mes)_3 \xrightarrow{\quad CO_2 \quad} [Cu_8Zn_3](Cp^*)_3(Mes)_4(CO_2)$$
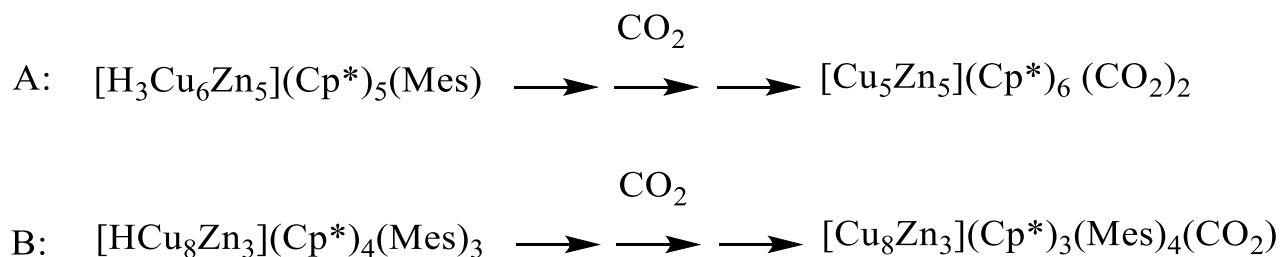
Scheme 11

Suggested reaction sequences for the formation of the two identified reaction products in the Cu/Zn library after CO₂ treatment.

Notably, the reaction time was shown to be a key parameter concerning the composition of the library. Prolonged reaction times (> 6 h) lead to very complex spectra with an increasing number of unprecedented peaks culminating in extremely complex spectra with many overlapping peaks after a total reaction time of 3 days. Precise adjustment of reaction conditions, which only lead to subtle spectral changes, is therefore considered to be a prerequisite for the investigation of reaction outcomes by LIFDI-MS. For the conditions applied (CO_2, 1 bar, RT, 6h), no other reproducible, significant changes apart from the two novel peaks discussed above were observed in LIFDI-MS spectra of the reaction solutions. In this context, it is of note that LIFDI-MS does not allow for quantification. Changes in library composition may well influence the ionization efficiency of other species. Further, the presence of product species, that are not ionizable by the LIFDI technique, cannot be excluded.

3.1.6 Size-focusing of cluster libraries

As explained above, LIFDI-MS is a powerful tool for the *in-situ* exploration of intermetalloid cluster libraries and assessment of their reactivity. Of note, the most reactive species in the library might not be the most prominent ones, rendering their isolation a difficult task. Nevertheless, isolation of specific cluster species is associated with a high gain of information by additional spectroscopic techniques (NMR analysis, structural information by SC-XRD, IR analysis). Synthesis of certain outstanding cluster species like the radical **1** was shown to be possible by precise adjustment of reaction conditions and monitoring the course of the reactions by LIFDI-MS, UV-Vis or NMR spectroscopy. The procedure is exemplary illustrated in the following for the mixture $[Cu_{7/8}Al_6](Cp^*)_6$ (**1/2**), for $[Cu_{10}Zn_2](Cp^*)_2(Mes)_6$ (**3**) and for the Au/Al cluster compounds $[H_xAu_7Al_6](Cp^*)_6$ (**7**) and $[Au_2Al_5](Cp^*)_5$ (**8**).

Size-focusing of Cu/Al cluster libraries by stoichiometry tuning

The following discussion is part of a published manuscript in the journal Dalton Transactions. [Reproduced (adapted) from M. Muhr, P. Heiss, M. Schütz, C. Gemel, M. H. Linden, H. B. Linden and R. A. Fischer, Enabling LIFDI-MS measurements of highly air sensitive organometallic compounds: A combined MS/glovebox technique. Dalton Trans. 2021, 50, 9031-9036 with permission from the Royal Society of Chemistry. Copyright 2021. Published by the Royal Society of Chemistry. Link: https://pubs.rsc.org/en/content/articlelanding/2021/dt/d1 dt00978h.]

The reaction of [CuMes] with 3.6 eq. of AlCp* produces a complex cluster library similar to the Cu/Zn one presented above with **2** as one of the major peaks in LIFDI-

3. Results and Discussion
3.1 Methodical part: Exploration of living cluster libraries by LIFDI-MS

MS analysis. Besides $[Cu_8Al_6](Cp^*)_6$ (**2**), the species $[Cu_6Al_7](Cp^*)_6$, $\{[Cu_7Al_7](Cp^*)_6 - 2H\}$ and an overlapping peak of a mixture of $\mathbf{1_H/1}$ are detected (see Figure 47 and Table 3). Noteworthy, peak identification is much easier in this case than for Cu/Zn libraries due to the larger difference in molecular mass and isotopic distributions between Cu and Al (^{27}Al is the only stable Al isotope). The species marked in bold in Table 3 are suggested to be molecular ions. They can all be described by the general formula $[Cu_aAl_b](Cp^*)_6$ (a+b =12, 13 or 14).

Addition of precise amounts of [CuMes] (overall final Cu:Al stoichiometry 1:1.2) to this library, followed by prolonged heating induces subtle spectral changes (see Figure 47 a)). Inspection of the peak at m/z = 1417 reveals it to correspond now to pure **1** instead of $\mathbf{1_H/1}$ (see Figure 47 b)). From these reaction solutions, isolation of the pure mixture **1/2** was possible after crystallization and a short work-up procedure. Obviously, all the other cluster species, especially those with unligated Al atoms, $[Cu_6Al_7](Cp^*)_6$ and $\{[Cu_7Al_7](Cp^*)_6 - 2H\}$, are removed or decomposed during the work-up procedure, potentially due to a high sensitivity or reactivity. Very interestingly, the amount of [CuMes] added to the original library is of crucial importance for the generation of pure **1**. Use of slightly less amounts resulted in isolation of mixtures of $\mathbf{1_H/1}$. The mechanism of the transformation of $\mathbf{1_H}$ to **1** remains however unclear and might be a project of further research.

The results nicely illustrate the following points: Without detailed analysis of reaction solutions by LIFDI-MS, feedback on the reaction design and access to pure **1**, as well as its subsequent reactivity assessment (*vide infra*) would not have been possible. Further, LIFDI-MS analysis of the reaction solution prior to crystallization sheds light on the existence of cluster species, which could not be captured by common crystallization procedures from these reaction solutions. Due to their naked Al atoms, these species might exhibit unique reactivity.

3. Results and Discussion

3.1 Methodical part: Exploration of living cluster libraries by LIFDI-MS

Table 3

List of ions observed in LIFDI-MS analysis of Cu/Al libraries before (Cu:Al stoichiometry 1:3.6) and after size-focusing towards the radical species [Cu$_7$Al$_6$](Cp)$_6$ (**1**) (final Cu:Al stoichiometry 1:1.2). Species in* **bold blue** *can be experimentally isolated as a co-crystallizate. Species marked in* **bold** *are supposed to be molecular ions according to chemical considerations.*

list of ion in Cu/Al library (Cu:Al = 1:3.6)	list of ions in Cu/Al library after size-focusing (Cu:Al = 1:1.2)
[CuAl$_4$](Cp*)$_4$	{[CuAl](Cp*)$_2$ -H}
[CuAl$_3$](Cp*)$_3$	[CuAl](Cp*)
[CuAl$_2$](Cp*)$_2$	[Cu$_2$Al$_2$](Cp*)$_3$
[Cu$_2$Al$_2$](Cp*)$_3$	[Cu$_2$Al](Cp*)$_2$
[Cu$_2$Al$_2$](Cp*)$_2$(Mes)	[Cu$_2$Al](Cp*)$_3$
[H$_3$Cu$_3$Al$_5$](Cp*)$_4$	
[Cu$_5$Al$_7$](Cp*)$_6$	
[Cu$_5$Al$_6$](Cp*)$_5$	
[Cu$_6$Al$_7$](Cp*)$_6$	**[Cu$_6$Al$_7$](Cp*)$_6$**
[Cu$_6$Al$_6$](Cp*)$_5$	[Cu$_6$Al$_6$](Cp*)$_5$
[Cu$_6$Al$_4$](Cp*)$_3$	[Cu$_6$Al$_4$](Cp*)$_3$
[Cu$_6$Al$_5$](Cp*)$_4$	
[Cu$_6$Al$_6$](Cp*)$_4$	
{[Cu$_7$Al$_2$](Cp*)$_4$(Mes)$_3$ - H}	
{[Cu$_7$Al$_5$](Cp*)(Mes)$_7$ -H} / [Cu$_7$Al$_7$](Cp*)$_5$(Mes)$_2$	{[Cu$_7$Al$_5$](Cp*)(Mes)$_7$ -H} / [Cu$_7$Al$_7$](Cp*)$_5$(Mes)$_2$
{[Cu$_7$Al$_7$](Cp*)$_6$ - 2H}	**{[Cu$_7$Al$_7$](Cp*)$_6$ - H}**
[(H)Cu$_7$Al$_6$](Cp*)$_6$	**[Cu$_7$Al$_6$](Cp*)$_6$**
[HCu$_7$Al$_6$](Cp*)$_5$	[HCu$_7$Al$_6$](Cp*)$_5$
[Cu$_7$Al$_4$](Cp*)$_4$	[Cu$_7$Al$_4$](Cp*)$_4$
[Cu$_7$Al$_6$](Cp*)$_4$	[Cu$_7$Al$_6$](Cp*)$_4$
{[Cu$_7$Al$_5$](Cp*)$_3$(Mes)$_6$ - H} / [Cu$_7$Al$_7$](Cp*)$_7$(Mes)	{[Cu$_7$Al$_4$](Cp*)$_3$ -H}
[HCu$_7$Al$_{19}$](Cp*)$_3$(Mes)$_3$	
[Cu$_8$Al$_6$](Cp*)$_6$	**[Cu$_8$Al$_6$](Cp*)$_6$**
[Cu$_8$Al$_6$](Cp*)$_5$	[Cu$_8$Al$_6$](Cp*)$_5$
{[Cu$_8$Al$_7$](Cp*)$_7$(Mes) - H}	[(H)Cu$_8$Al$_6$](Cp*)$_4$
[Cu$_8$Al$_6$](Cp*)$_6$(Mes)$_3$	{[Cu$_8$Al$_7$](Cp*)$_7$(Mes) - H}
	[H$_2$Cu$_8$Al$_6$](Cp*)(Mes)$_6$
	[Cu$_8$Al$_6$](Cp*)$_6$(Mes)$_3$

3. Results and Discussion
3.1 Methodical part: Exploration of living cluster libraries by LIFDI-MS
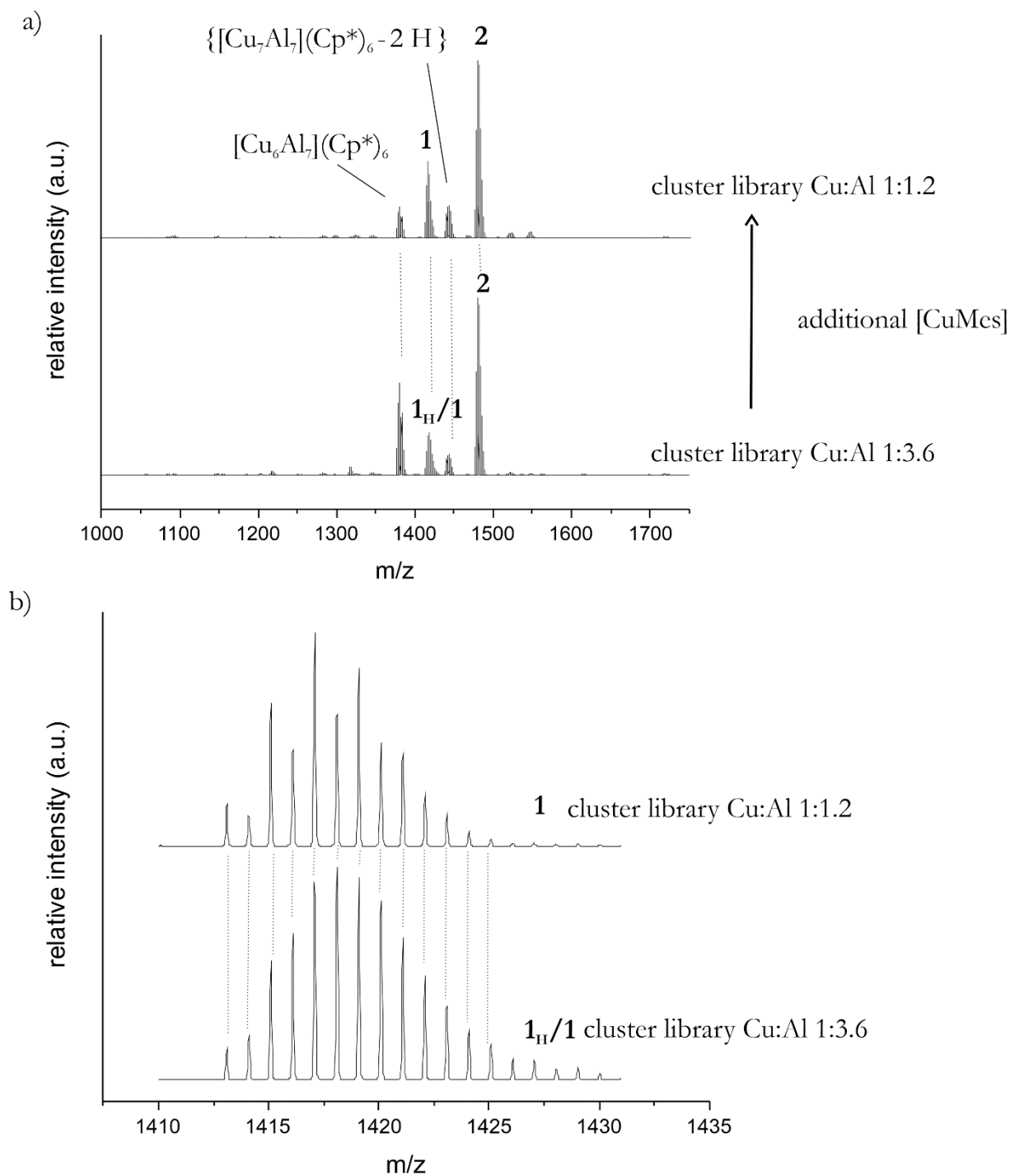
Figure 47
*Size-focusing of Cu/Al cluster libraries. a) Cut-out of the LIFDI-MS spectra of a Cu/Al library at different Cu:Al ratios. b) Enlarged peak at m/z = 1417, highlighting the efficient size-focusing process towards the radical species **1**.*

3. Results and Discussion
3.1 Methodical part: Exploration of living cluster libraries by LIFDI-MS

Size-focusing of Cu/Zn libraries by stoichiometry tuning

The cluster species $[Cu_{10}Zn_2](Cp^*)_2(Mes)_6$ (**3**) represents one of the molecular ion peaks in LIFDI-MS analysis of Cu/Zn libraries (see Table 1). Size-focusing towards this species was possible by precise adjustment of Cu:Zn stoichiometry and reaction conditions. Choice of the $[CuMes]:[Zn_2](Cp^*)_2$ stoichiometry was based on chemical considerations presented in Scheme 12. Noteworthy, partial reduction of Cu(I) to Cu(0) is accomplished by oxidation of ·ZnCp* units to Zn(II) species.

$$10\ [CuMes] + 3\ [Zn_2](Cp^*)_2 \longrightarrow [Cu_{10}Zn_2](Cp^*)_2(Mes)_6 + 6\ Zn(II)L_2$$

L = Mes, Cp*

6 x Cu(I)
4 x Cu(0)
2 x Zn(I)
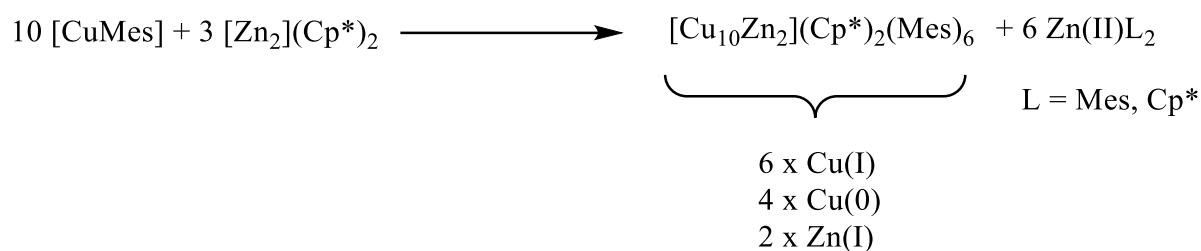
Scheme 12
*Chemical considerations concerning adjustment of the Cu:Zn stoichiometry for the size-focusing of Cu/Zn libraries towards compound **3**. Indeed $[Cu_{10}Zn_2](Cp^*)_2(Mes)_6$ was isolated from reaction solutions with the given Cu:Zn stoichiometry.*

Heating of $[CuMes]$ with 0.3 eq. of $[Zn_2](Cp^*)_2$ in toluene to 75 °C for seven days indeed leads to an *in-situ* LIFDI-MS spectrum of the reaction solution with **3**, {**3** + Mes} and $[Cu_9Zn_2](Cp^*)_3(Mes)_4$ as the most prominent peaks. The size-focusing process towards these species can nicely be monitored by LIFDI-MS (see Figure 48, bottom and middle). Whereas after a reaction time of 2 hours at room-temperature a complex library of more than 50 cluster species is produced, prolonged heating induces the size-distribution of the library to narrow down substantially. The library observed at room-temperature is nearly identical to the one analyzed by isotopic labeling with the very similar Cu:Zn stoichiometry of 1:0.75 (see Table S1). It is noted that the relative amount of $[Cu_9Zn_2](Cp^*)_3(Mes)_4$ in the final reaction solutions according to LIFDI-MS analysis was found to strongly depend on even very subtle and sometimes not controllable changes of the reaction conditions (temperature, stoichiometry, concentration). The very similar core compositions of **3** and $[Cu_9Zn_2](Cp^*)_3(Mes)_4$ might lead to the fact that these two clusters are likely to coexist within a given Cu:Zn stoichiometry range. Interestingly, alternate Cu:Zn stoichiometric ratios (especially Cu:Zn = 1:1.5) led to LIFDI-MS spectra with $[Cu_9Zn_2](Cp^*)_3(Mes)_4$ as the main peak after prolonged heating (see Figure S45). However, no isolation of the latter species was achieved from these solutions. In this context it is noted that quantification based on LIFDI-MS is not possible. Unfortunately, in *in situ* ^{1}H-NMR, compounds **3** and $[Cu_9Zn_2](Cp^*)_3(Mes)_4$ could not be detected due to overlapping peaks with many side products.

3. Results and Discussion

3.1 Methodical part: Exploration of living cluster libraries by LIFDI-MS

Pure compound **3** was isolated in a yield typical for highly sensitive molecular clusters (10 % based on Cu) and characterized from the size-focused reaction solutions. The LIFDI-MS spectrum of the isolated compound in shown in Figure 48, top (see chemical part for a detailed discussion of compound **3**). Interestingly, the peak {**3**+Mes} is also detected in the spectrum of the isolated compound. It is not clear whether this species is formed in solution by intermolecular ligand exchange processes or by adduct formation in the collision cell of the mass-spectrometer. The other peaks in the spectrum of isolated **3** are induced by fragmentation of **3** and are listed in Table S2 in the Appendix. As denoted above, the fragmentation behavior of isolated **3** was used as a model system to associate fragment ions to parent ions in mass spectra of complex Cu/Zn libraries (*vide supra*).
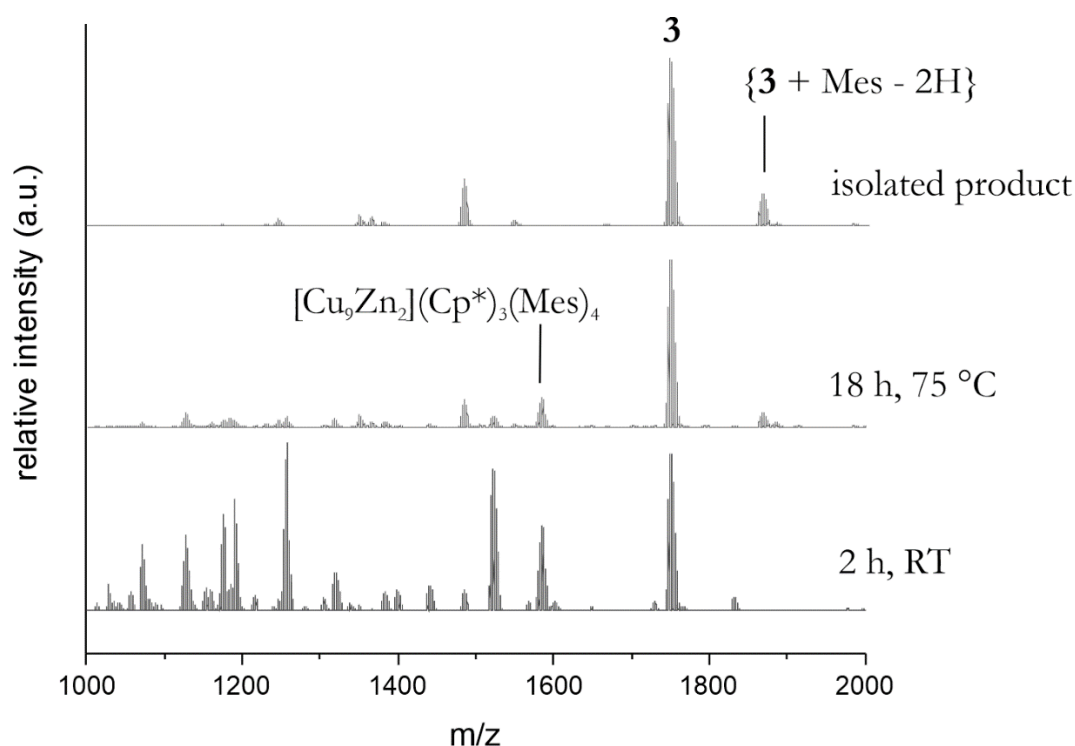
Figure 48
LIFDI-MS spectra illustrating the size-focusing process in the synthesis of **3** *([CuMes] + [Zn₂](Cp*)₂ 1:0.33, toluene) and spectrum of the isolated product (top).*

3.1.7 UV-Vis spectroscopy as a tool to monitor size-focusing processes

Quantitative analysis of UV-Vis data was conducted in collaboration with Tim Kratky from the group of Prof. Günther (chair of physical chemistry, TU Munich).

The reaction between the Au precursor [^{i}DippAuH] (^{i}Dipp = 1,3-bis(2,6-diisopropylphenyl)-2,3-dihydro-1H-imidazole) and AlCp* in a 1:1 stoichiometric ratio leads to the cluster species [$H_x Au_6 Al_6$](Cp*)$_6$ (**6**), [$Au_7 Al_6$](Cp*)$_6$ (**7**) and [$Au_8 Al_5$](Cp*)$_5$(^{i}Dipp) according to LIFDI-MS analysis of the reaction solutions (see Table 4). However, in this specific case, *in situ* LIFDI-MS analysis turned out to be problematic due to the extremely high ionizability of [Au_x(^{i}Dipp)$_y$]$^+$ aggregates, probably formed during ionization. The aggregate peaks dominate the spectra and render identification of Au/Al cluster peaks difficult and not well reproducible. Hence, a different strategy based on combinatorial use of *in situ* ^{1}H-NMR, UV-Vis and LIFDI-MS of isolated (purified) cluster products in combination with theoretical calculations was chosen to understand the product distribution obtained in this system.

Table 4
Au/Al species observed in LIFDI-MS spectra of Au/Al libraries with the stoichiometry Au:Al = 1:1. Species in **bold blue** *can be experimentally isolated as a co-crystallize. Species in* **bold** *are supposed to be molecular ions. Species in normal font are supposed to be fragments.*

Au/Al species observed in LIFDI-MS
[$Au_6 Al_6$](Cp*)$_5$
[$Au_6 Al_6$](Cp*)$_6$
[$Au_7 Al_6$](Cp*)$_5$
[$Au_7 Al_7$](Cp*)$_6$
[$Au_8 Al_5$](Cp*)$_5$(^{i}Pr)

LIFDI-MS analysis of an isolated black precipitate from the reaction between [^{i}DippAuH] and AlCp* (1:1) shows two molecular ion signals attributed to [$H_x Au_6 Al_6$](Cp*)$_6$ (**6**) and [$H_x Au_7 Al_6$](Cp*)$_6$ (**7**) (see Figure 77, chemical part). Noteworthy, this composition is confirmed by ^{1}H-NMR analysis of the isolated product. No selective isolation of **6** nor of **7** was achieved by varying the stoichiometry of the starting materials, even though **7** was shown to be formed to a slightly higher extent at lower AlCp* concentrations as shown by *in situ* ^{1}H-NMR analysis. Contrary to our expectations, no selective formation of **6** was achieved at higher AlCp* concentrations, rather the small cluster compound [$Au_2 Al_5$](Cp*)$_5$ (**8**) was isolated as the main product from these reaction solutions (see chemical part for

details). Noteworthy, the number of surface bound hydrides on **6** and **7** is not clear from experimental data; however, the presence of at least one hydride bound to **7** can be assumed due to the diamagnetism of the compound and due to IR data. DFT calculations to determine the total number of hydrides and their location in the structure are currently conducted in the group of *Prof. Saillard*. Preliminary results point towards one surface bound hydride at **7** ($[HAu_7Al_6](Cp^*)_6$) and towards two surface bound hydrides at **6** ($[H_2Au_6Al_6](Cp^*)_6$). Noteworthy, $[HAu_7Al_6](Cp^*)_6$ would be isoelectronic to $[HCu_7Al_6](Cp^*)_6$ (**1_H**).

These results suggest that **6** and **7** are accessed by energetically very similar reaction pathways (similar activation energy).

The use of external additives to influence product size-distributions is well known from colloid and nanoparticle synthesis.[199-202] Indeed, addition of a large excess (>10 eq.) of PPh$_3$ to the reaction between [*DippAuH] and AlCp* clearly leads to a size-focusing effect towards **7** as indicated by ^{1}H-NMR analysis of the isolated product (see chemical part for details). A selective, preparative access to **7** is thereby enabled.

Despite *in situ* ^{1}H-NMR analysis being a powerful technique for quantification, the appearance of paramagnetic species or of fluctional processes limits its applicability in cluster chemistry. Compounds **6** and **7** possess surprisingly different solubilities in organic solvents (**7** is much better soluble in toluene than **6**). The overall solubility of both compounds at room-temperature, however, is low, leading to considerable precipitation inside the NMR tube when conducting *in situ* NMR reactions. These issues generally render quantification by NMR problematic for cluster compounds with *a priori* unknown solubility, spin-state and solution behavior.

Quantification by UV-Vis spectroscopy is a very well established procedure in analytical chemistry. UV-Vis requires strongly dilute solutions in comparison to NMR. If reaction solutions containing **6** and **7** were diluted to 10^{-4} mol/l, complete dissolution of any precipitate was observed. Inspired by related work on pure Au clusters[203], it was therefore rationalized that UV-Vis could be used for relative quantification of **6** and **7** directly from diluted reaction solutions.

Pure, isolated compound **6/7** (cluster mixture $[H_xAu_{6/7}Al_6](Cp^*)_6$) and pure **7** ($[H_xAu_7Al_6](Cp^*)_6$) in toluene were investigated by UV-Vis spectroscopy at various defined concentrations to achieve calibration. The spectra of the pure compounds and the calibration curves are shown in the appendix (see Figures S46-S49).

3. Results and Discussion
3.1 Methodical part: Exploration of living cluster libraries by LIFDI-MS

Noteworthy, the **6:7** ratio in the mixture **6/7** was determined by ^{1}H-NMR analysis of a very dilute solution (no precipitation) to be 1:2.

Two wavelengths, namely 440 nm and 415 nm, were chosen to determine molar extinction coefficients of **6** and **7** using Lambert-Beers law (see appendix for details). The intensities extracted from the spectra of isolated **7** at different concentrations were considered for the calculation of the molar extinction coefficients of **7**. By knowing the ratio of **6:7** in the mixture from ^{1}H-NMR, determination of the extinction coefficients of **6** was possible from the mixture after subtraction of the contributions arising from **7** (see Table S3 for the determined extinction coefficients).

Next, the size-focusing process towards **7** upon PPh$_3$ addition was monitored by *in situ* UV-Vis spectrometry of diluted reaction solutions. The spectra are depicted in Figure 49. Noteworthy, the addition of PPh$_3$ induces the appearance of a shoulder at 436 nm in the spectra, which is associated to **7**. Figure 49 also indicates the wavelengths, which were used for relative quantification of **6** and **7**.

Assuming the intensities at 440 nm and 415 nm to be a linear combination of both **6** and **7**, the concentrations of **6** and **7** were determined using the previously determined extinction coefficients. The thus obtained ratios **6:7** in the reaction solution are visualized in Figure 50. Clearly, the size-focusing process towards **7** upon PPh$_3$ addition is observed. Noteworthy, **7** can be selectively obtained from the reaction solutions with 10 eq. PPh$_3$.

In a next step, it was tried to extend the principle to reaction solutions containing three Au/Al cluster compounds, namely $[Au_2Al_5](Cp^*)_5$ (**8**), $[H_xAu_6Al_6](Cp^*)_6$ and $[H_xAu_7Al_6](Cp^*)_6$ (**7**). However, unfortunately, no meaningful calibration curves were obtained upon UV-Vis analysis of dilute solutions of pure, isolated **8** (see appendix for details, Figure S50 and Figure S51). Clearly, **8** is transformed to another, unknown species upon dilution. It is supposed that compound **8** is much more reactive than **6** or **7** and reacts with trace amounts of water and oxygen at these extremly low concentrations (spectral changes are observed at $5 \cdot 10^{-5}$ mol/l; at this concentration one molecule of **8** is supposed to 10 molecules of water at a water content of 5 *parts per million*).

3. Results and Discussion

3.1 Methodical part: Exploration of living cluster libraries by LIFDI-MS
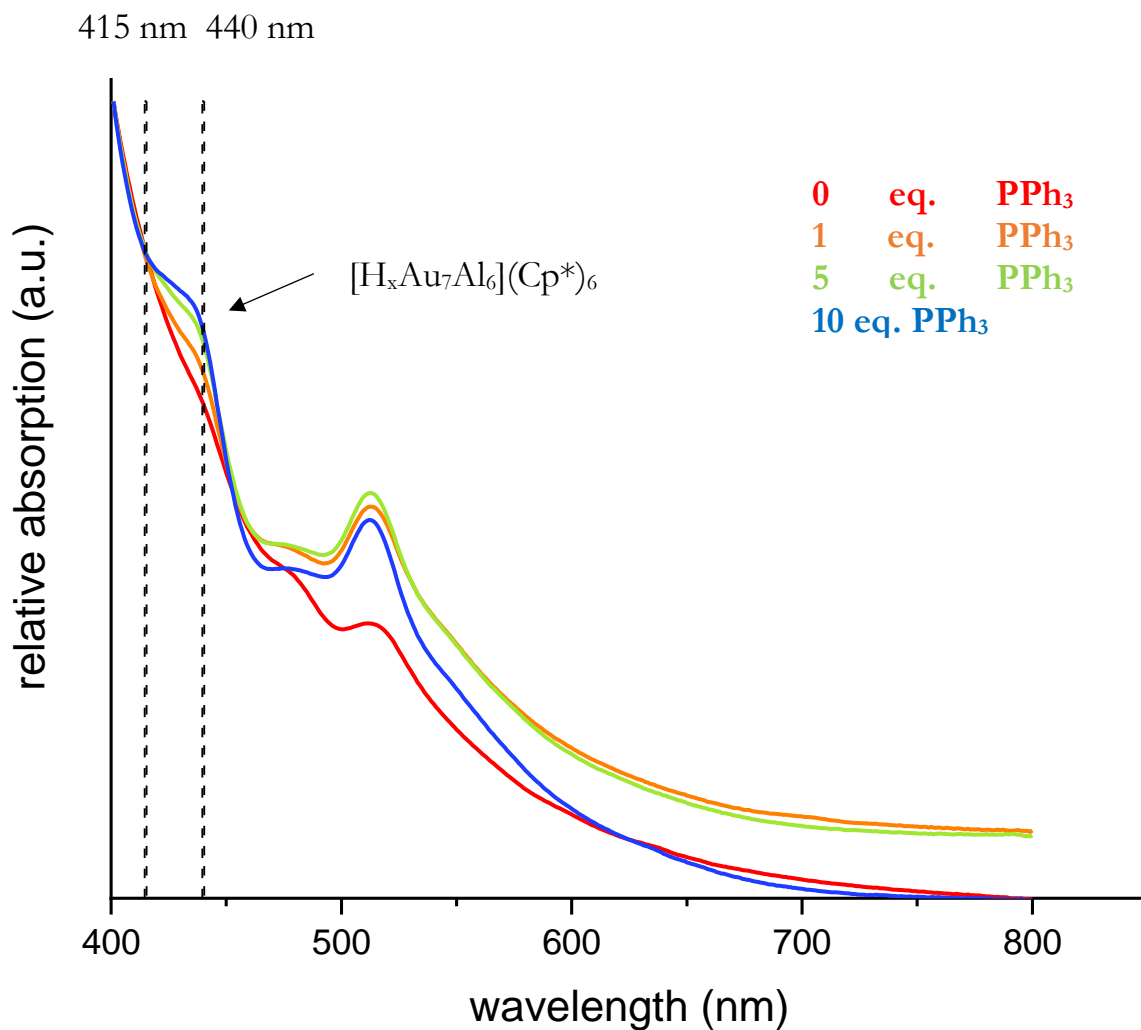
Figure 49
In situ UV-Vis spectra of the reaction between [^{i}DippAuH] + AlCp* (1:1, toluene, 75 °C, 2 h) with different amounts of PPh$_3$ added as an additive during the reaction. The wavelength used for quantification are marked by vertical dashed lines.

3. Results and Discussion
3.1 Methodical part: Exploration of living cluster libraries by LIFDI-MS
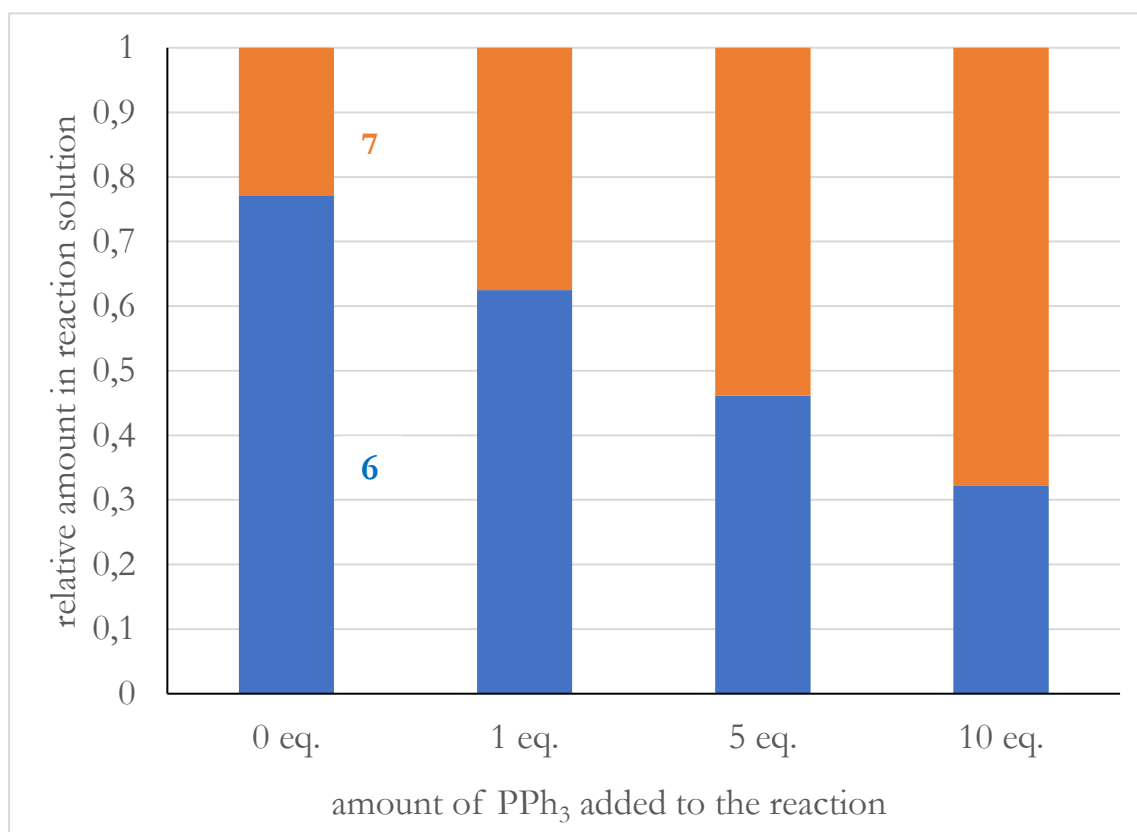
Figure 50
Quantitative analysis of the UV-Vis spectra depicted in Figure 49. The x-axis denotes the amounts of PPh$_3$ added to the reaction [iDippAuH] + AlCp (1:1). Fractions of [H$_x$Au$_6$Al$_6$](Cp*)$_6$ (**6**) and [H$_x$Au$_7$Al$_6$](Cp*)$_6$ (**7**) are visualized in blue and orange, respectively. [Figure created in collaboration with Tim Kratky].*

In conclusion, the Au/Al example highlights the importance of complementary methods (UV-Vis, NMR) in addition to LIFDI-MS analysis for the understanding of cluster libraries in solution. Characterization of cluster species in mixtures (**6**) and assignment of spectral features to members of a(n) (isolated) library is possible by simple combinatorics if a cluster library can be enriched in one of its components. Such a size-focusing effect cannot only be achieved by stoichiometric fine-tuning, but also by using external additives during cluster synthesis, such as in the selective synthesis of **7**. Further, UV-Vis was shown to be a suitable technique to monitor and quantify cluster species in reaction solutions.

3.1.8. Outlook and Perspectives

Large Cu/Al libraries

The presented methods to explore large intermetalloid cluster libraries by LIFDI-MS using (isotopic) labeling experiments for unambiguous peak identification and theoretical methods for structure elucidation is not limited to the systems presented above. Reaction of the triangular cluster $[Cu_2Al](Cp^*)_3$ (**9**) with $[H_6Cu_6](PPh_3)_6$ in a 3:1 molar ratio leads to dark reaction solutions with a complicated LIFDI-MS spectrum, similar to the Cu/Zn case. The spectrum is depicted in Figure 51. Even if some of the lighter cluster can be unambiguously identified, such as 1_H and **2**, identification of the larger clusters is difficult due to several matches with similar GoF, if PPh_3, Al, Cp^*, hydride H and Cu are considered as possible cluster constituents. Especially for large cluster, the number of possible matches is very high, as is shown exemplary in Figure 51 for some of the peaks. Nevertheless, the presence of intermetalloid Cu/Al clusters is unequivocally clear when regarding the possible compositions. Labeling strategies using $[Cu_2Al](Cp^{*Et})_3$, modified (labeled) PPh_3 ligands or isotopically enriched Cu precursor compounds are supposed to enable unambiguous identification of the peaks, such as it was presented in Figure 37 for the Cu/Zn case.

Noteworthy, the library depicted in Figure 51 is one of the rare cases, in which clusters with m/z > 2000 could be detected by LIFDI-MS at the present point of methodical development. Larger cluster nuclearities are supposed to be hardly ionizable by the LIFDI technique due to their decreased mobility on the LIFDI emitter (the clusters must move to the tips of the whiskers driven by the applied electric field in order to get ionized). Modified cluster ligands with well ionizable tags, such as polyphenyl groups, might be a possible solution for that problem. Alternatively, modification of the emitter´s surface, *e.g.* by application of additives, might enable a better surface mobility even of larger clusters. Further possible modifications could include continuous sample supply at moderate electric fields in combination with modified emitter geometries. For example, the use of geometrically well-defined emitter tips instead of undefined emitter surfaces ("wires") is anticipated to enable better reproducibility and maybe even quantification.

3. Results and Discussion

3.1 Methodical part: Exploration of living cluster libraries by LIFDI-MS

* possible matches

[H$_2$Cu$_{12}$Al$_{19}$](Cp*)$_9$

{[Cu$_{18}$](Cp*)$_{10}$ - 2H}

{[Cu$_{15}$Al$_{23}$](Cp*)(PPh$_3$)$_3$ - 2H}

{[Cu$_8$Al$_{15}$](Cp*)$_2$(PPh$_3$)$_5$ − H}

[H$_2$Cu$_8$Al$_{24}$](Cp*)$_6$(PPh$_3$)$_2$

[HCu$_9$Al$_{17}$](Cp*)$_5$(PPh$_3$)$_3$

[HCu$_{13}$Al$_{12}$](Cp*)$_8$(PPh$_3$)

* possible matches

{[Cu$_{13}$Al$_6$](Cp*)(PPh$_3$) − H}

{[Cu$_{14}$Al$_{24}$](Cp*)$_2$(PPh$_3$)$_2$ − H}

[Cu$_9$Al$_{11}$](Cp*)$_5$(PPh$_3$)$_3$ − H}

[Cu$_{12}$Al$_{13}$](Cp*)$_9$

{[Cu$_{18}$Al$_{19}$](Cp*)$_5$ − H}

* possible matches

{[Cu$_{13}$Al$_{12}$](Cp*)$_7$ − H}

{[Cu$_9$Al$_{17}$](Cp*)$_4$(PPh$_3$)$_2$ − H}

* possible matches

[Cu$_6$Al$_8$](Cp*)$_4$(PPh$_3$)
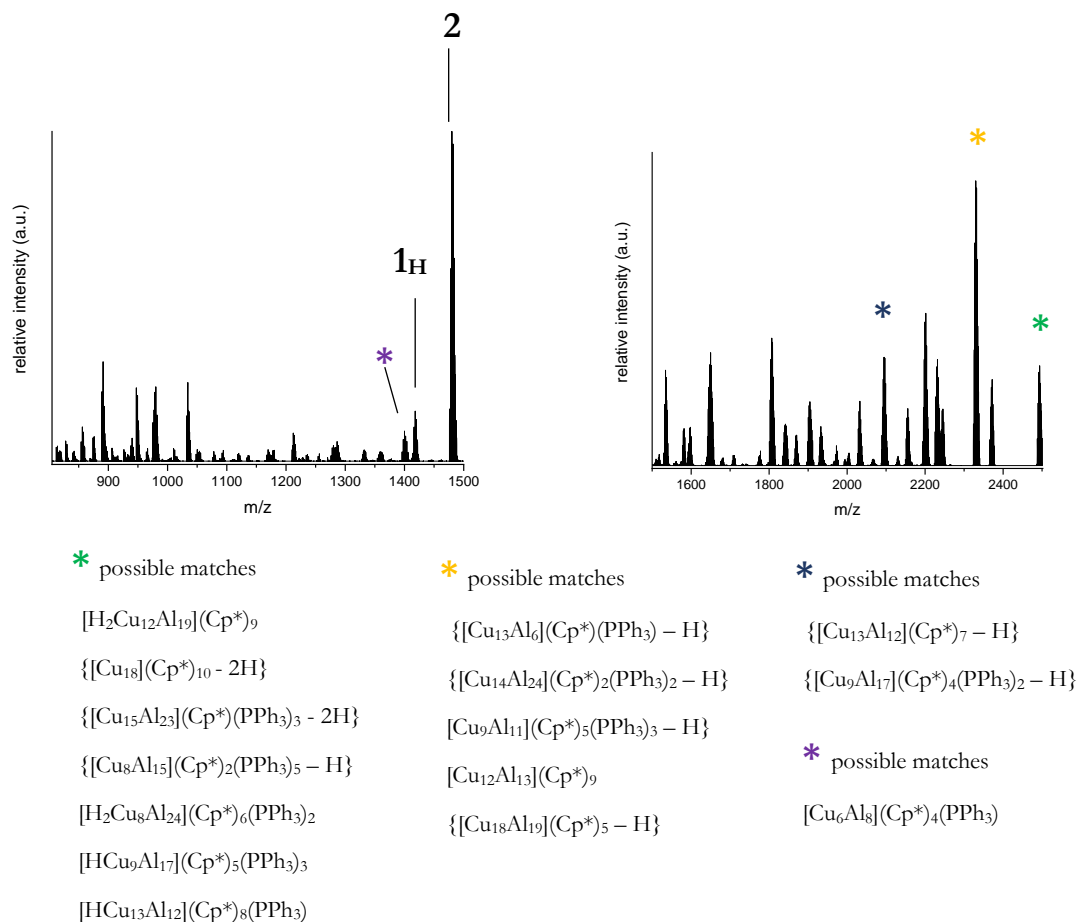
Figure 51

LIFDI-MS spectrum of a complicated Cu/Al library obtained upon reaction between [Cu$_2$Al](Cp)$_3$ (**9**) and [H$_6$Cu$_6$](PPh$_3$)$_6$ (3:1, toluene, 75 °C, 3 h). Assignment of the peaks is difficult and has to be conducted analoguously to the Cu/Zn libraries presented above. As an example for the complexity, some possible matches are shown for prominent peaks. "- H" denotes that the given sum formula is detected in its hydrogen abstracted form.*

3.2. Chemical part: Synthesis characterization, reactivity

In the following chemical part, the Cu/Zn, Cu/Al and Au/Al examples described in the methodical part will be discussed more in detail from a chemical point of view including interpretation of analytical data and structural information obtained from single crystal Xray diffraction. This part of the thesis will also include mechanistic insights in cluster formation and growth reactions as well as into reactivity patterns.

3.2.1. Exploring the "phase-width" in molecular Cu/Zn clusters

The following results on $[Cu_{10}Zn_2](Cp^*)_2(Mes)_6$ and $[CuZn_{10}](Cp^*)_7$ were published as an article in the journal Inorganic Chemistry (Link: https://doi.org/10.1021/acs.inorgchem.0c00943). [Reprinted (adapted) with permission from M. Schütz, M. Muhr, K. Freitag, C. Gemel, S. Kahlal, J.Y. Saillard, A. C. H. Da Silva, J. L. F. Da Silva, T. F. Fässler, R. A. Fischer, Inorg. Chem. 2020, 59, 13, 9077-9085. Copyright 2020 American Chemical Society.]

The Cu/Zn "brass" system is the archetypical Hume-Rothery phase and used in metallurgy and for the development of novel materials since ancient times. As mentioned in the introduction, the structural diversity of Hume-Rothery nanophases, such as γ-, δ-, and ε-brass, evolves in the Cu:Zn system only at Zn contents higher than 50 %. At Cu:Zn ratios below 40 %, α-brass exhibits a regular fcc structure based on that of metallic Cu. Between Zn contents of 40 % and 50 %, β-brass with a bcc packing is formed.

In all examples of molecular "embryonic brass" clusters reported so far, the Cu:Zn ratio is not far away from 1:1 with a slight bias to zinc, ranging from 1:1 in $[Cu_4Zn_4](CN^tBu)_4(Cp^*)_4$ to 1 : 2.5 in $[Cu_2Zn_5](Cp^*)_5^+$. In this dissertation, the structural variability, as well as the electronic bonding situation of intermetalloid, molecular Cu/Zn clusters was further investigated with special regard to the Cu:Zn ratio: How do molecular structures and electronic situations change in intermetalloid clusters over the whole Cu:Zn stoichiometry range, especially if the abundancy of one element is much higher? In this context, three new molecular clusters were synthesized and fully characterized, extending the "molecular phase diagram" (see Figure 52) of nano-brass clusters, namely the Zn-rich cluster $[CuZn_{10}](Cp^*)_7$ (**10**), its Cu-rich congener $[Cu_{10}Zn_2](Mes)_6(Cp^*)_2$ (**3**) and the "Hume-Rothery" cluster "micro-library" $[Cu_4Zn_{9/10}](Cp^*)_8$ (**4/5**). Figure 52 summarizes the thus obtained cluster "landscape" of neutral, ligated molecular nano-brass clusters.

3. Results and Discussion

3.2. Chemical part: Synthesis characterization, reactivity

The synthesis of **3** and **4/5** is closely related to the living Cu/Zn cluster libraries discussed in the methodical part and was also investigated by detailed *in situ* NMR studies to gain further mechanistic insight in cluster growth processes.
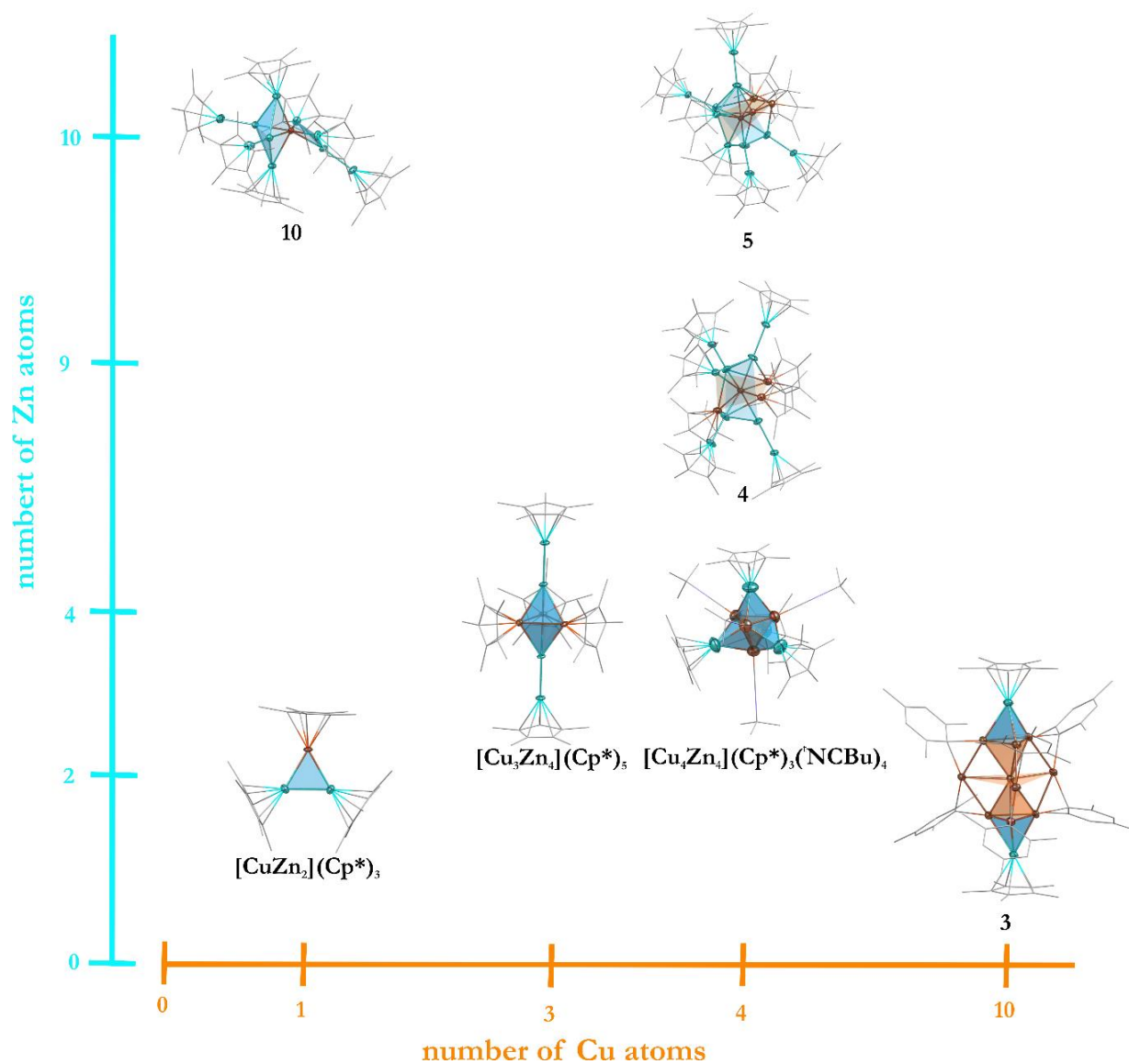
Figure 52

The landscape of neutral, molecular Cu/Zn clusters. The clusters [CuZn₂](Cp)₃, [Cu₃Zn₄](Cp*)₅ and [Cu₄Zn₄](Cp*)₄(ᵗNCBu) from previous reports[86, 88] were expanded by the Zn-rich cluster [CuZn₁₀](Cp*)₇ (**10**), the Cu-rich cluster [Cu₁₀Zn₂](Cp*)₂(Mes)₆ (**3**) and the micro-library [Cu₄Zn₉/₁₀](Cp*)₈ (**4/5**) in this dissertation.*

3.2.1.1. The Zn-rich cluster [CuZn$_{10}$](Cp*)$_7$ (**10**)

The synthesis of [CuZn$_{10}$](Cp)$_7$ was originally discovered by Kerstin Freitag during her PhD. project in the group of Prof. R. A. Fischer. Her preliminary results were reproduced in this dissertation and the species was completely characterized.*

Synthesis

Treatment of the NHC complex [(^{i}Dipp)CuH] (^{i}Dipp = 1,3-bis(2,6-diisopropylphenyl)-1H-imidazol-2-ylidene), *in situ* generated from [(^{i}Dipp)Cu(O^{t}Bu)] and (EtO)$_3$SiH, with two equivalents of [Zn$_2$](Cp*)$_2$ at -72 °C in diethylether leads to a deep-red solution after warming to room temperature (see Scheme 13). The reaction progress can be monitored by LIFDI-MS pointing to the formation of various [Cu$_x$(^{i}Dipp)$_y$] aggregates, as well as of a complicated mixture of [M$_8$]/[M$_{11}$]/[M$_{13}$] mixed metal Cu/Zn clusters (see Figure S52). However, when the concentrated reaction solution is cooled down to -30 °C, single crystals of [CuZn$_{10}$](Cp*)$_7$ (**10**) are formed as deep red octahedral fragments, as well as colorless crystals of unconsumed [Zn$_2$](Cp*)$_2$. Cluster **10** can only be manually separated from [Zn$_2$](Cp$_2$)* by crystal picking under an optical microscope in the glove box; however, an analytically quantitative separation of the crystals is not possible. All attempts to purify compound **10** by washing or recrystallization from different solvents failed due to the very similar solubilities of **10** and [Zn$_2$](Cp*)$_2$, and therefore, unfortunately, no meaningful data for elemental analysis were obtained.

Cluster **10** readily dissolves in common organic solvents (toluene, benzene, hexane, diethylether) and solutions in benzene are stable at room-temperature for several days before slow decomposition (metallic precipitate) occurs.

Notably, the excess of [Zn$_2$](Cp*)$_2$ in the synthesis of **10** is crucial. The use of stoichiometric amounts leads to unspecific reaction mixtures and no product can be isolated. Obviously, high concentrations of [Zn$_2$](Cp*)$_2$ are required to "trap" the Cu fragments formed in the competitive thermal decomposition of [^{i}DippCuH]. Due to the chemical instability of [^{i}DippCuH], the reaction of the thermally more stable analogous PPh$_3$ compound [H$_6$Cu$_6$](PPh$_3$)$_6$ was also investigated. However, Cp* transfer to copper was observed in this case as the dominating mechanism and the thermodynamically very stable half-sandwich complex [(PPh$_3$)CuCp*] was isolated as the only product. This illustrates the importance of the choice of the organometallic Cu-source and thus points to the kinetic control of the Cu/Zn cluster formation reactions.

3. Results and Discussion
3.2. Chemical part: Synthesis characterization, reactivity
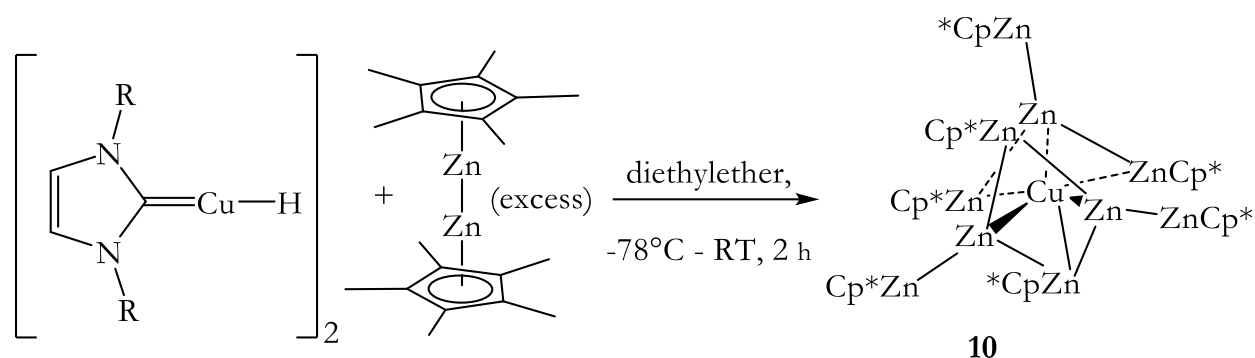
Scheme 13
*Synthesis of cluster **10**, [CuZn₁₀](Cp*)₇ = [Cu(ZnZnCp*)₃(ZnCp*)₄] (R = 2,6-diisopropylphenyl). The Cu-Zn connecting lines illustrate short contacts.*

Crystallographic characterization

The molecular structure of **10** in the solid state has been investigated by SC-XRD (see Figure 53). It should be noted that Cu and Zn could not be distinguished based on the SC-XRD data and the assignment of the elements to the metal positions as well as the elemental composition of **10** is based on NMR spectroscopy, mass spectrometry, as well as on density functional theory calculations (*vide infra*). Detailed crystallographic information is found in Table S4. Cluster **10** crystallizes in the orthorhombic space group P*nma* with four molecules per unit cell together with four molecules of heavily disordered diethylether per asymmetric unit. The molecule of **10** sits on a crystallographic symmetry plane and thus possesses C_s symmetry. The central Cu atom is hepta-coordinated by three Zn-ZnCp* units and four ZnCp* units. In all seven Zn units, the protecting Cp* ligands are η^5-coordinated, with Zn-Cp*$_{centroid}$ distances varying between 1.91 Å and 2.01 Å, which is typical for Zn-Cp* distances found in literature (*e.g.* 1.934 Å for [PdZn₈](Cp*)₄(Me)₄]).[204] The distances of the central Cu to the surrounding Zn atoms lie between 2.335(5) Å and 2.3997(5) Å, which is comparable to that found in the triangular cluster [CuZn₂](Cp*)₃ (2.381(1) Å) and indicates a dense sphere packing structure motive for **9**.[81] Notably, the Cu-ZnCp* distances (2.3997(5) for Cu1-Zn2 and 2.4136(5) for Cu1-Zn3) are distinctly longer than the Cu-ZnZnCp* distances (2.3477(3) Å and 2.3477(4) Å) with exception of the Cu1-Zn1 bond (2.335(5) Å).

3. Results and Discussion
3.2. Chemical part: Synthesis characterization, reactivity
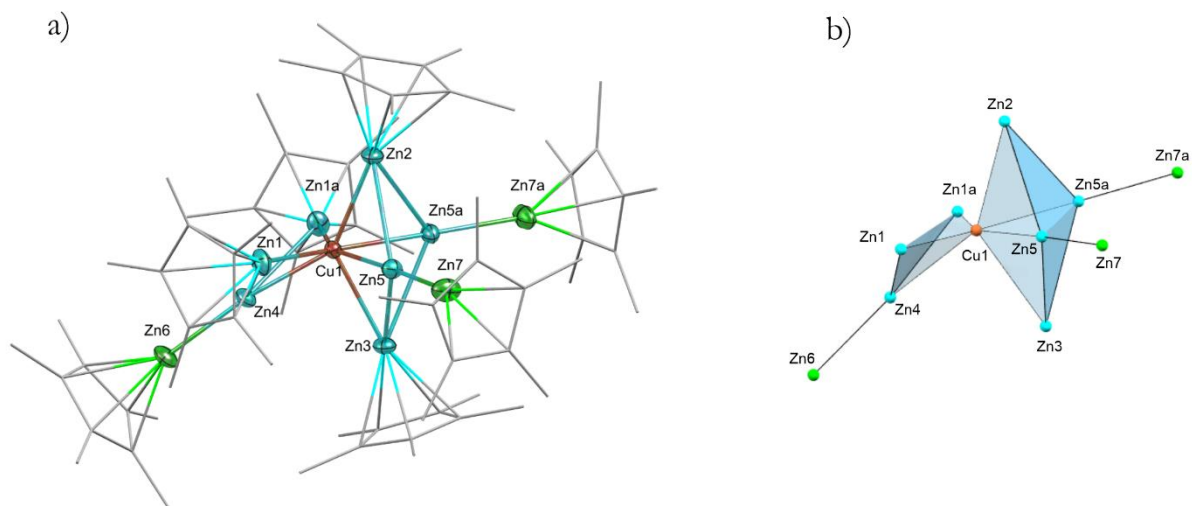
Figure 53

*a) Molecular structure of **10** in the solid state as determined by SC-XRD. Thermal ellipsoids are shown at the 50 % probability level, hydrogen atoms, co-crystallized solvent molecules and disordered groups are omitted for clarity and ligands are simplified as wireframes. Selected interatomic bond distances [Å] and angles [°]: Cu1-Zn5: 2.3477(3), Cu1-Zn1: 2.335(5), Cu1-Zn2: 2.3997(5), Cu1-Zn4: 2.3662(4), Cu1-Zn3: 2.4136(5), Zn4-Zn6: 2.3686(5), Zn5-Zn7: 2.390(5), Zn2-Zn5: 2.7489(4), Zn1-Zn4: 2.713(6), Zn5-Zn3: 2.7418(4), Cu1-Zn4-Zn6: 173.08(2), Cu1-Zn5-Zn7 172.0(2). b) Coordination geometry of Cu (orange) in **10** with Zn in the first (blue) and second coordination sphere (green).*

This phenomenon has also been observed in $[PdZn_8](Cp^*)_4(Me)_4$.[205] The Zn-Zn bond lengths within the Zn_2 units in **9** are 2.3686(5) Å (Zn4-Zn6) and 2.390(5) Å (Zn5-Zn7), *i.e.* they are elongated by 3-4 % with respect to $[Zn_2](Cp)^*_2$ (2.305 Å).[206] They are also significantly longer than those reported for $[Cu_3Zn_4](Cp^*)_5$ and $\{[Cu_2Zn_5](Cp^*_5)\}^+$ (2.299(6) – 2.318(2) Å).[88] The Zn-Zn-Cu moieties further show a significant deviation from linearity (Cu1-Zn4-Zn6: 173.08(2)° and Cu1-Zn5-Zn7 172.0(2) °). Longer Zn…Zn contacts (2.713(6) - 2.7489(4) Å) are also present between the Zn atoms coordinated to Cu. This is a characteristic feature of late transition-metal complexes of ZnR (R = Cp*, ZnCp*, Me).[207] Considering these contacts, the whole coordination sphere around Cu can be viewed as made up of two parts, a bent [(Cp*Zn)(ZnZnCp*)(ZnCp*)] assembly (Zn1-Zn4-Zn1a in Figure 53) as well as a [(Cp*Zn)(ZnZnCp*)(ZnCp*)(ZnZnCp*)] folded diamond (Zn2-Zn5-Zn3-Zn5a in Figure 53). The symmetry plane cuts each of these two pieces in two equivalent halves, with Zn(2), Zn(3) and Zn(4) lying on it, as well as Cu (see Figure 53).

Spectroscopic characterization of 10

The ^{1}H-NMR spectrum at room-temperature (Figure S54) of isolated single crystals of **10** in benzene-d$_6$ reveals one sharp singlet at 2.22 ppm beside a small signal attributable to [Zn$_2$](Cp*)$_2$ at 2.03 ppm. The occurrence of only one signal for all the Cp* ligands of **10** is surprising, as the symmetry of the molecule in the solid state suggests five distinct signals in the Cp* region, *i.e.* two singlets for the Zn-ZnCp* ligands with an integral ratio of 2 : 1 as well as three signals for ZnCp* ligands with an integral ratio of 2 : 1 : 1. At -90 °C in toluene-d^8, a splitting of the room temperature signal at 2.22 ppm into two discrete singlets at 2.23 ppm and 2.25 ppm with an integral ratio of 3:4 is observed (see Figure S54, bottom). Obviously, a fast exchange of all Cp* ligands is observed at room temperature, involving exchange between ZnCp* and ZnZnCp* ligands. Whether this exchange process is based on Zn-Zn or Zn-Cp* bond cleavage is not clear and cannot be decided on VT-NMR data only. The ^{13}C-NMR spectrum of **10** in benzene-d^6 at room-temperature shows two signals at 12.21 ppm and 111.10 ppm (Figure S53). Unfortunately, no ^{13}C-NMR spectrum could be recorded at -90 °C, due to decreased solubility of the compound at low temperatures. It should be noted that the NMR spectroscopic data are in line with the elemental composition and assignment resulting from density functional theory calculations, since the appearance of one coalesced signal for all Cp* ligands in the ^{1}H-NMR spectrum is consistent with Cu being in the center of the molecule.
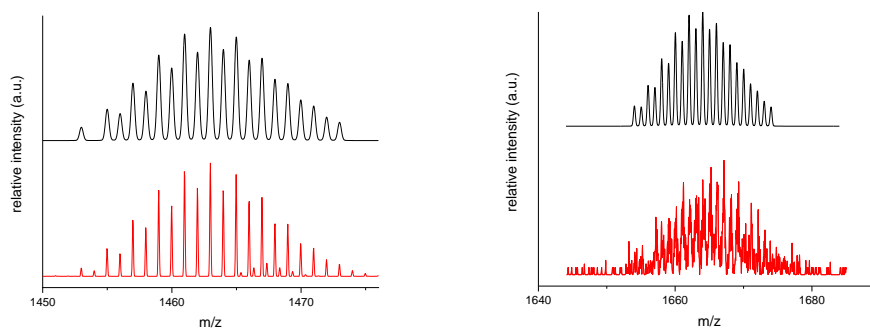
Figure 54
*Left: Ion signal of [**10** – ZnCp*]$^+$ (bottom, red) in LIFDI-MS (positive ion-mode) and calculated isotopic pattern (top, black). Right: Molecular ion signal of **10** (bottom, red) in LIFDI-MS (positive ion-mode) and calculated isotopic pattern (top, black).*

The mass spectrum (LIFDI) of **10** gives rise to various highly intensive ^{i}Dipp-adducts pointing to highly ionizable trace impurities present in the isolated crystals. The molecular ion peak of [CuZn$_{10}$](Cp*)$_7$ is detected as a weak signal at m/z = 1664. Unfortunately, the isotopic pattern observed for the molecular ion peak does not satisfy high resolution standards (see Figure 54, right) due to the weak intensity of

the signal. However, the fragment ion $[\mathbf{10} - ZnCp^*]^+$ is observed with high resolution and its isotopic pattern is well consistent with the calculated one for $[CuZn_9](Cp^*)_6$ (see Figure 54, left).

Computational analysis of 10

*The distribution of the elements Cu and Zn in the structure of compound **10** was computationally investigated by the group of Prof. Da Silva from Universidade de São Paulo (Brazil).*

The detailed theoretical bonding analysis was carried out by the group of Prof. Jean-Yves Saillard from the Université de Rennes (France).

The assignment of the copper location in **10** was obtained by geometry optimizations based on total energy DFT calculations of seven representative configurations (see Figure 55) corresponding to different occupations of the metal positions, using the all-electron full-potential Fritz–Haber institute *ab initio* molecular simulations (FHI-aims) package[208] with the PBE functional[209] (see computational details, Supporting Information). Unsurprisingly, the most stable structure is that with copper lying at the central position, in full agreement with the above discussed spectroscopic and structural data. It lies 0.67 eV below in energy than the next most stable configuration in which Cu is located at a more peripheral position.

In a following step, using the lowest energy structure, the electronic structure of **10** was then analysed by using the ADF program suite[210-211] at the BP86/TZ2P-D3 level (see computational details, Appendix). Although slightly distorted away from C_s symmetry, the optimized geometry of **10** at this level of theory was found to be close to its X-ray structure. The computed ^{1}H NMR chemical shifts (av. 2.06 and 1.95 ppm for ZnCp* and ZnZnCp*, respectively) as well as the ^{13}C ones (av. 10.66 and 113.16 ppm for ZnCp* and av. 7.74 and 111.57 ppm for ZnZnCp*) are consistent with the experimental data. Discarding first the long Zn…Zn contact and considering that each individual ZnCp* or ZnZnCp* unit is a 1-electron donor, the 7 electrons provided by the 7 organo-zinc ligands add up to the 11 valence electrons of Cu(0), making the later a 18-electron metal centre.

3. Results and Discussion

3.2. Chemical part: Synthesis characterization, reactivity
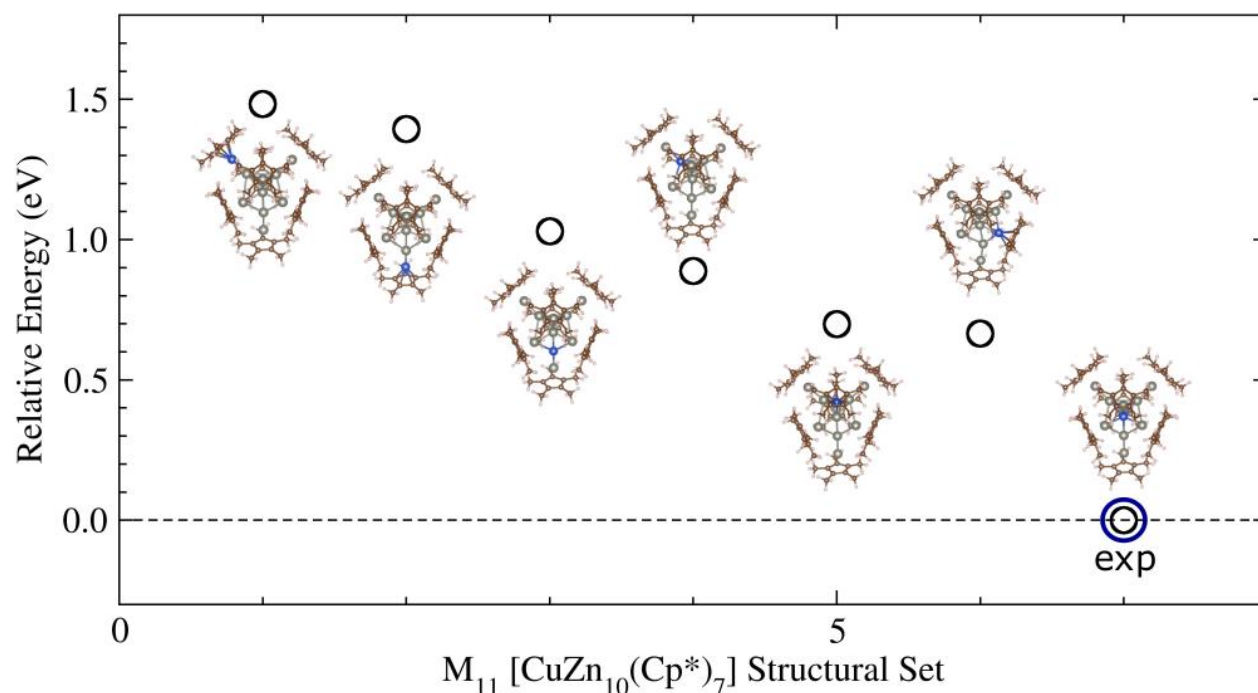
Figure 55
Optimized atomic configurations for [CuZn₁₀](Cp)₇ (**10**).*

This electron count is consistent with the computed substantial HOMO-LUMO gap (2.06 eV). However, the 18-electron rule should be considered carefully when applied to complexes in which the number of ligands is larger than the number of metal valence orbitals available for bonding. In such situations, delocalization over the ligand sphere is expected. This is what happens in **10** where the $3d^{10}4s^1$ copper centre has only four accepting orbitals (4s and 4p) to accommodate the 7 ligand electrons coming from seven organo-zinc σ-type orbital combinations. These seven combinations interact with the Cu orbitals in a manner roughly sketched in Figure 56. Four among the seven organo-zinc combinations interact with the copper 4s and 4p orbitals, leaving three of them non-bonding with Cu. Among the seven organo-zinc combinations, those which are the closest in energy to the copper AOs are expected to interact in a stronger way. These orbitals are the lowest among the seven, thus those which have Zn--Zn bonding character. In fact, they are the two lowest σ-type combinations (somewhat stabilized by 4p(Zn) AOs of the ZnZnCp* ligands) of each of the two subunits [(Cp*Zn)(ZnZnCp*)(ZnCp*)] and [(Cp*Zn)(ZnZnCp*)(ZnCp*)(ZnZnCp*)]. On the other hand, those having Zn--Zn antibonding character are expected to interact to a lesser extent. This is exemplified by a fragment decomposition analysis which indicates that the four lowest σ-type organo-zinc combinations have a global occupation of 5.98 electrons, whereas that of three highest ones is only 1.03 electrons. It results that the highest occupied levels of **10** have some Zn--Zn bonding character, whereas those having Zn--Zn

124

antibonding character are vacant. The diagram of Figure 56 is obviously oversimplified, but it allows explaining where bonding delocalization between the organo-zinc ligands originates from. It is worth noting that this situation is allowed because the organo-zinc σ-type orbitals lie at higher energy than the 3d(Cu) block. A lower energy would result in the occupation of their Zn--Zn antibonding combinations. Steric crowding among the ligand sphere tends also to favour such delocalization. The availability of 7 organo-zinc combinations to stabilize four Cu AOs is also favourable to a fluxional behaviour of the organo-zinc ligand sphere around the copper center.
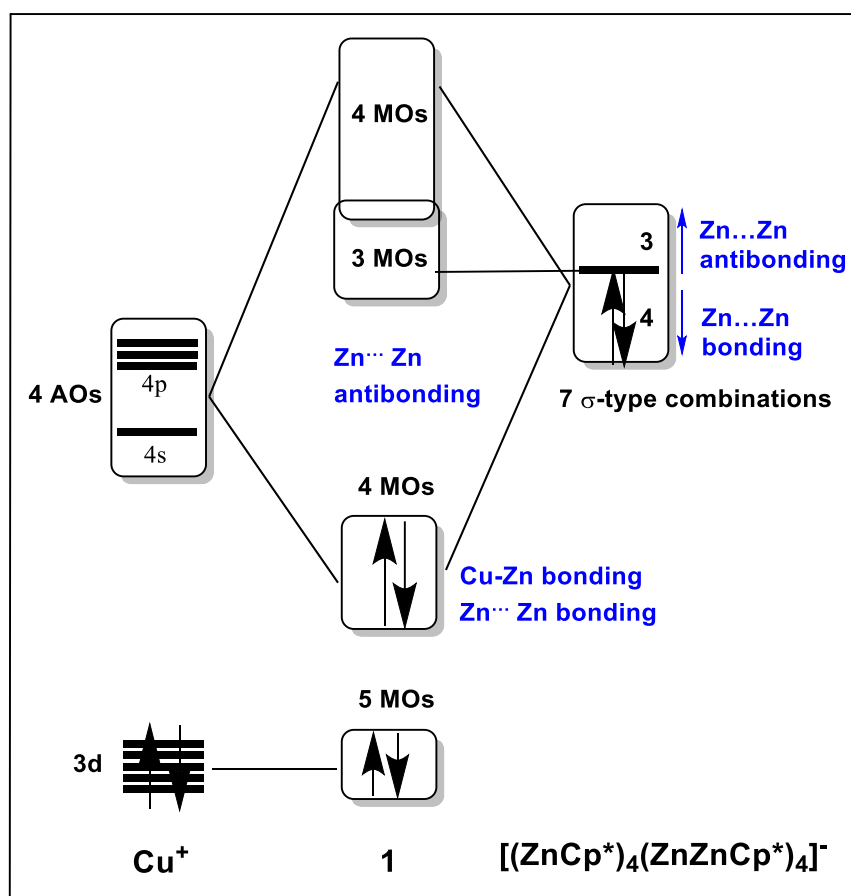
Figure 56
Simplified MO diagram sketching the interaction of the Cu valence AOs with the combinations of the σ-type frontier orbitals of the ZnCp and ZnZnCp* fragments in **10**. For the sake of simplicity Cu is considered in its +I oxidation state, making the whole ligand sphere an 8-electron donor system.*

The four highest occupied orbitals in Figure 56 have substantial Cu character, the computed natural atomic orbital (NAO) charge of Cu is negative (-0.66). Consistently, the seven zinc atoms bonded to Cu have positive NAO charges (avg.

+0.70), the three outer zinc atoms being less polarized (avg. +0.48). The computed Cu-Zn Wiberg indices are consistent with Cu-ZnCp* covalent bonding significantly stronger than Cu-ZnZnCp* bonding (avg. 0.255 and 0.094, respectively). Unsurprisingly, the computed Zn-Zn Wiberg indices (avg. 0.084) are much smaller than that corresponding to the Zn-Zn single bonds (avg. 0.490).

3.2.1.2 The Cu-rich cluster $[Cu_{10}Zn_2](Cp^*)_2(Mes)_6$ (**3**)

Synthesis

When [CuMes] is reacted with 0.33 eq of $[Zn_2](Cp)^*_2$ (per mole of Cu) in toluene and heated to 75 °C for several days, $[Cu_{10}Zn_2](Mes)_6(Cp^*)_2$ (**3**) is formed as the major reaction product (identified by LIFDI-MS, see Figure 48). After cooling the filtered and concentrated reaction solution to -30°C, **3** can be separated from the mixture in form of very air- and moisture sensitive black-green crystals (see Scheme 14). The molecular structure of **3** in the solid state has been determined by SC-XRD (see Figure 57), with the assignments of elements based on the elemental composition as derived from the molecular mass determined by LIFDI-MS, as well as on density functional theory calculations and NMR spectroscopic data (*vide infra*).
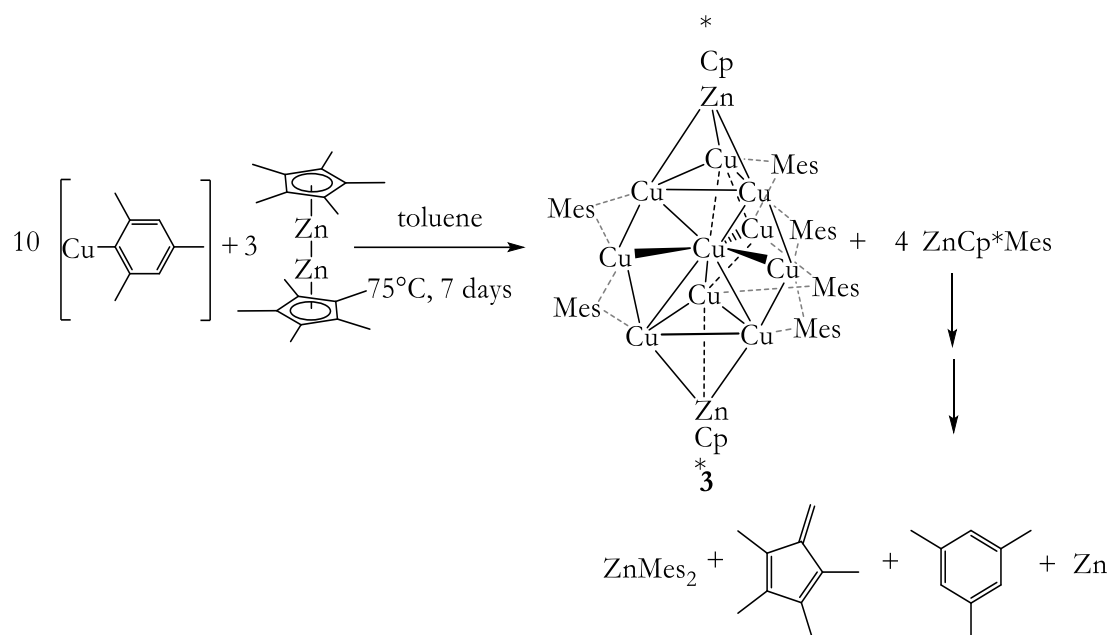
Scheme 14
Synthesis of the Cu-rich cluster [Cu₁₀Zn₂](Cp)₂(Mes)₆ (**3**). Note that ZnCp*Mes is identified as early side-product of the reaction, whereas after prolonged reaction times, ZnMes₂ is formed. The exact reaction pathway from ZnCp*Mes to ZnMes₂ is unclear, but formation of metallic Zn is postulated. Pentamethylfulvene and HMes were additionally detected in the reaction solutions.*

3. Results and Discussion
3.2. Chemical part: Synthesis characterization, reactivity

Cluster **3** is well soluble in toluene, but less soluble in benzene and only sparingly soluble in hexane. It can be obtained in analytically pure form after washing the isolated crystals with *n*-hexane. It is only moderately stable under argon atmosphere at room-temperature in the solid state as well as in solution. Prolonged heating to more than 100 °C leads to the formation of a metallic precipitate. Due to the high sensitivity of **3**, no meaningful data from elemental analysis could be obtained.

Mechanistic insights into the formation of 3

According to *in situ* ¹H-NMR analysis (see Figure S56), synthesis of compound **3** is accompanied by rapid initial formation of the half-sandwich zincocene complex MesZnCp*.[212] Upon prolonged heating, the species ZnMes$_2$[213], mesitylene and pentamethylfulvene (5-methylene-1,3-cyclopentadiene) are identified in the spectra. However, no peaks of the product species **3** can be identified in the spectra, probably due to the low concentration or solubility of **3**. ZnMes$_2$ was also obtained as a byproduct of **3** in the form of white crystals and identified by SC-XRD. The reaction is explained by ligand scrambling processes between two molecules of MesZnCp* accompanied by C-H activation of Cp* and reductive elimination reactions leading to HCp*, HMes and presumably to small amounts of metallic Zn. Notably, the observance of very fine metal mirrors at the wall of the reaction vessels is in line with this proposed reaction mechanism.

Crystallographic characterization of 3

Cluster **3** crystallizes in the triclinic space group P-1 with two molecules per unit cell and three disordered molecules of toluene per asymmetric unit. Detailed crystallographic information is found in the Appendix (Table S4). The metal core structure of **3** is close to ideal D$_{3h}$ symmetry and consists of two vertex-sharing tetrahedra Cu1-Cu2-Cu3-Cu4 and Cu4-Cu8-Cu9-Cu10 with Cu4 as the central vertex of both tetrahedra (see Figure 58 a)). The edges of this Cu$_7$ unit are bridged by three more Cu atoms (Cu5, Cu6, Cu7) forming a Cu$_3$ triangle around the central Cu4. Both tetrahedra are additionally capped by apical Zn atoms with an almost linear arrangement of Zn1-Cu4-Zn2. **3** is therefore structurally closely related to the Laves phase MgCu$_2$, in which the structural motif of two edge-sharing Cu$_4$-tetrahedra can also be found (see Figure 58 b) for illustration).[214] Noteworthy, the structural principle of tetrahedral building units is also inherent to Hume-Rothery phases ("stella quadrangula", see Figure 4). However, in **3**, the tetrahedral motifs (*e.g.* Cu1-4) are capped at the vertices by additional Cu atoms (Cu5-7) and not at the faces, such as typical for Hume-Rothery phases.

3. Results and Discussion
3.2. Chemical part: Synthesis characterization, reactivity

Most interestingly, the stacking sequence of atoms in **3** follows a A(Zn1)B(Cu1-3)A(Cu4-7)B(Cu8-9)A(Zn2) order, just as observed in hcp (hexagonal closed packed) solid-state structures (three Cu atoms are missing in the Cu4-7 plane for a perfect Cu anticuboctahedron). As Cu is the archetypical ccp (cubic closed packed) metal, this situation is very uncommon for molecular clusters of Cu. Figure 58 b) highlights the structural analogy between **3** and Mg (hcp packing). A similar extraordinary situation was found for the pure Cu cluster $[Cu_{53}(C\equiv CPhPh)_9(dppp)_6Cl_3]\{[NO_3]_9$ featuring a ABABC stacking principle (hybrid between hcp and ccp).[39] The structural analogy is depicted in Figure 58 b).

The Cu-Cu distances within the cluster core are all between 2.4223(7) Å and 2.7662(8) Å, which is well within the range of molecular compounds with direct Cu-Cu bonds reported in literature (2.3 Å for $[^iDippCuH]_2$[89], 3.424 Å for $\{[Ag_6Cu_2](dppe)_3(CCC_6H_4OCH_3)_6(MeCN)\}(ClO_4)_2$ (dppe= 1,2-bis(diphenylphosphino)ethane), 2.56 Å for Cu metal)[215-217], but slightly shorter than the mean Cu-Cu distance in $[H_4Cu_6Al_6](Cp^*)_6$ (2.531 Å)[92] and very similar to the one in $[Cu_4Zn_4](CN^tBu)_4(Cp^*)3(Cp)$ (2.471 Å).[86] The longest M-M distances (avg. 2.75 Å) are observed between the central Cu4 atom and the Cu triangle spanned by Cu5, Cu6 and Cu7. The Cu-Zn distances (avg. 2.45Å) are shorter with respect to $[Cu_4Zn_4](CN^tBu)_4(Cp^*)_3Cp$ (2.498(2) Å)[86] but very similar to those in $[Cu_3Zn_4](Cp^*)_5$ (2.431(2) − 2.458(2) Å),[88] reflecting the similar structural motifs of Zn capped Cu triangles. The Zn-Cp$^*_{centroid}$ distances are 1.91 Å and 1.92 Å, which is in line with literature values for terminal ZnCp* units in metal-rich molecules (1.83 Å – 2.19 Å) and especially comparable to those observed in $[Cu_3Zn_4](Cp^*)_5$ (1.901 / 1.922 Å).[88]

The six mesityl units are found in edge-bridging positions, each bridging one of the Cu-Cu contacts between the central Cu$_3$ triangle and the Cu$_3$ triangles of the two tetrahedral Cu$_4$ units. The Cu-C distances are all within the range of 1.992(5) Å and 2.044(4) Å and well in line with the Cu-C distance reported for $[Cu_5](Mes)_5$.[218]
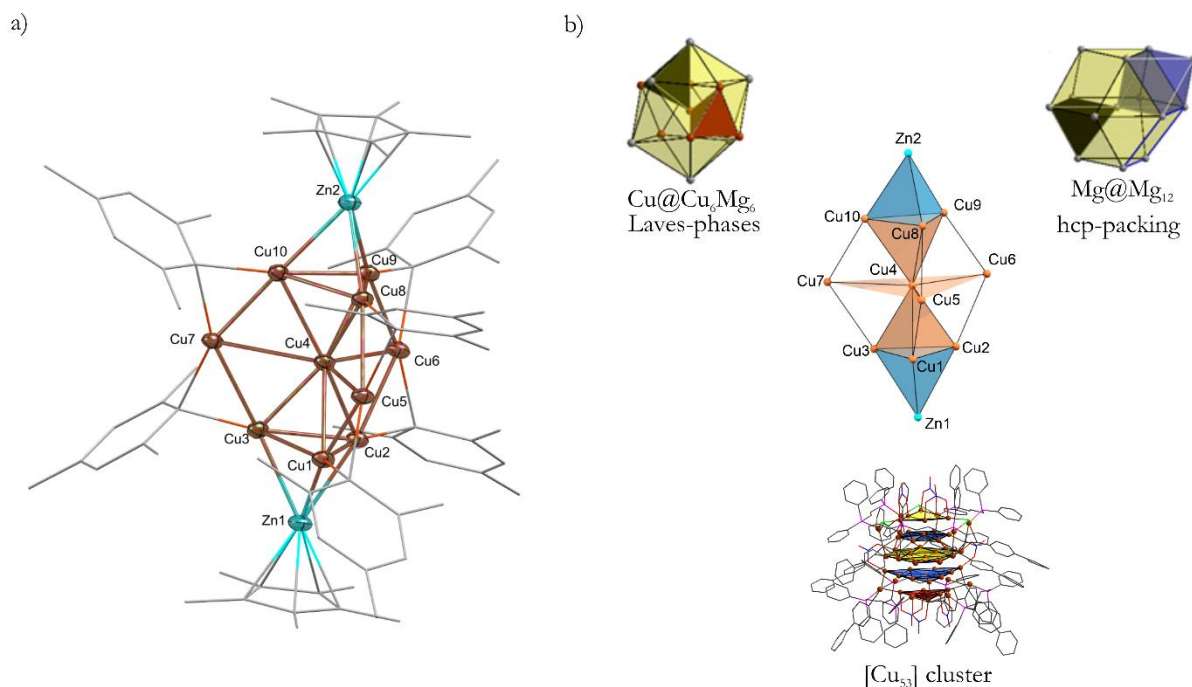
Figure 57

*a) Molecular structure of **3** in the solid state as determined by SC-XRD. Thermal ellipsoids are shown at the 50 % probability level, hydrogen atoms, co-crystallized solvent molecules and disordered groups are omitted for clarity and ligands are simplified as wireframes. Selected interatomic bond distances [Å] and angles [°]: Cu4-Cu10: 2.4617(8), Cu1-Cu5: 2.4223(7), Cu4-Cu3: 2.4566(7), Cu4-Cu7: 2.7662(8), Cu10-Zn2: 2.4659(8), Cu3-Zn1: 2.4528(8), Cu10-Zn2: 2.4658(7), Cu3-Zn1: 2.4526(7), Cu7-$C_{bridging\,mesityl}$: 2.030(4), Cu3- $C_{bridging\,mesityl}$: 2.012(4), Zn1-Cp*$_{centroid}$: 1.91, Zn2-Cp*$_{centroid}$: 1.92, Cu7-$C_{bridging\,mesityl}$-Cu3: 52.54(13), Cu10-Cu4-Cu8: 59.85(2), Cu7-Cu4-Cu6: 118.60(2); Cu10-Zn2-Cu8: 59.30(2). b): Cluster core geometry of **3** (middle, Cu = orange, Zn = blue). The stacking principle of metal atoms in **3** follows a hcp motif, such as in Mg (upper right side). The structural motif of edge-sharing tetrahedra is well known from Laves phases such as MgCu₂ (upper left side). A similar ABABC stacking principle was found in {[Cu53(C≡CPhPh)9(dppp)6Cl3]}⁺(middle, bottom).[39] The representation of {[Cu53(C≡CPhPh)9(dppp)6Cl3]}⁺ shows the ligands and chlorine atoms as wireframes (color code: C = grey, P = purple, Cl = green) and the Cu atoms in dark orange. The stacking planes are visualized in yellow, blue and red. [Parts of the figure were created by Dr. Wilhelm Klein and Prof. Thomas Fässler. They are also part of a review article published in the journal Chemical Society Reviews. Reproduced (adapted) from M. Schütz, C. Gemel, W. Klein, R. A. Fischer, T. F. Fässler, Intermetallic phases meet intermetalloid clusters. Chem. Soc. Rev., 2021, 50, 8496-8510 with permission from the Royal Society of Chemistry. Copyright 2021. Published by the Royal Society of Chemistry.]*

Spectroscopic characterization of 3

The ^{1}H-NMR spectrum of **3** in benzene-d^6 (see Figure S57) is consistent with the molecular structure found in the solid state and exhibits one singlet (12H) in the aromatic region at 6.76 ppm. In the aliphatic region, the mesitylene methyl groups split into two signals with an integral ratio of 2:1 (36H:18H) at 2.67 ppm and 2.03 ppm, respectively. The ZnCp* moieties give rise to a singlet signal (30H) at 1.62 ppm. Due to the high sensitivity of **3** small amounts of side products like mesitylene are found in the NMR spectra. Also, the ^{13}C-NMR (see Figure S58) spectrum is consistent with all other data with the aromatic mesitylene carbons found at 154.68, 140.57, 137.46 and 126.52 ppm and the CH$_3$ groups at 30.49 ppm and 21.18 ppm. The Cp* groups give rise to two signals at 110.23 ppm and 9.41 ppm. The ATR-IR spectrum of isolated **3** shows the typical bands for the hydrocarbon ligands. The isotopic pattern of the molecular ion peak of **3** in the LIFDI-mass spectrum is consistent with the calculated isotopic pattern for $[Cu_{10}Zn_2](Mes)_6(Cp^*)_2$ (Figure 58). Noteworthy, the elemental composition of **3** is unambiguously clear from labeling experiments with $[Zn_2](Cp^{*Et})_2$ and $[^{68}Zn_2](Cp^*)_2$.
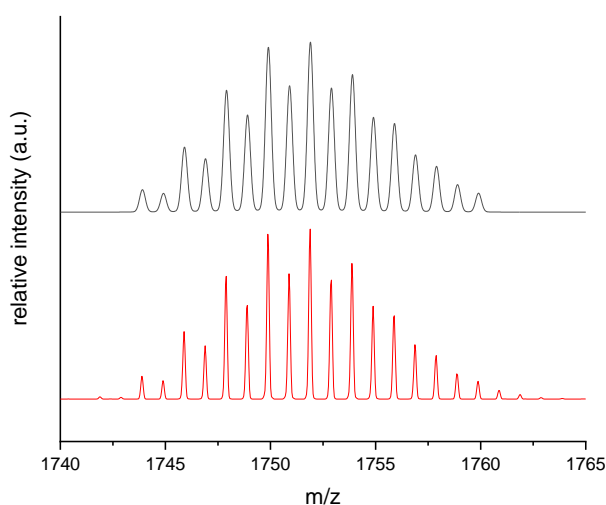
Figure 58
*a) Comparison of the experimental (as determined by positive ion-mode LIFDI-MS; bottom, red) and calculated (top, black) isotopic pattern of $[Cu_{10}Zn_2]Mes_6Cp^*_2$ (**3**).*

Computational analysis of 3

*The distribution of the elements Cu and Zn in the structure of compound **10** was computationally investigated by the group of Prof. Da Silva from Universidade de São Paulo (Brazil).*

The detailed theoretical bonding analysis was carried out by the group of Prof. Jean-Yves Saillard from the Université de Rennes (France).

The assignment of the two zinc locations over twelve metal sites in **3** was obtained by geometry optimization based on total energy DFT calculations of ten representative configurations in the same manner as proceeded for **10** (see computational details and Figure 59). Following the same trend, there is an excellent structural agreement between the XRD structure and the lowest energy configuration in which the two zinc atoms are located on the capping positions along the pseudo-three-fold axis.
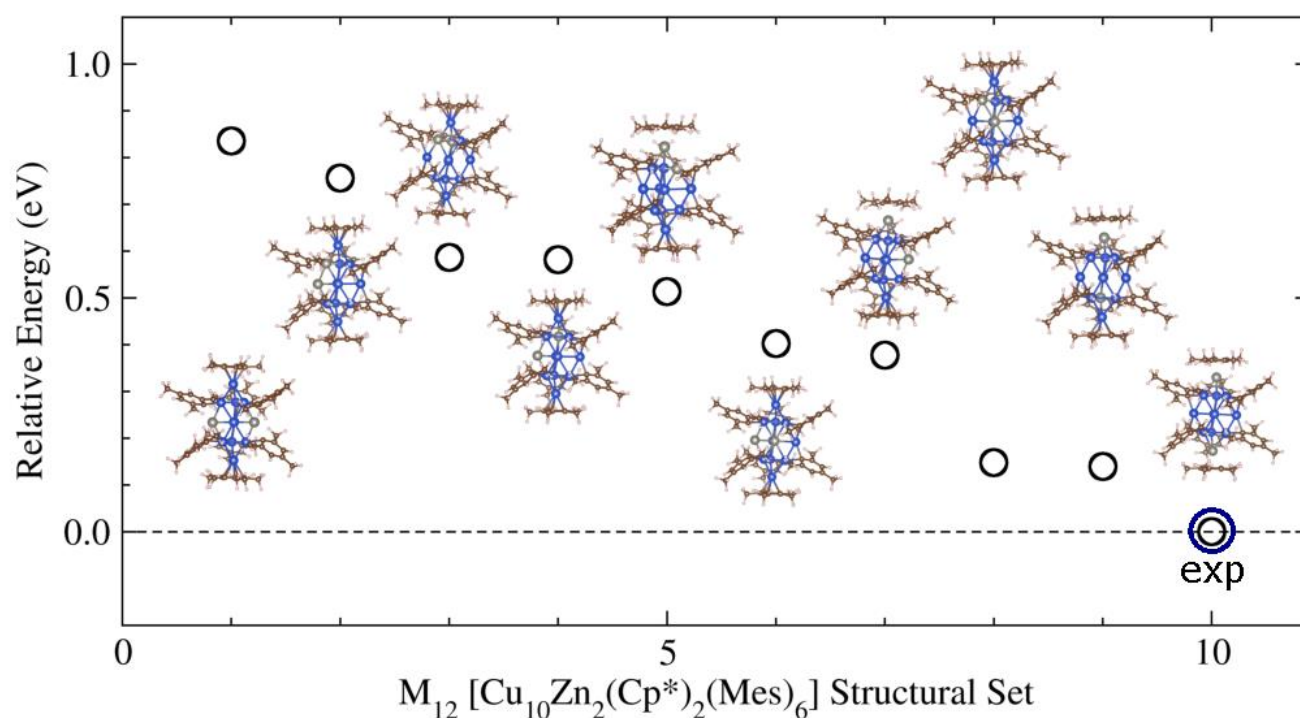
Figure 59
Optimized atomic configurations for [Cu$_{10}$Zn$_2$](Cp)$_2$(Mes)$_6$ (**3**).*

3. Results and Discussion
3.2. Chemical part: Synthesis characterization, reactivity

In the same way as for **10**, this low energy configuration was then investigated at the BP86/TZ2P-D3 level with the ADF2017 code (see computational details, Supporting Information) for analysing its electronic structure, which, as developed below, can be explained within the framework of the superatom concept.[33, 197, 219] The computed ¹H- and ¹³C- NMR chemical shifts are also consistent with their experimental counterparts (Table S5). The first question that arises with respect to electron distribution, is that of the metal oxidation states. Indeed, with six mesityl and two Cp* ligands, all formally anionic, the $[Cu_{10}Zn_2]$ group oxidation state is +8, that is, there are $[(10 \times 1) + (2 \times 2)] - 8 = 6$ metallic 4s electrons located somewhere on the metal core. This number is not a superatom closed-shell "magic" electron count, which makes sense owing to the fact that the regular superatom model assumes cluster spherical shapes,[33, 197, 219] which is obviously not the case for **3**. In any case, like in superatoms of group 11 metals, metal-metal bonding in **3** is expected to be mainly ensured by these valence s-type electrons.[197, 219-220] Like in group 11 superatoms, the computed HOMO-LUMO gap of **3** (1.51 eV), although significant, is not as large as that found usually at the GGA level for Cu(I) species.[221] A careful analysis of the occupied Kohn-Sham orbitals allowed identifying three of them with important 4s character, two of pseudo-a'_1 and one of pseudo-a''_2 symmetry. They are plotted in Figure 60. The highest one is the pseudo-a'_1 HOMO which is principally composed of the 4s AO of the central Cu4 atom, with some minor antibonding admixture from the other metal atoms. The two other 4s combinations have significant bonding character and therefore much lower energies. The lowest is the pseudo-a'_1 bonding counterpart of the HOMO. The other one, of pseudo-a''_2 symmetry, is bonding within each of the inner Cu_4 tetrahedra. Thus, in terms of a superatomic description, the electron configuration of **3** is $1S^2$ $1P_z^2$ $2S^2$, consistent with the very prolate shape of the cluster core. Thus, despite its substantial deviation from spherical symmetry, we believe that the superatom model still appears to be a useful limit reference for rationalizing the electronic structure of **3**. Consistently, the two LUMO's can be tentatively identified as the $1P_{x,y}$ orbitals. The weakly antibonding 2S HOMO lies 0.76 eV above the HOMO-1, suggesting the possibility of oxidizing **3** without major structural change. The Cu4 NAO charge (-0.47) is rather negative, indicative of an oxidation state close to –I, in agreement with the HOMO nature. That of the three outer Cu atoms (+0.63) is close to what is usually found for Cu(I).[221] The six other Cu atoms have an intermediate charge of +0.33. The Zn NAO charge (+0.97) is indicative of partly reduced Zn(II). Consistently, the Zn-Cu Wiberg indices are significant (avg. 0.197). The largest Cu-Cu Wiberg indices are within the two small triangles (avg. 0.151) and the smallest (avg. 0.043) correspond to the longest bonds, *i.e.* between the central and most inner Cu atoms. Overall, **3** can be viewed as a very elongated superatom with an unusual electron count associated with this prolate distortion. This unexpected situation is likely to be associated with the bridging ability of the ZnCp* capping units that offer the possibility to strongly bind to the top and the bottom of the cluster in addition to the bridging mesityl ligands stabilizing the Cu-core of the cluster.

a'₁ -4.01 eV (HOMO)   *a"₂* -9.21 eV

a'₁ -9.64 eV
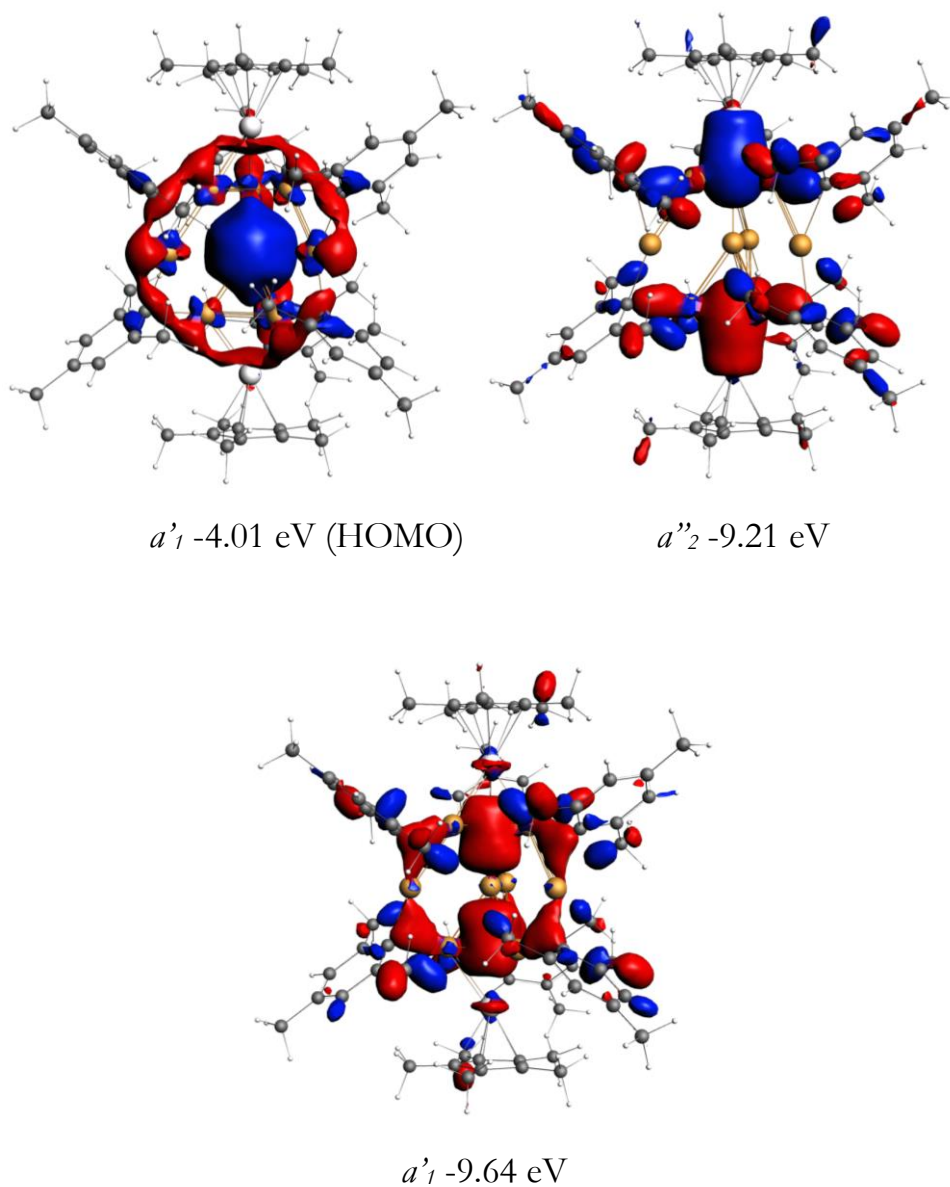
Figure 60
*The three occupied orbitals of **3** of large 4s character and responsible for metal-metal bonding in the [Cu₁₀Zn₂] core.*

3.2.1.3 The nano-brass "micro-library" $[Cu_4Zn_{9/10}](Cp^*)_8$ (**4/5**)

Synthesis

Reaction of [CuMes] with $[Zn_2](Cp^*)_2$ in a molar ratio of 1:0.75 at room-temperature leads to a dark red solution. Cooling the filtered reaction solution after a total reaction time of 2 h to -30 °C leads after several weeks to black crystals of **4/5** in addition to crystals of $[CuZn_2](Cp^*)_3$ and $[Cu_3Zn_4](Cp^*)_5$ (see Scheme 15). Noteworthy, prolonged reaction times did not lead to isolation of any product. It is suggested that the presence of $[CuZn_2](Cp^*)_3$, which is consumed after prolonged reaction times, is crucial as "seeding" crystals for the crystallization of **4/5** . The molecular structure of **4/5** in the solid state, being a co-crystallizate of $[Cu_4Zn_{10}](Cp^*)_8$ and $[Cu_4Zn_9](Cp^*)_8$, was analyzed by SC-XRD with assignment of the element positions based on DFT calculations (see Figure 41) as well as spectroscopic data (LIFDI-MS with isotopic labeling (^{68}Zn), X-ray photoelectron spectroscopy, ICP-MS analysis, NMR spectroscopy). **4/5** can be obtained in purified form by washing the crystallizate extensively with *n*-hexane. However, a quantitative separation from $[CuZn_2](Cp^*)_3$ still remains difficult. As a solid, it is stable under Ar atmosphere at room-temperature in solid-state as well as in solution but is unstable upon heating in solution to 90 °C leading to formation of HCp* and pentamethylfulvene as identified by ^{1}H-NMR spectroscopy. The pure Zn clusters $[H_2Zn_{4-6}](Cp^*)_8(Mes)_2$ were identified as products of the thermal treatment of **4/5** by LIFDI-MS analysis; however, assignment of these species is prone to some uncertainty and would require isotopic labeling with ^{68}Zn for unambiguous identification. **4/5** is well soluble in benzene and toluene but only very badly in hexane.

3. Results and Discussion
3.2. Chemical part: Synthesis characterization, reactivity

4
$[Cu_4Zn_9](Cp^*)_8$

5
$[Cu_4Zn_{10}](Cp^*)_8$
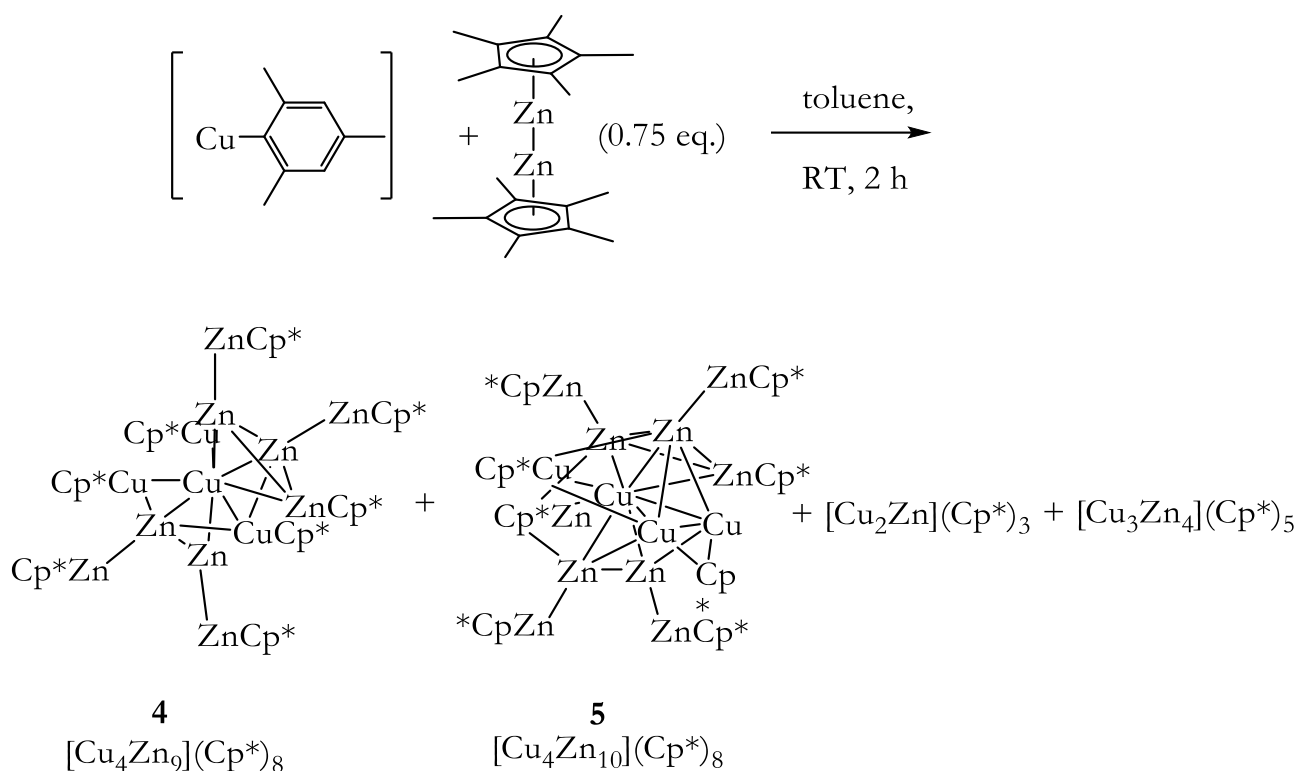
Scheme 15
*Synthesis of the Cu/Zn micro-library **4/5**. Clusters **4** and **5** can be separated from $[CuZn_2](Cp^*)_3$ and $[Cu_3Zn_4](Cp^*)_5$ by washing with n-hexane.*

Crystallographic characterization of 4/5

$[Cu_4Zn_9](Cp^*)_8$ (**4**) and $[Cu_4Zn_{10}](Cp^*)_8$ (**5**) co-crystallize in the triclinic space group P-1 with two molecules of **4** and **5** each per unit cell. Importantly, the presence of 8 (fully occupied) Cp* ligands is unambiguously clear from the crystallographic data. The co-crystallization of two compounds in one structure can be deduced from very close lying metal positions in the crystal structure at the MCp* positions. Assignment of the elements Cu and Zn to the atomic positions of the crystal structure was accomplished by DFT calculations (*Prof. Da Silva*, see methodological part and Figure 41). The results are currently verified by the group of *Prof. Saillard*. Therefore, the crystal structure has not been refined yet with ultimate elemental positions and the discussion of the structure is therefore given only on a qualitative level in the following.

The structure of **4** consists of four MCp* and four M-MCp* units coordinating to the central atom. According to the calculations, the central position is filled by Cu, which is coordinated by four Zn-ZnCp* units, one ZnCp* ligand and three CuCp* moieties. Interestingly, the structure may also be explained as superposition of three distorted tetrahedra: One central, Cu filled tetrahedron consisting of the four

135

unligated Zn atoms, surrounded by a tetrahedron of 3 CuCp* and one ZnCp* unit and one outer tetrahedron consisting of the outermost ZnCp* units (alternate description {Cu@[Zn$_4$]@[Zn$_1$Cu$_3$](Cp*)$_3$@[Zn$_4$](Cp*)$_4$}). Such structural motifs are well known from the corresponding solid-state alloys such as γ-brass Cu$_5$Zn$_8$ (see Figure 4, introduction). However, in the solid-state phase, mixing of Cu and Zn in one tetrahedral shell is not observed. The "stella quadrangula" motif of superimposed tetrahedra was also found in [Cu$_4$Zn$_4$](^{t}CNBu)$_4$(Cp*)$_3$(Cp), albeit with a much smaller degree of distortion in the innermost tetrahedron.[86] The fact that in **4** (and **5**), the innermost tetrahedron is filled by Cu may be a reason for that distortion.

In compound **5**, one of the CuCp* units coordinating to the central Cu atom is replaced by a Cu$_2$Cp* unit, in which the Cp* ligand is binding in a η^2-binding mode to two Cu atoms. As this replacement can statistically take place at all MCp* positions binding to the central atom, fractional occupied metal atom positions can be located in the crystal structure between these "inner" MCp* atoms due to crystallographic disorder. A similar situation of a η^2-bound Cp ligand was found in the [Cu$_2$Cp$_3$]$^-$ anion, in which a Cp ligand bridges two Cu atoms, as well as in [(Cp)Cu{(μ_3-NH)$_3$Ti$_3$(η^5-C$_5$Me$_5$)$_3$(μ_3-N)}].[222-223] According to the calculations, the Cp*Cu$_2$ moiety lies in direct vicinity to another CuCp* unit and opposite to two ZnCp* units.

Spectroscopic characterization of 4/5

LIFDI-MS spectra of isolated **4/5** exhibit three major peaks, which can be assigned to [Cu$_4$Zn$_{10}$](Cp*)$_8$ (molecular ion peak of **5**), [Cu$_4$Zn$_{10}$](Cp*)$_7$ and [Cu$_4$Zn$_9$](Cp*)$_7$ according to their isotopic patterns and *m/z* ratios (see Figure 61). Unambiguous assignment of the peaks is only possible by labeling experiments with [^{68}Zn$_2$](Cp*)$_2$ and the corresponding mass envelopes are included in Figure 61. Noteworthy, [Cu$_4$Zn$_{10}$](Cp*)$_7$ is supposed to be a fragment of [Cu$_4$Zn$_{10}$](Cp*)$_8$ (**5**) (Cp* cleavage). The molecular ion peak of [Cu$_4$Zn$_9$](Cp*)$_8$ (**4**) cannot be observed in LIFDI-MS analysis of the isolated crystals. Even though it is not clear from the LIFDI data alone whether the ion [Cu$_4$Zn$_{10}$](Cp*)$_7$ is a fragment of [Cu$_4$Zn$_{10}$](Cp*)$_8$ (**5**) or [Cu$_4$Zn$_9$](Cp*)$_8$ (**4**), the existence of [Cu$_4$Zn$_9$](Cp*)$_8$ is strongly supported by SC-Xray diffraction data (*vide supra*) and elemental analysis of the crystals (*vide infra*).

In addition to these peaks, a large variety of smaller clusters is detected in the mass spectrum of isolated **4/5** (see Figure S60, full range spectrum). These species are supposed to be fragments of the parent molecular ions and/or formed during the measurement process due to the thermal instability of compound **4/5**. Further, minor ($\leq$ 5 % on basis of NMR data) - but well ionizable – impurities of

3. Results and Discussion
3.2. Chemical part: Synthesis characterization, reactivity

$[CuZn_2](Cp^*)_3$ and $[Cu_3Zn_4](Cp^*)_5$ cannot be excluded with certainty due to the difficulty to separate these species. The ions identified in the spectra of the isolated compound **4/5** are listed in Table S2 in the Appendix.
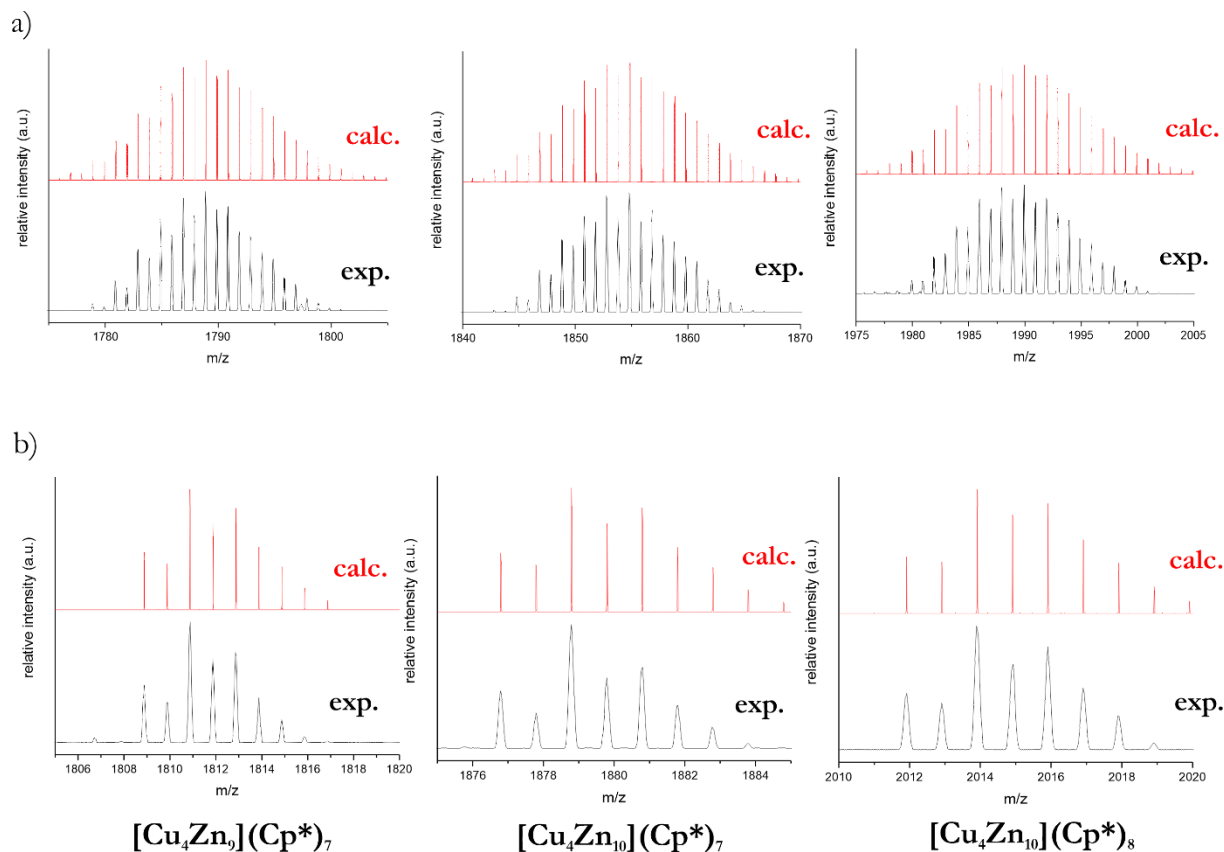
Figure 61

*Identification of **4/5** by LIFDI-MS. a) Comparison of calculated (red) and experimental (red) mass envelopes for $[Cu_4Zn_9](Cp^*)_7$, $[Cu_4Zn_{10}](Cp^*)_7$ and $[Cu_4Zn_{10}](Cp^*)_8$. b) Calculated (red) and experimental (black) isotopic patterns obtained by ^{68}Zn labeling experiments. $[Cu_4Zn_{10}](Cp^*)_7$ is supposed to be a fragment of $[Cu_4Zn_{10}](Cp^*)_8$ (Cp^* loss). Even though $[Cu_4Zn_9](Cp^*)_7$ might also be a fragment of $[Cu_4Zn_{10}](Cp^*)_8$, it is supposed to rather be a fragment of $[Cu_4Zn_9](Cp^*)_8$, as the presence of a second species with lower Zn content and 8 Cp* ligands is clear from SC-Xray diffraction data and elemental analysis.*

The elemental composition of **4/5** was also determined by ICP-MS analysis, giving a Cu:Zn ratio of 2.123 ± 0.031. Additional XPS analysis of the crystals gave a similar Cu:Zn ratio of 2.15 ± 0.1. The values are slightly lower than the ones expected for $[Cu_4Zn_{9/10}](Cp^*)_8$ (Cu:Zn = 2.25-2.5). The deviation can be explained by the

presence of ~5 % $[CuZn_2](Cp^*)_3$ in the sample. Nevertheless, the results strongly support the elemental composition and sum formulas.

The ^{1}H-NMR spectrum of **4/5** in toluene-d$_8$ (see Figure S61) shows two broad signals indicative of Cp* at 2.22 ppm and 2.27 ppm (integral ratio 1:1), which are assigned to MCp* (M = Cu, Zn) units and Zn-ZnCp* units, respectively. At -90 °C, four signals at 2.27 ppm, 2.29 ppm, 2.31 and 2.35 ppm are observed with integral ratios of 4:2:1:1 (see Figure S62). The signal with the highest integral at 2.27 ppm is assigned to Zn-ZnCp* units, whereas the one at 2.29 ppm is tentatively assigned to the two CuCp* units lying in direct vicinity to each other. The signals at 2.31 ppm and 2.35 ppm are thereafter assigned to the remaining CuCp* and ZnCp* units. The ^{13}C-NMR spectrum of **4/5** in toluene-d$_8$ (see Figure S63) shows four signals in the typical range of Cp* at 10.95 ppm, 11.75 ppm, 12.99 ppm (-CH$_3$) and 100.2 ppm, 111.40 ppm, 109.21 ppm (quaternary C atoms). As CuCp* units in intermetallic clusters tend to exhibit significantly upfield shifted quaternary carbon signals in ^{13}C-NMR (104.62 ppm in $[CuZn_2](Cp^*)_3$, 105.32 ppm in $[Cu_3Zn_4](Cp^*)_5$), the signals at 100.2 ppm and 11.75 ppm are attributed to CuCp* units. It is noted that NMR analysis of **4/5** is consistent with the assignment of the elements obtained by DFT calculations and by the symmetry of the structure (see Figure 41). Interestingly, fluctional Cp* exchange occurs within ZnZnCp* units and between CuCp* and ZnCp* units.

Noteworthy, the purity of $[Cu_4Zn_{9/10}](Cp^*)_8$ was also confirmed by powder-Xray diffraction (see Figure S65).

In situ studies on cluster formation of 4/5 and library composition

The reaction of [CuMes] with $[Zn_2](Cp^*)_2$ was investigated by means of time-dependent *in situ* ^{1}H-NMR spectroscopy and LIFDI-MS analysis in different stoichiometric Cu:Zn ratios (see also methodical part for the procedure of Cu/Zn library investigation by LIFDI-MS analysis). The reactions were conducted for Cu:Zn stoichiometries of 1:1.5, 1:3 and 3:1 and monitored over a duration of 2 days.

Applying a Cu:Zn ratio of 1:1.5 (as in synthesis of **4/5**), ^{1}H-NMR analysis indicates fast formation of the half-sandwich Zn(II) zincocene complex MesZnCp* already after a total reaction time of 30 minutes stemming from the reduction of [CuMes] with $[Zn_2](Cp^*)_2$ (see Figure S66). Further, the known embryonic Cu/Zn clusters $[CuZn_2](Cp^*)_3$, $[Cu_3Zn_4](Cp^*)_5$, as well as compound **4/5** are detected in the spectra (see Figure S66). When referenced to the residual proton signal of the solvent, the concentration of $[CuZn_2](Cp^*)_3$ was found to reach its maximum after 2 hours reaction time, followed by a constant decrease pointing towards its consumption in

cluster growth reactions (see Figure 62 a) for simplified illustration). In contrast, the concentration of **4/5** was found to be constant over several days. Notably, cluster **4/5** can only be crystallized after short reaction times (2-3 h) in the presence of $[CuZn_2](Cp^*)_3$; after prolonged reaction times (> 2 days) no crystals were obtained, even if **4/5** could still be detected by ^{1}H-NMR and LIFDI-MS analysis of reaction solutions. LIFDI-MS spectra of the reaction solutions reveal a variety of Cu/Zn clusters formed, which was in detail analyzed as described in the methodical part of this dissertation (see Table 1 for the molecular ions identified in the spectra). Notably, time-dependent LIFDI-MS analysis of the solutions did not reveal any new signals after prolonged reaction times at room-temperature, it is therefore supposed that the consumption of $[CuZn_2](Cp^*)_3$ leads to an overall higher concentration of the heavier clusters (see Figure 62 a) for simplified illustration). The ions $\{[Cu_3Zn_4](Cp^*)_6(Mes)_6 - H\}$, $[HCu_7](Cp^*)_2$, $[Cu_2Zn_3](Mes)_3$, $[Cu_4](Cp^*)(Mes)_2$, $[H_2Cu_3](Cp^*)_3$ and $[HCu_4](Cp^*)_2$ are observed only at this Cu:Zn stoichiometry in LIFDI-MS analysis.

When an excess of $[Zn_2](Cp^*)_2$ is reacted with [CuMes] (Cu:Zn ration = 1:3), *in situ* ^{1}H-NMR spectroscopy reveals formation of high amounts of $[CuZn_2](Cp^*)_3$ and $[Cu_3Zn_4](Cp^*)_5$, which persist at high concentration even under prolonged reaction times (see Figure S67 and Figure 62 b) for simplified illustration). Obviously, high concentrations of $[Zn_2](Cp^*)_2$ concentrations seem to complex Cu centers in the form of small (embryonic) coordination compounds. The total concentration of heavier clusters is therefore supposed to be lower than in samples with a Cu:Zn stoichiometry 1:1.5 (see Figure 62 b) for simplified illustration). Additionally, **4/5** is formed according to ^{1}H-NMR analysis and also detected in LIFDI-MS analysis (see Table S1). Indeed, crystals of **4/5** can be obtained together with high amounts of co-crystallizing $[CuZn_2](Cp^*)_3$ after various reaction times. LIFDI-MS spectra of the reaction solution reveal many fragment ions related to $[CuZn_2](Cp^*)_3$ and $[Cu_3Zn_4](Cp^*)_5$, being consistent with an overall high concentration of these species (Table S1). The ions $[Cu_7Zn_4](Cp^*)_4(Mes)_3$ and $[Cu_9](Cp^*)_2(Mes)_4$ are only observed at this Cu:Zn ratio applied. Noteworthy, none of these could be identified as a molecular ion.

Finally, an excess of [CuMes] was reacted with $[Zn_2](Cp^*)_2$ (Cu:Zn ratio: 1:0.75). Using this stoichiometric ratio of reactants, only very small amounts of **4/5** are formed at the beginning of the reaction according to ^{1}H-NMR analysis (see Figure S68 and Figure 62 c) for simplified illustration) besides Cp*ZnMes and unconsumed [CuMes]. Instead, the Cu-rich cluster $[Cu_{10}Zn_2](Mes)_6(Cp^*)_2$ (**3**) is detected as a very prominent peak in LIFDI-MS analysis. The LIFDI-MS spectra also reveal several species, which are supposed to be fragments or ligand exchange products of **3**, such as $[Cu_{10}Zn_2](Cp^*)_3(Mes)_5$, $[Cu_{10}Zn](Cp^*)_2(Mes)_4$, $[Cu_{10}Zn_2](Cp^*)_2(Mes)_5$ or $[Cu_{10}](Cp^*)(Mes)_6$ (see Table S1). Some of them were indeed identified as fragment

ions in LIFDI-MS analysis of isolated **3** (see Table S2). This points towards to the preferred formation of **3** under these reaction conditions even at room-temperature. Noteworthy, heating of such solutions results in size-focusing towards **3** (see Figure 48). In line with these observations, isolation of **4/5** was not possible from reaction solutions with this Cu:Zn stoichiometry of 1:0.75. The ions $[Cu_7Zn](Cp^*)_3(Mes)$, $[HCu_8](Cp^*)_2(Mes)_3$, $[Cu_4](Cp^*)_2(Mes)_2$, $[H_2Cu_9](Cp^*)(Mes)_5$, $[HCu_7](Cp^*)(Mes)_4$ in addition to ion peaks attributed to unconsumed [CuMes] starting material were observed only at this Cu:Zn stoichiometry. Noteworthy, many of them are supposed to be fragments of molecular ions listed in Table 1. It is supposed that fragmentation behavior is dependent on the composition of the library, which may well be explained by ligand exchange processes during ionization or even in the HCD cell set-up in the event of bimolecular collisions.

In conclusion, LIFDI-MS analysis of the reaction solutions with different Cu:Zn stoichiometry reveal only very subtle differences in library composition (Table S1). The main effect observed are ligand exchange and scrambling processes in the fragment ion species. Additionally, the preferred formation of $[CuZn_2](Cp^*)_3$, $[Cu_3Zn_4](Cp^*)_5$ and **4/5** at high to medium Zn concentrations, of $[Cu_{10}Zn_2](Cp^*)_2(Mes)_6$ at high Cu concentrations, respectively, is nicely reflected in the spectra. Notably, these observations are fully supported by quantitative *in situ* ^{1}H-NMR analysis.

3.2. Chemical part: Synthesis characterization, reactivity

a) Cu:Zn = 1:1.5

b) Cu:Zn = 1:3

c) Cu:Zn = 1:0.75

$[CuZn_2](Cp^*)_3$ $[Cu_4Zn_{9/10}](Cp^*)_8$ /   heavy clusters $[Cu_{10}Zn_2](Cp^*)_2(Mes)_6$
                      $[Cu_3Zn_4](Cp^*)_5$
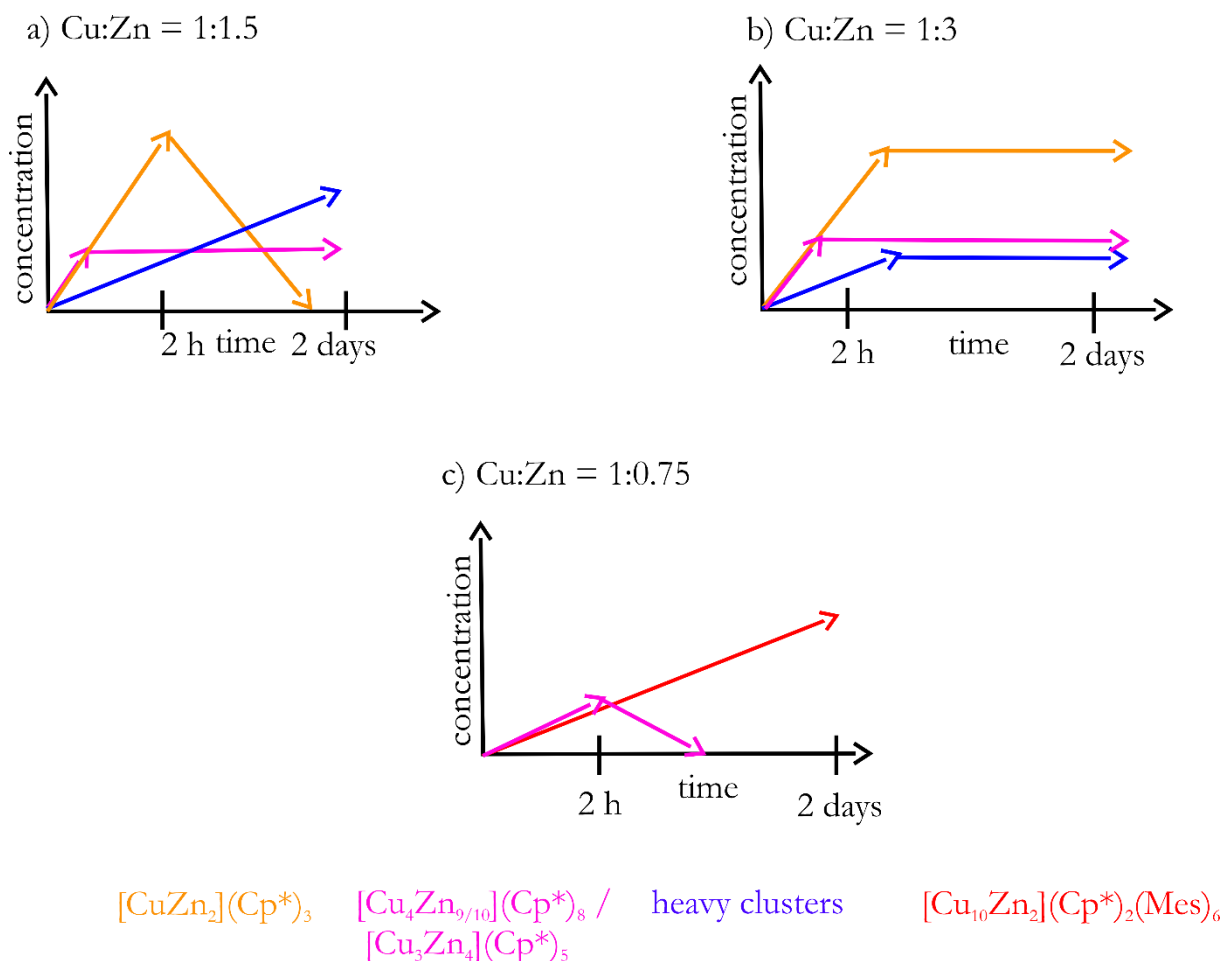
Figure 62
Simplified and tentative time vs. cluster concentration curves for the Cu:Zn stoichiometries 1:1.5 (a)), 1:0.3 (b)) and 1:0.75 (c)) in the [CuMes] + [Zn₂](Cp*)₂ reaction on the basis of in situ ¹H-NMR and LIFDI studies. Note that the arrows only indicate qualitative observations. The heavy clusters including [Cu₁₀Zn₂](Cp*)₂(Mes)₆ cannot be observed in in situ ¹H-NMR (low overall concentration, overlapping signals) but only in LIFDI-MS. Their concentration curves are therefore mainly based on chemical assumptions concerning cluster growth processes.

3.2.2 Reactivity of Cu/Zn cluster libraries

Chemical background and conceptual motivation of the reactions with CO_2 /H_2

The reactivity assessment of embryonic brass in the reduction of CO / CO_2 with hydrogen is inspired by the heterogenous methanol production from syn gas (CO / CO_2 /H_2) over Cu/ZnO/Al_2O_3 catalysts at harsh conditions of 493 − 573 K and 5-10 MPa (see also introduction, chapter 1.2.2).[23] The hydrogenation of CO_2 instead of CO is thereby considered to be beneficial in terms of environmental aspects and industrial importance.[224]

Despite the fact that this process has been subject of in-depth research over the last decades, a lot of uncertainity not only about the dominant mechanism of CO_2 reduction but also about the nature of the active site of the catalyst remains.[23] Two different reaction mechanisms have been proposed for the generation of methanol from CO_2.[23] In the first scenario, CO_2 is reduced to formate (HCOO), dioxomethylene (H_2COO), formaldehyde (H_2CO) and finally to the desired product CH_3OH. In the other proposed mechanism, CO is formed initially from CO_2 by the reverse water-gas-shift-reaction and subsequently CO is hydrogenated to form methanol. Evidence for the first mechanism was gained e.g. by infrared studies on CO_2 hydrogenation over Cu/SiO_2 and Cu/ZrO_2/SiO_2 surfaces.[225] However, the second mechanism was proposed as the dominating pathway for methanol production over Cu/ZrO_2 surfaces by a recent theoretical study.[226]

Concerning the active site, metallic Cu is considered to be the active center especially for H_2 dissociation on oxide supported catalysts. In these systems, the oxide support is supposed to the effect electronic stabilization of metallic Cu sites, as well as fine dispersion of the active centers over the whole catalyst surface.[23] Due to the fact that CO_2 adsorbs preferentially on oxide and H_2 dissociation is preferred on Cu, the catalytic reaction is supposed to occur on the oxide/Cu interface.[226] However, the exact valence of the catalytically active Cu centers at the interface is not clear so far. Metallic Cu and other low-valent Cu species ($Cu^{\delta+}$ and Cu^+) are all assumed to affect the catalytic activity.[226-228] Thereby, high catalytic activity is associated with Cu steps at the catalytical surface, which may further be stabilized by bulk defects like stacking faults.[24] Additionally, the presence of partially reduced ZnO_x at the catalyst surface, formed under experimental conditions, is supposed to enhance the catalytic activity. The reduced Zn centers are thereby considered to serve as an adsorption site for oxygen-bound intermediates.[24]

Molecular clusters and nanoparticles[23, 27] are considered as ideal candidates for a better understanding of electronic and geometric prerequisites for CO_2 reduction. Indeed, differences in reactivity concerning CO_2 adsorption and reduction were monitored for the members of the "embryonic brass" library by in situ LIFDI-MS analysis.

3. Results and Discussion
3.2. Chemical part: Synthesis characterization, reactivity

Reactivity of the Cu/Zn library towards CO₂

The reaction of Cu/Zn libraries (Cu:Zn = 1:1.5) with 1 bar CO_2 leads to changes in library composition as indicated by LIFDI-MS analysis. Careful adjustment of the reaction time induces only subtle changes in library composition, *i.e.* the appearence of two new peaks at m/z = 1543 and m/z = 1630 (see Figure 45). By isotopic labeling experiments (^{68}Zn), the peaks were identified as $[Cu_5Zn_5](Cp^*)_6(CO_2)_2$ and $[Cu_8Zn_3](Cp^*)_3(Mes)_4(CO_2)$. Inspection of the list of parent ions in the original library allows to suggest the starting material for these clusters, namely the hydride bearing clusters $[H_3Cu_6Zn_6](Cp^*)_5(Mes)$ and $[HCu_8Zn_3](Cp^*)_4(Mes)_3$. It has to be noted that the formulation of CO_2 ligands has to be regarded with some care, as LIFDI-MS only allows to unambiguously assign sum formulas to the peaks. In principle, a decomposition of the CO_2 into M-CO and M-O (M = Cu, Zn) is possible.[198]

Obviously, the hydride bearing clusters in the original library react first with CO_2. The reaction was also monitored by *in situ* ¹H-NMR analysis (see Figure S69). Already after short reaction times, the spectra indicate formation of pentamethylfulvene and of a peak at 4.41 ppm, which is very similar to the chemical shift of dissolved hydrogen (4.5 ppm in benzene-d₆). Free HCp* and mesitylene, as well as decamethylfulvalene are observed in low quantities. The results indicate cleavage of cluster bound ligands, *e.g.* by formation of pentamethylfulvene (C-H bond activation of Cp*), accompanied by reductive elimination of hydrogen, which possibly coordinates to library members in the form of surface bound hydrides. However, no signals of novel hydride species were observed in LIFDI-MS spectra of the reaction solution. The resulting free coordination sites are supposed to be prone to subsequent CO_2 adduct formation (potentially accompanied by cleavage of the CO_2 ligand). Additionally, the process is obviously accompanied by ligand exchange processes and subtle variations of the cluster core compositions may also occur (see Scheme 16). Interestingly, signals of $[Cu_2](Mes)_2$ are observed in ¹H-NMR spectra of the reaction solution. This is line with the loss of one [CuMes] unit in the reaction of $[H_3Cu_6Zn_6](Cp^*)_5(Mes)$ to $[Cu_5Zn_5](Cp^*)_6(CO_2)_2$ (see also Scheme 16 for illustration).

3. Results and Discussion
3.2. Chemical part: Synthesis characterization, reactivity
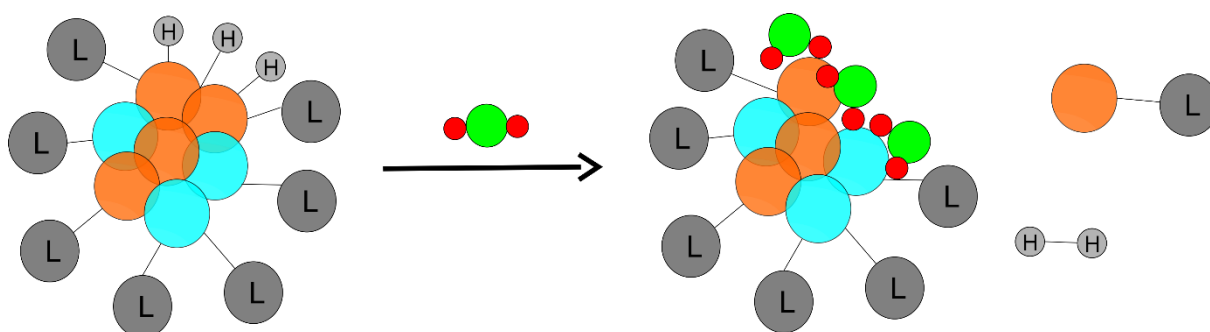
Scheme 16

Simplified illustration of the reactivity of ligated Cu/Zn clusters with CO_2 on basis of the data at hand. Open coordination sites at the clusters surface for CO_2 absorption are generated by elimination of H_2 or Cu-L. L = ligand (Cp*, Mes), Cu = orange, Zn = blue. Note that in principle cleavage of CO_2 into M-CO and M-O (M = Cu, Zn) is possible, as LIFDI-MS only allows to determine sum-formulas of the product species obtained.

The reaction was also investigated by XPS analysis of evaporated reaction solutions coupled with MS analysis of the gas phase. Noteworthy, evaporation of the solvent was shown to only marginally affect the integrity and composition of the library. When the sample was exposed to 1 mbar of CO_2, formation of hydrogen was observed, which is consistent with the results obtained by *in situ* ^{1}H-NMR analysis. Additionally, low amounts of formic acid were detected, proven by its characteristic fragmentation pattern. However, no mesitylene or HCp* could be observed, contrary to expectations from NMR analysis. Possibly, the formation of H-R (R= mesitylene, Cp*) occurs as a bimolecular process in solution, which is not possible in the solid state. This might lead to the preferential reductive elimination of hydrogen and the presence of H_2 also explains the formation of formic acid (sequential addition of H_2 and CO_2 also led to formate formation in solution, *vide infra*). Noteworthy, no such CO_2 reduction products could be detected in the solution experiments upon exposure to CO_2 alone. Interestingly, no CO_2 adsorption is reported in literature for Cu(110) or Zn surfaces, but only for ZnO_x particles.[229] Nevertheless, adsorption of CO_2 is proposed as the initial step in CO_2 hydrogenation from CO_2/H_2 mixtures.[230]
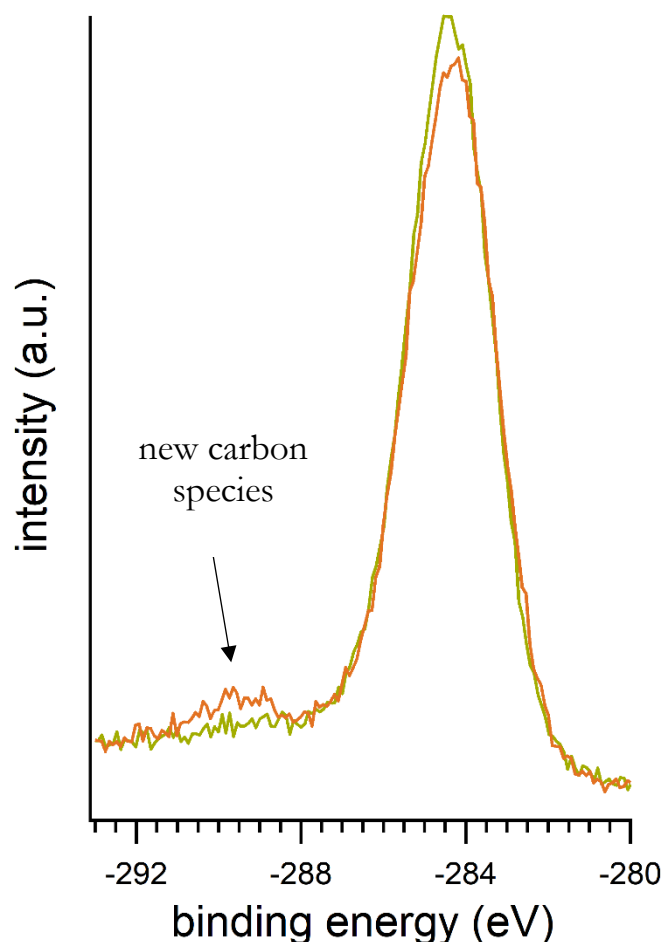
Figure 63
C 1s XPS spectrum of the evaporated Cu/Zn library (Cu:Zn = 1:1.5) before (green) and after
CO_2 exposure (1 bar). Clearly, formation of a new carbon species is discernible, which correlates
with the CO_2 uptake of certain clusters as observed in LIFDI-MS. [Figure created by Tim Kratky.]

XPS analysis of the sample after CO_2 exposure (900 mbar, 30 min, RT) indicates the presence of a novel carbon species at a high C 1s binding energy which originates from two bound O atoms (see Figure 63). This confirms a CO_2 adduct formation, such as observed by LIFDI-MS analysis.

FT-IR analysis of the reaction solutions in combination with theoretical analysis of the CO_2 cluster adducts by the group of *Prof. Da Silva* has currently been launched and will be a project of further research. Comparison between calculated and experimental IR bands is thought to further strengthen the interplay between computational and experimental approaches in the investigation of complex cluster libraries and their reactivity. These studies are also thought to verify the nature of the CO_2 units bound to the clusters (CO_2 ligand or M-CO + M-O).

3. Results and Discussion
3.2. Chemical part: Synthesis characterization, reactivity

Reactivity of the Cu/Zn library towards CO$_2$ and H$_2$

When the CO$_2$ pre-treated library is subjected to 2 bar of hydrogen pressure at room-temperature, *in situ* ^{1}H-NMR spectroscopy indicates formation of formate after a total reaction time of 4 hours at room-temperature. The reaction is further accompanied by formation of HCp*, mesitylene, pentamethylcyclopentane and 1,2,3,4,5-pentamethylcyclopent-1-ene in small amounts (see Figure S70). LIFDI-MS analysis of the reaction solution reveals formation of two major new peaks at *m/z* = 2305 and *m/z* = 2170 in addition to the unchanged peaks of the original CO$_2$ adduct species [Cu$_5$Zn$_5$](Cp*)$_6$(CO$_2$)$_2$ and [Cu$_8$Zn$_3$](Cp*)$_3$(Mes)$_4$(CO$_2$) (see Figure 64). Obviously, the latter two CO$_2$ adducts are inactive towards H$_2$.

Using labelling experiments with [Zn$_2$](Cp*^{Et})$_2$ and [^{68}Zn]$_2$(Cp*)$_2$, the two new peaks were unambiguously identified as [Cu$_{11}$Zn$_6$](Cp*)$_8$(CO$_2$)$_2$(HCO$_2$) and [Cu$_{11}$Zn$_6$](Cp*)$_7$(CO$_2$)$_2$(HCO$_2$). Noteworthy, the corresponding reaction with D$_2$ yields the species [Cu$_{11}$Zn$_6$](Cp*)$_8$(CO$_2$)$_2$(DCO$_2$) and [Cu$_{11}$Zn$_6$](Cp*)$_7$(CO$_2$)$_2$(DCO$_2$) with a Δm/z shift of 1 with respect to the original peaks (see Figure 65). Conducting the reaction with ^{13}CO$_2$ induces a Δm/z shift of three with respect to the original isotopic envelope (see Figure 65) being fully consistent with three CO$_2$ units bound to the reaction product. Whereas the incorporation of one H atom stemming from H$_2$ into the reaction product is doubtless, the exact nature of the CO$_2$ ligands remains unclear from mass spectrometric experiments alone. It is noted that three formate ligands are also in line with the determined sum formulas, if the possibility of CH activated Cp* ligands is taken into account.

3. Results and Discussion

3.2. Chemical part: Synthesis characterization, reactivity

Figure with two LIFDI-MS spectra (relative intensity vs m/z). Upper trace labeled "H$_2$ addition (2 bar, 18 h)" with two newly formed species marked by yellow ellipsoids near m/z 2170 and 2310. Lower trace labeled "library after CO$_2$ treatment (1 bar, 2 h)".

Legend:
✦ [Cu$_5$Zn$_5$](Cp*)$_6$(CO$_2$)$_2$ ✦ [Cu$_8$Zn$_3$](Cp*)$_3$(Mes)$_4$(CO$_2$)
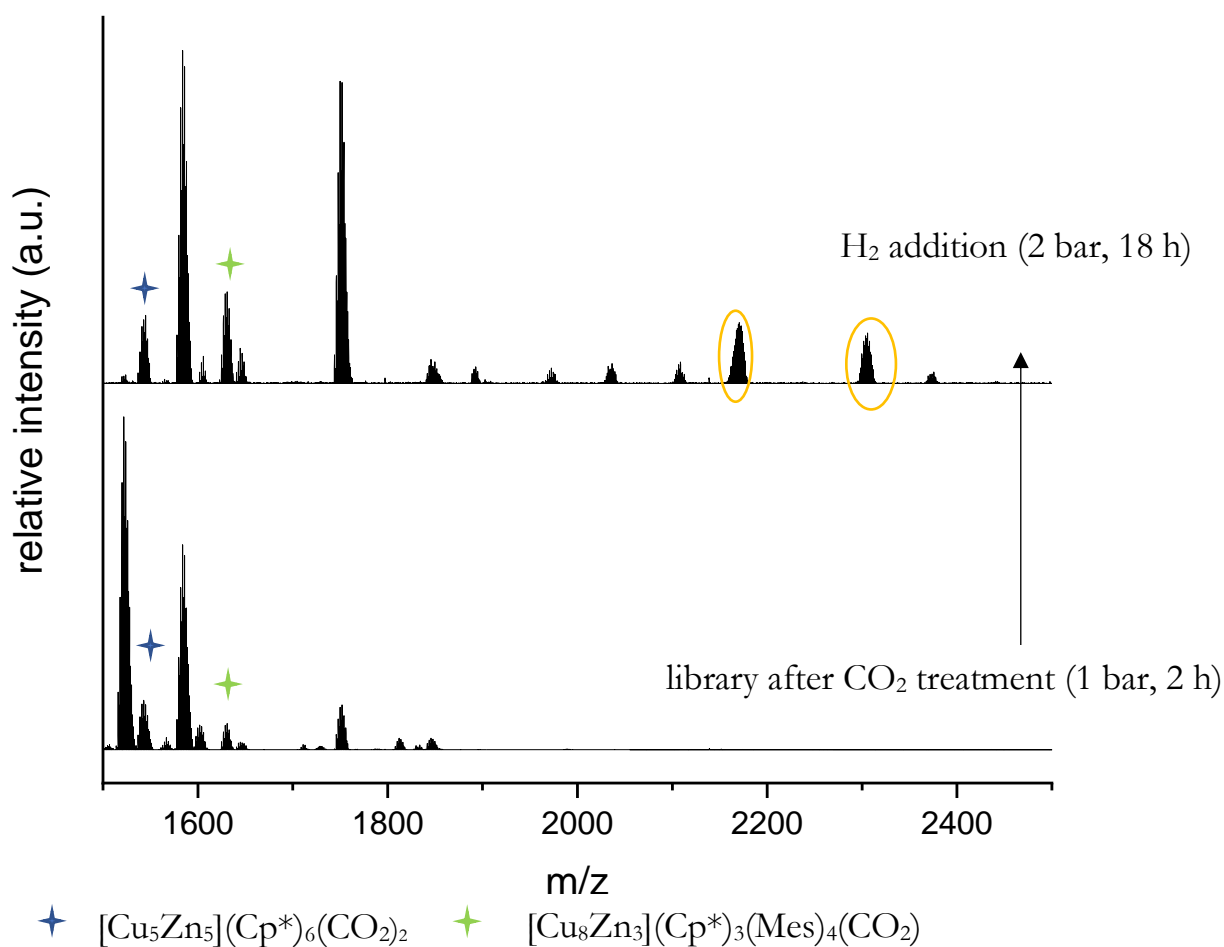
Figure 64
LIFDI-MS spectra of the Cu/Zn library (Cu:Zn = 1:1.5) after CO$_2$ treatment (lower trace) and after subsequent CO$_2$ + H$_2$ treatment (upper trace). The two newly formed species are marked by a yellow ellipsoid.

The reaction solutions were also investigated by *in situ* FT-IR spectroscopy (see Figure S71). Two new absorption bands are detected at wavenumbers of 1380 cm^{-1} and 1327 cm^{-1}, respectively. According to literature data, these bands might be associated to the C-H in plane bending / COO rocking, the C-O symmetric stretching vibration, respectively, of Cu-formate units.[231-232] Noteworthy, the C-O symmetric stretching vibration of Zn-bound formate is reported at higher wavenumbers (1366 cm^{-1}), hinting towards the presence of Cu bound formate in the reaction solutions.[233] However, for a clear assignment of the bands, theoretical calculations of the adduct species are necessary.
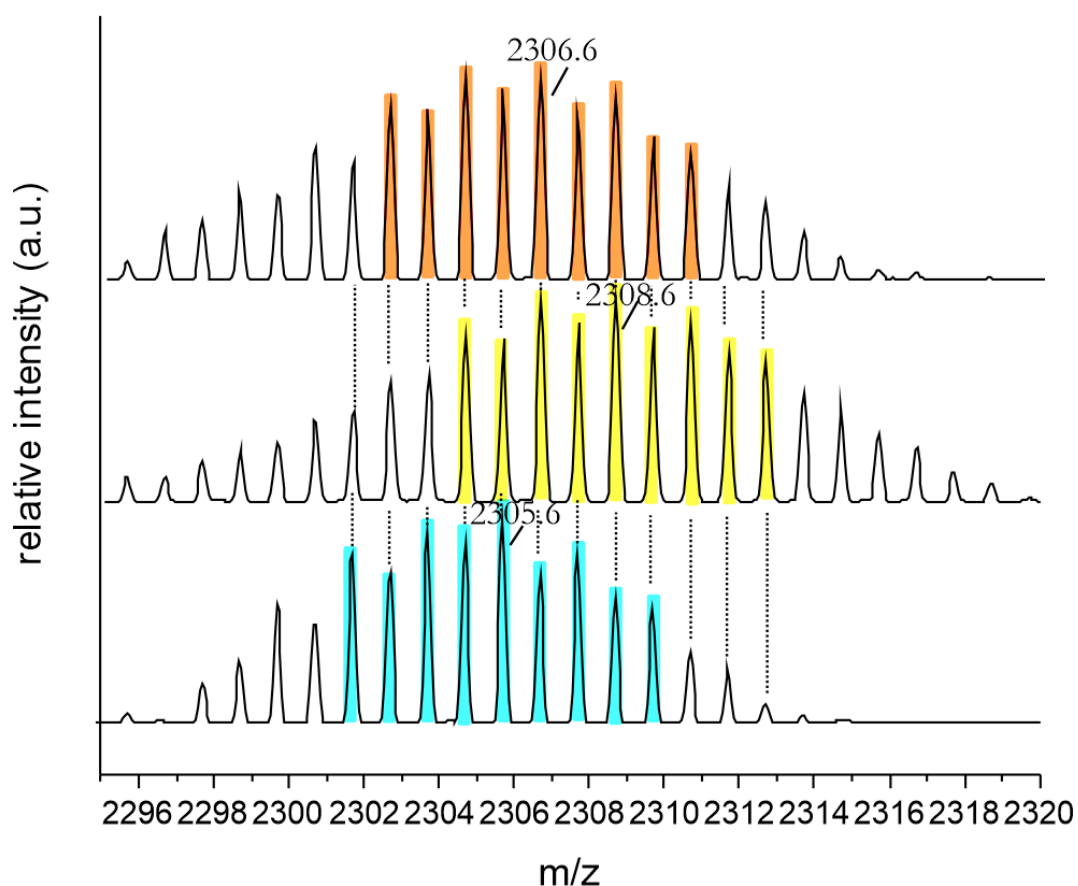
Figure 65
Visualization of the $\Delta m/z$ shift of 3 in the isotopic pattern of $[Cu_{11}Zn_6](Cp^*)_8(^{13}CO_2)_2(H^{13}CO_2)$ (yellow, middle trace) and of 1 in the isotopic pattern of $[Cu_{11}Zn_6](Cp^*)_8(CO_2)_2(DCO_2)$ (orange, upper trace) in comparison to the isotopic pattern of of $[Cu_{11}Zn_6](Cp^*)_8(CO_2)_2(HCO_2)$ (blue, bottom). In the middle and uppermost spectrum, a better experimental spectral resolution was achieved leading to broader mass envelopes. The correctness of assignment was verified by a computerized software written by Dr. C. Gemel.

Noteworthy, the formation of formate species is well in line with *in situ* FT-IR studies on solid state Cu/ZnO, Cu/SiO$_2$ and Cu/Al$_2$O$_3$ surfaces exposed to CO$_2$/H$_2$ mixtures.[198, 230]

3.2.3 Exploring Cu/Al cluster growth and reactivity

Main parts of the following results were published as an article in the journal Chemical Science. [Reprinted (adapted) with permission from M. Schütz, C. Gemel, M. Muhr, C. Jandl, S. Kahlal, J. Y. Saillard and R. A. Fischer, Exploring Cu/Al cluster growth and reactivity: From embryonic building blocks to intermetalloid, open-shell superatoms. Chem. Sci. 2021, 12, 6588-6599. Copyright 2021. Published by the Royal Society of Chemistry. Link: https://pubs.rsc.org/en/content/articlehtml/2021/sc/d1sc00268f.] Some of the results were also published in the journal Dalton Transactions. [Reproduced (adapted) from M. Muhr, P. Heiss, M. Schütz, C. Gemel, M. H. Linden, H. B. Linden and R. A. Fischer, Enabling LIFDI-MS measurements of highly air sensitive organometallic compounds: A combined MS/glovebox technique Dalton Trans. 2021, 50, 9031-9036 with permission from the Royal Society of Chemistry. Copyright 2021. Published by the Royal Society of Chemistry. Link: https://pubs.rsc.org/en/content/articlelanding/2021/dt/d1dt00978h.]

Similar to the Cu/Zn cluster system, the isolation of intermetalloid Cu/Al clusters is a sophisticated task, especially for larger nuclearities. Whereas the the hydrido M_{12} cluster $[H_4Cu_6Al_6](Cp^*)_6$ is accessible in good yield from $[H_6Cu_6](PPh_3)_6$ and $AlCp^*$, the large Mackay-type cluster $[Cu_{43}Al_{12}](Cp^*)_{12}$ can only be isolated in very small yield after a complicated work-up procedure from the reaction between [CuMes] and $AlCp^*$. Initially, no information about intermediates, which certainly exist on the way to this fascinating molecule, nor about mechanisms of its formation were available. This dissertation was aimed to shine a light into the dark reaction solutions of the [CuMes] / $AlCp^*$ system. High resolution *in situ* LIFDI-MS analysis was used in combination with *in situ* ^{1}H-NMR spectroscopy to identify intermediates, to unambiguously assign compositions and to assess reactivity patterns of specific clusters with small molecules (see also methodical part and Figures 35, 44).

Specifically, the "embryonic clusters" $[Cu_2Al](Cp^*)_3$ (**9**) and $[Cu_4Al_4](Cp^*)_5Mes$ (**11**) were isolated and fully characterized, along with a detailed bonding analysis on the DFT level of theory. Systematic investigation of cluster growth reactions involving these two building blocks and taking advantage of the direct feedback loop of mass spectrometry of reaction solutions into the parameter optimization of the cluster growth experiment led to the discovery of the M_{13}/M_{14} cluster mixture $[Cu_7Al_6](Cp^*)_6$ (**1**) $[HCu_7Al_6](Cp^*)_6$ (**1$_H$**) and $[Cu_8Al_6](Cp^*)_6$ (**2**) (see Scheme 17). Although these three clusters could not be separated from each other, and are accessible as mixtures only, the mass spectrometric approach allows for detailed insight into their reactivity, *e.g.* C-H and Si-H activation, as a function of the electronic structure (open *vs.* closed shell).

3. Results and Discussion
3.2. Chemical part: Synthesis characterization, reactivity

The chapter is organized in the following way: First, the principles of organometallic Cu/Al cluster synthesis and mechanistic findings are described. Second, the analytic characterization of compounds **1**, **1$_H$**, **2**, **9** and **11** is described in comparison to the already reported Cu/Al clusters and in relation to Cu/Al intermetallic solid-state phases. Along with the crystallographic information, the electronic structure of the clusters, *i.e.* bonding analysis on the DFT level of theory, is discussed which leads to the fourth and final section, which deals with the consequences for chemical reactivity.
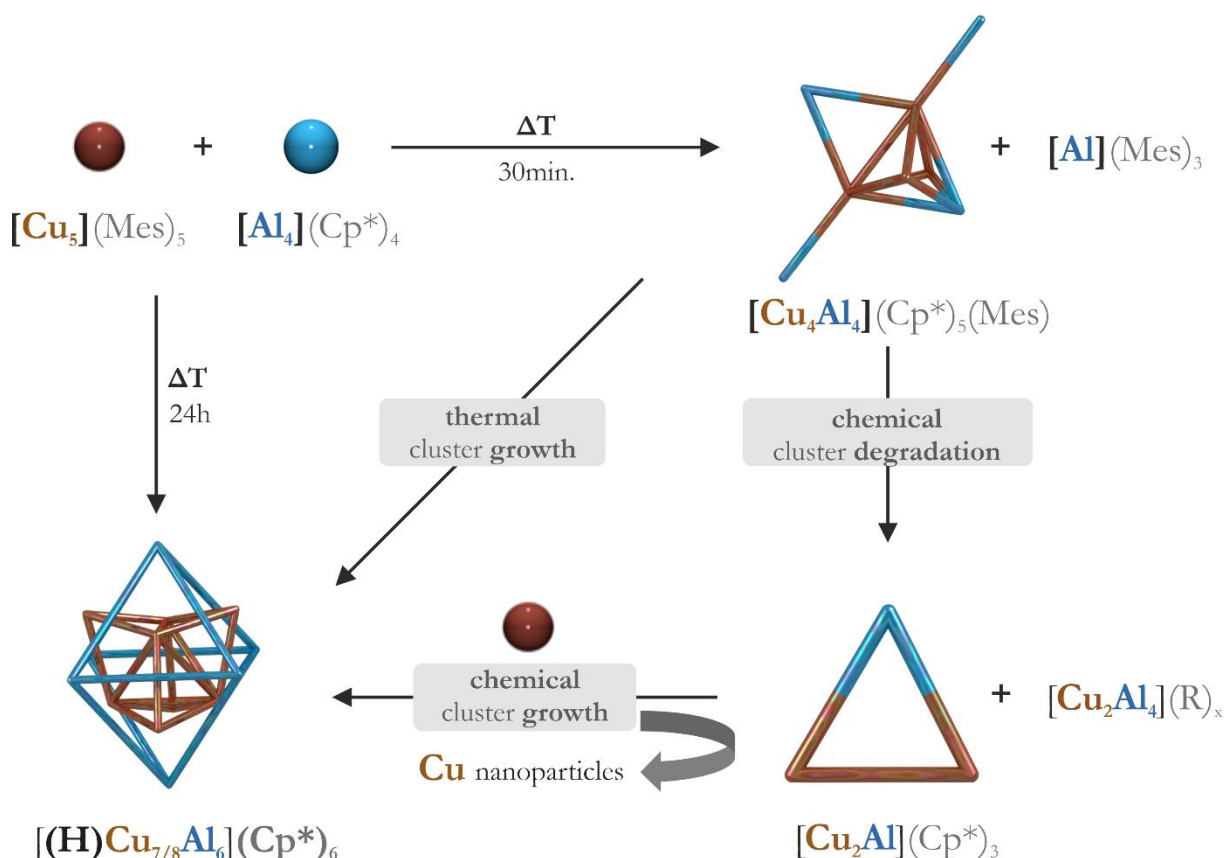
Scheme 17
Schematic representation of synthetic pathways to the new Cu/Al clusters [Cu$_4$Al$_4$](Cp)$_5$(Mes) (**11**), [Cu$_2$Al](Cp*)$_3$ (**9**), and the inseparable mixture of [HCu$_7$Al$_6$](Cp*)$_6$ (**1$_H$**), [Cu$_7$Al$_6$](Cp*)$_6$ (**1**), [Cu$_8$Al$_6$](Cp*)$_6$ (**2**). Cu atoms are illustrated in orange, Al atoms in blue, respectively. R denotes an organic ligand (Cp*, Mes, hexyne). Upon heating, cluster **11** can be transformed into a mixture of **1**, **1$_H$** and **2**. This mixture can be selectively obtained by a sequence of cluster degradation and growth reactions with additives involving the trimetallic cluster intermediate **9**. [Scheme created with the help of Dr. Christian Gemel.]*

3.2.3.1 Mechanistic investigations

Formation mechanism of [Cu₄Al₄](Cp*)₅(Mes) (11)

Heating a solution of [CuMes] with 1.32 eq. of AlCp* in toluene to 75 °C leads to a deep green solution within a few minutes. The reaction progress as monitored by *in situ* ^{1}H-NMR spectroscopy (see Figure S72) indicates rapid formation [Cu₄Al₄](Cp*)₅(Mes) (**11**) as the major reaction product with three Cp* signals (integral ratio 2:2:1) as well as one metal coordinated mesityl unit. Also the side products AlMes₃[234] and Mes₂AlCp* can be identified in these *in situ* ^{1}H-NMR spectra. Time dependent ^{1}H-NMR spectra indicate the ratio of **11** to be the highest after about 30-80 minutes. As shown in Figure S72, only small signals of other Cp* containing species are present at that time, which become more prominent at increased reaction times.

Observation of Mes₂AlCp* and AlMes₃ as side products in the formation of **11** is indicative of partial reduction of Cu(I) to Cu(0) by AlCp* accompanied by ligand transfer reactions between Al and Cu. Notably, 1.5 eq. of AlMes₃ and Mes₂AlCp* are formed per molecule of the [Cu₄Al₄](Cp*)₅(Mes) cluster **11** according to *in situ* ^{1}H-NMR (see Figure S72). A clear stoichiometric reaction would only include formation of one equivalent AlMes₃, however, it is supposed that the thermal instability of **11** (*vide infra*) leads to a competition between its formation (including formation of AlMes₃) and its decay (including formation of Mes₂AlCp*). **11** can be interpreted as an aggregate of redox-intermediates occurring in the reduction of Cu(I) and its subsequent coordination by AlCp*. We assume similar mechanisms to occur in the early stages of the synthesis of [Cu₄₃Al₁₂](Cp*)₁₂, as Mes₂AlCp* was also identified as a side product this reaction.[93]

Monitoring the reaction by LIFDI-MS analysis (see Figure S73) reveals a variety of intermetallic CuAl clusters with the exact composition being dependent on the reaction time (*vide infra*). However, the molecular ion peak of **11** cannot be detected at all, obviously **11** cannot be ionized without destruction by the LIFDI technique. Also, LIFDI-MS analysis of isolated single crystals of **11** did not yield a detectable molecular ion signal.

3. Results and Discussion
3.2. Chemical part: Synthesis characterization, reactivity

Targeted cluster degradation from [Cu₄Al₄](Cp*)₅(Mes) (11) to [Cu₂Al](Cp*)₃ (9)

The observation of triangular [Cu₂Al](Cp*)₃ (**9**) in thermal degradation of isolated [Cu₄Al₄](Cp*)₅(Mes) (**11**) (*vide infra*) was a motivation to search for a clean synthetic access to this small ("embryonic") building unit of Cu/Al clusters. As alkynes are known to stabilize Cu(I) centers and small Cu clusters[235-236], 3-hexyne was chosen from the organometallic "tool-box" as a degradation agent for [Cu₄Al₄](Cp*)₅(Mes) **11** to access smaller cluster units. Notably, alkynes are known to react with organometallic Al compounds to yield cycloaddition products.[237] When a toluene solution of **11** is treated with an excess of 3-hexyne (20 °C), a color change from deep-green to orange-brown is observed within a few minutes. The cluster degradation reaction from [Cu₄Al₄](Cp*)₅(Mes) (**11**) to [Cu₂Al](Cp*)₃ (**9**) is accompanied by consumption of four equivalents 3-hexyne per molecule of **11** as identified by *in situ* ^{1}H-NMR spectroscopy (see Figure S74). After a total reaction time of four days at room-temperature, **9** is clearly identified as main product by ^{1}H-NMR beside a variety of hexyne- and mesitylene containing side-products. LIFDI-MS analysis of the reaction solution reveals [Cu₂Al₄](Cp*)₃(Mes)(Hex)₂ (Hex = hexyne = C_6H_{10}) to be the main side product of the reaction (see Figure S75 and Table S7). However, to our surprise, no experimental evidence for the occurrence of cycloaddition products of AlCp* with 3-hexyne was gained.

The presence of [Cu₂Al₄](Cp*)₃(Mes)(Hex)₂ as main side product in the synthesis of **9** (*vide supra*) points towards a cluster degradation mechanism in which 3-hexyne extrudes CuCp* moieties from **11** by stabilizing the electron-deficient, low valent Cu(0) centers through coordination. A detailed analysis of the LIFDI-MS spectra of the reaction reveals a variety of other side products formed (see Table S7). Insight into the Cu and Al fate during the reaction can be gained by grouping the reaction products according to their Cu:Al ratio. Whereas Cu gets mainly incorporated into **9** and some Cu-rich clusters (*e.g.* [Cu₇/₈Al₆](Cp*)₆ (**1/2**) among others), the Al stoichiometry of the reaction is balanced by formation [Cu₂Al₄](Cp*)₃(Mes)(Hex)₂ and several other Al-rich clusters and Al-containing coordination compounds.

Thermal treatment of the [Cu₄Al₄](Cp*)₅(Mes) cluster 11 to yield the [(H)Cu₇/₈Al₆](Cp*)₆ clusters 1, 1_H and 2

When a solution of [Cu₄Al₄](Cp*)₅(Mes) is heated to 75 °C, *in situ* ^{1}H-NMR and LIFDI-MS analysis reveal initial formation of [Cu₂Al](Cp*)₃ (**9**), as well as of Mes₂AlCp* (see Supporting Information, Figure S76, S77). Further heating leads to consumption of **11** and rather selective formation of **1**, **1_H** and **2** as indicated by *in situ*

152

mass spectrometry (Figure S77). Obviously, the triangular cluster **9**, which can be considered as smallest building block of Cu/Al clusters is indeed an intermediate in cluster growth reactions from **11** to **1/2**. Interestingly, pentamethylfulvene ($C_{10}H_{14}$) is observed by *in situ* ^{1}H-NMR spectroscopy, pointing towards an intermolecular C-H bond activation of Cp* as the hydride source for $[HCu_7Al_6](Cp^*)_6$ (**1$_H$**). When *in situ* generated solutions of **11** are subjected to thermal treatment at 75 °C in contrast of using pure **11**, different results are obtained (see Figures S72, S73). Interestingly, ^{1}H-NMR and LIFDI-MS analysis reveal neither formation of **9** nor fulvene, but a much broader variety of Cu/Al clusters after prolonged heating times. Obviously, the presence of AlMes₃, which otherwise is removed during the workup of **11**, influences the course of the reaction, most reasonably by promoting ligand exchange reactions, *i.e.* by serving as a "ligand reservoir" for Mes ligands and as an acceptor for Cp* ligands to enable formation of the apparently very stable half-sandwich Cp*AlMes₂.

The [Cu₂Al](Cp)₃ triangular cluster 9 as a building block*

In contrast to the labile $[Cu_4Al_4](Cp^*)_5(Mes)$ cluster **11**, the triangular $[Cu_2Al](Cp^*)_3$ **9** is rather temperature-stable and can be heated up to 80 °C for several hours. The $[Cu_8Al_6](Cp^*)_6$ cluster **2** is formed in trace amounts only, as indicated by ^{1}H-NMR as well as mass spectrometry.

[CuMes] acts as a useful reagent for cluster growth. When **9** is treated with 1.2 equivalents of [CuMes], formation of Mes₂AlCp* and AlMes₃ is observed *in situ* ^{1}H-NMR experiments together with HCp*, pentamethylfulvene and decamethyl-1,1´-dihydrofulvalene (see Figure S78) as well as some remaining **9**. Obviously, the addition of [CuMes] to **9** leads to "abstraction" of AlCp*, reduction of Cu(I) units to Cu(0) and oxidation of Al(I) to Al(III) to yield Mes₂AlCp* as byproduct, thus increasing the amount of Cu(0) and decreasing at the same time the amount of stabilizing AlCp* in the system. Oxidation of some of the Cp* ligands also seems to play a role in Cu(I) reduction. The $[Cu_2Al](Cp^*)_3$ species **9** acts as donator of the Mes deprotection agent for [CuMes] and as a source of AlCp* as capping agent during the induced [Cu$_N$] core growth. Consequently, addition of two or more equivalents of [CuMes] results in rapid formation of a metallic precipitate upon heating, since all available AlCp* in the system is then consumed.

LIFDI-MS of the reaction with exactly 1.20 eq. of [CuMes] with respect to $[Cu_2Al](Cp^*)_3$ (**9**) shows $[Cu_8Al_6](Cp^*)_6$ (**2**) as the only present species beside some unreacted **9** (see Figure S79). This result was confirmed by SC-XRD analysis of single

crystals showing a pure [Cu_8] core of the cluster without ill-occupied vertices (see Table S6 for crystallographic information).

The fate of the stoichiometrically missing Cu in this reaction (see Scheme 17), can be elucidated by TEM analysis on evaporated reaction solutions revealing the presence of larger Cu nanoparticles (5 nm) (see Figure S84, left). However, obtaining a reliable mass or molar balance n(Cu) and n(Al) is difficult because of the low quantities of materials used. A balanced equation for the reaction can thus not be presented, so far. Nevertheless, **9** is therefore clearly an embryonic building block for the formation of larger clusters. Due to its inherent Cu:Al stoichiometry, exact tuning of the amount of Cu(I) added is necessary for the generation of larger Cu/Al clusters.

Alternative access to the cluster mixture [HCu$_{7/8}$Al$_6$](Cp*)$_6$ 1$_H$/2

An alternative access to the cluster mixture **1$_H$/2** was identified by reacting the trinuclear copper hydride precursor [H_3Cu_3](dppz)$_3$ with AlCp* (dppbz = 1.2-bis(diphenylphosphino)-benzene). Upon cooling the filtered reaction solution to -30 °C, single crystals of **1$_H$/2** suitable for SC-XRD were isolated in form of black needles in addition to free dppbz ligand and other unidentified and inseparable side-products. Reaction of the corresponding deuteride precursor, [D_3Cu_3](dppz)$_3$, leads to formation of **1$_D$** as clearly identified by *in-situ* LIFDI-MS analysis (see Figure S80). Notably, from the related reaction of [H_6Cu_6](PPh$_3$)$_6$ with AlCp*, the smaller cluster [$H_4Cu_6Al_6$](Cp*)$_6$ was isolated.[92] Obviously, reductive elimination of dihydrogen, H_2, leads to the formation of [H_xCu_y] aggregates and the subsequent trapping by AlCp* yields **1$_H$/2**. The reactions are summarized in Scheme 18.

3. Results and Discussion

3.2. Chemical part: Synthesis characterization, reactivity

a)

$$[H_3Cu_3](dppbz)_3 \xrightarrow[75\,°C,\ \textbf{3 h}]{+\ 2.45\ eq.\ AlCp^*,\ toluene,} [HCu_7Al_6](Cp^*)_6 + [Cu_8Al_6](Cp^*)_6 + dppbz$$

$$\mathbf{1_H} \qquad\qquad \mathbf{2}$$

2eq. dppbz, toluene, RT, **10 min**

$$[H_6Cu_6](PPh_3)_6 \xrightarrow[75\,°C,\ \textbf{18 h}]{+\ 6\ eq.\ AlCp^*,\ toluene,} [H_4Cu_6Al_6](Cp^*)_6$$

b)

$$[H_6Cu_6](PPh_3)_6 + 10\ mol\ \%\ dppbz \xrightarrow{fast} [H_3Cu_3](dppbz)_3 \xrightarrow{2.45\ eq.\ AlCp^*} \mathbf{1_H}\ +\ \mathbf{2}$$
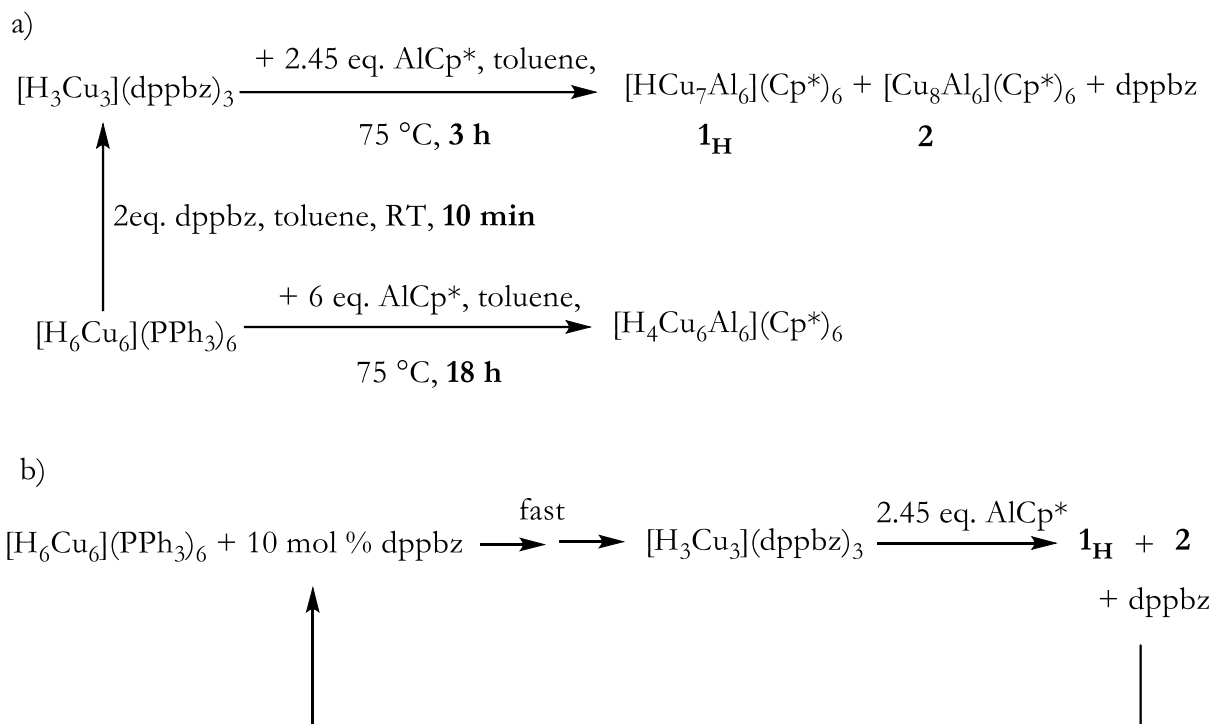
$$+\ dppbz$$

Scheme 18

a) Synthesis of $\mathbf{1_H}/\mathbf{2}$ out of $[H_3Cu_3](dppz)_3$ and $AlCp^*$ and of $[H_4Cu_6Al_6](Cp^*)_6$ out of $[H_6Cu_6](PPh_3)_6$ and $AlCp^*$. $[H_6Cu_6](PPh_3)_6$ can rapidly be converted to $[H_3Cu_3](dppz)_3$ upon exposure to the dppbz ligand. b) Catalytic amounts of dppbz ligand in the reaction between $[H_6Cu_6](PPh_3)_6$ and $AlCp^*$ lead to formation of $\mathbf{1_H}/\mathbf{2}$ instead of $[H_4Cu_6Al_6](Cp^*)_6$.

The influence of the phosphine (PPh_3 vs. dppbz) heteroatom ligand used on the $[Cu_aAl_b]$ cluster size obtained is however unclear so far and will be subject of further research. It is noted that according to *in situ* LIFDI-MS analysis, the use of catalytic amounts (10 mol%) of dppbz ligand in the reaction between $[H_6Cu_6](PPh_3)_6$ and $AlCp^*$ also selectively leads to the cluster species $\mathbf{1_H}/\mathbf{2}$ (see also experimental part). This is due to rapid conversion of $[H_6Cu_6](PPh_3)_6$ into $[H_3Cu_3](dppz)_3$ upon exposure to the chelate ligand dppbz (see Scheme 18 a)). The reaction from $[H_3Cu_3](dppz)_3$ with $AlCp^*$ to $\mathbf{1_H}/\mathbf{2}$ is at least 6 times faster than the reaction from $[H_6Cu_6](PPh_3)_6$ with $AlCp^*$ to $[H_4Cu_6Al_6](Cp^*)_6$ (according to *in situ* ^{1}H-NMR analysis). Reacting $[H_6Cu_6](PPh_3)_6$ with 10 mol % dppbz ligand in the presence of $AlCp^*$ therefore leads to rapid conversion of 10 mol % of $[H_6Cu_6](PPh_3)_6$ into $[H_3Cu_3](dppz)_3$, which itself reacts with $AlCp^*$ to form $\mathbf{1_H}/\mathbf{2}$ releasing again the dppbz ligand. The dppbz ligand again converts $[H_6Cu_6](PPh_3)_6$ to $[H_3Cu_3](dppz)_3$ closing the catalytic cycle (see Scheme 18 b)). Importantly, the Cu:Al stoichiometry turned out to have rather no effect at all in these reactions, highlighting the role of the phosphine ligands. It is noted that the selectivity of the presented catalytic reaction decreases rapidly upon preparative scale-up of the reaction. This is supposed to be due to different kinetics at higher concentrations (conducting the reaction in a preparative manner at very low concentrations is practically not feasible).

155

3. Results and Discussion
3.2. Chemical part: Synthesis characterization, reactivity

Interestingly, a similar effect of phosphane additives on the selectivity of cluster synthesis was also observed for the related Au/Al system (see chapter 3.3.3).

Size focusing to the cluster mixture 1/2 and selective synthesis of cluster 2.

Size-focusing of the mixture of the discussed interrelated Cu/Al clusters in favor of the cluster pair $[Cu_7Al_6](Cp^*)_6$ (**1**) and $[Cu_8Al_6](Cp^*)_6$ (**2**) was possible by starting from AlCp* and [CuMes] (molar ratio 1 : 0.28) at 75°C, followed after 4 h by addition of another 0.54 eq. of CuMes and further heating to 75 °C for 18 h (Scheme 17; overall Cu:Al stoichiometry applied 1:1.22). If the reaction of the organometallic sources of Cu and Al is conducted in precisely this way, the product clusters **1** and **2** are the major components in the equilibrated reaction mixture then observed in LIFDI-MS analysis (see Figure 47, Figure S81 and methodical part).

The reaction is accompanied by formation of Mes_2AlCp^* and $AlMes_3$ as identified by *in situ* ^{1}H-NMR (Figure S82). Notably, compounds **9** and **11** are observed as transient intermediates in the reaction by ^{1}H-NMR analysis before and after addition of the second portion of [CuMes], respectively. This underlines their role as building blocks in cluster growth reactions. It is noted that the use of slightly less [CuMes] in this size focused synthesis of **1/2** did not significantly change the molar ratio of **1:2** according to NMR and LIFDI-MS analysis. In these experiments, however, a mixture of **1** and **2** together with the hydridic species **1$_H$** is detected.

Based on these results a selective synthesis of **2** was developed by subjecting the primarily obtained cluster mixture **1/2** to different stoichiometric amounts of [CuMes]. Reaction with 5 molar eq. of [CuMes] leads to a complete consumption of $[Cu_7Al_6](Cp)_6$ as identified by *in situ* LIFDI-MS analysis as well as ^{1}H-NMR spectroscopy (vanishing of the corresponding paramagnetic signal even after short reaction times at room-temperature, see Figure S83 and Figure 43). Again, the reaction is accompanied by formation of Mes_2AlCp^* and $AlMes_3$.

Quantitative analysis of the ^{1}H-NMR spectra indicates increasing quantities of **2** being fully consistent with the LIFDI-MS spectra showing **2** as the only intense signal after 5 h reaction time. Indeed, single crystals of **2** were obtained from the filtered reaction solution in very small yield upon cooling to -30 °C. TEM images of evaporated reaction solutions again show the presence of smaller (5 nm) and larger Cu nano particles (ca. 50 nm) (see Figure S84, right). Both clusters **1** and **2** are expected to be susceptible to cluster growth reactions with [CuMes] and this may lead to larger clusters in the reaction solution which cannot any more be observed

by the LIFDI-MS instrumentation at this point of methodological development (see outlook of the methodical part for possible strategies how to resolve that issue).

3.2.3.2 Characterization of isolated species

Synthesis and characterization of [Cu₄Al₄](Cp*)₅(Mes) (11)

Synthesis

Heating of [CuMes] with AlCp* (1:1.3) in toluene to 75 °C for 30 minutes leads to dark green solutions and formation of compound **11** (see Scheme 19). Dark-green single crystals suitable for SC-XRD of **11** are obtained by cooling the filtered reaction solutions to -30 °C for several days. The refined molecular structure in the solid state is shown in Figure 66. Preparative access to pure **11** is possible by washing the crystallizate with small amounts of *n*-hexane and recrystallization from a minimum of toluene. Notably, the yield of the synthesis is low (5 %) due to very similar solubility properties of **11** and side-compounds, requiring several work-up steps. Compound **11** is highly air- and moisture sensitive but can be stored under argon-atmosphere at room-temperature without any signs of decomposition.
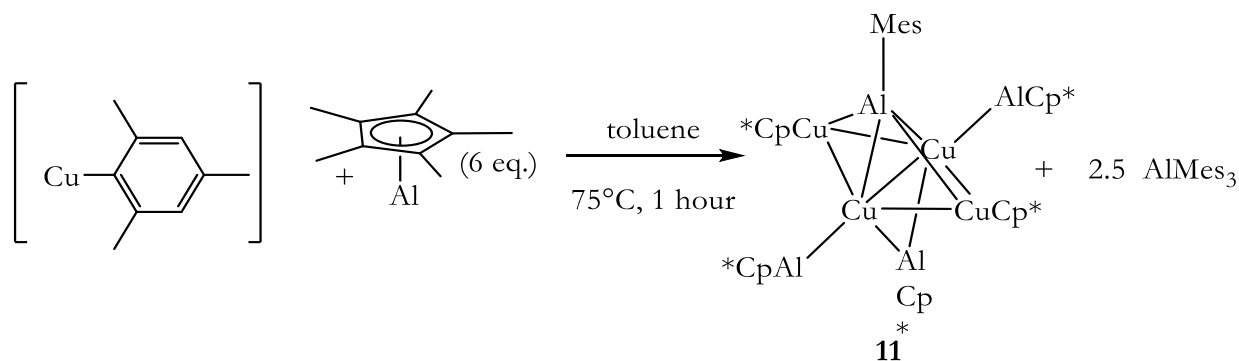
Scheme 19
Synthesis of [Cu₄Al₄](Cp)₅(Mes) (**11**).*

Crystallographic characterization of [Cu₄Al₄](Cp*)₅(Mes) (11)
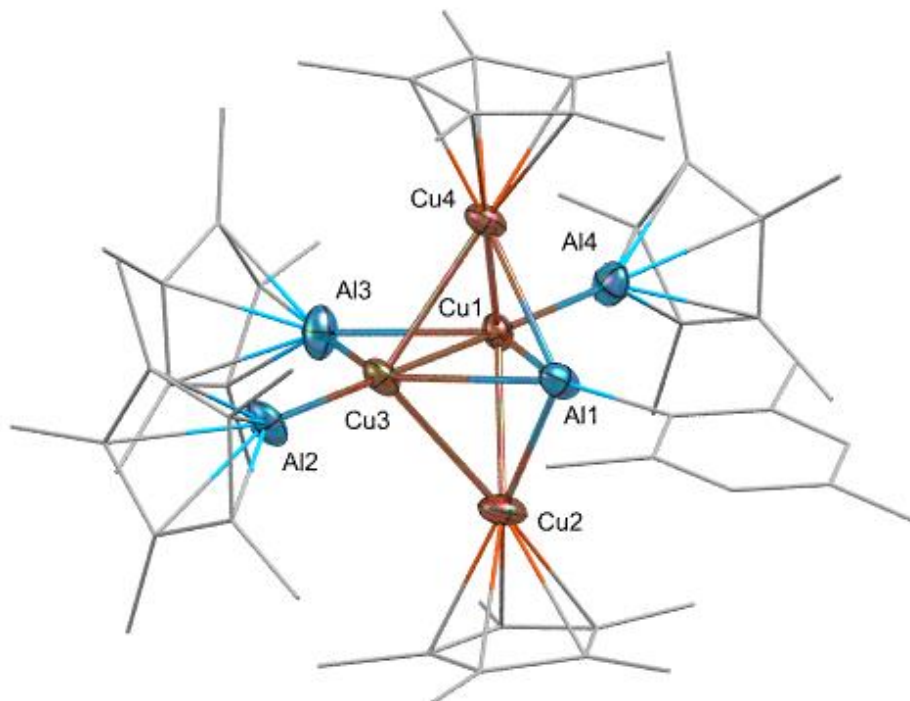
Figure 66
*Molecular structure of **11** in the solid state as determined by SC-XRD. Thermal ellipsoids are shown at the 50 % probability level, hydrogen atoms, co-crystallized solvent molecules and disordered groups are omitted for clarity and ligands are simplified as wireframes. Selected interatomic bond distances [Å] and angles [°]: Cu2-Cu3: 2.5335(13), Cu1-Cu2: 2.5441(2), Cu3-Al2: 2.3103(14), Cu1-Al4: 2.3190(14), Cu4-Al1: 2.3519(15) Å; Cu1-Al1: 2.4386(14) Å; Cu1-Al3: 2.4277(16) Å; Cu3-Al3: 2.4261(16) Å; Al3-Cp*centroid: 1.906, Al4-Cp*centroid: 1.958, Al2-Cp*centroid: 1.958, Cu4-Cp*centroid: 1.922, Cu2- Cp*centroid: 1.900, Al1-Cmesitylene: 1.966(5), Cu1-Cu2-Cu4: 106.16(4), Cu2-Cu3-Cu4: 107.20(4), Al2-Cu3-Cu1: 179.25(8), Al4-Cu1-Cu3: 178.89(7); Cu1-Al1-Cu3: 57.75(3).*

11 crystallizes in the monoclinic space group *P21/n* with four molecules per unit cell as well as three heavily disordered toluene molecules per asymmetric unit. Detailed crystallographic information can be found in Table S6. **11** consists of a [Cu₄(Cu1-Cu4)Al(Al1)] trigonal bipyramid, whereby the central Cu₂ unit is additionally coordinated by two "terminal" AlCp* (Al2, Al4) ligands, as well as by one bridging (Al3) AlCp*. Interestingly, to the best of our knowledge, **11** is the first crystallographically characterized compound featuring an Al^{I}Mes ligand. The bonding Cu-Cu distances in **11** (mean value 2.541 Å) are within the expected range

3. Results and Discussion
3.2. Chemical part: Synthesis characterization, reactivity

for this class of compounds[92,238]. The Cu-Cu-Cu bond angles are 106.16(4)° (Cu4-Cu1-Cu2) and 107.20(4)° (Cu2-Cu3-Cu4), whereas the central triangle of the bipyramid exhibits a Cu1-Al1-Cu3 angle of 57.75(3)°. The Cu-Al1 and Cu-Al3 distances (2.3519(15) Å (Cu4-Al1); 2.4386(14) Å (Cu1-Al1); 2.4277(16) Å (Cu1-Al3); 2.4261(16) Å (Cu3-Al3)) are slightly longer than the ones of terminally bound AlCp* (2.3103(14) Å (Cu3-Al2); 2.3190(14) Å (Cu1-Al4)). In general, the Cu-Al distances are shorter than those found in $[H_3Cu_6Al_6](Cp^*)_6(PhCHN)]$ (2.4027(14) – 2.7189(14) Å)[92] or the Hume-Rothery phases $CuAl_2$ (2.587(4))[10] and Cu_9Al_4 (2.468(2) – 2.737(3) Å)[11]. The horizontal axis of **11** is close to linearity with bond angles of 179.25(8)° (Al2-Cu3-Cu1) and 178.89(7)° (Al4-Cu1-Cu3). The Al-Cp*centroid distances are well comparable to other compounds featuring coordinated AlCp* groups.[93, 239] The Cu-Cp*centroid distances in **11** are found to be 1.900 Å and 1.922 Å. The Al1-C_{Mes} bond length (1.966(5) Å) is slightly shorter than the Al-C_{Mes} bond found in the corresponding Al(III) compound $Al(Mes)_3$ (1.995(8) Å).[240] It is noted that from an alternate point of view, a [Cu4] butterfly structural motif can be distinguished in the structure of **11**, which is known from other molecular Cu cluster compounds like $[Cu_4Te_4](P^iPr)_4$[241] and $[Cu_4](PPh_3)_2(mt)_4$[242] (mt = 2-mercaptothiazoline). Interestingly, similar structural motifs can also be identified in larger Cu/Al clusters. Thus, an Al atom surrounded by four butterfly-like arranged Cu atoms is found in the molecular structure of $[H_4Cu_6Al_6](Cp^*)_6$[92], while in the large cluster $[Cu_{43}Al_{12}](Cp^*)_{12}$, AlCp* occupies positions capping Cu_3 triangular faces.[93] In view of these structural analogies, **11** can be seen as a native "building block" for larger Cu/Al aggregates.

Spectroscopic characterization of [Cu₄Al₄](Cp*)₅(Mes) (11)

The ^{1}H-NMR spectrum of **11** in toluene-d[8] (see Figure S85) is fully consistent with the molecular symmetry found in the solid state. The Cp* groups give rise to three singlets at 2.10 ppm (CuCp*, 30H), 1.97 ppm (μ^2-AlCp*, 15H) and 1.92 ppm (terminal AlCp*, 30H). The aromatic protons of the mesitylene ligand is found ar 6.90 ppm (2H), while the methyl groups split into two signals at 2.31 (3H) and 2.28 ppm (6H). The ^{13}C NMR of **11** in toluene-d[8] (see Figure S86) exhibits three signals for the Cp* methyl groups at 10.78 and 11.97 ppm (AlCp*) as well as 13.13 ppm (CuCp*). The aromatic Cp* carbon atoms are found at 115.37 and 114.45 ppm (AlCp*) as well as 103.39 ppm (CuCp*). The mesitylene ligand gives rise to four signals at 143.10 ppm, 126.79 ppm, 32.46 ppm and 25.23 ppm; obviously, two aromatic signals could not be identified due to small signal intensities. The ATR-IR spectrum (see Figure S87) shows characteristic ν_{C-H} stretching vibrations at 2910.72 and 2840 cm^{-1}, as well as ν_{C-C} vibrational modes at 1485.23 cm^{-1}, 1423.43 cm^{-1}, and 1373.99 cm^{-1}. A band characteristic for an ν_{Al-C} stretching vibration is found at 418.17 cm^{-1}, which is in very good agreement with that reported for monomeric AlCp* in the gas phase.[243] A band at 455 cm^{-1} is tentatively assigned to metal-metal

vibration within the cluster core. The elemental analysis of **11** is in good agreement with the calculated values, therefore confirming the composition and purity of the compound.

Bonding analysis of [Cu$_4$Al$_4$](Cp)$_5$(Mes) (11)*

*Bonding analysis of **11** was carried out by Prof. Saillard et al.*

A rationalization of the bonding in **11** can start in considering it as made of six building units, namely one (edge-bridging) Al(η^5-Cp*), one Al-Mes, two Cu(η^5-Cp*) and two "linear" Cu-Al(η^5-Cp*) fragments. Assuming that six electrons are used for Cp* to M bonding (M = Al, Cu) and that the Cu-Al terminal bonds are localized 2-electron bonds, then the Al(η^5-Cp*), Al-Mes, Cu(η^5-Cp*) and "linear" Cu-Al(η^5-Cp*) fragments are 2-, 2-, 0- and 1-electron donor, respectively. Therefore, one is left with 6 electrons for the bonding within the [Cu$_4$Al$_2$] inner core of **11**. The M(η^5-Cp*) (M = Al, Cu) fragments have only one σ-type hybrid orbital to participate to the bonding. The Cu-R (R = AlCp*) and Al-R (R = Mes) units have three orbitals available. One is a σ-type hybrid and two are π-type np AOs, *i.e.*, "perpendicular" to the M-R bond.[244] With such a fragment orbital manifold and looking at the [Cu$_4$Al$_2$] core as an edge-bridged [Cu$_4$Al] trigonal bipyramid, it is easy to predict that there are only two bonding combinations of the fragment frontier orbitals that can be associated with the [Cu$_4$Al] trigonal bipyramid. They are the in-phase combination of the five σ-type hybrid and the π-bonding combination on the [Cu$_2$Al] triangular base of the bipyramid, stabilized by the out-of-phase combination of the two σ-type hybrids of the CuCp* capping units. These orbitals are sketched in Scheme 20 (left side and middle). They contain four of the six cluster electrons. The remaining electron pair is associated with the 2-electron/3-center bonding between the μ_2-AlCp* fragment and the Cu-Cu edge it bridges (right side of Scheme 20). Indeed the "linear" Cu-AlCp* units have enough frontier orbitals to participate to three bonding pairs.

3. Results and Discussion
3.2. Chemical part: Synthesis characterization, reactivity
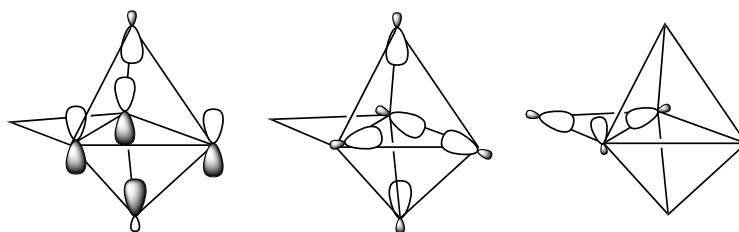
Scheme 20
Sketches of the three bonding MO containing the six electrons associated with the [Cu₄Al₂] core of
11.

This qualitative picture is supported by DFT calculations on **11** and on a simplified and symmetrized model of **11** in which all the methyl groups were replaced by hydrogens (see Figure 67). In the real cluster **11** the two "σ-type" cluster MOs of Scheme 20 somehow mix together and some supplementary mixing also occurs with other cluster MOs, in particular with those associated with the terminal Al-Cu bonds. The major computed data for **11** are gathered in Table S8. There is a good agreement between the optimized geometry and the X-ray structure. The computed ^{1}H- and ^{13}C-NMR chemical shifts match also nicely with their experimental counterparts (Figures S88, S89). From the Wiberg bond indices (WBI) one can see that the strongest Al-Cu bonds are those between Al(Mes) and the two Cu(Cp*) atoms. Cu-Cu bonding appears relatively weak (WBI$_{av}$ = 0.065). As expected, the more positively charged Cu and Al atoms are those bonded to Cp* ligands. It is of note that the Cp* ligands play a crucial role in stabilizing the structure of the very electron-deficient cluster **11**. Indeed, when the Cp*s are replaced by simple Cps in the calculation, the structure collapses during the geometry optimization process. The effect of the Cp* ligands is of double nature: Their electron-donating ability tends to satisfy as best as possible the electron demand of the cluster core, and they constitute a tight and rather rigid protecting shell around the cluster. Such a shield effect of Cp* ligands around metal cluster cores is already well documented.[88, 92-93, 245]
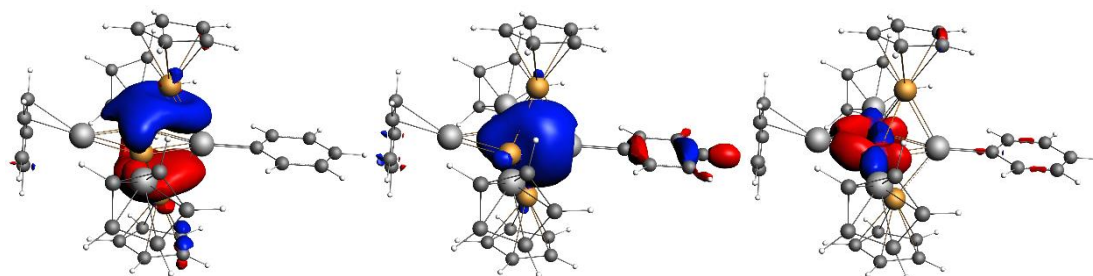
Figure 67
The three occupied Kohn-Sham orbitals containing the six metal-metal bonding electrons in the simplified model for **11**, *[Cu₄Al₄](Cp)₅(C₅H₅) (single-point calculation on a symmetrized model of C$_s$ symmetry).*

3. Results and Discussion

3.2. Chemical part: Synthesis characterization, reactivity

Synthesis and characterization of [Cu₂Al](Cp*)₃ (9)

Synthesis

When a toluene solution of **11** is treated with an excess of 3-hexyne, a color change from deep-green to orange-brown is observed within a few minutes. Cooling the filtered and diluted reaction solution after a total reaction time of four days to -30 °C for several days leads to yellow single crystals of the triangular cluster [Cu₂Al](Cp*)₃ (**9**) suitable for SC-XRD (see Scheme 21). The refined molecular structure of **9** in the solid state as determined by SC-XRD is shown in Figure 68. The composition of **9** has further been confirmed by LIFDI-MS, NMR and and elemental analysis. Preparative access to **9** is possible by treating *in situ* generated solution of **11** with an excess of 3-hexyne, followed by heating to 75 °C for 2 hours. From the obtained solutions, **9** is obtained in 14 % yield after crystallization at -30 °C, followed by washing with cold *n*-hexane. **9** is air-and moisture sensitive but can be stored at room-temperature under argon atmosphere.
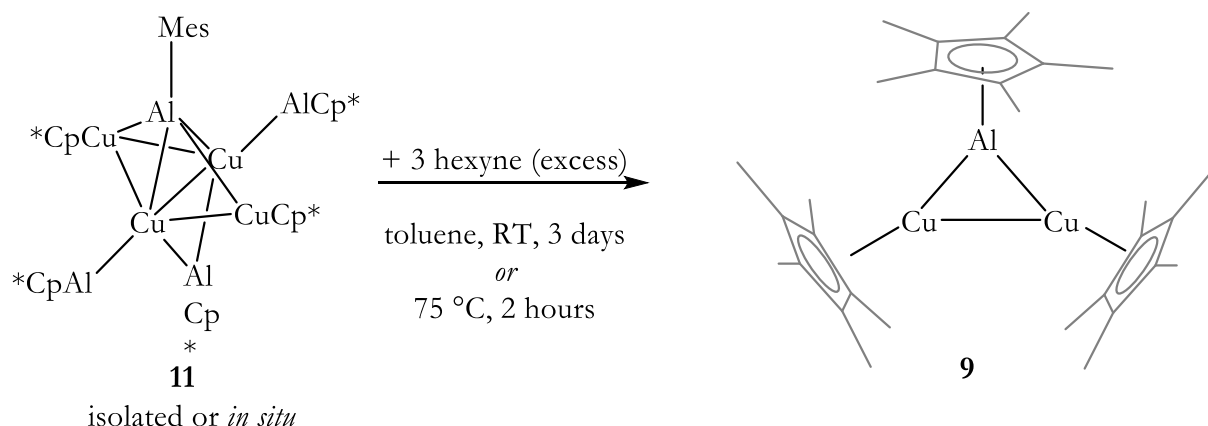
Scheme 21
*Synthesis of triangular **9** by targeted cluster degradation of **11**.*

Crystallographic characterization of [Cu₂Al](Cp*)₃ (9)

Compound **9** crystallizes in the triclinic space group *P-1* with two molecules per unit cell and is isostructural to the related isoelectronic triangular cluster [CuZn₂](Cp*)₃.[81] Detailed crystallographic information can be found in Table S6. The metal distribution within the cluster core is disordered over all three positions. Thus, all structural and geometric parameters involving the metal core are subject to some uncertainty and will therefore be discussed only on a qualitative level. The three metal

atoms span an almost equilateral triangle. The Cu1-Cu2 distance (2.265(8) Å) is significantly shorter than in other cluster compounds exhibiting Cu-Cu bonds, such as **11** (mean Cu-Cu bond distance 2.541 Å) or $[H_3Cu_6Al_6](Cp^*)_6(PhNHC)$ (mean distance 2.531 Å)[92]. Also the Cu-Cu distances within the $Cu_3Cp^*_3$ triangle in the trigonal bipyramidal cluster $[Cu_3Zn_4](Cp^*)_5$, (2.442(2)–2.446(2) Å)[88] are distinctly longer than in **11**. The two Cu-Al distances in **9** (2.314(15) Å and 2.40(2)) are comparable to those found in $[H_3Cu_6Al_6](Cp^*)_6(PhNHC)$ [92] or Hume-Rothery Cu/Al solid state structures (*vide supra*)[10-11]. The Cu-Cp*$_{centroid}$ distances in **9** (1.942 Å and 1.920 Å) are slightly longer than those in related compounds [81, 88], whereas the Al-Cp*$_{centroid}$ distance (1.933 Å) is within the range for complexes and clusters of AlCp* with transition metals.[92, 239]
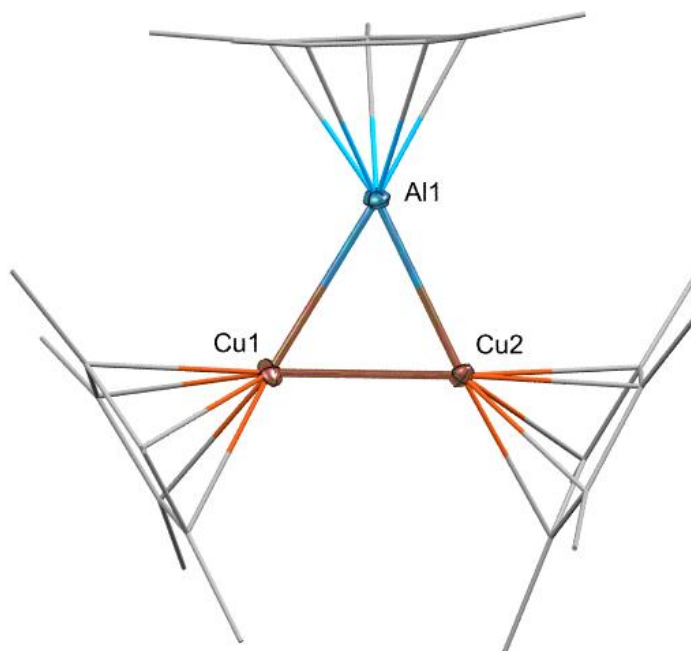
Figure 68
*Molecular structure of **9** in the solid state as determined by SC-XRD. Thermal ellipsoids are shown at the 50 % probability level, hydrogen atoms, co-crystallized solvent molecules and the disorder of the metal triangle are omitted for clarity and ligands are simplified as wireframes. Selected interatomic bond distances [Å] and angles [°]: Cu1-Cu2: 2.265(8), Cu2-Al: 2.314(15), Cu1-Al: 2.40(2), Cu1-Cp*$_{centroid}$: 1.942, Cu2-Cp*centroid: 1.920 Å, Al-Cp*$_{centroid}$: 1.933.*

3. Results and Discussion
3.2. Chemical part: Synthesis characterization, reactivity

Spectroscopic characterization of [Cu₂Al](Cp)₃ (9)*

The ^{1}H-NMR spectrum of **9** in benzene-d^6 (see Figure S90) shows two signals attributed to Cp* at 2.32 ppm (CuCp*, 30H) and 1.70 ppm (AlCp*, 15H), fully consistent with the symmetry of the molecular structure in the solid state. Accordingly, the ^{13}C-NMR (see Figure S91) exhibits signals for Cp* at 104.32 ppm / 12.55 ppm (CuCp*) and at 115.82 ppm / 9.87 ppm (AlCp*). The LIFDI-MS spectrum of **9** shows the molecular ion peak at m/z = 558.14 and with an isotopic pattern which is well consistent with the calculated pattern (see Figure S92). The ATR-IR spectrum of **9** (see Figure S93) is very similar to that of **11**, showing ν_{C-H} stretching bands at 2894.2 cm^{-1} and 2848.9 cm^{-1}, ν_{C-C} vibrations at 1421.4 cm^{-1} and 1371.9 cm^{-1} as well as a band at 418.2 cm^{-1}, which is assignable to a ν_{Al-C} stretching vibration. A very strong signal at 519.1 cm^{-1} is tentatively attributed to metal-metal vibrations of the M$_3$ triangle. Results from elemental analysis are consistent with calculated elemental composition.

Bonding analysis of [Cu₂Al](Cp)₃ (9)*

*Bonding analysis of **9** was carried out by Prof. Saillard et al.*

The DFT-optimized structure of **9** is of approximate C_{2v} symmetry, with Cu-Al bonds of 2.294 Å and 2.295 Å and a Cu-Cu bond of 2.421 Å. These values are expected to be more accurate that their X-ray counterparts (*vide supra*). The corresponding WBI values are 0.559, 0.557 and 0.199, respectively. Cu-Cu bonding in **9** is thus much stronger than in **11**. The 3-center/2-electron bonding within the triangle is made of the in-phase combination of the unique σ-type hybrid frontier orbital of the three MCp* (M = Cu, Al) constituting fragments and the two electrons provided by the AlCp* units. The corresponding Kohn-Sham orbital is the HOMO-7. It is plotted in Figure 69. Thus, **9** is isoelectronic to [Zn₂Cu](Cp*)₃,[81] or more simply, H₃$^+$. For the sake of comparison, the optimized geometry of the isoelectronic homometallic [Cu₃Cp*₃]$^{2-}$ hypothetical anion yielded Cu-Cu distances and WBI of 2.389 Å and 0.412, respectively, *i.e.* stronger Cu-Cu bonding than in **11**. The ^{1}H- (2.0 and 1.7 ppm) and ^{13}C-NMR chemical shift (Figure S94) computed for **9** are in good agreement with their experimental counterparts.
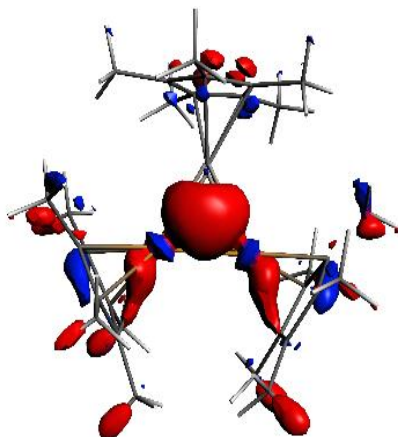
Figure 69
The 3-center bonding Kohn-Sham orbital (HOMO-7) associated with the 2-electron/3-center metal-metal bonding in 9.

Excursion: Metal aromaticity and NICS theory

The concept of aromaticity is one of the corner-stones in chemistry for the rationalization of reactivity and structure. In organic chemistry, the term aromaticity is used for planar systems with delocalized 4n + 2 valence electrons (*Hückel* rule). Other features of aromatic compounds include bond length equalization due to delocalization of the electron density, energetic stabilization due to resonance energy and specific reactivity patterns such as electrophilic substitution reactions.[246] However, for a long time, no unified criterion for quantification of aromatic properties was available. The NICS (nuclear independent chemical shift) theory, proposed by *Schleyer et al.* in 1996, has emerged as such a unified tool for the assessment of aromatic properties.[247] The proton chemical shift in NMR spectroscopy of aromatic compounds is usually abnormal, which is a consequence of the ring current of the delocalized electron density induced by an external magnetic field. However, the displacement values are relatively small (*e.g.* 7.3 ppm for CH in benzene vs. 5.6 for =CH in cyclohexene). NICS theory is based on the observation that *inside or above* aromatic systems, the chemical shift displacement in NMR spectroscopy is much more enhanced.[247] For example, the inner hydrogen atoms of annulene give a NMR signal at -3 ppm, whereas those at outer positions resonate at 9.28 ppm. Similar effects are observed for Li NMR chemical shifts in complexes of Li$^+$ with aromatic ring systems. NICS theory is based on these effects and uses *calculated, absolute magnetic shieldings* at ring centers as criterion for aromaticity and antiaromaticity. The signs of the computed values are reversed so that negative NICS values correspond to aromaticity, whereas positive NICS values denote anitaromaticity.[247] Figure 70 illustrates how the inner positions of a planar aromatic compounds experience a shielding effect due to the ring current of the delocalized

electron density, which is induced after application of an external magnetic field (*Ampère's* law).
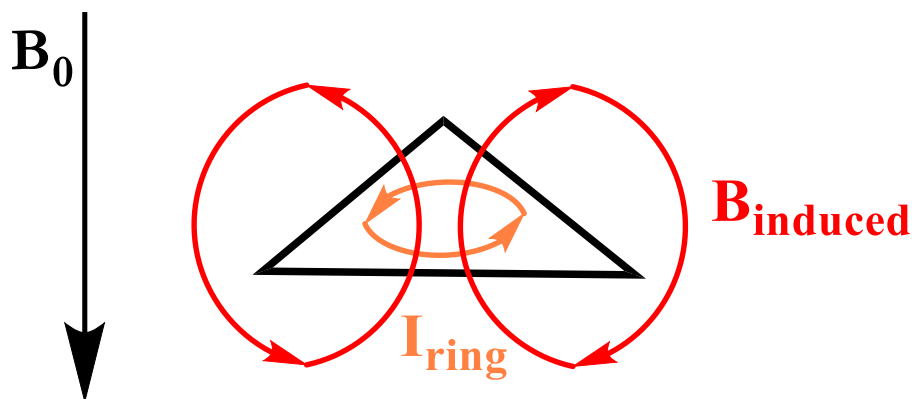
Figure 70
Schematic representation of the ring current (I_{ring}, orange arrows) induced in a triangular, aromatic molecule upon application of an external magentic field B_0. The ring current induces a magnetic field $B_{induced}$, which is of opposite direction as B_0. This induces a shielding effect of a hypothetical NMR active atom placed at the center above the triangle, which is calculated in NICS theory as a measure for aromaticity. [Own figure.]

The concept of aromaticity does not only apply to organic compounds, but also to metal containing species. First examples included metallabenzenes, such as osmabenzene, in which a carbon position of benzene is exchanged into a transition metal.[246] Later, all-metal aromatic and antiaromatic clusters have been studied by photoelectron spectroscopy in UHV, as well as by *ab initio* calculations.[248] The clusters $[MAl_4]^-$ (M = Na, Li, Cu) with a square-planar, aromatic Al_4^{2-} unit represent an example for that.[248] For metal clusters and compounds, the term "aromaticity" is more diverse than for organic compounds.[246] When only s-orbitals are involved in the delocalized orbital structure, one refers to σ-aromaticity. Likewise, the involvement of p-orbitals may result in $\sigma_{tangential/radial}$ or π-aromaticity. If d orbitals are involved, besides $\sigma_{tangential/radial}$ and $\pi_{tangential/radial}$ aromaticity, δ-aromaticity may occur. Conflicting aromaticity arises for example in systems, in which the s-orbitals consitute an aromatic subsystem, whereas *e.g.* the p-orbitals are involved in an antiaromatic subsystem. Such scenarios of conflicting aromaticity were reported for the clusters $[Li_3Al_4]^-$ and $[Li_4Al_4]$. In such cases, a NICS(r) analysis, *i.e.* determination of NICS values as a function of the radial position r at a certain molecular plane, can be helpful for analysis of the individual aromatic contributions.[249]

Triangular $[Cu_2Al](Cp^*)_3$ (**9**) integrates itself into a class of isolable, 2 e- compounds, for many of which σ-aromatic character was proven. A selection of such compounds is presented in Figure 71. In the triangular Au cluster $\{[Au_3](^iDipp)_3\}^+$, only 6s orbitals contribute to the delocalized 3 center – 2 electron bond.[87] A similiar situation is found in the Hg analogue $\{[Hg_3](dmpm)_4\}^+$ (dmpm =

3. Results and Discussion
3.2. Chemical part: Synthesis characterization, reactivity

bis(dimethylphosphino)methane).[250] Very recently, the all Cu analogue of [Cu$_2$Al](Cp*)$_3$, namely {[Cu$_3$](^{Et}CAAC)$_3$}[BF$_4$], was reported (^{Et}CAAC = cyclic(ethyl)(amino)carbene, here 1-(2,6-diisopropylphenyl)-4,4-diethyl-2,2-dimethyl-3,4-dihydro-2H-pyrrol-1-ium-5-ide).[251] As mentioned above, **9** features striking similarity to the embryonic brass clusters [CuZn$_2$](Cp*)$_3$ and [Zn$_3$](Cp*)$_3$$^+$, both of which exhibit negative NICS values of -42.3 ppm and -38.0 ppm.[81] Very interestingly, simple electron counting and *Hückels* rule (2 delocalized electrons = aromatic) allow for a very intriguing prediction of stable structures in this class of triangular metal clusters. Noteworthy, similar structures are also known with the metals Pd and Ga, namely the clusters {[Pd$_3$] (STol)$_3$(PAr$_3$)$_3$}$^+$ (Ar = C$_6$H$_4$F) and {[Ga$_3$](MesC$_6$H$_3$)$_3$}$^{2-}$.[252-253] In {[Pd$_3$](STol)$_3$(PAr$_3$)$_3$}$^+$, mainly d-orbitals contribute to aromaticity, whereas in {[Ga$_3$](MesC$_6$H$_3$)$_3$}$^{2-}$, the unhybridized p-orbitals of Ga consitute aromaticity. Both clusters can be regarded as isolelectronic to the π-aromatic cyclopropenyl cation.
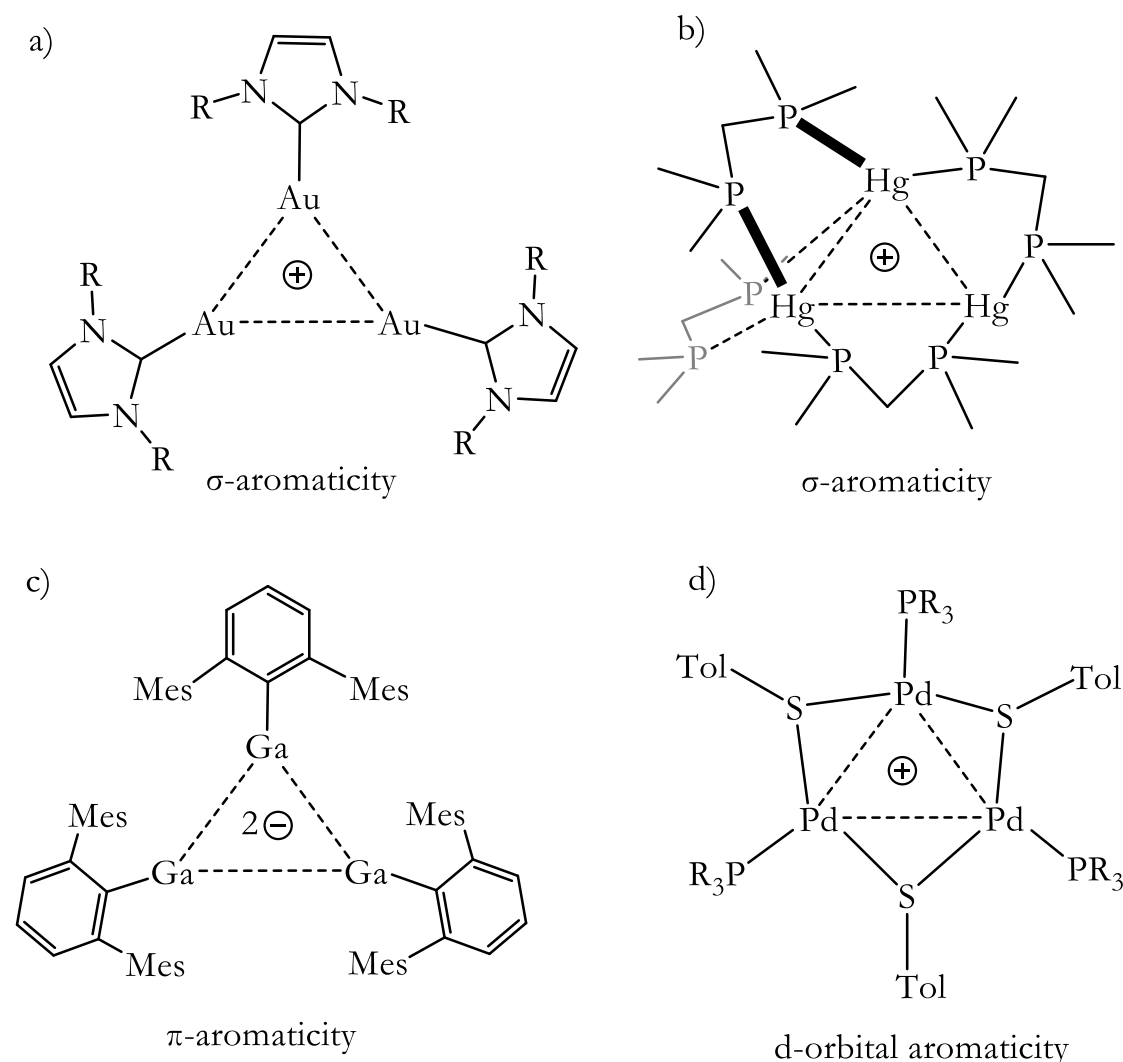
Figure 71
Examples for triangular compounds exhibiting metal-aromaticity. a) {[Au$_3$](^{i}Dipp)$_3$}$^+$ (R =2,6-diisopropylphenyl); a 2e σ-electronic compound.[87] b) {[Hg$_3$](dmpm)$_3$}$^{4+}$, the mercury analogon of a).[250] c) {[Ga$_3$](MesC$_6$H$_3$)$_3$}$^{2-}$, a 2e- π-electronic compound.[248] c) in{[Pd$_3$] (STol)$_3$(PAr$_3$)$_3$}$^+$ (R

$= C_6H_4F$), *d-orbitals contribute to the delocalized cluster orbitals involving all Pd atoms.* [249] *Note that several coordination adducts of* $\{[Pd_3] (STol)_3(PAr_3)_3\}^+$ *derivatives with Lewis acids have been reported mimicking the coordination behavior of aromatic donor ligands.* [254]

Synthesis and characterization of [Cu₇Al₆](Cp*)₆ (1), [HCu₇Al₆](Cp*)₆ (1ₕ) and [Cu₈Al₆](Cp*)₆ (2)

Synthesis

Precise adjustment of reaction conditions in the [CuMes] + AlCp* system ("size-focusing", see methodical part) leads to dark-brown reaction solutions with **1/2** as prominent peaks in LIFDI-MS analysis, besides several other signals attributed to intermetalloid Cu/Al clusters, such as $[Cu_6Al_7](Cp*)_6$ or $\{[Cu_7Al_7](Cp*)_6 - 2H\}$ (see Scheme 22 a)).

From these (unfiltered!) reaction solutions, pure **1/2** can be obtained as microcrystalline, black precipitate in 25 % yield upon cooling to -30 °C and washing with cold *n*-hexane. Unfortunately, no single-crystals of **1/2** suitable for SC-XRD could be obtained (only very small crystals of bad quality). This might be due to the exceptionally high sensitivity of the system, *e.g.* even filtration procedures under strict exclusion of air- and moisture led to (partial) decomposition of the samples. **1/2** can be stored under argon atmosphere in an isolated form at room-temperature.

The related mixture **1ₕ/2** is obtained by reaction of [Cu(dppbz)H]₃ with AlCp* at 75 °C in toluene (*vide supra*). From the filtered reaction solutions, **1ₕ/2** is obtained as dark, needle like single crystals suitable for X-ray diffraction upon cooling to -30 °C for several days (see Scheme 22 b)). The refined molecular structures in the solid state as determined by SC-XRD is shown in Figure 72. It is noted that despite lack of SC-XRD analysis of **1/2**, it can be regarded as isostructural to the closely related mixture **1ₕ/2** according to powder-Xray diffraction analysis (see Figure S95). For the mixture **1ₕ/2** no elemental/NMR/IR analysis is possible as it crystallizes as an inseparable mixture with free dppbz ligand and unidentified, hydride containing side-products. All attempts of isolating the single crystals under an optical microscope for further analysis were unsuccessful. However, the presence of the hydride in **1ₕ** is unequivocally indicated by LIFDI-MS analysis and isotopic labeling experiments starting from the corresponding Cu(I)-deuteride precursor (see Figure S80). This highlights the strength of mass-spectrometry and labeling studies for analysis of subtle differences between cluster species even in mixtures.

3. Results and Discussion

3.2. Chemical part: Synthesis characterization, reactivity

The different synthetic pathways to $1_H/1/2$ are summarized in Table 5.

Table 5
Access to different Cu/Al cluster mixtures as determined by LIFDI-MS analysis. The different reaction conditions are numbered in capital letters A-H. Detailed experimental conditions for these reactions can be found in the experimental section.

conditions	reaction	product mixture obtained	crystal structure	preparative synthesis possible
A	[Cu(dppbz)H]₃ + AlCp*	$1_H/2$	yes	no
B	[CuMes] + AlCp*	$1/2$	no	yes
C	thermal treatment **11**	$1/1_H/2$	no	no
D	**1/2** + [CuMes]	**2**	yes*	no
E	**9** + [CuMes]	**2**	yes	no
F	thermal treatment **1/2** (toluene)	$1/1_H/2$	no	no
G	**1/2** + (TMS)₃SiH	$1/1_H/2$	no	no
H	**1/2** + (TMS)₃SiD	$1/1_H/1_D/2$	no	no

*Likewise to entry F, a crystal structure of **2** was obtained for conditions H, showing a [Cu₈] kernel with fully occupied Cu positions.

3. Results and Discussion

3.2. Chemical part: Synthesis characterization, reactivity

a)

preparative access

b)

only single crystals
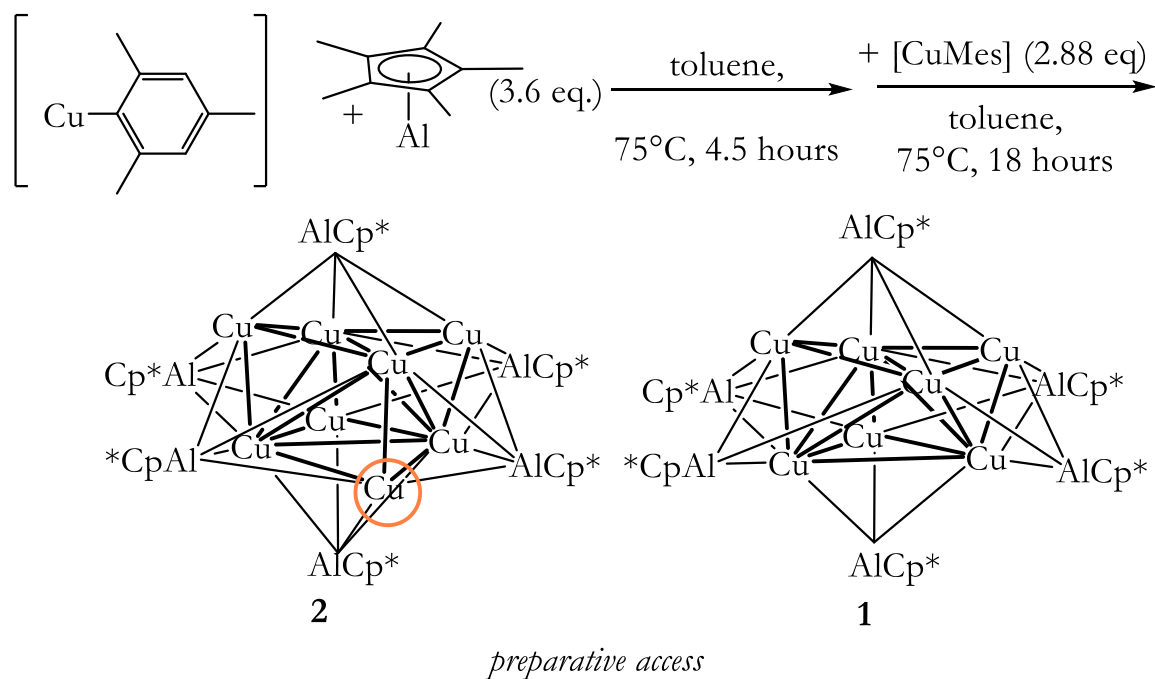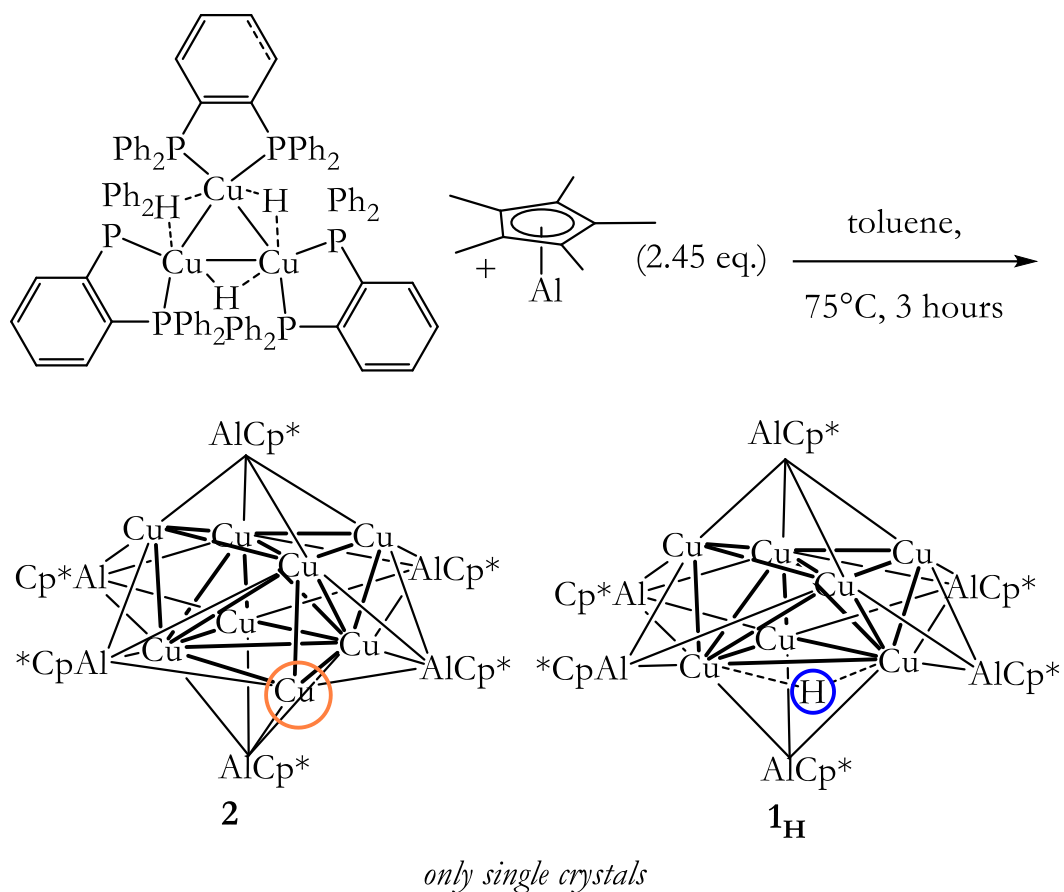
Scheme 22

*a) Synthetic (preparative) access to the micro-library **1/2**. b) Synthetic access to single crystals of the micro-library **1ₕ/2**.*

170

3. Results and Discussion
3.2. Chemical part: Synthesis characterization, reactivity

Crystallographic characterization of 1_H/2

Compounds **1_H/2** co-crystallize in the monoclinic space group *I2/m* with two molecules per unit cell. Detailed crystallographic information can be found in Table S6. The structure compromises a core of two nested copper tetrahedra embedded into an AlCp* octahedron (see Figure 72). Hereby, the outermost Cu positions (Cu2) are only partially occupied (composition according to refined crystal structure: $[Cu_{7.33}Al_6](Cp^*_6)$), being well consistent with a mixture of $[HCu_7Al_6](Cp^*)_6$ and $[Cu_8Al_6](Cp^*)_6$, just as determined by LIFDI-MS (*vide supra*). The hydride could not be located by SC-XRD but DFT calculations allow for an assessment of its binding mode (*vide supra*). The faces of the inner Cu tetrahedron (Cu1, Cu3, Cu5) are capped by the Cu atoms (Cu2, Cu2a, Cu4, Cu6) of the outer Cu tetrahedron resulting in an overall structural motif, which is well known as "stella quadrangula" from corresponding Hume-Rothery phases like γ-brass (Cu_5Zn_8) or Cu_9Al_4. The structural relationship between the species $[H_4Cu_6Al_6](Cp^*)_6$ (dicapped tetrahedron)[92] $[Cu_7Al_6](Cp^*)_6$ (triple capped tetrahedron) and $[Cu_8Al_6](Cp^*)_6$ (tetracapped tetrahedron) is a striking common motif when comparing these structures (see Figure 73). Additionally, the tetracapped tetrahedron to tricapped tetrahedron relationship is documented in the literature for copper clusters, although for Cu(I).[255-256]
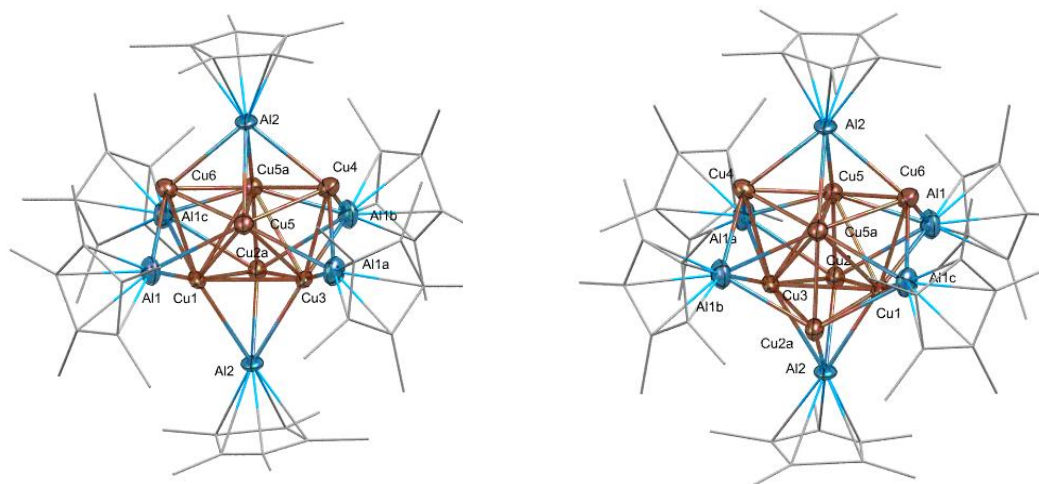
Figure 72

*Molecular structure of **1_H/2** in the solid state as determined by SC-XRD, the two co-crystallizing cluster **1_H** (left) and **2** (right) are shown separately. Thermal ellipsoids are shown at the 50 % probability level, hydrogen atoms, co-crystallized solvent molecules and disordered groups are omitted for clarity and ligands are simplified as wireframes. Selected interatomic bond distances [Å] and angles [°]: Cu1-Cu2: 2.311(3), Cu1-Cu5: 2.626(2), Cu1-Cu6: 2.381(2), Cu1-Cu3: 2.563(2), Cu2-Cu3: 2.314(3), Cu3-Cu5: 2.625(2), Cu3-Cu4: 2.390(2), Cu2-Cu5: 2.326(3), Cu6-Cu5: 2.404(2), Cu4-Cu5: 2.396(2), Cu1-Al1: 2.4850(15), Cu2-Al1: 2.588(2), Cu5-Al1:*

2.4966(18), Cu6-Al1: 2.5193(16), Cu1-Al2: 2.450(2), Cu2-Al2: 2.528(2), Cu3-Al2: 2.477(2), Al2-Cp*_{centroid}: 1.94, Al1-Cp*_{centroid}: 1.96; Cu5-Cu5a-Cu3: 59.0, Cu3-Cu1-Cu5: 60.77(5), Cu2-Cu1-Cu2a: 108.83(12), Cu1-Cu2-Cu3: 67.31(9), Cu2-Cu4-Cu2a: 58.9, Al1-Al1a-Al1b-A1c: 0.0, Al2-Al1b-Al2a-Al1: 0.0.

The structure can be also be described as a superposition of two AlCp* capped Cu-butterfly motifs (Cu4, Cu5, Cu5a, Cu6 / Cu1, Cu2, Cu2a, Cu3) giving a structural analogy to compound **11** (see Figure 73 for illustration). An Al atom surrounded by four butterfly-like arranged Cu atoms is also found in the molecular structure of $[H_4Cu_6Al_6](Cp^*)_6$[92], while in $[Cu_{43}Al_{12}](Cp^*)_{12}$, AlCp* occupies positions capping Cu_3 triangular faces.[93] In view of these structural analogies, **11** can be seen as a native "building block" for larger Cu/Al aggregates.

Cu-Cu distances in **1_H/2** vary between 2.311(3) Å (Cu1-Cu2) and 2.703 Å (Cu5-Cu5a) with a mean value of 2.447 Å, which is slightly shorter than in **11** or the closely related molecules $[H_3Cu_6Al_6](Cp^*)_6(PhCHN)$ and $[Cu_{43}Al_{12}](Cp^*)_{12}$. The Cu-Cu distances inside the inner Cu tetrahedron are thereby longer than those connecting the inner tetrahedron with the capping Cu atoms. The triangular faces of the inner tetrahedron span almost equilateral triangles with bond angles close to 60 ° (e.g. Cu5-Cu5a-Cu3: 59.0 °; Cu3-Cu1-Cu5: 60.77(5) °). The acute and obtuse angles between the outer and inner Cu tetrahedron vary between 108.83(12) ° (Cu2-Cu1-Cu2a) and 67.31(9) ° (Cu1-Cu2-Cu3). The outer tetrahedron itself is spanned by almost equilateral triangles (*e.g.* Cu2-Cu4-Cu2a: 58.9 °; Cu4-Cu6-Cu2a: 59.7 °). Al-Cu distances vary between 2.450(2) Å (Al2-Cu1) and 2.588(3) Å (Al1-Cu2). The mean Cu-Al distance of 2.51 Å is slightly longer than in **9** and **11**, but very similar to the mean distance in the solid-state phase $CuAl_2$ (vide supra). Very interestingly, the AlCp* shell adopts a perfect octahedral shape with dihedral angles of 0.0° between Al1-Al1a-Al1b-Al1c and Al2a-Al1-Al2-Al1b. Al-Cp*_{centroid} distances are with 1.94 Å (Al2-Cp*_{centr.}) and 1.96 Å (Al1-Cp*_{centr.}) very similar to those in **9, 11** as well as $[Cu_{43}Al_{12}](Cp^*)_{12}$ (*vide supra*).

Triangular motifs are common in all three compounds **9, 11, 1_H/2**. Whereas **9** itself is an almost equilateral triangle, in **11**, the central triangle of the bipyramid exhibits an angle of 57.75(3)°. The triangular faces of the inner tetrahedron in **1_H/2** span almost equilateral triangles with bond angles close to 60 °. The outer tetrahedron itself is spanned by almost equilateral triangles.

a)

b)
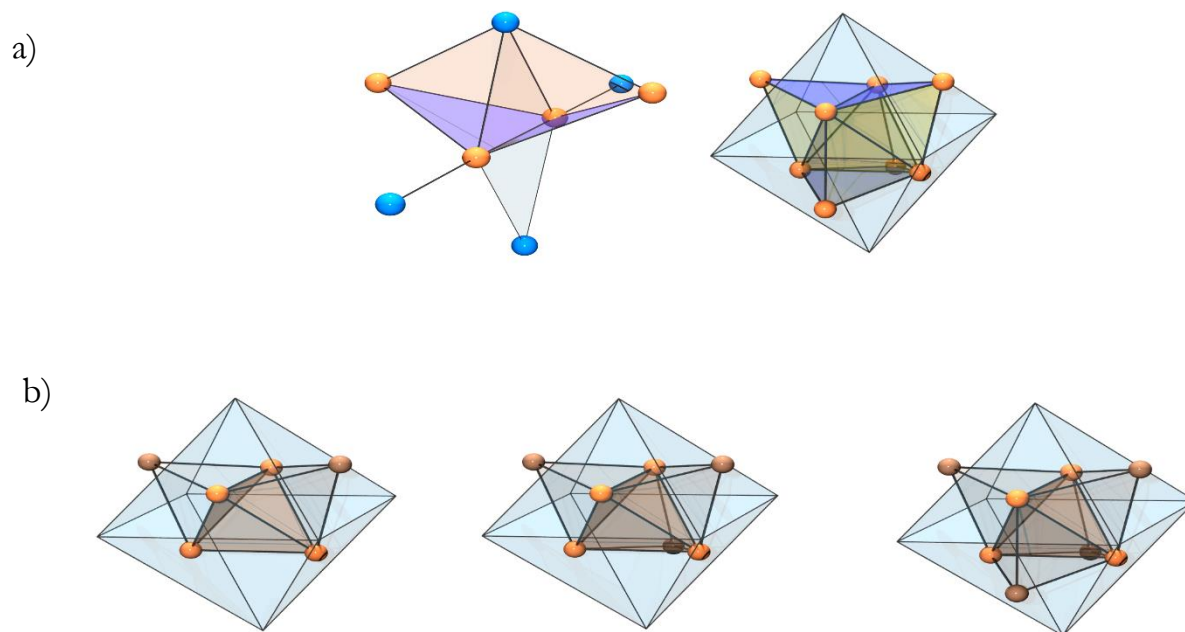
Figure 73

*a) Illustration of the butterfly [Cu4] motif (purple) in **11** (left) and **2** (right). b) Structural evolution of the Cu-kernels in [H4Cu6Al6](Cp*)6, **1H** and **2** (from left to right). Colour code: blue = Al, orange/ light brown = Cu. Organic ligands and Al atoms forming the octahedral shell of [H4Cu6Al6](Cp*)6, **1H** and **2** are omitted for clarity. Note the evolution starting with a di-capped [Cu4] tetrahedron in [H4Cu6Al6](Cp*)6 over tri-capped [Cu4] tetrahedron in [HCu7Al6](Cp*)6 to a tetra-capped tetrahedron in [Cu8Al6](Cp*)6.*

Excursion: Octahedral (MCp*)₆ shells (M = Al, Ni) in intermetalloid clusters

In Figure 73 b), the focus of structural analysis lies on the core structural motifs of the Cu/Al clusters $[H_xCu_{6-8}Al_6](Cp^*)_6$. Interestingly, despite the variability in core composition, all these structures feature an almost perfectly octahedral "shell" of AlCp* ligands. The structural motif of two interpenetrated tetrahedra surrounded by an octahedral shell is also found in solid-state Hume-Rothery phases such as γ-brass (Cu_5Zn_8) or Cu_9Al_4 (see Figure 4, introduction). In Cu_9Al_4, however, the octahedral positions are exclusively occupied by Cu and not Al.

The structural building principle $[M1_x](M2Cp^*)_6$ with an octahedral shell of M2Cp* units seems to be a rather general motif in the chemistry of Hume-Rothery inspired intermetalloid clusters. The structural situation is illustrated in the form of a general picture in Figure 74. Table 6 lists the hitherto known metal distributions M1 and M2 with octahedral (M2Cp*)₆ shell.

3. Results and Discussion

3.2. Chemical part: Synthesis characterization, reactivity

Table 6

Hitherto known examples of intermetalloid $[M1_x](M2Cp^*)_6$ clusters with an octahedral $(M2Cp^*)_6$ shell.

M1	M2
Cu	Al
Au	Al
Ga	Ni

In the case of Au/Al clusters, the clusters $[H_xAu_6Al_6](Cp^*)_6$ and $[H_xAu_7Al_6](Cp^*)_6$ were discovered and the chemistry of these species is also discussed in this dissertation (see chapter 3.2.4). Structural analysis by means of SC-Xray diffraction of the mixture $[H_xAu_{6/7}Al_6](Cp^*)_6$ and of pure $[H_xAu_7Al_6](Cp^*)_6$ reveals an octahedral shell of AlCp* ligands. However, resolution of the core geometries is in these cases not possible either due to unresolvable twinning or the fact that the crystals are a mixture of at least two species, as in the case of $[H_xAu_{6/7}Al_6](Cp^*)_6$ (see also dissertation[100] of *Jana Weßing*). Surprisingly, in the solid state, the octahedral shell of AlCp* ligands seems to be rather rigid and insensitive to geometric and compositional variations of the core. No severe disorder of the AlCp* ligands can be observed in any of the crystal structures. This might well be due to geometric constraints of the Cp* ligands and packing effects in the solid-state. In solution, however, rapid exchange between the AlCp* ligands at room-temperature is anticipated, as only one Cp* coalescence signal is observed for all the mentioned Cu/Al and Au/Al clusters. Note that the Cu/Al and Au/Al cluster examples correspond to the simplified model in Figure 31 a).

Another example represents the $M_{12/13/14}$ Ni/Ga cluster library $[Ni_7Ga_6](Cp^*)_6$, $[Ni_6Ga_7](Cp^*)_6$, $[Ni_7Ga_7](Cp^*)_6$ and $[Ni_6Ga_6](Cp^*)_6$, which is available from the reaction between $[Ni(cod)_2]$ and GaCp* (cod = cyclooctadiene).* Composition of this isolable, co-crystallizing cluster mixture was determined by LIFDI-MS analysis. SC-Xray diffraction analysis of the crystals reveals a homometallic shell of six NiCp* units, whereas the cluster core again is highly disordered. Noteworthy, the nature of the outer M2Cp* units was confirmed by solid-state MAS NMR, indicating that Ni occupies the Cp* bearing metal positions (see also Figure 31 b) for a simplified illustration). In contrast, the cluster core is mainly composed of Ga with only slight "doping" with one Ni atom in the clusters $[Ni_7Ga_6](Cp^*)_6$ and $[Ni_7Ga_7](Cp^*)_6$. Apparently, the reaction is accompanied by Cp* transfer from Ga to Ni. The example highlights that rigid shells of octahedral M2Cp* units represent a rather general and apparently structurally favored motif in intermetalloid clusters of Hume-Rothery composition. Whereas valuable information about these cluster shells can be drawn from SC-Xray experiments, determination of the nature and composition of the core

* unpublished results of Maximilian Muhr, Lena Staiger and Jana Weßing.

geometries often requires additional analytical (LIFDI-MS) and theoretical (DFT calculations) techniques.
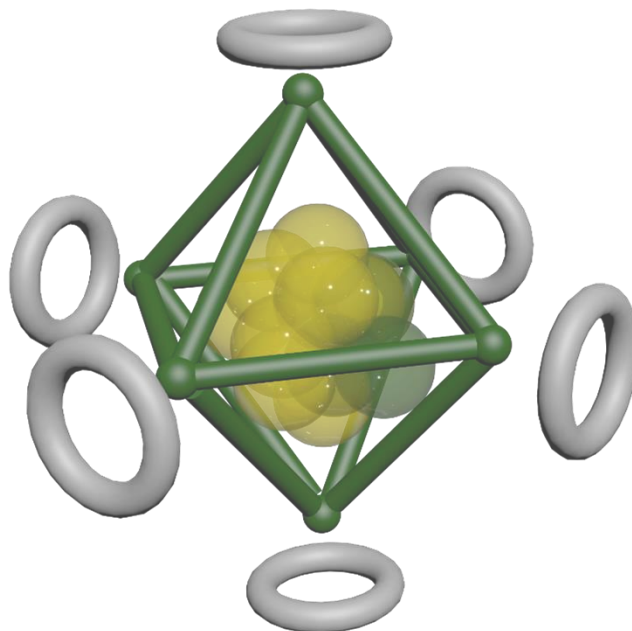
Figure 74
Schematic representation of an intermetalloid cluster with $(MCp^*)_6$ shell. Cp* ligands are simplified as grey circles and the octrahedral metal shell is illustrated in dark green. Noteworthy, structural information about the inner core (transparent spheres) is not always available from SC-XRD experiments due to disorder, twinning or co-crystallization effects. [Figure created by Lena Staiger].

Spectroscopic characterization of $[Cu_{7/8}Al_6](Cp^*)_6$ (1/2)

The ^{1}H-NMR of isolated **1/2** in benzene-d^6 (see Figure S96) gives rise to one sharp singlet at 1.94 ppm, which is attributed to diamagnetic $[Cu_8Al_6](Cp^*)_6$. A very broad signal is observed at -1.03 ppm, which is assigned to paramagnetic $[Cu_7Al_6](Cp^*)_6$. The ^{13}C-NMR of **1/2** (see Figure S97) in benzene-d^6 shows signals for Cp* at 12.89 ppm and 115.19 ppm, again assigned to diamagnetic **2**, while paramagnetic **1** could not be identified in the ^{13}C-NMR spectrum. LIFDI-MS analysis of isolated **1/2** shows the molecular ion peaks of $[Cu_8Al_6](Cp^*)_6$ (**2**) at m/z = 1480 together with $[Cu_7Al_6](Cp^*)_6$ (**1**) at m/z = 1417 with isotopic patterns well in line with the calculated ones (see Figure 35 and methodical part). Elemental analysis of **1/2** closely matches the values expected for $[Cu_8Al_6](Cp^*)_6$ indicating that the amount of $[Cu_7Al_6](Cp^*)_6$ is below 5 mass %. This is in full agreement with SQUID measurements of the sample, indicating an overall diamagnetic behavior over the whole temperature range with only very small paramagnetic contributions. As expected, the ATR-IR spectrum of **1/2** (see Figure S98) is very similar to the ones of **9** and **11**. ν_{C-H} stretching bands

are found at 2906 cm^{-1} and 2850 cm^{-1}, ν_{C-C} vibrations at 1489 cm^{-1} , 1423 and 1369 cm^{-1} and the ν_{Al-C} stretching vibration at 414 cm^{-1}.

Bonding analysis of 1/2

*The bonding analysis of **1/2** is described in the methodical part as a representative example for bonding-reactivity assessment (see page 95). It further illustrates, how hydrides can be located in intermetalloid clusters by theoretical methods. Relevant computed data for compounds **1/2** is further given in Table S9.*

3.2.3.3 Reactivity of intermetalloid Cu/Al clusters

*The reactivity of the mixture **1/2** was in detail investigated in this dissertation with regard to a radical reactivity of the open-shell cluster **1**. Thereby, the ability of **1** to undergo C-H and Si-H activation reactions resulting in formation of **1$_H$** was discovered. Analysis of the reaction solutions was mainly conducted by LIFDI-MS analysis and the procedure/spectra interpretation is presented in the methodical section. The organic side-products of the reactions were analyzed by NMR and GC-MS analysis allowing for a fundamental understanding of the reactions´ mechanism and scope. These results are presented in the following paragraph.*

C-H and Si-H activation reactions

When isolated [Cu$_{7/8}$Al$_6$](Cp*)$_6$ (**1/2**) is heated in toluene to 110 °C for several days, partial transformation of [Cu$_7$Al$_6$](Cp*)$_6$ (**1**) into [HCu$_7$Al$_6$](Cp*)$_6$ (**1$_H$**) is observed in LIFDI-MS analysis (see Figure 44 a) and Scheme 23 a)). Pentamethylfulvene was identified as an organic reaction product by GC-MS (see Table S10). However, no reaction at all is observed in toluene-d$_8$ (also no formation of pentamethylfulvene according to ^{1}H-NMR analysis) indicating C-H bond activation of toluene playing a crucial role in the reaction pathway. **1** is supposed to initially react with toluene by H radical transfer forming **1$_H$** and toluyl radicals, which intermolecularly C-H activate (cluster bound) Cp* ligands in a second reaction step, finally resulting in formation of pentamethylfulvene. Noteworthy, cleavage of pentamethylfulvene from the cluster core would then result in a 1e$^-$ reduced, Cp* deprotected cluster (see Scheme 23 a)) The presence of the deprotected cluster [Cu$_8$Al$_6$](Cp*)$_5$ as a small peak in LIFDI-MS analysis is consistent with this hypothesis (see Figure S99). Noteworthy, toluyl radicals are resonance stabilized. They were also shown to rearrange to the aromatic benzyl radical in the gas phase.[257-258] As no coupling products from toluene were detected in GC-MS, the formed tolyl radicals are supposed to have only a very limited lifetime before undergoing C-H activation of coordinated Cp* forming the

thermodynamically more stable molecule pentamethylfulvene. It is therefore not clear, whether the original C-H activation of toluene occurs at the -CH$_3$ or at the aromatic -CH position. It is further noted that substantial isotope effects in such H atom transfer reactions from toluene are known in literature.[259-260]

The reactive open-shell character of [Cu$_7$Al$_6$](Cp*)$_6$ **1** is further illustrated by conversion of isolated **1/2** with (TMS)$_3$SiH (tris(trimethylsilyl)silane) at 110 °C in toluene to a mixture of **1/1$_H$/2** in addition to the novel cluster species {[Cu$_7$Al$_6$](Cp*)$_6$(Si(SiMe$_3$)$_3$ − H} and {[Cu$_8$Al$_6$](Cp*)$_6$(Si(SiMe$_3$)$_3$ - H} (see Figure S101 and Scheme 10 and Scheme 23 b) ; "- H" denotes that the given formula unit is detected in LIFDI-MS in its hydrogen abstracted form). *In-situ* ^{1}H-NMR analysis indicates consumption of **1** (see Figure S100). Unfortunately, no signal of the hydride species **1$_H$** was observed, even at extended scan-rate and -range, probably due the fluctional character of the hydride. *In-situ* ^{1}H-NMR and GC-MS analysis of the reaction mixture reveal formation of a variety of polysilanes, such as *e.g.* hexamethyldisilane, pentamethyldisilane or tetramethyldisilane (see Table S10 and Scheme 23 b)), pointing to a radical H-transfer mechanism. These silane species are interpretated as disproportionation products of intially generated [(TMS)$_3$Si]· radicals.[261] [(TMS)$_3$Si]· might be formed by Si-H and/or C-H activation of (TMS)$_3$SiH. Noteworthy, silyl radicals are well known to undergo comproportionation (Si-Si bond formation), as well as disproportionation reactions including intermolecular C-H activation of Si-CH$_3$ groups.[261] The reaction products {[Cu$_7$Al$_6$](Cp*)$_6$(Si(SiMe$_3$)$_3$ − H} and {[Cu$_8$Al$_6$](Cp*)$_6$(Si(SiMe$_3$)$_3$) - H} observed in LIFDI-MS analysis give further evidence for such a radical mediated course of the reaction, as they represent adducts of C-H activated [(TMS)$_3$Si]· radicals with the parent clusters **1$_H$** and **2**.

When **1/2** is converted with the deuterated analogon (TMS)$_3$SiD, a mixture of **1/1$_H$/1$_D$/2** is observed (see Figure 44 b)).

Reaction with tetrakis(trimethylsilyl)silane (TMS)$_4$Si yielded a mixture of **1$_H$/1** together with {[Cu$_8$Al$_6$](Cp*)$_6$(SiMe$_3$)-H} as novel species observed in LIFDI-MS analysis (see Figure S102 for LIFDI-MS and Figure S103 for *in situ* ^{1}H-NMR). In this case, (TMS)$_3$SiH together with pentamethylfulvene were detected in GC-MS analysis again pointing towards a radical H-transfer mechanism. The presence of {[Cu$_8$Al$_6$](Cp*)$_6$(SiMe$_3$)-H} in LIFDI-MS analysis allows to suggest a balanced reaction equation between **1/2** and (TMS)$_4$Si, which is presented in Scheme 23 c).

3. Results and Discussion
3.2. Chemical part: Synthesis characterization, reactivity

a)

$$[Cu_{7/8}Al_6](Cp^*)_6 \; + \; \text{(toluene)} \quad \xrightarrow{110\,°C} \quad [(H)Cu_{7/8}Al_6](Cp^*)_6 \; + \; \text{(toluyl radical)}$$

$$\mathbf{1/2} \qquad\qquad\qquad\qquad\qquad \mathbf{1/1_H/2}$$

1 e$^-$ reduced, Cp*
deprotected cluster

b) $\quad [Cu_{7/8}Al_6](Cp^*)_6 \; + \; (TMS)_3SiH \quad \xrightarrow{110\,°C} \quad [(H)Cu_{7/8}Al_6](Cp^*)_6 \; + \; [(TMS)_3Si]^\bullet$

$$\mathbf{1/2} \qquad\qquad\qquad\qquad\qquad\qquad \mathbf{1/1_H/2}$$

$$[(TMS)_3Si]^\bullet \quad \longrightarrow \quad \longrightarrow \quad Me_3Si\text{-}SiMes_3 \; + \; Me_3Si\text{-}SiHMe_2 \; + \; Me_2HSi\text{-}SiHMe_2$$

$$[(TMS)_3Si]^\bullet \; + \; [Cu_{7/8}Al_6](Cp^*)_6 \quad \longrightarrow \quad \{[Cu_{7/8}Al_6](Cp^*)_6(Si(SiMe_3)_3 \text{ - } H\}^*$$

$$\mathbf{1/2}$$

c) $\quad 1.5 \; [Cu_{7/8}Al_6](Cp^*)_6 \; + (TMS)_4Si \quad \xrightarrow[\text{3 days}]{110\,°C, \text{ toluene-}d_8}$

$$\mathbf{1/2}$$

$$[HCu_7Al_6](Cp^*)_6 \; + \; \{[Cu_8Al_6](Cp^*)_6(SiMe_3) \text{ - } H\} \; + \; (TMS)_3SiH \; + \quad \text{(pentamethylfulvene)} \quad + \; Cp^*$$

deprotected
cluster

$$\mathbf{1_H}$$
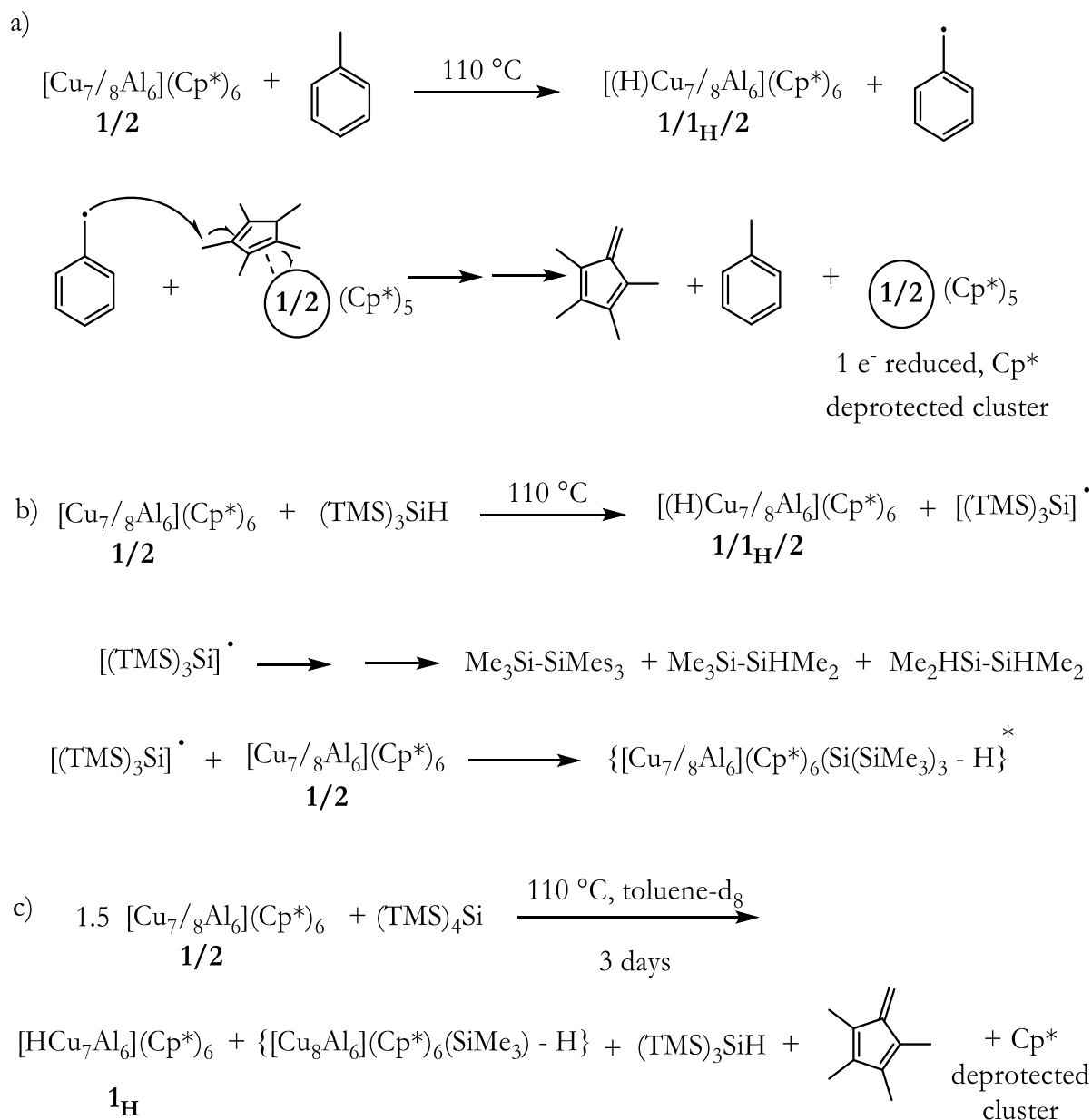
Scheme 23
a) Toluene activation by [Cu₇/₈Al₆](Cp)₆ (**1/2**) leading [(H)Cu₇/₈Al₆](Cp*)₆ and proposed reaction fate of the formed toluyl radicals. Only pentamethylfulvene could be detected as organic reaction product by GC-MS. The cleavage of pentamethylfulvene from a Cp* protected cluster is supposed to be initiated by the toluyl radicals and to lead to a 1 e- reduced, Cp* deprotected cluster. b) Proposed reaction equation for the reaction between [Cu₇/₈Al₆](Cp*)₆ and (TMS)₃SiH leading to [(H)Cu₇/₈Al₆](Cp*)₆. The disproportionation products of [(TMS)₃Si]· radicals were detected by GC-MS. * Product detected by LIFDI-MS. Hydrogen abstraction is supposed to occur in the LIFDI machine. c) Proposed balanced reaction equation for the reaction of [Cu₇/₈Al₆](Cp*)₆ with (TMS)₄Si.*

From these results it is concluded that the reactive open shell cluster **1** is inclined to C-H and Si-H bond activation reactions with the corresponding closed shell hydride cluster **1$_H$** as the thermodynamically stable reaction product. While no C-D activation occurs with toluene-d$_8$ under the conditions applied, Si-D activation is observed, competitively occurring to the C-H activation reactions of toluene and of Si-CH$_3$ groups. Notably, no C-H activation was observed when heating **1/2** in methylcyclohexane. The result can be explained by the α-Si and β-Si effect stabilizing carbon centered radicals in α- and β-positions to a Si atom.[262] Notably, in (TMS)$_3$SiH and (TMS)$_4$Si, carbon atoms possess Si neighbors in α- and β-position. For example, α-chlorosilanes were shown to be favorable reduced by a radical mechanism than their all-carbon α-chloroalkane counterparts.[263] Additionally, ·CH$_2$Si(Me)$_3$ radicals were generated from SiMe$_4$ and observed in ESR experiments, whereas from CMe$_4$, no such radicals have been obtained.[264] Hyperconjugation is made responsible as stabilizing effect for β-Si radicals, but the origin of the α-Si effect is still under some debate in literature. It is therefore concluded that the ability of **1** to undergo C-H activation is limited to systems which are chemically able to stabilize the resulting carbon centered radicals (resonance stabilization or α-/β-Si effect).

All reactions described in this paragraph are very slow and require long heating times at high temperatures (7 days, 110 °C) to achieve only partial transformation of **1** to **1$_H$**. It is supposed that even more extended reaction times of several weeks would result in quantitative formation of **1$_H$**, however such reactions are of limited usefulness due to unwanted parasitic side-reactions (reaction with trace-amounts of moisture, oxygen, thermal decomposition).

3.2.3.4 Outlook and Perspectives for Cu/Al cluster chemistry

Generation of Cu/Al libraries using the embryonic builing block [Cu$_2$Al](Cp)$_3$ (9)*

The reaction of the [Cu$_2$Al] triangle **9** with *Stryker´s* reagent [H$_6$Cu$_6$](PPh$_3$)$_6$ in a <u>3:1 ratio (HCu:Al = 2:1)</u> in toluene (HCu:Al stoichiometry = 2:1) at 75 °C results in rapid formation of the thermodynamically very stable half-sandwich complex [Cp*CuPPh$_3$] as indicated by ^{1}H-NMR spectroscopy, LIFDI-MS analysis and SC-XRD of isolated colorless crystals obtained directly from the dark reaction solutions.

LIFDI-MS analysis of the reaction solution also reveals formation of a variety of large Cu/Al clusters with m/z ≤2500 (see Figure 51 in the outlook of the methodical part and Scheme 24). In ^{1}H-NMR, only **2** can be identified as cluster species

3. Results and Discussion
3.2. Chemical part: Synthesis characterization, reactivity

according to its Cp* signal (see Figure S104). Interestingly, the reaction of $[H_6Cu_6](PPh_3)_6$ with AlCp* only results in formation of the known cluster $[H_4Cu_6Al_6](Cp^*)_6$. Obviously, triangular **9** is cleaved by PPh_3 ligands resulting in liberation of AlCp*, which subsequently coordinates to "naked" $[H_xCu_x]$ fragments resulting in the formation of large clusters. Noteworthy, formation of hydrogen in trace amounts is observed in *in situ* ^{1}H-NMR analysis explaining the formation of Cu(0) cluster cores by reductive elimination of hydrogen from $[H_xCu_x]$. Analysis of the LIFDI-MS spectra reveals the cluster species $[HCu_7Al_6](Cp^*)_6$ (**1$_H$**), $[Cu_8Al_6](Cp^*)_6$ (**2**), but for the larger clusters, unambigous assignment was not achieved so far. Labeling experiments (with AlCp*^{Et} or labeled PPh_3) are suggested for their identification, just as applied for the complicated Cu/Zn libraries in this dissertation. When the reaction was repeated in this HCu:Al stoichiometry (2:1) upon addition of extra, "free" PPh_3, size-focusing towards the two known clusters $[H_xCu_6Al_6](Cp^*)_6$ and $[Cu_8Al_6](Cp^*)_6$ (**2**) was observed by LIFDI-MS (see Figure 75).
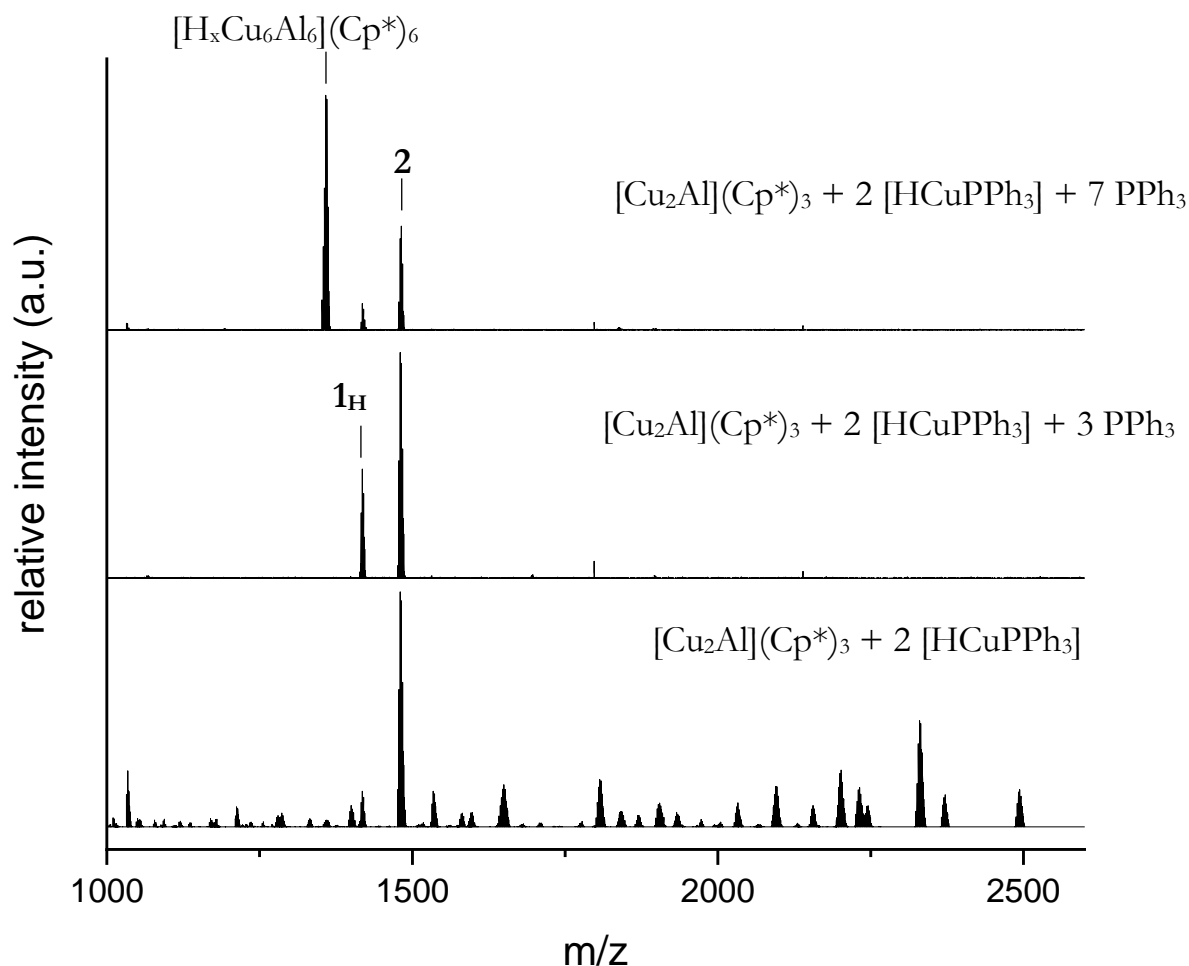
Figure 75
Size-focusing and size-control of large Cu/Al libraries upon phosphane (PPh₃) addition. The figure shows in situ LIFDI-MS spectra of the respective reaction solutions. Bottom: A large Cu/Al library is obtained upon reaction of [Cu₂Al](Cp)₃ with [HCuPPh₃] in a stoichiometric ratio in*

which every PPh₃ is captured by a "Cp*Cu" unit as [Cp*CuPPh₃]. Note that peak assignment is difficult for this library due to several possible matches for most of the heavier cluster peaks. For some tentative assignment it is referred to Figure 51 in the outlook of the methodical part, which shows the same spectrum. Middle: Repeating the reaction between [Cu₂Al](Cp*)₃ and [HCuPPh₃] upon addition of 3 equivalents of extra PPh₃ leads to a size-focusing towards [HCu₇Al₆](Cp*)₆ (1ₕ) and [Cu₈Al₆](Cp*)₆ (2). Top: Repeating the reaction between [Cu₂Al](Cp*)₃ and [HCuPPh₃] upon addition of 7 equivalents of extra PPh₃ leads to a size-focusing towards [HₓCu₆Al₆](Cp*)₆ (x = 1-4) in addition to some 1ₕ and 2. Note that cluster size is therefore controllable by the amount of PPh₃ added in the course of the reaction.

The presence of free PPh₃ in solution therefore influences the selectivity of the reaction and the size distribution of the obtained library. Under conditions with low concentrations of "free" PPh₃ in solution, *i.e.* when a CuCp* moiety is offered for every PPh₃ ligand as "scavanger" unit, large cluster libraries are observed. Addition of "free" PPh₃ induces higher selectivity and formation of smaller cluster units, probably by stabilizing the very reactive [HₓCuₓ] intermediates (see Scheme 24). Notably, by applying this principle, selective syntheses were also achieved in the closely related Au/Al cluster system (*vide infra*).

$$[HCuPPh_3] + [Cu_2Al](Cp^*)_3 + PPh_3 \xrightarrow{\text{toluene, 75 °C}} \text{large cluster library} + [Cp^*CuPPh_3]$$

$$x \qquad\qquad y \qquad\qquad z \qquad\qquad\qquad\qquad\qquad\qquad 2\,y$$
$$z = 2y - x$$

increasing amount of additional PPh₃
toluene, 75 °C

size-focused library of Cu/Al clusters + [Cp*CuPPh₃]
2 y

x = 2, y = 1 -> [HₓCu₆Al₆](Cp*)₆ + [Cu₈Al₆](Cp*)₆
x = 1, y = 1 -> micro-library **12**
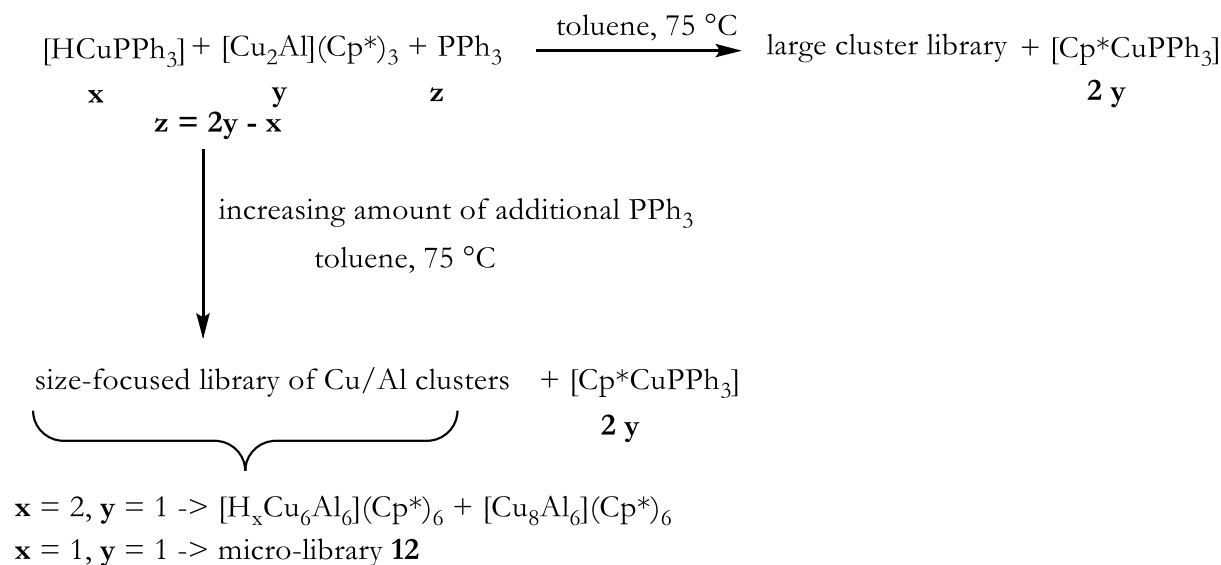
Scheme 24
General scheme for the generation of Cu/Al libraries from [Cu₂Al](Cp)₃, PPh₃ and [HCuPPh₃]. **x**, **y** and **z** denote stoichiometric ratios. At certain stoichiometric PPh₃ ratios (**z = 2y-x**), large cluster libraries (m/z > 2000 in LIFDI-MS) are formed. Increasing amounts of free PPh₃ in the solutions lead to size-focusing towards smaller Cu/Al libraries (m/z <1600 in LIFDI-MS).*

When **9** is reacted with [H₆Cu₆](PPh₃)₆ in a 6:1 ratio (HCu:Al = 1:1) upon addition of 3 eq. of extra PPh₃ to achieve complete cleavage of **9** by formation of

3. Results and Discussion

3.2. Chemical part: Synthesis characterization, reactivity

[Cp*CuPPh$_3$], a complex library very similar to the one in Figure 51 is observed in LIFDI-MS analysis, however with much lower signal intensity of the heavier clusters and the clusters [Cu$_6$Al$_7$](Cp*)$_6$ and [Cu$_6$Al$_6$](Cp*)$_6$ are detected as new species. In the higher m/z region (>2000), unambiguous assignment is again difficult, also due to the very low signal intensities. The reaction was repeated with higher amounts of PPh$_3$ added. Again, a size-focusing effect is nicely observed in LIFDI-MS analysis, resulting in a smaller library of five members upon addition of 12 eq. PPh$_3$ per mole of [H$_6$Cu$_6$](PPh$_3$)$_6$.

From the latter solution, isolation of black single crystals (denoted as micro-library **12**) is possible (see Scheme 25).

1) **X** = /, **Y** = H   [H$_x$Cu$_6$Al$_6$](Cp*)$_6$
2) **X** = Cu, **Y** = H   [HCu$_7$Al$_6$](Cp*)$_6$
3) **X** = Cu, **Y** = Cu [Cu$_8$Al$_6$](Cp*)$_6$
4) **X** = /, **Y** = Al   [Cu$_6$Al$_7$](Cp*)$_6$
5) **X** = Cu, **Y** = Al {[Cu$_7$Al$_7$](Cp*)$_6$ -H}
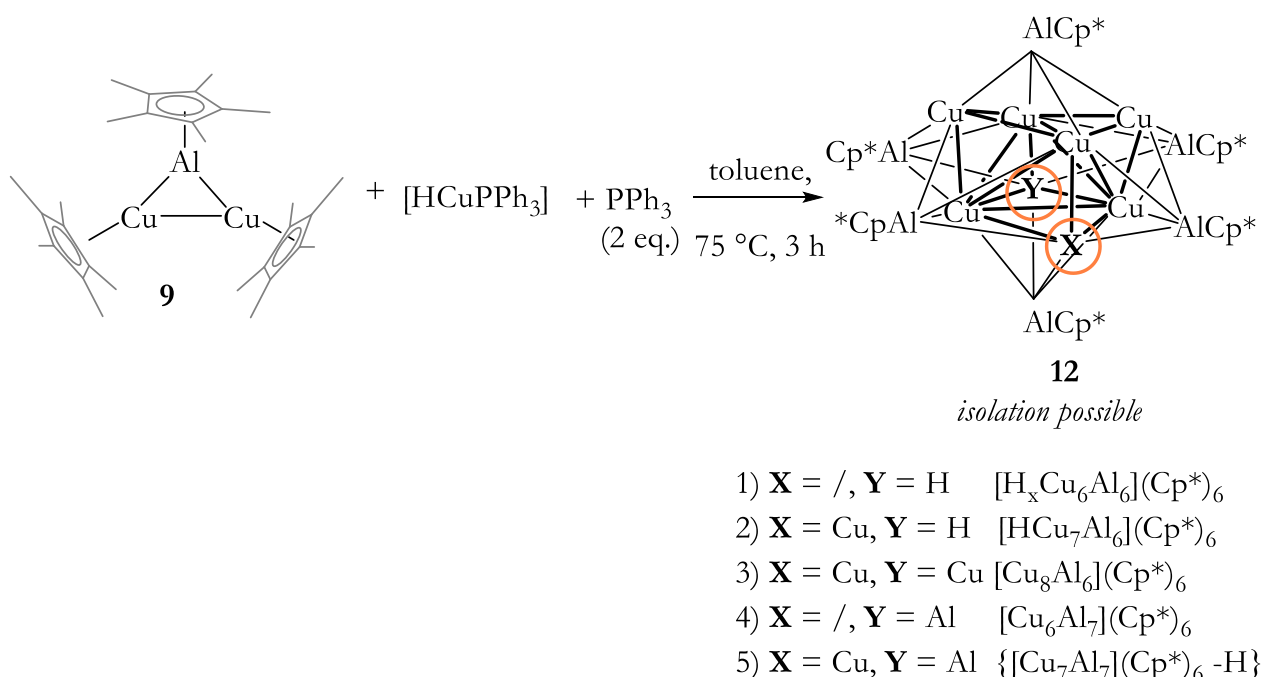
Scheme 25
*Preparation of the micro-library **12**. The components of the micro-library were determined by LIFDI-MS.*

The LIFDI-MS spectrum of these crystals is depicted in Figure 76. It shows the known clusters [H$_x$Cu$_6$Al$_6$](Cp*)$_6$, **1$_H$** and **2** in addition to [Cu$_6$Al$_7$](Cp*)$_6$ and {[Cu$_7$Al$_7$](Cp*)$_6$ – H}. Note that for the latter one, it is not clear whether the species contains a C-H activated Cp* ligand or whether hydrogen abstraction occurs inside the mass spectrometer. ^{1}H-NMR analysis of the isolated crystals reveals [H$_4$Cu$_6$Al$_6$](Cp*)$_6$ to be the major component of the mixture (see Figure S105). However, the signal attributed to **2** has very low intensity. Additionally to [H$_4$Cu$_6$Al$_6$](Cp*)$_6$ and **2**, two novel Cp* containing species are observed at 1.949 ppm

182

and 1.975 ppm, which might be associated with $\{[Cu_7Al_7](Cp^*)_6 - H\}$ and $\mathbf{1_H}$. Noteworthy, $[Cu_6Al_7](Cp^*)_6$ is expected to be paramagnetic. A broad signal at -2.10 ppm might be attributed to this species. Analysis of SC-Xray diffraction data for **12** reveals an octahedral shell of 6 AlCp* ligands and a core with 16 partially occupied metal positions. Refinement of the core structure does not give any hint for the incorporation of Al atoms in the core, rather $[H_xCu_6Al_6](Cp^*)_6$ is determined as overall composition. Its structure features a di-capped $[Cu_4]$ tetrahedron, just as reported previously. It is unclear so far, why the additional cluster species detected in ¹H-NMR analysis of the crystals and in LIFDI-MS cannot be located in the crystal structure. Possibly, co-crystallization in single crystalline form is unfavoured or some of the species are only stable or formed in solution. Noteworthy, the presence of unligated Al atoms in $\{[Cu_7Al_7](Cp^*)_6 - H\}$ and $[Cu_6Al_7](Cp^*)_6$ may well be linked with unusual reactivity towards small molecules.

The exposure of intermetalloid Cu/Al libraries towards reactants such as H_2, CO_2, CH_4 or organic functionalities is supposed to lead to novel fundamental insight into structure-reactivity relationships (see Introduction and Figure 31). Especially the micro-library **12** represents as ideal candidate for such studies, as it contains hydride bearing clusters such as $[H_xCu_6Al_6](Cp^*)_6$ and $\mathbf{1_H}$, as well as clusters with a naked Al atom, such as $[Cu_6Al_7](Cp^*)_6$ and $[Cu_7Al_7](Cp^*)_6$. The exposure of this library to hydrogen is suggested as a first experiment to monitor its reactivity. Hydrogen seems to be an ideal candidate as it was already shown to react with isolated $[H_4Cu_6Al_6](Cp^*)_6$ in the following way:

Treatment of $[H_4Cu_6Al_6](Cp^*)_6$ with 5 bar hydrogen at room-temperature for <u>a few hours</u> leads to a shift of the Cp* attributed signal from 2.01 ppm to 2.04 ppm in *in situ* ¹H-NMR spectra of the reaction solution (see Figure S106). In parallel, a new hydride signal is observed at 1.30 ppm, whereby the original hydride signal vanishes completely. Integration of the two new peaks proposes the sum formula of the product formed to be $[H_{8-10}Cu_6Al_6](Cp^*)_6$ (see Scheme 26). Very interestingly, release of hydrogen pressure results in reappearance of the signals of the starting material, hinting towards a reversible hydrogen uptake. Unfortunately, no LIFDI-MS signals of the new hydride species are available so far. Solution IR spectroscopy is suggested to further elucidate the nature of the reaction product.

If $[H_4Cu_6Al_6](Cp^*)_6$ is supposed to 5 bar hydrogen atmosphere <u>for several days</u>, the initial reaction product is prone to further reactions (see Scheme 26). In ¹H-NMR spectroscopy, eight new Cp* signals are then observed in the region typical for Cu/Al clusters (see Figure S107). They split up into two pairs of four signals each with equal integrals. Unfortunately, no meaningful LIFDI-MS data of the reaction product could be obtained so far due to very low signal intensities

3. Results and Discussion
3.2. Chemical part: Synthesis characterization, reactivity

$\{[Cu_7Al_7](Cp^*)_6 - H\}$

$[Cu_6Al_7](Cp^*)_6$

$[Cu_6Al_7](Cp^*)_6$

$[H_xCu_6Al_6](Cp^*)_6$

$[HCu_7Al_6](Cp^*)_6$

$\{[Cu_7Al_7](Cp^*)_6 - H\}$

$[Cu_8Al_6](Cp^*)_6$

*

* = unclear assignment
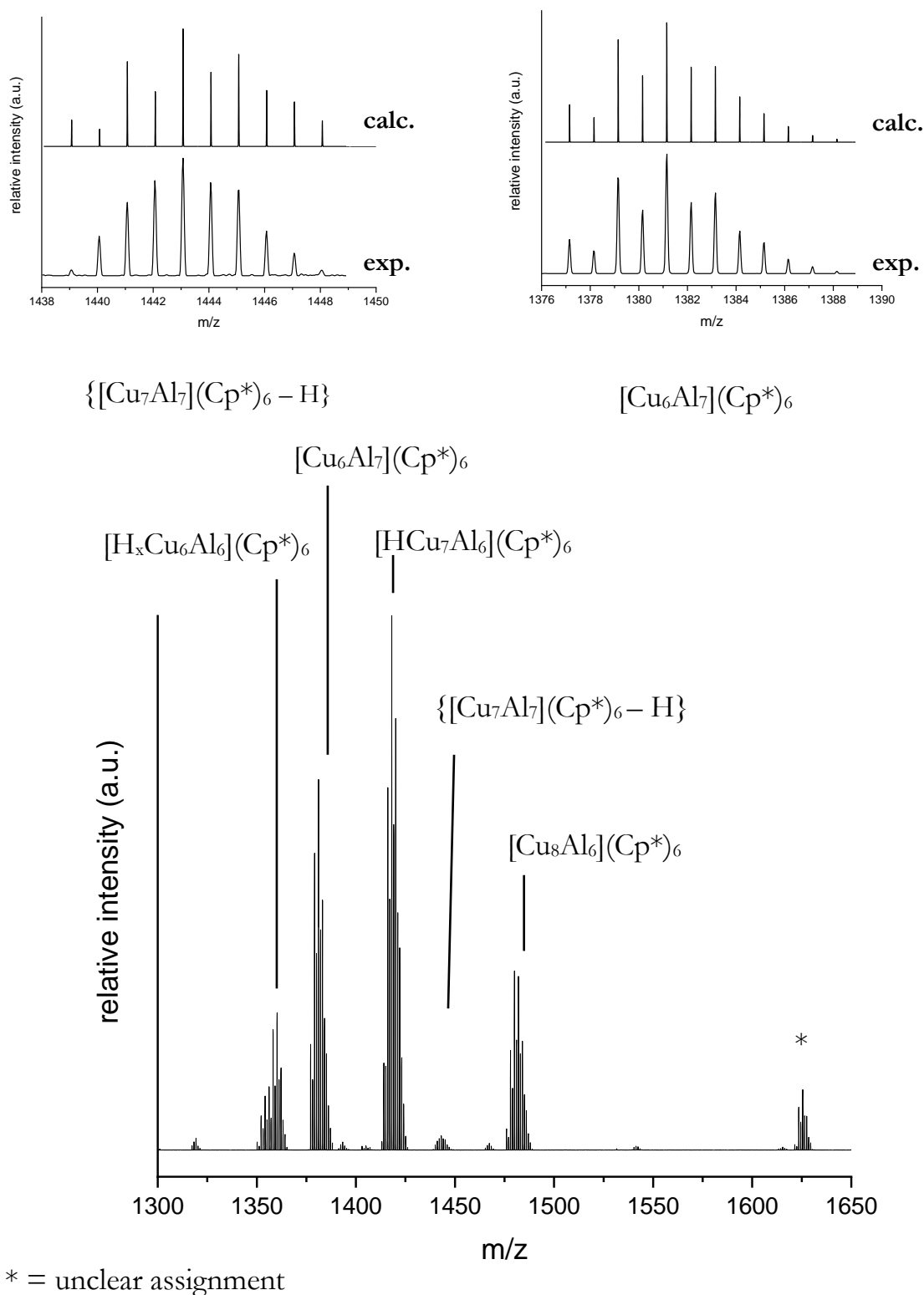
Figure 76
*Bottom: LIFDI-MS spectrum of isolated crystals of the micro-library **12** obtained from the reaction **9** + [H₆Cu₆](PPh₃)₆ + PPh₃ (6:1:12). Top: Comparison between calculated and experimental mass envelopes of {[Cu₇Al₇](Cp*)₆ − H} and [Cu₆Al₇](Cp*)₆.*

184

Despite the difficulties in analysis of the reaction products, the reaction behavior of Cu/Al cluster libraries is supposed to be very promising. Analysis of reactivity differences between isolated $[H_4Cu_6Al_6](Cp^*)_6$, the micro-library $\mathbf{1_H}/\mathbf{2}$ and the micro-library $\mathbf{12}$ might allow to assess the reaction behavior of specific species even in mixtures by the rules of combinatorics.

$$[H_4Cu_6Al_6](Cp^*)_6 \underset{\text{pressure release}}{\overset{\text{benzene-}d_6,\ 5\ \text{bar } H_2,\ 2\ h}{\rightleftharpoons}} [H_{8\text{-}10}Cu_6Al_6](Cp^*)_6$$

benzene-d_6, 5 bar H_2, 3 days

formation of > 2 new clusters
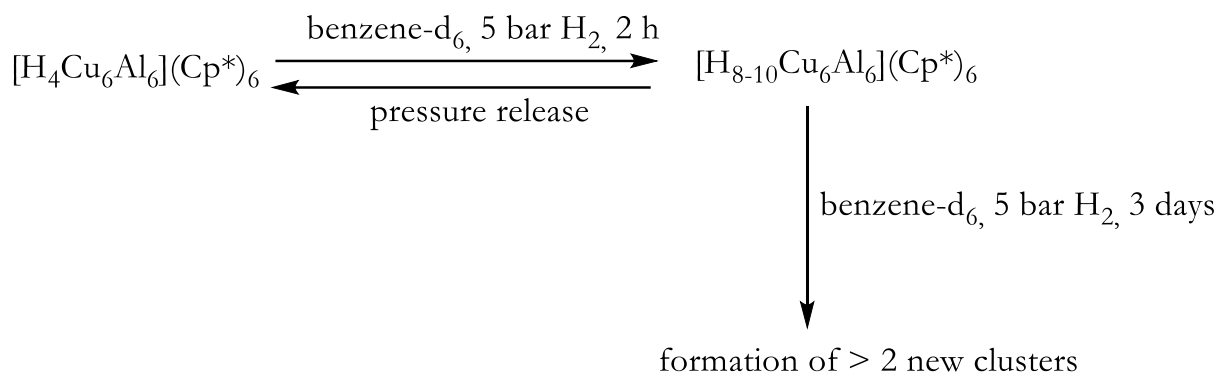
Scheme 26
Preliminary reaction scheme for the reaction of [H₄Cu₆Al₆](Cp*)₆ with hydrogen.

3.2.4 Size-focusing and characterization of Au/Al cluster libraries

3.2.4.1 Synthesis and characterization of $[H_xAu_{6/7}Al_6](Cp^*)_6$ (**6/7**)

The following synthesis was initially discovered during the dissertation of Jana Weßing at the chair of Prof. R. A. Fischer. In her dissertation, Jana Weßing achieved initial characterization of the obtained product. However, the exact nature of the clusters obtained remained unidentified. The work of Jana Weßing was therefore reproduced and continued in this dissertation project.

Synthesis

Reaction of the Au(I) precursor [*i*DippAuH] with one equivalent of AlCp* in toluene at 75 °C leads to a dark red solution within a reaction time of 30 minutes (see Scheme 27). Cooling the filtered reaction solution to -30 °C after a total reaction time of 2 hours leads to a black precipitate after several days. Isolation of the precipitate, followed by extensive washing with benzene leads to isolation of $[H_xAu_{6/7}Al_6](Cp^*)_6$ (**6/7**) in very low yield (5 % based on Au). The low yield is explained by very similar solubility properties of **6/7** and *i*Dipp containing side products, requiring extensive washing procedures. **6/7** is very air- and moisture sensitive and rapidly decomposes

upon exposure to traces of moisture. It has only very limited solubility in organic solvents such as toluene, *n*-hexane or benzene. Notably, the structures of **6/7** in Scheme 27 are suggested structures based on the analogy between **6** and $[H_4Cu_6Al_6](Cp^*)_6$ and between **7** and **1**, respectively.
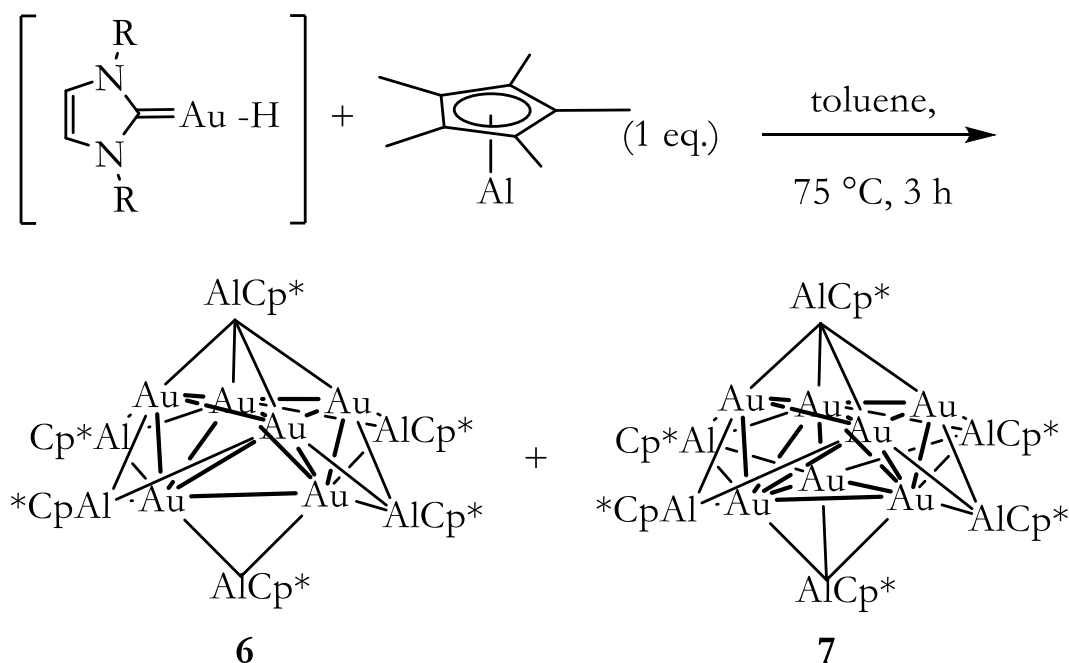
Scheme 27
*Synthesis of the cluster microlibrary $[H_xAu_{6/7}Al_6](Cp^*)_6$ (**6/7**). Hydrides are not shown due to uncertainty about their location. R = 2,6-diisopropylphenyl.*

Spectroscopic characterization

LIFDI-MS analysis of the product shows two major peaks, which can be unambiguously assigned to the ions $\{[Au_6Al_6](Cp^*)_6\}^+$ ($\{$**6** $- H_x\}^+$) and $\{[Au_7Al_6](Cp^*)_6\}^+$ ($\{$**7** $- H_x\}^+$) according to their isotopic patterns, which are fully consistent with the calculated envelopes (see Figure 77). Note that in LIFDI-MS, no hydride ligands bound to the $[Au_6Al_6]$ and $[Au_7Al_6]$ kernels can be detected. However, the presence of at least one hydride can be concluded for **7** from the diamagnetism (NMR active) of the compound, as $[Au_7Al_6](Cp^*)_6$ would be paramagnetic (19 VE) such as $[Cu_7Al_6](Cp^*)_6$. IR spectroscopic results strongly suggest the presence of hydrides for **6** and **7** (*vide infra*). Obviously, $[Au_8Al_5](Cp^*)_5(^iDipp)$, which observed as a small peak in LIFDI-MS of the reaction solution, is removed during crystallization or the workup procedure. The ^1H-NMR spectrum of **6/7** in benzene-d$_6$ (see Figure S108 and Figure 78 a)) shows only two peaks at 1.99 ppm and 1.94 ppm, which are assigned to $[H_xAu_7Al_6](Cp^*)_6$ and $[H_xAu_6Al_6](Cp^*)_6$, respectively. Integration of the peaks gives a ratio for

3. Results and Discussion
3.2. Chemical part: Synthesis characterization, reactivity

$[H_xAu_6Al_6](Cp^*)_6/[H_xAu_7Al_6](Cp^*)_6$ of 2:1 in the isolated mixture. Noteworthy, no signal of surface bound hydrides can be unambiguously identified in the ^{1}H-NMR spectrum. Acquisition of ^{13}C-NMR spectra of **6/7** is challenging due to very limited solubility of the compound in organic solvents. The spectrum in benzene-d$_6$ (see Figure S109 and Figure 78 b)) shows two peaks of cluster bound Cp* ligands at 13.00 ppm (-CH_3 groups of **6**), 115.20 ppm (quaternary carbon of Cp* of **6**) and 115.50 ppm (quaternary carbon of Cp* of **7**), besides signals attributed to free HCp*, which is explained by the low solubility of **6/7** in comparison to HCp* and its high sensitivity towards trace amounts of water. The IR spectrum of **6/7** (see Figure S110 and Figure 78 c)) is complicated and exhibits the characteristic C-H stretching (2790 -3012 cm^{-1}), -CH_3 deformation (903 – 1240 cm^{-1}) and C-C stretching (1270-1454 cm^{-1}) modes of the Cp* ligand. Modes below 1000 cm^{-1} (554 – 889 cm^{-1}) are attributed to C-C stretching and deformation modes involving the ring system. The Al-Cp* stretching frequency is found at 445 cm^{-1}. A characteristic M-H (M = Au, Al) stretching frequency is discernible at 1580 -1630 cm^{-1}. The band exhibits maximum absorption at 1600 cm^{-1}. This value is very similar to IR frequencies observed for $[AuH_4]^-$ (1676.4 cm^{-1}, 1678.8 cm^{-1}) and $[H_2AuH_3]$ (1651.5 cm^{-1}, 1666.8 cm^{-1}) in matrix isolation experiments, whereas the frequencies observed for [AuH] (2226.6 cm^{-1}) and also for isolated [^{i}DippAuH] (1976 cm^{-1}) are found at higher wavenumbers.[265-266] Interestingly, bands in **6/7** are tendentially shifted towards lower wavenumbers and much broader than in pure **7**. The fact that the sample is a mixture of two clusters with slightly different core geometries is made responsible for this observation. Obviously, this concerns especially the ring associated modes between 500 cm^{-1} and 1000 cm^{-1}. Noteworthy, for **7** the presence of at least one hydride can be concluded from the diamagnetism of the compound as observed by NMR analysis. For **6**, the presence of hydrides seems likely due to the additional M-H absorption band in IR spectroscopy, which is lacking in the IR spectrum of pure **7** (see Figure S110 and Figure 78 c)). DFT calculations to predict the number of hydrides are currently conducted by the group of *Prof. Saillard*. Preliminary results from these calculations strongly favor the presence of one hydride in **7** ($[HAu_7Al_6](Cp^*)_6$) and of two hydrides in **6** ($[H_2Au_6Al_6](Cp^*)_6$).

The UV-Vis spectrum of isolated **6/7** in toluene shows a very prominent absorption band at 494 nm – 540 nm with a maximum absorption at 517 nm (see Figure S111 and Figure 78 d)). A minor absorption band is observed around 478 nm in addition to a small shoulder at 440 nm.

3. Results and Discussion
3.2. Chemical part: Synthesis characterization, reactivity
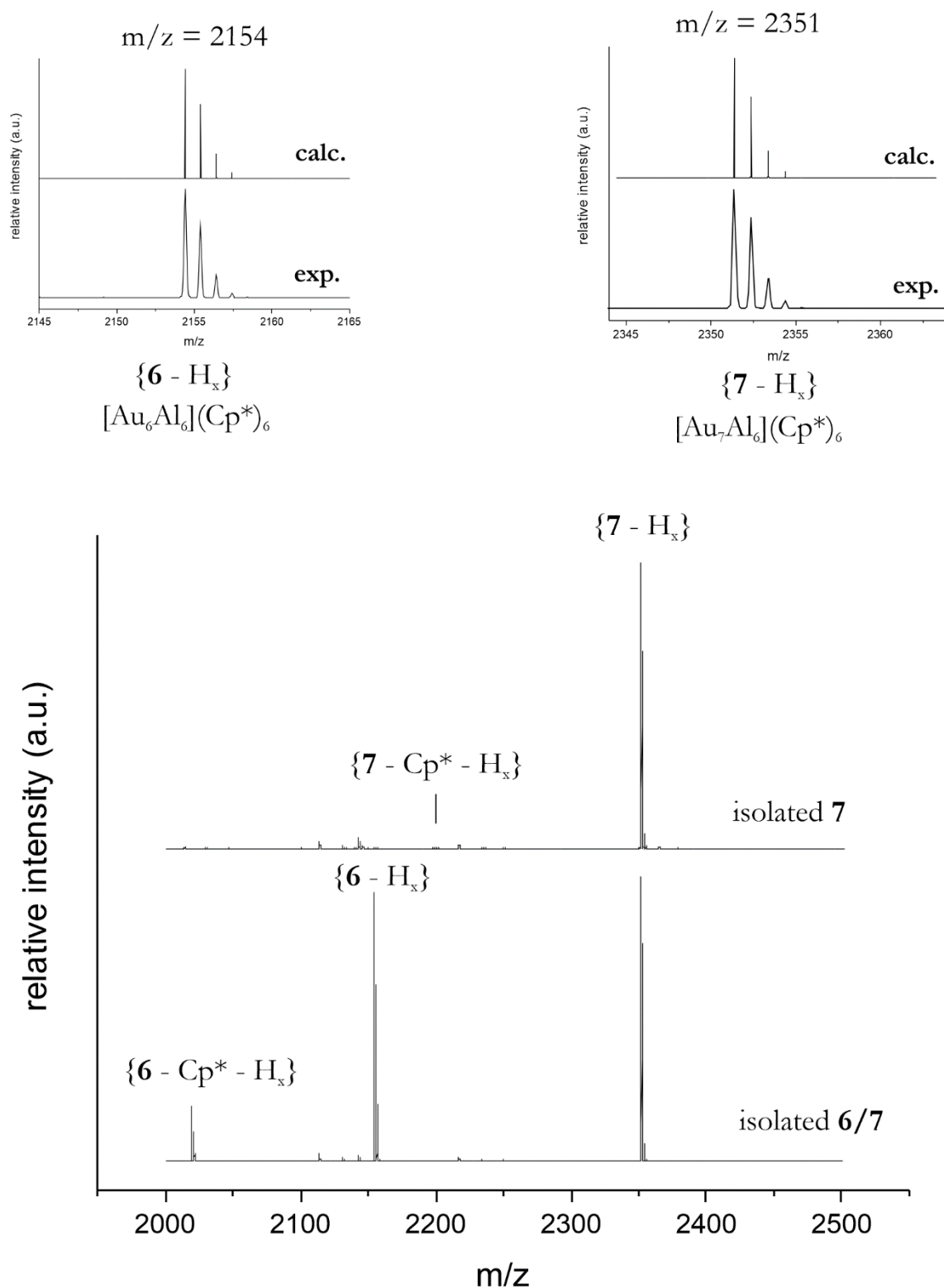
Figure 77

*Bottom: Comparison of LIFDI-MS spectra of isolated **6/7** and pure **7**. Top: Comparison of calculated and experimental patterns for the hydride-free base peaks {[Au₆Al₆](Cp*)₆}⁺ (m/z = 2154) and {[Au₇Al₆](Cp*)₆}⁺(m/z = 2351). Note that in LIFDI-MS no hydrides attached to the Au/Al clusters can be observed. However, their presence can be concluded from IR spectroscopy and from the diamagnetism of compound **7**.*

3.2.4.2 Synthesis and characterization of $[H_xAu_7Al_6](Cp^*)_6$ (**7**)

Synthesis

A selective synthesis of **7** is achieved by addition of a high excess of PPh$_3$ to the reaction between [*i*DippAuH] and AlCp*. If [*i*DippAuH] is reacted with AlCp* for 2 hours in toluene at 75 °C upon addition of 10 equivalents of PPh$_3$, **7** is the main species formed according to *in situ* ^{1}H-NMR and UV-Vis analysis (*vide infra*, Scheme 28, Figures 49-50 and Figure S121). **7** is isolated from the reaction solutions upon cooling the filtered solutions to -30 °C for several days followed by washing the obtained crystals with small amounts of *n*-hexane. Noteworthy, small amounts of **6** in the isolated precipitate are easily removed during work-up due to a better solubility of **6** in organic solvents. Macroscopic properties of **7** are basically identical to the mixture **6/7**.
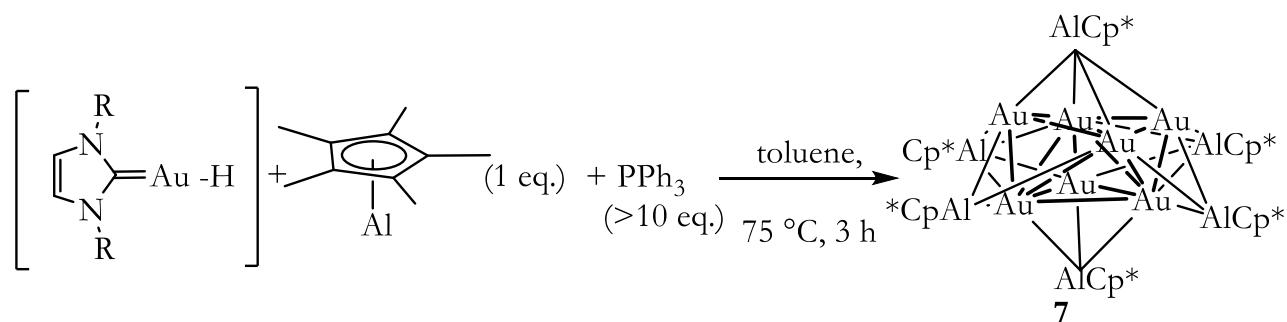
Scheme 28
Synthesis of [H$_x$Au$_7$Al$_6$](Cp)$_6$ (**7**). Hydride ligands are not shown due to uncertainty about their location. R = 2,6-diisopropylphenyl.*

Spectroscopic characterization

The purity of **7** is confirmed by ^{1}H-NMR analysis in benzene-d$_6$, exhibiting only one peak at 1.99 ppm as the only signal besides very small impurities of PPh$_3$ and co-crystallized toluene (see Figure S112 and Figure 78 a)). The ^{13}C-NMR spectrum shows the quaternary carbon signal of the Cp* ligands of **7** at 115.50 pm (see Figure S113 and Figure 78 b)). Unfortunately, no signal of the -*C*H$_3$ carbon atoms could be identified in the spectra, probably due to overlap with the signals of free HCp*. Likewise, the LIFDI-MS spectrum of isolated **7** shows the molecular ion peak of {**7** - H$_x$}${}^+$ at m/z = 2351 as the only Au/Al cluster signal (see Figure 77). The IR spectrum of isolated **7** is similar to the one of **6/7**, yet much simpler (see Figure S110 and Figure 78 c)). The characteristic C-H stretching (2790 -3012 cm^{-1}), C-H

189

3. Results and Discussion

3.2. Chemical part: Synthesis characterization, reactivity

deformation (1178 – 1335 cm^{-1}; 729 cm^{-1}) and C-C stretching (1380-1497 cm^{-1}) modes of the Cp* ligand are again identified in the spectrum in addition to the Al-Cp* stretching frequency at 445 cm^{-1}. A characteristic Au-H stretching frequency is discernible at 1720 -1780 cm^{-1}. The band exhibits maximum absorption at 1753 cm^{-1}, as well as two shoulders at 1735 cm^{-1} and 1770 cm^{-1}.
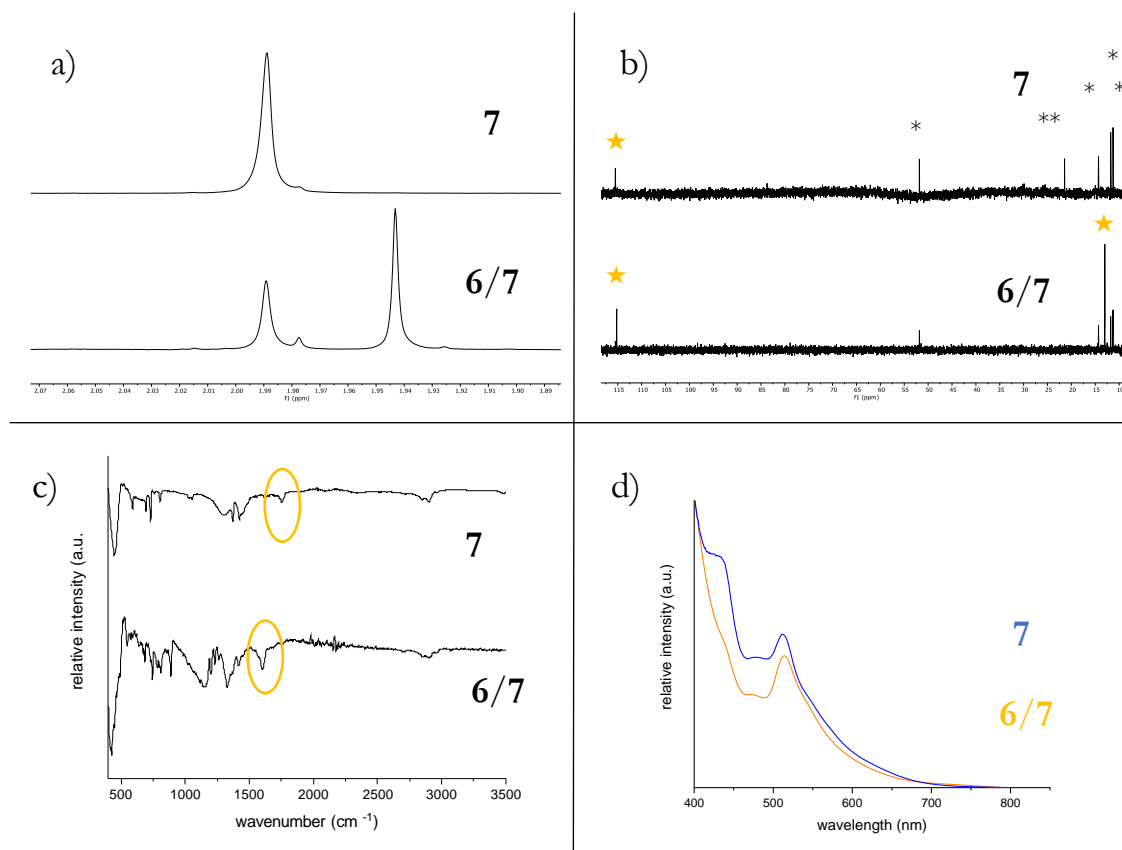
Figure 78

*Summarized analytical data for the compound **6**/**7** and **7**. The full-range spectra can be found in enlarged version in the appendix. a) ^{1}H-NMR spectra (benzene-d$_6$). b) ^{13}C-NMR spectra (benzene-d$_6$). Signals marked with * are attributed to HCp* and those marked with ** to co-crystallized toluene. Signals attributed to the clusters are marked with yellow stars. Note that the -CH$_3$ carbon signal of **7** overlaps with signals of HCp*. Quaternary carbon signals of **6** and **7** differ only very marginally in their chemical shift (115.2 ppm and 115.5 ppm). c) ATR-IR data. Au-H stretching regions are marked with yellow ellipsoids. d) UV-Vis data.*

The UV-Vis spectrum of isolated **7** in toluene is similar to the one of **6/7** (see Figure S111 and Figure 78 d)). Besides the prominent absorption band at 494 nm – 540 nm (maximum: 514 nm) and the minor band at 480 nm, the shoulder at 415-463 nm is much more pronounced than in the spectrum of **6/7**.

3. Results and Discussion

3.2. Chemical part: Synthesis characterization, reactivity

Analytical data of both **6** and **7** is summarized in Figure 78.

Crystallographic characterization

Single crystals of **7** suitable for Xray diffraction are obtained upon slow cooling of dilute reaction solutions to -30 °C for several days. However, the obtained data does not fulfill high-quality publication standards due to unresolvable twinning. Unfortunately, all efforts to obtain better quality crystals by variation of the crystallization conditions (concentration, temperature, solvent) were met by failure. Nevertheless, some qualitative information may be drawn from the SC-XRD experiments.

The molecular structure of **7** in the solid-state compromises a Au core with several partially occupied Au sites embedded into an octahedral shell of six AlCp* ligands. However, due to twinning effects, a high residual electron density is found in the core region, which could not be further refined. The crystallographic situation somehow resembles the one of $[(H)Cu_{7/8}Al_6](Cp^*)_6$, in which two different sites where found for one cluster molecule and in which one Cu atom was identified to be only partially occupied. Unresolvable core structures are a common problem in single-crystal analysis of intermetalloid clusters. In $[Ni_xGa_y](Cp^*)_6$ for example, the Ga core of the cluster could not be unambiguously refined since the compound represents a co-crystallizate of several different cluster species. Likewise, the crystal structure of **7** does not allow for any conclusions about the geometry of the Au core. However, the crystal structure clearly establishes the core-shell arrangement of **7** with AlCp* at the cluster´s outside and Au being the core element, such as it is known for the corresponding Cu/Al chemistry.[92-93] The presence of Al in the core cannot be excluded on basis of the SC-XRD data alone. However, according to the sum-formulas determined by LIFDI-MS and the fact that AlCp* occupies the six "shell positions", a pure $[Au_7]$ kernel can be assumed. Due to the structural and chemical analogy of **7** to $[HCu_7Al_6](Cp^*)_6$, the structure of the latter can serve as a starting point for structure optimization at the DFT level of theory. Results of these calculations conducted by *Prof. Saillard et al.* will be presented in a publication in near future.

191

3. Results and Discussion
3.2. Chemical part: Synthesis characterization, reactivity

3.2.4.3 Synthesis and characterization of embryonic [Au$_2$Al$_5$](Cp*)$_5$ (**8**)

Synthesis

Heating of [^{i}DippAuH] with excess of AlCp* (> 1.5 eq.) leads to dark reaction solutions. Cooling of these solutions to -30 °C after filtration yields dark single crystals suitable for SC-XRD after several days (see Scheme 29). The refined single-crystal structure reveals the nature of the compound to be [Au$_2$Al$_5$](Cp*)$_5$ (**8**) (see Figure 79). According to *in situ* ^{1}H-NMR analysis of the reaction solution, **8** is not the only product of the reaction, but formed in parallel to **6** and **7** (see Figures S122-S124). *In situ* NMR and UV-Vis studies indicate the highest concentrations of **8** at high AlCp* stoichiometries and after prolonged reaction times (several days). **8** can be obtained in low yield (7 % based on Au) from these reaction solutions upon washing the isolated crystals with *n*-hexane. **8** is sensitive towards air and moisture but can be stored at room-temperature under argon without signs of decomposition.
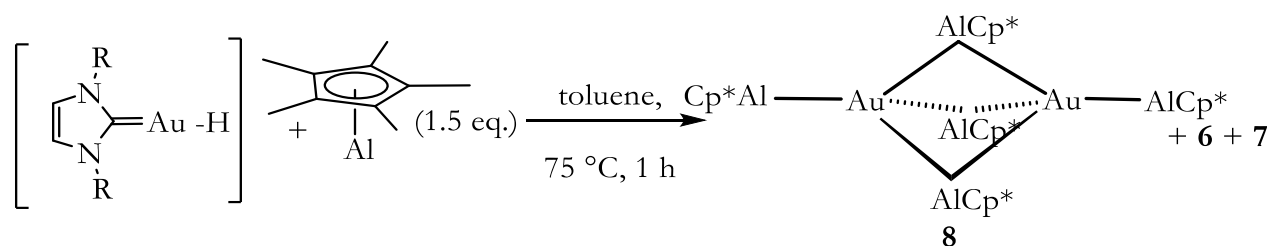
Scheme 29
Synthesis of [Au$_2$Al$_5$](Cp)$_5$ (**8**). R = 2,6-diisopropylphenyl.*

Crystallographic characterization

Compound **8** crystallizes in the monoclinic space group *P2$_1$/n* with four cluster molecules per unit cell and four molecules of co-crystallized toluene. Detailed crystallographic information is found in Table S11. **8** consists of a digold-centered trigonal-bipyramidal structure with idealized *D$_{3h}$* symmetry. The central Au$_2$ unit is surrounded by two terminal AlCp* units and three bridging AlCp* units. It is therefore regarded as gold analogon to the known cluster compounds [Pd$_2$(AlCp*)$_5$], [M$_2$(GaCp*)$_5$] (M= Pd, Pt) and [Ni$_2$(AlCp*)$_5$].[89, 267] Au-Al distances in **8** vary between 2.3972(15) Å (Au2-Al2) and 2.5566(14) Å (Au1-Al3) with a mean value of Au-AlCp*$_{terminal}$ = 2.4086 Å and Au-AlCp*$_{bridging}$ = 2.5485 Å. Interestingly, the Au-Al bonds to the terminal AlCp* units are slightly shorter than to the bridging AlCp* moieties, such as also observed in [Pd$_2$(AlCp*)$_5$].[89]

192

3. Results and Discussion

3.2. Chemical part: Synthesis characterization, reactivity
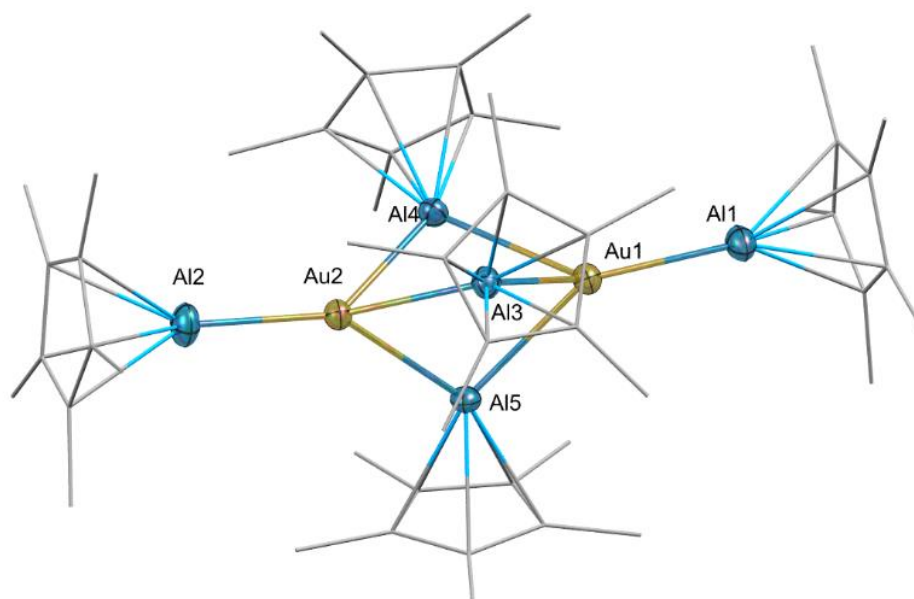
Figure 79

Molecular structure of [Au₂Al₅](Cp)₅ (**8**) in the solid state as determined by SC-XRD. Hydrogen atoms are omitted for clarity and organic ligands are drawn as wireframes. Color code: Au = yellow, Cu = orange, Al = blue. Interatomic distances [Å] and angles [°]: Au1-Au2: 3.881, Au1-Al1: 2.4200(15), Au1-Al4: 2.5565(14), Au1-Al3: 2.5566(14), Au1-Al5: 2.5651(14), Au2-Al2: 2.3972(15), Au2-Al3: 2.5358(14), Au2-Al4: 2.5365(14), Au2-Al5: 2.5404(14), Al1-Cp*centroid: 1.890, Al4-Cp*centroid: 1.993, Al2-Au2-Au1: 175.14, Cp*centroid -Al2-Au2: 176.09, Al2-Au2-Al4: 137.79(5), Al2-Au2-Al5: 144.36(5), Al2-Au2-Al3: 135.67(5), Al1-Au1-Au2: 174.69, Cp*centroid -Al1-Au1: 176.13, Al1-Au1-Al4: 136.46(5), Al1-Au1-Al5: 144.42(5), Al1-Au1-Al3: 138.27(5), Au2-Al4-Au1: 99.27, Au2-Al3-Au1: 99.29, Au2-Al5-Au1: 98.95(5).*

Crystallographically characterized Au-Al bonds are rare for molecular compounds. A Au->Al donor acceptor interaction was observed upon coordination of the Lewis pair Mes₂PC(=CHPh)Al(^{t}Bu) to Au-R (R = C₆F₅, CCPh).[268] However, the observed Au-Al distances in these compounds (2.897(2) Å, 2.758(1) Å, respectively) are significantly longer than in **8**. Au-Al distances in **8** are however well comparable to those in the trimetallic cluster [Ni(AuPPh₃)₆(AuCl)₃(AlCp*)] (2.596(5) Å – 2.633(6) Å).[269] Strongly polarized Au$^{\delta-}$-Al$^{\delta+}$ bonds of similar bond length (2.402(3) Å - 2.6045(18) Å) were identified in complexes of the [(NON)Al]⁻ aluminyl ligand (NON = 4,5-bis(2,6-diisopropylanilido)-2,7-di-tert-butyl-9,9-dimethylxanthene) with Au.[270] Noteworthy, The Au2-Al2 bond in **8** is with 2.3972(15) Å the shortest molecular Au-Al bond reported so far and well within the sum of the covalent radii of the two elements (2.57 Å).[271] Overall, Au-Al bond distances in **8** are slightly shorter than in the solid-state alloy AuAl₂ (2.58 Å).[272] Notably, the Au-Au distance in **8** (Au1-Au2= 3.881 Å) is much longer than in related dimeric molecules or small clusters featuring direct Au-Au bonding.[269, 273-274]

Al-Cp*$_{centroid}$ distances are very similar to the corresponding distances in other complexes and clusters of AlCp* with transition metals (*vide supra*). The central axis of **8** slightly deviates from linearity (Al2-Au2-Au1 = 175.14 ° and Al1-Au1-Au2: 174.69 °). This deviation from linearity is more pronounced than in the related molecules [Pd$_2$(AlCp*)$_5$] (Al-Pd1-Pd2 = 179.00(5) °)[89] and [Ni$_2$(AlCp*)$_5$] (Al-Ni1-Ni2 = 179.13(2) °)[267]. The bridging AlCp* units cap the central Au$_2$ unit with obtuse angles between 98.94 ° (Au2-Al5-Au1) and 99.29 ° (Au2-Al3-Au1). The bridging Al atoms Al3, Al4 and Al5 themselves span an almost equilateral triangle with Al-Al-Al angles close to 60 °.

Spectroscopic characterization of 8

The ^{1}H-NMR spectrum of **8** in benzene-d$_6$ exhibits two broad Cp* attributed signals at 2.19 ppm and 1.85 ppm with an integral ratio of 3:2, which are assigned to the bridging, the terminal, respectively, AlCp* moieties (see Figure S114). Noteworthy, a similar splitting of the signals is observed for the analogous Pd compound [Pd$_2$(AlCp*)$_5$], albeit with the terminal AlCp* signals being the higher down-field shifted. The ^{13}C-NMR spectrum of **8** in toluene-d$_8$ (see Figure S115) shows the two signals of the -CH_3 groups of the terminal and bridging AlCp* moieties at 13.65 ppm and 10.23 ppm. However, only one signal at 114.19 ppm is observed for the quaternary carbon atoms. Interestingly, despite the missing Au-Au bond in **8**, the compound is diamagnetic (formally 2 x 6s^1 configuration). The situation is likely to be similar to the one in diamagnetic Fe$_2$(CO)$_9$, in which there is no Fe-Fe bond, but rather a reordering of electron density to result formally in a Fe(-I) (18 VE) and a Fe(I) (16 VE) center. Electron deficiency is therefore delocalized on the two metal centers.

LIFDI-MS analysis of the isolated product shows the molecular ion peak {**8**-H}$^+$ as weak signal at m/z = 1203.4 (see Figure 80) besides several fragment species of **8**, such as {[AuAl$_2$](Cp*)$_2$}$^+$ (*m/z* = 521), {[AuAl$_3$](Cp*)$_3$}$^+$ (*m/z* = 683) and {[HAuAl$_4$](Cp*)$_4$}$^+$ (*m/z* = 845). Obviously, **8** is unstable under the measurement conditions; similar effects were observed for the embryonic Cu/Al cluster [Cu$_4$Al$_4$](Cp*)$_5$(Mes) (**11**), which did not yield a molecular ion signal at all. Further, the spectrum of isolated **8** shows the larger Au/Al clusters **6** and **7**, as well as numerous [Au$_x$(^{t}Dipp)$_y$]$^+$ aggregates. As the formation of **6** and **7** occurs in parallel during synthesis of **8**, slight impurities of these larger clusters in the final sample cannot be excluded. The presence of [Au$_x$(^{t}Dipp)$_y$]$^+$ is explained by their extremly high ionizability leading to intense signals even at very low concentrations.

3. Results and Discussion

3.2. Chemical part: Synthesis characterization, reactivity
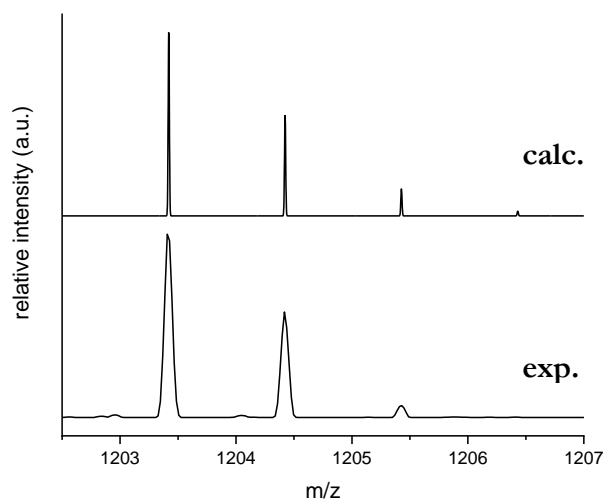
Figure 80
Comparison between experimentally observed (LIFDI-MS, positive ion mode, bottom) and calculated mass envelopes (top) of {[Au₂Al₅](Cp)₅ -H}.*

The IR spectrum of **8** (see Figure S116) shows the characteristic modes of the Cp* ligand, as well as the Al-Cp* stretching frequency at 455 cm^{-1} (*vide supra*). In consistency with the other analytical data, no signal of a surface bound hydride is observed in the spectrum. The UV-Vis spectrum of isolated **8** (see Figure S111 b)) consists of a broad, weak band at 516 nm, a band centered at 417 nm, as well as a broad and intense band at 406 nm. In the UV region, a sharp band at 331 nm is detected.

3.2.4.4 Mechanistic investigations

In situ studies of the synthesis of **6** and **7** were conducted mainly by *in situ* ^{1}H-NMR analysis and UV-Vis. Noteworthy, the signal positions of **6** , **7**, respectively are known from the isolated compounds (*vide supra*) by combinatoric comparison of their NMR spectra with LIFDI-MS spectra. However, in this specific case, LIFDI-MS is only of limited use for the analysis of the reaction solutions. The ^{i}Dipp ligand turned out to be extremely well ionizable and $[Au_x(^iDipp)_y]^+$ aggregates strongly dominate the spectra rendering the identification of Au/Al cluster peaks very difficult.

Reduction mechanism of Au(I)

Monitoring the reaction between [^{i}DippAuH] and AlCp* in a 1:1 molar ratio by *in situ* ^{1}H-NMR analysis indicates rapid consumption of the starting material at 75 °C. Compound **6** is identified as the major reaction product according to its Cp* attributed signal (see Figure S117) besides several other Cp* containing (cluster) products. LIFDI-MS analysis of the reaction solutions reveals the cluster $[Au_8Al_5](Cp^*)_5(^iDipp)$ as a very small peak besides the peaks attributed to **6** and **7**.

As a major side-product, uncoordinated ^{i}Dipp ligand is detected in the ^{1}H-NMR spectra. Detailed investigations of other ^{i}Dipp attributed species identifies [H_2AlCp*^{i}Dipp] as intermediate side product after short reaction times. Notably, the assignment of this species is based on *in situ* NMR test experiments between free ^{i}Dipp ligand and Cp*AlH$_2$ (detailed information on these reactions is found in Figures S127-S129 and summarized in Scheme S1). LIFDI-MS analysis of the reaction solutions also shows a signal of $\{[H_xAlCp^{*i}Dipp]\}^+$. Further heating of the reaction solution induces formation of HCp* as observed in ^{1}H-NMR analysis. Separate test reactions between excess ^{i}Dipp and H_2AlCp* showed formation of HAlCp*$_2$, HCp*, AlCp* and $\{[Al_2{}^iDipp_2H_5]\}^+$ upon heating of the reaction solutions. Notably, no significant hydrogen evolution is observed in the *in situ* ^{1}H-NMR spectra of the reaction between [^{i}DippAuH] and AlCp*.

The observations indicate reduction of Au(I) by AlCp* leading to liberation of ^{i}Dipp and formation of H_2AlCp*, undergoing a rich (dynamic) coordination chemistry with the free carbene ligand. Thereby, disproportionation of the adduct [H_2AlCp*^{i}Dipp] is supposed to lead - *via* HAlCp*$_2$ - to reformation of AlCp* and of HCp* as the final product of the reduction process of Au(I). Indeed, significant amounts of Cp*$_2$AlH are detected in *in situ* ^{1}H-NMR spectra of reactions between [^{i}DippAuH] and AlCp* at higher starting concentrations of AlCp*.

Size-focusing of cluster libraries

The influence of the stoichiometric ratio of the reactants applied on the **6:7** ratio obtained was investigated by ^{1}H-NMR spectroscopy. Reaction of [^{i}DippAuH] with 0.75 eq. of AlCp* results in enhanced formation of **7** as indicated by ^{1}H-NMR spectroscopy of the reaction solutions (see Figure S118). However, a size-focusing effect towards this species cannot be achieved by stoichiometry tuning alone.

As expected, the use of higher AlCp* concentrations (Au:Al = 1:1.25-1:1.5) results in preferred initial formation of **6**, such as expected by stoichiometric considerations (see Figures S119-S120). However, an additional cluster species (1.938 ppm) is then formed significantly, especially at Au:Al ratios of 1:1.5. Noteworthy, isolation of pure **6** is not possible from reactions at these Au:Al stoichiometries, rather **8** is isolated as reaction product. Addition of even higher AlCp* concentrations results in significant formation of **8** (see Figures S122-S124).

The size-focusing of the Au/Al libraries by the use of external additives is inspired by similar concepts in nanoparticle synthesis. [199-202] An interaction between the additive and the nanoparticles´ surface is thereby crucial to achieve selectivity by influencing the thermodynamic landscape and enabling novel reaction pathways.[201] PPh$_3$ was chosen as the additive of choice for the Au/Al cluster system, as phosphine ligands are known to stabilize Au clusters obtained by reduction from Au(I) precursors.[275] For example, the use of PPh$_3$ enabled selective synthesis of Au clusters, such as *Schmid´s* famous [Au$_{55}$](PPh$_3$)$_{12}$Cl$_6$ cluster.[50] However, PPh$_3$ is also known to be prone to ligand exchange reactions[276-277] and therefore seemed an ideal candidate for the stabilization of reaction intermediates in the [^{i}DippAuH] + AlCp* system by reversible coordination.

Addition of PPh$_3$ (10 eq.) to the reaction [^{i}DippAuH] and AlCp* (Au:Al = 1:1) induces preferred formation of cluster **7** as indicated by ^{1}H-NMR spectroscopy and UV-Vis spectroscopy (see Figure 49 and 50) . Selective size-focusing towards **7** is possible either by use of large amounts of PPh$_3$ (50 eq.) for a Au:Al stoichiometry of 1:1, or by use of a slight excess of Au (Au:Al = 1:0.75) in combination with moderate phosphine concentrations. For example, for a Au:Al stoichiometry of 1:0.75, already 1 eq. of PPh$_3$ proved to be sufficient to achieve selective formation of **7**. The observations indicate that selective formation of **7** occurs from preformed [L$_x$Au$_y$(PPh$_3$)$_z$] (y>z) aggregates (L = ^{i}Dipp, H, AlCp*), which are in equilibrium with free PPh$_3$ and Au precursor compound. Importantly, no reaction at all was observed between [^{i}DippAuH] and PPh$_3$ alone. This leads to the conclusion that the above mentioned [L$_x$Au$_y$(PPh$_3$)$_z$] aggregates are formed after the reduction step of Au(I) to

3. Results and Discussion
3.2. Chemical part: Synthesis characterization, reactivity

Au(0). Noteworthy, the observation of small amounts of coordinated PPh$_3$ in *in situ* ^{1}H-NMR spectra of the reaction is in line with this hypothesis (see Figure S121). Interestingly, species **6/7** themselves are prone to dynamic coordination of PPh$_3$, as their signals were shown to be slightly shifted in ^{1}H-NMR spectra of PPh$_3$ containing solutions. In ^{31}P-NMR spectra of the reaction solution, only one coalescence signal of all PPh$_3$ ligands is discernible at -5.35 ppm. It is noted that use of alternate phosphines like PMe$_3$ or P(OPh)$_3$ did not lead to comparable results, rather complete decomposition including the formation of Au mirrors occurred in these cases.

Formation and decay of [Au$_2$Al$_5$](Cp*)$_5$ (8)

In situ ^{1}H-NMR investigations of the reaction of [^{i}DippAuH] with excess of AlCp* reveals **8** to be formed in small amounts after prolonged reaction times (18 h, 75 °C) at a Au:Al ratio of 1:1.5. Applying even higher Al stoichiometries (Au:Al 1:2 – 1:3) leads to faster formation of **8** in parallel to the larger clusters **6** and **7** and remaining AlCp* ligand. Prolonged heating leads to increasing quantities of **8**, accompanied by decreasing signal intensities of **6**, **7** and AlCp*. It is concluded that **6** and **7** are formed as early (kinetic) products in the reaction between [^{i}DippAuH] and AlCp*, regardless of the stoichiometry applied. However, in the presence of AlCp* ligand, cluster degradation of **6** and **7** towards the smaller Au/Al cluster **8** takes place. Indeed, heating of a preformed, *in situ* generated solution of **6/7** with 2 eq. AlCp* leads to very slow formation of **8** as indicated by *in situ* ^{1}H-NMR analysis (see Figure S125).

Isolated **8** is quite temperature stable. *In situ* ^{1}H-NMR analysis of a solution of **8** kept at 75 °C for several hours shows no major changes besides formation of [H$_x$Au$_6$Al$_6$](Cp*)$_6$ (**6**) in trace amounts. Treatment of isolated **8** with [^{i}DippAuH] (2 eq.) at 75°C results in a rapid color change from dark green to red. *In situ* ^{1}H-NMR of the solution indicates complete consumption of **8** already after 30 minutes reaction time and formation of [H$_x$Au$_6$Al$_6$](Cp*)$_6$ (**6**) in addition to an unknown Cp* containing species (see Figure S126). As expected, [AlCp*H$_2$^{i}Dipp] is identified as major side-product besides some unreacted [^{i}DippAuH]. LIFDI-MS analysis of the solution reveals **6** and [H$_x$Au$_7$Al$_6$](Cp*)$_6$ (**7**) as the only Au/Al cluster products. The results clearly demonstrate that **8** is a building block for the generation of larger nuclearity Au/Al clusters upon addition of Au(I) sources. **6** unambiguously is a product of these cluster growth reactions. Whether **7** also is amongst the reaction products, however, is not clear so far, as it could only be identified in LIFDI-MS analysis but not in the ^{1}H-NMR spectrum of the reaction solution. Interestingly, **8** therefore behaves almost identical as triangular [Cu$_2$Al](Cp*)$_3$ does upon addition of [CuMes] (*vide supra*).

198

3.2.4.5 Outlook and Perspectives for Au/Al cluster libraries

Synthesis of trimetallic Cu/Au/Al clusters

In analogy to the reaction between triangular $[Cu_2Al](Cp^*)_3$ (**9**) and $[H_6Cu_6](PPh_3)_6$, **9** was reacted with [^{i}DippAuH]. As expected, *in situ* ^{1}H-NMR of the reaction (stoichiometry of reactants 1:2) reveals formation of the very stable half-sandwich complex [Cp*Cu^{i}Dipp] (see Figure S130). However, LIFDI-MS analysis of the reaction solution did not yield any detectable cluster signal. It is supposed that the reaction yields very large clusters, probably escaping LIFDI-MS analysis at this point of methodical development due their large m/z ratio. Therefore, the stoichiometry of reactants was varied and PPh$_3$ was additionally added to the solutions to achieve cleavage of **11** by formation of [Cp*CuPPh$_3$]. The different stoichiometric ratios between the reactants applied is listed in Table 7.

Table 7
*Different stoichiometric ratios of reactants tested in the reaction $[Cu_2Al](Cp^*)_3$ (**9**) + [^{i}DippAuH] + PPh$_3$.*

experiment number	**9**	[^{i}DippAuH]	PPh$_3$
A	1	1	1
B	1.5	1	2
C	5	4	5

When **9** is reacted with [^{i}DippAuH] and one equivalent of PPh$_3$ (conditions A), LIFDI-MS of the reaction solution reveals mainly formation of **6** and **7** (see Scheme 30 a)). However, also the trimetallic cluster $[Au_6CuAl_6](Cp^*)_6$ is detected at m/z = 2217.3, besides several other trimetallic clusters with albeit very small signal intensity (see Figure S132). ^{1}H-NMR analysis in toluene-d$_8$ of the reaction (see Figure S131) likewise shows the signals attributed to **6** and **7**, in addition to a novel Cp* cluster signal at 1.97 ppm, which is therefore assigned to $[H_xAu_6CuAl_6](Cp^*)$. As expected, [Cp*CuPPh$_3$] and [^{i}DippCuCp*] are observed as side-products of the reaction. Cooling the filtered reaction solution to -30 °C for several months yields small black crystals suitable for SC-XRD in very small yield. The refined crystal structure as determined in the solid-state is shown in Figure 81 and detailed crystallographic information is summarized in Table S11. It consists of a [Au$_4$] quadrangle capped by two apical AlCp* ligands, three horizontal AlCp* ligands, as well as one horizontal CuCp* moiety. Unfortunately, the synthesis of $[Au_4CuAl_5](Cp^*)_6$ (**13**) could not be reproduced so far, nor could a molecular ion peak of the species be found in the

3. Results and Discussion
3.2. Chemical part: Synthesis characterization, reactivity

LIFDI-MS spectrum of the reaction solution or the isolated precipitate. Obviously, $[Au_4CuAl_5](Cp^*)_6$ is only a minor fraction of the formed cluster library and separation of its crystals from side products is hardly feasible due to their identical color (black). A size-focusing towards $[Au_4CuAl_5](Cp^*)$, *i.e.* a selective synthesis, could not be achieved so far. However, the results (LIFDI-MS and SC-XRD) clearly demonstrate that synthesis of trimetallic Au/Cu/Al clusters is possible from **9** and [*i*DippAuH].
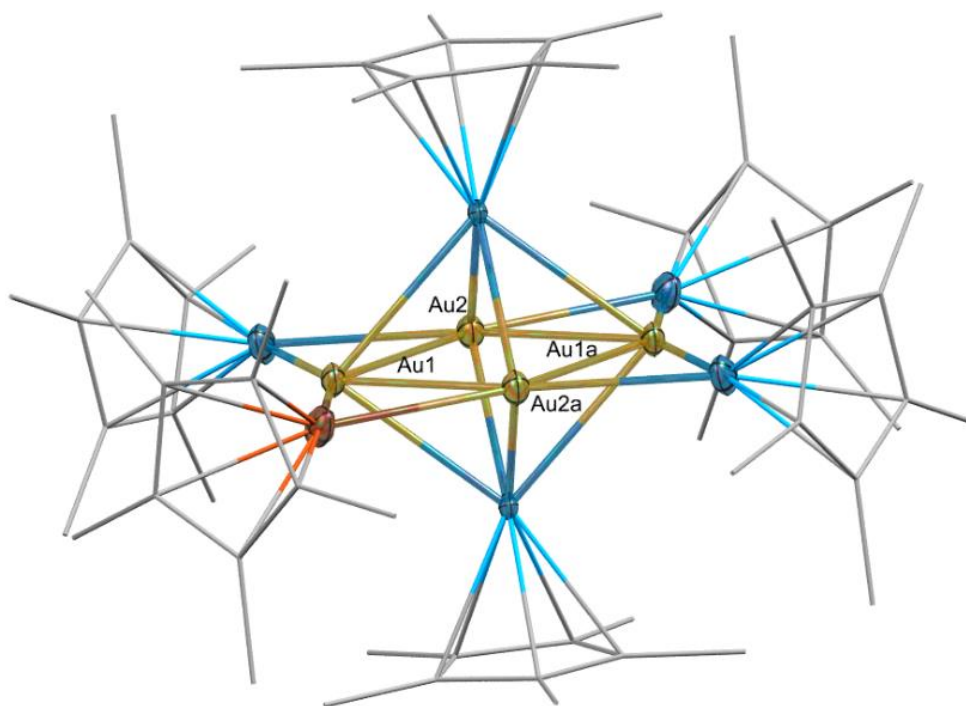
Figure 81
Molecular structure of [Au₄CuAl₆](Cp)₆ (**13**) in the solid state as determined by SC-XRD. Note that no reproducible synthetic access to this compound could be found so far. Hydrogen atoms are omitted for clarity and organic ligands are drawn as wireframes. Color code: Au = yellow, Cu = orange, Al = blue. Interatomic distances [Å] and angles [°]: Au1-Al$_{apical}$ = 2.675(6), Au1-Al$_{horizontal}$ = 2.522(3), Au2-Al$_{apical}$ = 2.664(4), Au2-Al$_{horizontal}$ = 2.528(3), Au1-Au2 = 2.7764(8), Au2-Cu = 2.528(3), Au1-Cu = 2.522(3), Cp$_{centroid}$-Al$_{apical}$ = 1.941, Cp$_{centroid}$-Cu = 1.896 = Cp$_{centroid}$-Al$_{horizontal}$, Cu-Au1-Au2a = 56.74, Au1-Au2-Au1a = 89.53, Al1-Au2-Al$_{apical}$ = 85.58, Cp*$_{centroid}$-Al$_{apical}$-Al$_{apical}$ = 146.82, Au1-Au2-Al$_{apical}$ = 58.45.*

In the experiments B and C, a slight excess of **9** with respect to [*i*DippAuH] was used. In experiment C, 20 % of all CuCp* units of **9** were thought to be left uncoordinated by *i*Dipp or PPh₃ in order to favor Cu incorporation into the formed cluster species. Indeed, in both experiments, enhanced formation of trimetallic

200

clusters was observed in LIFDI-MS analysis of the reaction solutions (see Figure 82, Figures S133-S135 and Table 8).

The reaction conditions are summarized in Scheme 30 b).

Table 8
Intensity of cluster peaks observed in LIFDI-MS spectra of the experiments A, B and C in Table 7.

ion peaks in LIFDI-MS	conditions A	conditions B	conditions C
$[Au_7Al_6](Cp^*)_6$	*intense*	*medium*	*intense*
$[Au_6Al_6](Cp^*)_6$	*intense*	*weak*	*weak*
$[Au_6CuAl_6](Cp^*)_6$	*medium*	*medium*	*intense*
$[Au_5Cu_2Al_6](Cp^*)_6$	*weak*	*medium*	*medium*
$[Au_5CuAl_6](Cp^*)_6$	very weak	*medium*	*weak*
$[Au_4Cu_3Al_6](Cp^*)_6$	*weak*	*intense*	*medium*
$[Au_4Cu_2Al_6](Cp^*)_6$	*very weak*	*intense*	*weak*
$[Au_3Cu_4Al_6](Cp^*)_6$	*weak*	*intense*	*weak*

3. Results and Discussion
3.2. Chemical part: Synthesis characterization, reactivity

a)

$$[Cu_2Al](Cp^*)_3 \ + \ [^iDippAuH]$$

9   1 eq.

1 eq.

1 eq. PPh$_3$ → $[H_xAu_6Al_6](Cp^*)_6 \ + \ [H_xAu_7Al_6](Cp^*)_6$

6   **7**

$+ \ [Au_4CuAl_5](Cp^*)_6 \ + \ [Cp^*Cu\text{-}L]$

13

10 eq. PPh$_3$ → $[H_xAu_7Al_6](Cp^*)_6 \ + \ [Cp^*Cu\text{-}L]$

7

b)

$$[Cu_2Al](Cp^*)_3 \ + \ [^iDippAuH] \ \xrightarrow{1.25 - 2 \text{ eq. PPh}_3} \ [H_xAu_yCu_zAl_6](Cp^*)_6 \ + \ [Cp^*Cu\text{-}L]$$

9

1.25 - 1.5 eq.   1 eq.

y + z = 6/7

3 < y < 7
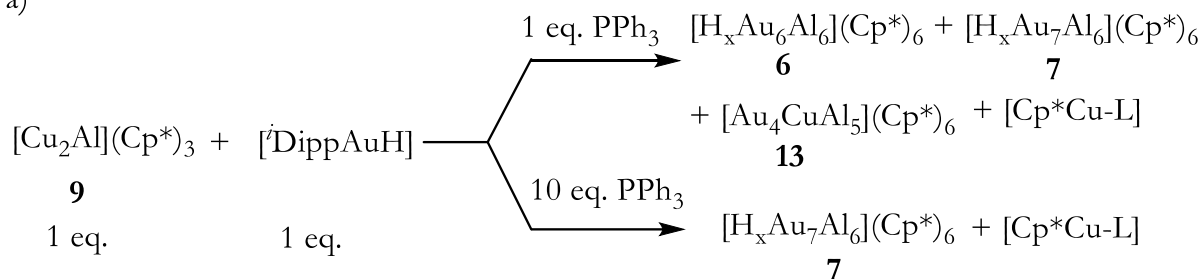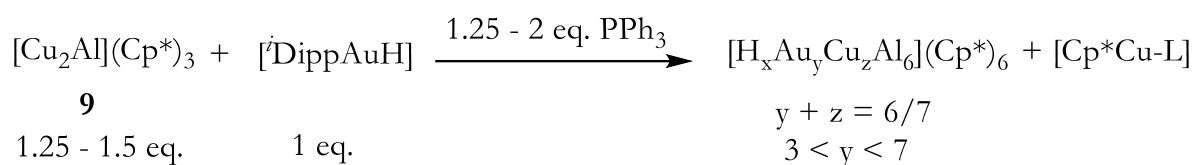
ternary cluster libraries

Scheme 30
Reaction equations for the conversion of [Cu₂Al](Cp)₃ (**9**) with [ⁱDippAuH] upon addition of PPh₃. L = PPh₃ / ⁱDipp. a) Use of a 1:1 stoichiometric ratio between **9** and [ⁱDippAuH] leads to the Au/Al clusters **6**/**7** upon cleavage of triangular **9** with PPh₃. [Au₄CuAl₅](Cp*)₆ (**13**) and other ternary Au/Cu/Al clusters are only observed as side-products. Use of large amounts of PPh₃ (10 eq.) reproduces the selective synthesis of **7**, as in the use of AlCp* instead of **9**. b) Use of slight excess of [Cu₂Al](Cp*)₃ leads to ternary Au/Cu/Al cluster libraries as observed in LIFDI-MS analysis.*
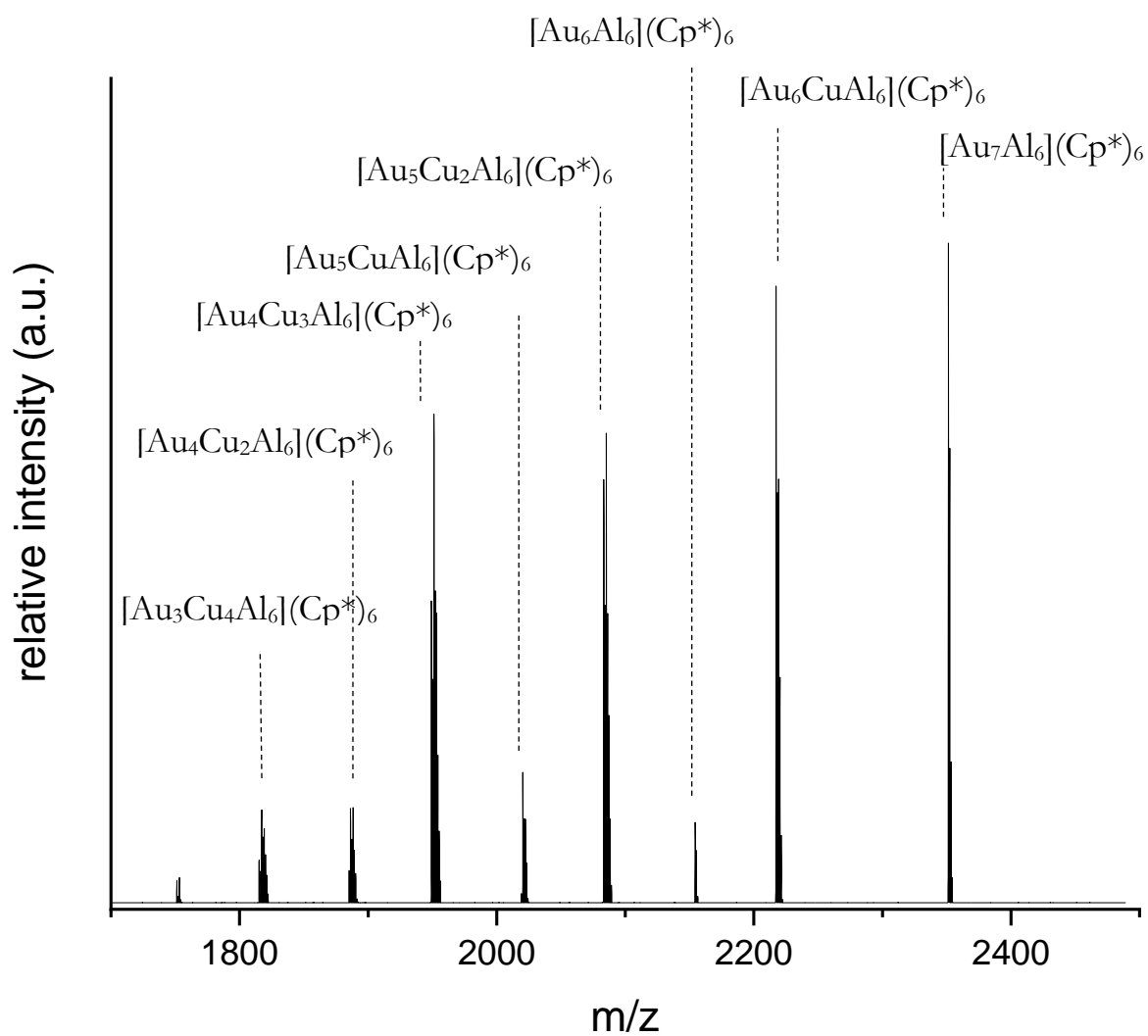
Figure 82
*A ternary cluster library: In situ LIFDI-MS spectrum of the reaction **9** + [^{i}DippAuH] + PPh$_3$*
(5:4:5) (75 °C, 2 h, entry C in Table 7).

4. Conclusion

In this work, *"living libraries"* of intermetalloid, Cp* ligated clusters in solution were systematically investigated using a novel approach based on *in situ* LIFDI-MS analysis and supported by *in situ* NMR and UV-Vis spectroscopy. Specifically, cluster growth and reactivity pathways were investigated for the systems Cu/Zn, Cu/Al and Au/Al.

The Cu/Zn "nano-brass" library $[Cu_aZn_b](Cp^*)_c(Mes)_d$ ((a+b) ≥ (c+d)), obtained by reaction of the organometallic precursors [CuMes] and $[Zn_2](Cp^*)_2$, was in detailed analyzed by LIFDI-MS analysis. A novel algorithm enabling a fundamental understanding of this and related systems is presented. It starts with identification of mass peaks by means of labeling experiments (Cp^{*Et}, ^{68}Zn). Subsequently, the fragmentation behavior was assessed by stepped collision energy experiments in the HCD cell /orbitrap system, which is unprecedented for the LIFDI ionization technique. By this, the molecular ions present in the cluster solution could be revealed. In collaboration with the group of *Prof. Saillard* (*Rennes*) and *Prof. Da Silva* (*São Paulo*), theoretical analysis of selected cluster candidates including *ab initio* structure optimizations was initiated. Finally, the reactivity of the Cu/Zn library towards CO_2 and H_2 was investigated, conceptually motivated by the use of Cu/Zn(O) materials as catalysts for methanol production from CO_2/H_2 or CO/H_2. Using LIFDI-MS, two specific clusters from the original library were shown to undergo CO_2 uptake after reductive elimination of ligands or ligand-metal fragments. The sum formulas of the thus obtained adducts could unambiguously be addressed by means of labelling experiments ($^{13}CO_2$, ^{68}Zn, Cp^{*Et}). Subsequent treatment of the obtained libraries with H_2 leads to the production of formate, however, no exact reaction pathway can be presented so far.

The power of mass-spectrometric methods for the assessment of subtle reactivity differences between species in mixtures is further demonstrated for the isolable Cu/Al micro-library $[Cu_{7/8}Al_6](Cp^*)_6$. Whereas the closed-shell superatom $[Cu_8Al_6](Cp^*)_6$ is rather inert, the radical nature of the open-shell superatomic $[Cu_7Al_6](Cp^*)_6$ cluster is reflected in its reactivity towards addition of one Cu core atom leading to $[Cu_8Al_6](Cp^*)_6$, and as well by its ability to undergo σ(C-H) and σ(Si-H) activation reactions of toluene and $(TMS)_3SiH$ (TMS= tris(trimethylsilyl)) leading to the hydride species $[HCu_7Al_6](Cp^*)_6$. Subtle differences of one H atom, such as between $[Cu_7Al_6](Cp^*)_6$ and $[HCu_7Al_6](Cp^*)_6$ are well recognized by the LIFDI-MS technique.

UV-Vis in combination with ^{1}H-NMR and LIFDI-MS analysis was used to monitor the composition of Au/Al libraries obtained from [*i*DippAuH] and AlCp*. For the

4. Conclusion

first time, addition of phosphine additives into the cluster formation reaction was found to result in highly enhanced selectivity regarding the cluster reaction products. Whereas $[H_xAu_6Al_6](Cp^*)_6$ and $[H_xAu_7Al_6](Cp^*)_6$ were shown to be the major components in reaction mixtures with a Au:Al stoichiometry of 1:1, addition of PPh$_3$ to the reaction mixture enabled a selective synthesis of $[H_xAu_7Al_6](Cp^*)_6$. The size-focusing process towards this species was quantified by UV-Vis analysis. Further optimization of the Au:Al stoichiometry led to isolation of the first embryonic Au/Al cluster $[Au_2Al_5](Cp^*)_5$. $[Au_2Al_5](Cp^*)_5$ was found to be formed out of larger Au/Al clusters ($[H_xAu_{6/7}Al_6](Cp^*)_6$) upon AlCp* exposure. The reaction sequence can be inverted by reacting "embryonic" $[Au_2Al_5](Cp^*)_5$ with Au(I) sources to access larger Au/Al nuclearities.

In the course of the above mentioned investigations, the new Cu/Zn clusters $[Cu_{10}Zn_2](Cp^*)_2(Mes)_6$ and $[Cu_4Zn_{9/10}](Cp^*)_8$ were discovered and fully characterized. Synthesis of the cluster $[CuZn_{10}](Cp^*)_7$ was reproduced and the product was fully characterized. Whereas $[CuZn_{10}](Cp^*)_7$ represents a 18 VE complex of Cu, $[Cu_{10}Zn_2](Cp^*)_2(Mes)_6$ can be interpretated as 6 electron superatom with prolate distortion from spherical symmetry. The three novel Cu/Zn clusters therefore represent the phase diagram of brass on a molecular level with the co-crystallizate $[Cu_4Zn_{9/10}](Cp^*)_8$ being the molecular analogue to the rich structural diversity of Hume-Rothery phases. Further theoretical analysis of this molecule will be presented soon.

In the [CuMes] + AlCp* system, cluster growth reactions were explored and monitored by *in situ* LIFDI-MS and ^{1}H-NMR. Feedback into experimental design allowed for an informed choice and precise adjustment of reaction conditions and led to isolation of the intermetallic cluster $[Cu_4Al_4](Cp^*)_5(Mes)$. It reacts with excess of 3-hexyne to yield the triangular cluster $[Cu_2Al](Cp^*_3)$. The two embryonic clusters $[Cu_4Al_4](Cp^*)_5(Mes)$ and $[Cu_2Al](Cp^*)_3$, respectively, were fully characterized and shown to be intermediates in thermally and chemically induced cluster growth reactions leading to formation of the inseparable mixture of the closely related clusters $[Cu_7Al_6](Cp^*)_6$, $[HCu_7Al_6](Cp^*)_6$ and $[Cu_8Al_6](Cp^*)_6$.

Working with mixtures of compounds is well established in biochemistry (proteomics) and combinatorial chemistry. In this dissertation, principles from these disciplines were for the first time successfully transferred to the field of organometallic, Hume-Rothery inspired cluster chemistry in solution. Many obstacles might still be on the way when dealing with the fascinating world of metal rich molecules and clusters. Nevertheless, the presented concepts and approaches combining experiments and theory might enable a more fundamental and systematic

4. Conclusion

understanding of the rich chemistry of intermetalloid clusters in solution and of their reactivity towards molecules of industrial or social interest.

5. Experimental

5.1 Materials and Methods

Spectroscopy

NMR spectra were recorded on a Bruker Avance III AV400US (1H, 400 MHz) and a Bruker Avance II 500 with a cryo-probe (13C, 125 MHz). The deuterated solvents were degassed and stored over molecular sieves. Chemical shifts are given relative to TMS and were referenced to the residual solvent peak as internal standards. Chemical shifts are reported in parts per million, downfield shifted from TMS, and are consecutively reported as position (δH or δC), relative integral, multiplicity (s = singlet, d = doublet, q = quartet and m = multiplet) and assignment. Variable temperature (VT) NMR spectra were recorded on a Bruker DRX 400 spectrometer (1H, 400 MHz). FT-IR spectra were measured in an ATR setup with a Bruker Alpha FTIR spectrometer under an inert gas atmosphere in a glove-box. Raman scattering was performed on a Renishaw inVia Raman microscope RE04 using an excitation wavelength of 532 nm. Abbreviations for vibration spectroscopy data is as follows: s = sharp, b = broad, i = intense, w = weak. UV-Vis spectra were measured in toluene under inert atmosphere in quartz cuvettes (d = 1 cm) with an Agilent Carry 60 spectrometer.

Elemental Analysis (EA)

EA measurements were conducted in the Microanalytical Laboratory Kolbe in Mülheim an der Ruhr.

Spectrometry

Mass spectrometry was conducted on filtered solutions with an Exactive™ PlusOrbitrap system from the Thermo Scientific company and a Micromass LCT-QTOF-Micro mass spectrometer; Ionisation method: Liquid injection field desorption ionization (LIFDI; special ionization cell obtained from Linden CMS GmbH, Leeste, Germany; http://www.linden-cms.de), solvent: toluene. The sample is applied on a tungsten wire which is coated with thousands of micro graphite dendrites. By applying a potential between the emitter and the counter electrode of 10 kV the sample molecules are ionized and subsequently accelerated to the counter

electrode and eventually to the detector. The resulting ions are radical cations, *e.g.* [M]•+.

GC-MS measurements

A few drops of water were added to the respective diluted reaction solution in toluene. The mixture was filtered over neutral aluminium oxide and afterwards again over standard filter paper. Measurements were conducted with an Agilent GC-7890 with Autosampler.

TEM measurements

TEM measurements were performed and interpreted by Tomanec Ondřej and Prof. Radek Zboril (Regional Center of Advanced Technologies and Materials, 78371 Olomouc, Czech Republic).

Samples were measured by High Resolution Transmission Electron Microscope (HRTEM) Titan G2 (FEI) with Image corrector on accelerating voltage 80 kV. STEM images were taken with HAADF detector 3000 (Fishione). Energy Dispersive Spectrometry (EDS) was performed by Super-X system with four silicon drift detectors (Bruker).

X-ray photoelectron spectroscopy (XPS)

XPS measurements were conducted by Tim Kratky (chair of physical chemistry, Prof. Günther).

X-ray photoelectron spectra were recorded on a *Leybold-Heraeus* LHS 10 spectrometer using a non-monochromatized Al K_α source (1486.7 eV). The cluster samples were drop-casted on a Si wafer. Sample preparation and transfer into the XPS spectrometer were carried out under argon atmosphere.

The analyzer was operated at a constant pass energy of 100 eV leading to an energy resolution with a full width at half-maximum (fwhm) of ~1.1 eV. The energy scale of the spectra was corrected for sample charging by using the C 1s signal (284.5 eV, adventitious carbon). All spectra were recorded in an ultra-high vacuum chamber at a pressure below 5×10^{-8} mbar. Core level spectra were deconvoluted by using Voigt functions and linear background subtraction.

5. Experimental
5.1 Materials and Methods

X-ray crystallography

Single crystal Xray crystallography was in part performed by Dr. Christian Jandl for the compounds **1$_H$/2** *(data collection and interpretation) and for pure* **2** *(data collection). Data interpretation was conducted by Dr. Wilhelm Klein for the compounds* **8** *and* **13**.

Data were collected on a single crystal x-ray diffractometer equipped with a CMOS detector (Bruker APEX III, ϰ-CMOS), a TXS rotating anode or an IMS microsource (see Tables S4, S6, S11) with MoK$_\alpha$ radiation (λ = 0.71073 Å) and a Helios optic using the APEX3 software package.[278] Measurements were performed on single crystals coated with perfluorinated ether. The crystals were fixed on top of a kapton micro sampler and frozen under a stream of cold nitrogen. A matrix scan was used to determine the initial lattice parameters. Reflections were corrected for Lorentz and polarisation effects, scan speed, and background using SAINT.[279] Absorption correction, including odd and even ordered spherical harmonics was performed using SADABS.[280] Space group assignments were based upon systematic absences, E statistics, and successful refinement of the structures. The structures were solved using SHELXT with the aid of successive difference Fourier maps, and were refined against all data using SHELXL-2014/2017 in conjunction with SHELXLE.[281-283] Hydrogen atoms were calculated in ideal positions as follows: Methyl hydrogen atoms were refined as part of rigid rotating groups, with a C–H distance of 0.98 Å and $U_{iso(H)}$ = 1.5·$U_{eq(C)}$. Other H atoms were placed in calculated positions and refined using a riding model, with methylene and aromatic C–H distances of 0.99 Å and 0.95 Å, respectively, other C–H distances of 1.00 Å, all with $U_{iso(H)}$ = 1.2·$U_{eq(C)}$. Non-hydrogen atoms were refined with anisotropic displacement parameters. Full-matrix least-squares refinements were carried out by minimizing $\Sigma w(F_o^2 - F_c^2)^2$ with the SHELXL weighting scheme.[282] Neutral atom scattering factors for all atoms and anomalous dispersion corrections for the non-hydrogen atoms were taken from *International Tables for Crystallography*.[284] A split layer refinement was used for disordered groups and additional restraints on distances, angles and anisotropic displacement parameters were employed to ensure convergence within chemically reasonable limits, if necessary. Heavily disordered co-crystallized solvent molecules were treated as a diffuse contribution to the overall scattering without specific atom positions using the PLATON/SQUEEZE procedure.[285] Images of the crystal structures were generated with Mercury and Povray (polyhedral illustrations).[286-287]

5. Experimental

5.1 Materials and Methods

Computational Details

Computational work was carried out by Prof. Saillard et al. and Prof. Da Silva et al. The following experimental descriptions are therefore written by these collaboration partners.

Atomic Structure Generation for Theoretical Total Energy Calculations

The initial atomic structure configurations for clusters $[CuZn_{10}](Cp^*)_7$, $[Cu_{10}Zn_2](Cp^*)_2(Mes)_6$ and $[Cu_4Zn_{9/10}](Cp^*)_7$ were obtained as follows: The initial cluster frameworks determined by X-ray diffraction (XRD) were considered. However, the occupation of the metal sites by Cu or Zn is not fully ascertained by XRD, owing to their closeness in atomic numbers. Thus, the occupation of the metal sites was determined by total energy density functional theory (DFT) calculations. We generated several trial configurations using the XRD frameworks in which the Cu *vs.* Zn occupation of the metal sites were randomly fixed, keeping the chemical composition of the clusters fixed, in order to identify the lowest energy positional isomer. Although the number of sites is relatively small, the number of trial configurations is large due to the many possible combinations. Hence, it has a substantial computational cost. Thus, we employed the K-means algorithm to remove similar trial configurations, reducing the initial set to a smaller set of trial structures on which full geometry optimization were performed.

Theoretical Ab initio Total Energy Calculations

Our total energy calculations were based on the spin-polarized density functional theory (DFT) framework within the Perdew–Burke–Ernzerhof (PBE) formulation for the exchange-correlation energy functional.[209] The Kohn–Sham (KS) orbitals were expanded using numeric atom-centered orbitals (NAOs), as implemented in the all-electron full-potential Fritz–Haber institute ab initio molecular simulations (FHI-aims) package.[208] In the FHI-aims framework, we employed the second improvement of the minimal basis set for the NAOs, namely, the light-tier 2 (following the FHI-aims terminology).[208] The electrons were described by the zero-order regular approximation (atomic ZORA).[288] For the self-consistency of the electron density, we employed a total energy criterion of $1 \times 10-5$ eV along with a Gaussian broadening parameter of 1 meV, which is crucial to avoid possible fractional electron occupation of the electronic states near the highest occupied molecular orbitals

5. Experimental

5.1 Materials and Methods

(HOMO) and lowest unoccupied molecular orbital (LUMO). The geometry optimizations were carried out using the modified Broyden–Fletcher–Goldfarb–Shanno (BFGS) algorithm. The equilibrium geometries were found once the atomic forces on all atoms were smaller than 0.025 eV/Å.

Electronic Structure Analysis

The FHI-aims lowest energy configurations of $[CuZn_{10}](Cp^*)_7$ and $[Cu_{10}Zn_2](Cp^*)_2(Mes)_6$ (see above), which incidentally coincide with their XRD structures, were thereafter fully optimized with the Amsterdam Density Functional (ADF2017) code[210, 289] using the BP86 functional[290-291] together with Grimme's empirical DFT-D3 corrections[291] and the ADF standard STO-TZ2P basis set. Analytical computations of vibrational frequencies were performed for ascertaining their energy minimum nature for all cluster compounds analyzed. Electronic structures were analyzed with the help of the ADF-GUI graphical interface.[292] Natural atomic orbital (NAO) populations and Wiberg bond indices were computed with the natural bond orbital NBO6.0 program[293] implemented in the ADF2017 package. The NMR chemical shifts were computed according to the gauge-independent atomic orbitals (GIAO) method assuming the Zero Order Regular Approximation (ZORA) for the $S = \frac{1}{2}$ complex $[Cu_7Al_6](Cp^*)_6$.[294]

General procedure (work-flow) for computerized peak identification in LIFDI-MS

Mass spectra evaluation was carried out with a computer program written by Dr. Christian Gemel ("MassSpecApp"). The basic principles of the program and work-flow are described in the following.

The program starts spectrum analysis by automated pattern recognition. Local maxima above a given treshold value (parameter can be changed by the user; default is 10^{-2} with respect to the highest peak in the spectrum) are recognized as peaks. Thereafter, the peaks are automatically grouped into peakgroups and subsequently (isotopic) patterns by a recursive process. The algorithm starts at the highest remaining peak in the peaklist and searches to the left and to the right for peaks that are distant by an exact m/z shift of $1/z$ from each other (within a given error range ε, can be changed by the user). The charge z is provided as input value (default z = 1, can be changed by the user). When a peak is recognized as part of a peakgroup, it is deleted from the peaklist. The condition for interrupting the recursive process is the absence of a peak in the peaklist. The result of this process is a list of peakgroups, which are then further considered as isoptopic patterns when they contain a minimum number of peaks (default is 5; parameter can be changed by the user).

5. Experimental
5.1 Materials and Methods

For the process of pattern analysis, the user provides a list of possible fragments by loading a file. This list contains all "fragments" (metal atoms, ligands, solvents, etc...) the observed ions could possibly consist of. The program then generates weight matches for each pattern by combining these fragments to ions in a recursive process. For each pattern which is analyzed, all possible fragment combinations up to the m/z value of the respective pattern are calculated The pattern centroid (intensity weighted average, $(m/z)_{\text{centroid}}$) is used as the experimental average weight. All those fragment combinations are accepted which molar weight M_w falls into the range:

$$(m/z)_{\text{centroid}} - 2.1 < M_w < (m/z)_{\text{centroid}} + 4.1 \quad (1.9)$$

The subtraction of 2.1 accounts for a possible loss of 2 hydrogen atoms and the addition of 4.1 accounts for the possibility of up to four additional hydrogens, which are not part of the individual fragments (*e.g.* hydride ligands). The result is a list of fragment formulas for each pattern, which fulfill the above weight criterium. Since this list is very often extremely long (depending on the m/z values of the patterns and the M_W of the individual fragments), the pattern analysis continues by a "sieving" step. First, the isotopic patterns for each fragment (= sum formula) are calculated by the EnviPat algorithm.[295] By comparing the exact m/z values of the calculated and the experimental patterns, an "offset" value is calculated, *i.e.* an exact m/z difference between each experimental and the corresponding calculated peak. Only those patterns are further considered, which have an average offset value below a given threshold (default 0.2, can be changed by the user). The program thereafter calculates the goodness of fit value "GoF" of the experimental pattern to the calculated one and of the calculated one to the experimental one. The formulas for these "GoF$_{\text{experimental to calculated}}$" (GoF $_{\text{exp. to calc.}}$) and "GoF$_{\text{calculated to experimental}}$" (GoF $_{\text{calc. to exp.}}$) are as follows:

$$GoF_{calc.to\ exp.} = \frac{\sum_j(\frac{I_j}{\alpha} - T_j)^2}{\sum_j T_j^2} \quad with\ \alpha = \frac{\sum_j I_j T_j}{\sum_j T_j^2} \quad (2.0)$$

$$GoF_{exp.\ to\ calc.} = \frac{\sum_j(\frac{T_j}{\alpha} - I_j)^2}{\sum_j I_j^2} \quad with\ \alpha = \frac{\sum_j I_j T_j}{\sum_j I_j^2} \quad (2.1)$$

In these formulas, j denotes the individual isotopic peaks inside the pattern. I_j is defined as intensity of the jth peak in the calculated pattern and T_j as the intensity of the jth peak in the experimental pattern.

5. Experimental
5.1 Materials and Methods

A total GoF between 0 (identical patterns) and 1 (no fit at all) is finally calculated as the average between "GoF$_{\text{experimental to calculated}}$"and "GoF$_{\text{calculated to experimental}}$". In the output file, for every pattern, the possible pattern matches are listed with their corresponding GoF$_{\text{final}}$ value. The patterns can also be visually compared to the calculated ones of the pattern matches.

Sometimes (especially for Cu/Zn libraries), several matches are found with very similar GoF$_{\text{final}}$ values. By comparing the results of Cp*, Cp*$^{\text{Et}}$ and ^{68}Zn labeled spectra, in most of the cases, only one final pattern match is identified.

General procedure for the analysis of fragmentation behavior in LIFDI-MS by CE vs. I plots

LIFDI-MS spectra of the Cu/Zn libraries were recorded at a heating rate of the emitter of 60 mA/s at (normalized) collision energies of 10, 11, 12, 13, 14, 15, 17 and 18. Every measurement was conducted at least 5 times under the same conditions for determination of the variation coefficient of the peak intensity.

Integrals of the peaks of interest in the mass spectra were determined by an in-house computer programm written by *Dr. Christian Gemel.* The integrals determined are relative integrals with respect to the total integral of the spectrum.

For every collision energy, the average peak intensity $\bar{I}$ was calculated. The coefficient of variation of the peak intensity $\sigma(I)$ was calculated by the following formula:

$$\sigma(I) = \sqrt{\frac{\sum_i (x_i - \bar{I})^2}{(n-1)}} \quad (2.2)$$

x_i denotes the measured *i*-th peak intensity and n denotes the total number of measurements at this collision energy. The coefficient of variation of the respective average peak intensity $\sigma(\bar{I})$ was thereafter calculated as follows:

$$\sigma(\bar{I}) = \frac{\sigma(I)}{\sqrt{n}} \quad (2.3)$$

For analysis of the fragmentation behavior, *CE* was plotted against $\bar{I}$ with error bars corresponding to $\pm \ \sigma(\bar{I})$. For the ease of analysis, linear regression analysis was

5. Experimental

5.1 Materials and Methods

conducted for CE = 10 – 15 and for CE = 10 -17. For this, the following weighted sums are defined:

$$S = \sum_i \frac{1}{\sigma_i^2} \quad (2.4)$$

$$S_{CE} = \sum_i \frac{CE_i}{\sigma_i^2} \quad (2.5)$$

$$S_I = \sum_i \frac{x_i}{\sigma_i^2} \quad (2.6)$$

$$S_{CE \cdot I} = \sum_i \frac{CE_i \cdot x_i}{\sigma_i^2} \quad (2.7)$$

$$S_{CE^2} = \sum_i \frac{CE_i^2}{\sigma_i^2} \quad (2.8)$$

Note that CE_i is defined as the normalized i-th collision energy (adopting values between 10 and 18). The slope of the regression line is calculated as follows:

$$slope = \frac{SS_{CE \cdot I} - S_{CE} S_I}{SS_{CE^2} - S_{CE}^2} \quad (2.4)$$

Accordingly, the error of the slope σ_{slope} is calculated:

$$\sigma_{slope} = \sqrt{\frac{S}{SS_{CE^2} - S_{CE}^2}} \quad (2.5)$$

It is noted that the integration method used here produces a bias at higher collision energies (CE > 15). This is due to the significant production of light fragments (Cp*, Mes, Cu, Zn) under these conditions, which are lying outside the measurement range (measurement of heavier clusters of interest is only possible with m/z set to be > 200). Therefore, the determined integrals at higher collision energies are supposed to overestimate the actual integrals.

5.2 Synthesis

General

All experiments were conducted using standard Schlenk and glovebox techniques under an atmosphere of purified argon. All solvents and chemicals, respectively, were carefully dried (water content < 5 ppm) and saturated with argon prior to their use. Basic starting materials were purchased from standard suppliers. ^{68}ZnO was purchased from *BuyIsotope* (Sweden).The organometallic starting compounds were prepared according to the following literature procedures:

AlCp*[296]	*[CuMes] = [Cu₅](Mes)₅*[218]	*[H₆Cu₆](PPh₃)₆*[123]
[Zn₂](Cp*)₂[206]	*[Zn₂](Cp*^{Et})₂*[206]	*[^{i}DippAuH]*[266]
[^{i}DippCuH][215]	*[H₄Cu₆Al₆](Cp*)₆*[92]	*[^{68}Zn₂](Cp*)₂*[297]
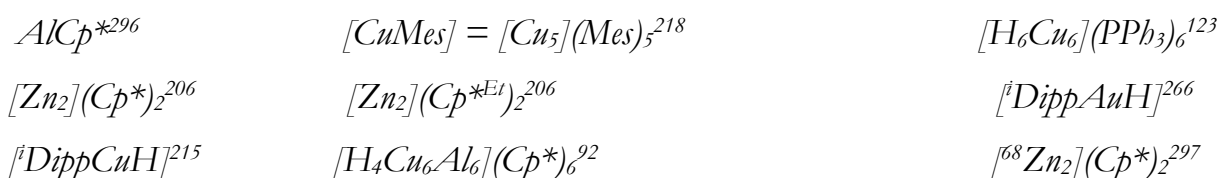
Synthesis of [CuZn₁₀](Cp)₇ = [Cu(ZnZnCp*)₃(ZnCp*)₄] (10)*

A sample of 274 mg (0.52 mmol) of [^{i}DippCu(O^{t}Bu)] were suspended in 8 ml of diethylether and cooled to -75 °C. A volume of 0.15 ml of HSi(OEt)₃ (0.81 mmol) were added dropwise to the solution leading to an immediate color change to yellow. The solution was stirred for 4 hours at -75 °C before a suspension of 420 mg [Zn₂](Cp*)₂ (1.0 mmol) in 7 ml diethylether was added at that temperature. The resulting solution was allowed to warm to room-temperature and stirred for 2 hours, accompanied by a color change to deep-red. The solution was concentrated in vacuum, filtered and left for crystallization at -30 °C for several weeks leading to a mixture of red crystals of **10** and colorless ones of [Zn₂](Cp*)₂, which was isolated and washed with a minimum amount of n-hexane. The yield could not be determined due to the inseparability of the two types of crystals. The assignment of the spectroscopic data of the manually separated single crystals of **10** is as follows:

^{1}H-NMR (298 K, 400 MHz, C₆D₆, manual separation of single crystals): 2.22 (s, 105H, Cp*)

^{1}H-NMR (208 K, 400 MHz, C₆D₆, manual separation of single crystals): 2.25 (s, 45H, ZnZnCp*), 2.27 (s, 60H, ZnCp*)

^{13}C-NMR (298 K, 400 MHz, C₆D₆, manual separation of single crystals): 12.21 (s, C₅(*C*H₃)₅ groups), 111.10 (s, *C*₅(CH₃)₅)

Raman (298 K): ν [cm^{-1}] = 2850 (b, w), 1575 (b), 1025 (s, w), 980 (s), 142 (s).

LIFDI-MS: m/z (a.u.) = 1664 ([M]$^+$), 1462 ([M-ZnCp*]$^+$).

Synthesis of [Cu$_{10}$Zn$_2$](Mes)$_6$(Cp*)$_2$ (3)

A sample of 200 mg (1.1 mmol) of [CuMes] and 132 mg (0.3 mmol) of [Zn$_2$](Cp*)$_2$ were dissolved in 25 ml of toluene and heated to 75 °C for 7 days. The dark solution was filtered *via* a passivated glass frit, concentrated under reduced pressure (4 ml) and left for crystallization at -30 °C for several weeks. Dark-green crystals of **3** were isolated in 9.1 % yield (based on Cu) and washed with a minimum amount of *n*-hexane (3 x 0.3 ml).

^{1}H-NMR (298 K, 400 MHz, C$_6$D$_6$): 1.62 (s, 30 H, ZnCp*), 2.03 (s, 18H, CH$_3$ (Mes)), 2.67 (s, 36H, CH$_3$ (Mes)), 6.76 (s, 12H, CH$_{aryl}$ (Mes)).

^{13}C-NMR (298 K, 400 MHz, C$_6$D$_6$): 9.41 (s, methyl groups (ZnCp*)), 21.18 (s, methyl groups (Mes)), 30.49 (s, methyl groups (Mes)), 110.23 (s, ring carbon atoms (Cp*)), 126.52 (s, ring carbon atoms (Mes)), 137.46 (s, ring carbon atom (ZnCp*)), 140.57 (s, ring carbon atoms (Mes)), 154.68 (s, ring carbon atoms (Mes)).

ATR-IR (298 K): ν [cm^{-1}] = 3011 (w), 2962, 2908, 2855, 1594 (s), 1444, 1413, 1380, 1283 (w), 1258 (s, i), 1081 (i), 1013 (i), 863 (w), 842 (w), 791 (i), 661-698, 574 (w), 544 (w), 527 (w).

LIFDI-MS: m/z (a.u.) = 1751 ([M]$^+$).

Synthesis of [Cu$_4$Zn$_{9/10}$](Cp*)$_8$ (4/5)

220 mg (1.2 mmol) of [CuMes] and 366 mg (0.9 mmol) of [Zn]$_2$Cp*$_2$ were dissolved in 50 ml of toluene. The resulting red solution was stirred for 2 hours at room temperature, concentrated under reduced pressure (4 ml), filtered and left for crystallization at -30 °C for one week. The resulting crystallizate (yellow, red and black crystals) was washed extensively with *n*-hexane (5-10 ml) until only black crystals of **4/5** remained.

Yield: 20 mg (19 % based on Cu).

^{1}H-NMR (298 K, 400 MHz, C$_7$D$_8$): 2.22 (s (broad), 60H, (CuZnCp*)), 2.27 (s (broad), 60H, (ZnCp*)).

^{1}H-NMR (208 K, 400 MHz, C$_7$D$_8$): 2.27 (s, 60H, (CuZnCp*)), 2.29 (s, 30H, (ZnCp*)), 2.31-2.35 (two overlapping singlets, 30H, (ZnCp*)).

^{13}C-NMR (298 K, 500 MHz, cryo-probe, C_7D_8): 10.95 (s, CH_3 (Cp*)), 12.99 (s, CH_3 (Cp*)), 109.21 (s, quaternary C 8Cp*)), 111.40 (s, quaternary C (Cp*)).

IR (ATR, 298 K): ν [cm^{-1}] = 2962 (w, shoulder), 2888, 2850 (s), 2723 (w), 1711-1827, 1450, 1419 8s), 1376 (s), 1256 (w), 1147 (w), 1019, 937, 797, 723, 690, 587 (s), 459.

LIFDI-MS: m/z = 1987 ($[Cu_4Zn_{10}](Cp*)_8]^+$), 1852 ($[Cu_4Zn_{10}](Cp*)_7]^+$), 1788 ($[Cu_4Zn_9](Cp*)_7]^+$).

ICP-MS: Zn/Cu ratio calculated for $[Cu_4Zn_{9/10}](Cp*)_8$: 2.25-2.5; found experimentally: Zn/Cu = 2.123 $\pm$ 0.031

XPS: Zn/Cu ratio calculated for $[Cu_4Zn_{9/10}](Cp*)_8$: 2.25-2.5; found experimentally: Zn/Cu = 2.15

*Note: The experimentally determined Cu content is slightly higher than expected for **4/5**. This deviation is explained by impurities of $[CuZn_2](Cp*)_3$, which is only hardly separable from **4/5** even by extensive washing.*

Synthesis of $[Cu_4Al_4](Cp*)_5(Mes)$ (11)

232.56 mg (1.4 mmol, 1.31 eq.) of AlCp* and 200 mg (1.1 mmol, 1 eq.) of [CuMes] were dissolved in 20 ml of toluene and heated to 75 °C for 60 minutes resulting in a dark green solution. The solution was filtered *via* canula, concentrated under reduced pressure (10 ml) and left for crystallization at -30 °C for one week. The resulting needle-like crystals were isolated, washed with *n*-hexane (3 x 0.25 ml) and recrystallized from a minimum amount of toluene at -30 °C giving pure **11**.

Yield: 5 % (based on Cu).

^{1}H-NMR (400mHz, 298 K, C_7D_8): 6.90 (s, 2H, CH_{aryl}(Mes)), 2.31 (s, 3H, -CH_3(Mes)), 2.28 (s, 6 H, -CH_3(Mes)), 2.10 (s, 30H, -CH_3(CuCp*)), 1.97 (s, 15H, -CH_3(AlCp*$_{bridging}$)), 1.92 (s, 30H, -CH_3(AlCp*$_{apical}$)).

^{13}C-NMR (400 mHz, 298 K, C_7D_8): 143.10 (s, quaternary C(Mes)), 126.79 (s, quaternary C(Mes)), 115.37 (s, quaternary C(AlCp*)), 114.45 (s, quaternary C(AlCp*)), 103.39 (s, quaternary C(CuCp*)), 32.46 (s, CH_3(Mes)), 25.23 (s, -CH_3(Mes)), 13.13 (s, -CH_3(CuCp*)), 11.97 (s, -CH_3(AlCp*)), 10.78 (s, -CH_3(AlCp*)).

IR (ATR, 298 K): ν [cm^{-1}] = 2897 (b), 2835 (b), 1482 (w), 1415 (s), 1376 (s), 1376 (s), 1023 (w), 846, 800, 731 (w), 590, 538 (w), 453 (s, i), 422 (s).

Elemental analysis [%]: Calculated for $Cu_4Al_4C_{59}H_{86}$: C: 61.22, H: 7.49, Al: 9.32, Cu: 21.96; found: C: 60.14, H: 7.61, Al: 9.25, Cu: 21.68.

5. Experimental

5.2 Synthesis

*Note: Despite the reaction being rather selective according to in-situ NMR analysis, pure **11** is only accessible in small yields (5 %) due to very similar solubility properties of **11** and side products (AlCp*Mes₂, AlMes₃) requiring an extensive washing and recrystallization procedure.*

Synthesis of [CuAl₂](Cp*)₃ (9)

232.6 mg (1.4 mmol, 1.31 eq.) of AlCp* and 200 mg (1.1 mmol, 1 eq.) of [CuMes] were dissolved in 20 ml of toluene and heated to 75 °C for 60 minutes resulting in a dark-green solution. 3 ml (26.4 mmol, 24 eq.) of 3-hexyne were added under vigourous stirring resulting in a color change to dark brown. The solution was heated to 75 °C for 60 minutes, filtered *via* canula, concentrated under reduced pressure (10 ml) and left for crystallization at -30 °C for one week. The resulting yellow-orange crystals were isolated, washed with *n*-hexane (3 x 0.3 ml) and dried to yield pure **9**.

Yield: 14 % (based on Cu).

^{1}H-NMR (400mHz, 298 K, C₆D₆): 2.32 (s, 30H, -CH_3(CuCp*)), 1.70 (s, 15H, -CH_3(AlCp*)).

^{13}C-NMR (400 mHz, 298 K, C₆D₆): 115.82 (s, quaternary C(AlCp*)), 104.32 (s, quaternary C(CuCp*)), 12.55 (s, -CH_3(CuCp*)), 9.87 (s, -CH_3(AlCp*).

IR (ATR, 298 K): ν [cm^{-1}] = 2894 (b), 2848 (b), 2716 (w), 1480 (w), 1425, 1375, 1261 (w), 1160 (w), 1049-1115 (w), 1020, 799, 729, 694, 591, 518 (i), 430, 420.

Elemental analysis [%]: Calculated for Cu₂AlC₃₀H₄₅: C: 64.37, H: 8.10, Al: 4.82, Cu: 22.70; found: C: 63.22, H: 8.01, Al: 4.89, Cu: 22.02.

Synthesis of [Cu₇/₈Al₆](Cp*)₆ (1/2)

500 mg (3.1 mmol, 1 eq.) of AlCp* and 156.3 mg (0.86 mmol, 0.28 eq.) of [CuMes] were suspended in 50 ml of toluene and heated to 75 °C for 4.5 hours resulting in a deep-green solution. Additional 305 mg (1.7 mmol, 0.55 eq.) [CuMes] were added and the mixture was heated to 75 °C for 24 hours. The dark-brown solution was concentrated under reduced pressure to half its volume and cooled to -30 °C for 7 days. The black precipitate was isolated by means of canula filtration, washed with *n*-hexane at -78 °C (4 x 0.4 ml) and dried under reduced pressure to yield pure **1/2**.

Yield: 23 % (based on Cu).

^{1}H-NMR (400mHz, 298 K, 0.007 mmol/ml, C₆D₆): 1.94 ppm (s, [Cu₈Al₆](Cp*)₆), -1.03 ppm (broad paramagnetic signal, [Cu₇Al₆](Cp*)₆).

5. Experimental
5.2 Synthesis

^{13}C-NMR (500 mHz, cryo-probe, 298 K, C$_6$D$_6$): 115.19 (s, quaternary C([Cu$_8$Al$_6$](Cp*)$_6$)), 12.89 (s, -CH$_3$(([Cu$_8$Al$_6$](Cp*)$_6$)).

IR (ATR, 298 K): 2962 (w), 2903, 2850, 1489 (w), 1423 (s), 1369 (s), 1264 (w), 1157-1017 (b), 799, 729, 587 (w), 414 (s, i);

Elemental analysis [%]: Calculated for Cu$_8$Al$_6$C$_{60}$H$_{90}$: C: 48.64, H: 6.12, Cu: 34.31, Al: 10.93; found: C: 48.16, H: 6.04, Cu: 34.77, Al: 10.76.

*Note: The synthesis of **1/2** turned out to be very sensitive even to subtle changes of reaction conditions. Small variations of the CuMes:AlCp* ratio employed resulted in isolation of a mixture of **1/1$_H$/2** instead of **1/2**. In situ ^{1}H-NMR analysis suggests Cp* to be the origin of the hydride ligand in these cases, as pentamethylfulvene was detected as a reaction product. The stepwise addition of [CuMes] allowed for a better reaction control and isolation of pure **1/2** as described above.*

Synthesis of [H₃Cu₃](dppbz)₃ (dppbz = 1.2-bis(diphenylphosphinobenzene)

68.1 mg (0.035 mmol, 1 eq.) of [H$_6$Cu$_6$](PPh$_3$)$_6$ and 95.3 mg (0.21 mmol, 6 eq.) of dppbz were suspended in 1.5 ml of toluene and stirred for several hours resulting in a color change from red to yellow. The solution was kept standing without stirring overnight resulting in a yellow precipitate, which was subsequently isolated by filtration. After recrystallized from 0.5 ml of hot toluene, [Cu(dppbz)H]$_3$ was isolated as yellow powder in 50 % yield based on Cu. ^{1}H- and ^{31}P-NMR analysis of the product is consistent with values reported in literature.[298]

Synthesis of (TMS)₃SiD

2.5 g (7.6 mmol, 1 eq.) of (TMS)$_3$SiBr and 300 mg (1.04 eq.) of LiAlD$_4$ were heated in 100 ml diethylether under reflux conditions for three days under argon atmosphere. 1M KOH solution (50 ml) in water was added slowly and the mixture was extracted three times with diethylether. The organic layer was separated, dried over anhydrous MgSO$_4$, filtered and the solvent was removed under reduced pressure resulting in (TMS)$_3$SiD in 50 % yield, which was dried over molecular sieve for further use.

^{1}H-NMR (toluene-d$_8$): 0.24 (s, 27H, Si-CH$_3$).

5. Experimental
5.2 Synthesis

Synthesis of [H$_x$Au$_{6/7}$Al$_6$](Cp*)$_6$ (6/7)

[^{i}DippAuH] (150 mg, 0.256 mmol) and AlCp* (41.56 mmol, 0.256 mmol) were heated in 15 ml of toluene at 75 °C for 3 h. The red reaction solution was filtered and stored at -30 °C for several weeks. The formed dark crystallizate was isolated by means of filtration and washed with *n*-hexane (3 x 0.1 ml) and benzene (3 x 0.1 ml) resulting in pure **6/7**.

Yield: 5 % (based on Au).

^{1}H-NMR (298 K, 400 MHz, C$_6$D$_6$): 1.99 (s (broad), 90H, C*H$_3$* (Cp*) of **7**), 1.94 (s (broad), 90H, C*H$_3$* (Cp*) of **6**).

^{13}C-NMR (298 K, 500 MHz, cryo-probe, C$_6$D$_6$): 12.99 (s, *CH$_3$* (Cp*) of **6**), 115.2 (s, quaternary *C* (Cp*) of **6**), 115.5 (very small, s, quaternary *C* (Cp*) of **7**).

IR (ATR, 298 K): ν [cm^{-1}] = 2959 (w), 2904, 2845, 1756 (w), 1595, 1411, 1358, 1325, 1264, 1230, 1201, 1158 – 915 (b, i), 889, 809, 781, 742, 685, 638, 546, 426.

UV-Vis (298 K, toluene): 517 nm (broad), 478 nm (very weak), 440 nm (shoulder, weak), 309 nm (sharp).

LIFDI-MS: m/z = 2154 ([Au$_6$Al$_6$](Cp*)$_6$]$^+$), 2351 ([Au$_7$Al$_6$](Cp*)$_6$]$^+$).

*Note: Due to the high sensitivity of the mixture **6/7** in comparison to pure **7**, no meaningful values were obtained from elemental analysis of the sample.*

Synthesis of [H$_x$Au$_7$Al$_6$](Cp*)$_6$ (7)

[^{i}DippAuH] (150 mg, 0.256 mmol), AlCp* (41.56 mmol, 0.256 mmol) and PPh$_3$ (650 mg, 2.55 mmol, 10 eq.) were heated in 15 ml of toluene at 75 °C for 3 h. The hot, red reaction solution was filtered and stored at -30 °C for three days. The formed dark crystallizate was isolated by careful decantation and washed with *n*-hexane (3 x 0.3 ml) resulting in pure **7**.

Yield: 17 % (based on Au).

^{1}H-NMR (298 K, 400 MHz, C$_6$D$_6$): 1.99 (s (broad), 90H, C*H$_3$* (Cp*) of **7**).

^{13}C-NMR (298 K, 500 MHz, cryo-probe, C$_6$D$_6$): 115.5 (s, quaternary *C* (Cp*) of **7**).

IR (ATR, 298 K): ν [cm^{-1}] = 3552 (w), 3483 (w), 2964 (w), 2902, 2850, 1753, 1452 (shoulder), 1421, 1371, 1310 (b, i), 1050 (w), 1027 (w), 801, 729, 694, 587, 451 (i).

UV-Vis (298 K, toluene): 514 nm (broad), 480 nm (very weak), 415 - 463 nm (shoulder, strong), 298 nm (sharp).

LIFDI-MS: m/z = 2351 ([Au$_7$Al$_6$](Cp*)$_6$]$^+$).

5. Experimental
5.2 Synthesis

Elemental analysis [%]: Calculated for $Au_7Al_6C_{60}H_{90}$: C: 30.64, H: 3.86, Al: 6.88, Au: 58.62; found: C: 29.95, H : 3.88, Al: 6.73, Au: 58.41.

*Note: Despite all efforts (cryo-probe, high number of scans), no clear assignment of the -**C**H₃ (Cp*) signal of **7** in ¹³C-NMR spectroscopy was possible and only the quaternary carbon signal could be detected. It is supposed that the -**C**H₃ carbon signal is overlapping with the signals of free HCp*, which cannot be avoided due to the very high sensitivity of **7** and its low solubility in comparison to organic molecules.*

Synthesis of [Au₂Al₅](Cp*)₅ (8)

[*i*DippAuH] (100 mg, 0.17 mmol) and AlCp* (69.13 mg, 0.426 mmol) were heated in 5 ml of toluene to 75 °C for two days. The dark-brown reaction solution was concentrated to half its volume under reduced pressure, filtered and cooled to -30 °C for one week resulting in dark crystals of **8**. The crystals were isolated by decantation and washed with a minimum amount of *n*-hexane (3 x 0.1 ml).

Yield: 7 % (based on Au)

¹H-NMR (298 K, 400 MHz, C_6D_6): 2.19 (s (very broad), 45H, bridging AlCp*), 1.85 (s (very broad), 30H, terminal AlCp*).

¹³C-NMR (298 K, 500 MHz, cryo-probe, C_7D_8): 114.19 (s, quaternary C), 13.65 (s, -CH_3), 10.23 (s, -CH_3).

LIFDI-MS: m/z = 1203 ([**8**-H]⁺).

IR (ATR, 298 K): ν [cm⁻¹] = 2964 (w), 2900, 2848, 2712 (w), 1487 (w), 1417, 1369, 1176 (w), 1019, 799, 578, 455 (i).

UV-Vis (298 K, toluene): 498-536 nm (weak, broad), 478 nm (broad), 406 nm (very broad), 331 nm (sharp).

Elemental analysis [%]: Calculated for $Au_2Al_5C_{50}H_{75}$: C: 49.84, H : 6.27, Al: 11.20, Au: 32.69; found: C: 49.00, H: 6.22, Al: 10.87, Au: 32.51.

Experimental procedure for the generation of Cu/Zn libraries

[CuMes] and [Zn₂](Cp*)₂ were mixed in toluene (5 ml) resulting in a deep-red solution and stirred at room-temperature for 2 hours before analysis *via* LIFDI-MS. The reaction can be scaled down when keeping the overall concentration of reactants constant. Reactions with [⁶⁸Zn₂](Cp*)₂ and [Zn₂](Cp*^{Et})₂ were carried out accordingly. The different Cu/Zn rations applied are listed in the following Table 9:

5. Experimental

5.2 Synthesis

Table 9
Amount of [CuMes], [Zn₂](Cp)₂, [⁶⁸Zn₂](Cp*)₂ and [Zn₂](Cp*^Et)₂ used for the generation of Cu/Zn libraries.*

Cu/Zn ratio	[CuMes] [mg]	[Zn₂](Cp*)₂ [mg]	[⁶⁸Zn₂](Cp*)₂ [mg]	[Zn₂](Cp*^Et)₂ [mg]
1:0.75	22 (0.12 mmol)	18.3 (0.046 mmol)	18.5 (0.046 mmol)	19.8 (0.046 mmol)
1:1.5	22 (0.12 mmol)	36.6 (0.091 mmol)	37.0 (0.091 mmol)	39.6 (0.091 mmol)
1:3	22 (0.12 mmol)	73.2 (0.18 mmol)	73.2 (0.18 mmol)	79.2 (0.18 mmol)

Experimental procedure for the reactions of Cu/Zn libraries with CO_2

The Cu/Zn library (Cu:Zn ratio 1:1.5) in toluene was prepared in a *Schlenk* flask (*vide supra*) and the flask was purged with CO_2 (1 bar). The solution was stirred for 3 h resulting in formation of the CO_2 adducts $[Cu_5Zn_5](Cp^*)_6(CO_2)_2$ and $[Cu_8Zn_3](Cp^*)_4(CO_2)$. Prolonged reaction times (>6 h) led to further, so far unidentified reaction products.

Alternatively, the reaction can be conducted in a Young-NMR tube: 11 mg (0.0602 mmol) of [CuMes] and 18.5 mg (0.046 mmol, 0.75 eq.) of $[Zn_2](Cp^*)_2$ were dissolved in 0.5 ml of toluene-d₈. After two hours at room-temperature, the NMR tube was pressurized with 2 bar CO_2 (without prior evacuation). After 18 h reaction time, the CO_2 adducts $[Cu_5Zn_5](Cp^*)_6(CO_2)_2$ and $[Cu_8Zn_3](Cp^*)_3(Mes)_4$ can be observed by LIFDI-MS analysis.

Note: Prolonged reaction times are necessary in the NMR reactions, probably due to the smaller liquid-gas interface and due to the absence of stirring (kinetic effects).

Experimental procedure for the reactions of Cu/Zn libraries with CO_2 and H_2

The Cu/Zn library was treated with CO_2 in a Young-NMR tube (*vide supra*). After a total reaction time of 18 h at room-temperature, CO_2 was released from the tube (glove-box). The tube was pressurized with 3 bar H_2 without prior evacuation. Formate is detected by NMR after 4 hours reaction time; the species

5. Experimental
5.2 Synthesis

$[Cu_{11}Zn_6](Cp^*)_8(CO_2)_2(HCO_2)$ can be observed by LIFDI-MS after 18 h at room-temperature.

Experimental procedures for conditions described in Table 5

Conditions A: Reaction of [H₃Cu₃](dppbz)₃ with AlCp / Synthesis of 1_H/2*

20 mg (13.0 μmol, 0.4 eq.) $[H_3Cu_3](dppbz)_3$ and 5.20 mg (0.032 mmol, 1.0 eq.) AlCp* were heated at 75 °C for 2 h in 2.5 mL toluene resulting in a dark solution. Cooling the concentrated and filtered reaction solution to -30 °C for several days leads to an inseparable mixture of few dark single-crystals of **1_H/2** suitable for SC-XRD in addition to free dppbz ligand and other side-products.

For *in-situ* LIFDI-MS experiments, the synthesis of **1_H/2** can also be conducted as follows:

12.3 mg (6.27 μmol, 0.2 eq.) of $[H_6Cu_6](PPh_3)_6$, 5 mg (0.031 mmol, 1 eq.) of AlCp* and 3.4 mg (7.62 μmol, 1.2 eq) of dppbz were heated in 1 ml of toluene for three hours resulting in a dark solution. In the same manner, preparation of **1_D/2** was conducted using $[D_6Cu_6](PPh_3)_6$ as starting material.

Conditions C: Thermal treatment of 11

5 mg (4.3 μmol) of isolated **11** were dissolved in 0.5 ml of toluene-d₈ or benzene-d₆ in a sealed Young-NMR tube and heated to 75 °C for six hours.

Conditions D: Conversion of isolated 1/2 with [CuMes]

5 mg (3.4 μmol, 1 eq.) of isolated **1/2** and 3.1 mg (0.017 mmol, 5 eq.) of [CuMes] were dissolved in 0.5 ml of benzene-d₆ in a sealed Young-NMR tube and heated to 75 °C for several hours.

10 mg (6.8 μmol, 1 eq.) of isolated **1/2** and 12.4 mg (0.068 mmol, 10 eq.) of [CuMes] were dissolved in 1 ml of toluene and heated to 75 °C for 5 hours resulting in a

metallic precipitate (Cu). Filtration of the solution and storage at -30 °C led to crystallization of pure **2** as determined by SC-XRD in very small yield.

Conditions E: Conversion of 9 with [CuMes]

5 mg (8.9 μmol, 1 eq.) of isolated **9** and 1.9 mg (10.4 μmol, 0.4 eq) of [CuMes] were dissolved in 0.5 ml of benzene-d_6 in a sealed Young-NMR tube and heated to 75 °C for 6 hours. Conducting the reaction toluene and cooling the filtered reaction solution to -30 °C for several weeks led to few single crystals of pure **2** as determined by SC-XRD.

Conditions F: Thermal treatment of 1/2 in toluene

5 mg (3.4 μmol) of isolated **1/2** were heated in 0.5 ml of toluene to 110 °C for 5 days in a sealed Young-NMR tube.

Conditions G/H: Conversion of isolated 1/2 with excess (TMS)₃SiH and (TMS)₃SiD

10 mg (6.8 μmol) of isolated **1/2** and 0.3 ml (1 mmol) of (TMS)$_3$SiH / 0.3 ml (1 mmol) of (TMS)$_3$SiD were dissolved in 2.5 ml of toluene and heated to 110 °C for 5 days.

For the *in-situ* ^{1}H NMR reaction, 5 mg (3.4 μmol) of isolated **1/2** and 10 mg (40.3 μmol) of (TMS)$_3$SiH were dissolved in 0.5 ml of toluene-d_8 and heated to 110 °C for 5 days.

Experimental procedures for the determination of extinction coefficients in the Au/Al system

For the determination of extinction coefficients, a sample of [H$_x$Au$_7$Al$_6$](Cp*)$_6$, [H$_x$Au$_{6/7}$Al$_6$](Cp*)$_6$, [Au$_2$Al$_5$](Cp*)$_5$, respectively, was dissolved in 3 ml of toluene in an UV-Vis cuvette (see Table 10 for the amounts used). UV-Vis spectra were recorded of these original solutions. Afterwards, dilution series were made by diluting

the solutions with a factor of 2 per series and UV-Vis spectra were recorded for each series.

Table 10
Amounts of $[H_xAu_7Al_6](Cp^*)_6$, $[H_xAu_{6/7}Al_6](Cp^*)_6$ and $[Au_2Al_5](Cp^*)_5$ used for the determination of extinction coefficients.

sample	$[H_xAu_7Al_6](Cp^*)_6$	$[H_xAu_{6/7}Al_6](Cp^*)_6$	$[Au_2Al_5](Cp^*)_5$
amount used [mg]	1.3 ($5.5 * 10^{-4}$ mmol)	1.5	1.5 ($1.25 * 10^{-4}$ mmol)

Experimental procedures for the investigation of Au/Al cluster libraries by UV-Vis (PPh₃ influence)

[^{i}DippAuH] (10 mg, 17.1 µmol) and AlCp* (2.8 mg, 17.1 µmol) were heated together with different amounts of PPh$_3$ in 1 ml of toluene to 75 °C for 2 h. 0.1 ml of the reaction solutions were diluted to a total volume of 3 ml with fresh toluene and investigated by UV-Vis. The amounts of PPh$_3$ used are listed in the following Table 11.

Table 11
Amounts of PPh₃ used in Au/Al cluster library generation in the UV-Vis experiments. Au:Al stoichiometry was kept constant 1:1.

PPh$_3$ stoichiometry w. r. t. Au	0 eq.	1 eq.	5 eq.	10 eq.
amount of PPh$_3$ used [mg]	0 (0.0 mmol)	4.5 (17.1 µmol)	22.4 (85.4 µmol)	44.7 (17.1 mmol)

5. Experimental
5.2 Synthesis

Experimental procedures for the generation of trimetallic Au/Cu/Al libraries

[Cu$_2$Al](Cp*)$_3$, [^{i}DippAuH] and PPh$_3$ were mixed in 0.5 ml of toluene-d$_8$ and heated to 75 °C for 2 hours. The amounts of starting materials used are listed in Table 12.

Table 12
Amounts of [Cu$_2$Al](Cp)$_3$, [^{i}DippAuH] and PPh$_3$ used for the generation of trimetallic cluster libraries. Experiment numbers refer to Table 7.*

experiment number	[^{i}DippAuH] [mg]	[Cu$_2$Al](Cp*)$_3$ [mg]	PPh$_3$ [mg]
A	5.25 (9.0 μmol)	5 (8.5 μmol)	2.3 (8.8 μmol)
B	5.00 (8.5 μmol)	7.14 (12.8 μmol)	4.5 (17.2 μmol)
C	5 (8.5 μmol)	5.96 (10.5 μmol)	2.8 (10.7 μmol)

6. Appendix

6.1 Supporting information for the methodical part

The following supporting data documentation refers to pages 72-91.

Table S1: Species identified in LIFDI-MS spectra of Cu/Zn libraries obtained by mixing [CuMes] + $[Zn_2](Cp^*)_2$ (toluene, RT, 2 h). The table also lists at which other stoichiometry the respective ion is observed.

green = species identified by Cp*Et and ^{68}Zn label

light green = species identified by ^{68}Zn label

white = species identified in a spectrum of another stoichiometry

Cu:Zn 1:3	Cu:Zn 1:1.5	Cu:Zn 1:0.75
$\{[Zn](Cp^*)_2 -H\}$	$[Cu_5](Mes)_4$ also in 1:0.75	$[Cu_7Zn](Cp^*)_2(Mes)_4$ also in 1:3 und 1:1.5
$[Cu](Cp^*)_2$	$[Cu_4](Mes)_4$, $[Cu_3Zn](Mes)_4$	$[Cu_4](Mes)_4$, $\{[Cu_4](Mes)_3 - H\}$
$[Cu_3](Cp^*)_2$	$[Cu_3Zn_3](Cp^*)_4$ also in 1:3	$[Cu_5](Mes)_4$ also in 1:1.5
$[Cu_3Zn_3](Cp^*)_4$	$[HCu_3Zn](Cp^*)_3$ also in 1:3	$[Cu_9Zn](Cp^*)_3(Mes)_3$ also in 1:3 und 1:1.5
$[HCu_3Zn](Cp^*)_3$ also in 1:1,5	$[Cu_3Zn_4](Cp^*)_5$ also in 1:3	$[Cu_3Zn_4](Cp^*)_5$ also in 1:3 und 1:1.5
$[Cu_3Zn_4](Cp^*)_5$ also in 1:1.5	$ZnCp^*Mes$	$[Cu_5Zn](Cp^*)_3(Mes)$ also in 1:3 und 1:1.5
$ZnCp^*Mes$	$[CuZn](Cp^*)_2$	$ZnCp^*Mes$
$\{[Cu_3Zn_2](Cp^*)_3 -H\}$	$[HCu_3Zn_2](Cp^*)_3$ also in 1:3, $[H_3Cu_5](Cp^*)_3$	$[Cu_7Zn](Cp^*)_3(Mes)_2$ also in 1:3 und 1:1.5
$[Cu_7Zn](Cp^*)_2Mes$ also in 1:1.5 und 3:1	$[Cu_7Zn](Cp^*)_2(Mes)_4$ also in 1:3 und 3:1	$[Cu_7Zn_3](Cp^*)_3(Mes)_4$ also in 1:3 und 3:1
$[Cu_7Zn_3](Cp^*)_3(Mes)_4$ also in 1:1.5 und 3:1	$[Cu_7Zn_3](Cp^*)_3(Mes)_4$ also in 1:3 und 3:1	$[HCu_7](Cp^*)_2(Mes)$ also in 1:3 und 3:1
$[Cu_3Zn_2](Cp^*)_4$ also in 1:1,5	$[Cu_3Zn_2](Cp^*)_4$ also in 1:3, $[Cu_7Zn_2](Cp^*)_2(Mes)_5$ also in 1:3	$[Cu_7](Cp^*)_2(Mes)_4$ also in 1:3 und 3:1
$[Cu_7](Cp^*)_2(Mes)_4$ also in 1:1.5	$[Cu_7](Cp^*)_2(Mes)_4$ also in 1:3	$[Cu_7](Cp^*)_3(Mes)$ also in 1:3 und 3:1
$[HCu_9Zn_2](Cp^*)_3(Mes)_4$ also in 1:1.5	$[Cu_7Zn](Cp^*)_3(Mes)_2$ also in 1:3	$[Cu_7](Cp^*)_2(Mes)_3$ also in 1:3 und 3:1

6. Appendix

6.1 Supporting information for the methodical part

$[Cu_7](Cp^*)_2(Mes)_3$ also in 1:1.5	$[HCu_7](Cp^*)_2$	$[H_2Cu_7Zn](Cp^*)_4(Mes)$ also in 1:3 und 3:1
$[Cu_5Zn_2](Cp^*)_4$ also in 1:1.5	$[Cu_7](Cp^*)_2(Mes)_3$ also in 1:3	$[Cu_7Zn](Cp^*)_3(Mes)$
$[H_3Cu_3](Cp^*)_3$	$[Cu_5Zn_2](Cp^*)_4$ also in 1:3	$[HCu_8](Cp^*)_2(Mes)_3$
$[Cu_5Zn](Cp^*)_3(Mes)$ also in 1:1.5	$[H_3Cu_2Zn](Cp^*)_3$ also in 1:0.75 and 1:3	$[Cu_4](Cp^*)_2(Mes)_2$
$[Cu_9Zn](Cp^*)_3(Mes)_3$ also in 1:1.5	$[Cu_5Zn](Cp^*)_3(Mes)$ also in 1:3	$[H_2Cu_9](Cp^*)(Mes)_5$
$[HCu_5](Cp^*)_2(Mes)$ also in 1:1.5	$[Cu_9Zn](Cp^*)_3(Mes)_3$ also in 1:3	$[HCu_8Zn_3](Cp^*)_4(Mes)_3$ also in 1:1.5
$[Cu_7](Cp^*)_2(Mes)_2$ also in 1:1.5	$[Cu_7](Cp^*)_2(Mes)_2$ also in 1:3	$[Cu_5](Cp^*)(Mes)_3$ also in 1:1.5
$[Cu_7](Cp^*)_3(Mes)$ also in 1:1.5	$[HCu_5](Cp^*)_2(Mes)$ also in 1:3	$[Cu_9Zn](Cp^*)_3(Mes)_3$ also in 1:3 und 1:1.5
$[Cu_9](Cp^*)_3(Mes)_2$ also in 1:1.5 and 1:0.75	$[Cu_{10}Zn_3](Cp^*)_3(Mes)_5$ also in 1:0.75	$[Cu_7Zn_2](Cp^*)_2(Mes)_5$ also in 1:3 und 1:1.5 (B)
$[HCu_8Zn](Cp^*)_4$ also in 1:1.5	$[Cu_3](Cp^*)_2$, $\{[Cu_2Zn](Cp^*)_2 - H\}$ also in 1:0.75	$[Cu_7](Cp^*)_2(Mes)_2$ also in 1:3 und 1:1.5 (A/B)
$[Cu_7Zn_2](Cp^*)_3(Mes)_3$ also in 1:1.5	$[Cu_9](Cp^*)_3(Mes)_2$ also in 1:3 and 1:0.75	$[Cu_5](Cp^*)_2(Mes)_2$ also in 1:3 und 1:1.5
$[HCu_5Zn](Cp^*)_3$ also in 1:1.5	$[Cu_7Zn_2](Cp^*)_3(Mes)_3$ also in 1:0.75	$\{[Cu_3](Mes)_3 - H\}$
$[H_2Cu_7Zn](Cp^*)_4$, also in 1:1.5	$[HCu_5Zn](Cp^*)_3$ also in 1:3 $[Cu_4Zn_2](Cp^*)_3$	$[Cu_{10}](Cp^*)(Mes)_6$
$[Cu_9](Cp^*)_2(Mes)_2$ (no unambigous assignment)	$[H_2Cu_7Zn](Cp^*)_4$ also in 1:3	$[Cu_7](Cp^*)_3(Mes)_2$ also in 1:3
$[Cu_7Zn_4](Cp^*)_4(Mes)_3$	$[Cu_9](Cp^*)_2(Mes)_2$ also in 1:3	$[Cu_9](Cp^*)_2(Mes)_2$ also in 1:3 und 1:1.5
$[Cu_9](Cp^*)_3(Mes)$ also in 1:1.5	$[Cu_2Zn_3](Mes)_3$	$[Cu_9](Cp^*)_3(Mes)$ also in 1:3 und 1:1.5
$[Cu_7](Cp^*)_3(Mes)_2$ also in 3:1	$[Cu_9](Cp^*)_3(Mes)$ also in 1:3	$[Cu_{10}Zn_2](Cp^*)_2(Mes)_6$ also in 1:3 und 1:1.5
$[HCu_7](Cp^*)_2(Mes)$ also in 1:1.5	$[Cu_7](Cp^*)_3(Mes)_2$ also in 1:3	$[Cu_{10}Zn_3](Cp^*)_3(Mes)_5$ also 1:1.5
$[HCu_4](Cp^*)_2$ also in 1:1.5	$[HCu_7](Cp^*)_2(Mes)$ also in 1:3	$[Cu_7Zn_2](Cp^*)_3(Mes)_3$ also in 1:1.5
$[Cu_3](Cp^*)_3$ also in 1:1.5	$[Cu_4Zn_{10}](Cp^*)_8$ also in 1:3	$[Cu_4](Cp^*)(Mes)_3$ also in 1:3 und 1:1.5
$[Cu_9Zn](Cp^*)_3(Mes)_2$ also in 3:1	$\{[Cu_3Zn_4](Cp^*)_6(Mes)_6 - H\}$	$[HCu_5](Mes)_3$

6. Appendix

6.1 Supporting information for the methodical part

$[Cu_4Zn_{10}](Cp^*)_8$ also in 1:1.5	$[Cu_{10}Zn_2](Cp^*)_2(Mes)_6$ also in 1:3 and 1:0.75	$[Cu_{10}Zn_2](Cp^*)_3(Mes)_5$
$[Cu_9](Cp^*)_2(Mes)_4$	$[Cu_5](Cp^*)_2(Mes)_2$ also in 1:3	$[Cu_9Zn](Cp^*)_3(Mes)_2$ also in 1:3
$[Cu_4](Cp^*)_2(Mes)$ also in 1:1.5	$[H_3Cu_6Zn_5](Cp^*)_5(Mes)$ also in 1:3	$[Cu_{10}Zn](Cp^*)_2(Mes)_4$
$[Cu_{10}Zn_2](Cp^*)_2(Mes)_6$ also in 1:1.5 and 1:3	$[Cu_4](Cp^*)(Mes)_2$	$[HCu_7](Cp^*)(Mes)_4$
$[Cu_7Zn](Cp^*)_3(Mes)_2$ also in 1:1.5	$[Cu]_7(Cp^*)_3(Mes)$ also in 1:3	$[Cu_5Zn_2](Cp^*)_4$ also in 1:1.5 und 1:3
$[Cu_7Zn](Cp^*)_4(Mes)$ also in 1:1.5	$[Cu_7Zn](Cp^*)_4(Mes)$ also in 1:3	
$[HCu_7](Cp^*)_3$ also in 1:1.5	$[HCu_7](Cp^*)_3$ also in 1:3	$[HCu_5Zn_6](Cp^*)_5(Mes)$ also in 1:3 und 1:1.5
$[Cu_7Zn_2](Cp^*)_4(Mes)$ also in 1:1.5	$[Cu_7Zn_2](Cp^*)_4(Mes)$ also in 1:3	$[H_2Cu_5Zn_6](Cp^*)_5(Mes)$
$[Cu_4Zn_{10}](Cp^*)_7$ also in 1:1.5	$[Cu_4Zn_{10}](Cp^*)_7$ also in 1:3	$[Cu_7Zn_2](Cp^*)_4(Mes)$ also in 1:1.5
$[Cu_5Zn_6](Cp^*)_5(Mes)$ also in 1:1.5	$[Cu_4](Cp^*)_2(Mes)$	$[Cu_9](Cp^*)_3(Mes)_2$ also in 1:1.5
$[CuZn](Cp^*)_2$	$[Cu_5](Cp^*)(Mes)_3$ also in 1:0.75	$[Cu_{10}Zn](Cp^*)_3(Mes)_3$ also in 1:3 und 1:1,5
$[Cu_7Zn](Cp^*)_2(Mes)_4$ also in 1:1.5	$[Cu_{10}Zn](Cp^*)_3(Mes)_3$ also in 1:3	$[Cu_5Zn_2](Cp^*)_4(Mes)$ also in 1:3 und 1:1.5
$[H_3Cu_2Zn](Cp^*)_2$ also in 1:1.5 and 1:0.75	$[HCu_4](Cp^*)_2$	$[Cu_{10}Zn_2](Cp^*)_2(Mes)_5$
$[Cu_9Zn_2](Cp^*)_3(Mes)_4$ also in 1:1.5	$[Cu_9Zn_2](Cp^*)_3(Mes)$ also in 1:3	$\{[Cu_3] (Cp^*)_2(Mes) -H\}$
$[HCu_9]Cp^*(Mes)_4$ also in 1:1.5	$[H_2Cu_3](Cp^*)_3$	$[Cu_9Zn_3](Cp^*)_4(Mes)_3$ also in 1:3 und 1:1.5
$[Cu_5](Cp^*)_2(Mes)_2$ also in 1:1.5	$[HCu_8Zn_3](Cp^*)_4(Mes)_3$ also in 1:3	$[Cu_3Zn_2](Cp^*)_4$ also in 1:3 und 1:1.5
$[Cu_9Zn_3](Cp^*)_4(Mes)_3$ also in 1:1.5	$[HCu_8Zn](Cp^*)_4$ also in 1:3	$\{[Cu_4](Mes)_4 -H\}$
$[HCu_5Zn_2](Cp^*)_4(Mes)$ also in 1:1.5	$[HCu_9]Cp^*(Mes)_4$ also in 1:3	$[Cu_3](Cp^*)_2$ also in 1:3
$[Cu_7Zn_2](Cp^*)_2(Mes)_5$ also in 1:1.5	$[Cu_4](Cp^*)(Mes)_3$ also in 1:3	$[Cu_3Zn_3](Cp^*)_4$ also in 1:3 und 1:1.5
$[Cu_{10}Zn](Cp^*)_3(Mes)_3$ also in 1:1.5	$[Cu_9Zn_3](Cp^*)_4(Mes)_3$ also in 1:3	$[HCu_3Zn_2](Cp^*)_3$ also in 1:3 und 1:1.5
	$[HCu_5Zn_2](Cp^*)_4(Mes)$ also in 1:3	$[CuZn](Cp^*)_2$ also in 1:1.5

6. Appendix
6.1 Supporting information for the methodical part

| | | $[H_3Cu_2Zn](Cp^*)_2$ also in 1:3 |
| | | $[HCu_5](Cp^*)_2(Mes)$ also in 1:1.5 |

Table S2: Fragments identified in LIFDI-MS spectra of isolated Cu/Zn clusters.

in isolated $[Cu_4Zn_{9/10}](Cp^*)_8$ -> thermal instability	in isolated $[Cu_{10}Zn_2(Cp^*)_2(Mes)_6]$	in isolated $[CuZn_2](Cp^*)_3$
$\{[Cu_3Zn_2](Cp^*)_3 - H\}$	$[Cu_{10}Zn_2](Cp^*)_2(Mes)_6$	$[CuZn](Cp^*)_2$
$\{[Cu_2Zn_2](Cp^*)_3 - 2H\}$	$[Cu_{10}]Cp^*(Mes)_6$	$[H_4Cu_3](Cp^*)_2$
$[Cu_3Zn_3](Cp^*)_4$	$ZnCp^*Mes$	$[CuZn_2](Cp^*)_2$
$[HCu_4](Cp^*)_2$	$\{[Cu_{10}Zn_2](Cp^*)_2(Mes)_7 - H\}$	$[CuZn_2](Cp^*)_3$
$[Cu_3Zn_4](Cp^*)_5$	$[HCu_{10}](Mes)_6$	$\{[Cu_3Zn_2](Cp^*)_3 - H\}$
$[Cu_4Zn_4](Cp^*)_5$	$[H_2Zn_2]Cp^*$	$\{[Cu_2Zn_4](Cp^*)_4 - H\}$
$[Cu_3Zn_2](Cp^*)_4$	$[Cu_{10}]Cp^*(Mes)_5$	$\{[Cu_2Zn_2](Cp^*)_3 - H\}$
$[Cu_4Zn_{10}](Cp^*)_8$	$[Cu_{10}]Cp^*(Mes)_4$	$[Cu_7Zn](Cp^*)_4/$ $\{[Cu_6Zn_2](Cp^*)_4 - H\}$
$[Cu_4Zn_{10}](Cp^*)_7$	$[Cu_{10}Zn]Cp^*(Mes)_6$	$[H_4Cu_2Zn_2](Mes)_3$
$\{[Cu_7Zn_4](Cp^*)_5 - H\}/$ $[H_2Cu_9Zn_2](Cp^*)_5$	$[Cu_{10}](Cp^*)_2(Mes)_4$	$[Cu_3Zn_4](Cp^*)_5$
$[HCu_8Zn](Cp^*)_4$	$[CuZn]Cp^* Mes$	$[HCu_4](Cp^*)_2$
$[H_4Cu_6Zn_7](Cp^*)_7$	$[Cu_3]Cp^*Mes$	$[HCu_7](Cp^*)_3$
$[Cu_5Zn_2](Cp^*)_4$	$[CuZn](Cp^*)_2Mes$	$[Cu_3Zn_2](Cp^*)_4$
$[HCu_5Zn](Cp^*)_3/$ $[Cu_4Zn_2](Cp^*)_3$	$\{[Cu_{10}Zn_2](Cp^*)_3(Mes)_6 - H\}$	$[Cu_2](Cp^*)_3$
$\{[Cu_6Zn_4](Cp^*)_5 - 2H\}$	$[Cu_6] (Mes)_5$	$[Cu_5Zn_2](Cp^*)_4$
$[Zn_2](Cp^*)_3$	$[Cu_6](Mes)_5 /$ $\{[Cu_5Zn](Mes)_5 -H\}$	$\{[Cu_5Zn](Cp^*)_3 - H\}$
$[Cu_7Zn](Cp^*)_4$	$\{[Cu_2Zn](Cp^*)_2Mes - H\}$	$[H_4Zn_3](Mes)_3$
$[H_2Cu_6Zn_6](Cp^*)_6$	$\{[Cu_{10}Zn]Cp^*(Mes)_7 - H\}$	
$[H_4Cu_6Zn_5](Cp^*)_6$	$[H_2Cu_{12}](Cp^*)_2(Mes)_8/$ $[HCu_{11}Zn](Cp^*)_2(Mes)_8$	
$[HCu_7](Cp^*)_3$	$\{[Cu_3Zn](Cp^*)_2(Mes)_2 - H\}$	
$[H_4Cu_9Zn_2](Cp^*)_5 /$ $[H_3Cu_9Zn_3](Cp^*)_5$	$[Cu_7]Cp^*(Mes)_5$	
$[H_4Cu_{10}Zn_3](Cp^*)_6/$ $[H_3Cu_9Zn_4](Cp^*)_6$	$[CuZn]Cp^*Mes$	
$[H_4Cu_8Zn](Cp^*)_5$	$\{[Cu_2Zn]Cp^*(Mes)_2 - 2H\}$	

$[H_4Cu_{10}Zn_6](Cp^*)_8$ / $[H_3Cu_9Zn_7](Cp^*)_8$		

The following supporting data documentation refers to pages 83-92.

CE vs. I plots for all peaks in the Cu/Zn (1:1.5) library

Note: Peak intensities were determined as relative integrals with respect to the overall integral of all peaks in the spectrum. This leads to a bias in integration at CE > 15 due to the enhanced formation of lighter fragments with m/z < 200, lying outside the measurement range. Actual peak intensities are therefore expected to be lower than detected at CE > 15.
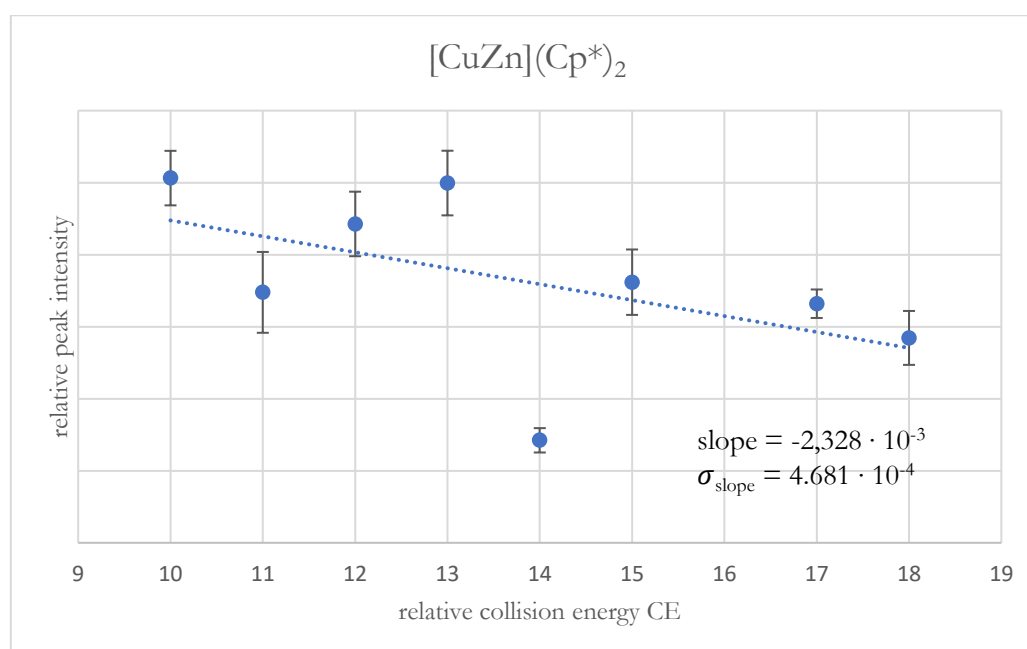
Figure S1: *CE vs. I plot of the ion* $\{[CuZn](Cp^*)_2\}^+$.

The ion was identified in the LIFDI-MS spectrum of isolated [CuZn$_2$](Cp*)$_3$. The CE vs. I plot is indicative of a molecular ion. The species is supposed to be a fragment of [CuZn$_2$](Cp*)$_3$, which is formed (thermally) during the ionization process. Consequently, it shows a CE vs. I behavior like a molecular ion.
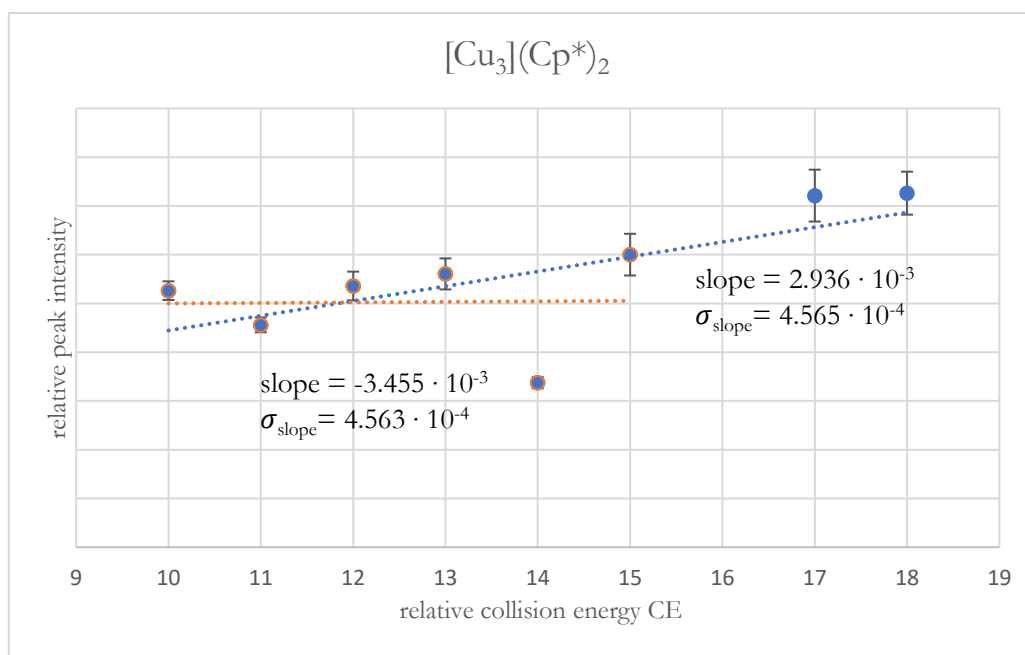
Figure S2: *CE vs. I* plot of the ion $\{[Cu_3](Cp^*)_2\}^+$.

The CE vs. I plot is indicative of a fragment ion. The species was observed in the LIFDI-MS spectrum of isolated $[CuZn_2](Cp^*)_3$.
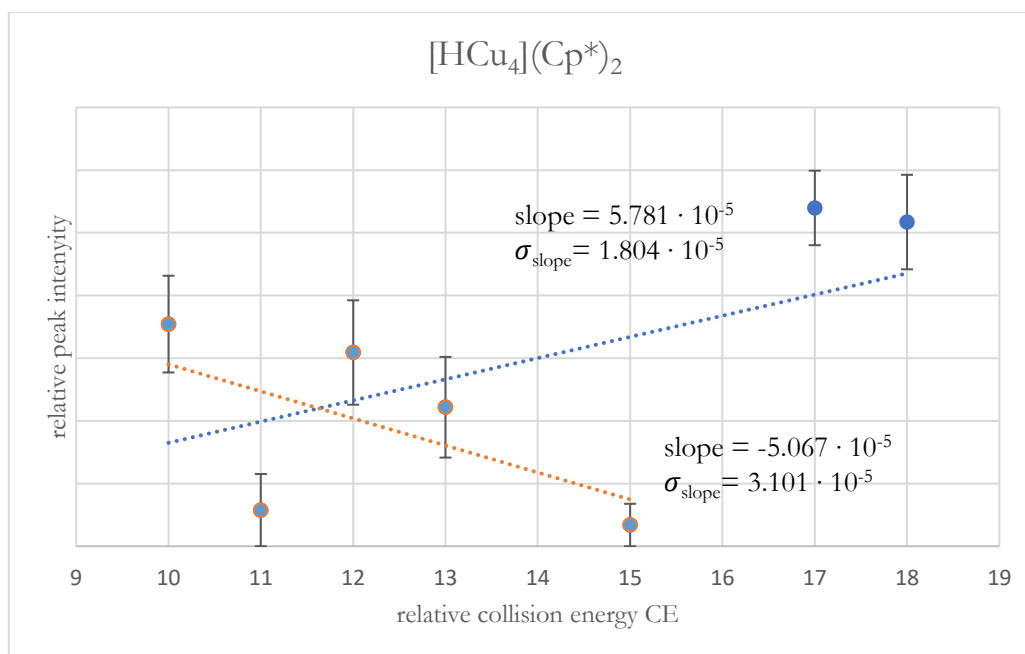
Figure S3: *CE vs. I* plot of the ion $\{[HCu_4](Cp^*)_2\}^+$.

*The species was identified in the LIFDI-MS spectrum of isolated $[CuZn_2](Cp^*)_3$ and $[Cu_4Zn_{9/10}](Cp^*)_8$ (**4/5**). The CE vs. I plot is indicative of a molecular ion if considering collision energies from 10-15. At higher collision energies, data interpretation is difficult due to the bias in*

6. Appendix

6.1 Supporting information for the methodical part

integration. The species is supposed to be a fragment, which is formed (thermally) during the ionization process. Consequently, it shows a CE vs. I behavior like a molecular ion.
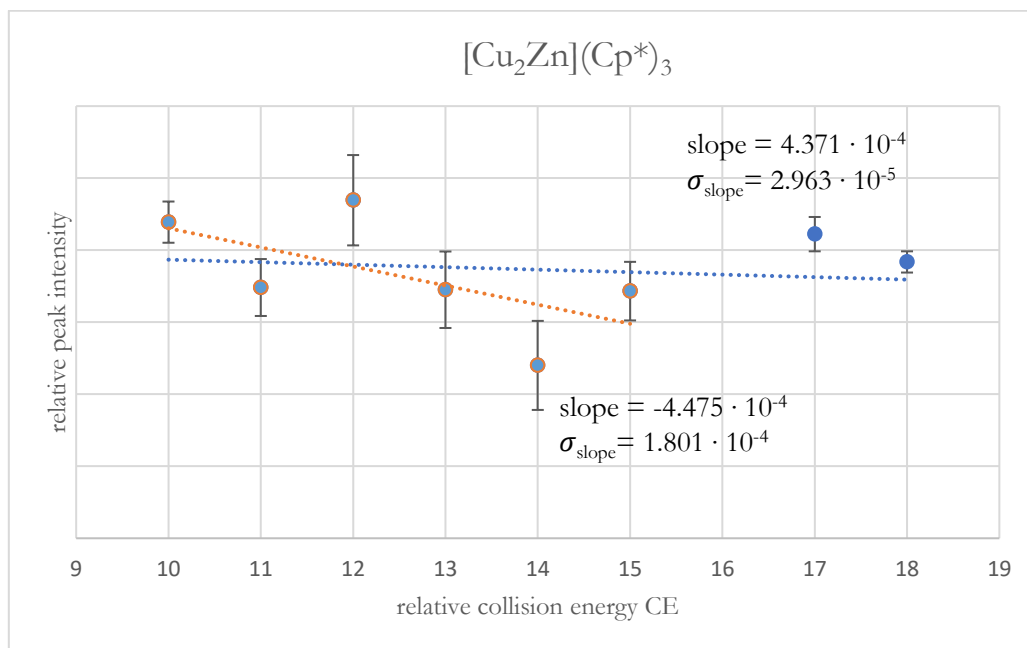
Figure S4: *CE vs. I plot of the ion* {[Cu₂Zn](Cp*)₃}⁺.

A clear assignment of the species is not possible. According to the slope in the CE = 10-15 region, the species might be a molecular ion.
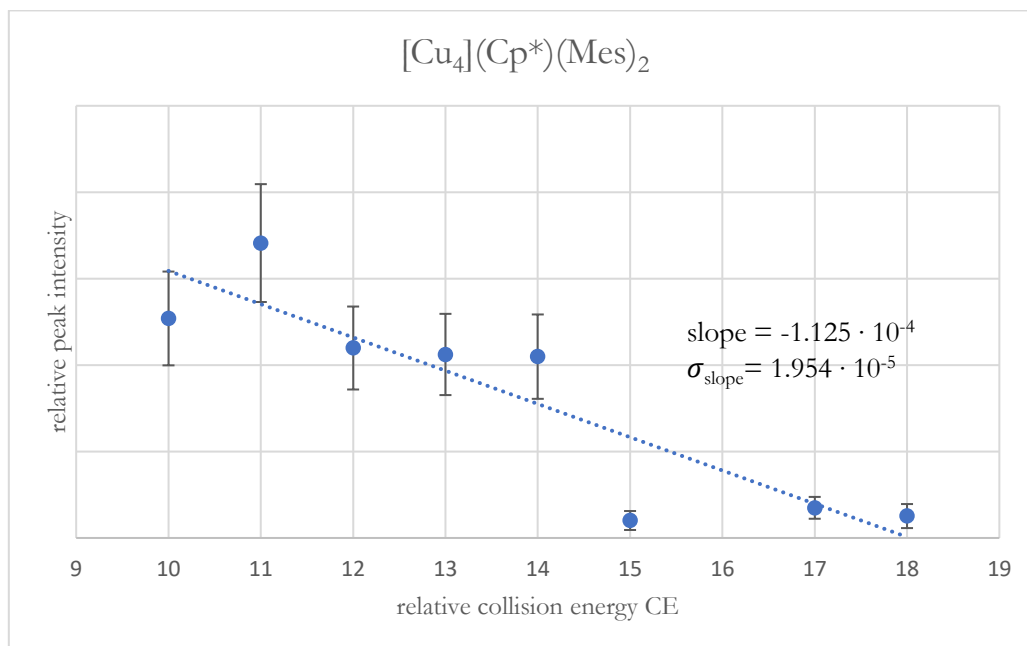
Figure S5: *CE vs. I plot of the ion* {[Cu₄](Cp*)(Mes)₂}⁺.

*The species is clearly assigned as a molecular ion according to the CE vs. I plot. However, it may also be a fragment formed during ionization.*

6. Appendix
6.1 Supporting information for the methodical part
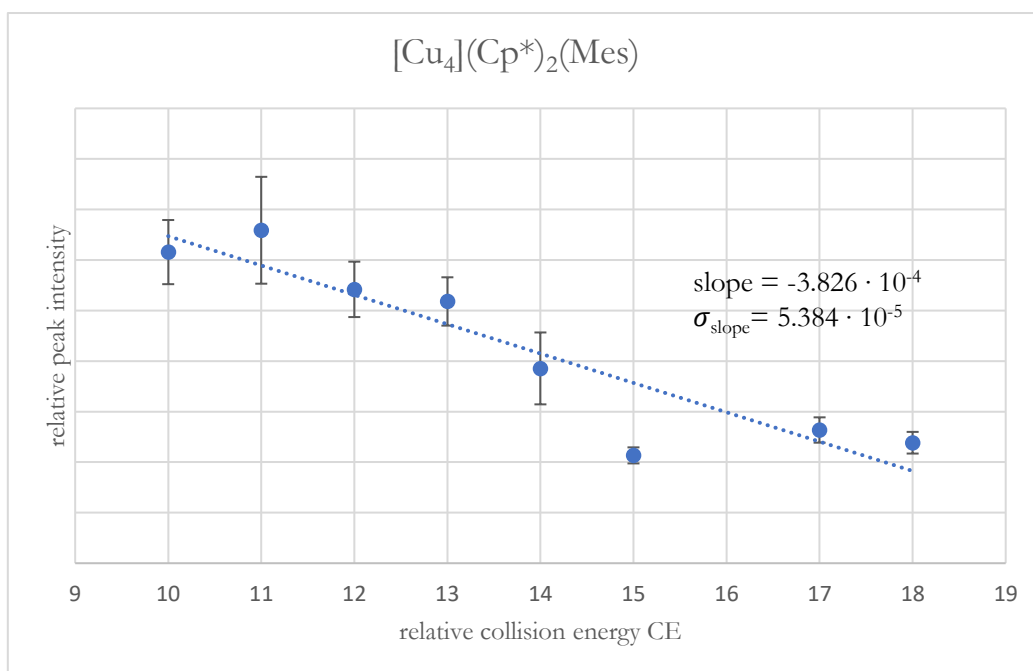
Figure S6: *CE vs. I* plot of the ion $\{[Cu_4](Cp^*)_2(Mes)\}^+$.

The species is clearly assigned as a molecular ion according to the CE vs. I plot. However, it may also be a fragment formed during ionization.
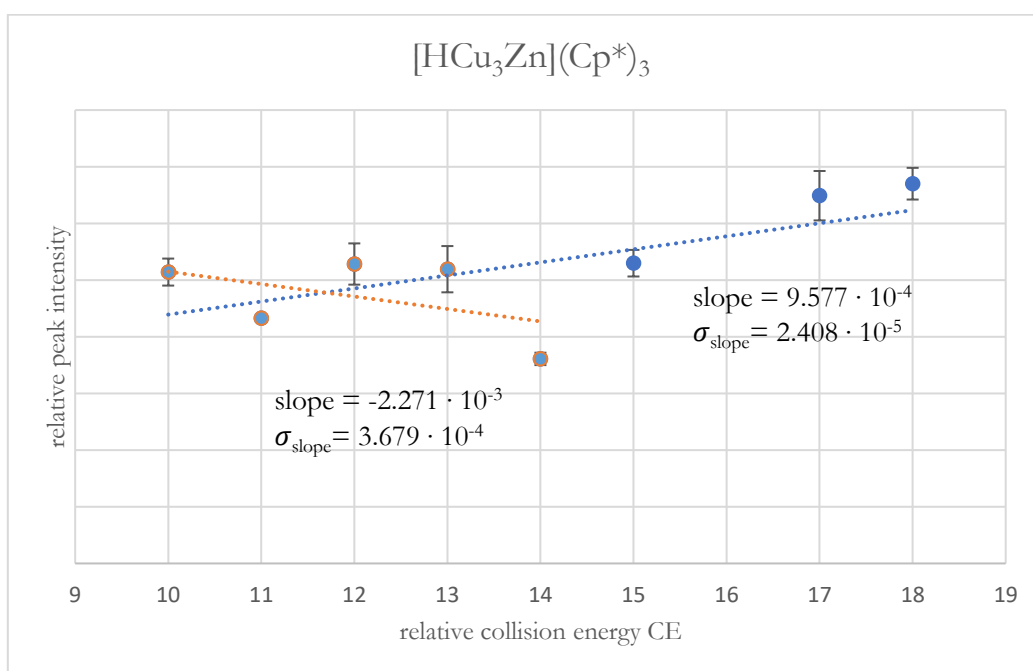
Figure S7: *CE vs. I* plot of the ion $\{[HCu_3Zn](Cp^*)_3\}^+$.

A clear assignment of the species is not possible. However according to the CE = 10-14 region, it may be assigned as a molecular ion.
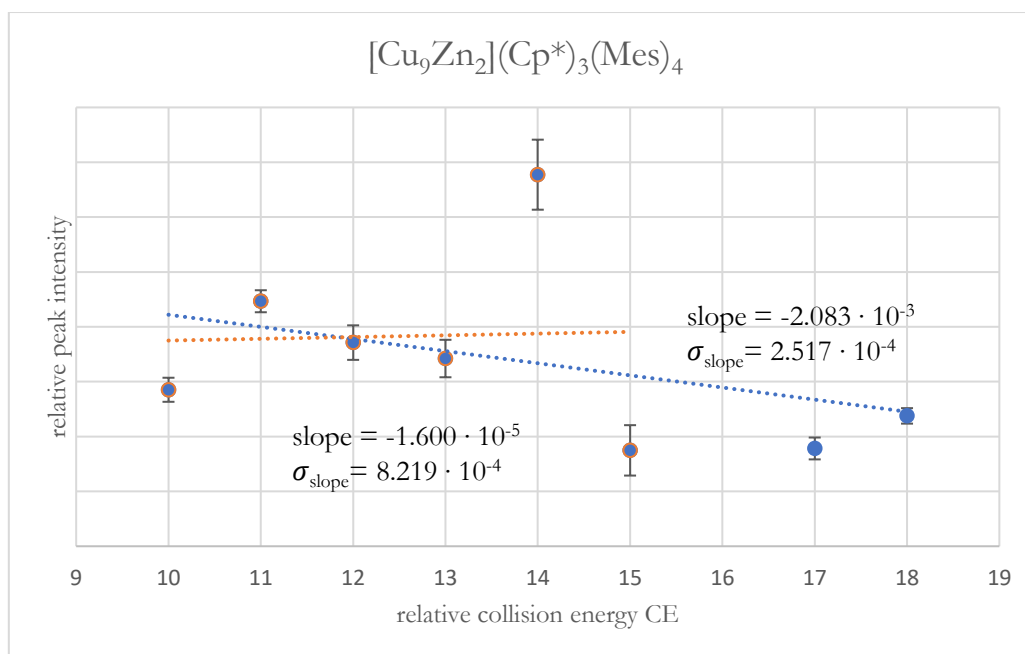
6. Appendix

6.1 Supporting information for the methodical part
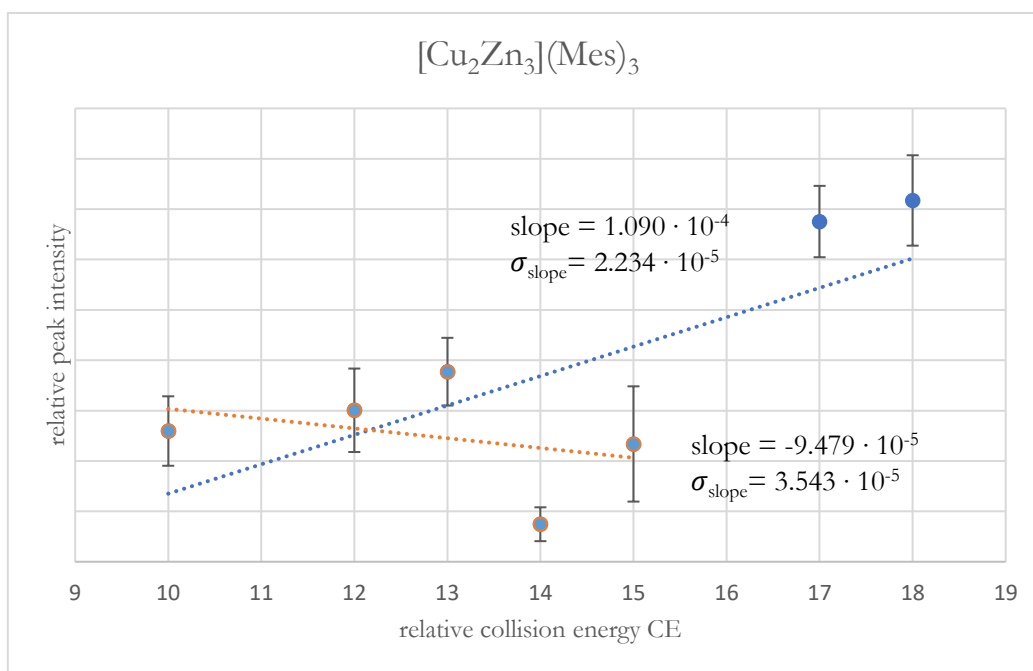
Figure S8: *CE vs. I* plot of the ion $\{[Cu_2Zn](Mes)_3\}^+$.

A clear assignment of the species is not possible. However according to the CE = 10-14 region, it may be assigned as a molecular ion.
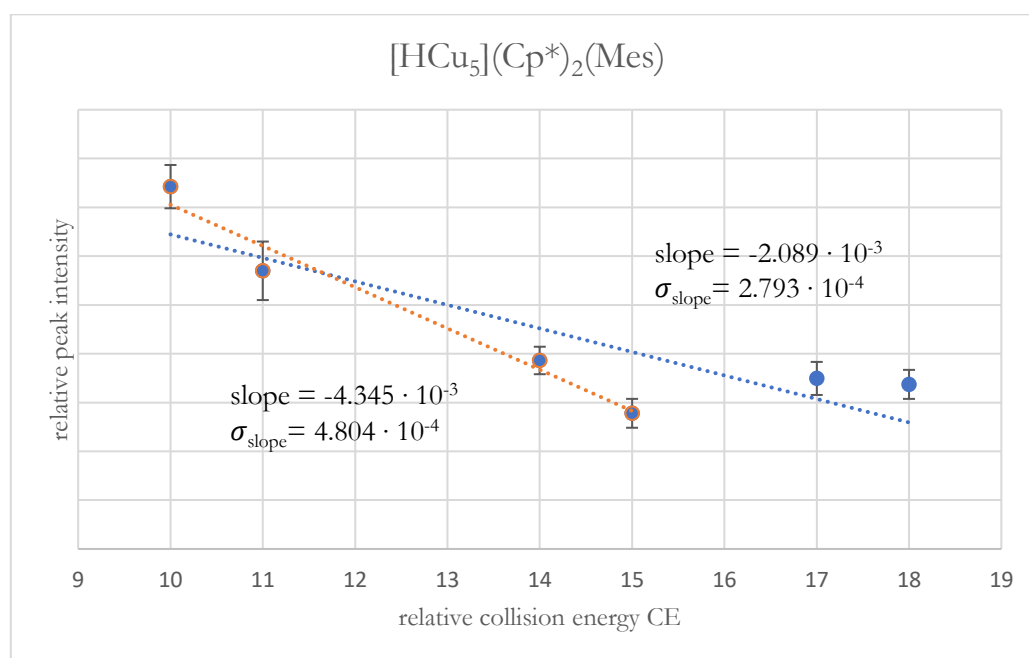
Figure S9: *CE vs. I* plot of the ion $\{[HCu_5](Cp^*)_2(Mes)\}^+$.

The species is clearly assigned as a molecular ion according to the CE vs. I plot. However, it may also be a fragment formed during ionization. The slight increase in peak intensity at CE > 15 is supposed to be due to the bias in integration.
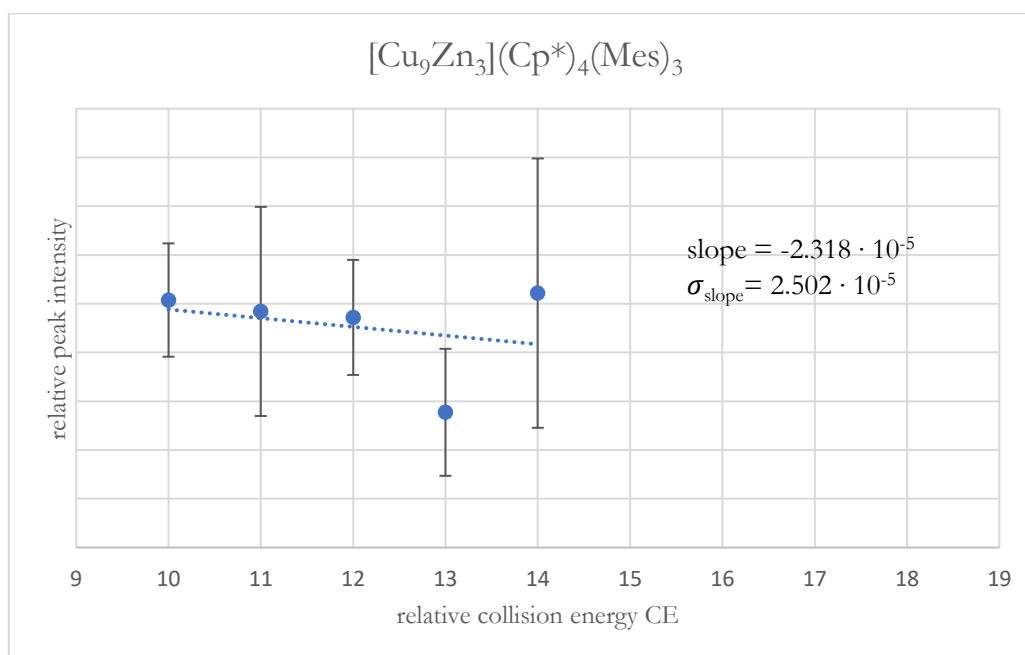
6. Appendix
6.1 Supporting information for the methodical part
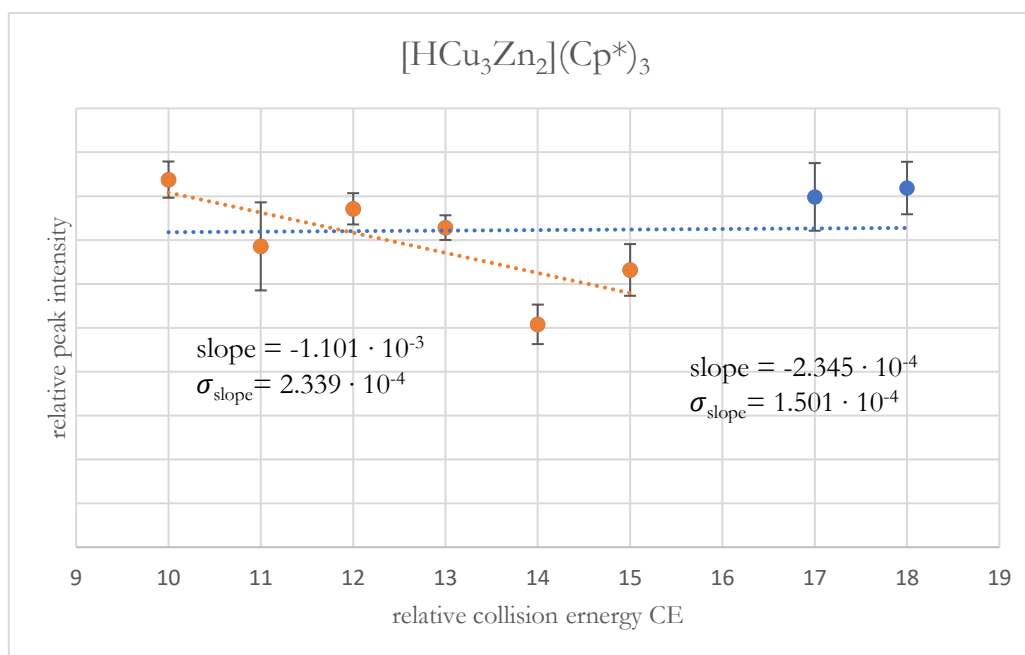
Figure S10: *CE vs. I* plot of the ion $\{[HCu_3Zn_2](Cp^*)_3\}^+$.

*The species was identified in LIFDI-MS spectra of isolated $[Cu_4Zn_{9/10}](Cp^*)_8$ **(4/5)**. The CE vs. I plot is indicative of a molecular ion if considering collision energies from 10-15. At higher collision energies, data interpretation is difficult due to the bias in integration. The species is supposed to be a fragment of $[CuZn_2](Cp^*)_3$, which is formed (thermally) during the ionization process. Consequently, it shows a CE vs. I behavior like a molecular ion.*
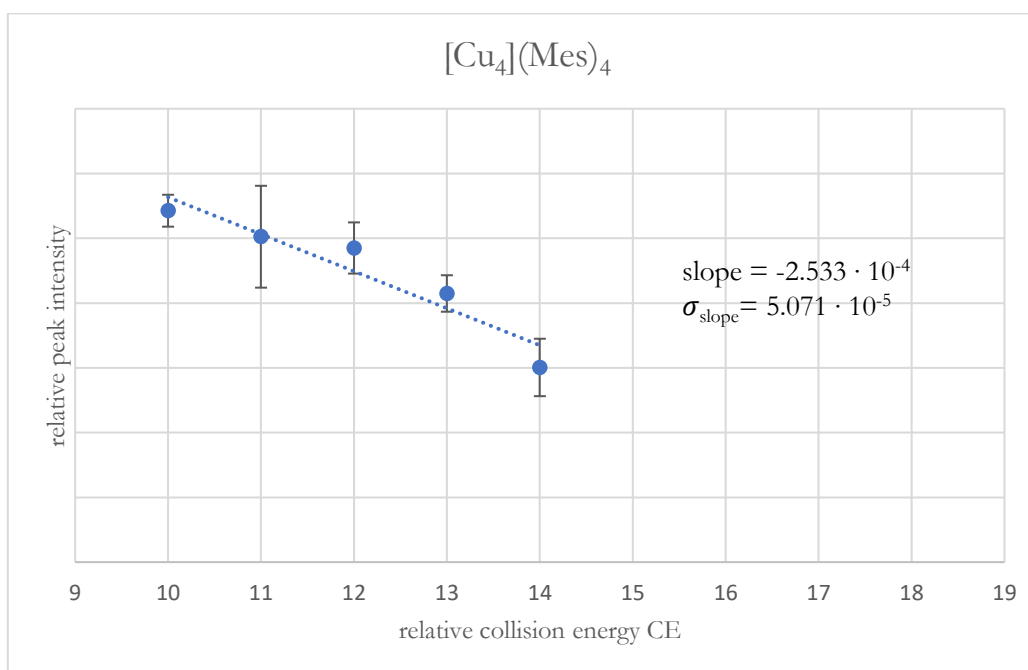
Figure S11: *CE vs. I* plot of the ion $\{[Cu_4](Mes)_4\}^+$.

According to the CE vs. I plot, the species clearly is assigned as molecular ion. However, it is supposed that the species is formed out of $[Cu_5](Mes)_5$ by loss of one CuMes unit during ionization.

6. Appendix

6.1 Supporting information for the methodical part
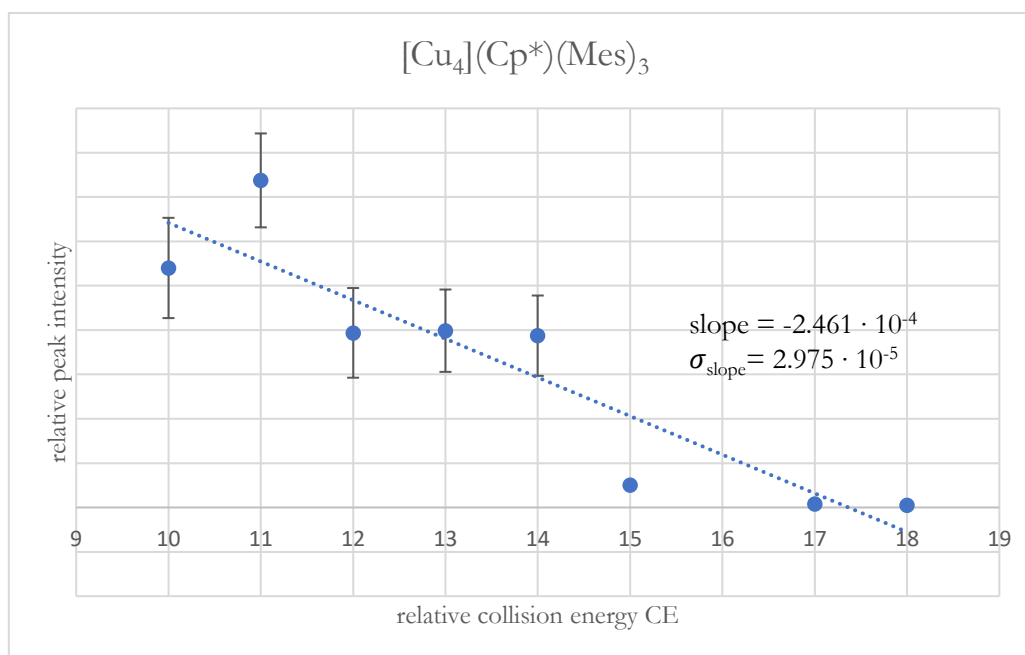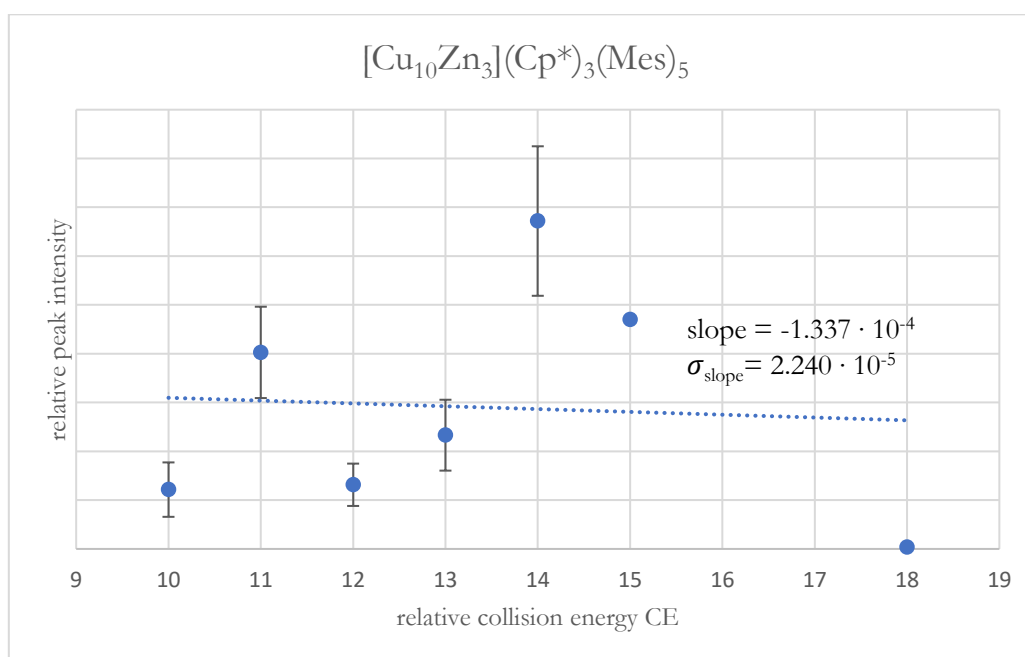

Figure S12: *CE vs. I* plot of the ion $\{[Cu_4](Cp^*)(Mes)_3\}^+$.

The species is clearly assigned as a molecular ion according to the CE vs. I plot. However, it may also be a fragment formed during ionization.
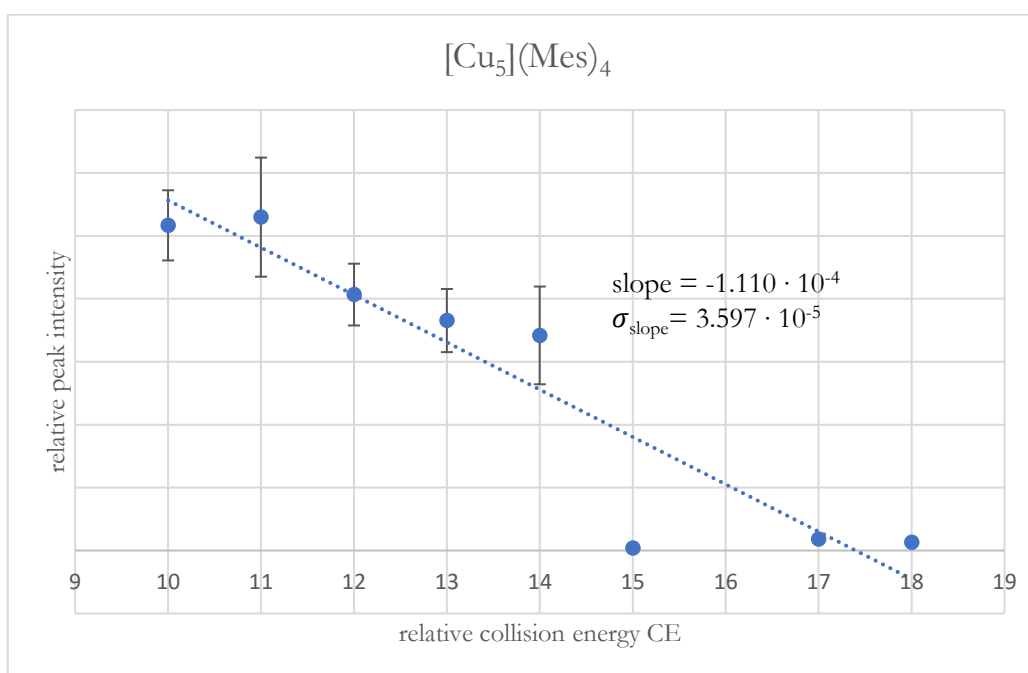
Figure S13: *CE vs. I* plot of the ion $\{[Cu_5](Mes)_4\}^+$.

According to the CE vs. I plot, the species clearly is assigned as molecular ion. However, it is supposed that the species is formed out of $[Cu_5](Mes)_5$ by loss of one Mes unit during ionization.

6. Appendix

6.1 Supporting information for the methodical part
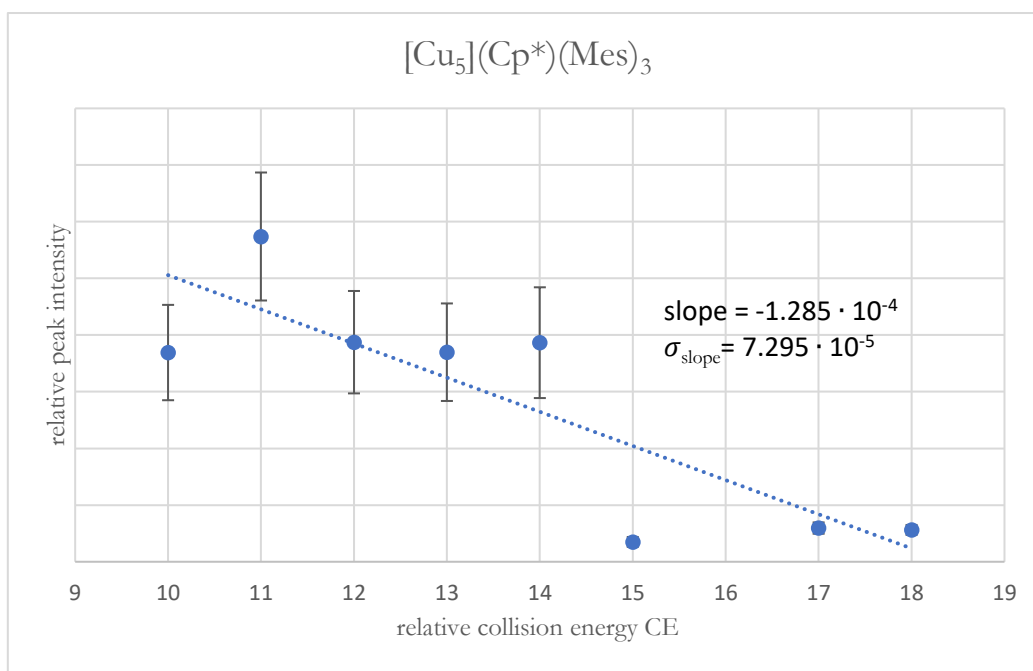
Figure S14: *CE vs. I* plot of the ion $\{[Cu_5](Cp^*)(Mes)_3\}^+$.

The species is clearly assigned as a molecular ion according to the CE vs. I plot. However, it may also be a fragment formed during ionization.
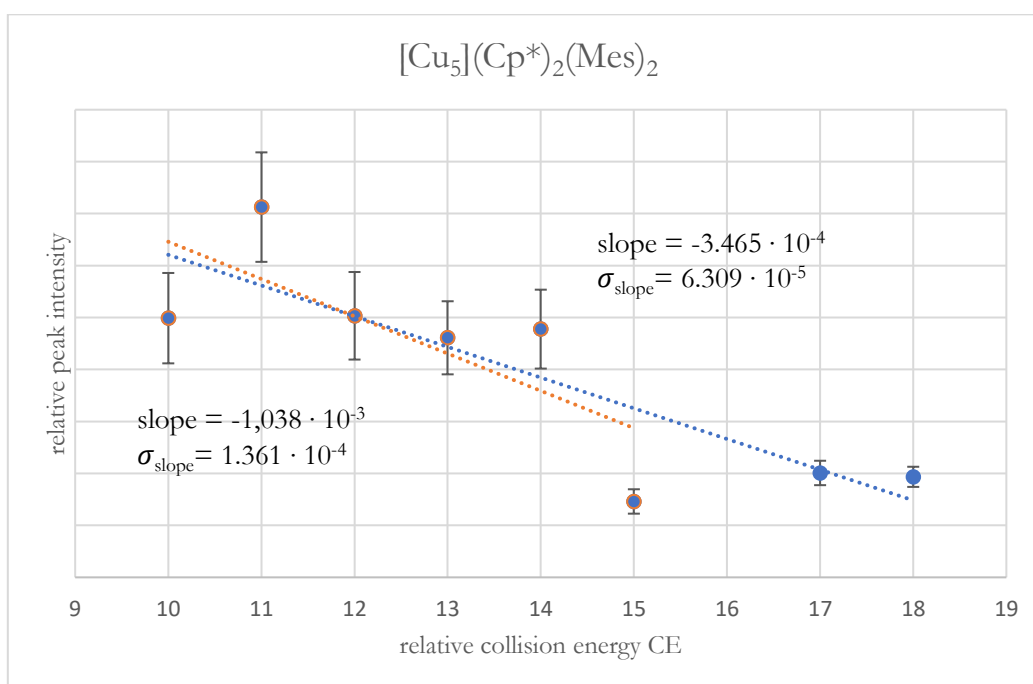
Figure S15: CE vs. I plot of the ion $\{[Cu_5](Cp^*)_2(Mes)_2\}^+$.

The species is clearly assigned as a molecular ion according to the CE vs. I plot. However, it may also be a fragment formed during ionization.

6. Appendix
6.1 Supporting information for the methodical part
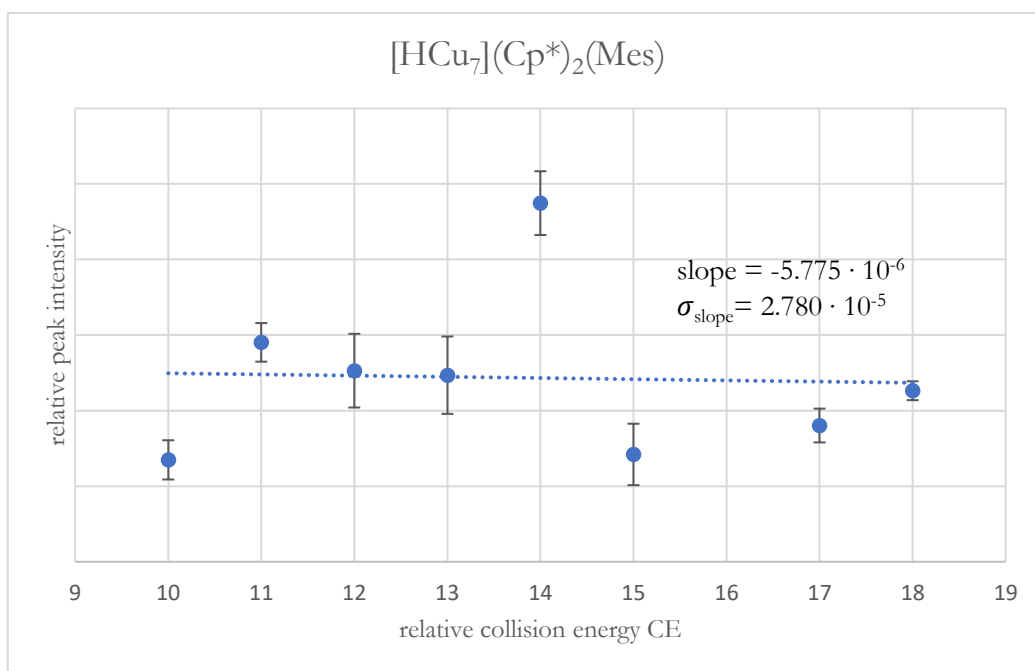
Figure S16: *CE vs. I* plot of the ion $\{[HCu_7](Cp^*)_2(Mes)\}^+$.

A clear assignment of the species is not possible.
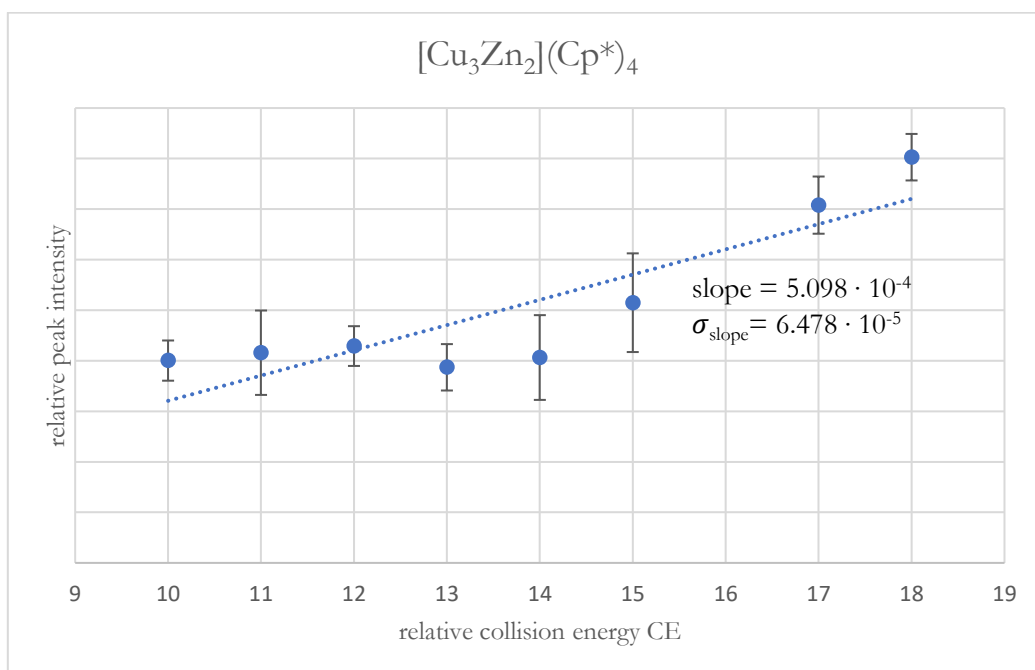
Figure S17: *CE vs. I*

plot of the ion $\{[Cu_3Zn_2](Cp^*)_4\}^+$.

A clear assignment is difficult to make for this species, as the CE vs. I plot in the CE>15 region has to be regarded with care due to the bias in integration. However, an assignment as a fragment ion seems likely.

6. Appendix

6.1 Supporting information for the methodical part
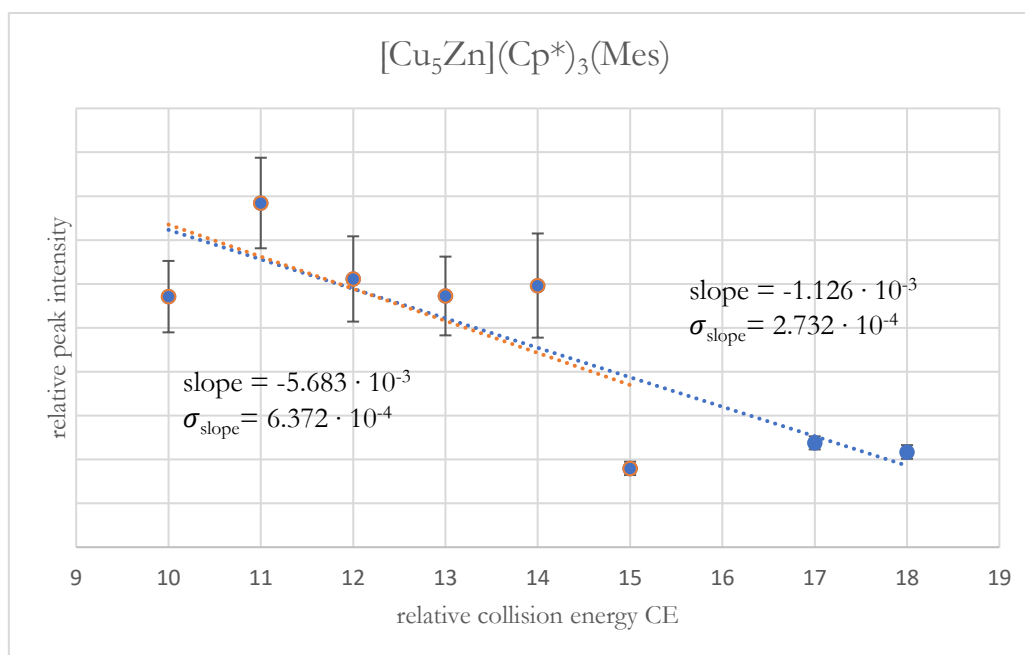
Figure S18: *CE vs. I* plot of the ion $\{[Cu_5Zn](Cp^*)_3(Mes)\}^+$.

The species is clearly assigned as a molecular ion according to the CE vs. I plot. However, it may also be a fragment formed during ionization.
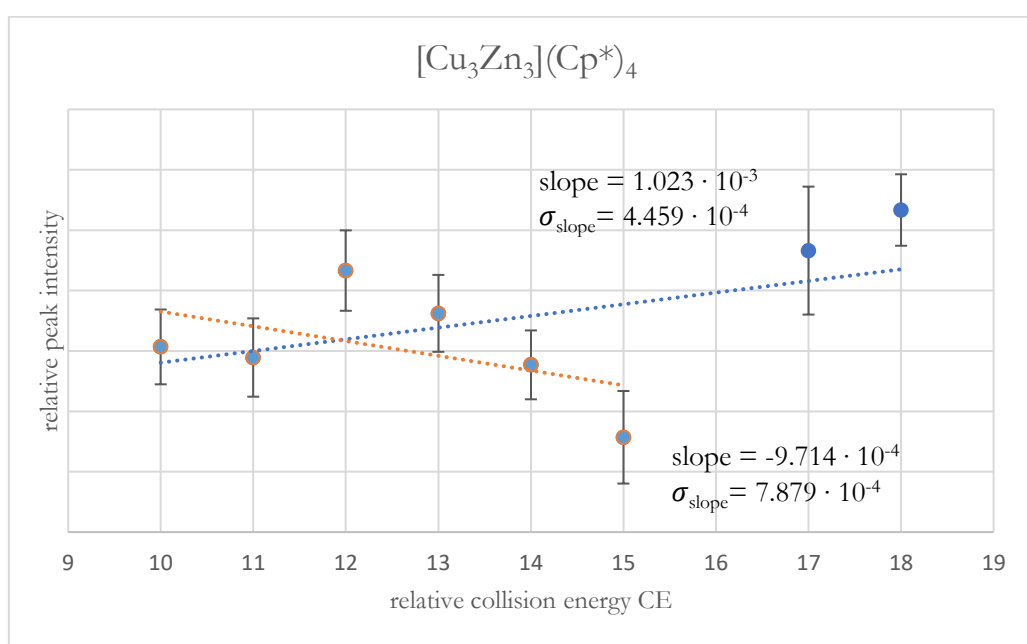
Figure S19: *CE vs. I* plot of the ion $\{[Cu_3Zn_3](Cp^*)_4\}^+$.

*The species was identified in LIFDI-MS spectra of isolated $[Cu_4Zn_{9/10}](Cp^*)_8$ (**4/5**). It is supposed to be formed (thermally) during ionization out of **4/5**, showing consequently the behavior of a molecular ion in the CE vs. I plot. The data at CE > 15 has to be regarded with care due to bias in data integration.*

6. Appendix
6.1 Supporting information for the methodical part
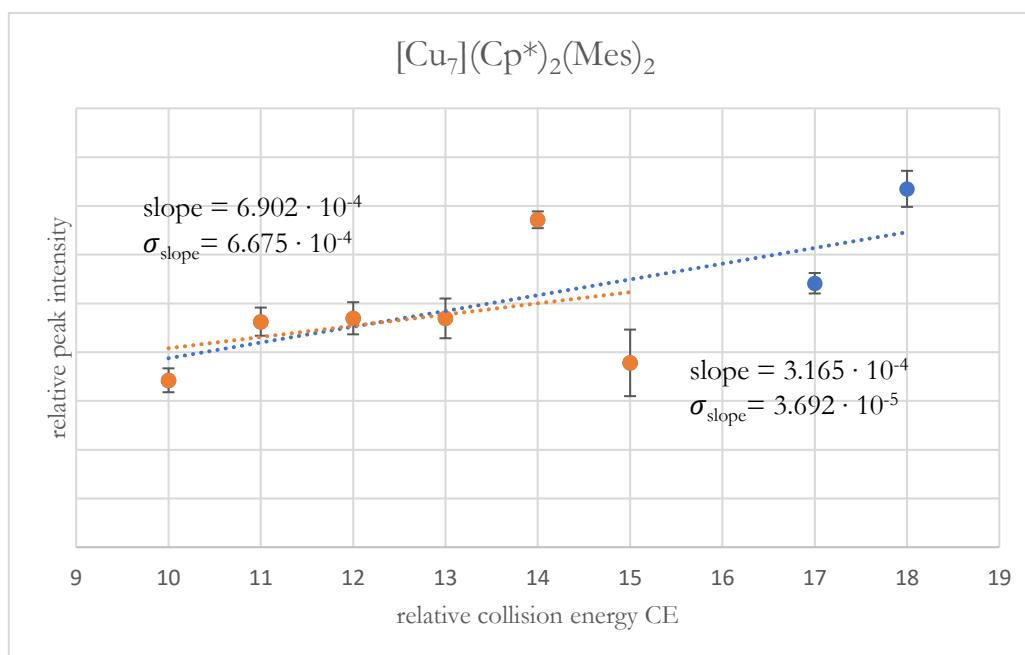
Figure S20: *CE vs. I* plot of the ion $\{[Cu_7](Cp^*)_2(Mes)_2\}^+$.

Due to the bias in integration at CE > 15, a clear assignment is difficult for this species. However, it is likely to be a fragment ion (positive slope also in the CE = 10 − 15 region).
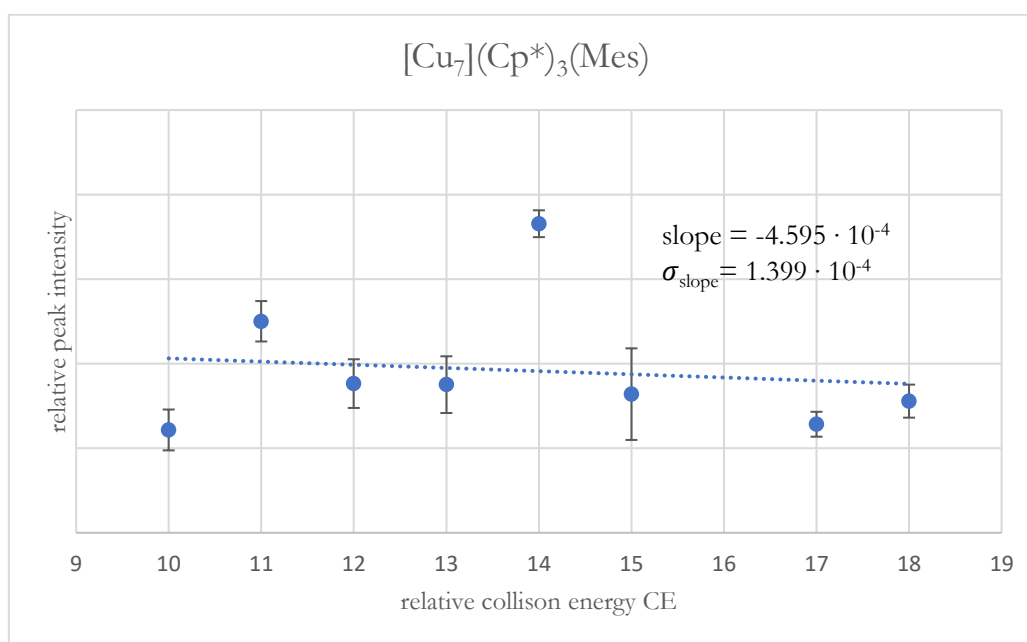
Figure S21: *CE vs. I* plot of the ion $\{[Cu_7](Cp^*)_3(Mes)\}^+$.

Due to the steady-state behavior, a clear assignment is not possible for this species.

6. Appendix

6.1 Supporting information for the methodical part
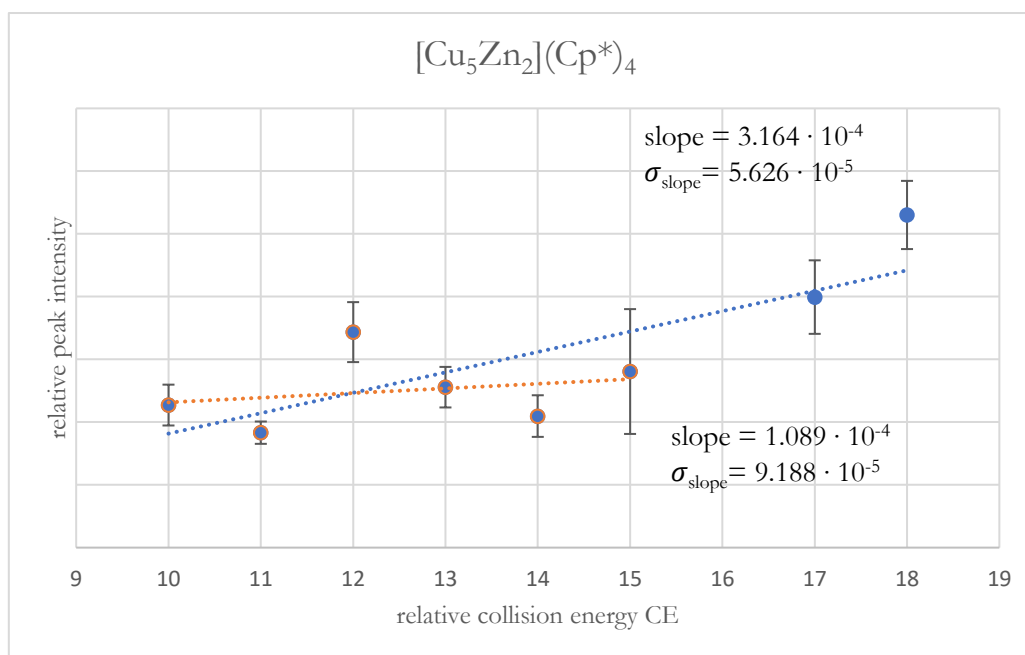
Figure S22: *CE vs. I* plot of the ion $\{[Cu_5Zn_2](Cp^*)_4\}^+$.

A clear assignment for this species is difficult due to the bias in integration at CE > 15. However, it is supposed to be a fragment ion.
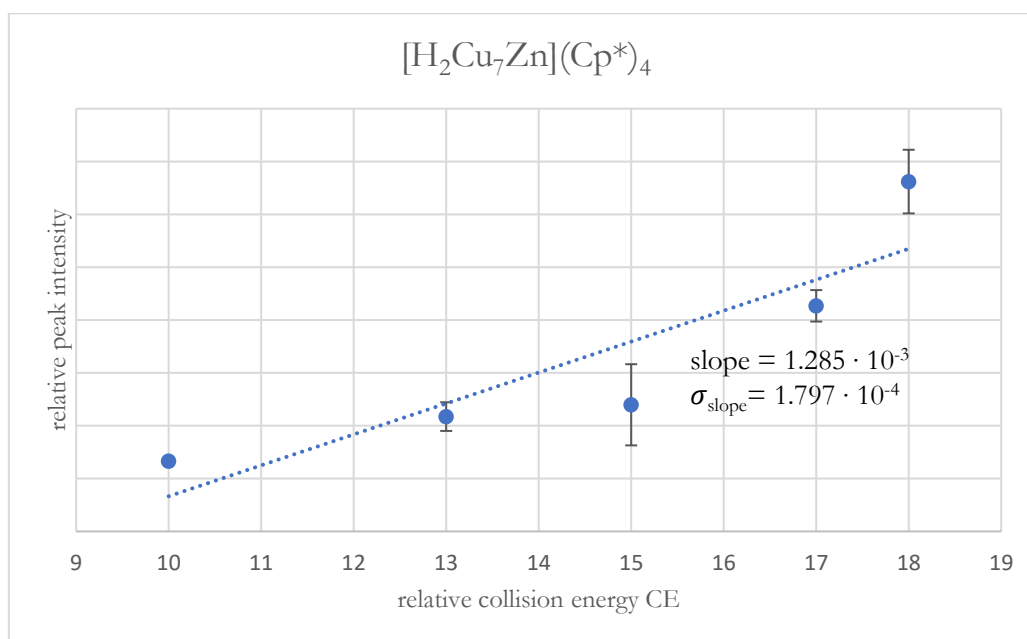
Figure S23: *CE vs. I* plot of the ion $\{[H_2Cu_7Zn](Cp^*)_4\}^+$.

The species is identified as a fragment in isolated [CuZn_2](Cp^*)_3. It shows also the behavior of a fragment ion in the CE vs. I plot.

6. Appendix

6.1 Supporting information for the methodical part
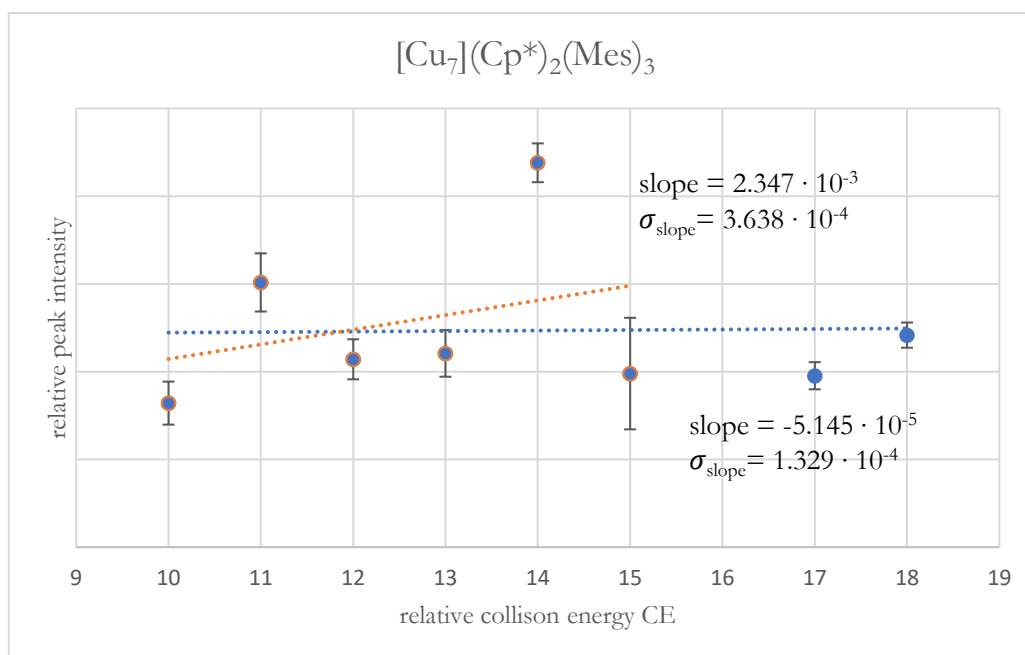
Figure S24: *CE vs. I* plot of the ion $\{[Cu_7](Cp^*)_2(Mes)_3\}^+$.

A clear assignment is not possible for this species (no clear trend).
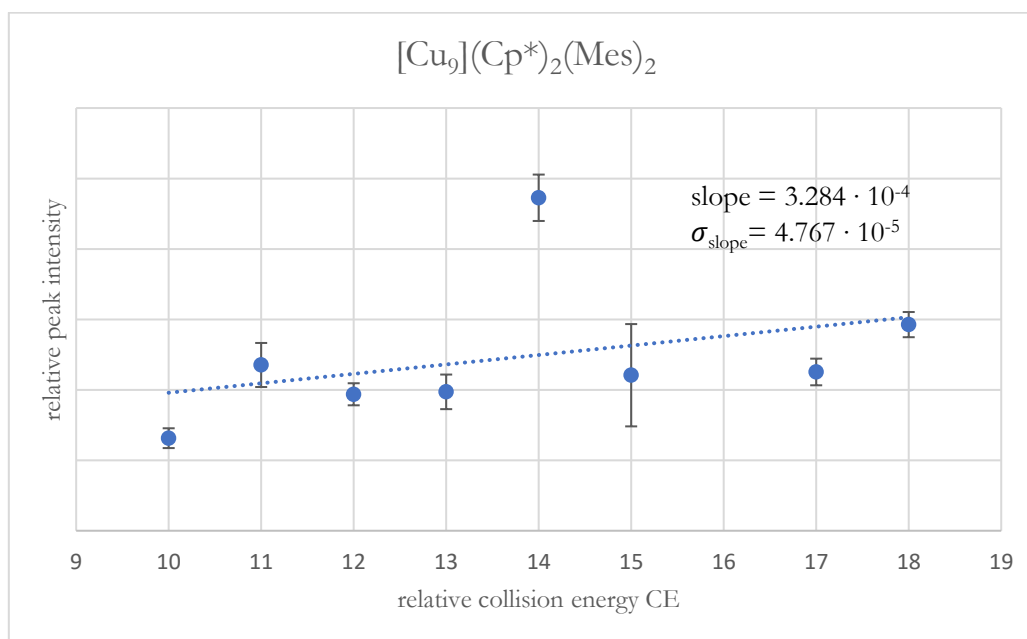
Figure S25: *CE vs. I* plot of the ion $\{[Cu_9](Cp^*)_2(Mes)_2\}^+$.

A clear assignment is not possible for this species due to the bias in integration at CE >15.

6. Appendix

6.1 Supporting information for the methodical part
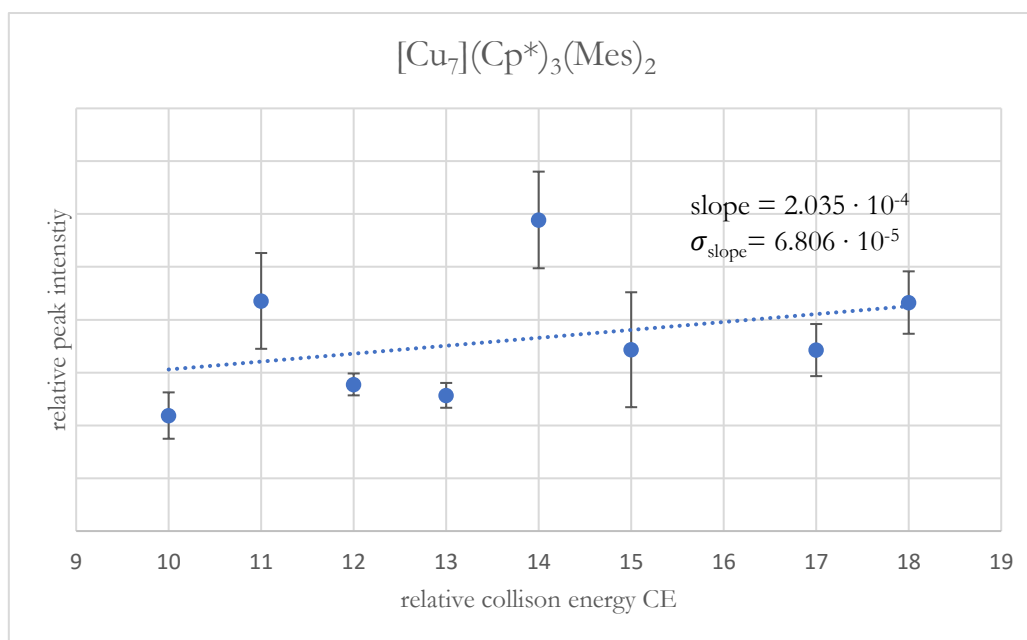
Figure S26: *CE vs. I* plot of the ion ${[Cu_7](Cp^*)_3(Mes)_2}^+$.

A clear assignment is not possible for this species due to the bias in integration at CE > 15.
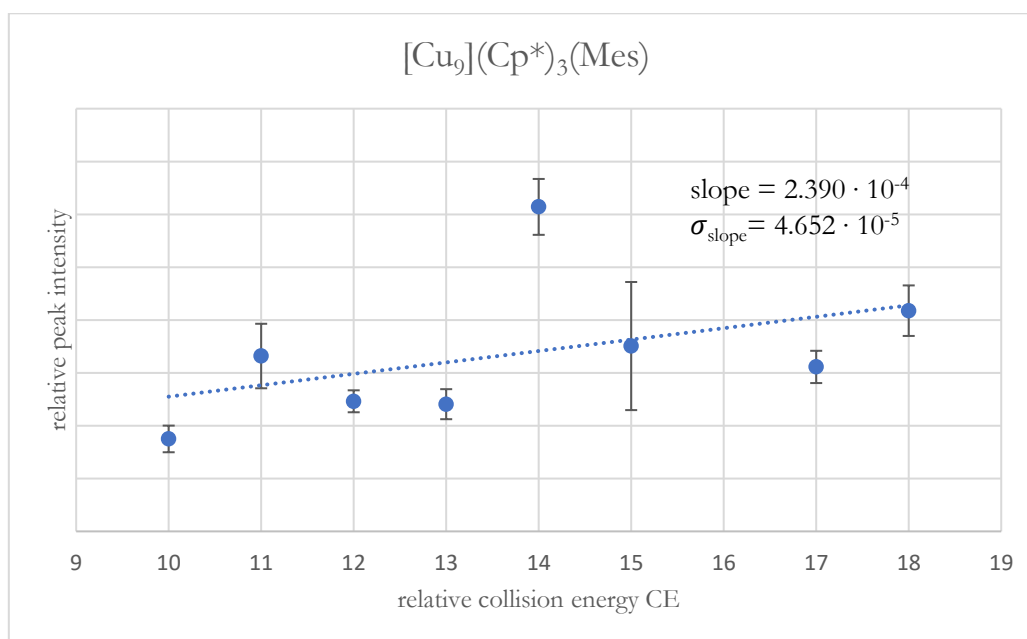
Figure S27: *CE vs. I* plot of the ion ${[Cu_9](Cp^*)_3(Mes)}^+$.

A clear assignment is not possible for this species due to the bias in integration at CE > 15.

6. Appendix

6.1 Supporting information for the methodical part
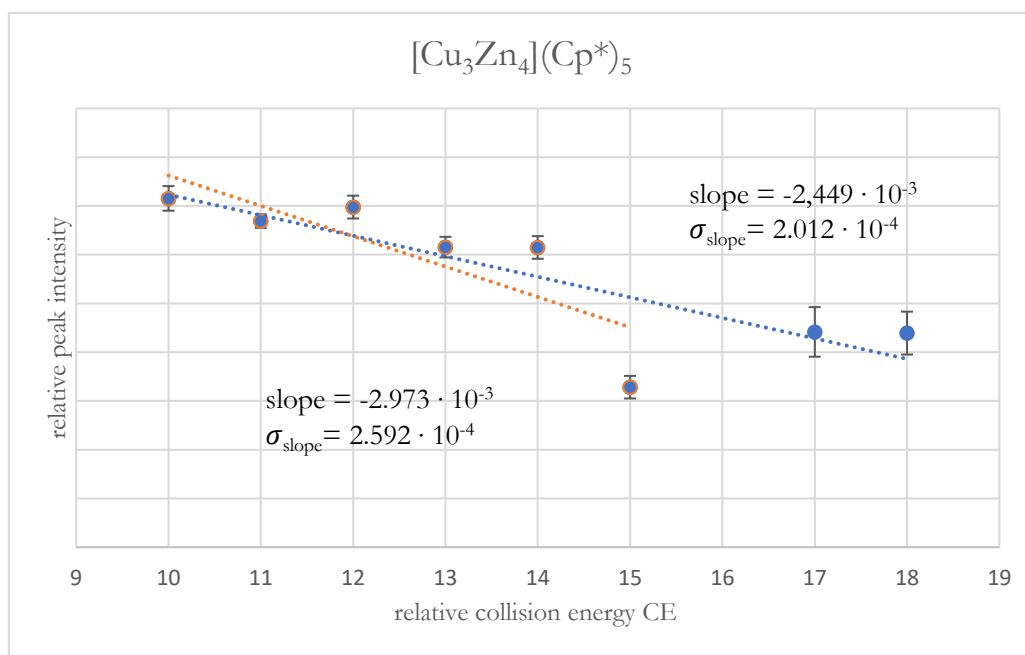
Figure S28: *CE vs. I* plot of the ion $\{[Cu_3Zn_4](Cp^*)_5\}^+$.

The species is clearly assigned as a molecular ion and can also be isolated.
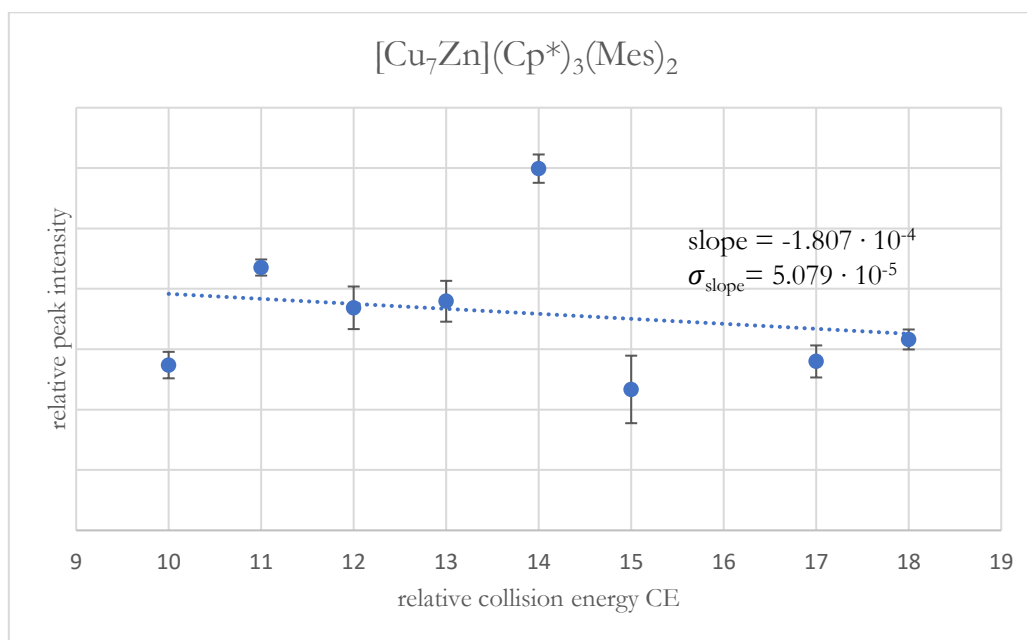
Figure S29: *CE vs. I* plot of the ion $\{[Cu_7Zn](Cp^*)_3(Mes)_2\}^+$.

A clear assignment is difficult for this species. However, it is likely to be a molecular ion, as the peak intensities at CE >15 are expected to be even lower than detected. However, it may also be a fragment formed during ionization.

6. Appendix

6.1 Supporting information for the methodical part
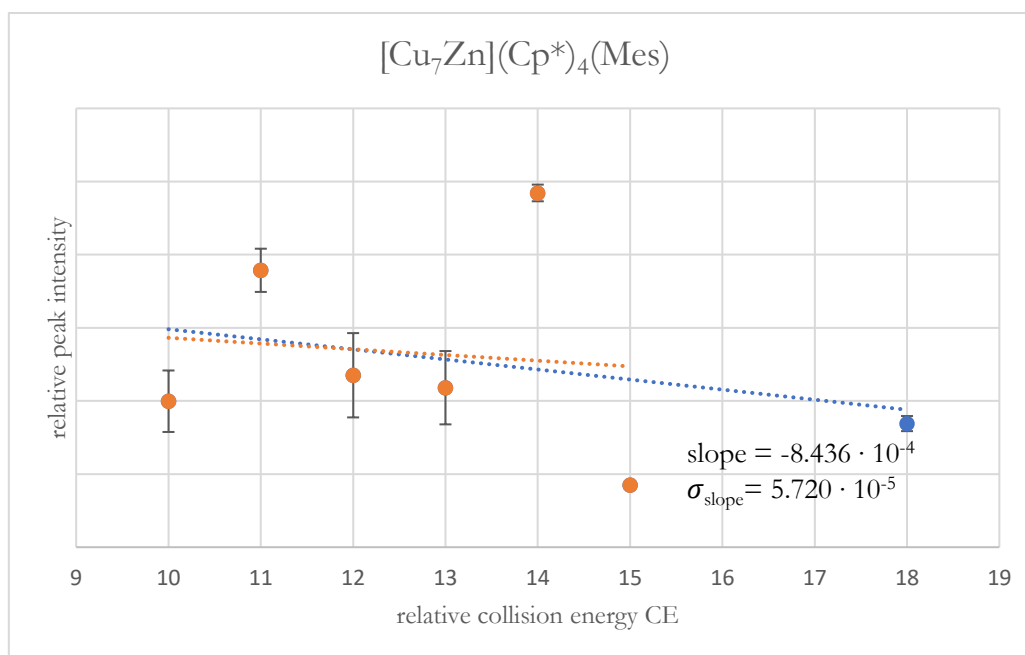
Figure S30: *CE vs. I* plot of the ion $\{[Cu_7Zn](Cp^*)_4(Mes)\}^+$.

The species is clearly assigned as a molecular ion according to the CE vs. I plot. However, it may also be a fragment formed during ionization.
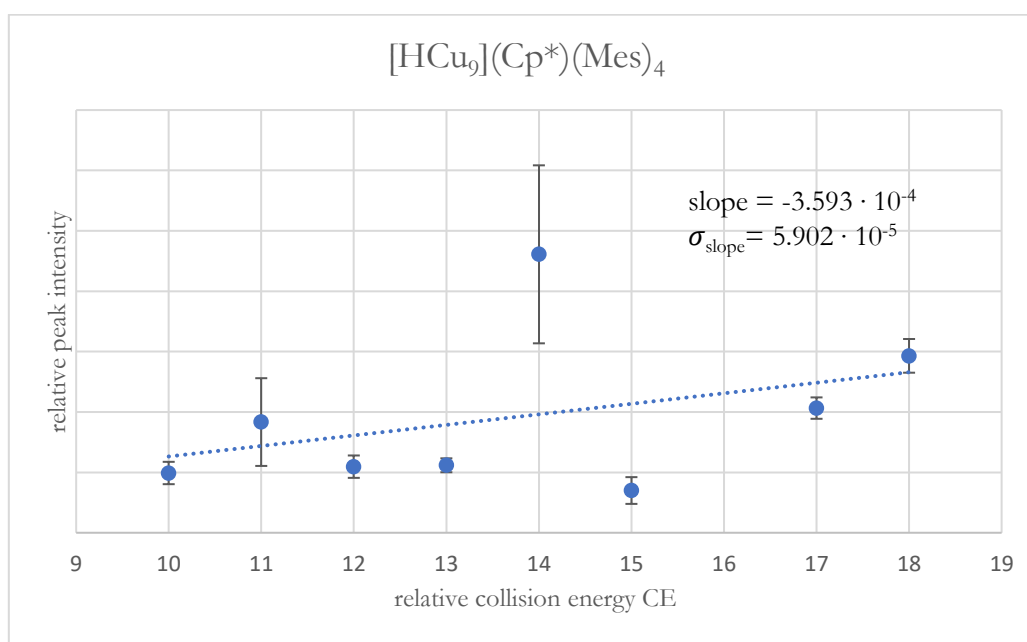
Figure S31: *CE vs. I* plot of the ion $\{[HCu_9](Cp^*)(Mes)_4\}^+$.

A clear assignment is not possible for this species due to the bias in integration at CE > 15.

6. Appendix

6.1 Supporting information for the methodical part
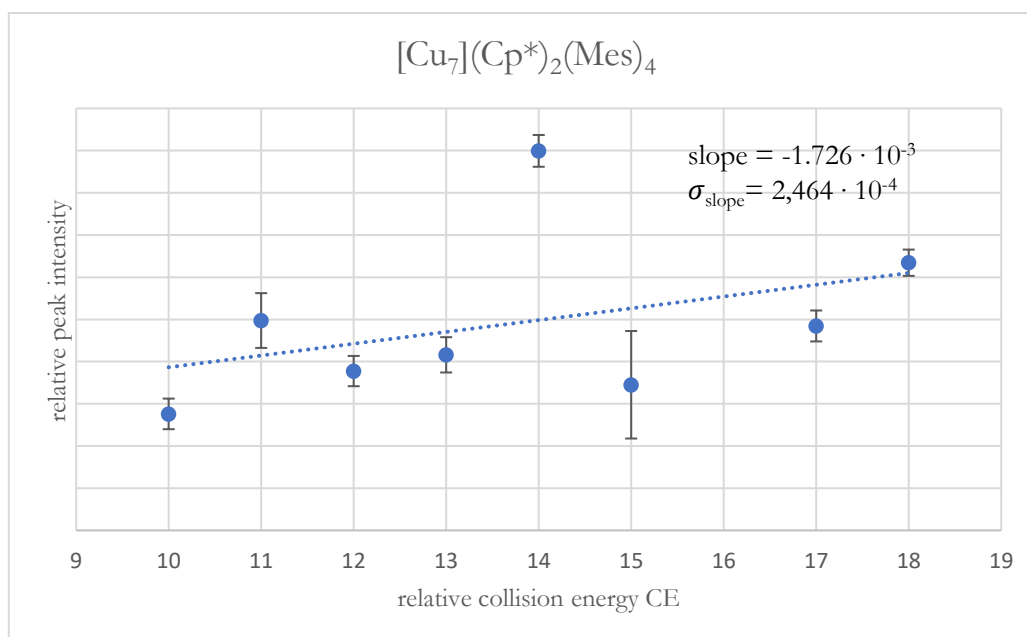
Figure S32: *CE vs. I* plot of the ion $\{[Cu_7](Cp^*)_2(Mes)_4\}^+$.

A clear assignment is not possible for this species due to the bias in integration at CE > 15.
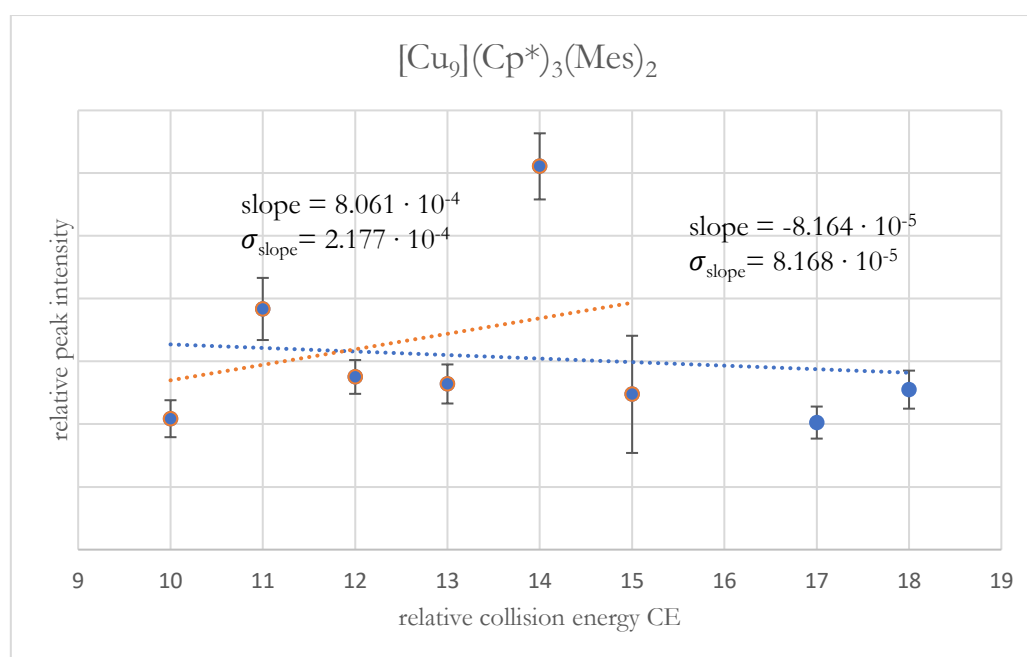
Figure S33: *CE vs. I* plot of the ion $\{[Cu_9](Cp^*)_3(Mes)_2\}^+$.

A clear assignment is not possible for this species.

6. Appendix

6.1 Supporting information for the methodical part
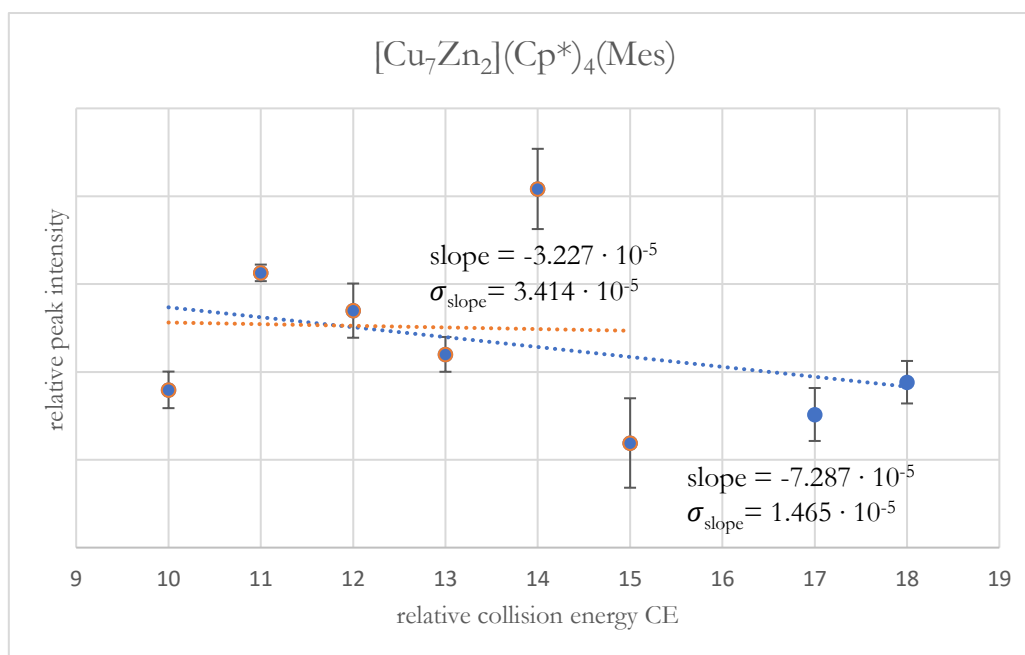
Figure S34: *CE vs. I* plot of the ion $\{[Cu_7Zn_2](Cp^*)_4(Mes)\}^+$.

The species can be assigned as molecular ion if considering that a slight increase in peak intensity at CE > 15 is supposed to be caused by the bias in integration. It may however also be a fragment formed during ionization.
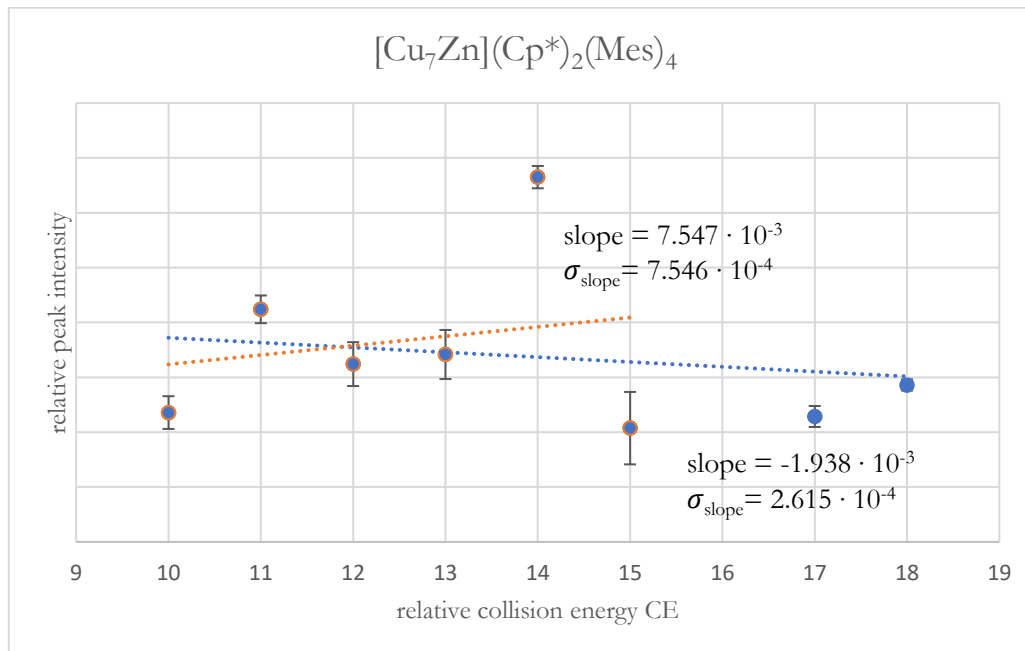
Figure S35: *CE vs. I* plot of the ion $\{[Cu_7Zn](Cp^*)_2(Mes)_4\}^+$.

A clear assignment cannot be made for this species, however, it is likely to be molecular ion as the peak intensities at CE >15 are expected to be even lower than detected. However, it may also be a fragment formed during ionization.

6. Appendix
6.1 Supporting information for the methodical part
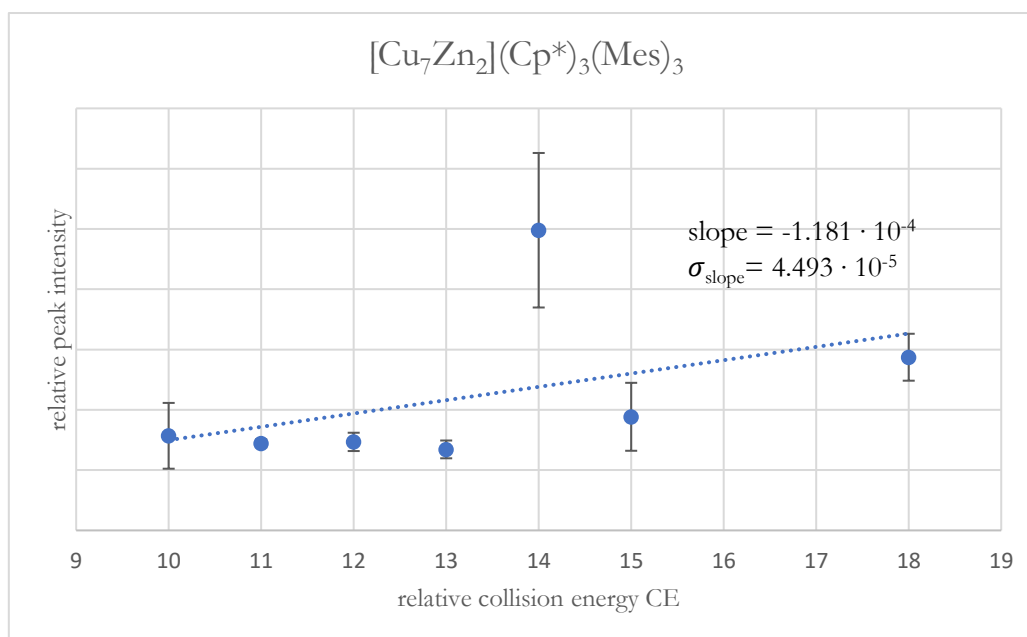
Figure S36: *CE vs. I* plot of the ion $\{[Cu_7Zn_2](Cp^*)_3(Mes)_3\}^+$.

A clear assignment cannot be made for this species due to the bias in integration at CE > 15.
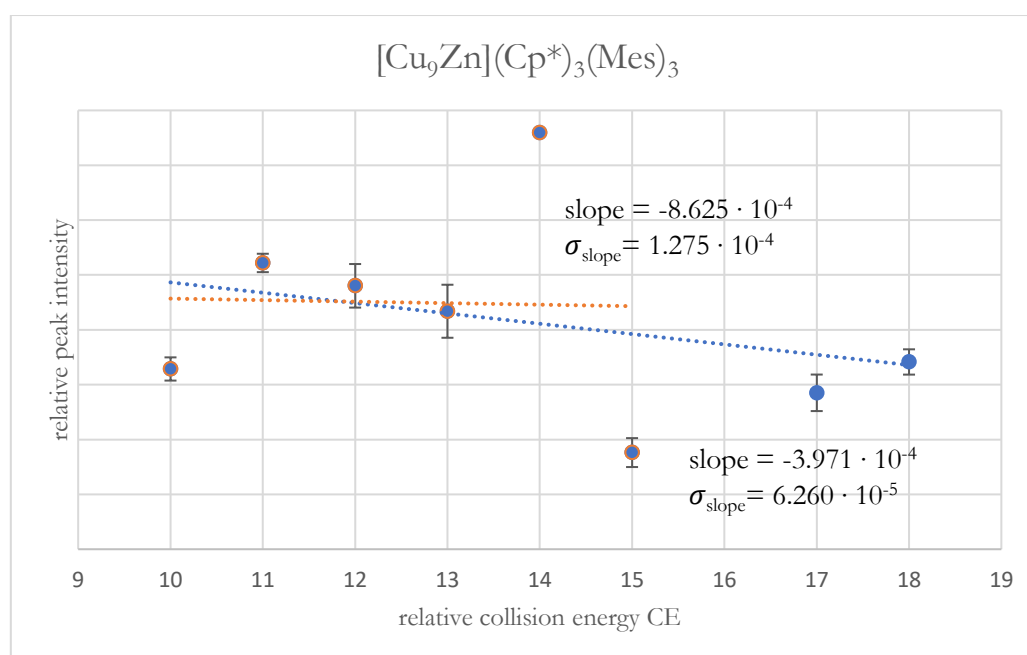
Figure S37: *CE vs. I* plot of the ion $\{[Cu_9Zn](Cp^*)_3(Mes)_3\}^+$.

The species can be assigned as molecular ion if considering that a slight increase in peak intensity at CE > 15 is supposed to be caused by the bias in integration.

6. Appendix
6.1 Supporting information for the methodical part
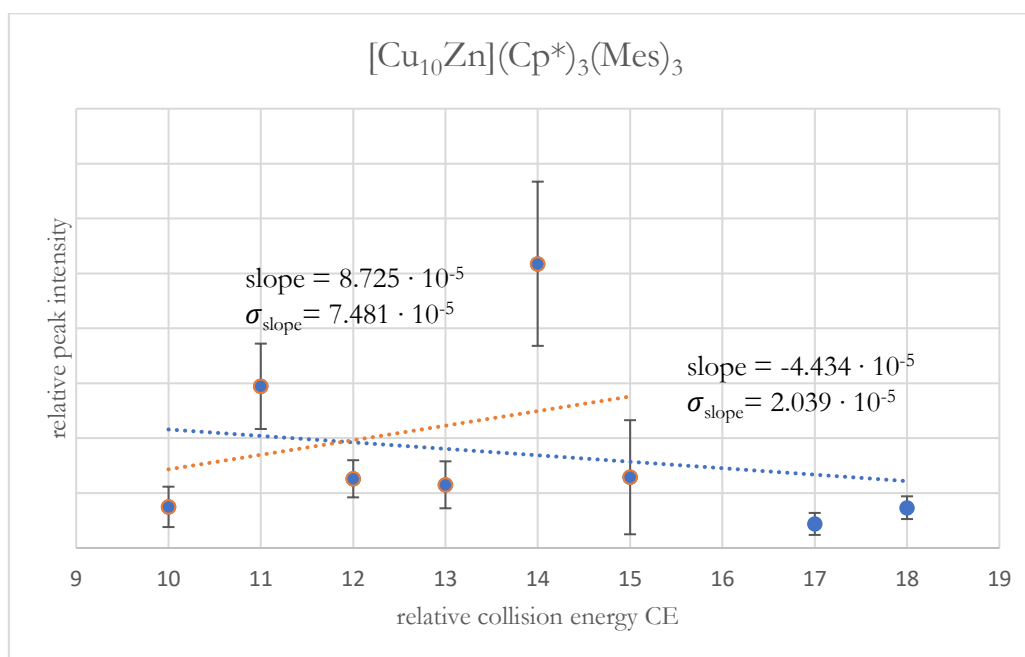
Figure S38: *CE vs. I* plot of the ion $\{[Cu_{10}Zn](Cp^*)_3(Mes)_3\}^+$.

The species is assigned as molecular ion. Due to the bias in integration, the intensity values at CE = 17 and 18 are supposed to be actually even lower than detected.

Figure S39: *CE vs. I* plot of the ion $\{[Cu_9Zn_2](Cp^*)_3(Mes)_4\}^+$.

The species is assigned as molecular ion. Due to the bias in integration, the intensity values at CE = 17 and 18 are supposed to be even lower than detected.

6. Appendix

6.1 Supporting information for the methodical part
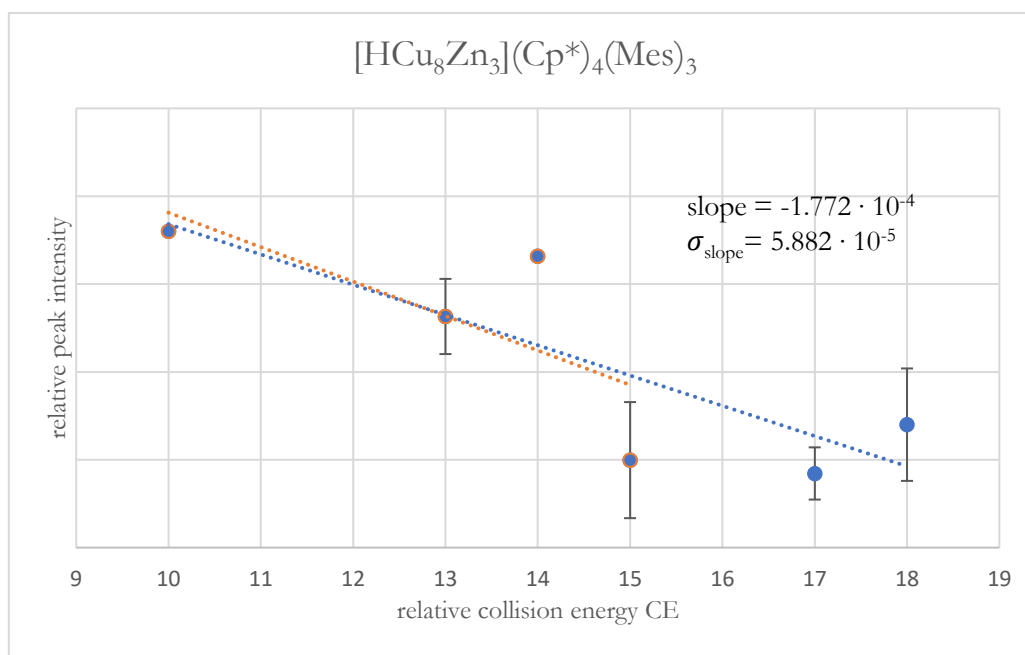
Figure S40: *CE vs. I* plot of the ion $\{[HCu_8Zn_3](Cp^*)_4(Mes)_3\}^+$.

The species is assigned as molecular ion. Due to the bias in integration, the intensity values at CE = 17 and 18 are supposed to be actually even lower than detected.

Figure S41: *CE vs. I* plot of the ion $\{[Cu_9Zn_3](Cp^*)_4(Mes)_3\}^+$.

The species is assigned as a molecular ion.

6. Appendix

6.1 Supporting information for the methodical part
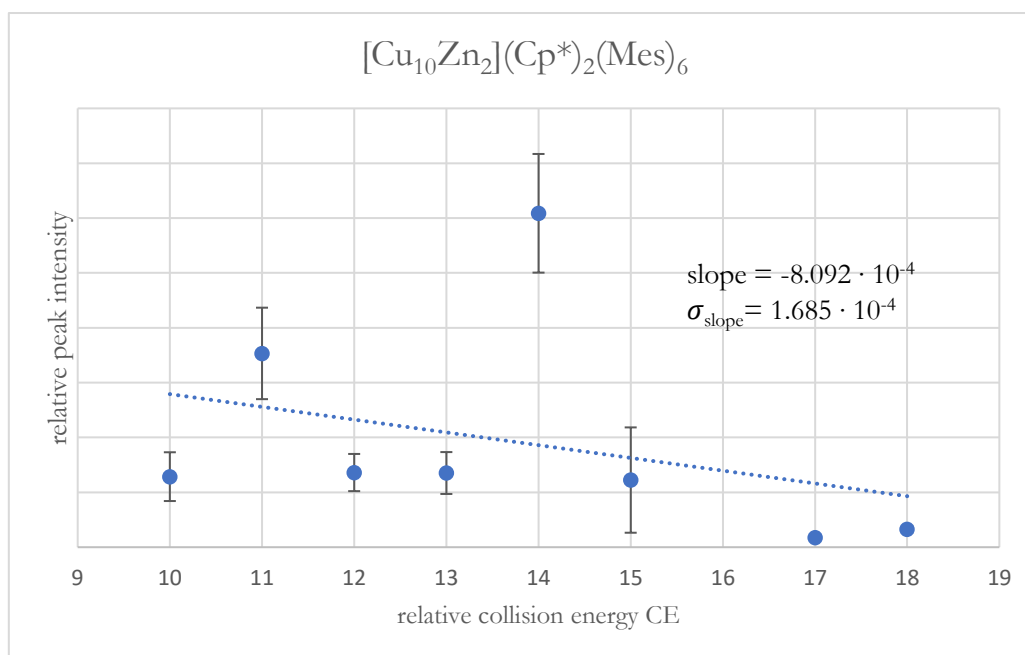
Figure S42: *CE vs. I* plot of the ion $\{[Cu_{10}Zn_2](Cp^*)_2(Mes)_6\}^+$.

The species as assigned as molecular ion and can also be isolated.

Figure S43: *CE vs. I* plot of the ion $\{[Cu_{10}Zn_3](Cp^*)_3(Mes)_5\}^+$.

A clear assignment cannot be made for this species.

6. Appendix
6.1 Supporting information for the methodical part
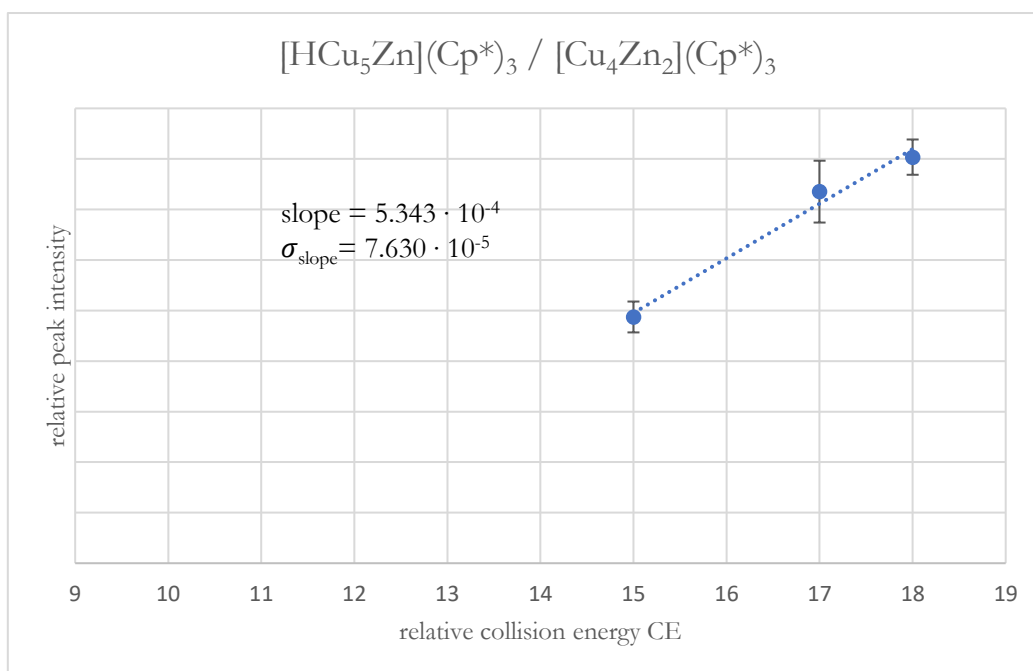
Figure S44: *CE vs. I* plot of the ion $\{[HCu_5Zn](Cp^*)_3\}^+$ and $[Cu_4Zn_2](Cp^*)_3$.

*Both ions were identified by labeling experiments with ^{68}Zn. In the unlabeled spectra however, their peaks are overlapping. Both ions can be assigned as fragments according to the CE vs. I plots. The ions were also identified as a fragment ions in spectra of isolated $[Cu_4Zn_{9/10}](Cp^*)_8$ (**4/5**).*

Size-focusing of Cu/Zn libraries by stoichiometry tuning

The following supporting data documentation refers to pages 108-109.
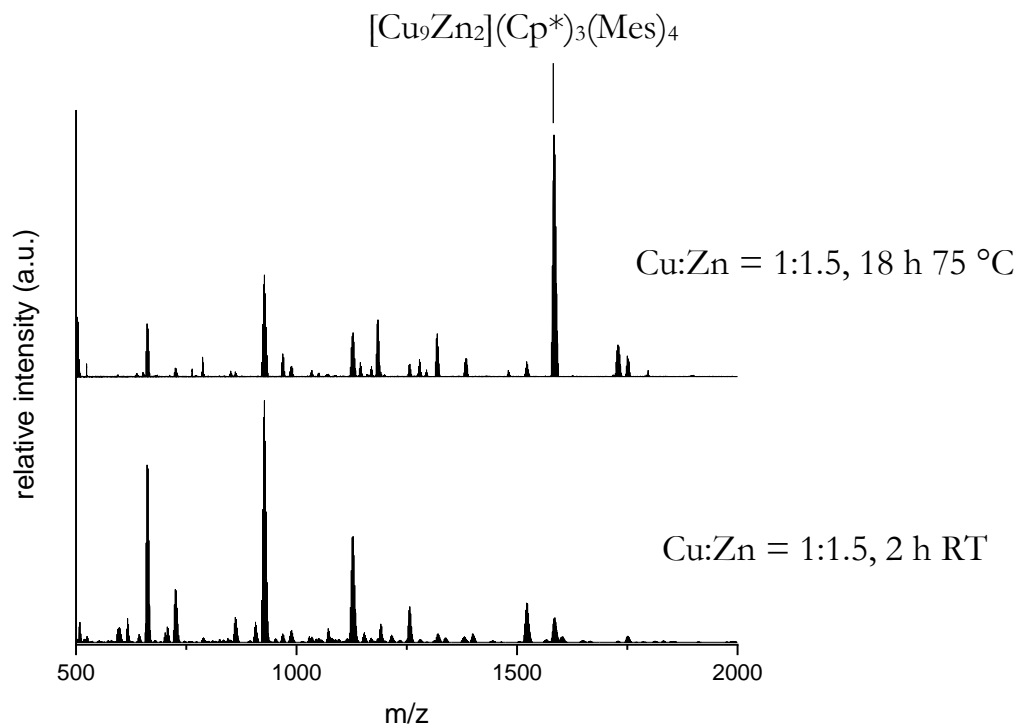
Figure S45: LIFDI-MS spectra of the Cu:Zn = 1:1.5 reaction solution before and after heating to 75 °C.

The spectra clearly show the influence of Cu:Zn stoichiometry on the size-focusing process (compare with Figure 48). Whereas with an optimized Cu:Zn stoichiometry of 10:6, a size-focusing towards [Cu₁₀Zn₂](Cp*)₂(Mes)₆ is observed upon heating of the reaction solutions, use of higher Zn contents results in LIFDI-MS spectra with the molecular ion [Cu₉Zn₂](Cp*)₃(Mes)₄ a major peak. All attempts to isolate this species from the reaction solutions were unfortunately met with failure and only very small amounts of an amorphous material in addition to few crystals of [Cu₁₀Zn₂](Cp*)₂(Mes)₆ could be obtained. Possibly, the overall concentration of [Cu₉Zn₂](Cp*)₃(Mes)₄ in the solutions is low due to formation of larger nuclearity Cu/Zn clusters or even nanoparticles, which cannot be detected by the LIFDI technique at the current stage of methodical development (see outlook of the methodical part).

UV-Vis spectroscopy as a tool to monitor size-focusing processes

The following supporting data documentation refers to pages 110-114.

Main parts of the principles of UV-Vis data interpretation were developed in collaboration with Tim Kratky.
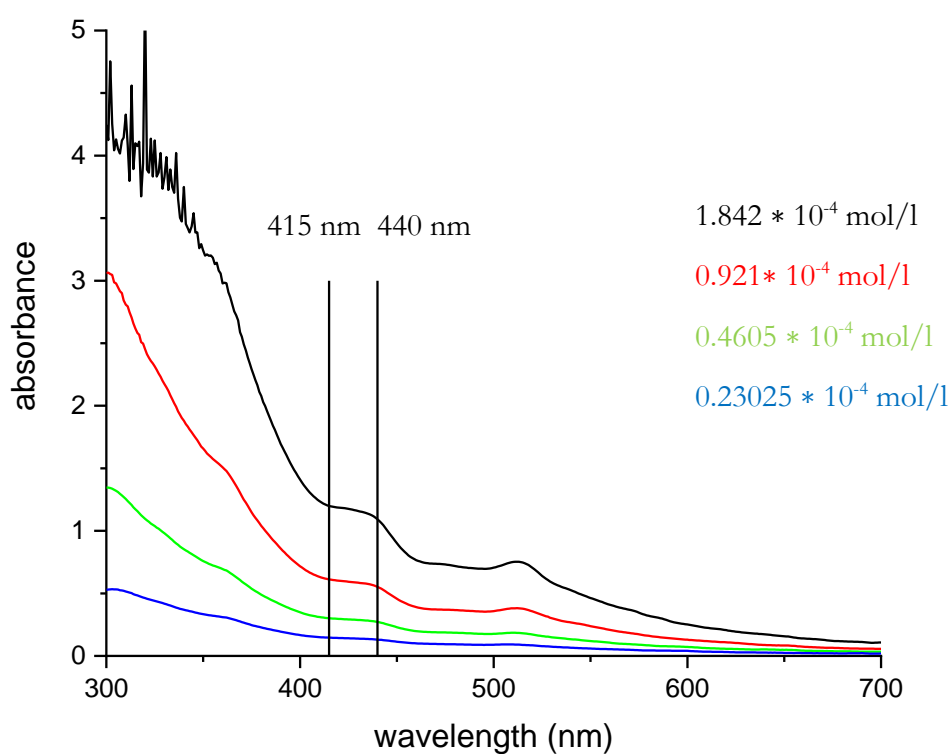
Figure S46: UV-Vis dilution series of isolated $[H_xAu_7Al_6](Cp^*)_6$ for the determination of extinction coefficients. The vertical lines mark the wavelengths for which extinction coefficients were determined.

6. Appendix

6.1 Supporting information for the methodical part
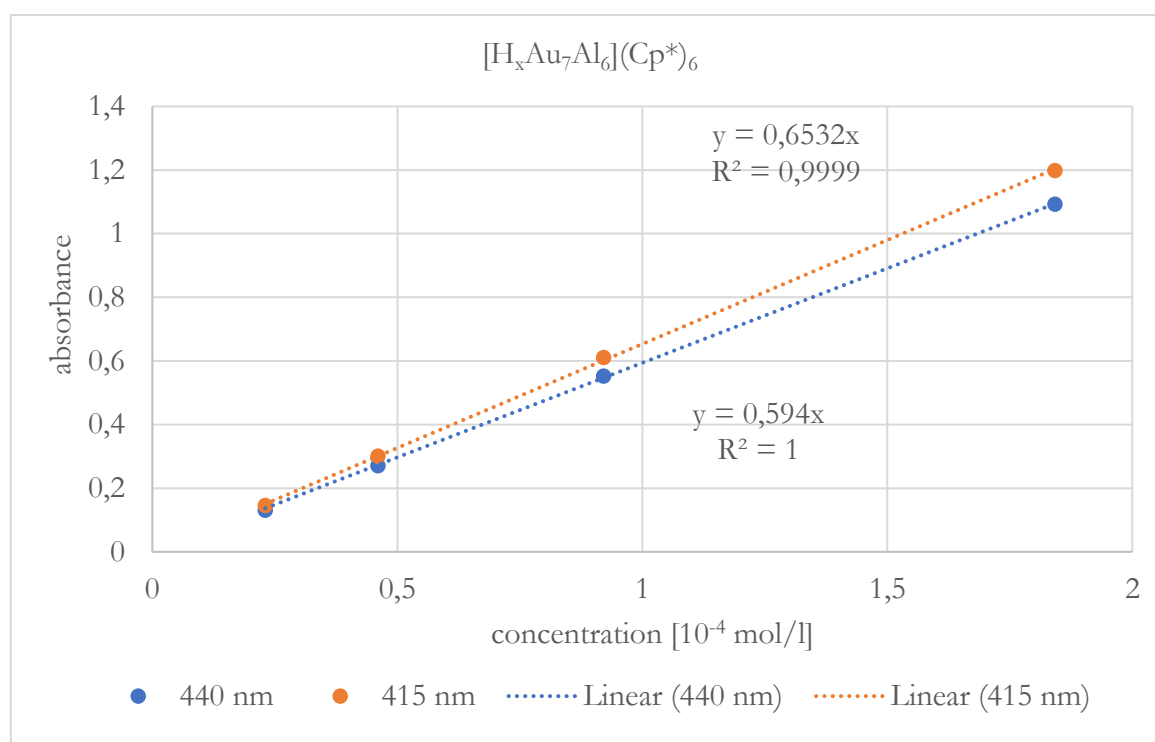
Figure S47: Determination of the extinction coefficients of $[H_xAu_7Al_6](Cp^*)_6$ at 440 nm and 415 nm by linear regression of UV-Vis data (calibration line). Due to Lambert-Beers law, the y-intercept was set to 0.
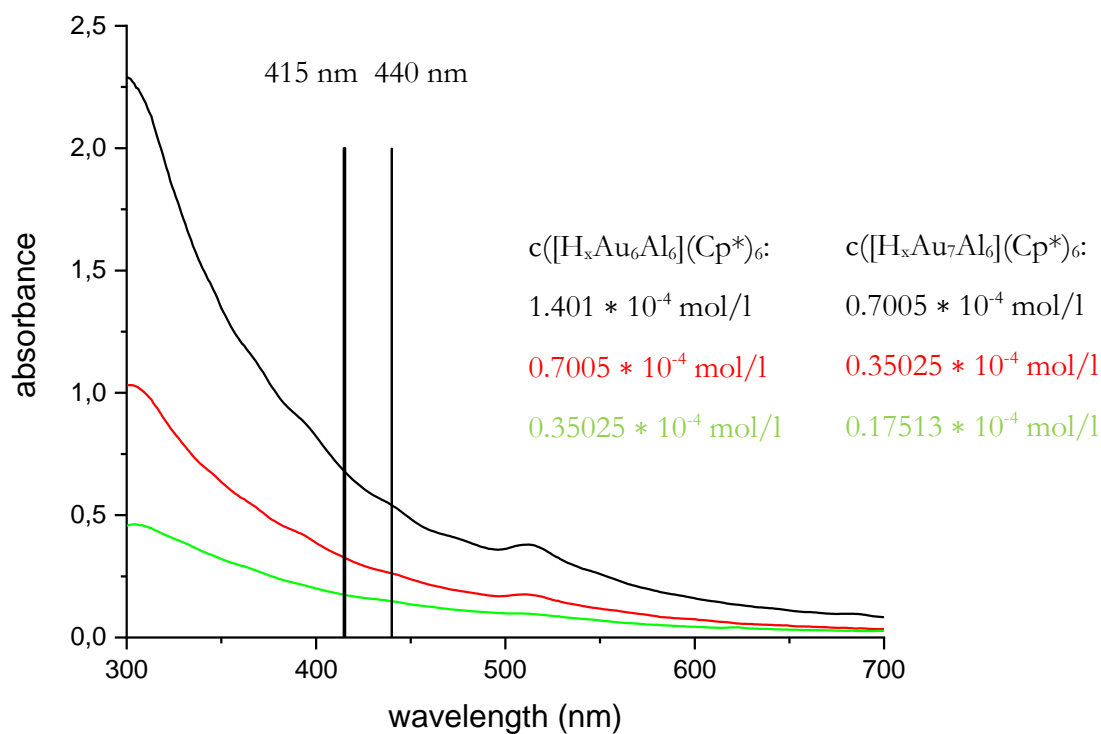
Figure S48: UV-Vis dilution series of isolated $[H_xAu_{6/7}Al_6](Cp^*)_6$ for the determination of extinction coefficients. The vertical lines mark the wavelengths at which extinction coefficients were determined.

6. Appendix
6.1 Supporting information for the methodical part
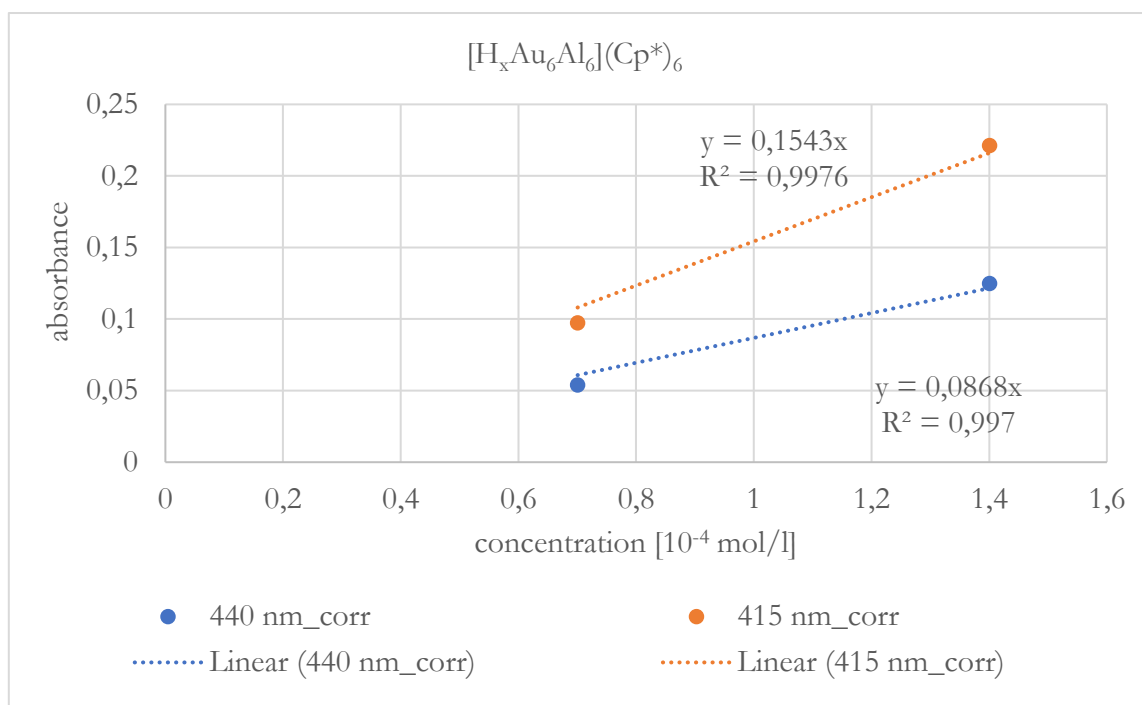
Figure S49: Determination of the extinction coefficients of $[H_xAu_6Al_6](Cp^*)_6$ at 440 nm and 415 nm by linear regression analysis of UV-Vis data (calibration curve). Due to Lambert-Beers law, the y-intercept was set to 0.

UV-Vis intensities of the isolated compounds $[H_xAu_7Al_6](Cp^*)_6$ and $[H_xAu_{6/7}Al_6](Cp^*)_6$ at 440 nm and 415 nm were analyzed by linear regression to determine the extinction coefficients following Lambert-Beers law. Note that $[H_xAu_6Al_6](Cp^*)_6$ (6) is not available in pure form but only as a mixture together with $[H_xAu_7Al_6](Cp^*)_6$ (7). Determination of the extinction coefficient of $[H_xAu_6Al_6](Cp^*)_6$ from the data obtained for the mixture $[H_xAu_{6/7}Al_6](Cp^*)_6$ was possible by knowing the ratio of the mixture components from ^{1}H-NMR analysis ($[H_xAu_6Al_6](Cp^*)_6$: $[H_xAu_7Al_6](Cp^*)_6$ = 2:1). The absorbance A of $[H_xAu_6Al_6](Cp^*)_6$ at the respective concentration could therefore be calculated by subtracting the contribution of $[H_xAu_7Al_6](Cp^*)_6$ from the measured absorbance of the mixture $[H_xAu_{6/7}Al_6](Cp^*)_6$:

$$A\,(6) = A\,(6/7) - c(7) * \varepsilon(7) \quad (2.9)$$

In this formula, c(7) is the concentration of $[H_xAu_7Al_6](Cp^*)_6$ in the mixture and ε(7) the extinction coefficient of $[H_xAu_7Al_6](Cp^*)_6$ at the respective wavelength as determined from the calibration experiments with isolated, pure $[H_xAu_7Al_6](Cp^*)_6$. c(7) is obtained as follows:

$$c(7) = \frac{m}{(M_W(7) + 2 * M_W(6)) * V} \quad (3.0)$$

$$M_W(7) = molecular\ weight\ ([H_xAu_7Al_6](Cp^*)_6) = 2351\ g/mol \quad (2.6)$$

6. Appendix

6.1 Supporting information for the methodical part

$$M_w(\textbf{6}) = molecular\ weight\ ([H_xAu_6Al_6](Cp^*)_6) = 2154\ g/mol \quad (3.1)$$

$$m = weight\ of\ [H_xAu_{6/7}Al_6](Cp^*)_6)\ sample\ taken$$

$$V = volume\ of\ toluene.$$

The extinction coefficients of [H$_x$Au$_6$Al$_6$](Cp*)$_6$ and [H$_x$Au$_7$Al$_6$](Cp*)$_6$ obtained at the respective wavelengths are summarized in the following Table S3:

Table S3: Extinction coefficients ε [$\frac{1}{mol*cm}$] and corresponding error-squares R^2 of [H$_x$Au$_6$Al$_6$](Cp*)$_6$ and [H$_x$Au$_7$Al$_6$](Cp*)$_6$.

compound	ε (415 nm)	ε (440 nm)
[H$_x$Au$_6$Al$_6$](Cp*)$_6$	0.1543 (R^2 = 0,9976)	0.0868 (R^2 = 0,997)
[H$_x$Au$_7$Al$_6$](Cp*)$_6$	0,6532 (R^2 = 0,9999)	0.594 (R^2 = 1.0000)

The concentrations of [H$_x$Au$_6$Al$_6$](Cp*)$_6$ and [H$_x$Au$_7$Al$_6$](Cp*)$_6$ in the dilute reaction solutions could thereafter be obtained by solving the following linear equations:

$$\begin{pmatrix} \varepsilon_{415\ nm}(\textbf{6}) & \varepsilon_{415\ nm}(\textbf{7}) \\ \varepsilon_{440\ nm}(\textbf{6}) & \varepsilon_{440\ nm}(\textbf{7}) \end{pmatrix} * \begin{pmatrix} c(\textbf{6}) \\ c(\textbf{7}) \end{pmatrix} = \begin{pmatrix} A_{415\ nm} \\ A_{440\ nm} \end{pmatrix}. \quad (3.2)$$
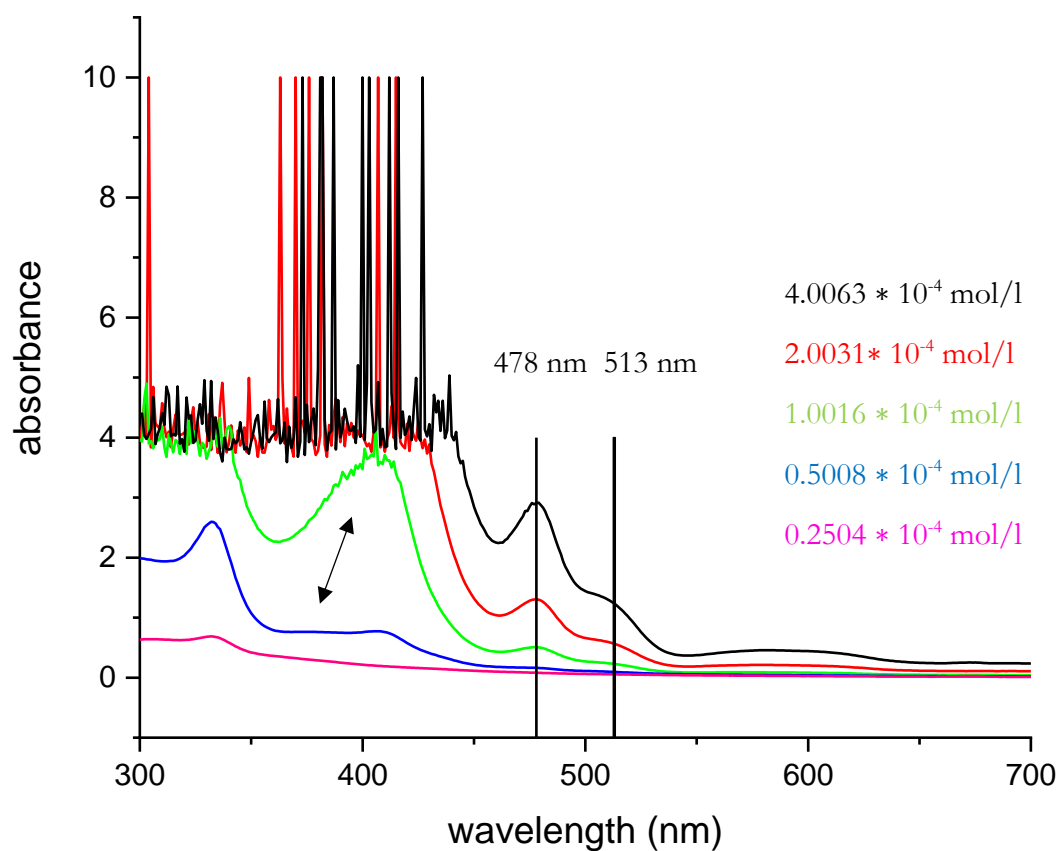
Figure S50: UV-Vis dilution series of isolated $[Au_2Al_5](Cp^*)_5$ for the determination of extinction coefficients. The vertical lines mark the wavelengths for which extinction coefficients were determined. Note the remarkable spectral change at the band at 400 nm at low concentrations (marked by an arrow). This change was reproducibly observed.

6. Appendix
6.1 Supporting information for the methodical part
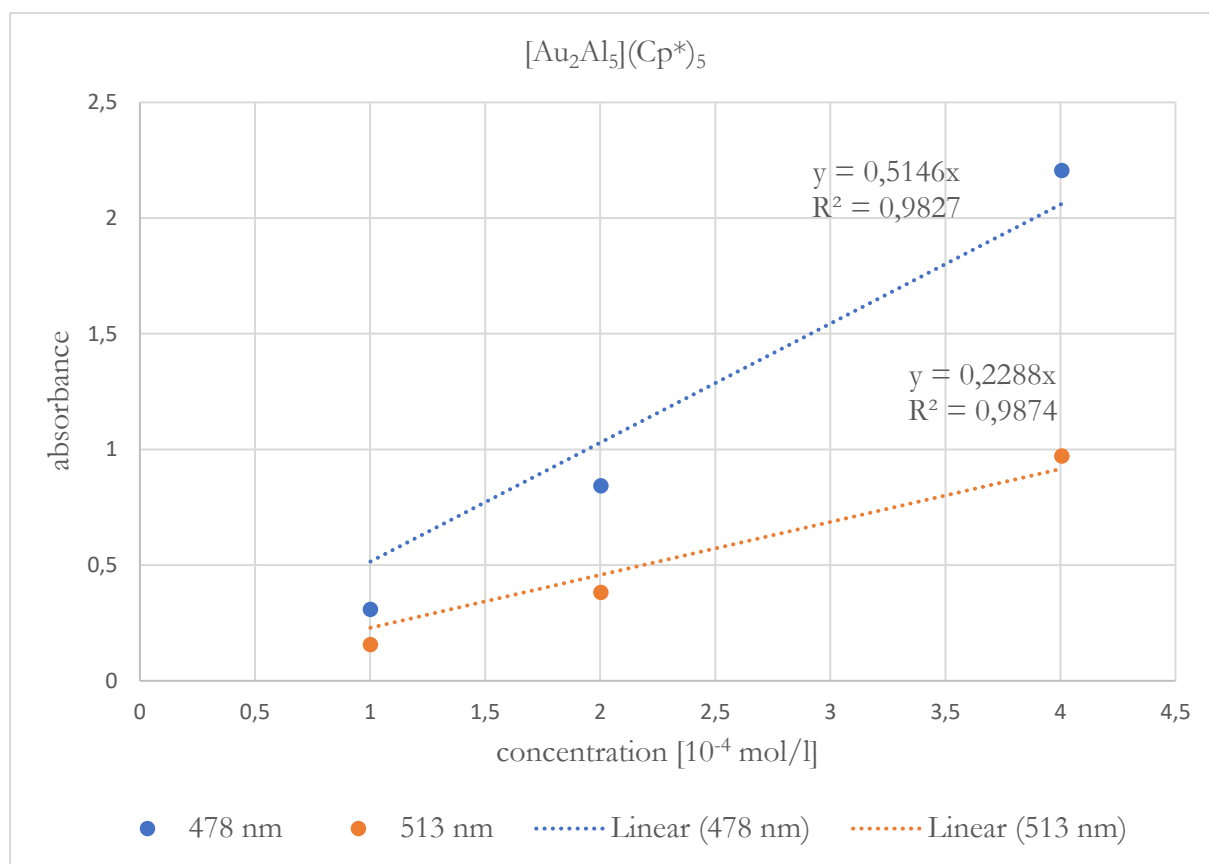
Figure S51: Determination of the extinction coefficients of $[Au_2Al_5](Cp^*)_5$ at 478 nm and 513 nm by linear regression analysis of UV-Vis data (calibration curve).

Determination of extinction coefficients for $[Au_2Al_5](Cp^*)_5$ is more complicated than for $[H_xAu_6Al_6](Cp^*)_6$ and $[H_xAu_7Al_6](Cp^*)_6$. A spectral change of the band at 400 nm is clearly visible at lower concentrations rendering this band inappropriate for the determination of an extinction coefficient. The situation is better for the bands at 513 nm and 478 nm, however, the linear regression analysis reveals that absorbance at low concentrations ($< 2 * 10^{-4}$ mol/l) is lower than expected. These observations lead to the conclusion that $[Au_2Al_5](Cp^*)_5$ is unstable in solution at very low concentrations, probably due to its high sensitivity towards traces of water or oxygen, which become significant at these low concentrations even when working under inert conditions.

6.2 Supporting information for the chemical part

6.2.1 Crystallographic information for Cu/Zn clusters

Table S4: Crystallographic information for the Cu/Zn clusters **3**, **10** and **4/5**.

	10	3	4/5
chemical formula	$C_{70}H_{105}CuZn_{10}$	$C_{74}H_{96}Cu_{10}Zn_2$	*
CCDC number	1993672	1993671	-
formula weight	1663.99	1751.79	*
temperature	100(2) K	100(2) K	100(2) K
λ [Å]	0.71073	0.71073	0.71073
crystal size [mm]	0.120 x 0.120 x 0.120	0.045 x 0.094 x 0.249	0.097 x 0.124 x 0.162
crystal habit	red fragment	green fragment	black fragment
crystal system	orthorhombic	triclinic	triclinic
space group	P*nma*	P-1	P-1
unit cell dimensions	a = 24.2661(14) Å b = 20.0177(11) Å c= 15.5275(9) Å α = 90° β = 90° γ = 90°	a = 12.4074(12) Å b = 16.9704(17) Å c= 22.465(2) Å α = 75.965(3)° β = 89.083(3)° γ = 75.103(3)°	a = 12.558(2) b = 16.667(3) c = 25.165(5) α =99.142(6) β = 99.801(5) γ = 111.556(5)
volume [$Å^3$]	7542.5(7)	4429.3(8)	4684.2(16)
Z	4	2	2
ϱ (calculated) [g/cm^3]	1.465	1.134	*
absorption coefficient [mm^{-1}]	3.429	2.909	3.370
F(000)	3416	1780	2023
diffractometer	BRUKER D8 VENTURE DUO IMS	BRUKER D8 VENTURE	BRUKER D8 VENTURE DUO IMS
radiation source	IMS microsource, Mo	TXS rotating anode, Mo	IMS microsource, Mo
θ range for data collection [°]	2.36 – 26.02	1.96-25.35	2.00 - 25.35
index ranges	-29 ≤ h ≤ 29 -24 ≤ k ≤ 24 -19 ≤ l ≤ 19	-14 ≤ h ≤ 14 -20 ≤ k ≤ 20 -27 ≤ l ≤ 27	-15 ≤ h ≤ 15 -20 ≤ k ≤ 20 -30 ≤ k ≤ 30
reflections collected	208987	174146	84203
independent reflections	7652 [(R_{int}) = 0.0448]	16188 [(R_{int}) = 0.0792]	17129 [(R_{int}) = 0.0834]

coverage of independent reflections	99.9 %	99.9 %	96.2 %
absorption correction	Multi-scan	Multi-scan	Multi-scan
max. and min. transmission	0.6370 and 0.7454	0.6396 and 0.7453	0.7360 and 0.6110
structure solution technique	direct methods	direct methods	direct methods
structure solution program	SHELXT (Sheldrick 2014)	SHELXT (Sheldrick 2014)	SHELXT 2014/5 (Sheldrick 2014)
refinement method	full matrix least squares on F^2	full matrix least squares on F^2	full matrix least squares on F^2
refinement program	SHELXL 2017/1 (Sheldrick 2017)	SHELXL 2014/7 (Sheldrick 2014)	SHELXL 2017/1 (Sheldrick 2017)
function minimized	$\sum w(F_0^2 - F_c^2)^2$	$\sum w(F_0^2 - F_c^2)^2$	$\sum w(F_0^2 - F_c^2)^2$
data/restraints/parameters	7652/1048/699	16188/0/803	17129/543/1069
goodness of fit on F^2	1.043	1.011	1.037
$\Delta/\sigma_{max.}$	0.002	0.001	0.001
final R indices [I>2σ]	R1 = 0.0214, wR2 = 0.0491	R1 = 0.0401, wR2 = 0.0972	*
final R indices [all data]	R1 = 0.0252, wR2 = 0.0506	R1 = 0.0664, wR2 = 0.1107	*
$\Delta F_{max.}$, $\Delta F_{min.}$ [e / $Å^{-3}$]	0.478, -0.394	1.342, -0.720	*

The exact location of the elements Cu and Zn in the crystal structure of [Cu₄Zn₉/₁₀](Cp)₈ was determined by DFT calculations (see Figure 41), as these elements cannot be distinguished by standard SC-XRD techniques. The results of these calculations were obtained shortly before publication of this dissertation and are currently verified by the group of Prof. Saillard. The crystal structure of [Cu₄Zn₉/₁₀](Cp*)₈ is therefore not fully refined yet. The refined crystal structure with location of Cu and Zn as determined by the calculations will be presented in a publication in near future.*

6.2.2 Characterization of [CuZn$_{10}$](Cp*)$_7$ (**10**)

The following supporting data documentation refers to pages 119-126.
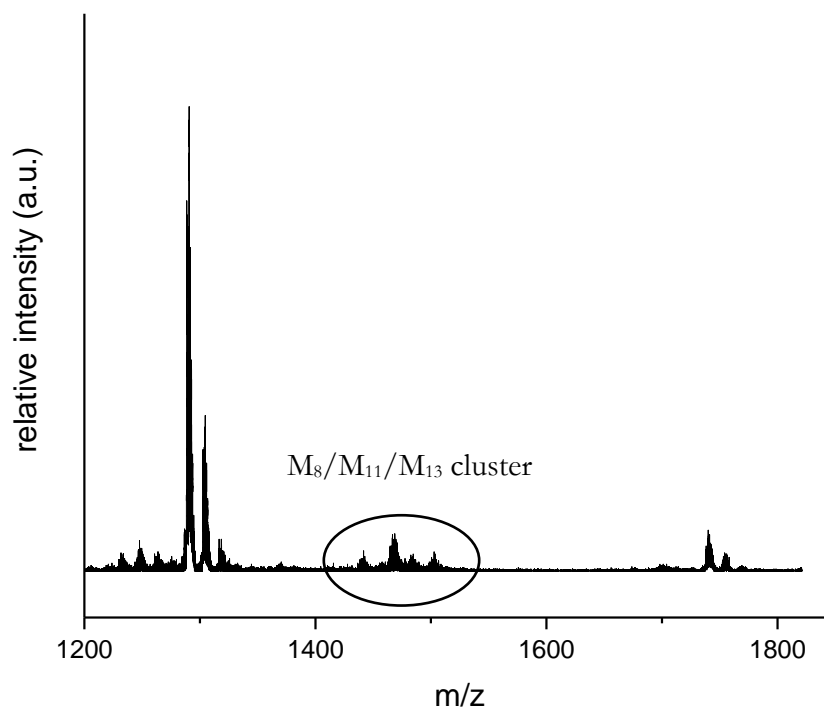
Figure S52: LIFDI-MS of the reaction [^{i}DippCuH] + [Zn$_2$](Cp*)$_2$ after 2 hours at room-temperature. Peaks at m/z < 1400 and at m/z >1700 are attributed to [Cu$_x$(^{i}Dipp)$_y$] aggregates.

Besides signals attributed to [Cu$_x$(^{i}Dipp)$_y$] aggregates, several M$_8$/M$_{11}$ and M$_{13}$ Cu/Zn clusters with strongly overlapping peaks are detected in LIFDI-MS spectra of the reaction solution.
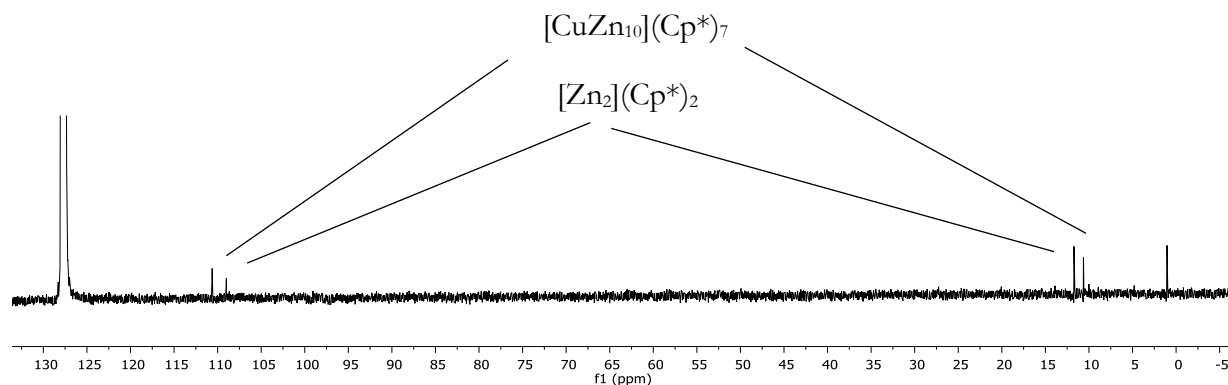
Figure S53: ^{13}C-NMR spectrum (benzene-d$_6$) of [CuZn$_{10}$](Cp*)$_7$ + [Zn$_2$](Cp*)$_2$ at 298 K. The peak at 126 ppm is attributed to the solvent residual signal and the one at 0.92 ppm to silicon grease.

6. Appendix
6.2 Supporting information for the chemical part
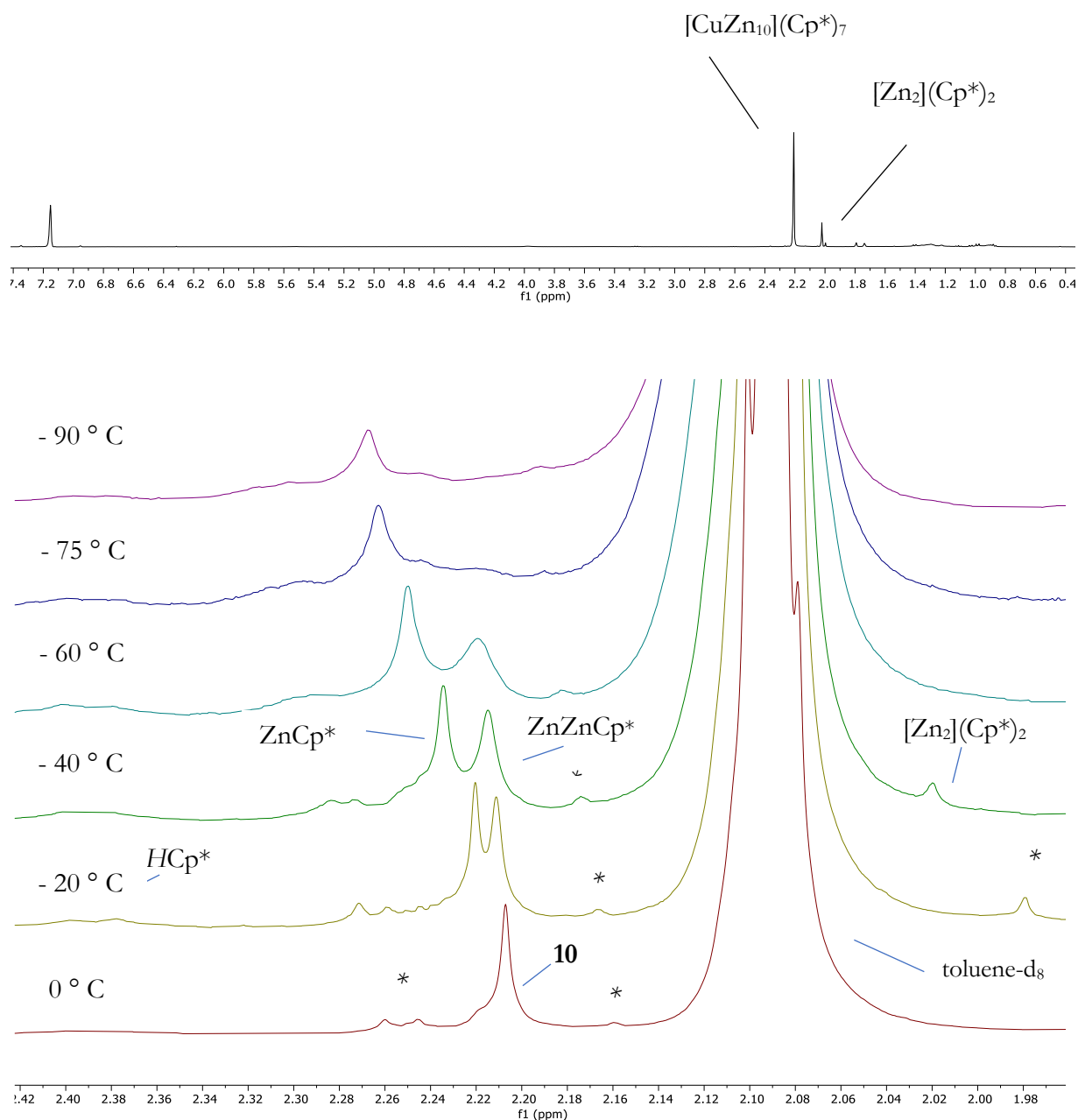
Figure S54: Top: ^{1}H-NMR spectrum (benzene-d$_6$) of [CuZn$_{10}$](Cp*)$_7$ (**10**) + [Zn$_2$](Cp*)$_2$ (298 K). Bottom: Variable temperature ^{1}H-NMR spectra of **10** in toluene-d$_8$ focused on the splitting of the signal corresponding to **10**.

* = unidentified species

Note: In the variable temperature ^{1}H-NMR spectra, a splitting of the signal corresponding to [CuZn$_{10}$](Cp)$_7$ is observed at -40 °C - -60 °C which is assigned to the ZnCp* and ZnZnCp* moieties in the molecule. Below -60 °C, a further broadening of the peak is observed pointing towards a second coalescence point between the sets of symmetry equivalent ZnCp* and ZnZnCp* units. Unfortunately, the origin of the peaks at 2.24-2.26 ppm, 2.16 ppm and 1.97 ppm could not be*

264

identified. It is assumed that they correspond to side- or decomposition products of [CuZn$_{10}$](Cp*)$_7$, probably caused by the limited stability of [CuZn$_{10}$](Cp*)$_7$ in solution. It is noted that no high-temperature spectra of [CuZn$_{10}$](Cp*)$_7$ are shown due to rapid decomposition above +20 °C.
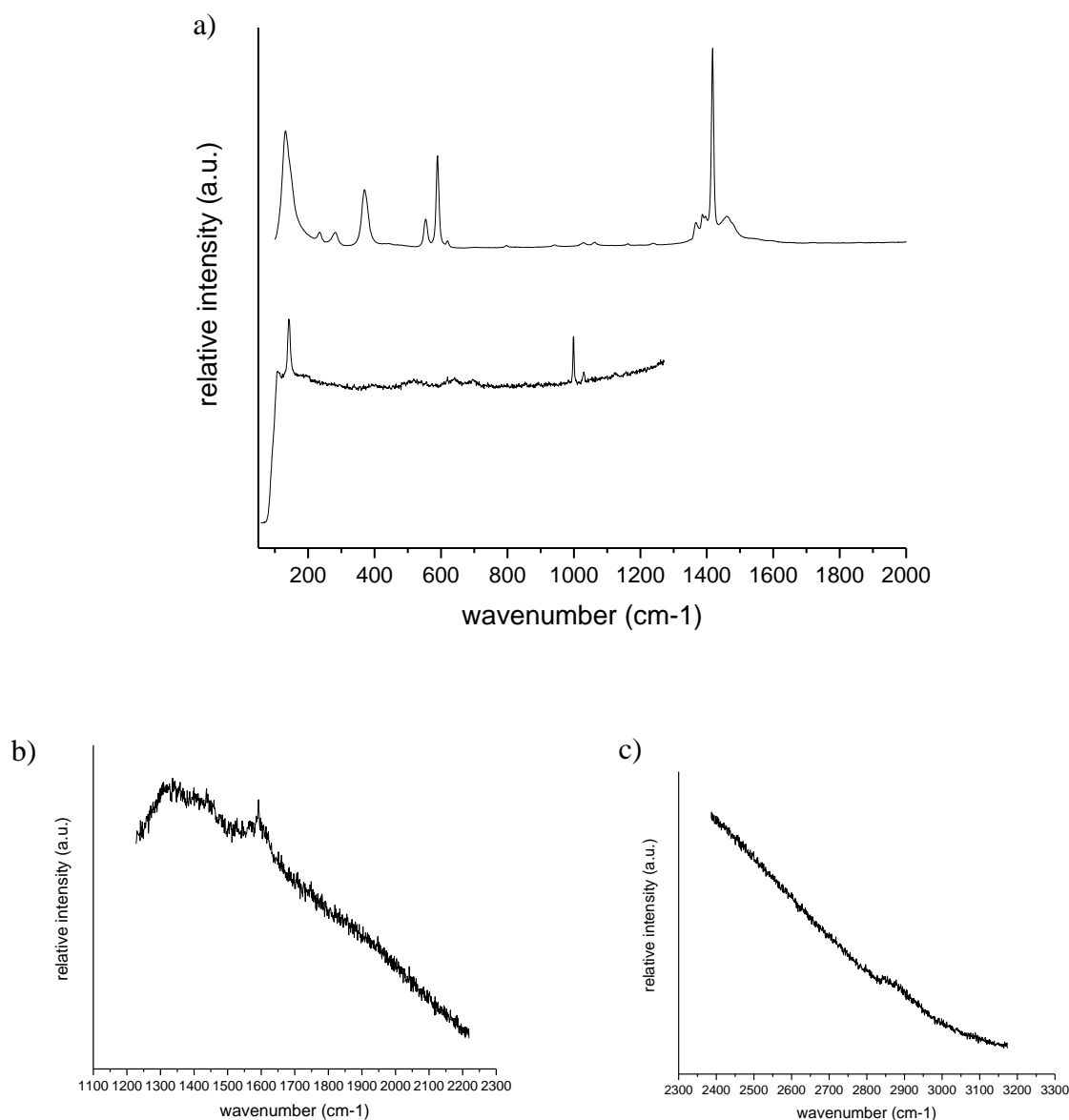
Figure S55: a) Raman spectra of [Zn$_2$]Cp*$_2$ (top) and [CuZn$_{10}$](Cp*)$_7$ (bottom). b) Raman spectrum of **10** in the region 1100 cm-1 – 2200 cm^{-1}. c) Raman spectrum of [CuZn$_{10}$](Cp*)$_7$ in the region 2300 cm^{-1} – 3200 cm^{-1}.

Note: Clean Raman spectra of [CuZn$_{10}$](Cp*)$_7$ were available by using a Raman microscope, which allows focusing on single crystals. The Raman spectrum of [CuZn$_{10}$](Cp*)$_7$ exhibits only very weak signals corresponding to Cp* C-H stretching vibrations (2850 cm^{-1}) as well as Cp*

breathing vibrations (1575 cm⁻¹). The poor signal to noise ratio is a consequence of the high fluorescence background of the compound, which can also not be reduced by variation of the excitation wavelengths. Further vibrations are found at 1025 cm⁻¹, 980 cm⁻¹ and 142 cm⁻¹; the latter is tentatively assigned to a M-M vibration. Interestingly, a very similar vibration is found in isolated [Zn₂](Cp)₂.*

6.2.3. Characterization of [Cu₁₀Zn₂](Cp*)₂(Mes)₆ (**3**)

The following supporting data documentation refers to pages 126-133.
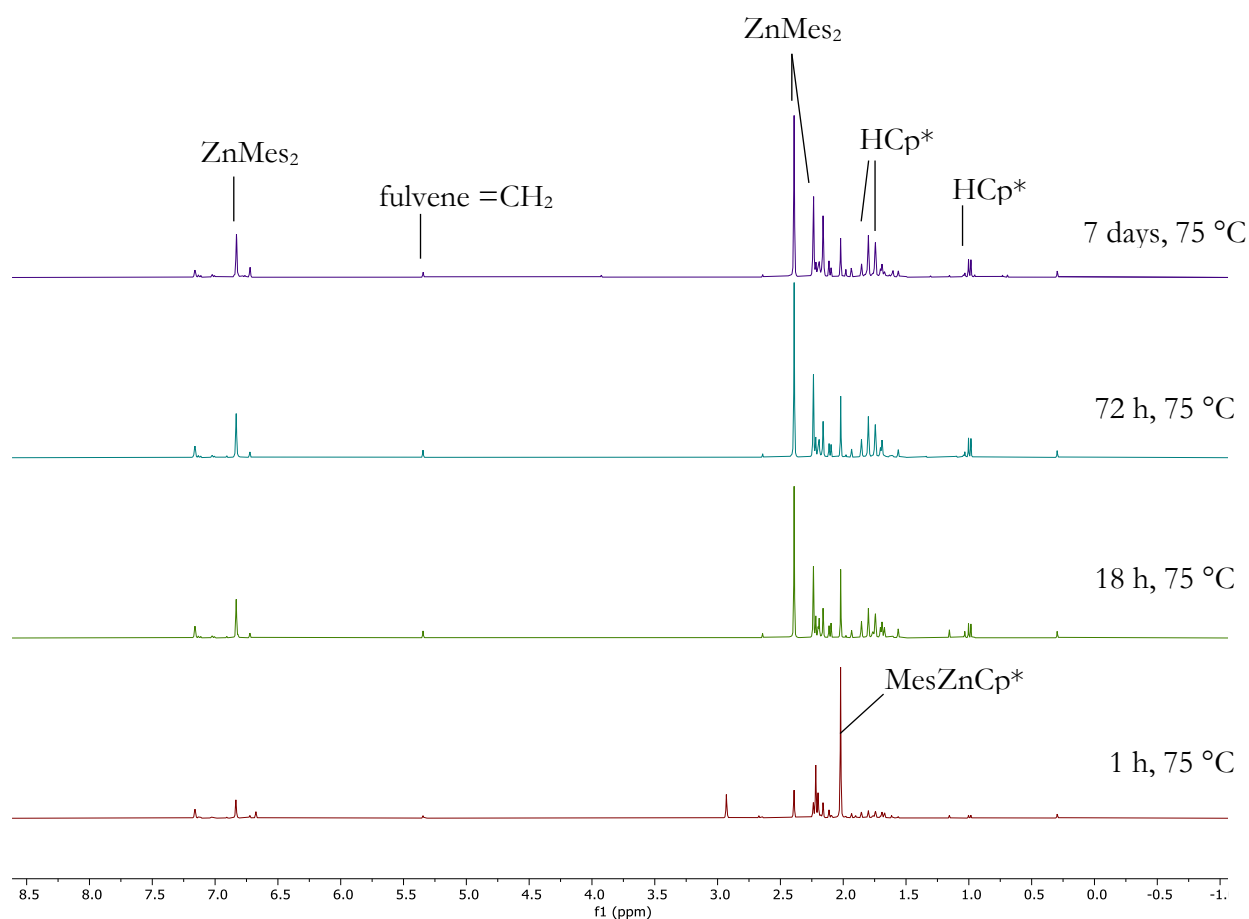
Figure S56: *In situ* ¹H-NMR spectra (benzene-d₆) of the synthesis of [Cu₁₀Zn₂](Cp*)₂(Mes)₆ (**3**).

6.2 Supporting information for the chemical part
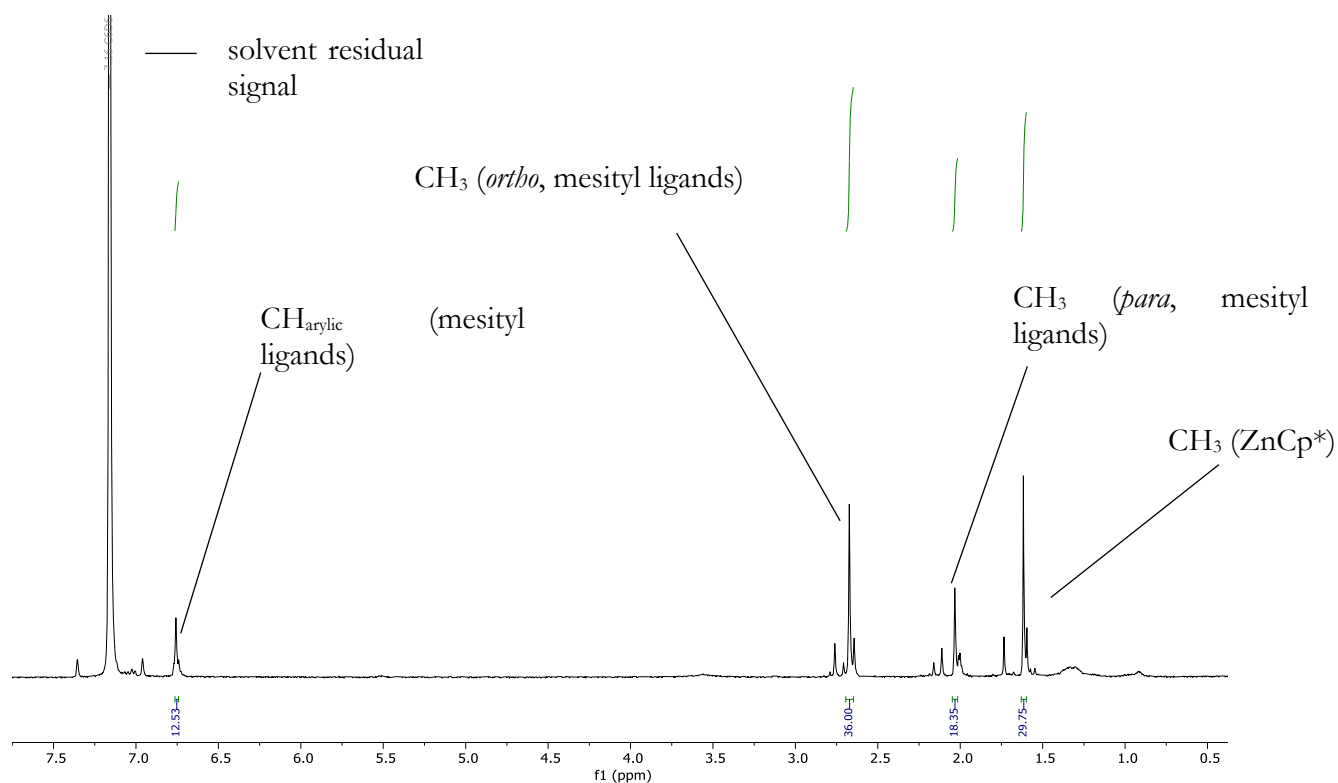
Figure S57: ^{1}H-NMR spectrum (benzene-d$_6$) of [Cu$_{10}$Zn$_2$](Cp*)$_2$(Mes)$_6$ (**3**) (298 K).
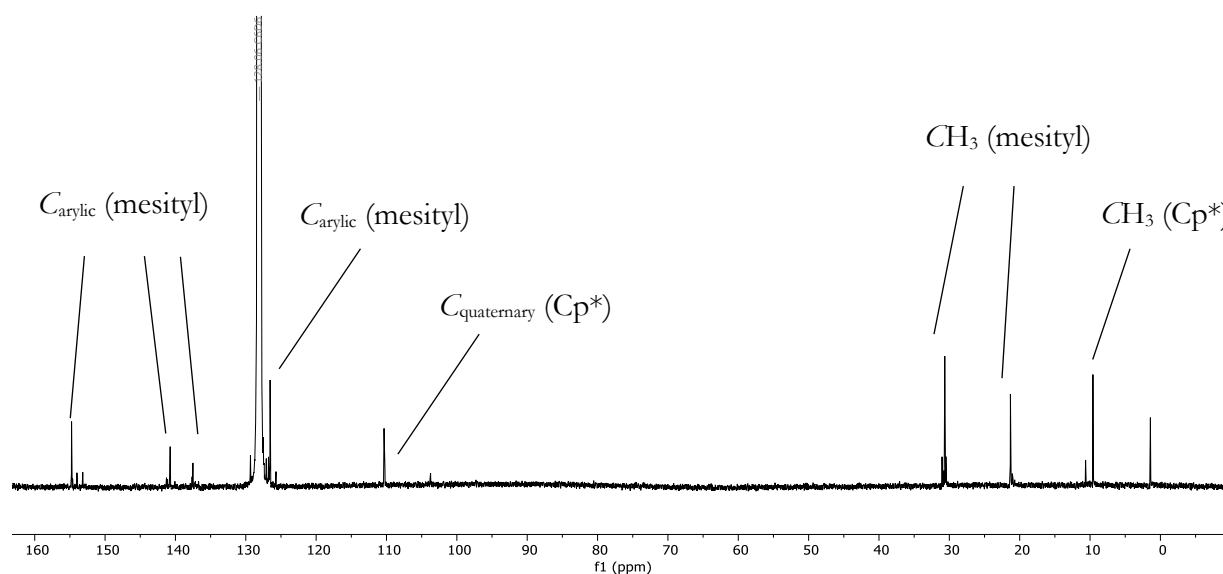
Figure S58: ^{13}C-NMR spectrum of [Cu$_{10}$Zn$_2$](Cp*)$_2$(Mes)$_6$ (**3**) (benzene-d$_6$) in benzene-d$_6$ (298 K). The peak at 126 ppm is the solvent residual signal and the one at 0.92 ppm is attributed to silicon grease.

The ^{1}H-NMR and ^{13}C-NMR spectra of isolated [Cu$_{10}$Zn$_2$](Cp)$_2$(Mes)$_6$ (**3**) are fully consistent with the symmetry and composition of the compound as determined by SC-XRD. Several small impurities in the ^{1}H-NMR spectrum of **3** (e.g. mesitylene) are due to the extremly high sensitivity of the isolated compound.*

6. Appendix
6.2 Supporting information for the chemical part
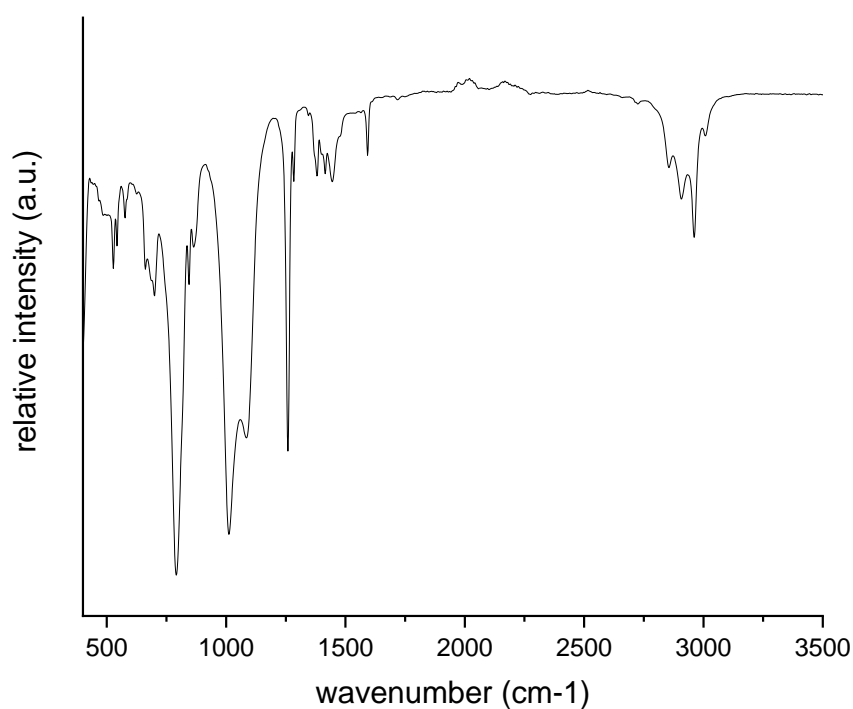
Figure S59: ATR-IR spectrum of [Cu$_{10}$Zn$_2$](Cp*)$_2$(Mes)$_6$.

The ATR-IR spectrum of [Cu$_{10}$Zn$_2$](Cp)$_2$(Mes)$_6$ (**3**) shows characteristic ν$_{C-H}$ stretching vibrations in the region 2855-3011 cm^{-1} for both the mesityl and Cp* ligands. The bands between 500 cm^{-1} and 1700 cm^{-1} are mainly assigned to ν$_{C-C}$ vibrations.*

Table S5: Computed and experimental ^{1}H and ^{13}C NMR chemical shifts for **3**.

Signal (multiplicity)	δ_{exp}	δ_{calc}
H (12)	6.76	6.70
H (36)	2.67	2.46
H (18)	2.03	1.94
H (30)	1.62	1.19
C (6)	140.57	143.49
C (12)	154.68	154.85
C (6)	137.46	141.19
C (12)	126.52	124.79
C (12)	30.49	28.31
C (6)	21.18	18.08
C (10)	110.23	113.25
C (10)	9.41	6.50

6.2.4 Characterization of $[Cu_4Zn_{9/10}](Cp^*)_8$ (**4/5**)

The following supporting data documentation refers to pages 134-138.
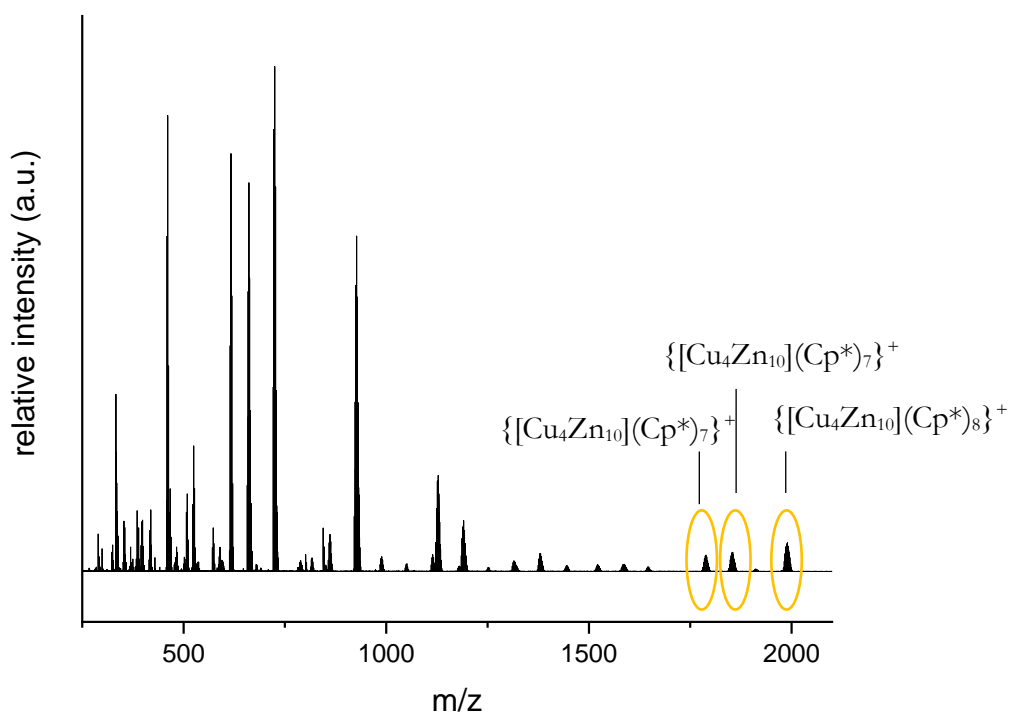
Figure S60: Full-range LIFDI-MS spectrum of isolated $[Cu_4Zn_{9/10}](Cp^*)_8$ (**4/5**).

*The LIFDI-MS spectrum of $[Cu_4Zn_{9/10}](Cp^*)_8$ (**4/5**) shows the signals of $[Cu_4Zn_{10}](Cp^*)_8$, $[Cu_4Zn_{10}](Cp^*)_7$ and $[Cu_4Zn_9](Cp^*)_7$. Obviously, $[Cu_4Zn_{10}](Cp^*)_7$ is a fragment ion of $[Cu_4Zn_{10}](Cp^*)_8$. $[Cu_4Zn_9](Cp^*)_7$ is supposed to be a fragment of $[Cu_4Zn_9](Cp^*)_8$. The molecular ion of $[Cu_4Zn_9](Cp^*)_8$ is not detected. All the other peaks are fragments or cluster rearrangement products, and their identity is listed in Table S2. They are supposed to be generated during the ionization process due to the thermal instability of the compound.*

6. Appendix
6.2 Supporting information for the chemical part
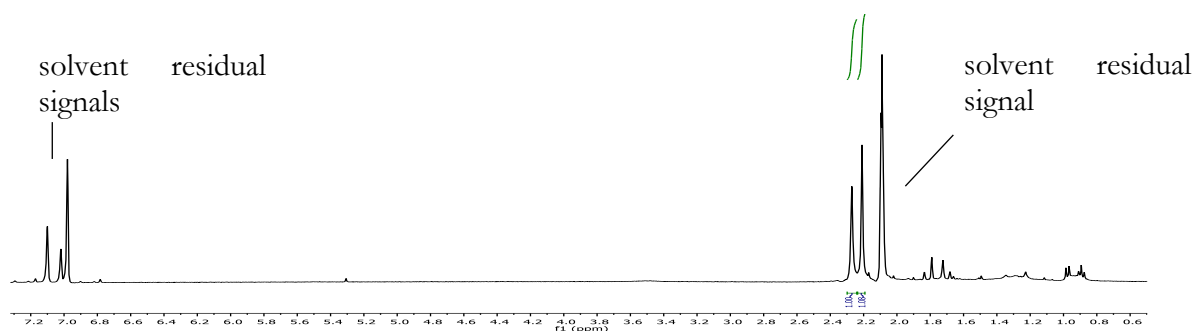
Figure S61: ^{1}H-NMR spectrum of $[Cu_4Zn_{9/10}](Cp^*)_8$ (**4/5**) in toluene-d_8 (298 K).
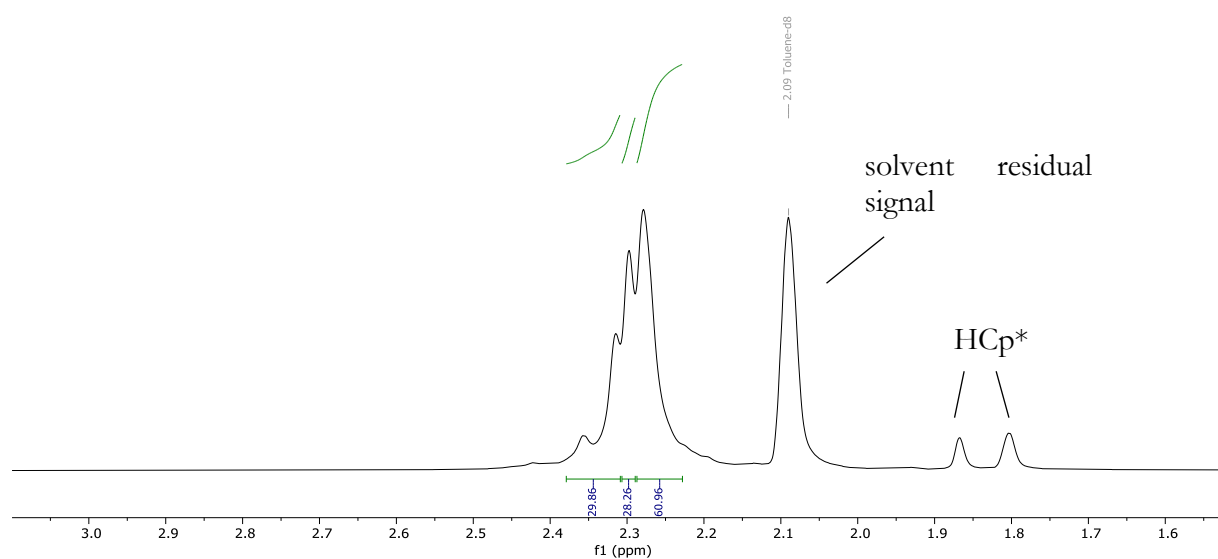
Figure S62: ^{1}H-NMR spectrum of $[Cu_4Zn_{9/10}](Cp^*)_8$ (**4/5**) in toluene-d_8 at -90°C (208 K).

The -90 °C ^{1}H-NMR spectrum of $[Cu_4Zn_{9/10}](Cp^*)_8$ shows a 1:1:2:4 (tentative assignment: 1x ZnCp*, 1x CuCp*, 2x CuCp*, 4x ZnZnCp*) signal splitting of the Cp* attributed signals.
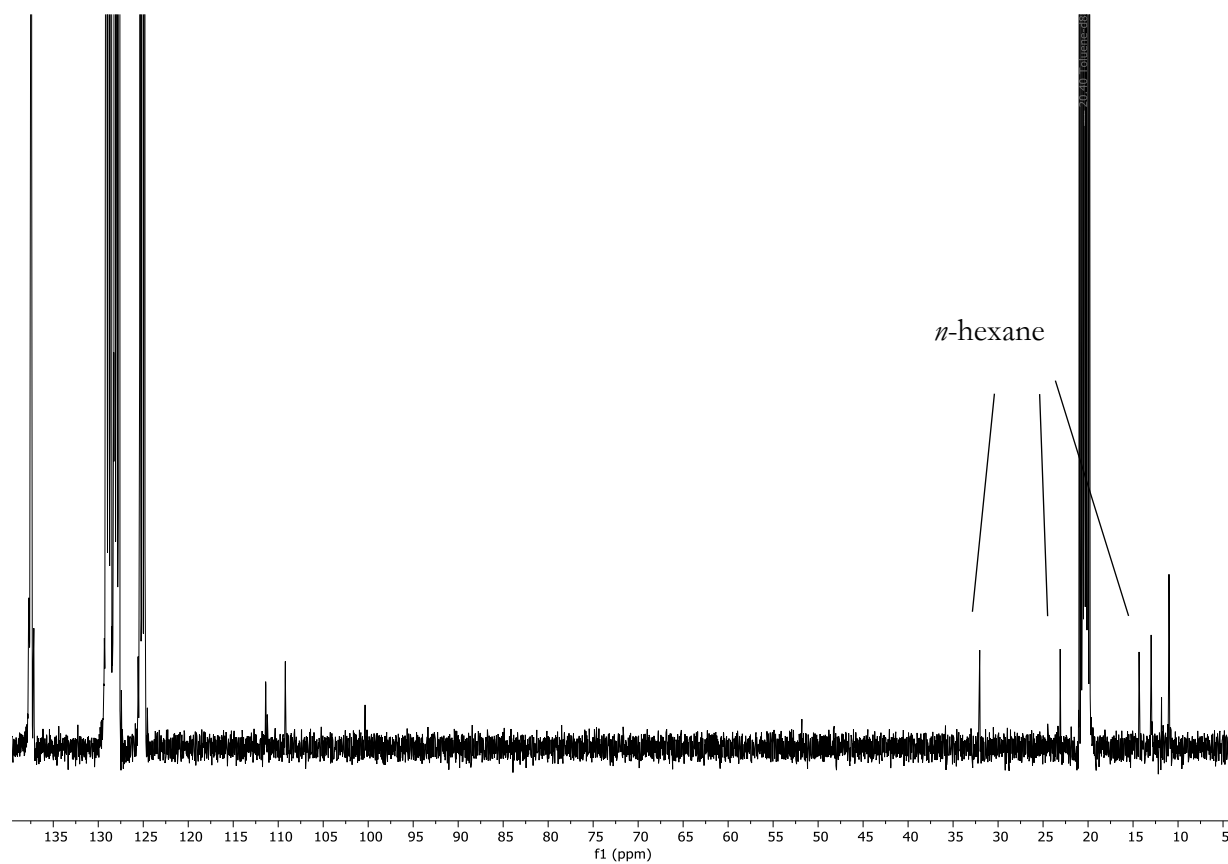
Figure S63: ^{13}C-NMR spectrum of [Cu$_4$Zn$_{9/10}$](Cp*)$_8$ (**4/5**) in toluene-d$_8$ (298 K). Peaks at 20 ppm, 125 ppm, 127-130 ppm and 137.5 ppm are solvent residual signals.
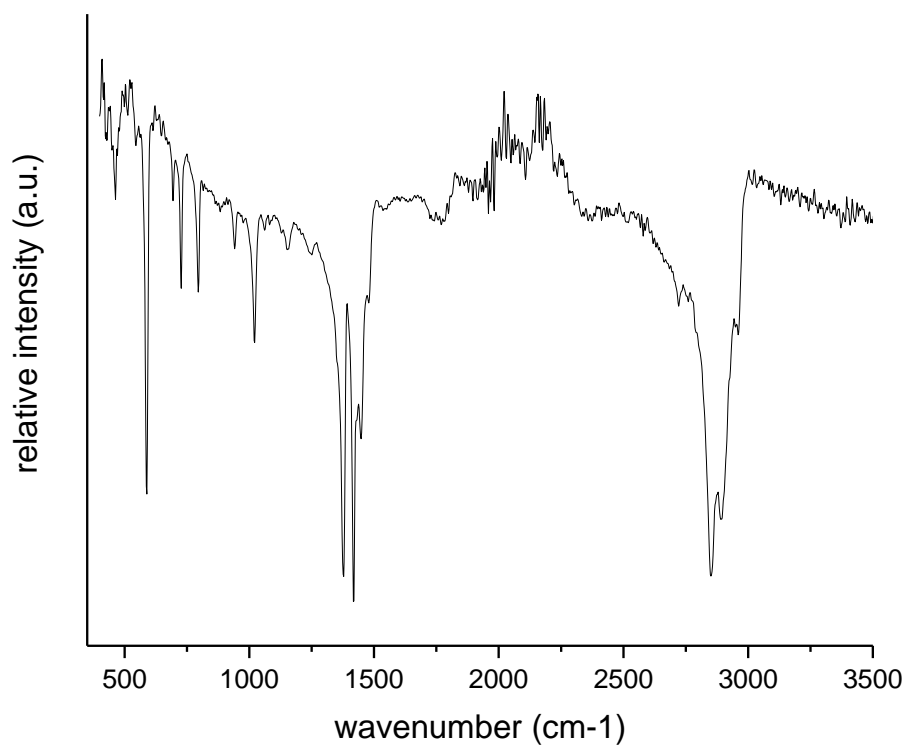
Figure S64: IR spectrum of $[Cu_4Zn_{9/10}](Cp^*)_8$ (**4/5**).

The IR spectrum shows characteristic v_{C-H} stretching vibrations of the Cp* ligands in the region 2500 - 3000 cm^{-1}. The bands between 500 cm^{-1} and 1700 cm^{-1} are mainly assigned to v_{C-C} vibrations.
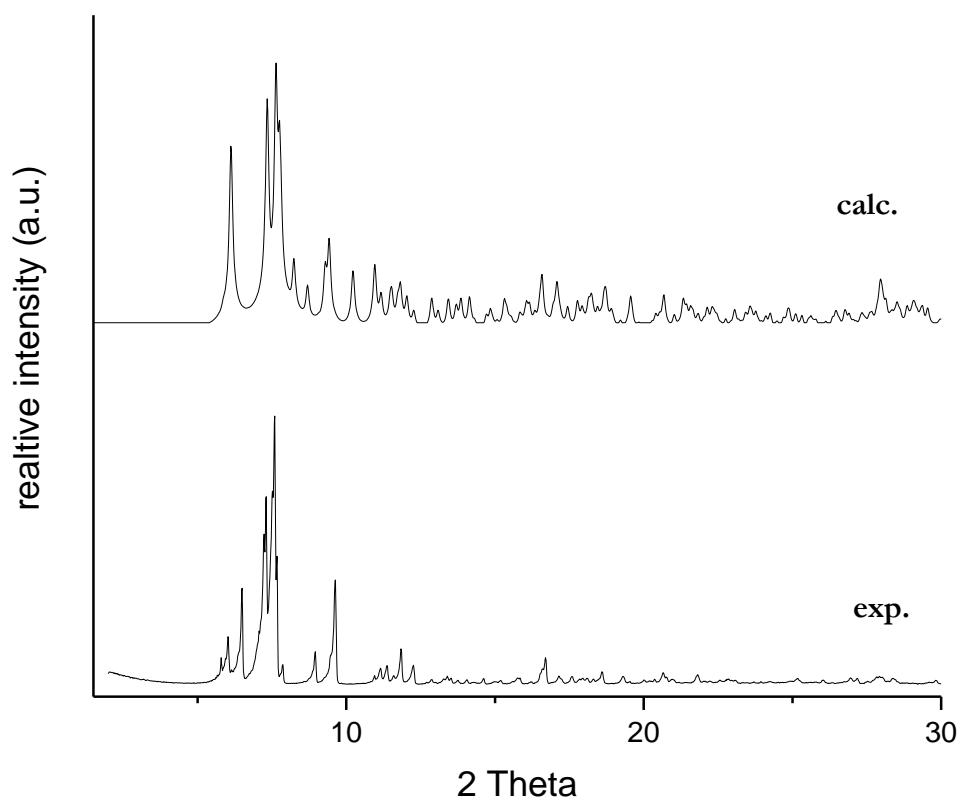
Figure S65: Powder-XRD pattern of $[Cu_4Zn_{9/10}](Cp^*)_8$ (**4/5**) and calculated pattern.

The powder-Xray diffraction pattern of $[Cu_4Zn_{9/10}](Cp^*)_8$ shows large coincidence with the calculated one from SC-XRD, thereby confirming the purity of the isolated material.

In situ studies on cluster formation of 4/5 and library composition

The following supporting data documentation refers to pages 138-141.
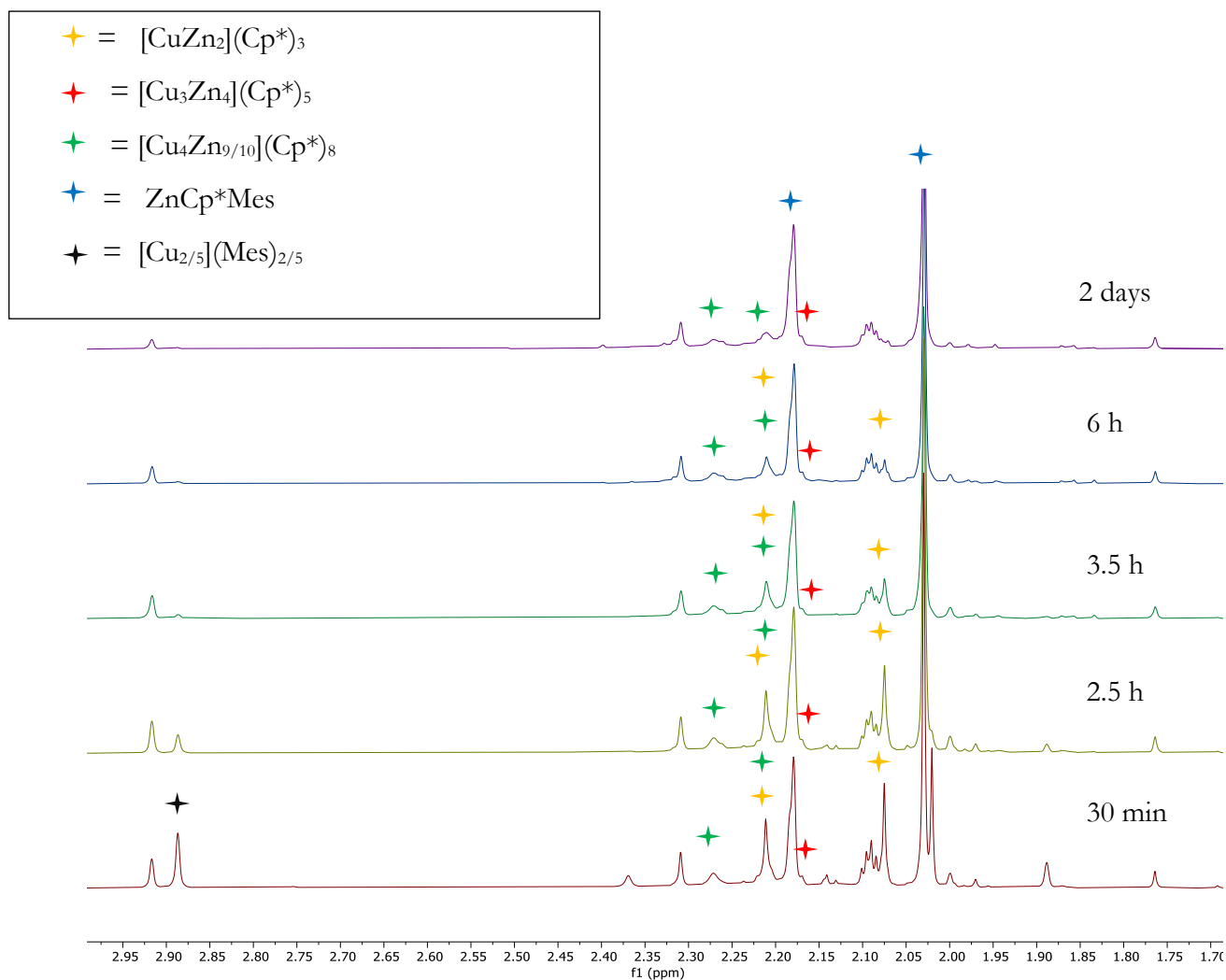
Figure S66: ^{1}H-NMR spectra (toluene-d_8) of the reaction solution [CuMes] + [Zn$_2$](Cp*)$_2$ (1:0.75) at room-temperature. The multiplet at 2.09 ppm is the solvent residual signal.

6. Appendix

6.2 Supporting information for the chemical part
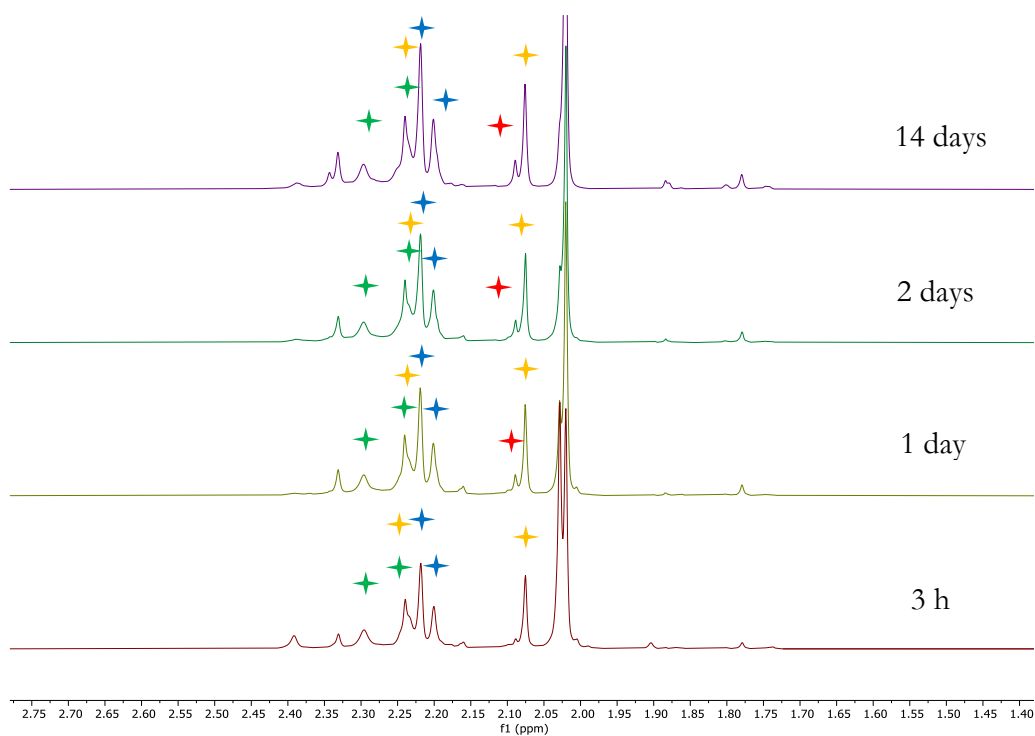
Figure S67: ^{1}H-NMR spectra (benzene-d$_6$) of the reaction solution [CuMes] + [Zn$_2$](Cp*)$_2$ (1:1.5) at room-temperature.
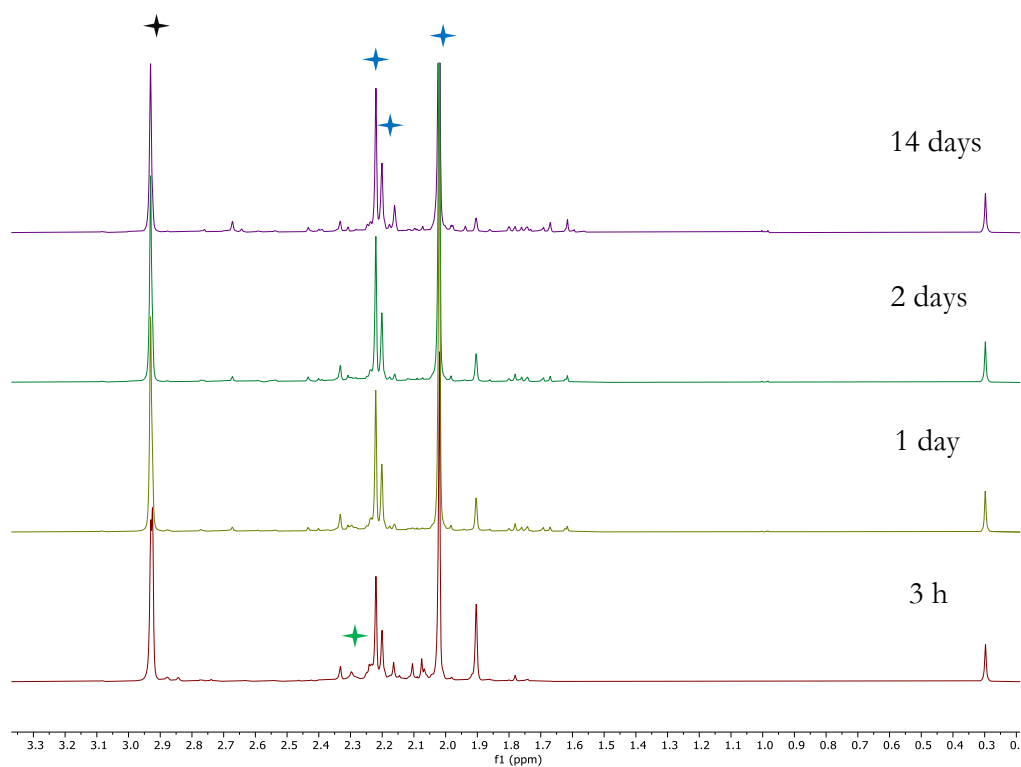
Figure S68: ^{1}H-NMR spectra (benzene-d$_6$) of the reaction solution [CuMes] + [Zn$_2$](Cp*)$_2$ (1:0.38) at room-temperature.

The in situ ^{1}H-NMR spectra of Cu:Zn libraries generated from [CuMes] and [Zn$_2$](Cp*)$_2$ at different Cu:Zn stoichiometries show Cp*ZnMes$_2$ as major reaction product, which is formed upon reduction of Cu(I) with [Zn$_2$](Cp*)$_2$. The triangular cluster [CuZn$_2$](Cp*)$_3$ is formed at medium to high Zn concentrations. Whereas at a Cu:Zn stoichiometry of 1:1.5, embryonic [CuZn$_2$](Cp*)$_3$ is consumed in the time course of the reaction (after several days), it persists in solution at a Cu:Zn stoichiometry of 1:3. Besides [CuZn$_2$](Cp*)$_3$, [Cu$_3$Zn$_4$](Cp*)$_5$ is identified in the spectra of these Cu:Zn stoichiometries. [Cu$_4$Zn$_{9/10}$](Cp*)$_8$ is also formed at Cu:Zn concentrations of 1:1.5 and 1:3 without major changes in concentration over time. At the Cu:Zn stoichiometry of 1:0.38, only very small amounts of [Cu$_4$Zn$_{9/10}$](Cp*)$_8$ are detected after short reaction times. No other cluster species can be identified by NMR at this Cu:Zn ratio.

6.2.5 Reactivity of Cu/Zn cluster libraries

The following supporting data documentation refers to pages 142-148.

6.2.5.1 Reactivity towards CO_2
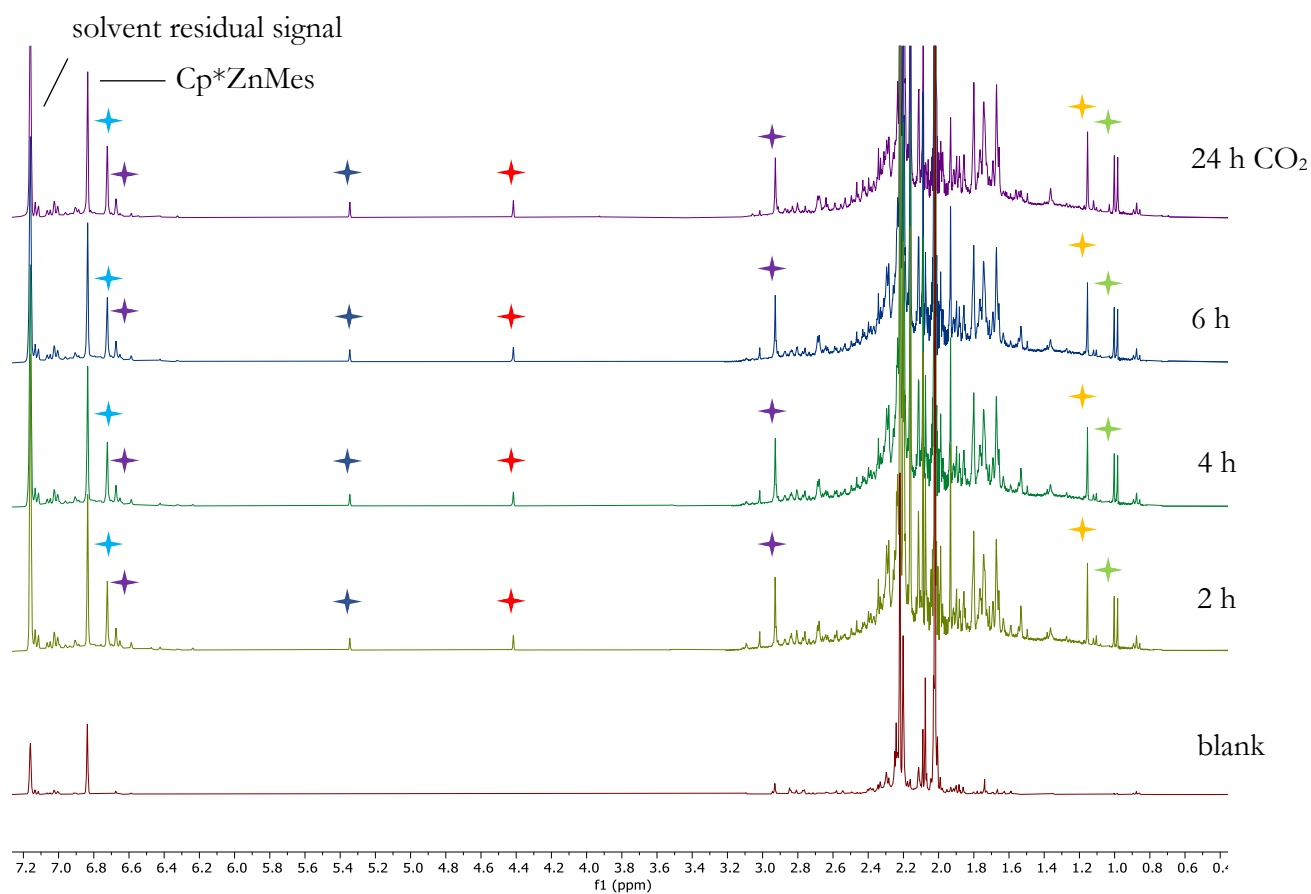
Figure S69: Time dependant *in-situ* ^{1}H-NMR (benzene-d$_6$) of the reaction of the Cu/Zn library (Cu:Zn 1:1.5) with CO_2 (1 bar, RT).

✦ fulvene ✦ fulvalene ✦ HCp* ✦ mesitylene ✦ hydrogen (coordinated) ✦ [Cu$_2$](Mes)$_2$

6. Appendix

6.2 Supporting information for the chemical part

*Note: In the region 1.4 ppm – 2.4 ppm, signals of Cp*ZnMes, [CuZn$_2$](Cp*)$_3$, [Cu$_3$Zn$_4$](Cp*)$_5$ and [Cu$_4$Zn$_{9/10}$](Cp*)$_8$ (**4/5**) can be observed. This indicates that these species do not react with CO$_2$, such as observed in LIFDI-MS analysis. Formation of fulvalene, HCp* and mesitylene was observed in varying amounts when reproducing the experiment. This is probably due to the very high sensitivity of the library towards traces of moisture. If they are involved as product species in CO$_2$ adduct formation is therefore not clear. However, reductive elimination of e.g. HMes to open coordination sites for CO$_2$ binding seems to be a plausible mechanism.*

6.2.5.2 Reactivity towards CO_2 and H_2
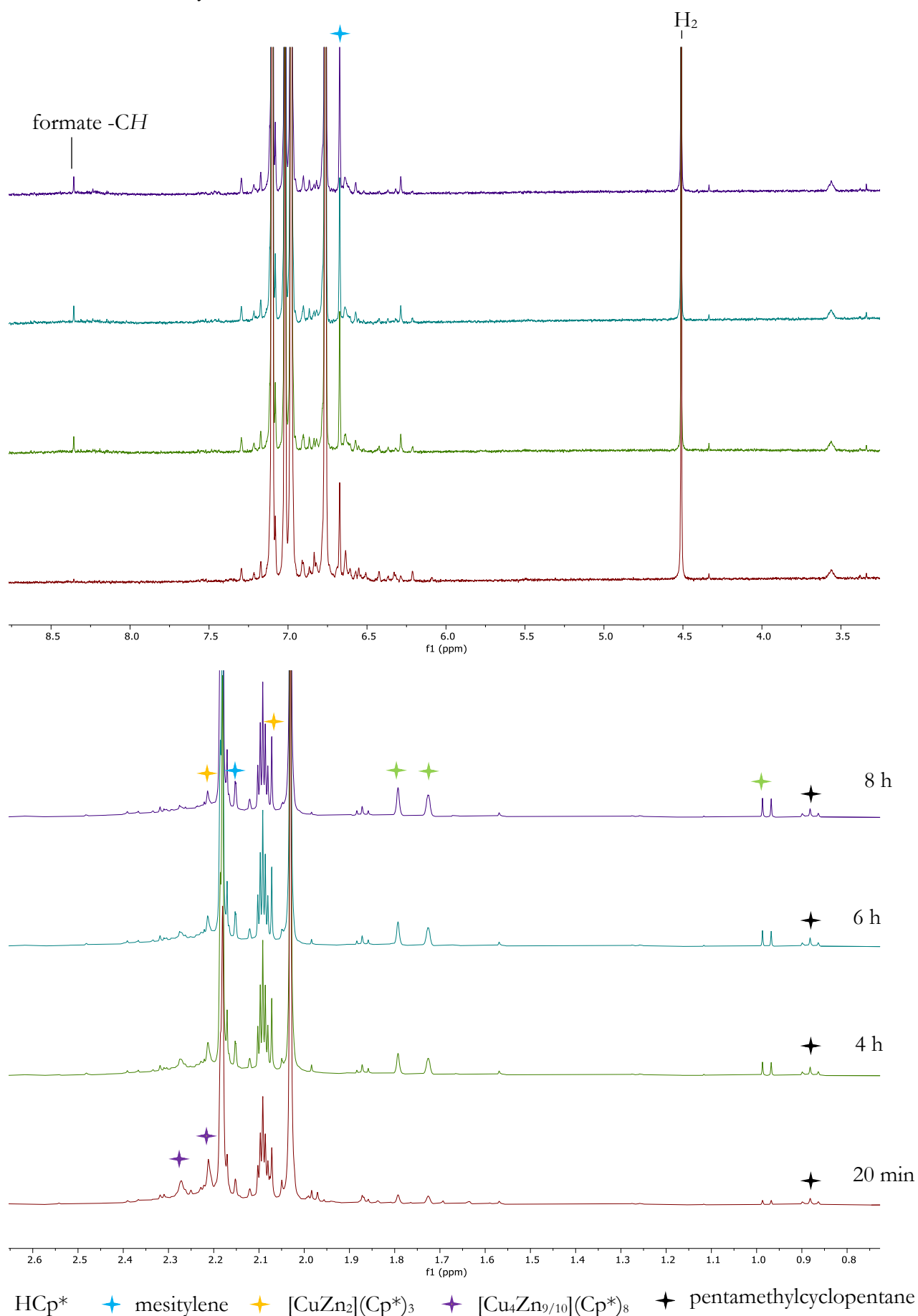
Figure S70: Time dependent *in-situ* ^{1}H-NMR (toluene-d_8) of the treatment of the Cu/Zn library (Cu:Zn 1:1.5) with H_2 (2 bar, RT) <u>after</u> reaction with CO_2 (1 bar, 2h, RT).

279

Note: The signals at 2.03 ppm, 2.18 ppm and 6.76 ppm are referred to Cp*ZnMes and the ones at 2.09 ppm and 6.97-7.09 ppm to toluene-d8.
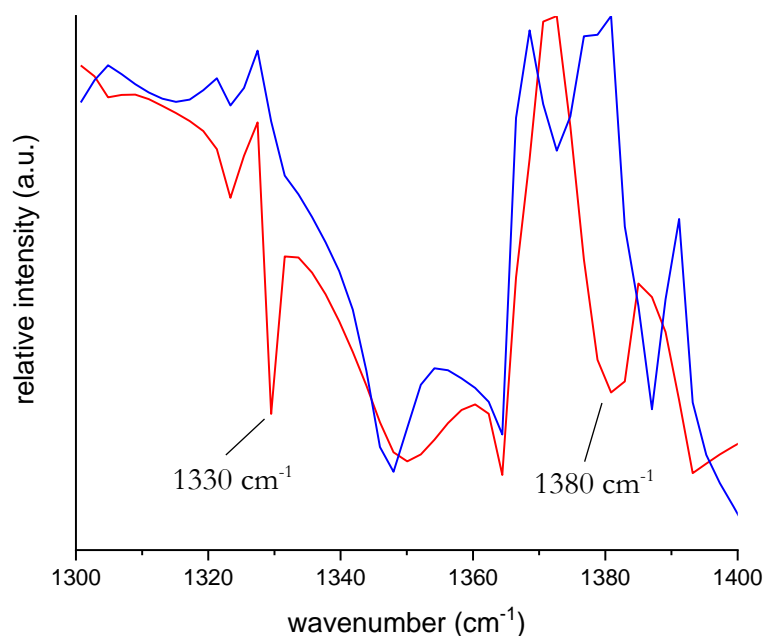
Figure S71: Cut-outs of the FT-IR spectra of the original Cu/Zn library (Cu:Zn = 1:1.5) (blue) and of the Cu/Zn library (Cu:Zn = 1:1.5) after CO_2/H_2 treatment (red).

The bands at 1330 cm^{-1} and 1380 cm^{-1} are tentatively assigned to Cu-formate units (C-H in plane bending / COO rocking, the C-O symmetric stretching vibration, respectively).

6.2.6 Crystallographic information of Cu/Al clusters

Table S6: Crystallographic information for Cu/Al clusters **1$_H$/2**, **2**, **9** and **11**.

	11	**9**	**1$_H$/2**	**2**
chemical formula	$C_{59}H_{86}Cu_4Al_4$	$C_{30}H_{45}Cu_2Al$	$Cu_{7.33}Al_6C_{60}H_{90}$	$Cu_8Al_6C_{60}H_{90}$
formula weight	1157.40	559.74	1438.63	1481.60
temperature	100(2) K	100(2) K	100(2)	100(2)
λ [Å]	0.71073	0.71073	0.71073	0.71073
crystal size [mm]	0.208x0.261x0.815	0.025x 0.055 x 0.075	0.048x 0.102x 0.193	0.093x0.142x0.187
crystal habit	black-green fragment	yellow-orange fragment	black needle	black fragment
crystal system	monoclinic	triclinic	monoclinic	monoclinic
space group	P 2$_1$/n	P-1	*I 2/m*	*C 2/m*
unit cell dimensions	a = 14.6563(11) Å b = 25.306(2) Å c= 19.6043(16) Å α = 90° β = 92.589(3)° γ = 90°	a = 10.6817(8) Å b = 10.6837(8) Å c= 15.0961(12) Å α = 75.703(2)° β = 72.180(2)° γ = 60.202(2)°	a = 12.9999(9) Å b = 17.2545(13) Å c = 16.5285(17) Å α = 90° β = 97.7410(16)° γ = 90°	a = 19.603(4)Å b = 17.296(4)Å c = 12.944(2)Å α = 90° β = 123.107(7) γ = 90°
volume [Å^3]	7263.7(10)	1413.85(19)	3673.7(5)	3676.4(13)
Z	4	2	2	2
ϱ (calculated) [g/cm^3]	1.058	1.315	1.301	0.158
absorption coefficient [mm^{-1}]	1.232	1.551	2.181	0.583
F(000)	2432	592	1481	163
diffractometer	BRUKER D8 VENTURE DUO IMS	BRUKER D8 VENTURE	BRUKER D8 VENTURE	BRUKER D8 VENTURE DUO IMS

6. Appendix

6.2 Supporting information for the chemical part

radiation source	IMS microsource, Mo	TXS rotating anode, Mo	TXS rotating anode, Mo	IMS microsource, Mo
θ range for data collection [°]	2.08 – 25.39	2.39-25.76	2.36-25.68	2.355-25.693
index ranges	$-17 \leq h \leq 17$ $-30 \leq k \leq 30$ $-23 \leq l \leq 23$	$-12 \leq h \leq 13$ $-12 \leq k \leq 12$ $-18 \leq l \leq 18$	$-15 \leq h \leq 15$ $-21 \leq k \leq 20$ $-20 \leq l \leq 20$	$-23 \leq h \leq 23$ $-21 \leq k \leq 21$ $-15 \leq l \leq 15$
reflections collected	278735	60165	46509	86379
independent reflections	13338 $[(R_{int}) = 0.1132]$	5328 $[(R_{int}) = 0.0299]$	3607 $[(R_{int}) = 0.0412]$	3610 $[(R_{int}) = 0.0271]$
coverage of independent reflections	99.9 %	98.6 %	99.9 %	99.9%
absorption correction	Multi-scan	Multi-scan	Multi-scan	Multi-Scan
max. and min. transmission	0.5707 and 0.7452	0.7073 and 0.7452	0.9030 and 0.6780	0.7453 and 0.6940
structure solution technique	direct methods	direct methods	direct methods	direct methods
structure solution program	SHELXS-97 (Sheldrick 2008)	SHELXS-97 (Sheldrick 2008)	SHELXS-13/1 (Sheldrick 2008)	SHELXS-13/1 (Sheldrick 2008)
refinement method	full matrix least squares on F^2	full matrix least squares on F^2	full matrix least squares on F^2	full matrix least squares on F^2
refinement program	SHELXL 2014 (Sheldrick 2014)	SHELXL 2014 (Sheldrick 2014)	SHELXL 2014 (Sheldrick 2014)	SHELXL 2018/3 (Sheldrick 2018)
function minimized	$\sum w(F_0^2 - F_c^2)^2$	$\sum w(F_0^2 - F_c^2)^2$	$\sum w(F_0^2 - F_c^2)^2$	$\sum w(F_0^2 - F_c^2)^2$
data/restraints/parameters	13338/840/833	5328/145/334	3607/160/249	3610/217/248
goodness of fit on F^2	1.059	1.269	1.118	1.097
$\Delta/\sigma_{max.}$	0.543	0.001	0.001	0.018

6. Appendix

6.2 Supporting information for the chemical part

final R indices [I>2σ]	R1 = 0.0718, wR2 = 0.1499	R1 = 0.0389, wR2 = 0.0872	R1 = 0.0572, wR2 = 0.1882	R1 = 0.0790, wR2 = 0.2315
final R indices [all data]	R1 = 0.0960, wR2 = 0.1437	R1 = 0.0405, wR2 = 0.0878	R1 = 0.0683, wR2 = 0.1974	R1 = 0.0816, wR2 = 0.2361
$\Delta F_{max.}$, $\Delta F_{min.}$ [e / Å^{-3}]	0.853, -0.847	0.532, -0.639	0.617, -0.579	2.932/-0.823

The following supporting data documentation refers to pages 151-157.

6.2.7 Mechanistic investigations in Cu/Al cluster growth processes

6.2.7.1 Formation mechanism of $[Cu_4Al_4](Cp^*)_5(Mes)$ (**11**)

⭐ AlMes$_3$

⭐ Mes$_2$AlCp*

⭐ $[Cu_4Al_4](Cp^*)_5(Mes)$

⭐ $[Cu_8Al_6](Cp^*)_6$
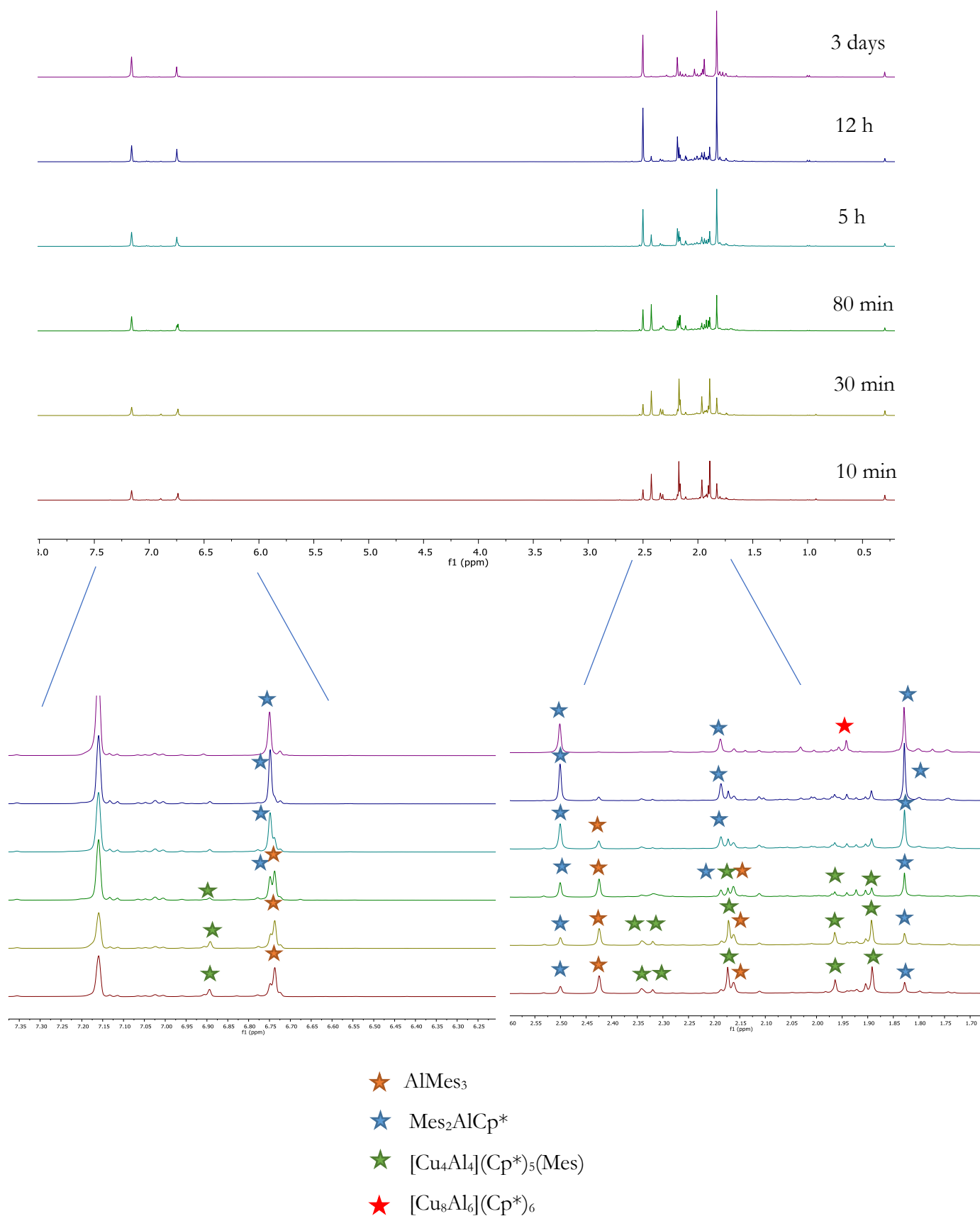
Figure S72: *In-situ* ^{1}H-NMR spectra (benzene-d$_6$) of the reaction [CuMes] + AlCp* (1:1.3), 75 °C.

The in situ ^{1}H-NMR spectra of the [CuMes] + AlCp* (1:1.3, 75 °C) reaction reveal formation of the Al(III) oxidation products AlMes$_2$ and Cp*AlMes$_2$. [Cu$_4$Al$_4$](Cp*)$_5$(Mes) is formed after short reaction times and can be isolated from the respective solutions. Due to thermal instability of [Cu$_4$Al$_4$](Cp*)$_5$(Mes), prolonged heating leads to its decay and to formation of [Cu$_8$Al$_6$](Cp*)$_6$ amongst other clusters (several small peaks, see also corresponding LIFDI-MS data, Figure S73).

6. Appendix
6.2 Supporting information for the chemical part

[Cu₆Al₇](Cp*)₆   [Cu₆Al₇](Cp*)₆ / [HCu₇Al₇](Cp*)₆   {[Cu₇Al₇](Cp*)₆ -H} / [Cu₇Al₇](Cp*)₆
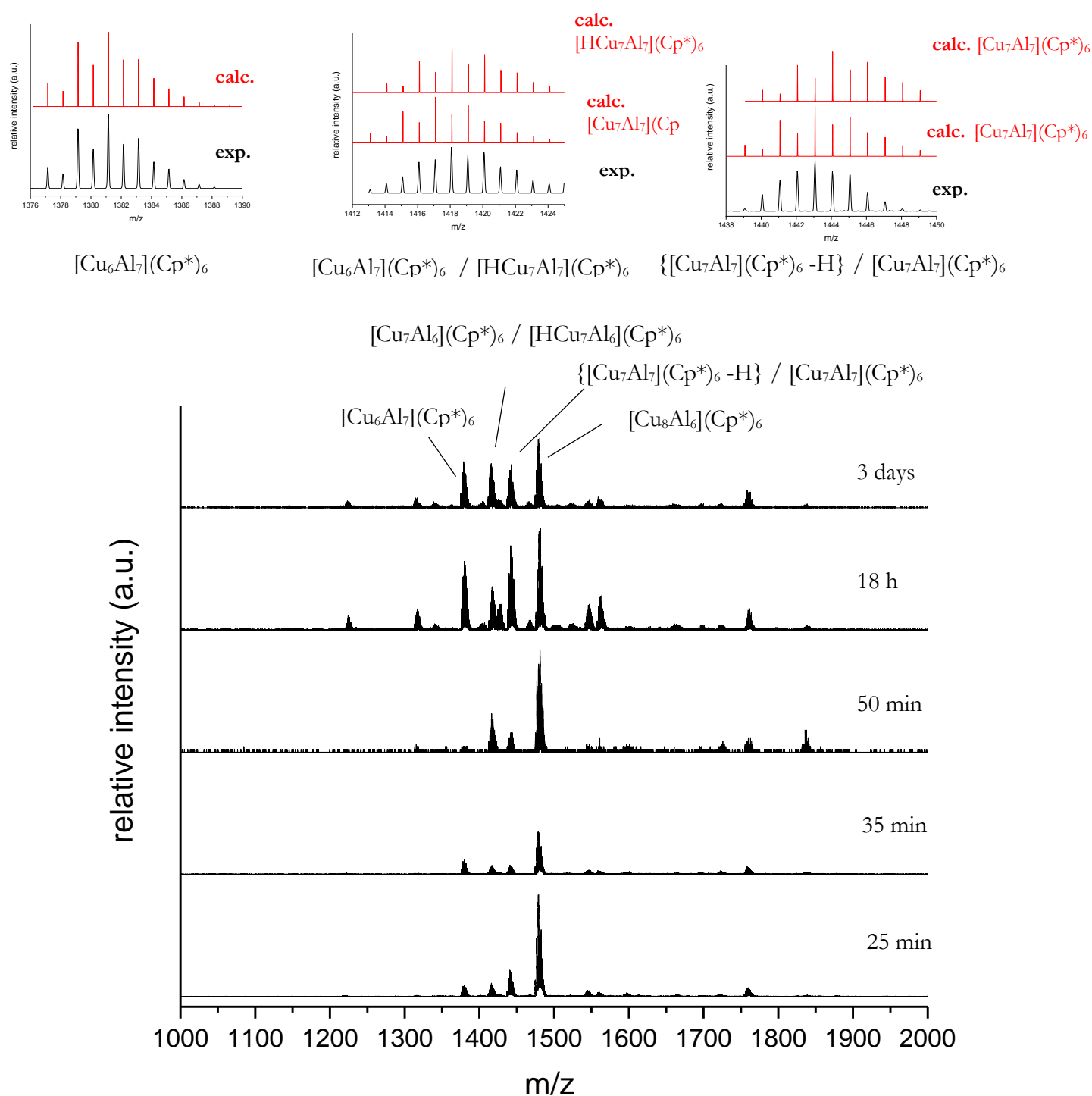
Figure S73: Bottom: LIFDI-MS spectra of the reaction solution [CuMes] + AlCp* (1:1.3, 75°C) after different reaction times. Top: Comparison between calculated (red) and experimental (black, determined by LIFDI-MS) mass-envelopes for the species [Cu₆Al₇](Cp*)₆ and {[Cu₇Al₇](Cp*)₆ -H}. The isotopic pattern of [Cu₈Al₆](Cp*)₆ is depicted and analyzed in Figure 35 (main text).

Note: The peak at m/z = 1443 is found to be a mixture between the deprotonated cluster {[Cu₇Al₇](Cp)₆ -H} and [Cu₇Al₇](Cp*)₆. Likewise, the peak at m/z = 1418 is a mixture between the radical **1** and the hydride **1H**.*

286

6.2.7.2 Targeted cluster degradation from [Cu₄Al₄](Cp*)₅(Mes) (**11**) to [Cu₂Al](Cp*)₃ (**9**)

addition of 3-hexyne, RT, 4 days

addition of 3-hexyne, RT, 48 h

addition of 3-hexyne, RT, 36 h

addition of 3-hexyne, RT, 24 h

addition of 3-hexyne, RT, 12 h

addition of 3-hexyne, RT, 30 min

starting material **11**

8.5 8.4 8.3 8.2 8.1 8.0 7.9 7.8 7.7 7.6 7.5 7.4 7.3 7.2 7.1 7.0 6.9 6.8 6.7 6.6 6.5 6.4 6.3 6.2 6.1 6.0 5.9 5.8 5.7 5.6 5.5 5.4 5.3 5.2 5.1 5.0 4.9 4.8 4.7
f1 (ppm)

★ = [Cu₂Al](Cp*)₃
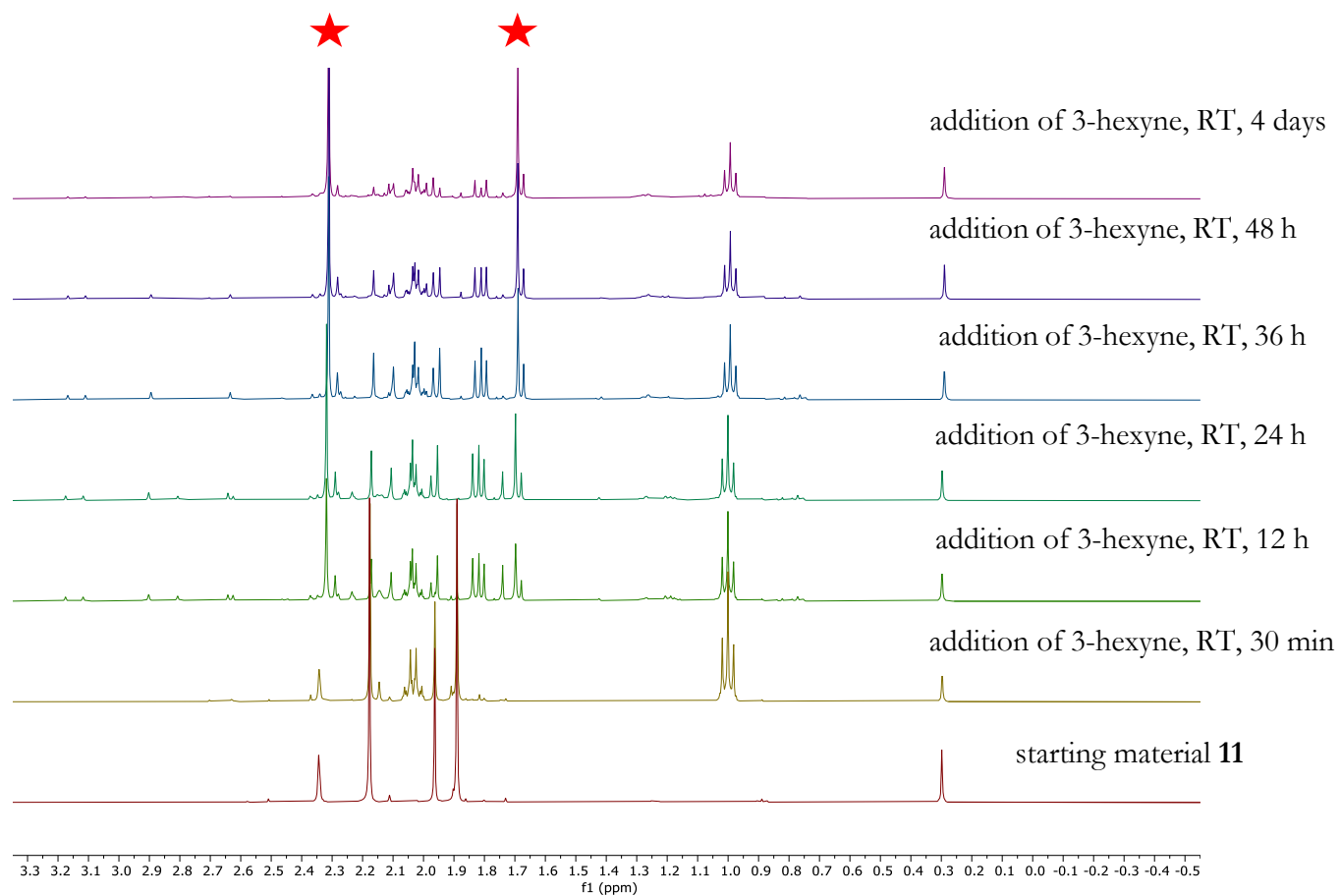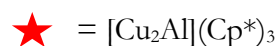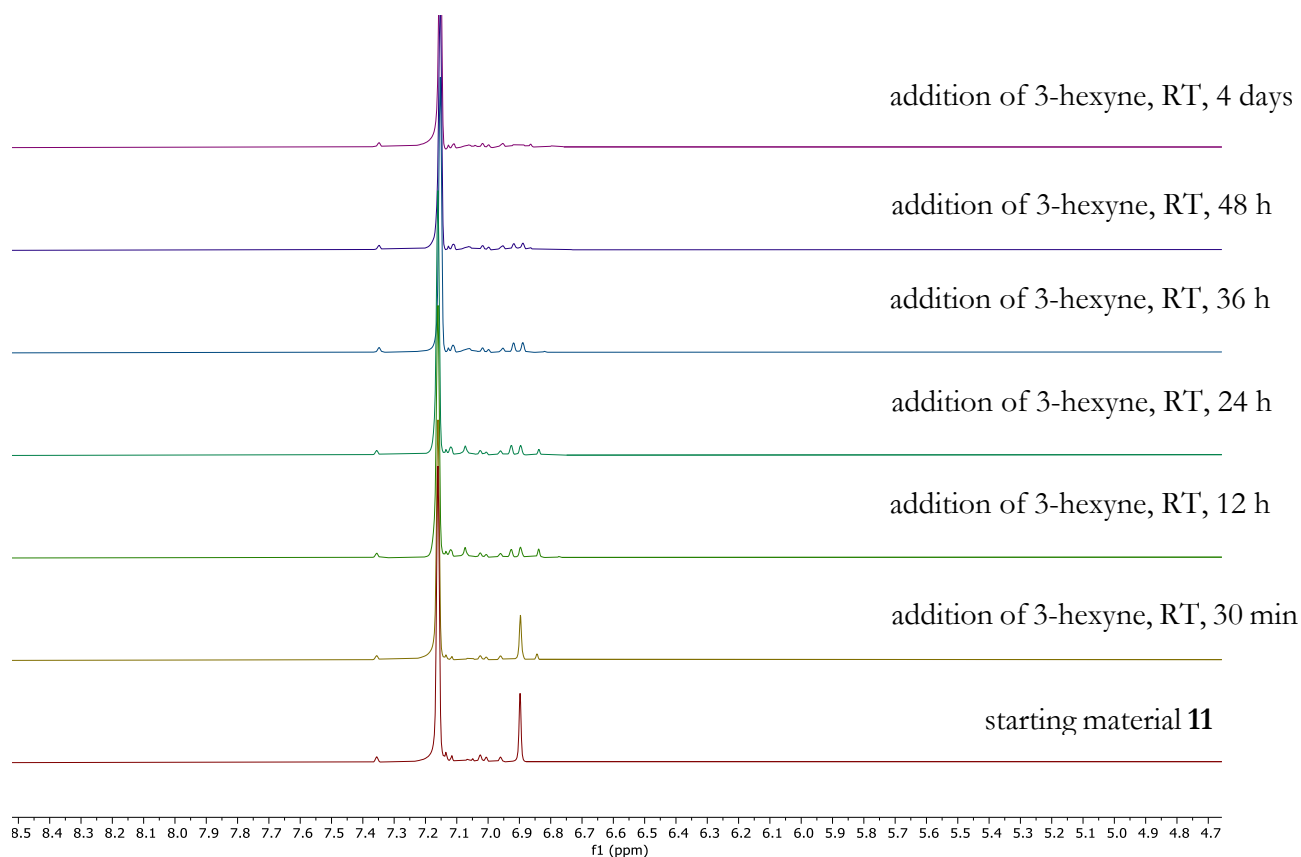
Figure S74: *In-situ* ¹H NMR spectra (benzene-d₆) of the conversion of [Cu₄Al₄](Cp*)₅(Mes) **11** with 3-hexyne (8 eq.). Up: Aliphatic region, Bottom: Aromatic region of the spectra. The triplet at 0.99 ppm, as well as the multiplett at 2.05 ppm are attributed to 3-hexyne, which is used in excess. The signal at 0.29 ppm is attributed to silicon grease.

The spectra clearly show consumption of [Cu₄Al₄](Cp)₅(Mes) upon addition of 3-hexyne and slow formation of triangular [Cu₂Al](Cp*)₃. Several side products can be distinguished in the spectra (e.g. the signal group at 1.85 ppm). However, no clear assignment can be made for these species. LIFDI-MS analysis (see Figure S75) provides an overview about the plethora of species formed as side-products in the cluster degradation.*

$[Cu_2Al_4](Cp^*)_3(Mes)(Hex)_2$ ★

$[Cu_2Al](Cp^*)_3$ ★

$[Cu_6Al_7](Cp^*)_6$ ★

$[Cu_8Al_6](Cp^*)_6$ ★
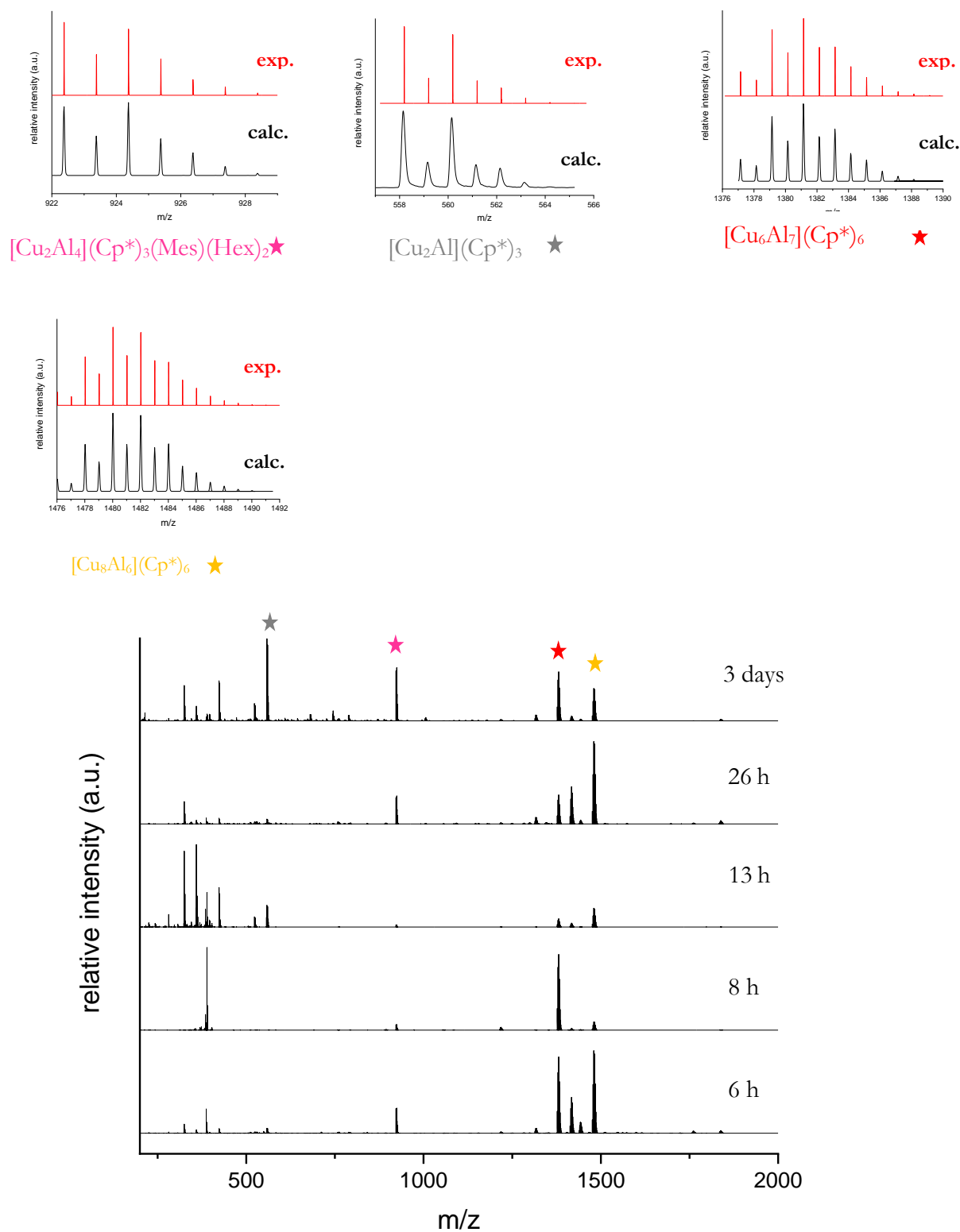
Figure S75: Bottom: Time-dependent LIFDI-MS spectra of the reaction solution $[Cu_4Al_4](Cp^*)_5(Mes)$ + 3-hexyne (10. Eq.), RT. Top: Enlarged isotopic pattern as determined by LIFDI-MS (red) and calculated mass envelopes (black) for selected peaks.

Table S7: Species observed in LIFDI-MS analysis of the reaction $[Cu_4Al_4](Cp^*)_5(Mes)$ + 3-hexyne (10 eq.), RT.

after 6 h	after 8 h	after 13 h	after 26 h	after 3 days
$[Cu_8Al_6](Cp^*)_6$	$[Cu_8Al_6](Cp^*)_6$	$[Cu_8Al_6](Cp^*)_6$	$[Cu_8Al_6](Cp^*)_6$	$[Cu_8Al_6](Cp^*)_6$
$[Cu_7Al_6](Cp^*)_6$	$[Cu_6Al_4](Cp^*)_3$	$[Cu_7Al_6](Cp^*)_6$	$[Cu_7Al_6](Cp^*)_6$	$[HCu_7Al_6](Cp^*)_6$
$\{[Cu_7Al_6](Cp^*)_6\ \text{-2H}\}$	$\{[Cu_7Al_7](Cp^*)_6\ \text{-H}\}$	$\{[Cu_7Al_7](Cp^*)_6\ \text{-H}\}$	$\{[Cu_7Al_7](Cp^*)_6\ \text{-H}\}$	$\{[Cu_7Al_7](Cp^*)_6\ \text{-H}\}$
$[Cu_8Al_6](Cp^*)_6(Mes)_3$	$[Cu_8Al_6](Cp^*)_6(Mes)_3$	$[Cu_8Al_6](Cp^*)_6(Mes)_3$	$[Cu_8Al_6](Cp^*)_6(Mes)_3$	$[Cu_8Al_6](Cp^*)_6(Mes)_3$
$\{[Cu_8Al_7](Cp^*)_7(Mes)\ \text{-H}\}$				
$[H_3Cu_3Al_2](Mes)(Hex)_2$ (small)		$[Cu_2Al](Cp^*)_2(Hex)$	$[H_3Cu_3Al_2](Mes)(Hex)_2$	$[Cu_3Al_5](Cp^*)_2(Hex)_5$
			$[Cu_3Al_2](Cp^*)(Mes)(Hex)_3$	$[Cu_3Al_2](Cp^*)(Mes)(Hex)_3$
				$[Cu_5Al_2](Cp^*)(Mes)(Hex)_4$
				$[Cu_5Al_2](Cp^*)(Mes)(Hex)_3$
$[Cu_6Al_6](Cp^*)_5$	$[Cu_6Al_6](Cp^*)_5$	$[Cu_6Al_6](Cp^*)_5$	$[Cu_6Al_6](Cp^*)_5$	$[Cu_6Al_6](Cp^*)_5$
$[HCuAl_4](Cp^*)(Hex)$		$[CuAl_4](Cp^*)_2(Hex)$	$[CuAl_4](Cp^*)_2(Hex)$	$[H_4CuAl_3](Cp^*)_3$
$[Cu_2Al_3](Cp^*)_3(Hex)(H)_2$	$[Cu_2Al_3](Mes)_2(Hex)(H)_2$		$[H_2Cu_2Al_3](Cp^*)_3(Hex)$	
$[Cu_2Al_3](Cp^*)_2(Mes)(Hex)$	$[Cu_2Al_3](Cp^*)_2(Mes)(Hex)_2$		$[Cu_2Al_3](Cp^*)_2(Mes)$	
			$[H_4CuAl_3](Cp^*)_3$	$[H_4CuAl_3](Cp^*)_3$
			$[H_4Cu_2Al_5](Hex)_3$	
$[Cu_2Al_4](Cp^*)_3(Mes)(Hex)_2$	$[Cu_2Al_4](Cp^*)_3(Mes)(Hex)_2$	$[Cu_2Al_4](Cp^*)_3(Mes)(Hex)_2$	$[Cu_2Al_4](Cp^*)_3(Mes)(Hex)_2$	$[Cu_2Al_4](Cp^*)_3(Mes)(Hex)_2$
$[Cu_2Al_4](Cp^*)_2(Mes)(Hex)_2$				$[HCu_2Al_4](Cp^*)_2(Mes)(Hex)_2$
$[Cu_2Al_4](Cp^*)_3(Mes)(Hex)$			$[Cu_2Al_4](Cp^*)_3(Mes)(Hex)$	$[Cu_2Al_4](Cp^*)_3(Mes)(Hex)$
$[Cu_2Al_4](Cp^*)_2(Mes)_2(Hex)_2$				$[Cu_2Al_2](Cp^*)(Mes)(Hex)_3$
$[Cu_2Al_4](Cp^*)_2(Mes)(Hex)$			$[Cu_2Al_4](Cp^*)_2(Mes)(Hex)$	
$[HCu_2Al_4](Cp^*)_2(Mes)(Hex)_3$				
$[Cu_5Al_7](Cp^*)_6$	$[Cu_5Al_7](Cp^*)_6$	$[Cu_5Al_7](Cp^*)_6$	$[Cu_5Al_7](Cp^*)_6$	$[Cu_5Al_7](Cp^*)_6$
			$[Cu_3Al_5](Cp^*)_2(Hex)_5$	$[Cu_4Al_6](Cp^*)_2(Hex)_6$
$[H_4Cu_5Al_{19}](Hex)_9$ (small)			$[HCu_2Al_6](Cp^*)_3(Hex)$	$[Cu_2Al_5](Cp^*)_3(Hex)_4$
$[Cu_6Al_8](Mes)_3(Hex)_4$			$[H_4Cu_5Al_{19}](Hex)_9$ (small)	$[HCu_3Al_8](Cp^*)(Mes)(Hex)_6$
$[Cu_5Al_{16}](Cp^*)(Mes)_2(Hex)_6$				
$[Cu_5Al_7](Cp^*)_6$	$[Cu_6Al_7](Cp^*)_6$	$[Cu_6Al_7](Cp^*)_6$	$[Cu_6Al_7](Cp^*)_6$	$[Cu_6Al_7](Cp^*)_6$
$[Cu_2Al](Cp^*)_3$		$[Cu_2Al](Cp^*)_3$	$[Cu_2Al](Cp^*)_3$	
$[Cu_2Al](Cp^*)_2$		$[Cu_2Al](Cp^*)_2$	$[Cu_2Al](Cp^*)_2$	
$[Cu](Cp^*)_2$			$[Cu](Cp^*)_2$	$[Cu_2](Cp^*)_2$
				$[HCu_2Al](Cp^*)_2(Mes)$

yellow: Cu-rich clusters; blue: Cu:Al 1:1 clusters; green: small, Cu-rich clusters; light green: Al-rich coordination compound; blue / pink: Al rich-clusters, $[Cu_2Al_4](Cp^*)_3(Mes)(Hex)$ = main side product; red: large, Al-rich clusters; grey: **11** and fragments thereof;

6.2 Supporting information for the chemical part
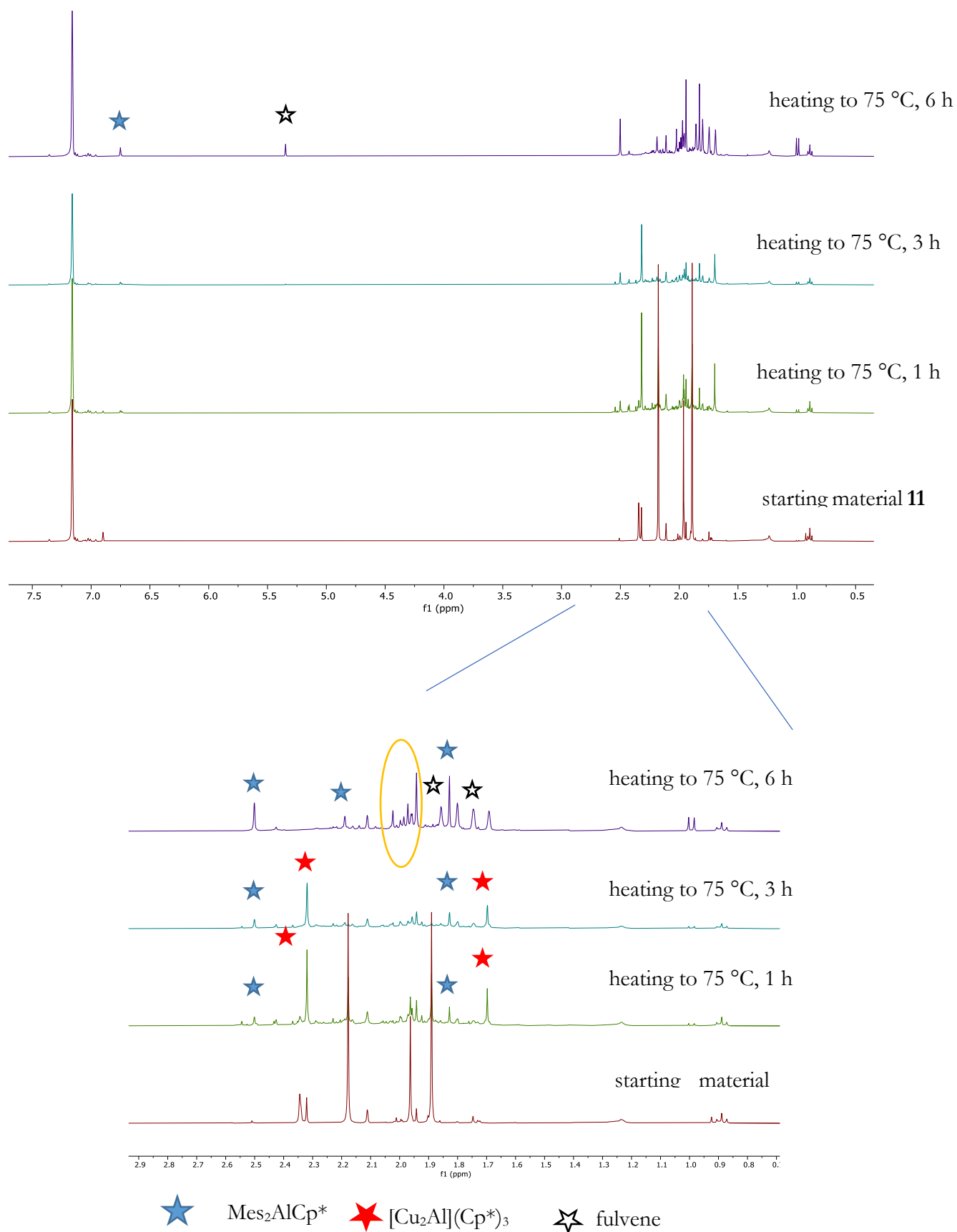
Figure S76: *In situ* ^{1}H-NMR spectra (benzene-d_6) of heating isolated [Cu$_4$Al$_4$](Cp*)$_5$(Mes) (**11**). The signal of [Cu$_8$Al$_6$](Cp*)$_6$ is marked by a yellow ellipsoid.

6. Appendix

6.2 Supporting information for the chemical part

The spectra show thermally induced formation of [Cu₈Al₆](Cp*)₆ out of [Cu₄Al₄](Cp*)₅(Mes) upon extrusion of the Al(III) species Cp*AlMes₂. Fulvene is detected as additional product, probably stemming from the autoreduction of Cp*Cu(I) units. Triangular [Cu₂Al](Cp*)₃ is detected as an intermediate reaction product pointing towards its role in cluster growth reactions.
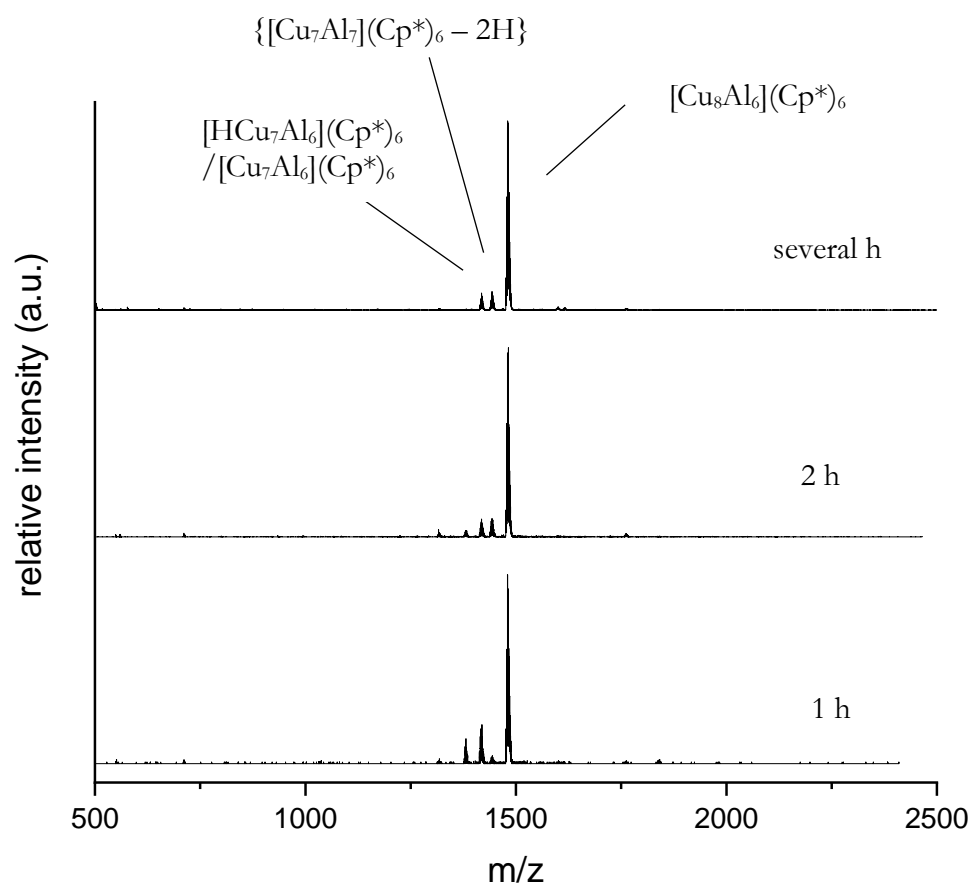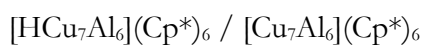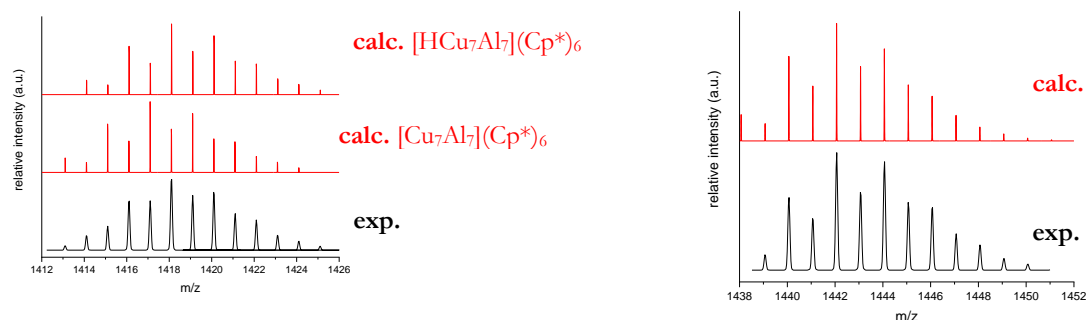
Figure S77: Bottom: LIFDI-MS spectra of a solution of isolated [Cu₄Al₄](Cp*)₅(Mes) (**11**) in toluene heated to 75 °C. Top: Comparison between experimental (black, LFIDI-MS) and calculated (red) isotopic patterns for selected peaks.

The LIFDI-MS shows [Cu₈Al₆](Cp*)₆, [(H)Cu₇Al₆](Cp*)₆ and {[Cu₇Al₇](Cp*)₆ − 2H}as products of the thermal degradation of [Cu₄Al₄](Cp*)₅(Mes).

6.2.7.3 The [Cu₂Al](Cp*)₃ triangular cluster **9** as a building block
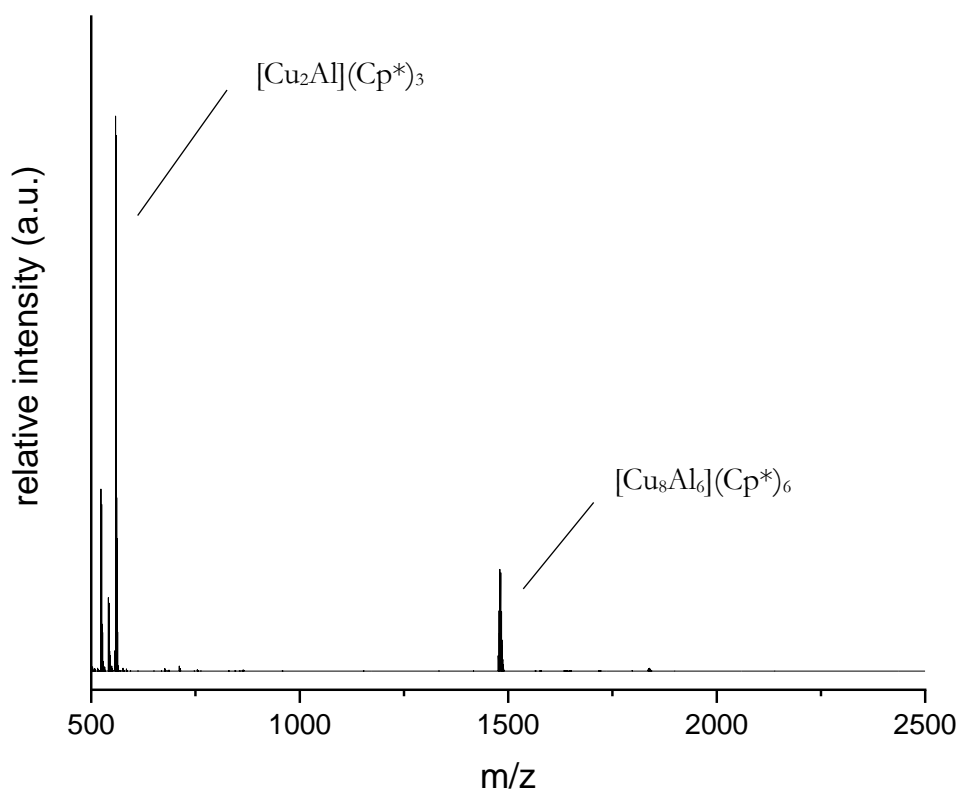
Figure S78: *In-situ* LIFDI-MS spectra of the conversion of [Cu₂Al](Cp*)₃ (**9**) with [CuMes] (1:1.2, toluene, 75°C, 7 h).

[Cu₈Al₆](Cp)₆ is formed as a product of the reaction between [Cu₂Al](Cp*)₃ (**9**) with [CuMes] besides Cu nanoparticles (see Figure S84).*

★ Mes$_2$AlCp*

★ AlMes$_3$

★ [CuMes]

★ [Cu$_2$Al](Cp*)$_3$
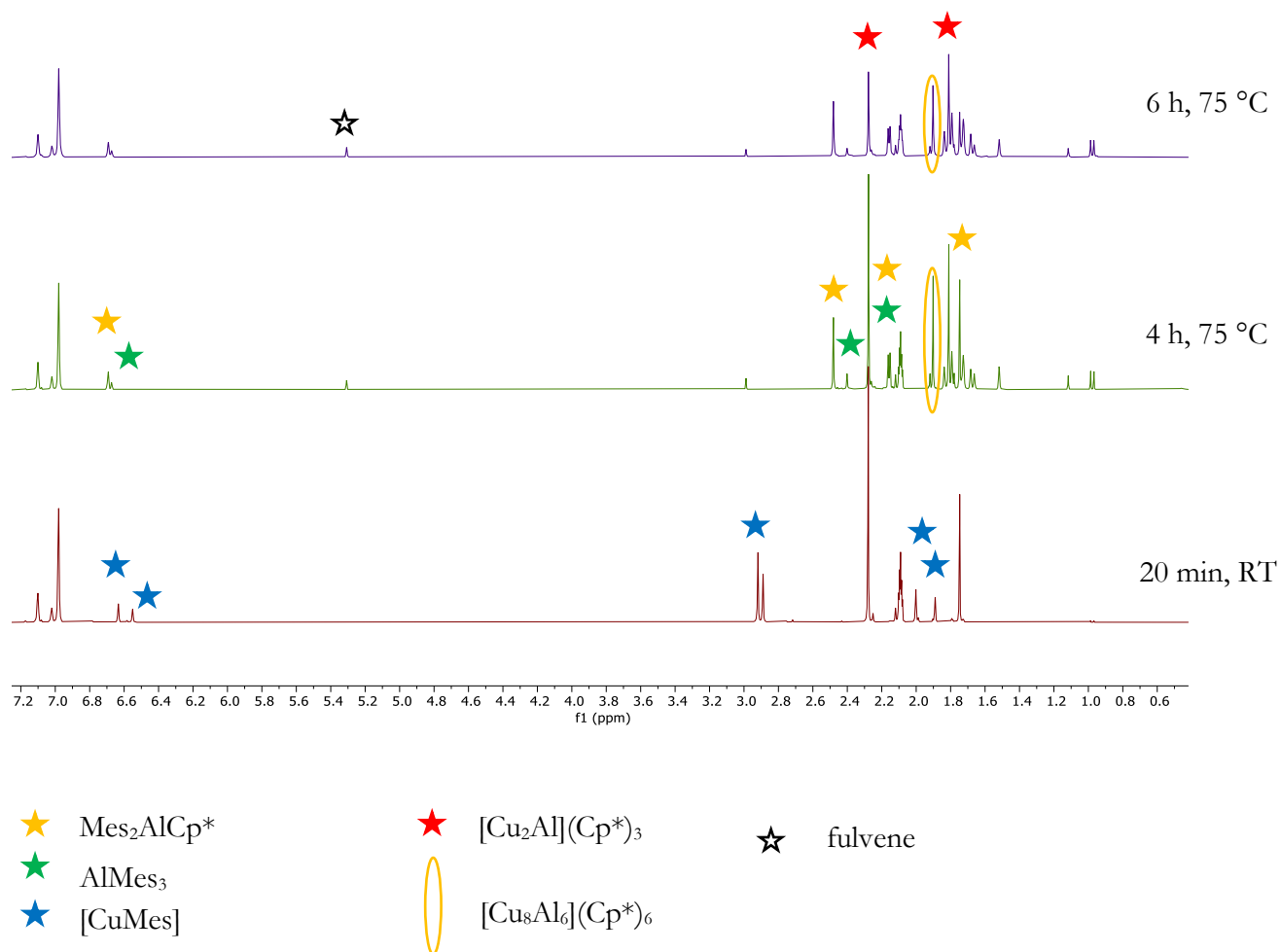
⬭ [Cu$_8$Al$_6$](Cp*)$_6$

☆ fulvene

Figure S79: *In-situ* ^{1}H-NMR spectra (toluene-d$_8$) of the conversion of [Cu$_2$Al](Cp*)$_3$ (**9**) with [CuMes] (1:1.2).

Cluster grwoth from [Cu$_2$Al](Cp)$_3$ to [Cu$_8$Al$_6$](Cp*)$_6$ is accompanied by formation of Cp*AlMes$_2$ and fulvene as oxidation products of the reduction of Cu(I).*

6.2.7.4 Alternative access to the cluster mixture [(H)Cu$_{7/8}$Al$_6$](Cp*)$_6$ (**1$_H$/2**)

a)
[Cu(dppbz)$_2$]

[HCu$_7$Al$_6$](Cp*)$_6$

[Cu$_8$Al$_6$](Cp*)$_6$

[H$_3$Cu$_3$](dppbz)$_3$ + AlCp* (1: 2.46)
toluene, 3 h, 75 °C

b)

m/z = 1418

exp.

calc.

[HCu$_7$Al$_6$](Cp*)$_6$

from [H$_3$Cu$_3$](dppbz)$_3$

m/z = 1419

exp.

calc.

[DCu$_7$Al$_6$](Cp*)$_6$

from [D$_3$Cu$_3$](dppbz)$_3$

m/z = 1417

exp.

calc.

[Cu$_7$Al$_6$](Cp*)$_6$

from [CuMes] + AlCp*
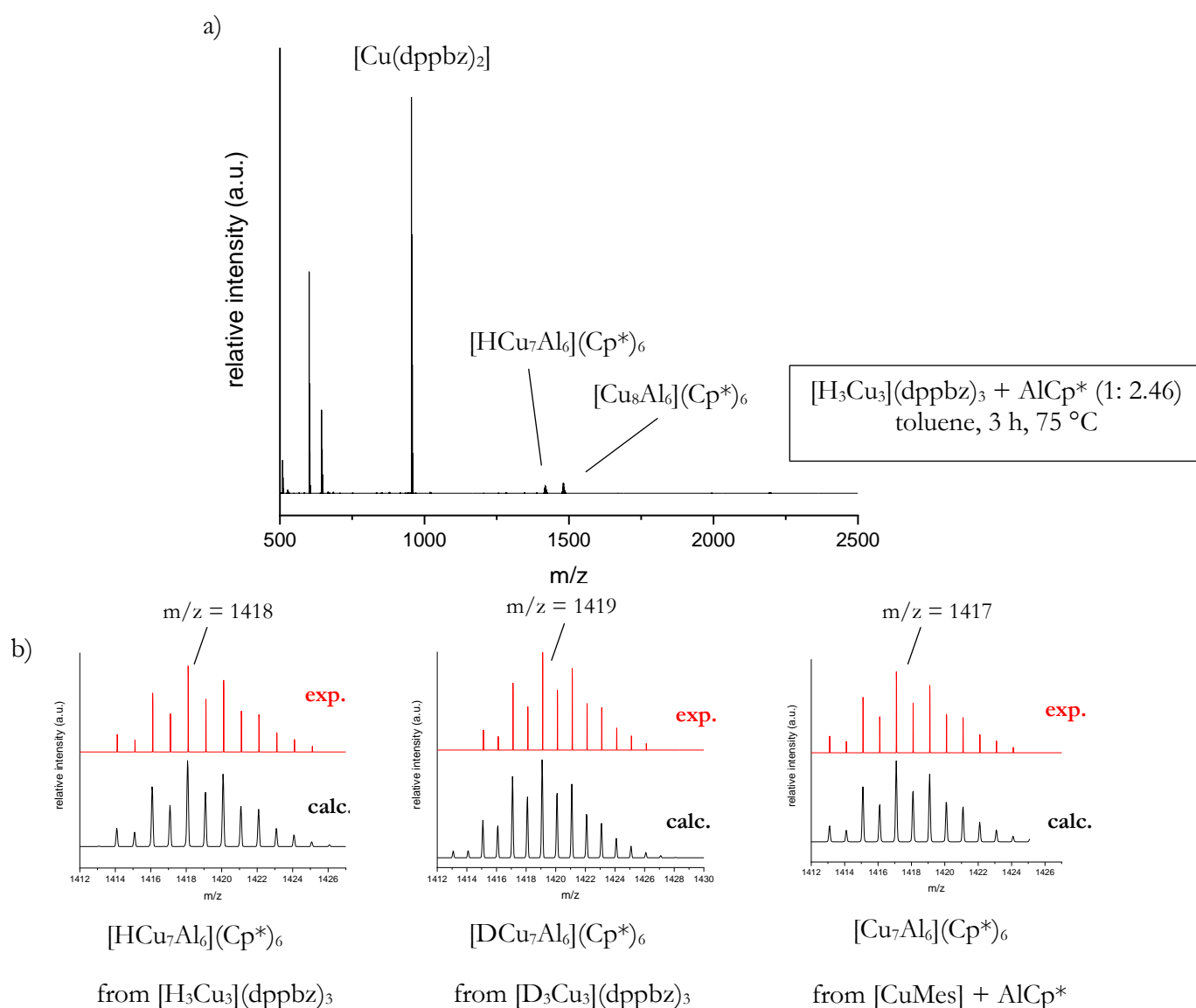
Figure S80: a) Full range LIFDI-MS spectrum of the reaction solution [H$_3$Cu$_3$](dppbz)$_3$ + AlCp* (1: 2.46, toluene, 3 h, 75 °C). b) Comparison of experimental (black) and calculated mass envelopes (red) of the species **1$_H$, 1$_D$** and **2**.

The reaction of [H$_3$Cu$_3$](dppbz)$_3$ (dppbz = 1.2-bis(diphenylphosphino)benzene) with AlCp yields [HCu$_7$Al$_6$](Cp*)$_6$ and [Cu$_8$Al$_6$](Cp*)$_6$. Likewise, reaction of [D$_3$Cu$_3$](dppbz)$_3$ with AlCp* yields [DCu$_7$Al$_6$](Cp*)$_6$ and [Cu$_8$Al$_6$](Cp*)$_6$.*

6.2.7.5 Size focusing to the cluster mixture [Cu$_{7/8}$Al$_6$](Cp*)$_6$ (**1/2**) and selective synthesis of [Cu$_8$Al$_6$](Cp*)$_6$ (**2**)
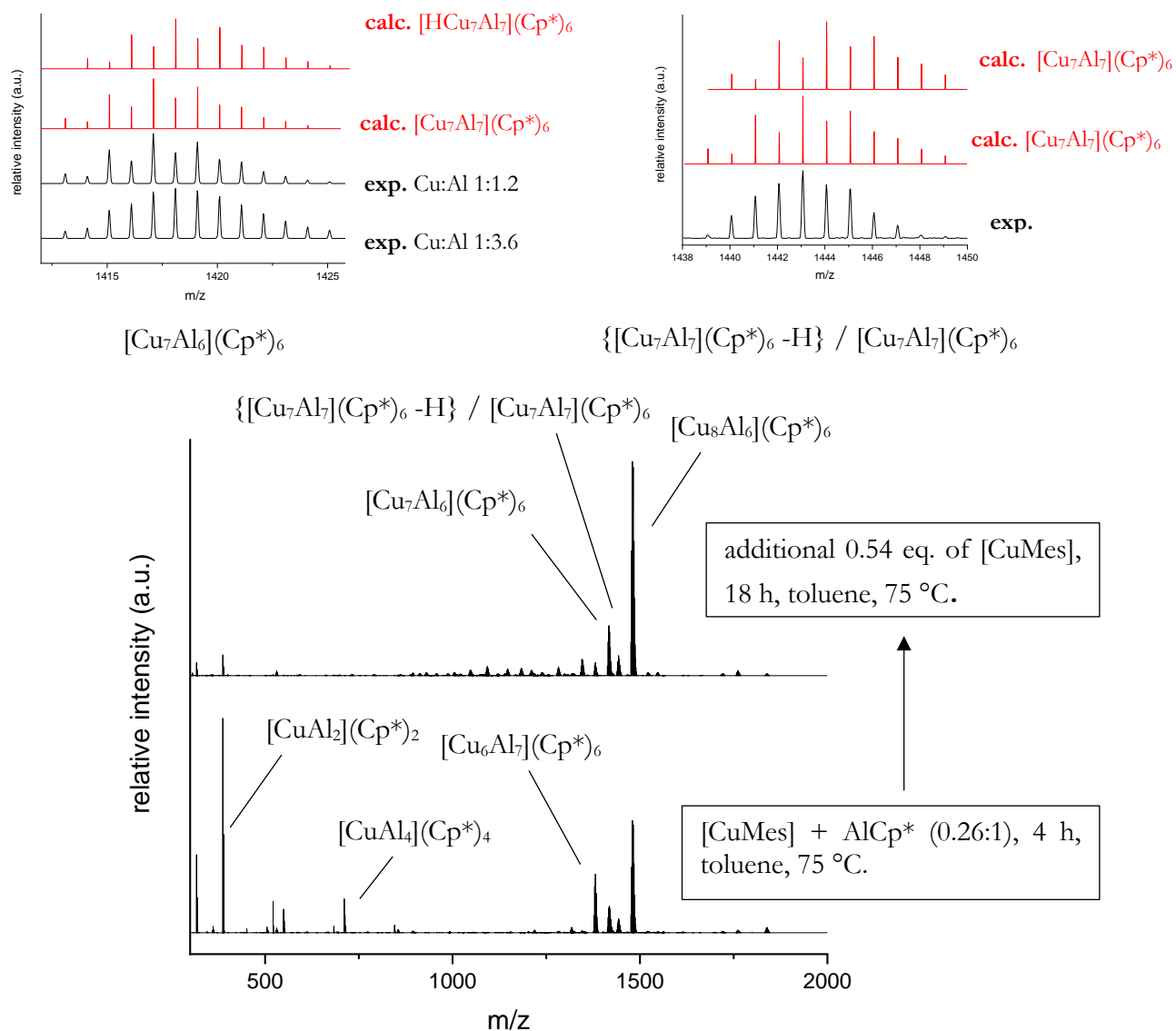
Figure S81: Full-range *in situ* LIFDI-MS spectra of the synthesis of [Cu$_{7/8}$Al$_6$](Cp*)$_6$ (**1/2**).

The spectra illustrate the size-focusing process towards the radical species [Cu$_7$Al$_6$](Cp)$_6$. Whereas in the Al-rich library, a mixture between [Cu$_7$Al$_6$](Cp*)$_6$ and its hydride congener [HCu$_7$Al$_6$](Cp*)$_6$ is detected, the final reaction solution only contains [Cu$_7$Al$_6$](Cp*)$_6$ according to LIFDI-MS analysis. From the final solutions, [Cu$_{7/8}$Al$_6$](Cp*)$_6$ can be obtained as micro-crystalline precipitate upon slow cooling. The side-product [Cu$_7$Al$_7$](Cp*)$_6$ (detected in LIFDI-MS as a mixture between [Cu$_7$Al$_7$](Cp*)$_6$ and {[Cu$_7$Al$_7$](Cp*)$_6$ - H}) is not contained in the isolated precipitate.*

★   AlMes$_3$ ★   AlCp*   ★   [Cu$_8$Al$_6$](Cp*)$_6$

★   Mes$_2$AlCp*   ★   [Cu$_7$Al$_6$](Cp*)$_6$
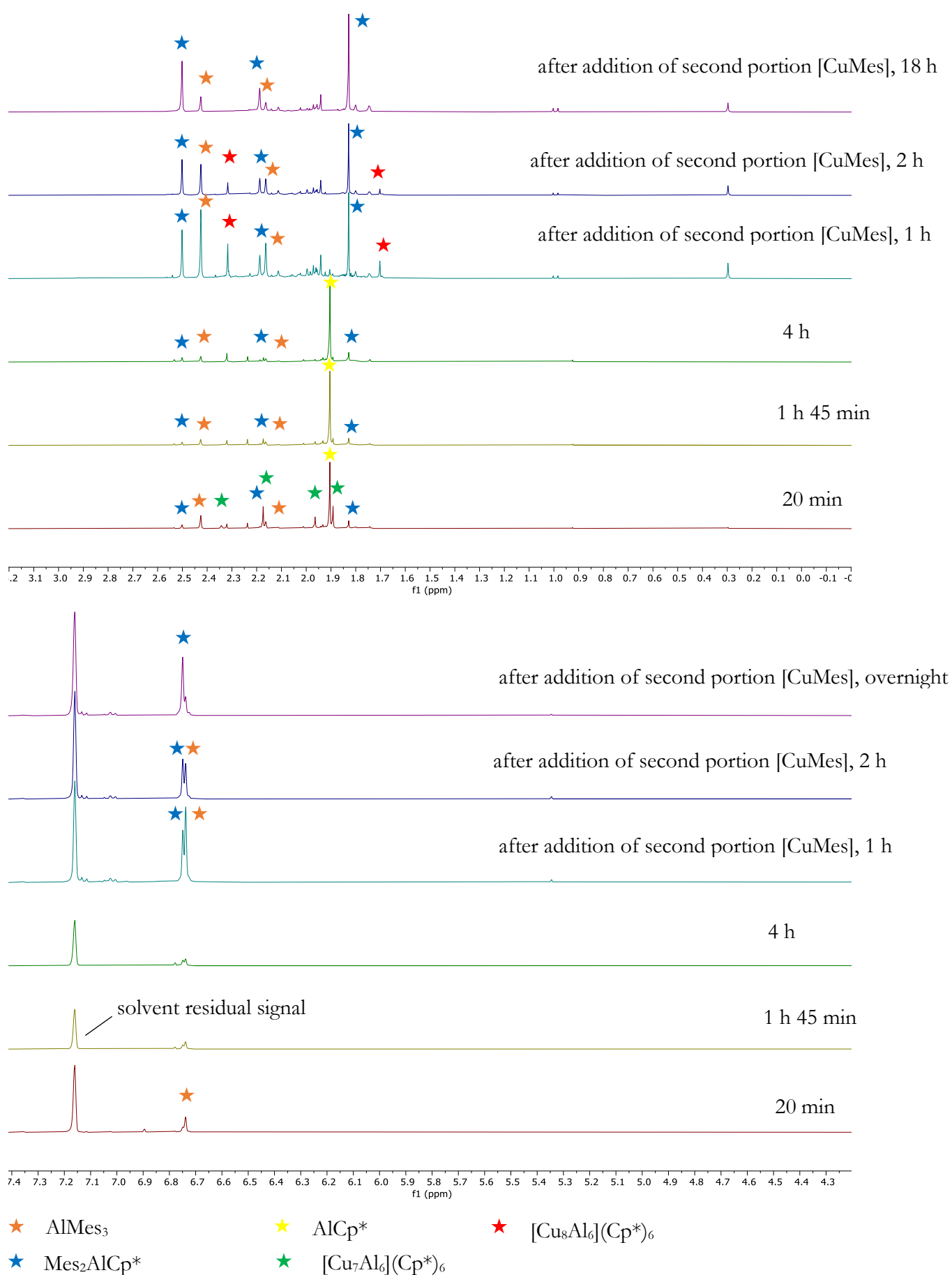
Figure S82: *In-situ* NMR spectra (benzene-d$_6$) of synthesis of [Cu$_{7/8}$Al$_6$](Cp*)$_6$ (**1/2**).

6. Appendix

6.2 Supporting information for the chemical part
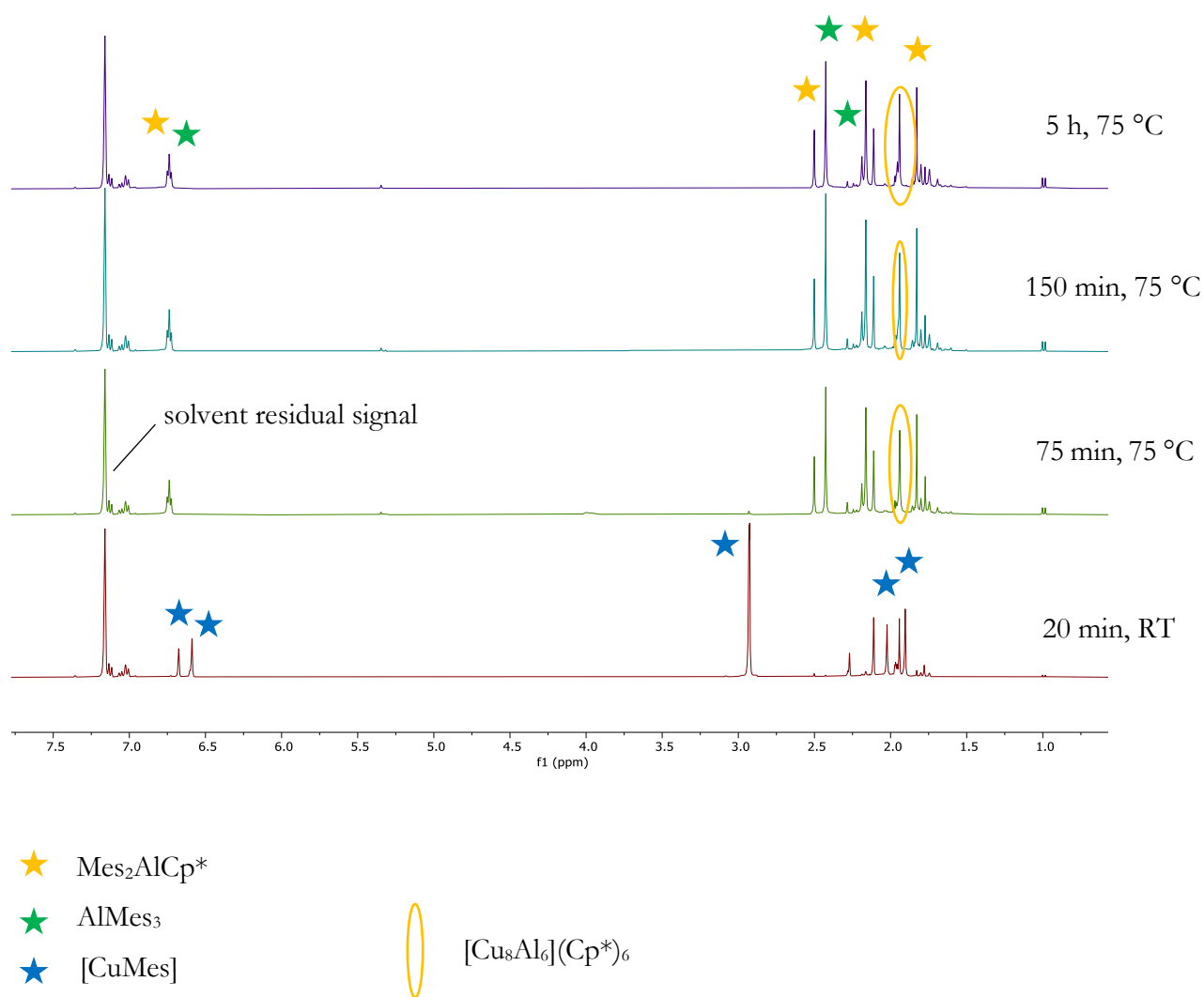
Figure S83: *In-situ* ^{1}H-NMR spectra (benzene-d_6) of the conversion $[Cu_{7/8}Al_6](Cp^*)_6$ (**1/2**) with [CuMes] (1:5).

Note: The small peak at 2.11 ppm, as well as the aromatic signals at 6.9 ppm -7.15 ppm are caused by toluene, which is co-crystallised with $[Cu_{7/8}Al_6](Cp^*)_6$.

In the cluster growth reactions starting from $[Cu_{7/8}Al_6](Cp^*)_6$ with [CuMes], Cp^*AlMes_2 is again identified as Al(III) oxidation product. With respect to the solvent residual signal, the intensity of the peak attributed to $[Cu_8Al_6](Cp^*)_6$ is increased over time, accompanied by a vanishing of the paramagnetic signal attributed to $[Cu_7Al_6](Cp^*)_6$ (not shown). As a conclusion, $[Cu_8Al_6](Cp^*)_6$ is formed as the initial reaction product of the cluster growth starting from $[Cu_7Al_6](Cp^*)_6$. This is in line with an expected higher reactivity of the radical species $[Cu_7Al_6](Cp^*)_6$ (see also methodical part). Cu nanoparticles were identified as an additional reaction product (see Figure S84). Obviously, $[Cu_8Al_6](Cp^*)_6$ is prone to further cluster growth reactions.
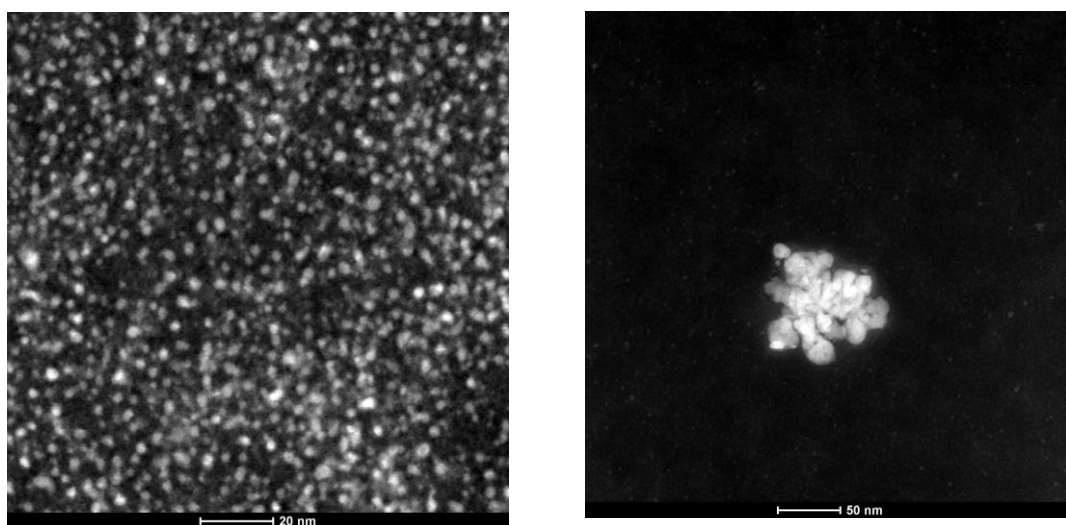
Figure S84: Left: TEM image of evaporated reaction solution of [CuMes] + [Cu$_2$Al](Cp*)$_3$ (conditions E in Table 5); Right: TEM image of evaporated reaction solution of [CuMes] + [Cu$_{7/8}$Al$_6$](Cp*)$_6$ (conditions D in Table 5).

6.2.8. Characterization of [Cu₄Al₄](Cp*)₅(Mes) (**11**)

The following supporting data documentation refers to pages 157-161.
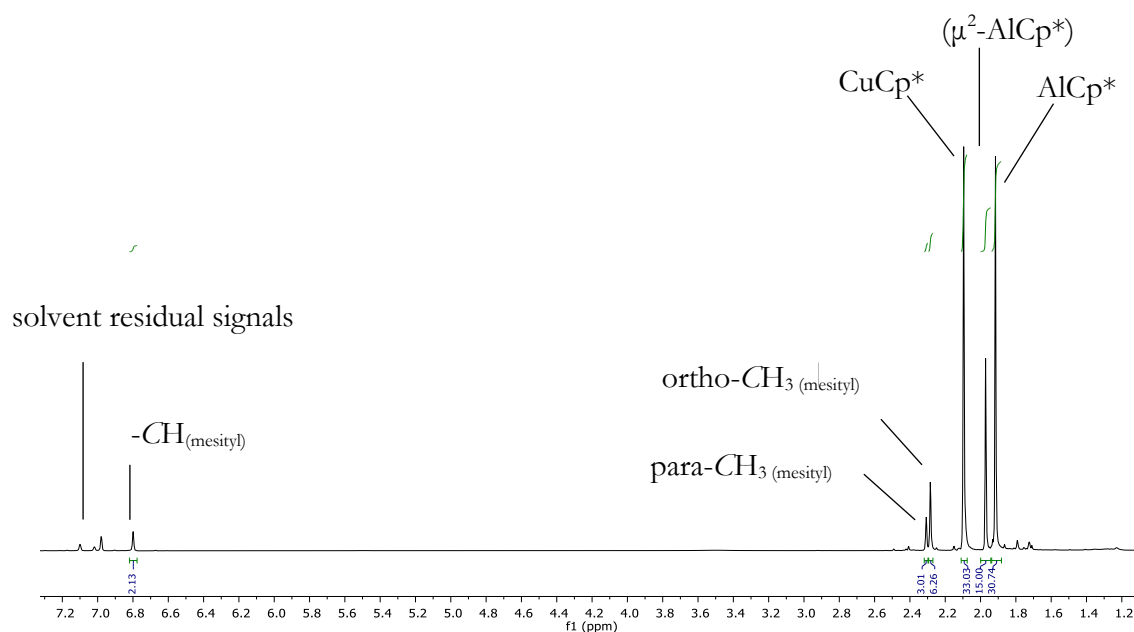
Figure S85: ¹H-NMR spectrum (toluene-d₈) of [Cu₄Al₄](Cp*)₅(Mes) (**11**) at room-temperature.
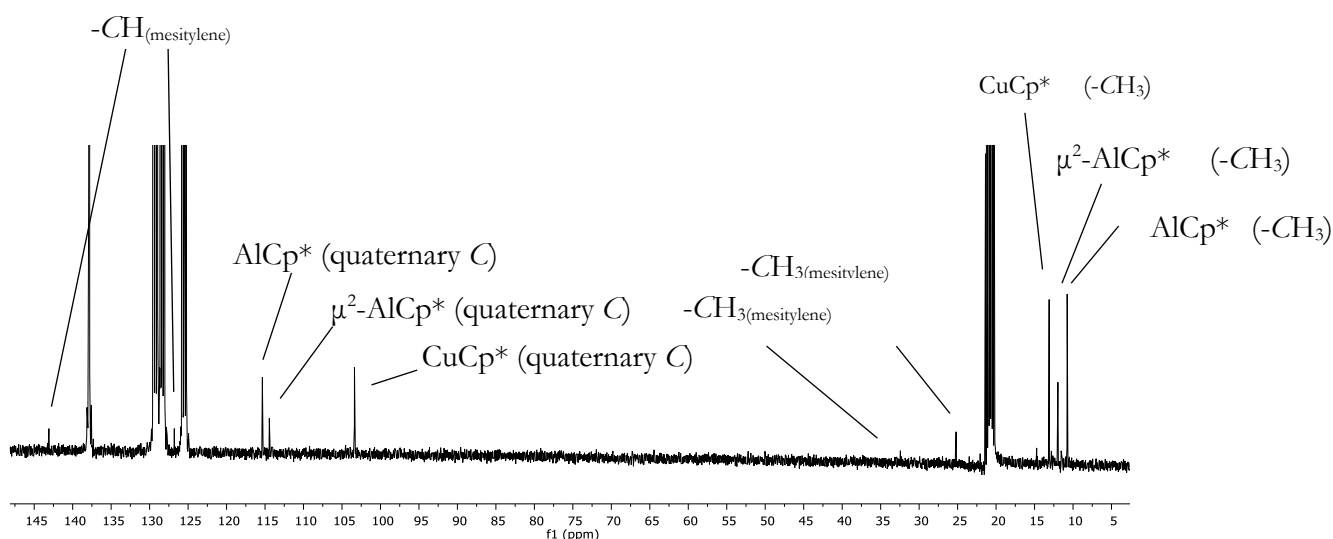
Figure S86: ¹³C-NMR spectrum (toluene-d₈) of [Cu₄Al₄](Cp*)₅(Mes) (**11**) at room-temperature. Signals at 20 ppm, 125 ppm, 127.5 ppm and 137.5 ppm are solvent residual signals.

¹H- and ¹³C-NMR spectra of isolated [Cu₄Al₄](Cp)₅(Mes) (**11**) are fully consistent with the symmetry and composition of the compound in the solid-state as determined by SC-XRD.*
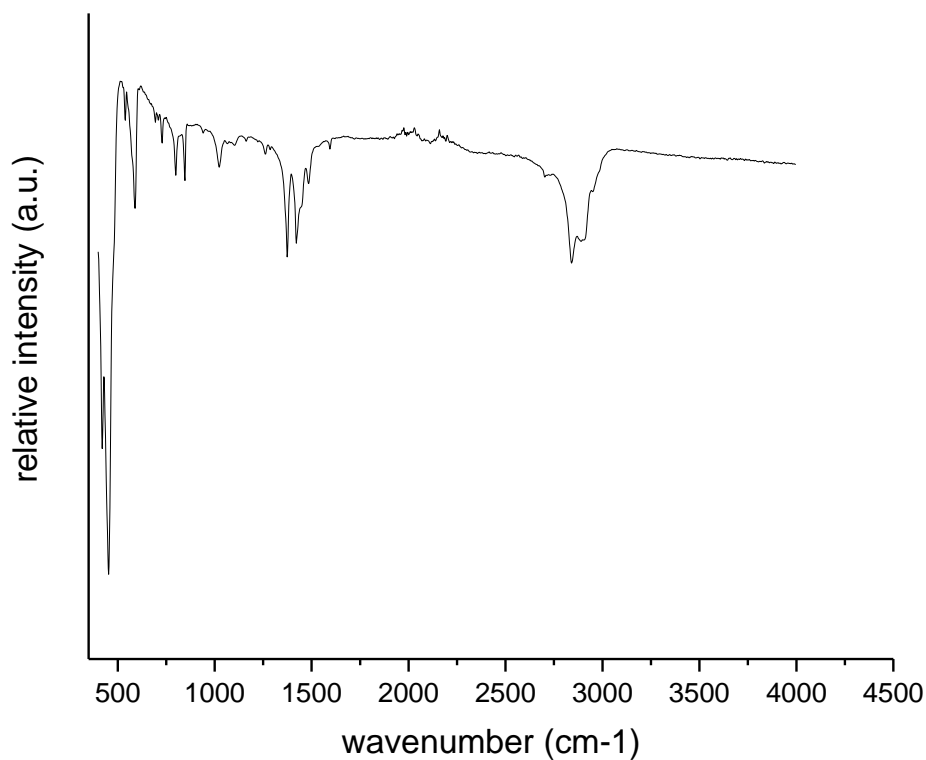
Figure S87: ATR-IR spectrum of [Cu$_4$Al$_4$](Cp*)$_5$(Mes) (**11**).

The IR spectrum shows the bands typical for the Cp* and Mes ligands (characteristic v_{C-H} stretching vibrations in the region 2500 - 3000 cm^{-1} and v_{C-C} vibrations between 500 cm^{-1} and 1700 cm^{-1}). The strong band at 418.17 cm^{-1} is attributed to the v_{Al-C} stretching vibration of the AlCp* units.

6. Appendix

6.2 Supporting information for the chemical part
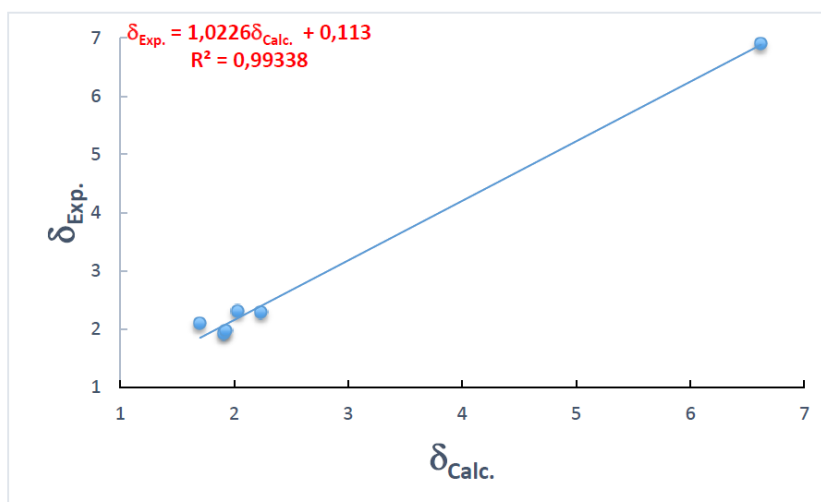
Figure S88: Correlation between experimental (δ_{Exp}) and DFT-computed (δ_{Calc}) ^{1}H NMR chemical shifts for [Cu$_4$Al$_4$](Cp*)$_5$(Mes) (**11**).
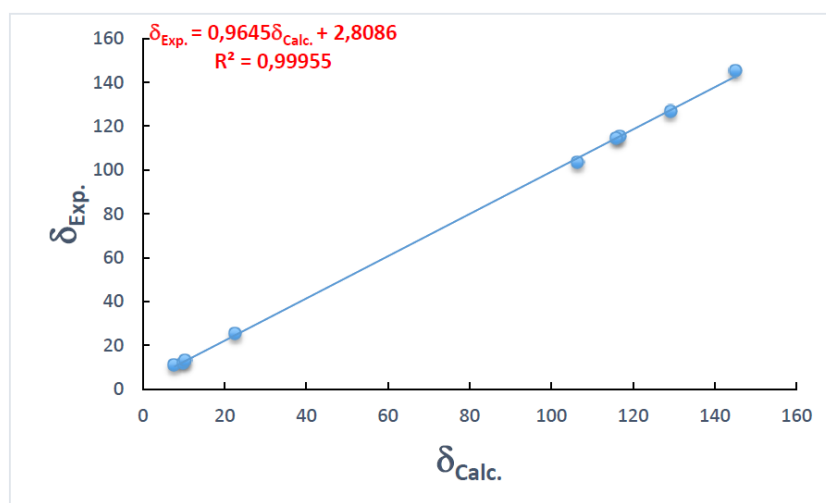
Figure S89: Correlation between experimental (δ_{Exp}) and DFT-computed (δ_{Calc}) ^{13}C NMR chemical shifts for [Cu$_4$Al$_4$](Cp*)$_5$(Mes) (**11**).

6.2 Supporting information for the chemical part

Table S8: Relevant computed data for $[Cu_4Al_4](Cp^*)_5(Mes)$ (**11**). Distances are in Å. WBI = Wiberg bond index).

HOMO-LUMO Gap (eV)			1.28		
NBO charges within the Cu₄Al bipyramid	**Cu1**	**Cu3**	**Cu2**	**Cu4**	**Al1**
	0.15	0.15	0.40	0.41	0.50
NBO charges of μ₂- and terminal Al	**Al3**	**Al2**	**Al4**		
	0.69	0.83	0.86		
Within the Cu₄Al bipyramid	**Dist. [WBI]**		**(μ₂-Al)-Cu**	**Dist. [WBI]**	
Al1-Cu1	2.445 [0.250]		Al3-Cu1	2.398 [0.297]	
Al1-Cu3	2.476 [0.251]		Al3-Cu3	2.435 0.266	
Al1-Cu2	2.363 [0.510]		**Terminal Al-Cu**	**Dist. [WBI]**	
Al1-Cu4	2.390 [0.479]		Al4-Cu1	2.294 [0.442]	
Cu2-Cu1	2.522 [0.071]		Al2-Cu3	2.302 [0.431]	
Cu2-Cu3	2.562 [0.042]				
Cu4-Cu1	2.543 [0.061]				
Cu4-Cu3	2.484 [0.104]				
Cu1-Cu3	2.441 [0.045]				

6.2.9 Characterization of $[Cu_2Al](Cp^*)_3$ (**9**)

The following supporting data documentation refers to pages 162-168.
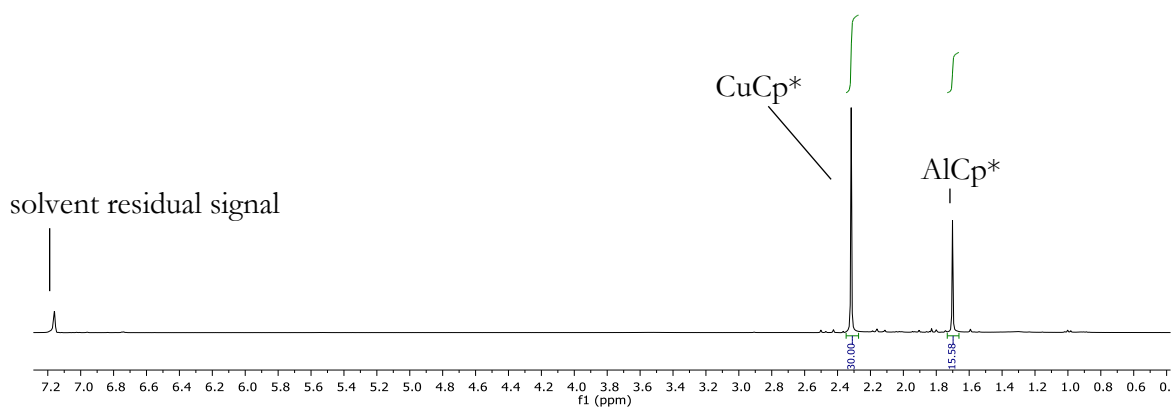
Figure S90: ^{1}H-NMR spectrum (benzene-d_6) of $[Cu_2Al](Cp^*)_3$ (**9**).
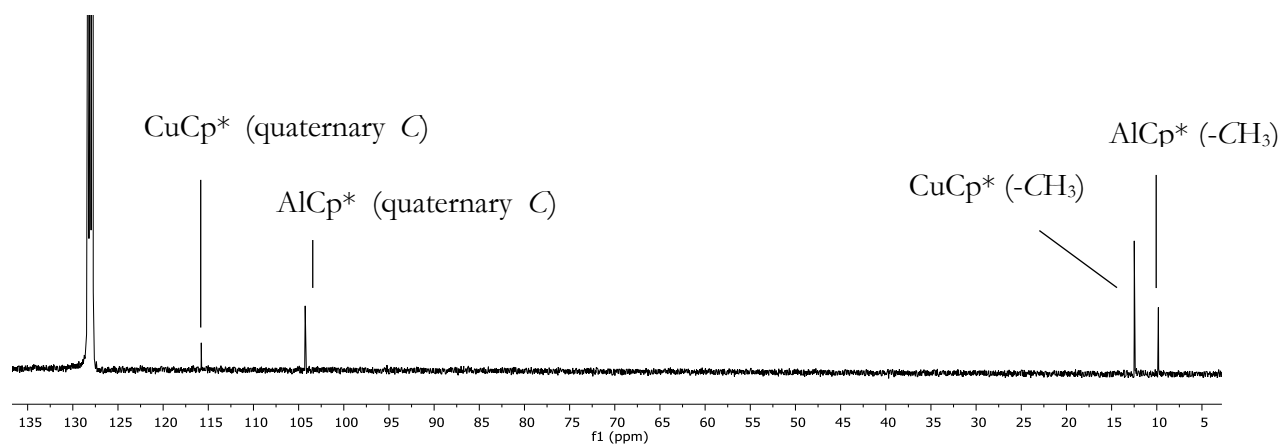
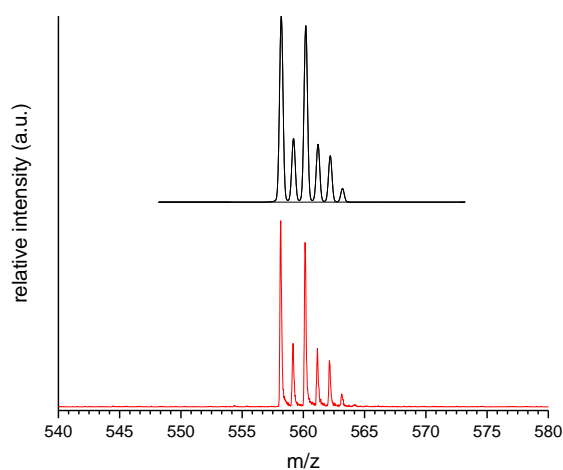**Figure S91:** ^{13}C-NMR spectrum (benzene-d$_6$) of [Cu$_2$Al](Cp*)$_3$ (**9**). The signal at 128 ppm is solvent residual signal.

^{1}H- and ^{13}C-NMR spectra of isolated [Cu$_2$Al](Cp)$_3$ (**9**) are fully consistent with the symmetry and composition of the compound in the solid-state as determined by SC-XRD.*
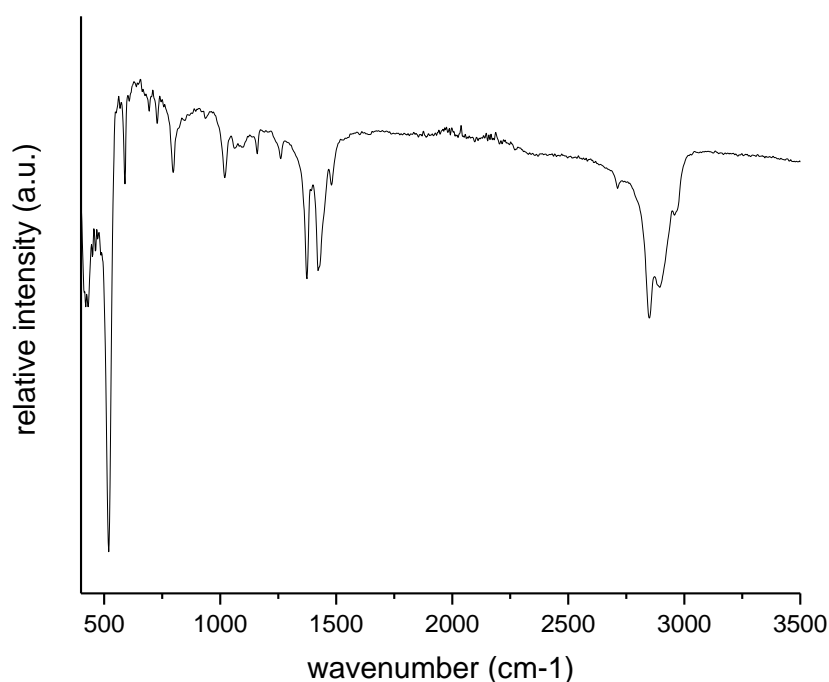

Figure S92: Comparison of the experimental (as determined by LIFDI-MS; bottom, red) and calculated (top, black) isotopic pattern of [Cu$_2$Al]Cp*$_3$ (**9**).

LIFDI-MS analysis of isolated [Cu$_2$Al]Cp$_3$ (**9**) unambiguously confirms its composition.*

6. Appendix

6.2 Supporting information for the chemical part

Figure S93: ATR-IR spectrum of [Cu₂Al](Cp*)₃ (**9**).

Vibrations of the Cp* ligand are assigned as for [Cu₄Al₄](Cp*)₅(Mes) (vide supra, characteristic v_{C-H} stretching vibrations in the region 2500 - 3000 cm^{-1} and v_{C-C} vibrations between 500 cm^{-1} and 1700 cm^{-1}). The band at 418.2 cm^{-1} is attributed to the v_{Al-C} stretching vibration of the AlCp* unit. The strong band at 519 cm^{-1} is tentatively assigned to metal-metal vibrations inside the cluster triangle.
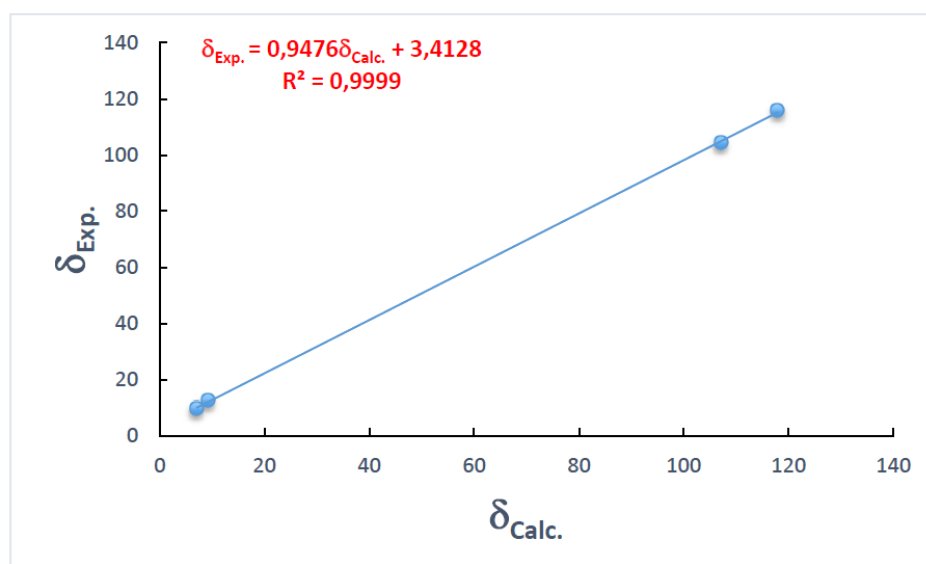
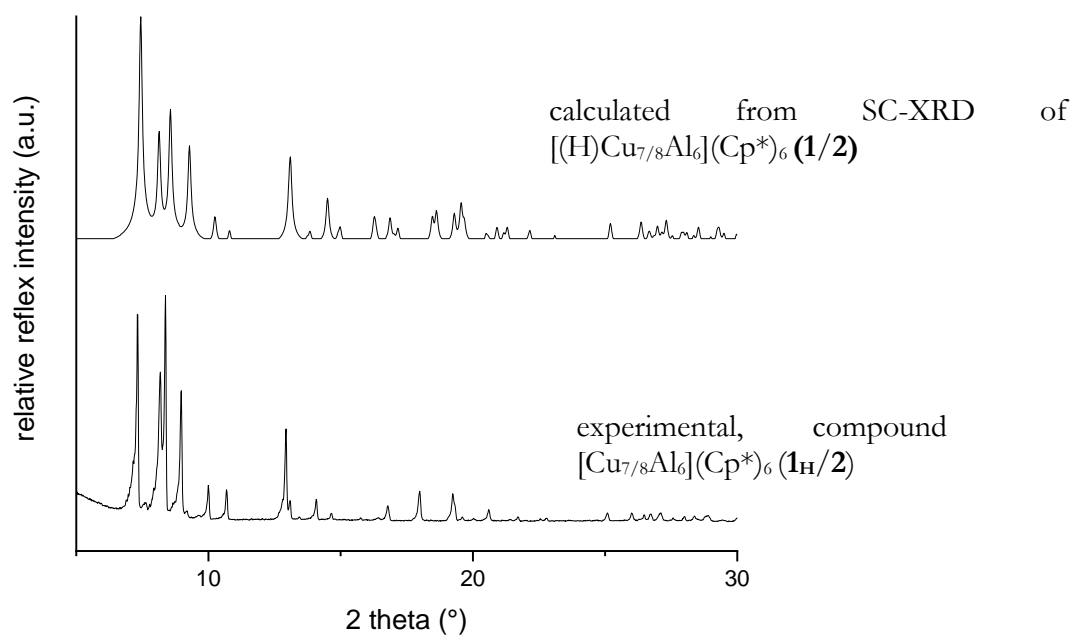**Figure S94:** Correlation between experimental (δ_{Exp}) and DFT-computed (δ_{Calc}) ¹³C NMR chemical shifts for [Cu₂Al](Cp*)₃ (**9**).

6.2.10 Characterization of $[Cu_7Al_6](Cp^*)_6$ (**1**), $[HCu_7Al_6](Cp^*)_6$ (**1_H**) and $[Cu_8Al_6](Cp^*)_6$ (**2**)

The following supporting data documentation refers to pages 168-176.

calculated from SC-XRD of $[(H)Cu_{7/8}Al_6](Cp^*)_6$ (**1/2**)
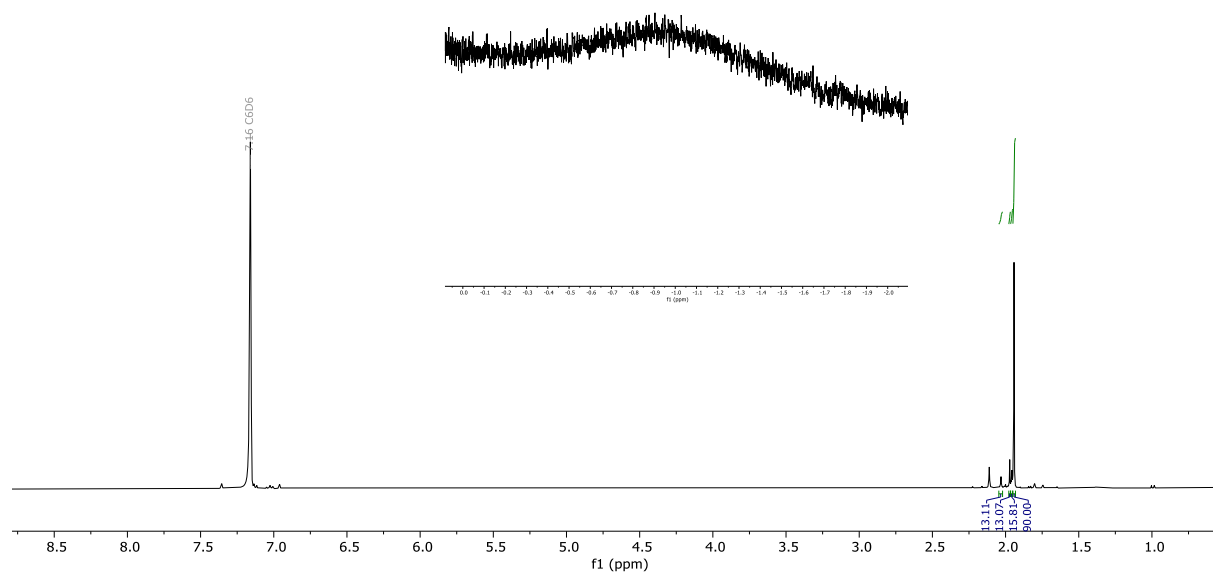
experimental, compound $[Cu_{7/8}Al_6](Cp^*)_6$ (**1_H/2**)

Figure S95: Powder-X-ray diffraction pattern of $[Cu_{7/8}Al_6](Cp^*)_6$ (**1/2**) (bottom) and calculated pattern based on SC-Xray diffraction data of $[(H)Cu_{7/8}Al_6](Cp^*)_6$ (**1_H/2**) (top).

Powder X-ray diffraction data of the micro-library $[Cu_8Al_6](Cp^*)_6$ / $[Cu_7Al_6](Cp^*)_6$ confirms that the compound is isostructural to $[Cu_8Al_6](Cp^*)_6$ / $[HCu_7Al_6](Cp^*)_6$, for which SC-XRD data is available.

Figure S96: ^{1}H-NMR spectrum (benzene-d_6) of [Cu$_{7/8}$Al$_6$](Cp*)$_6$ (**1/2**). The inset shows the signal attributed to paramagnetic [Cu$_7$Al$_6$](Cp*)$_6$ (**1**) at -0.95 ppm.

Note: Several small signals are observed at 2.03 ppm, 1.97 ppm and 1.95 ppm, probably assignable to minor quantities of smaller Cu/Al clusters also detected in LIFDI-MS spectra of the isolated product (see Figure 33). No significant spectral changes were observed in ^{1}H-NMR spectra recorded at variable temperature, however, with significant precipitation of the sample at low temperatures.
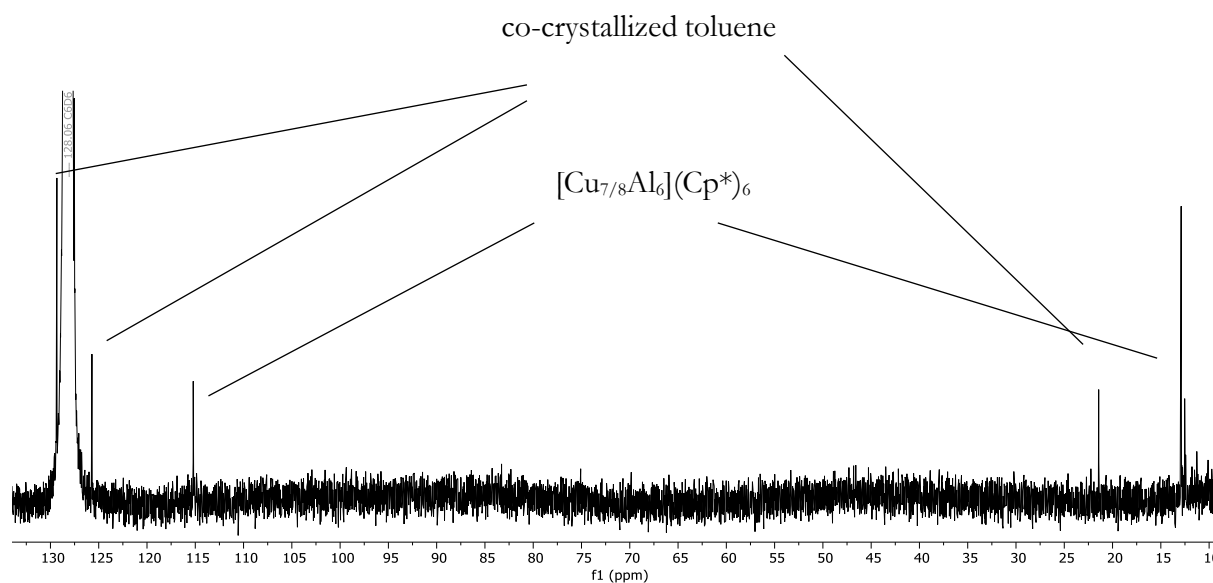

Figure S97: ^{13}C-NMR spectrum (benzene-d_6) of [Cu$_{7/8}$Al$_6$](Cp*)$_6$ (**1/2**). Signal at 128 ppm is solvent residual signal.

6. Appendix
6.2 Supporting information for the chemical part

^{1}H- and ^{13}C-NMR data of isolated [Cu$_{7/8}$Al$_6$](Cp*)$_6$ show mainly one singlet signal attributed to [Cu$_8$Al$_6$](Cp*)$_6$. In ^{1}H-NMR analysis, a broad paramagnetic signal is discernible at -0.95 ppm, which is attributed to the radical cluster [Cu$_7$Al$_6$](Cp*)$_6$.
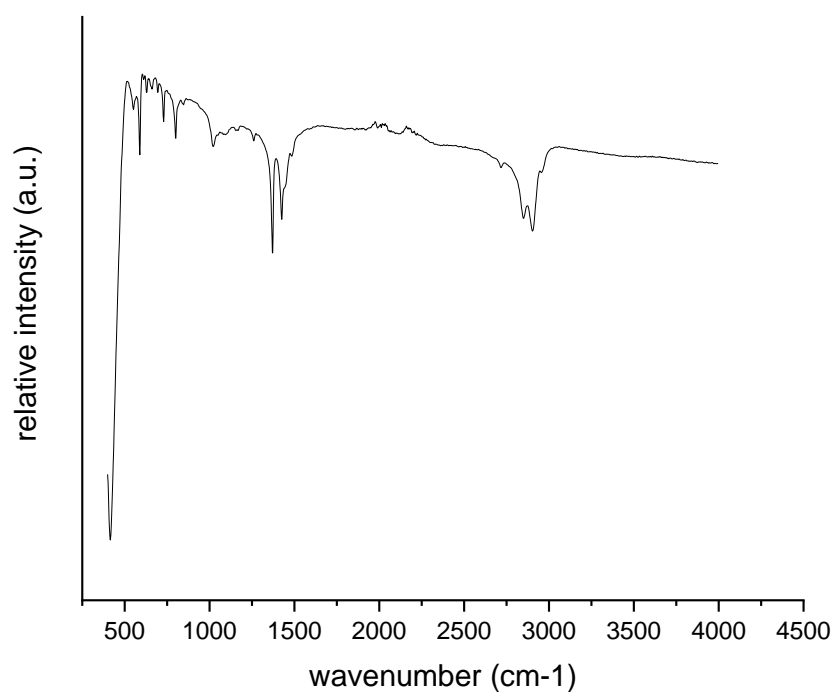
Figure S98: ATR-IR spectrum of [Cu$_{7/8}$Al$_6$](Cp*)$_6$ (**1/2**).

For IR interpretation it is referred to the spectra of the closely related compounds [Cu$_4$Al$_4$](Cp*)$_5$(Mes) and [Cu$_2$Al](Cp*)$_3$.

6. Appendix

6.2 Supporting information for the chemical part

Table S9: Relevant computed data for $[Cu_8Al_6](Cp^*)_6$ (**2**), $[Cu_7Al_6](Cp^*)_6$ (**1**) and $[HCu_7Al_6](Cp^*)_6$ (**1$_H$**). Distances are in Å. WBI = Wiberg bond index (in brackets). Values in parenthesis are the numbers of averaged quasi-equivalent atoms, owing to the fact that **2** is pseudo-T_h, whereas **1, 1$_H$(a)** and **1$_H$(b)** are close to 3-fold symmetry.

| Compound		**2**	**1**	**1$_H$(a)**	**1$_H$(b)**
HOMO-LUMO Gap (eV)		1.17	-	1.16	1.81
NBO charges (av.)	Cu(inner)	0.16 (4)	0.16 (3) 0.34 (1)	0.25 (3) 0.33 (1)	0.28 (3) 0.25 (1)
	Cu(cap)	0.24 (4)	0.21 (3)	0.26 (3)	0.23 (3)
	Al	0.28 (6)	0.21 (3) 0.45 (3)	0.16 (3) 0.49 (3)	0.48 (3) 0.26 (3)
	μ_3-H			-0.35	-0.58
Distances [WBI]	(μ_3-H)-Cu (av. and range)			1.795 [0.128] 1.788-1.800	1.810 [0.045] 1.807-1.813
	Cu(inner)-Cu(inner) (av. and range)	2.745 [0.030]	2.941 [0.026] 2.568-3.318	3.085 [0.022] 2.599-3.616	3.047 [0.014] 2.586-3.457
	Cu(cap)-Cu(inner) (av. and range)	2.505 [0.023]	2.580 [0.023] 2.502-2.684	2.535 [0.030] 2.438-2.598	2.573 [0.021] 2.489-2.753
	Al-Cu(cap) (av. and range)	2.530 [0.289]	2.494 [0.300] 2.413-2.625	2.524 [0.279] 2.396-2.762	2.505 [0.301] 2.405-2.737

6.2.11 Reactivity of intermetalloid Cu/Al clusters

6.2.11.1 C-H and Si-H activation reactions

The following supporting data documentation refers to pages 176-179.
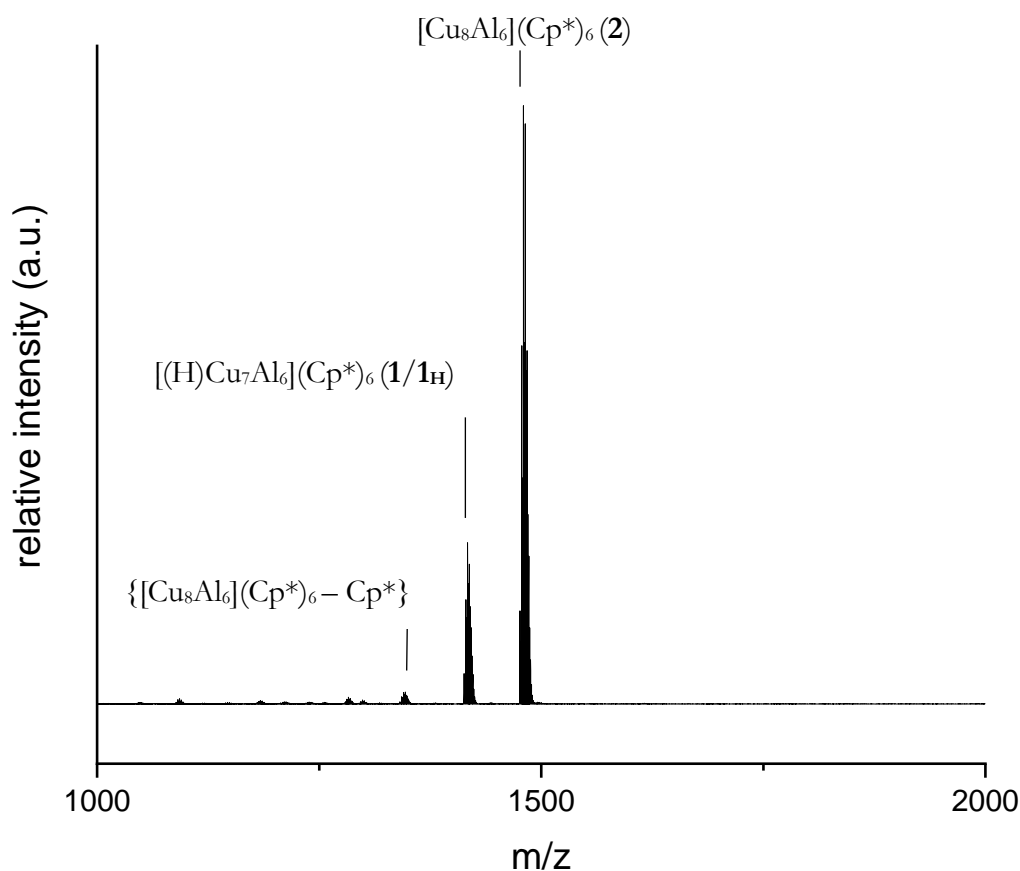
Figure S99: Full range *in-situ* LIFDI-MS spectrum of a solution of $[Cu_{7/8}Al_6](Cp^*)_6$ (**1/2**) heated in toluene-h_8 to 110 °C for 5 days.

*After heating $[Cu_{7/8}Al_6](Cp^*)_6$ (**1/ 2**) in toluene to 110 °C for several days, LIFDI-MS analysis indicates partial formation of the hydride species $[HCu_7Al_6](Cp^*)_6$ (**1$_H$**), whereas the peak attributed $[Cu_8Al_6](Cp^*)_6$ remains unchanged. The reaction was not observed in toluene pointing towards toluene playing a crucial role in the mechanism (initial formation of toluyl radicals). Pentamethylfulvene was detected by GC-MS as a side-product. It is suggested that initially formed toluyl radicals activate cluster bound Cp* ligands resulting in formation of pentamethylfulvene and 1e- reduced, Cp* deprotected cluster species, such as $\{[Cu_8Al_6](Cp^*)_6 - Cp^*\}$.*
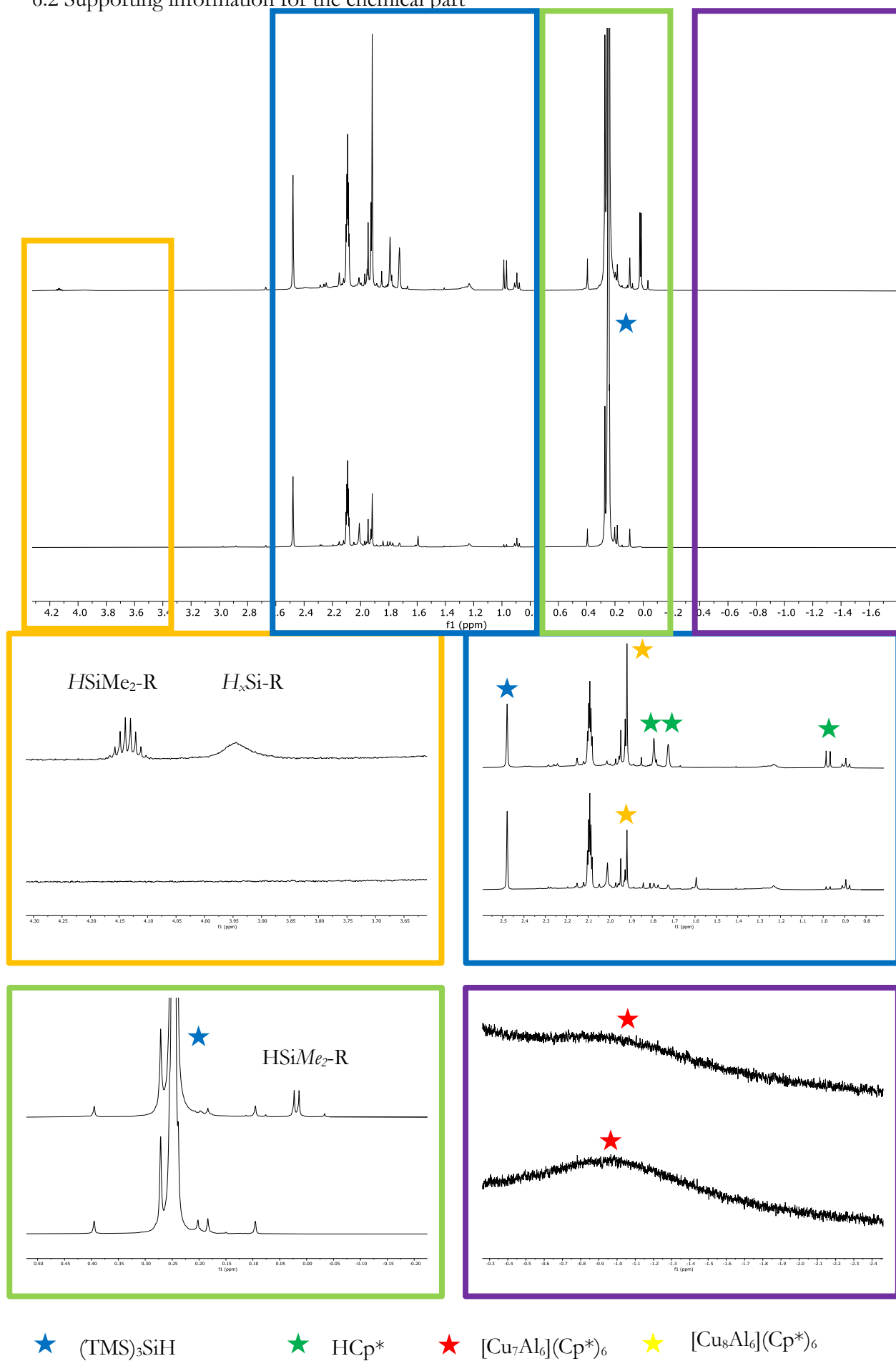
6. Appendix

6.2 Supporting information for the chemical part

Table S10: Reaction conditions applied in C-H and Si-H activation reactions with isolated $[Cu_{7/8}Al_6](Cp^*)_6$ (**1/2**) and reaction products observed by LIFDI-MS (cluster species) and GC-MS (organic species).

silane species added	solvent	product cluster observed in LIFDI-MS	species identified by GC-MS
(TMS)₃SiH	toluene-h₈	1/1ₕ/2; {[Cu₇Al₆](Cp*)₆(Si(TMS)₃) − H}, {[Cu₈Al₆](Cp*)₆(Si(TMS)₃) − H}	**HSiMe₃:** m/z = 73.1 [-H]⁺, 59.1 [-Me]⁺ **HMe₂Si-SiMe₃:**[299] m/z = 133 [+H]⁺, 117 [-Me]⁺, 103 [-2xMe]⁺, 87 [-3xMe]⁺, 73 [-HMe₂Si]⁺, 59 [-HMe₂Si, -Me]⁺ **Me₃Si-SiMe₃:**[300] m/z = 147.1 [+H]⁺, 131 [-Me]⁺, 117 [-2xMe]⁺, 103 [-3xMe]⁺, 87 [-4xMe +H]⁺, 73 [-SiMe3]⁺, 59 [-Me, -SiMe₃]⁺ **Me₃Si-SiH₂-SiMe₃:**[301] 176.1 [M]⁺, 161.0 [-Me]⁺, 145.0 [-2xMe, -H]⁺, 131 131 [-3xMe]⁺, 117 [-4xMe +H]⁺,101 [-SiMe₃, -2H]⁺, 88 [SiMe₄]⁺, 73 [SiMe₃]⁺, 59 [SiMe₂]⁺ **(C₇H₇)Si((TMS)₃:**[302] m/z = 341.1 [+3H]⁺, 325 [-Me + 2H]⁺, 267 [-SiMe₃ + H], 253 [-SiMe3, -Me, +3H]⁺, 236 [-SiMe₃, -2xMe, +H]⁺, 193 [-2xSiMe₃, +H]⁺, 154, 133 [HMe₂Si-SiMe₃ +H]⁺, 87, 73 [SiMe₃]⁺, 59 [HSiMe₂]⁺;
(TMS)₃SiH	toluene-d₈	1/1ₕ/2; {[Cu₇Al₆](Cp*)₆(Si(TMS)₃) − H}, {[Cu₈Al₆](Cp*)₆(Si(TMS)₃) − H}	**HSiMe₃:** m/z = 73.1 [-H]⁺, 59.1 [-Me]⁺ **(HSiMe₂)₂(SiMe₃)SiH:** m/z = 220.2 [M]⁺, 205.2 [-Me]⁺, 177, 161, 145.1, 129.1, 105.1, 91.0, 73.0, 57.1
(TMS)₃SiD	toluene-h₈	1/1ₕ/1_D/2	
(TMS)₄Si	toluene-d₈	1/1ₕ/2; {[Cu₈Al₆](Cp*)₆(SiMe₃) − H}	**Pentamethylfulvene:**[*] m/z = 134.1 [M]⁺, 119.1 [-Me]⁺, 103 [- 2x Me -H]⁺, 103, 91, 77, 51; **(TMS)₃SiH:**[*] 248.1, 207, 190.9, 174.1 [-SiMe₃H]⁺, 159.0, 145.0, 129.0, 91.0, 73.1, 59.0;
none	toluene-h₈	1/1ₕ/2	**Pentamethylfulvene:**[*] m/z = 134.1 [M]⁺, 119.1 [-Me]⁺, 103 [- 2x Me -H]⁺, 103, 91, 77, 51
none	toluene-d₈	1/2	
none	methyl-cyclohexane	1/2	

[*]: identified by software database

311

★ (TMS)₃SiH   ★ HCp*   ★ [Cu₇Al₆](Cp*)₆   ★ [Cu₈Al₆](Cp*)₆

Figure S100: *In-situ* ¹H-NMR spectra (toluene-d₈) of the conversion of [Cu₇/₈Al₆](Cp*)₆ (**1/2**) with (TMS)₃SiH.

6. Appendix

6.2 Supporting information for the chemical part

Note: The silane reaction products could not unambiguously identified by in-situ ^1H NMR spectroscopy. However, suggestions for functional groups of the species can be made and are inserted as text boxes in the spectra.[303] It is noted that these suggestions are consistent with the GC-MS results. ^{29}Si spectra of the solution were recorded but due to low concentrations of the silane reaction products, no meaningful signals apart from unconsumed (TMS)₃SiH were observed.
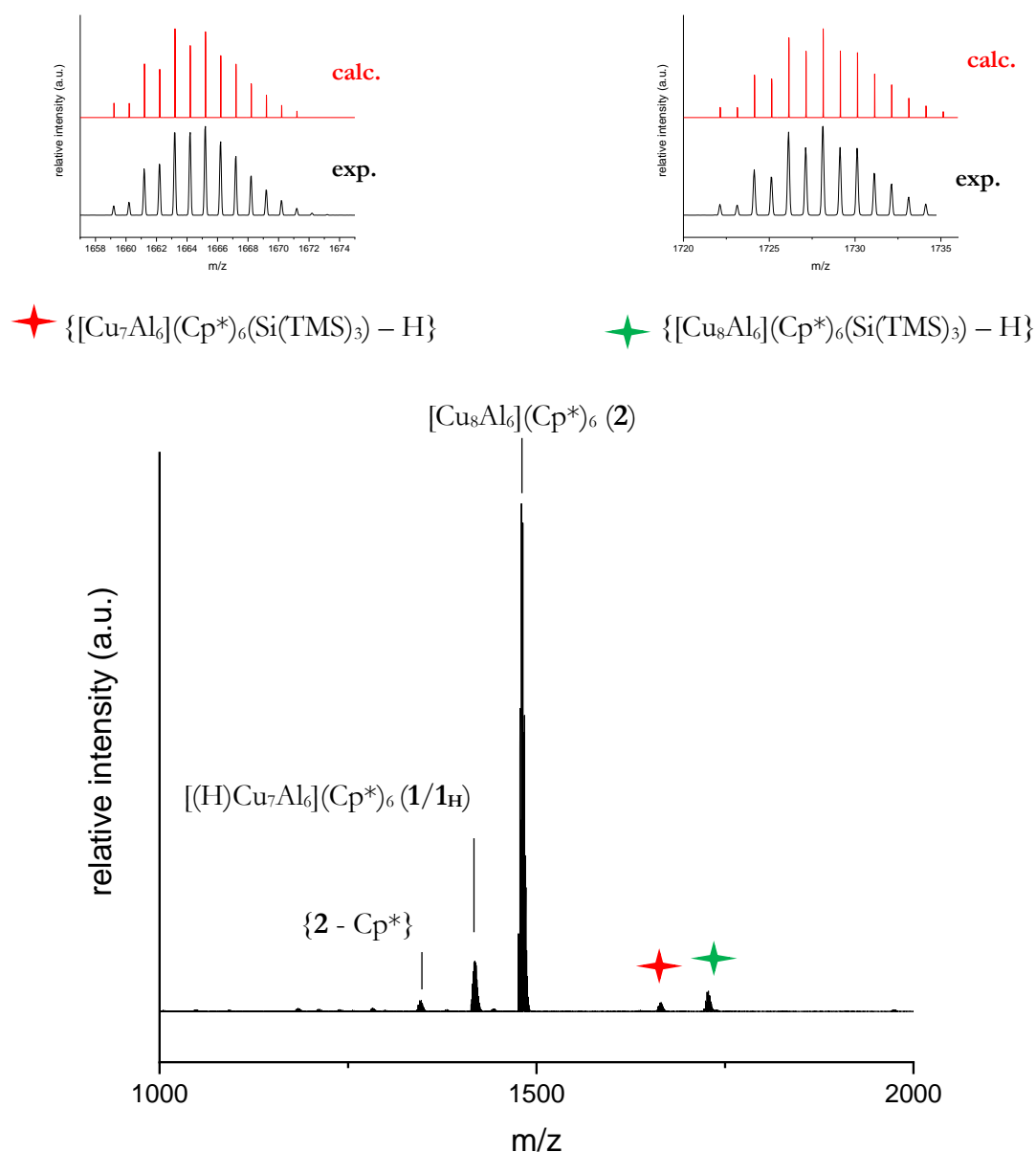
Figure S101: *In-situ* LIFDI-MS spectrum of the conversion of $[Cu_{7/8}Al_6](Cp^*)_6$ (**1/2**) with (TMS)₃SiH (toluene-h₈, 110 °C, 5 days).

The reaction of [Cu₇/₈Al₆](Cp)₆ (**1/2**) with (TMS)₃SiH in toluene-h₈ <u>and</u> toluene-d₈ yields a mixture of [HCu₇Al₆](Cp*)₆ and [Cu₇Al₆](Cp*)₆. Noteworthy, no activation of toluene-d₈ by [Cu₇Al₆](Cp*)₆ is observed proving an activation of (TMS)₃SiH by the radical [Cu₇Al₆](Cp*)₆.*

6. Appendix

6.2 Supporting information for the chemical part

According to the silane reaction products identified in in situ ^{1}H-NMR and GC-MS, the reaction is of radical nature, just as expected. This is also in line with observation of the species $\{[Cu_8Al_6](Cp^*)_6(Si(TMS)_3) - H\}$ and $\{[Cu_7Al_6](Cp^*)_6(Si(TMS)_3) - H\}$ in in situ LIFDI-MS analysis.
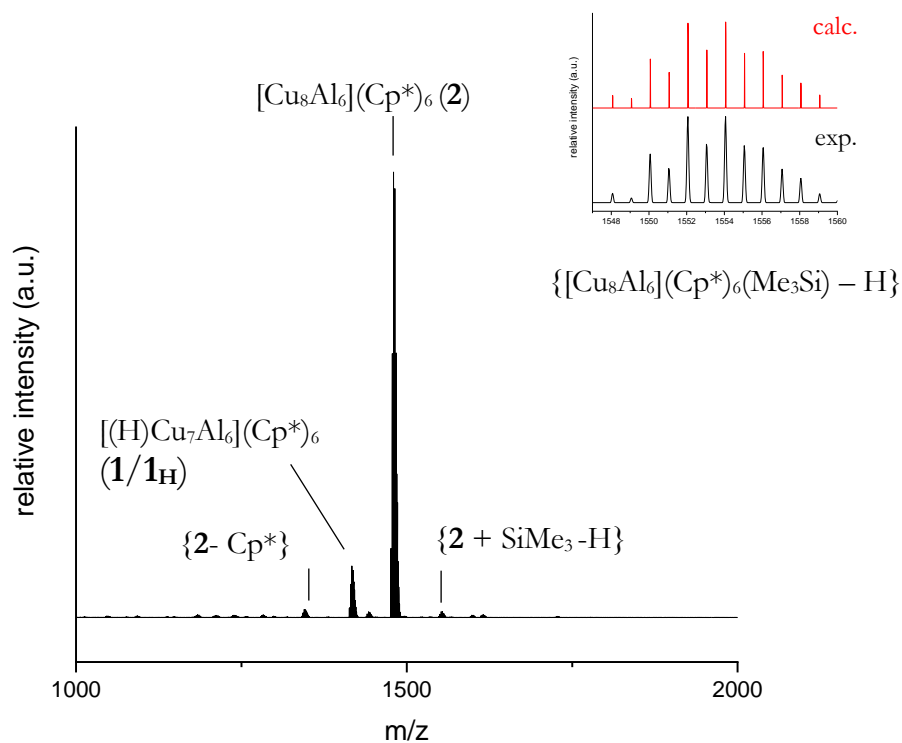
Figure S102: *In-situ* LIFDI-MS spectrum of the conversion $[Cu_{7/8}Al_6](Cp^*)_6$ (**1/2**) with $(TMS)_4Si$ (toluene-d$_8$, 110 °C, 5 days).

6. Appendix

6.2 Supporting information for the chemical part
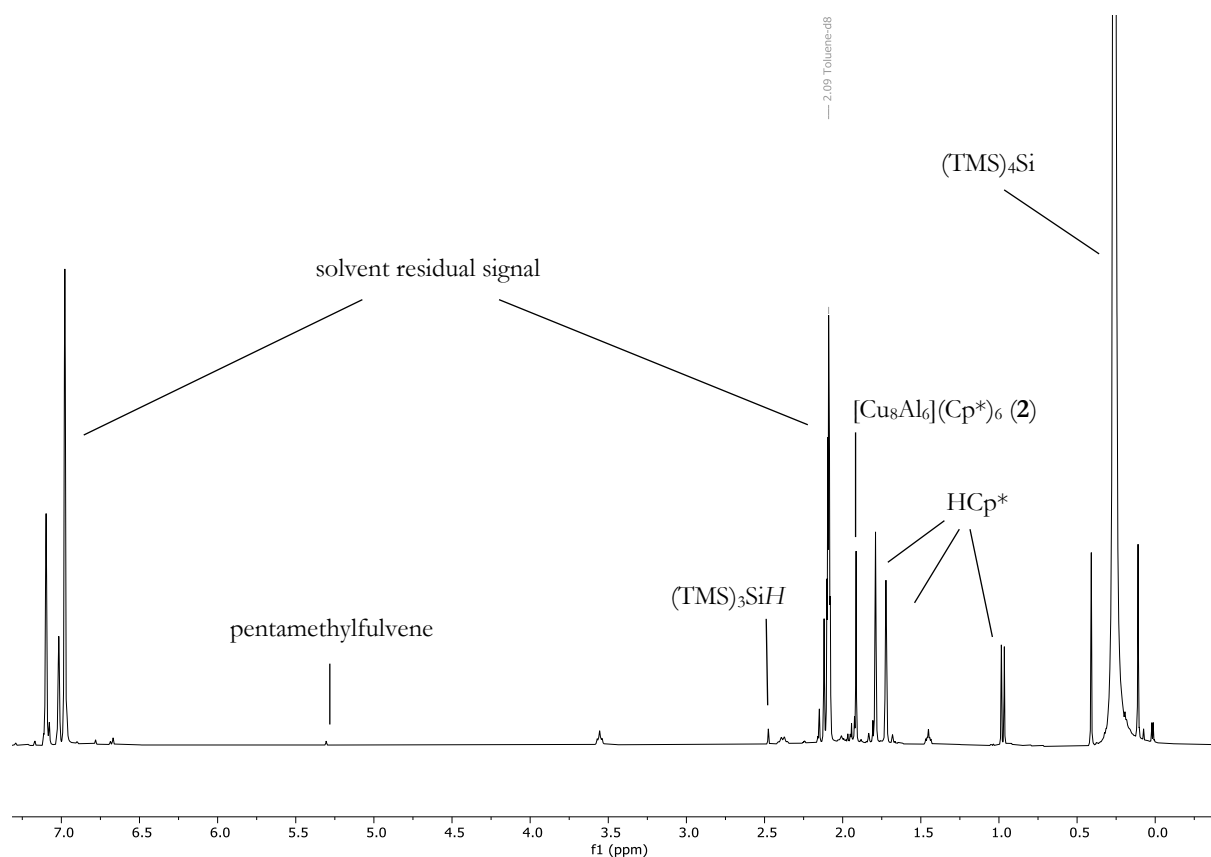
Figure S103: *In-situ* ^{1}H-NMR spectra (toluene-d$_8$, 110 °C, 5 days) of the conversion of [Cu$_{7/8}$Al$_6$](Cp*)$_6$ (**1/2**) with (TMS)$_4$Si. Signals at > 6.9 ppm and at 2.09 ppm are solvent residual signals.

The reaction of [Cu$_{7/8}$Al$_6$](Cp)$_6$ with (TMS)$_4$Si in toluene-d$_8$ yields a mixture of [HCu$_7$Al$_6$](Cp*)$_6$ and [Cu$_7$Al$_6$](Cp*)$_6$ as indicated by LIFDI-MS analysis of the reaction mixture. The further reaction products pentamethylfulvene, (TMS)$_3$SiH and {[Cu$_8$Al$_6$](Cp*)$_6$(Me$_3$Si) − H} (identified by GC-MS, NMR and LIFDI-MS) are fully consistent with a radically mediated C-H bond activation of (TMS)$_4$Si.*

6.2.12 Formation of Cu/Al libraries out of [Cu$_2$Al](Cp*)$_3$ and [H$_6$Cu$_6$](PPh$_3$)$_6$

The following supporting data documentation refers to pages 179-185.
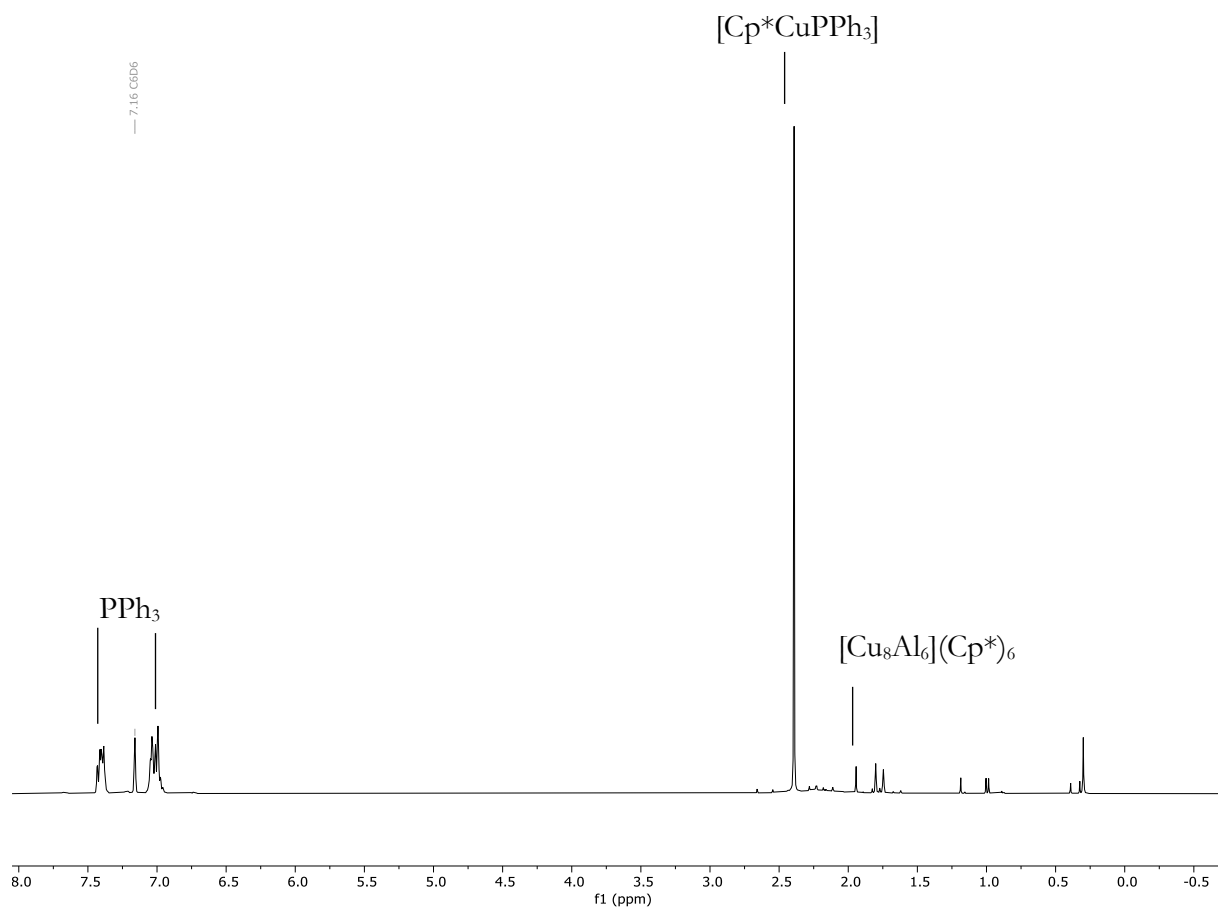
Figure S104: *In-situ* ^{1}H-NMR spectrum (benzene-d$_6$) of the reaction between [Cu$_2$Al](Cp*)$_3$ and [H$_6$Cu$_6$](PPh$_3$)$_6$ (3:1, 75 °C, 3 h). The peak at 7.15 ppm is solvent residual signal.

6. Appendix

6.2 Supporting information for the chemical part
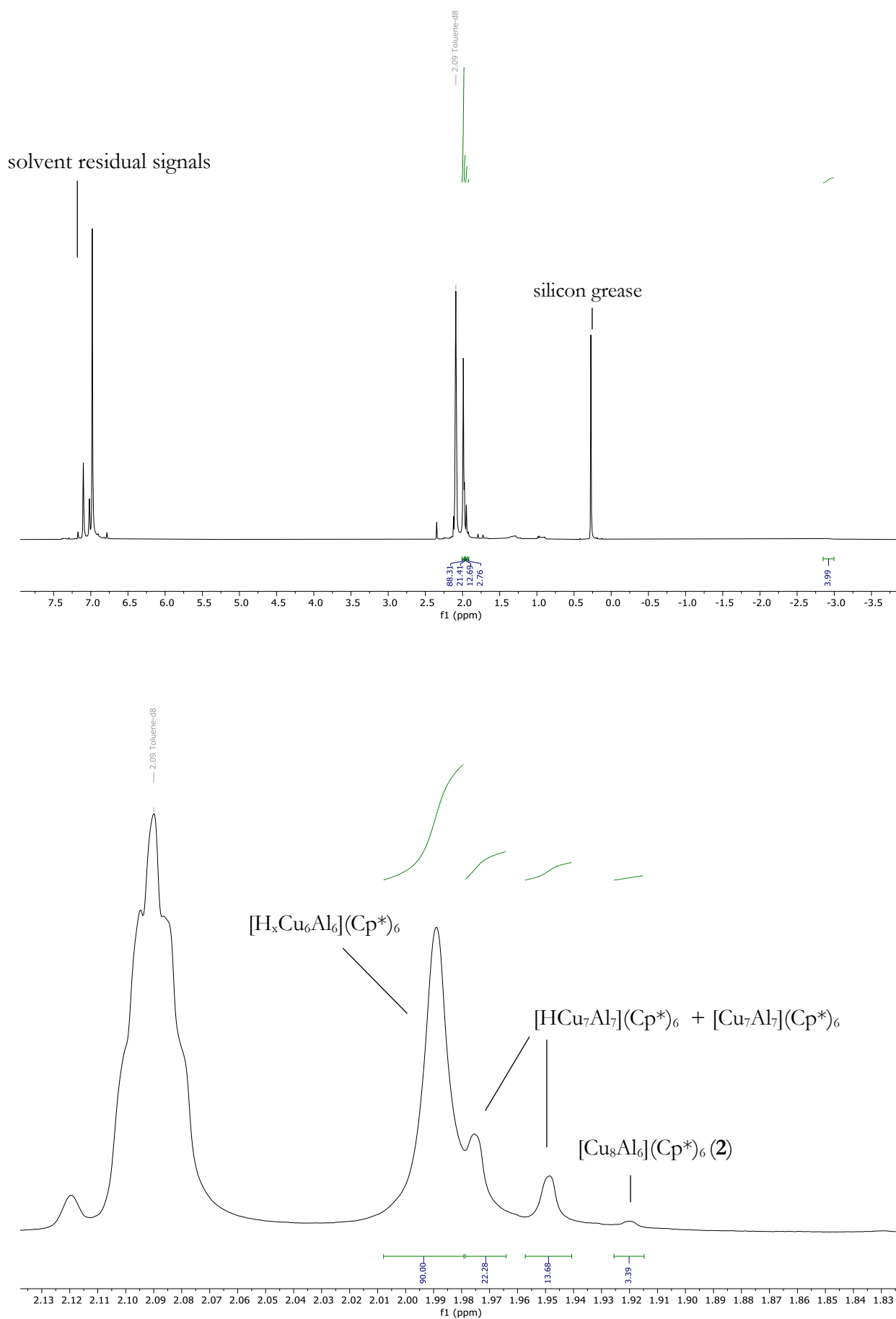
Figure S105: Full range (top) and zoom-in (bottom) of ^{1}H-NMR spectra of the isolated single crystals of the reaction $[Cu_2Al](Cp^*)_3 + [H_6Cu_6](PPh_3)_6 + PPh_3$ (6:1:12).

The reaction of [Cu₂Al](Cp*)₃ with [H₆Cu₆](PPh₃)₆ in a 3:1 molar ratio leads to formation of [Cp*CuPPh₃] and a large library of Cu/Al clusters (see Figure 51, outlook of the methodical part). Use of a stoichiometric ratio of 6:1 leads upon addition of 12 equivalents of external PPh₃ to a size-focusing effect. From these reaction solutions, crystals can be obtained, the NMR of which is shown in Figure S105. The corresponding LIFDI-MS spectrum is depicted in Figure 76 (main text). In the NMR spectrum, the main peak can be assigned to [H₆Cu₆Al₆](Cp*)₆. A smaller peak is attributed to [Cu₈Al₆](Cp*)₆. The remaining two peaks are tentatively assigned to [Cu₇Al₇](Cp*)₆ and [HCu₇Al₆](Cp*)₆.

6.2.13 Reactivity of [H₄Cu₆Al₆](Cp*)₆ towards H₂

The following supporting data documentation refers to pages 183-185.
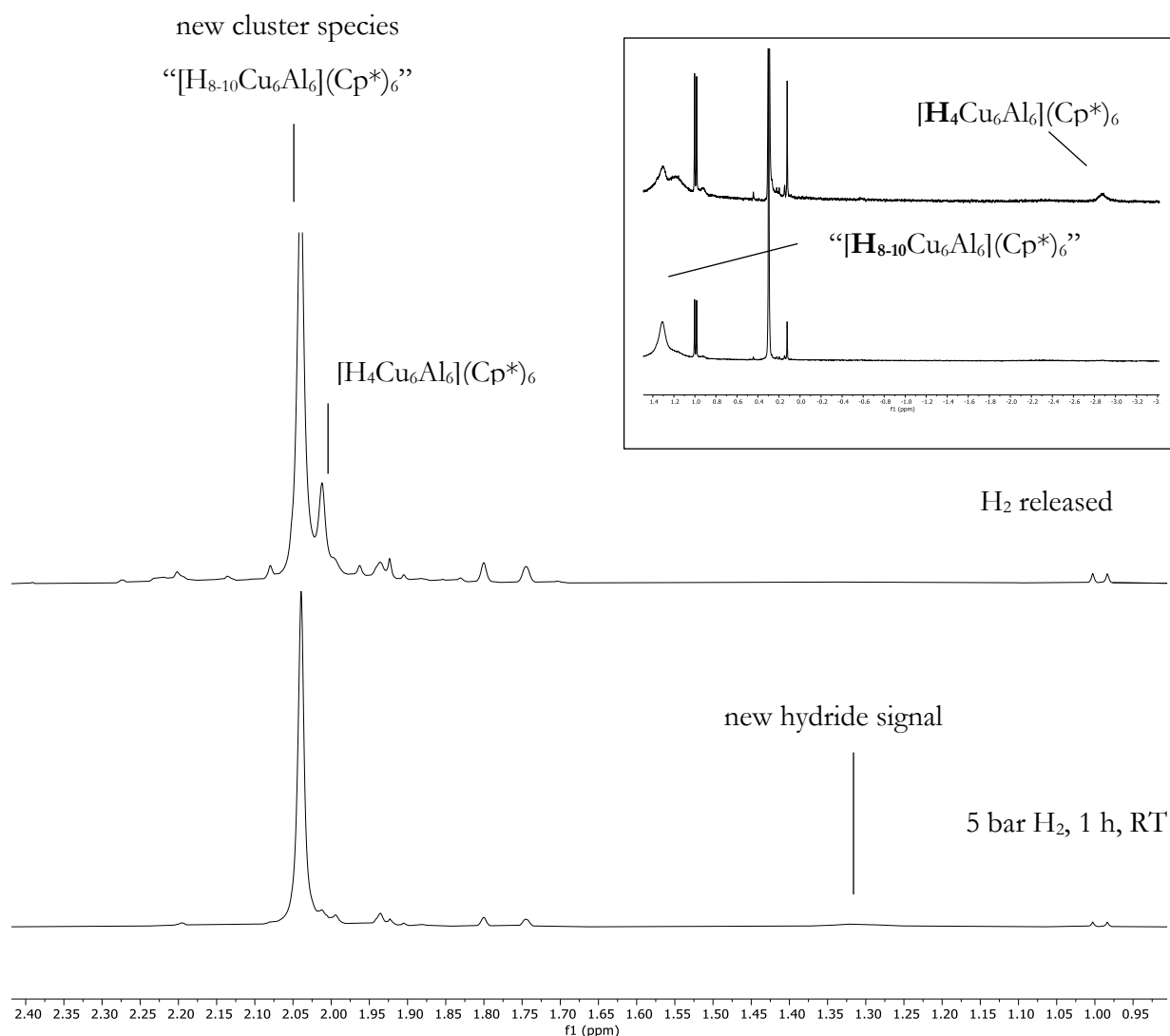
Figure S106: ¹H-NMR spectra of the reversible reaction of [H₄Cu₆Al₆](Cp*)₆ with hydrogen (5 bar, RT) in benzene-d₆. The upper box shows a zoom of the hydride associated peaks. The peaks at

318

0.99 ppm, 1.75 ppm, 1.80 ppm correspond to HCp*. The peak at 0.29 pm corresponds to silicon grease.
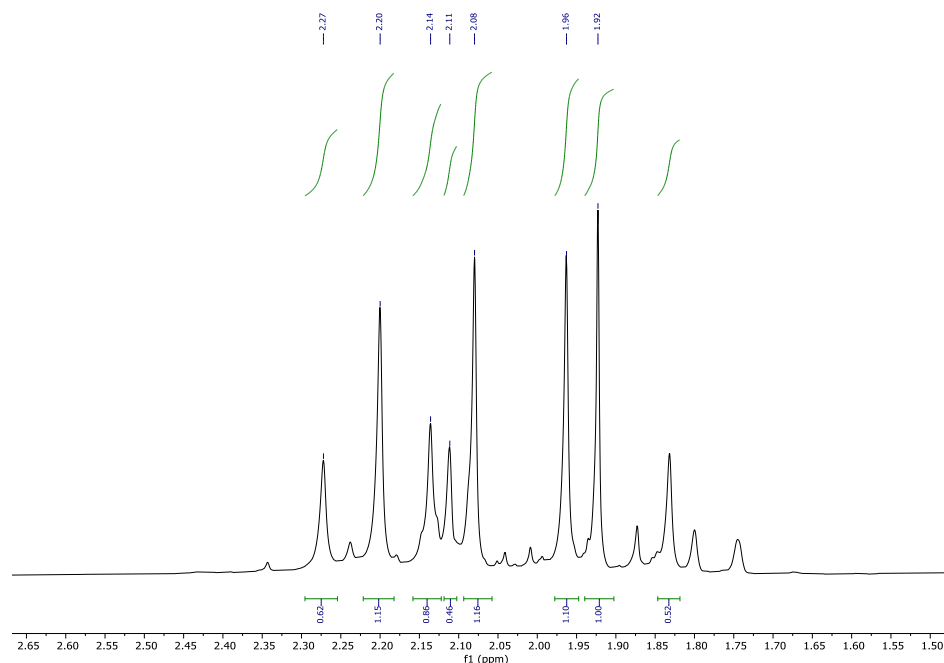
Figure S107: Cut-out of the ^{1}H-NMR spectrum (benzene-d$_6$) of the reaction of [H$_4$Cu$_6$Al$_6$](Cp*)$_6$ with hydrogen (5 bar, RT, 3 days). The peaks at 1.75 ppm and 1.80 ppm correspond to HCp*.

Exposure of [H$_4$Cu$_6$Al$_6$](PPh$_3$)$_6$ to 5 bar H$_2$ results after several hours in a new cluster species with a new hydride signal at 1.30 ppm and a new Cp* signal at 2.04 ppm in ^{1}H-NMR analysis. According to integration of the signals, the species is tentatively assigned as [H$_{8-10}$Cu$_6$Al$_6$](Cp*)$_6$. Noteworthy, this reaction is reversible upon release of the H$_2$ pressure. Prolonged exposure to 5 bar H$_2$ for several days results in irreversible formation of several new cluster species according to ^{1}H-NMR analysis.

6.2.14 Crystallographic information for Au/Al and Cu/Au/Al clusters

Table S11: Crystallographic information for the compounds **8** and **13**.

	8	13
chemical formula	$C_{57}H_{83}Al_5Au_2$	$C_{60}H_{90}Cu_{0.94}Al_{5.06}$
CCDC number	-	-
formula weight	1297.06	1795.59
temperature	100(2) K	100(2) K
λ [Å]	0.71073	0.71073
crystal size [mm]	0.113x0.155x0.314	0.101x0.144x0.179
crystal habit	dark needle	dark fragment
crystal system	monoclinic	monoclinic
space group	P 2_1/n	I 2/m
unit cell dimensions	a = 11.5893(9) Å b = 37.149(3) Å c= 13.9089(11) Å α = 90° β = 104.188(3)° γ = 90°	a = 13.6124(15) Å b = 17.792(2) Å c= 15.542(3) Å α = 90° β = 107.968(4)° γ = 90°
volume [Å^3]	5805.5(8)	3580.6(8)
Z	4	2
ϱ (calculated) [g/cm^3]	1.484	1.665
absorption coefficient [mm^{-1}]	5.157	8.535
F(000)	2592	1718
diffractometer	BRUKER D8 VENTURE	BRUKER D8 VENTURE
radiation source	TXS rotating anode, Mo	TXS rotating anode, Mo
θ range for data collection [°]	1.894 – 25.908	2.289 – 25.475
index ranges	-14 ≤ h ≤ 14 -45 ≤ k ≤ 45 -17 ≤ l ≤ 17	-16 ≤ h ≤ 16 -21 ≤ k ≤ 21 -18 ≤ l ≤ 18
reflections collected	213543	85143
independent reflections	11270 [(R_{int}) = 0.0460]	3423 [(R_{int}) = 0.4668]
coverage of independent reflections	99.9 %	99.9 %
absorption correction	Multi-scan	Multi-scan
max. and min. transmission		0.5707 and 0.7452
structure solution technique	Direct Methods	Direct Methods
structure solution program	SHELXS-97 (Sheldrick 2008)	SHELXS-97 (Sheldrick 2008)

6. Appendix
6.2 Supporting information for the chemical part

refinement method	full matrix least squares on F^2	full matrix least squares on F^2
refinement program	SHELXL 2014 (Sheldrick 2014)	SHELXL 2014 (Sheldrick 2014)
function minimized	$\sum w(F_0^2 - F_c^2)^2$	$\sum w(F_0^2 - F_c^2)^2$
data/restraints/parameters	11270/75/639	3423/0/175
goodness of fit on F^2	1.291	1.101
$\Delta/\sigma_{max.}$	0.002	0.000
final R indices [I>2σ]	R1 = 0.0306, wR2 = 0.0665	R1 = 0.0753, wR2 = 0.2017
final R indices [all data]	R1 = 0.0334, wR2 = 0.0678	R1 = 0.0875, wR2 = 0.2106
$\Delta F_{max.}, \Delta F_{min.}$ [e / Å^{-3}]	2.158, -1.755	5.652, -3.002

6.2.15 Characterization of [H$_x$Au$_{6/7}$Al$_6$](Cp*)$_6$ (**6/7**)

The following supporting data documentation refers to pages 185-188.
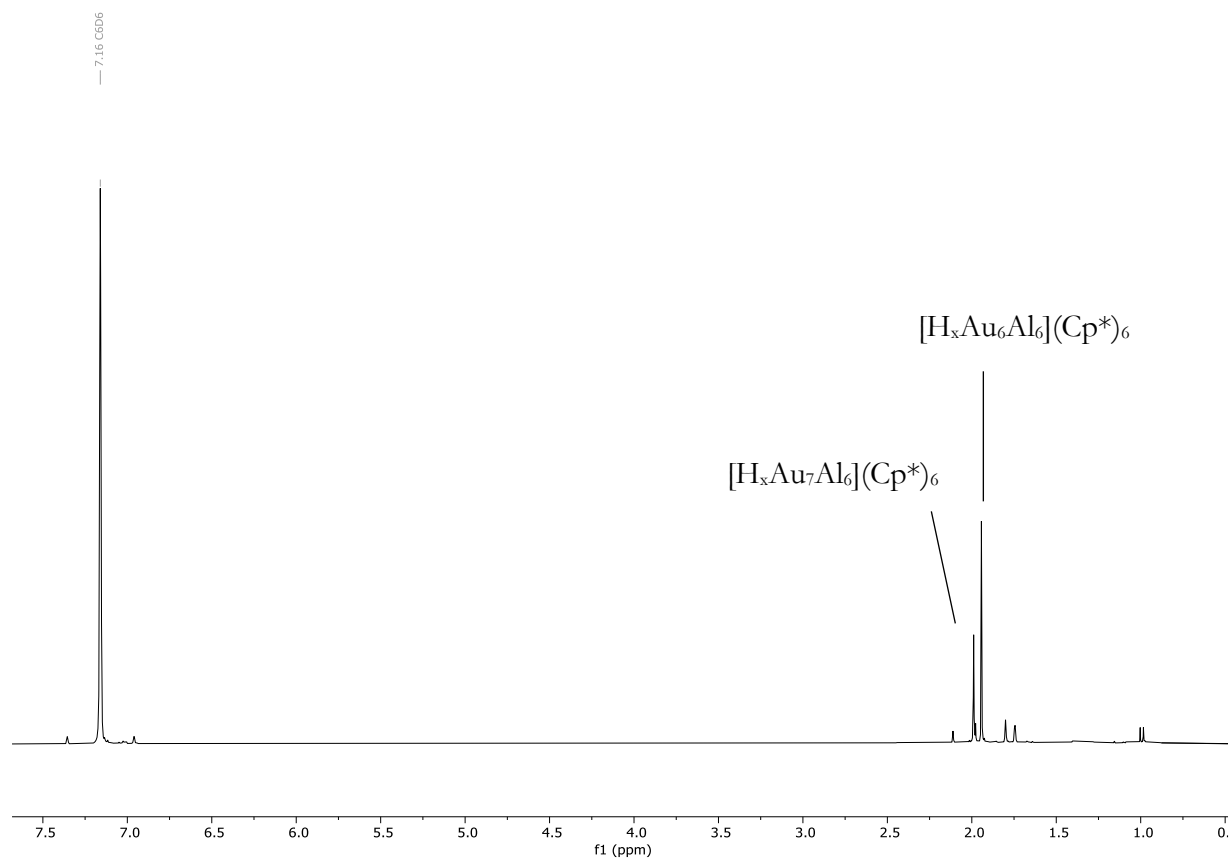
Figure S108: ^{1}H-NMR (benzene-d$_6$) spectrum of isolated [H$_x$Au$_{6/7}$Al$_6$](Cp*)$_6$ (**6/7**).

6. Appendix
6.2 Supporting information for the chemical part
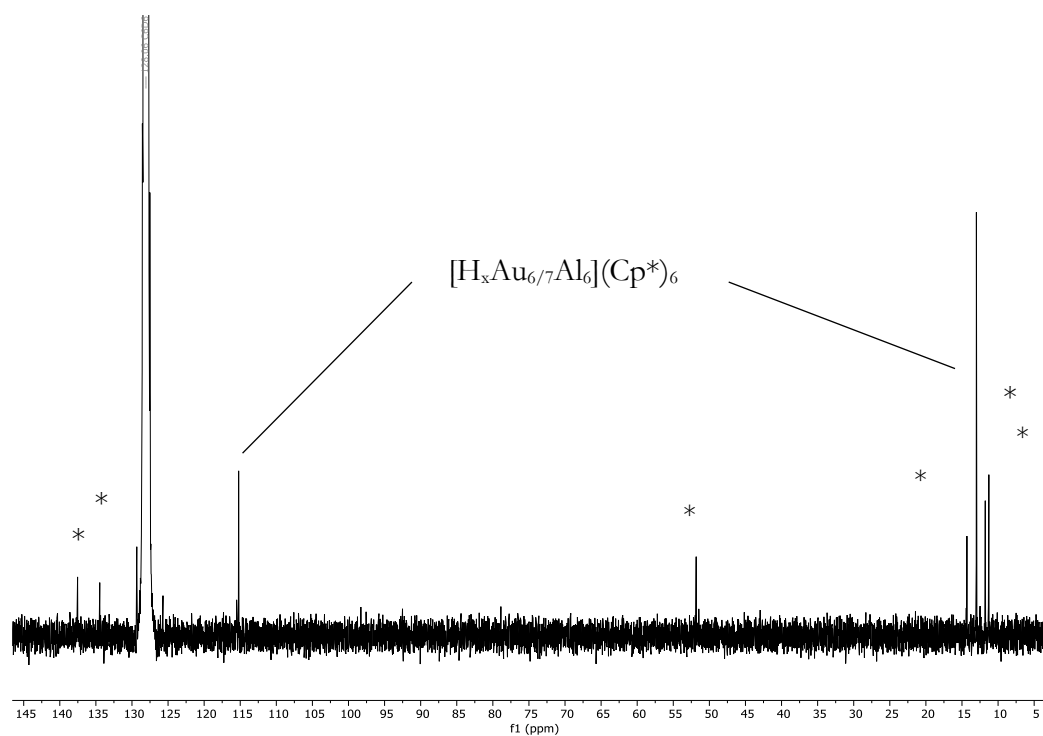
Figure S109: ^{13}C-NMR spectrum (benzene-d_6) of isolated $[H_xAu_{6/7}Al_6](Cp^*)_6$ (**6/7**). Signals marked with * are attributed to free pentamethylcyclopentadiene (HCp*).
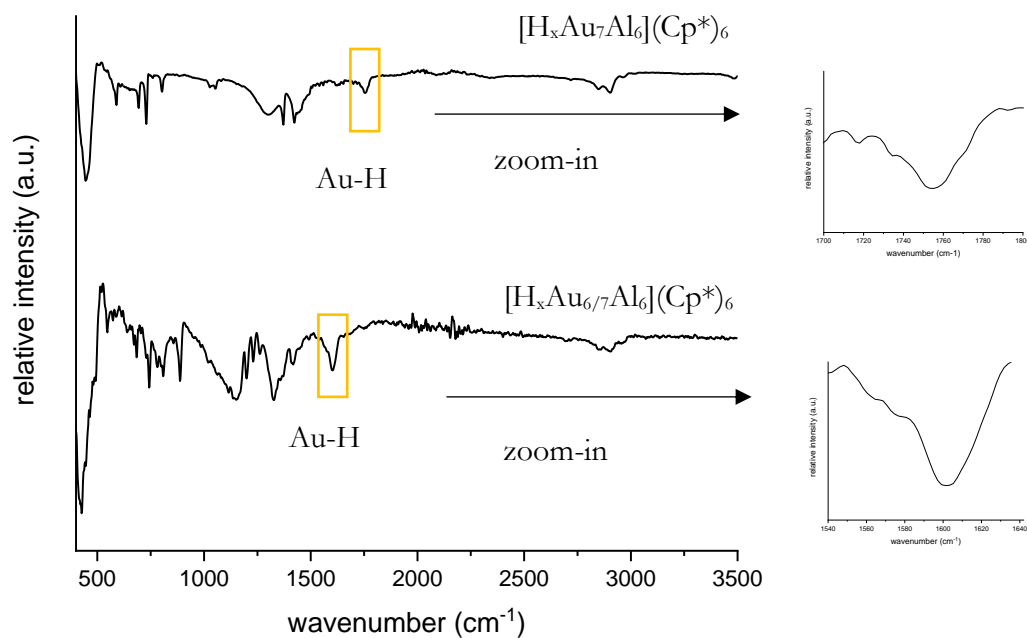
Figure S110: Comparison of ATR-IR spectrum of the isolated $[H_xAu_{6/7}Al_6](Cp^*)_6$ (**6/7**) mixture (bottom) with pure $[H_xAu_7Al_6](Cp^*)_6$ (**7**) (top). The Au-H hydride regions are additionally shown as zoom-in.

6. Appendix

6.2 Supporting information for the chemical part

a)

b)
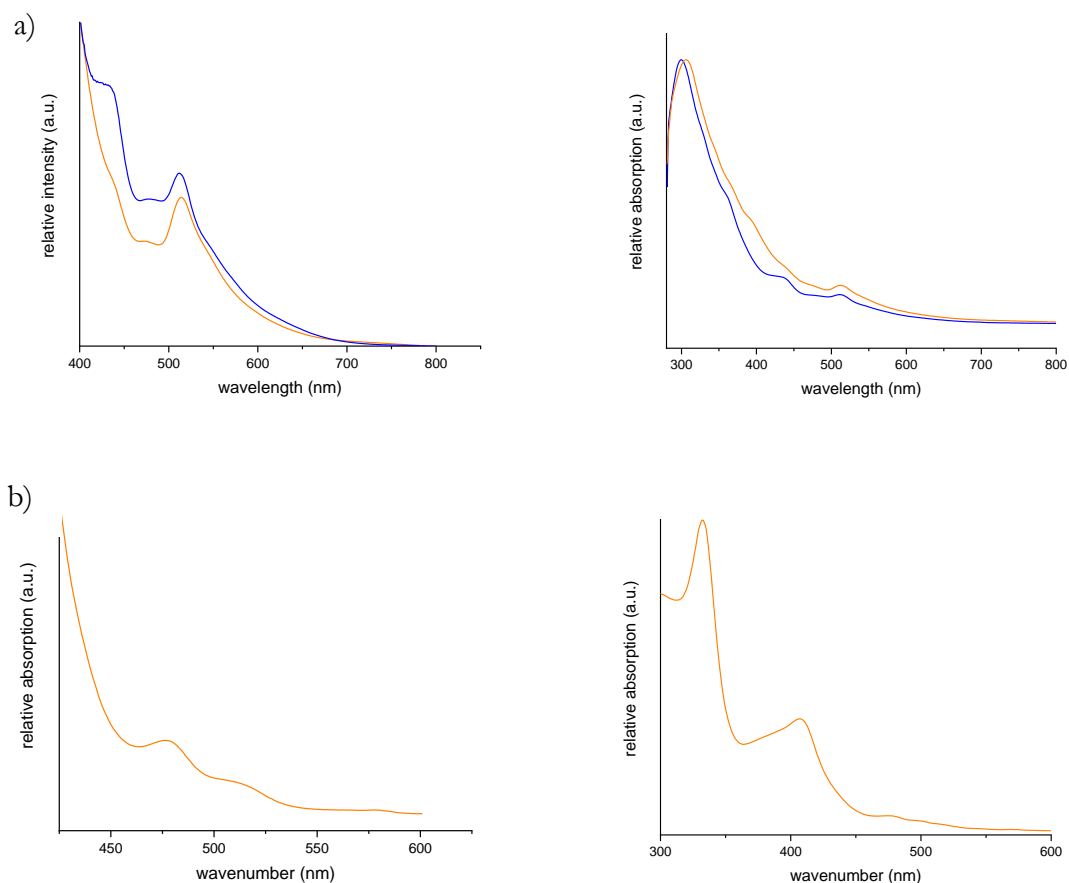
Figure S111: a) Comparison of UV-Vis spectra of isolated $[H_xAu_{6/7}Al_6](Cp^*)_6$ (**6/7**) (orange) and pure $[H_xAu_7Al_6](Cp^*)_6$ (**7**) (blue). Left: Enlarged Vis region. Right: Full-range spectrum. b) UV-Vis spectrum of isolated $[Au_2Al_5](Cp^*)_5$ (**8**). Left: Enlarged Vis region. Right: Full-range spectrum.

6.2.16 Characterization of [H$_x$Au$_7$Al$_6$](Cp*)$_6$ (**7**)

The following supporting data documentation refers to pages 189-191.
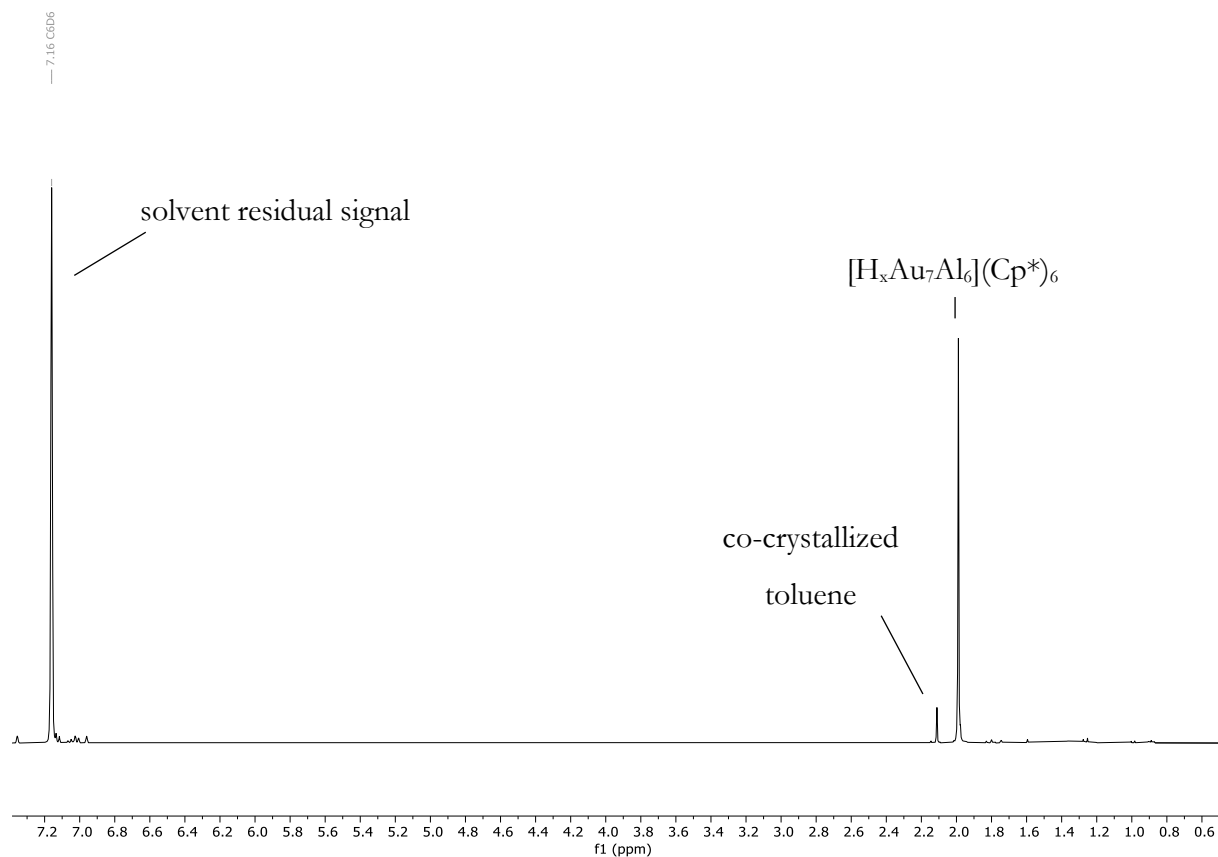
Figure S112: ^{1}H-NMR (benzene-d$_6$) spectrum of isolated [H$_x$Au$_7$Al$_6$](Cp*)$_6$ (**7**).

6. Appendix
6.2 Supporting information for the chemical part
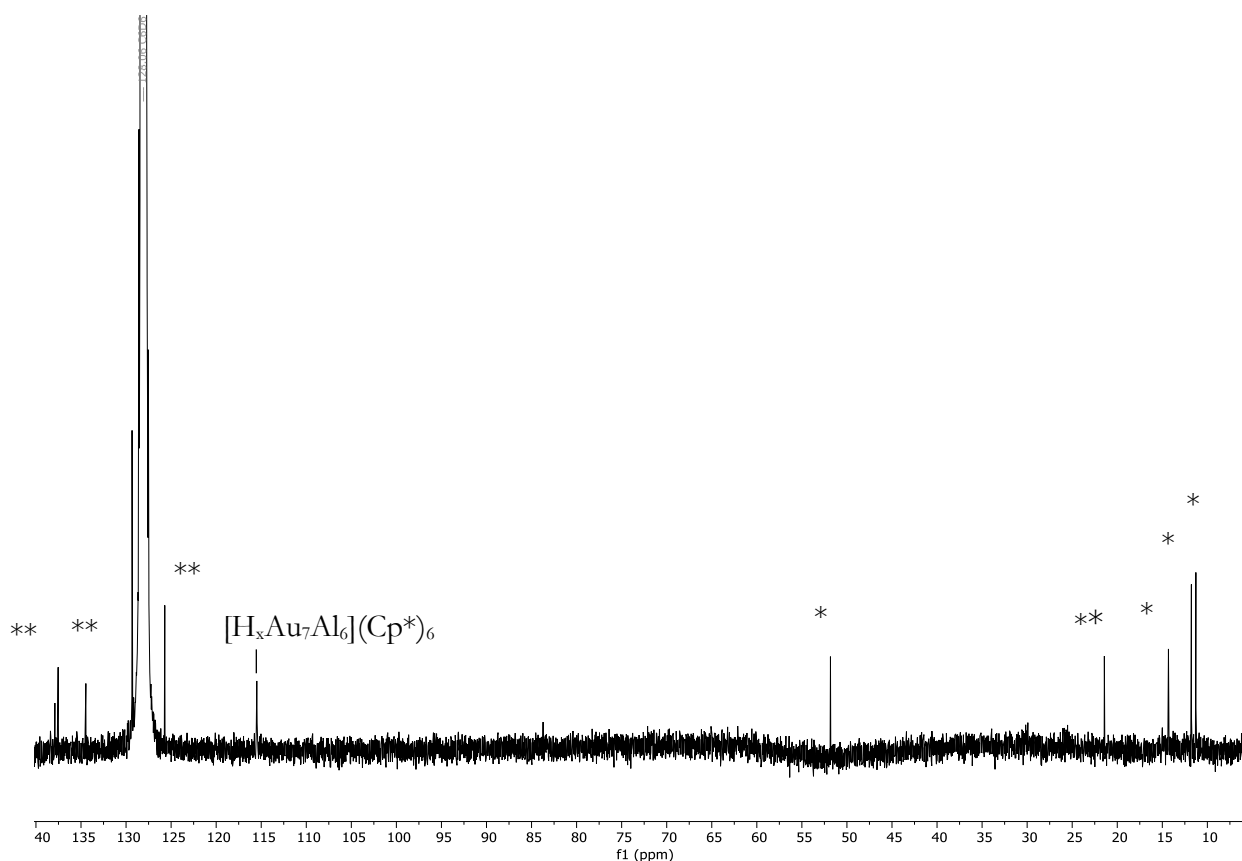
Figure S113: ^{13}C-NMR spectrum (benzene-d$_6$) of isolated [H$_x$Au$_7$Al$_6$](Cp*)$_6$ (**7**). Signals marked with * are attributed to free pentamethylcyclopentadiene (HCp*). Signals marked with ** are attributed to co-crystallized toluene. The signal at 128 ppm is solvent residual signal.

The NMR spectroscopic results from isolated [H$_x$Au$_{6/7}$Al$_6$](Cp)$_6$ and [H$_x$Au$_7$Al$_6$](Cp*)$_6$ allow for a clear assignment of peak positions to [H$_x$Au$_6$Al$_6$](Cp*)$_6$ and [H$_x$Au$_7$Al$_6$](Cp*)$_6$ by combinatorics. Composition of the isolated species is known from LIFDI-MS analysis (see Figure 77). Note that the -CH$_3$ signal of [H$_x$Au$_7$Al$_6$](Cp*)$_6$ is supposed to overlap with peaks from HCp* in ^{13}C-NMR analysis. The relatively high intensity of HCp* attributed signals in the ^{13}C-NMR spectra is attributed to the low solubility of [H$_x$Au$_7$Al$_6$](Cp*)$_6$ in comparison to HCp* and to its high sensitivity.*

6.2.16 Synthesis and characterization of [Au₂Al₅](Cp*)₅ (**8**)

The following supporting data documentation refers to pages 192-195.
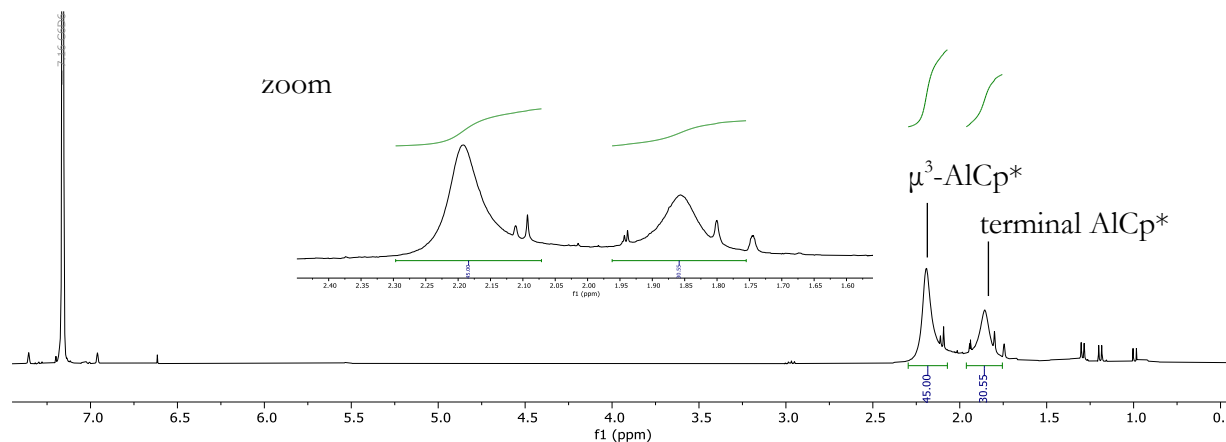
Figure S114: ^{1}H-NMR (benzene-d$_6$) spectrum of isolated [Au$_2$Al$_5$](Cp*)$_5$ (**8**) and zoom of the cluster relevant region. The peak at 7.15 ppm is solvent residual signal. The small peaks < 1.5 ppm and at 6.75 ppm are caused by slight ^{f}Dipp impurities. The small peaks are 1.75 ppm and 1.80 ppm are attributed to HCp* and the one at 2.09 ppm to co-crystallized toluene. The other small peaks at 1.94 ppm and 2.11 ppm are of unknown origin.
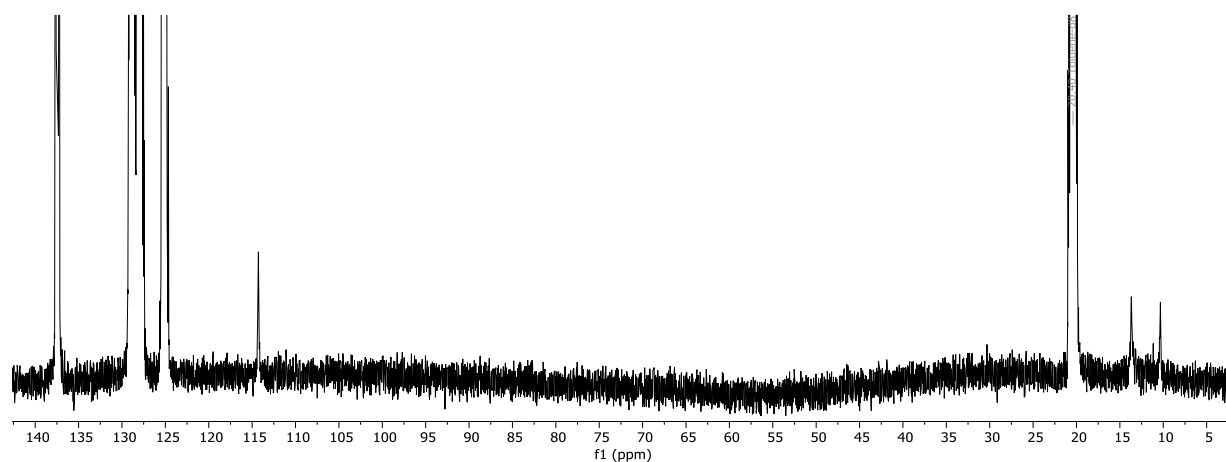
Figure S115: ^{13}C-NMR spectrum (toluene-d$_8$) of [Au$_2$Al$_5$](Cp*)$_5$ (**8**). Peaks at 21 ppm, 125 ppm, 128 ppm and 137.5 ppm are solvent residual signal.

The NMR spectroscopic data of [Au₂Al₅](Cp)₅ is fully consistent with the symmetry and composition of the compound in the solid-state as determined by SC-XRD.*
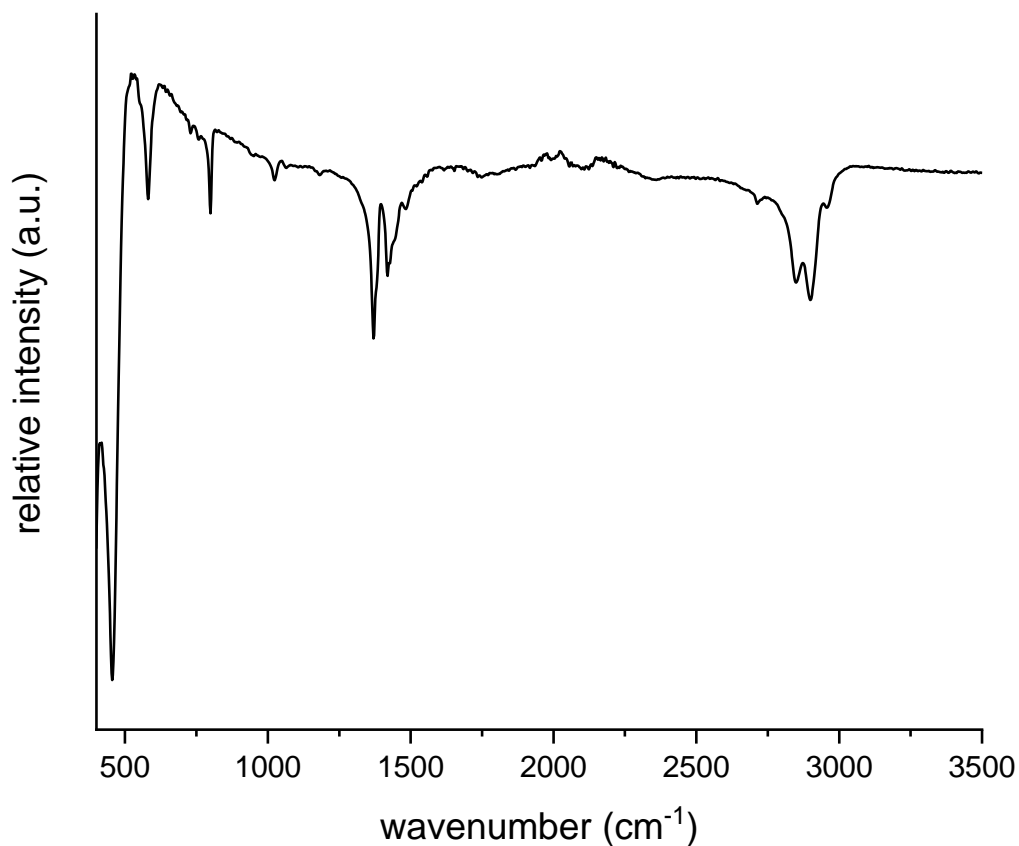
Figure S116: ATR-IR spectrum of [Au$_2$Al$_5$](Cp*)$_5$ (**8**).

The IR spectrum shows bands typical for Cp (characteristic v_{C-H} stretching vibrations in the region 2500 - 3000 cm^{-1} and v_{C-C} vibrations between 500 cm^{-1} and 1700 cm^{-1}). The strong band at 455 cm^{-1} is attributed to the v_{Al-C} stretching vibration of the AlCp* units. No Au-H hydride signals can be identified in the spectrum.*

6.2.17 Mechanistic investigations in Au/Al cluster chemistry

The following supporting data documentation refers to pages 196-198.

6.2.17.1 Reduction mechanism of Au(I)
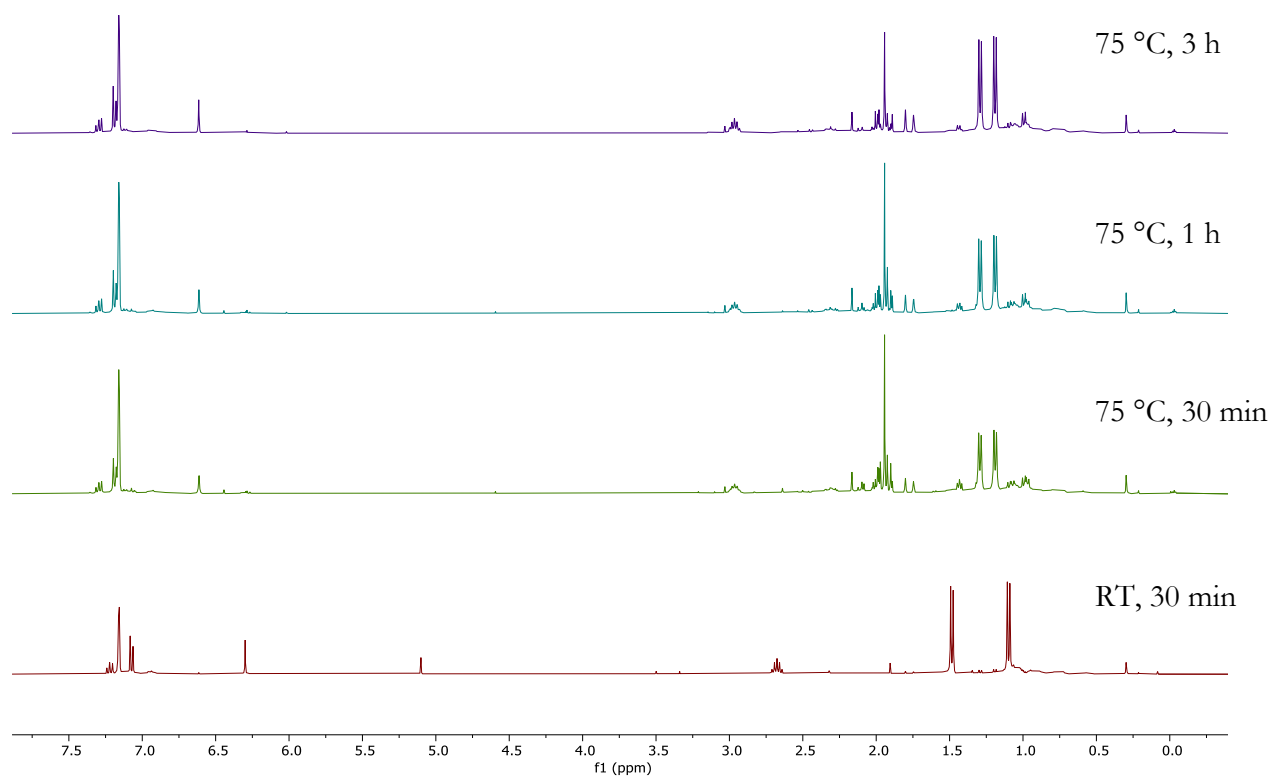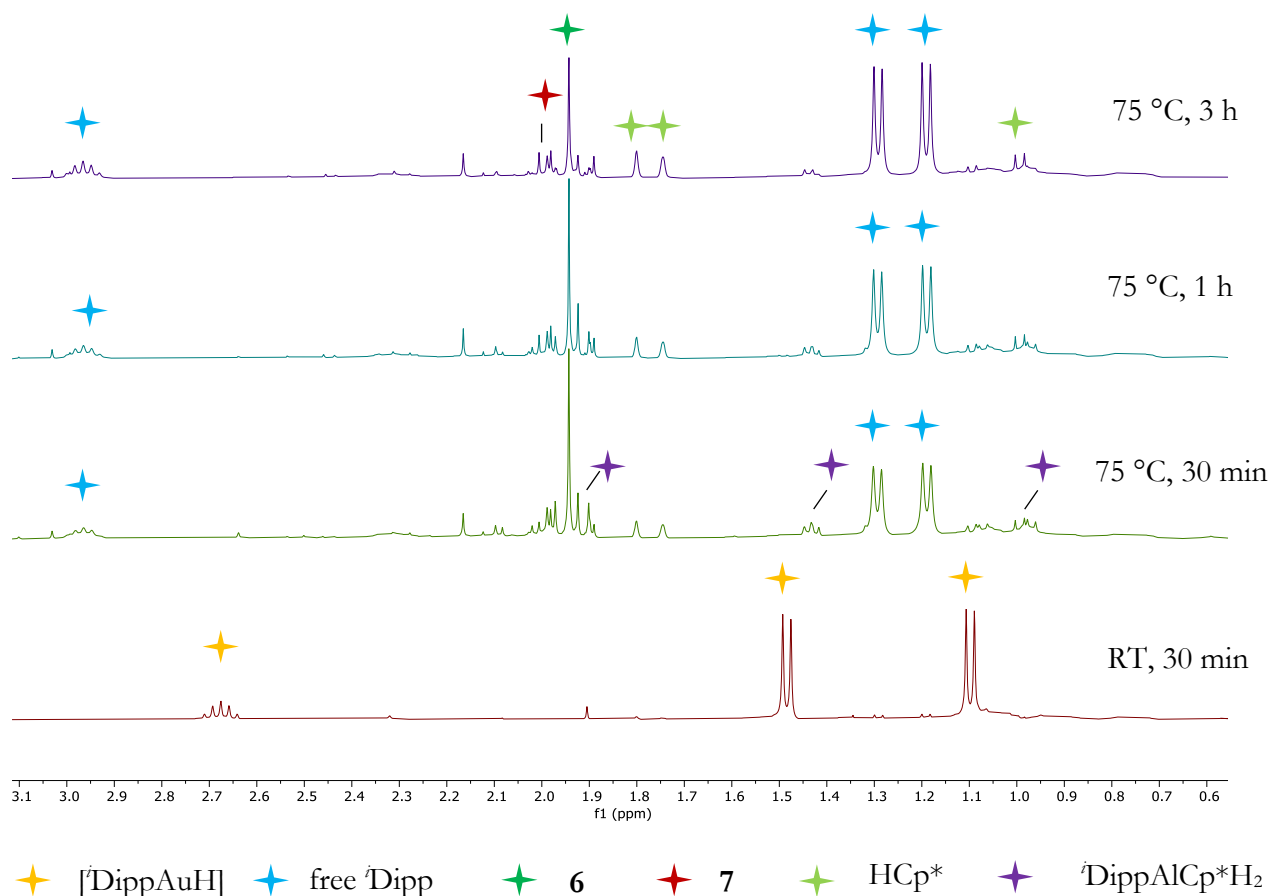
Figure S117: *In situ* ¹H-NMR spectra (benzene-d₆) of the reaction [ᵗDippAuH] + AlCp*
(1:1). Note that **6** = [HₓAu₆Al₆](Cp*)₆ and **7** = [HₓAu₇Al₆](Cp*)₆.

6.2 Supporting information for the chemical part

Figure S118: *In situ* ^{1}H-NMR spectra (benzene-d_6) of the reaction [^{i}DippAuH] + AlCp* (1:0.75, 75 °C, 2 h).

6.2 Supporting information for the chemical part

✦ AlCp*₂H

Figure S119: *In situ* ¹H-NMR spectra (benzene-d₆) of the reaction [ᴵDippAuH] + AlCp* (1:1.25, 75 °C, 2 h).

Figure S120: *In situ* ^{1}H-NMR spectra (benzene-d$_6$) of the reaction [*DippAuH] + AlCp* (1:1.5, 75 °C, 2 h).

Higher AlCp* stoichiometric ratios favor formation of [H$_x$Au$_6$Al$_6$](Cp*)$_6$ compared to [H$_x$Au$_7$Al$_6$](Cp*)$_6$. However, a size-focusing towards [H$_x$Au$_6$Al$_6$](Cp*)$_6$ is not possible. At a Au:Al stoichiometry of 1:1.5, formation of [Au$_2$Al$_5$](Cp*)$_5$ starts to begin.

6. Appendix

6.2 Supporting information for the chemical part
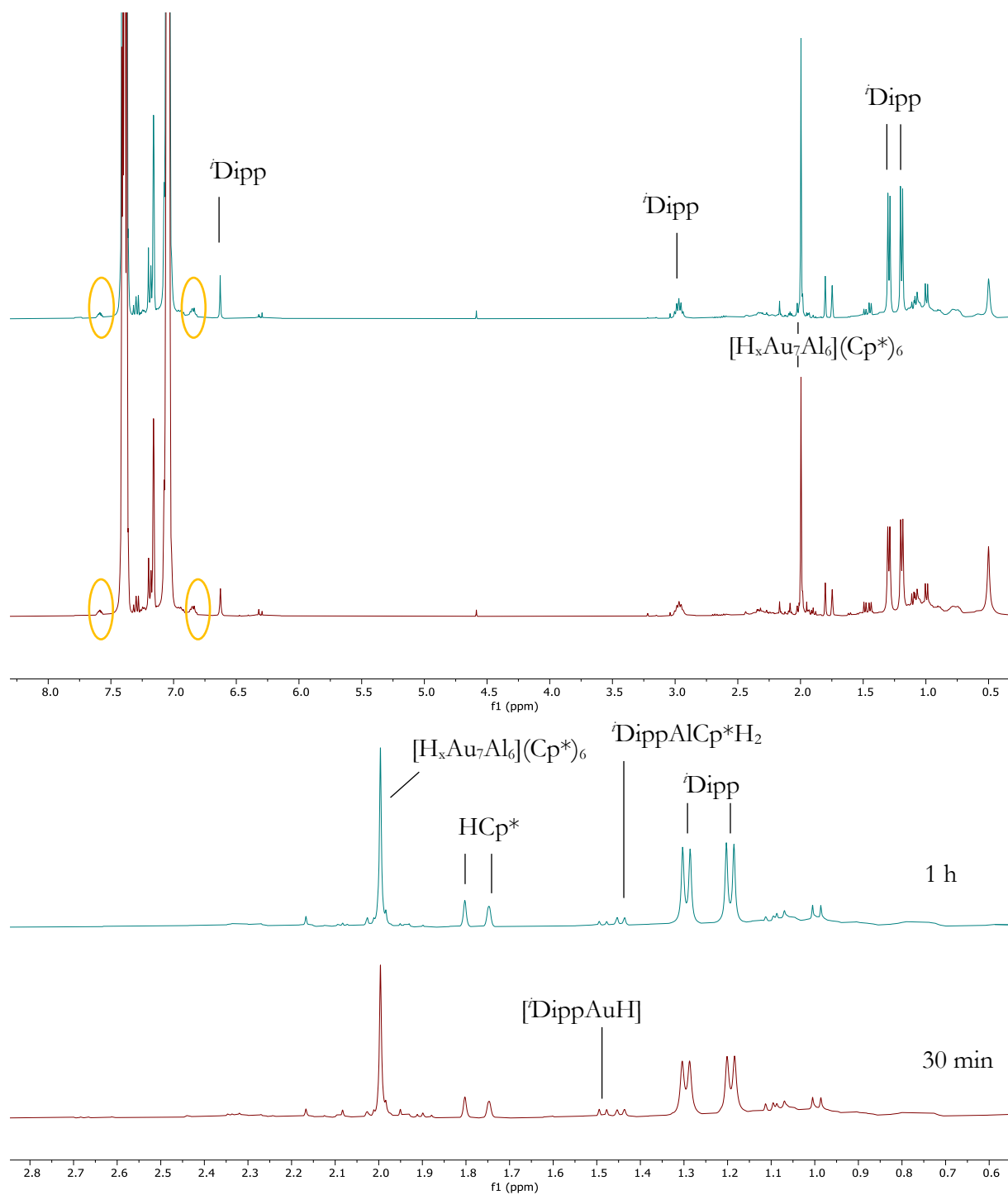
Figure S121: *In situ* ^{1}H-NMR spectra (benzene-d$_6$) of the reaction [^{i}DippAuH] + AlCp* + PPh$_3$ (1:0.75:10, 75 °C). The intense signals at 7.1 ppm and 7.4 ppm are attributed free PPh$_3$. The signal at 7.16 ppm is solvent residual signal. Yellow ellipsoids mark signals attributed to (dynamically) coordinated PPh$_3$.

Clearly, [H$_x$Au$_7$Al$_6$](Cp)$_6$ is formed selectively at a Au:Al stoichiometry of 0.75:1 upon addition of 10 eq. PPh$_3$.*

6.2.17.3 Formation mechanism of [Au₂Al₅](Cp*)₅ (**8**)
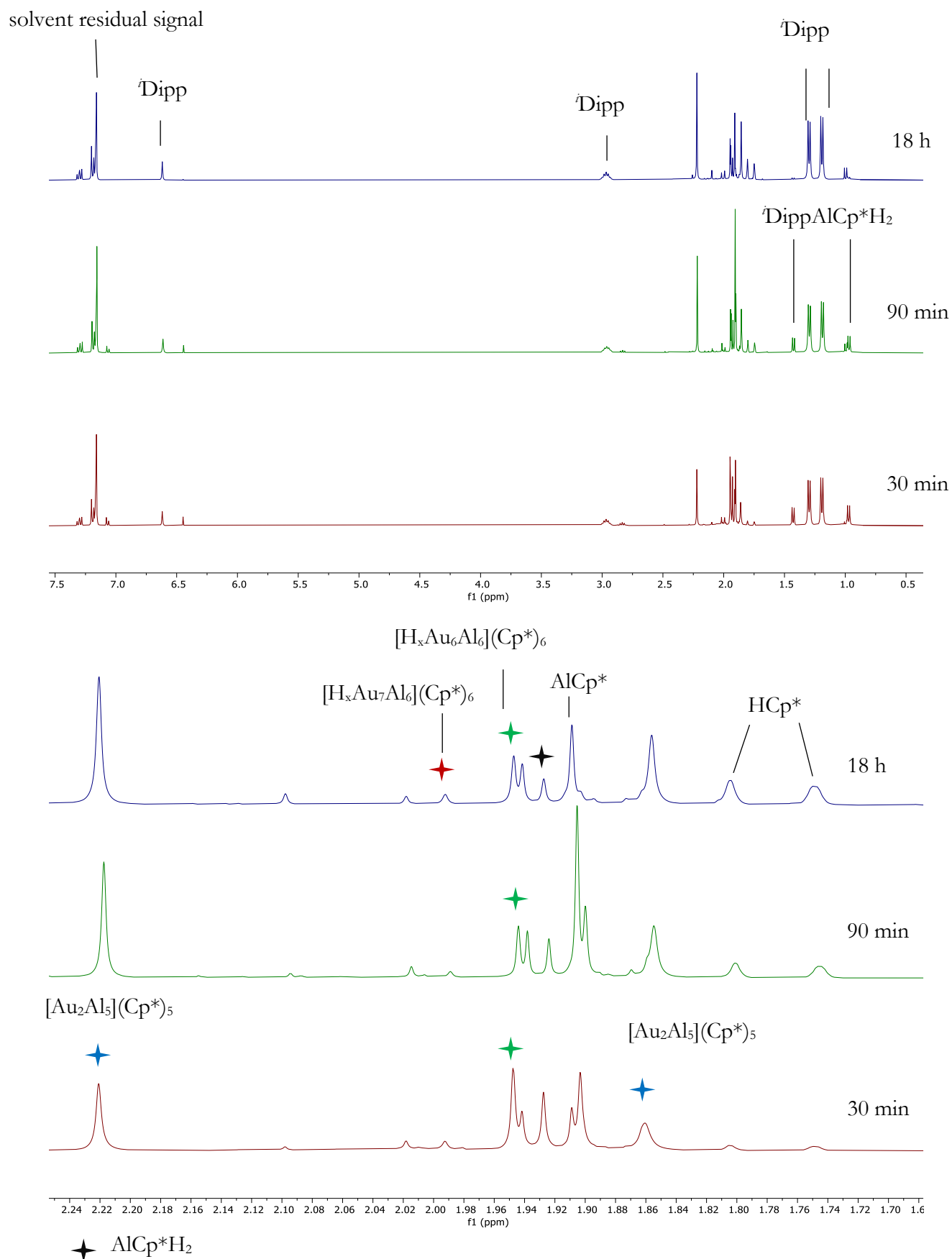
Figure S122: Time-dependant *in situ* ¹H-NMR spectra (benzene-d₆) of the reaction [ⁱDippAuH] + AlCp* (1:2, 75 °C).

335

6. Appendix

6.2 Supporting information for the chemical part
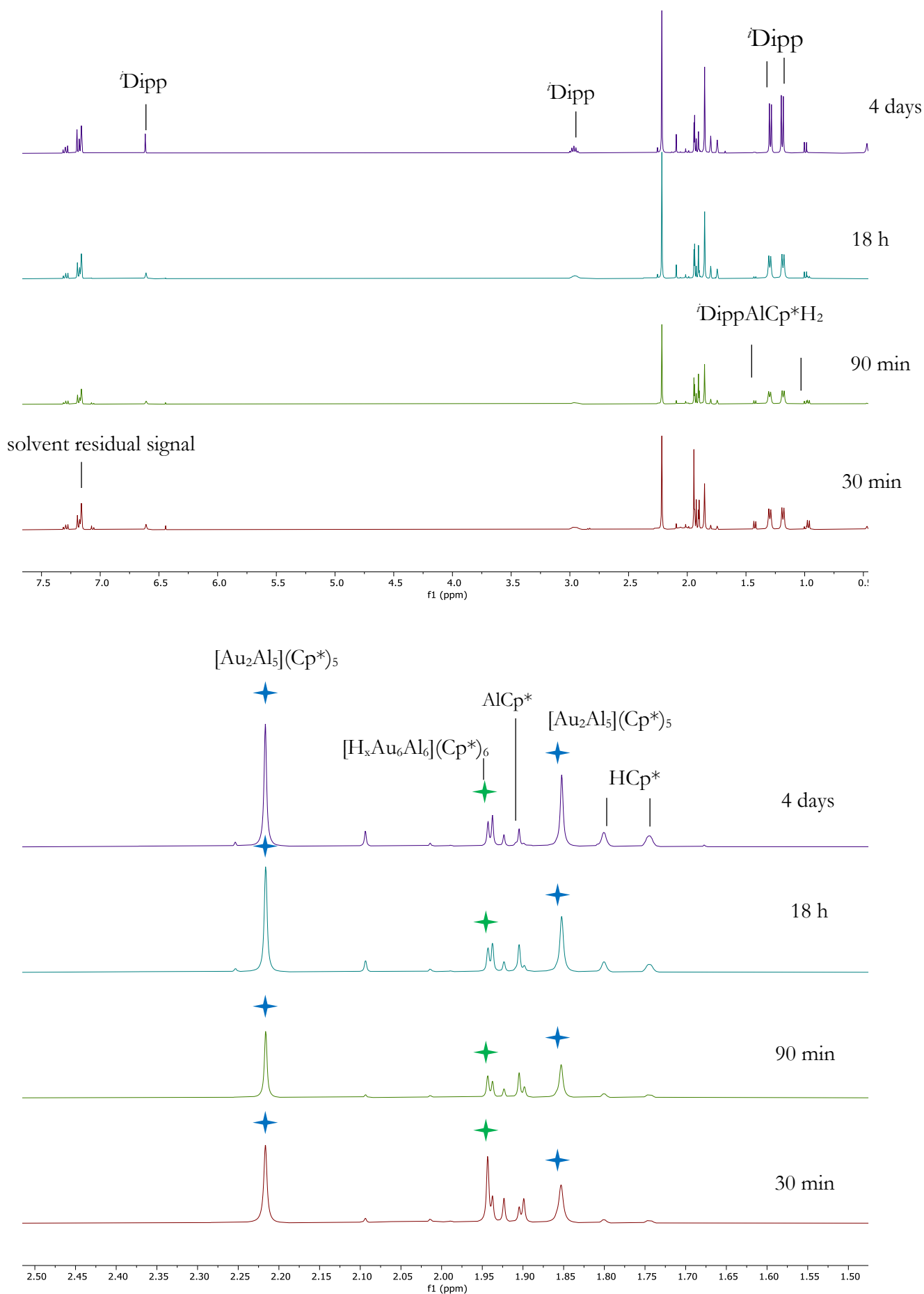
Figure S123: Time-dependant *in situ* ^{1}H-NMR spectra (benzene-d$_6$) of the reaction [^{i}DippAuH] + AlCp* (1:2.5, 75 °C).

solvent residual signal
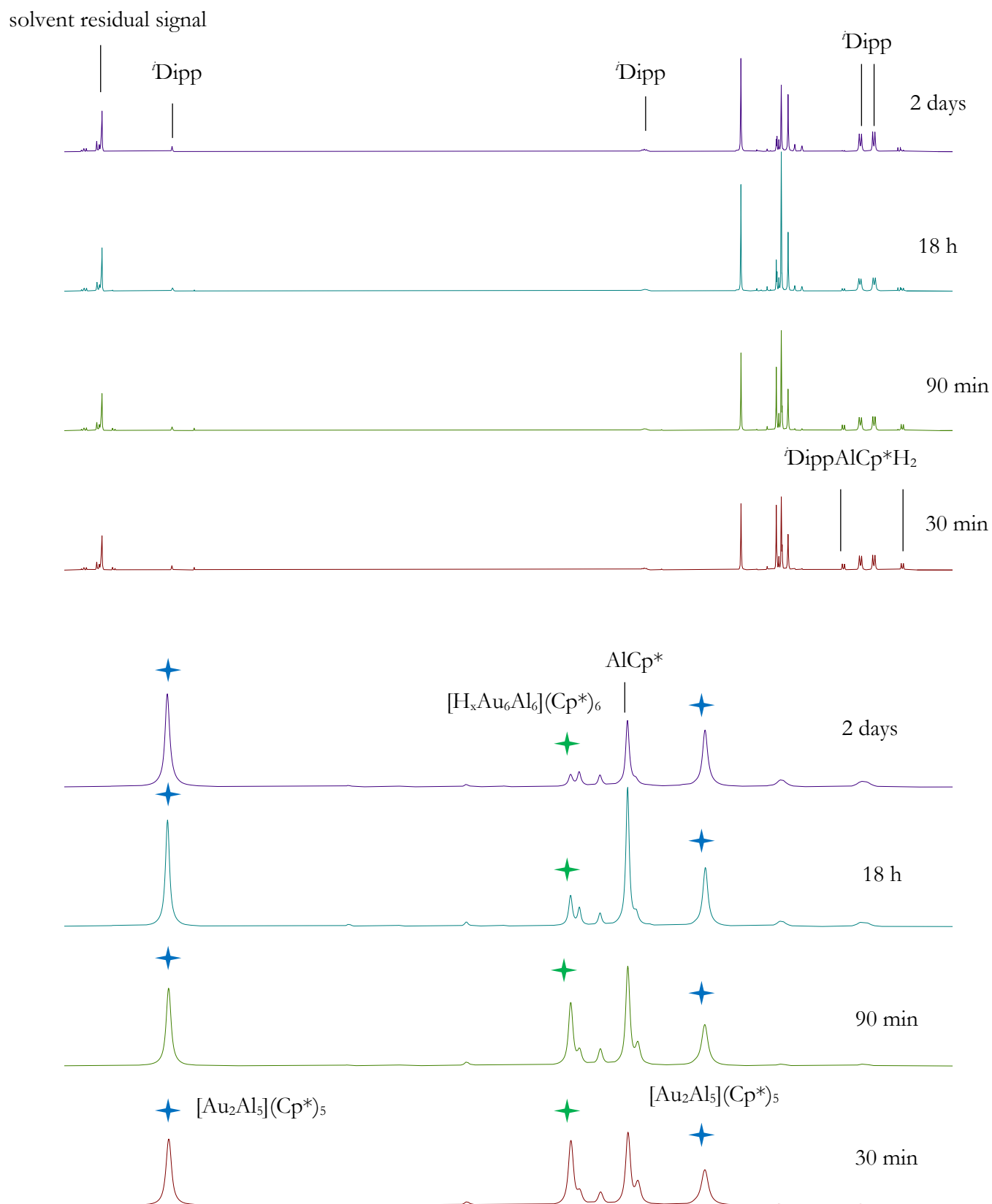
Figure S124: Time-dependant *in situ* ^{1}H-NMR spectra (benzene-d$_{6}$) of the reaction [^{i}DippAuH] + AlCp* (1:3, 75 °C).

6. Appendix

6.2 Supporting information for the chemical part
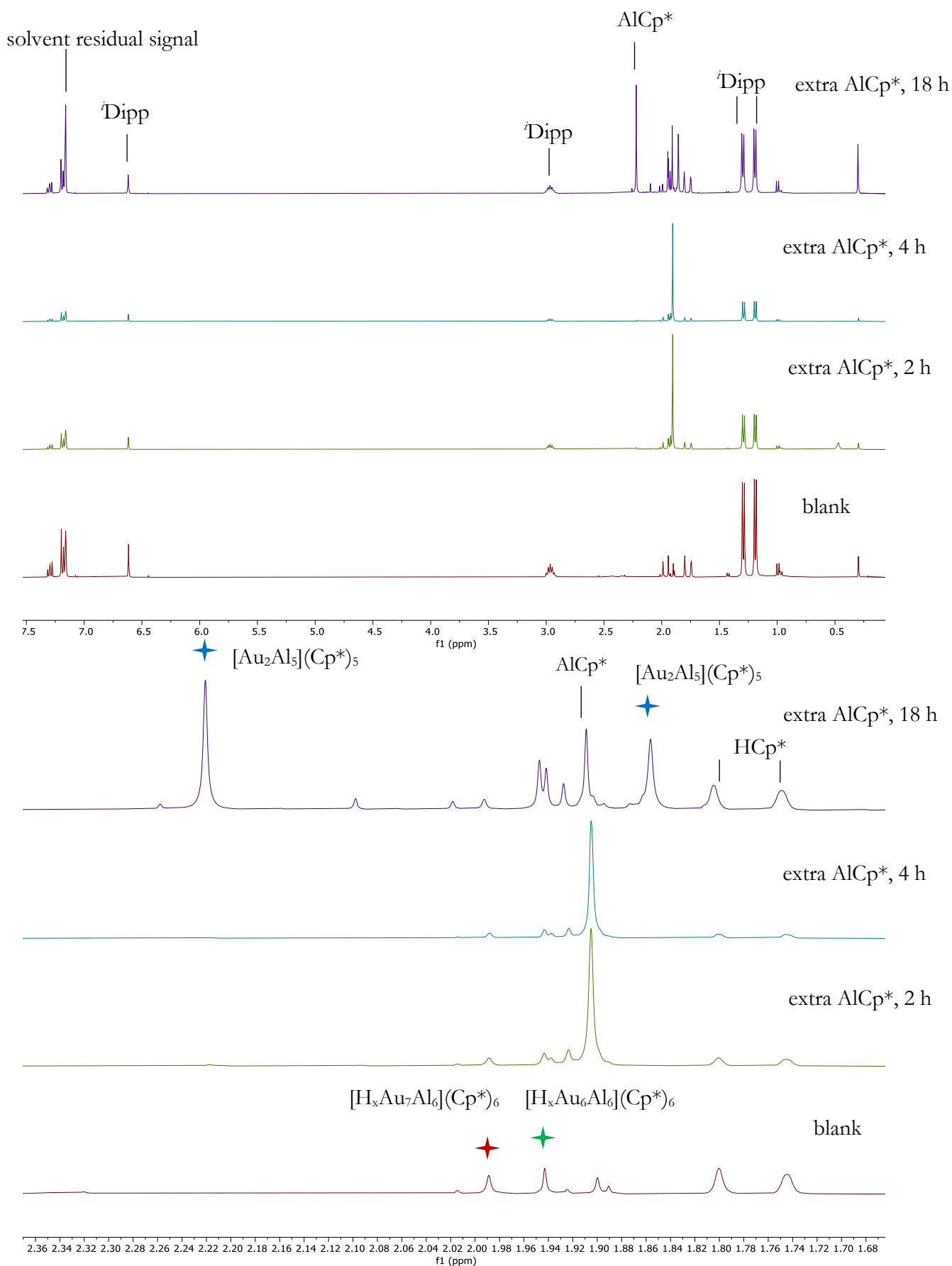
Figure S125: Time dependant *in situ* ^{1}H-NMR spectra (benzene-d$_6$) of the conversion of *in situ* generated [H$_x$Au$_{6/7}$Al$_6$](Cp*)$_6$ (**6/7**) (blank) with extra AlCp*.

6. Appendix

6.2 Supporting information for the chemical part

The spectra illustrate that [Au₂Al₅](Cp*)₅ is preferable formed at high AlCp* concentrations and after prolonged reaction times at 75 °C. [HₓAu₆Al₆](Cp*)₆ is formed initially but its concentration is decreasing over time. This leads to the conclusion that [Au₂Al₅](Cp*)₅ is formed out of [HₓAu₆Al₆](Cp*)₆ in the presence of AlCp*. This was verified by a test experiment, in which in situ generated [HₓAu₆/₇Al₆](Cp*)₆ was exposed to AlCp*.
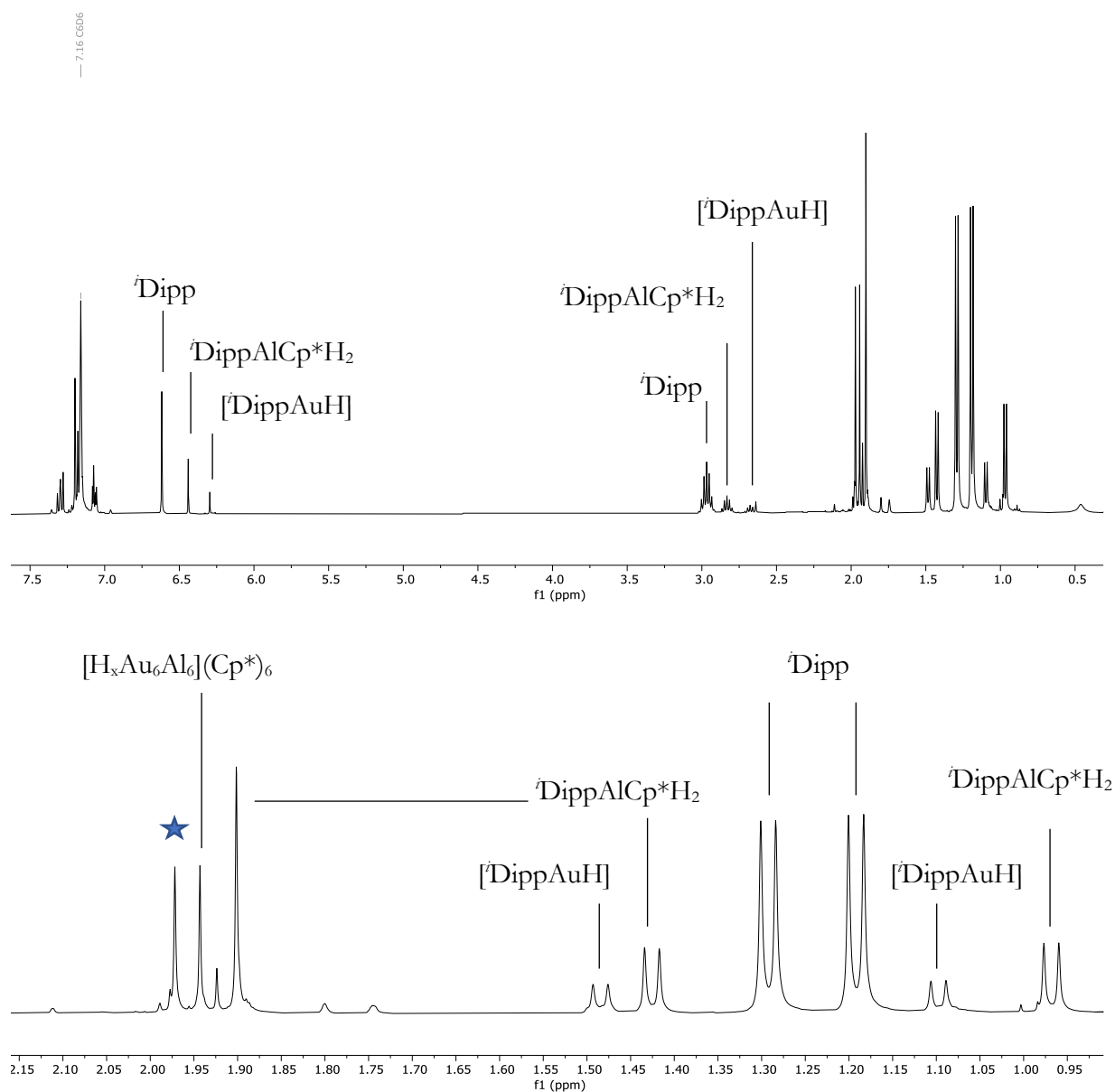
★ unknown species

Figure S126: *In situ* ¹H-NMR spectrum (benzene-d) of the reaction [Au₂Al₅](Cp*)₅ (**8**) + [ᶦDippAuH] (1:2, 75 °C, 30 min).

The reaction of [Au₂Al₅](Cp*)₅ with [ᶦDippAuH] leads to formation of AlCp*H₂(ᶦDipp) and of [HₓAu₆Al₆](Cp*)₆. Very similar reactivity was observed in the reaction between [Cu₂Al](Cp*)₃ and [CuMes]. LIFDI-MS of the reaction solution indicates formation of [HₓAu₆Al₆](Cp*)₆ and [HₓAu₇Al₆](Cp*)₆. However, [HₓAu₇Al₆](Cp*)₆ is not detected in the ¹H-NMR spectrum (the

signal marked by the blue star does not have the chemical shift of [H$_x$Au$_7$Al$_6$](Cp)$_6$). Clearly, [Au$_2$Al$_5$](Cp*)$_5$ is a building block for the generation of larger Au/Al clusters upon addition of Au(I) sources.*

6.2.17.3 Additional investigations between Cp*AlH$_2$ and ^{i}Dipp
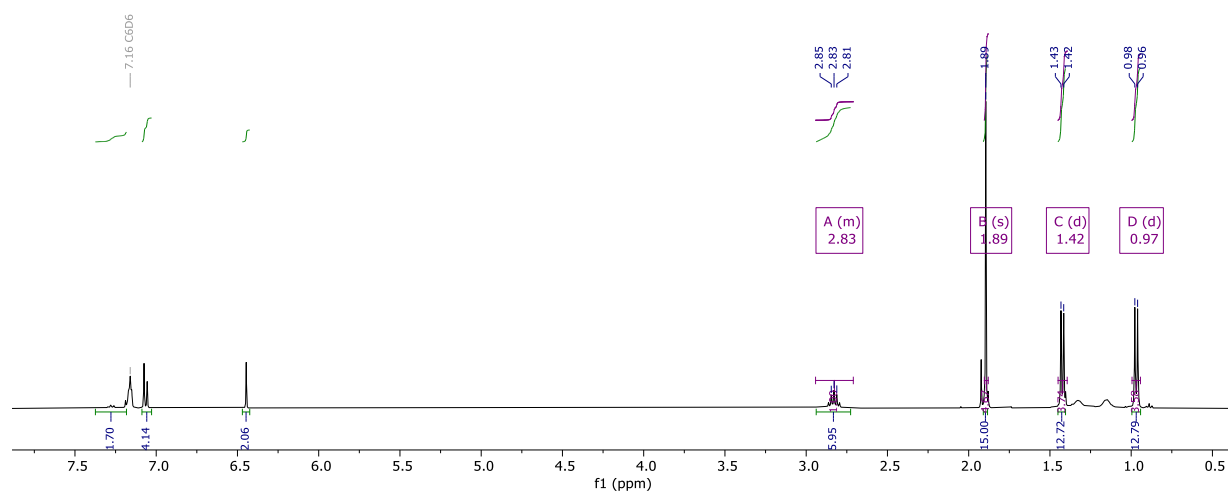
Figure S127: *In situ* ^{1}H-NMR spectrum (benzene-d$_6$) of the reaction Cp*$_2$AlH$_2$ + ^{i}Dipp (1:1, RT, 2 h).
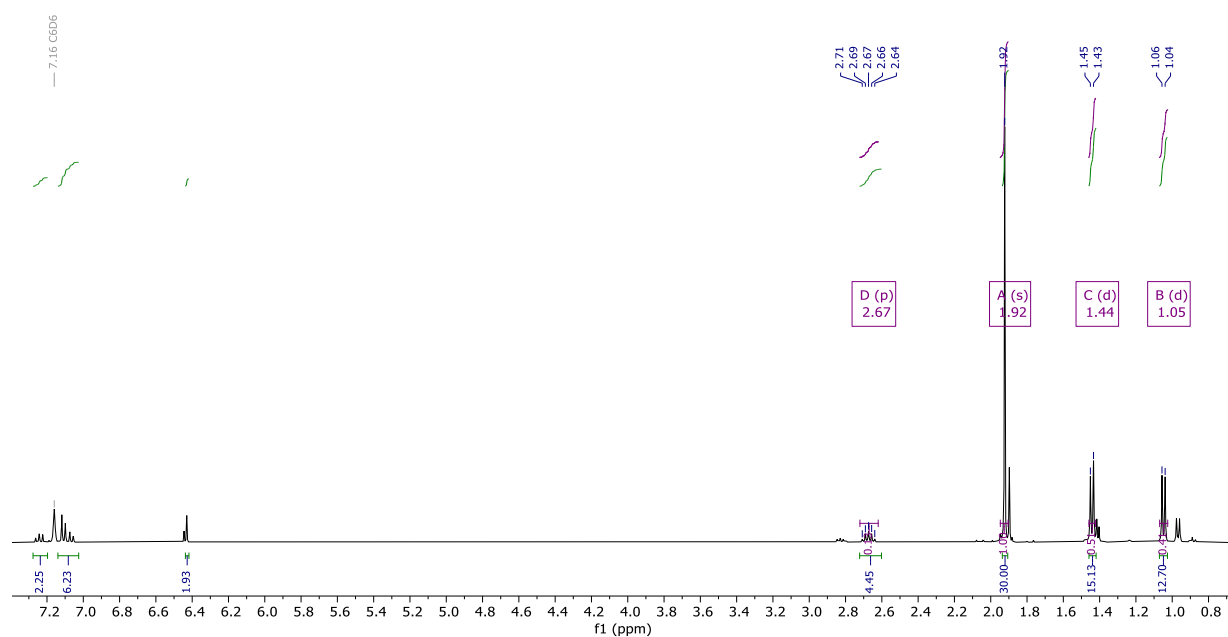
Figure S128: *In situ* ^{1}H-NMR spectrum (benzene-d$_6$) of the reaction Cp*$_2$AlH$_2$ + ^{i}Dipp (1:0.5, RT, 2 h).

6. Appendix
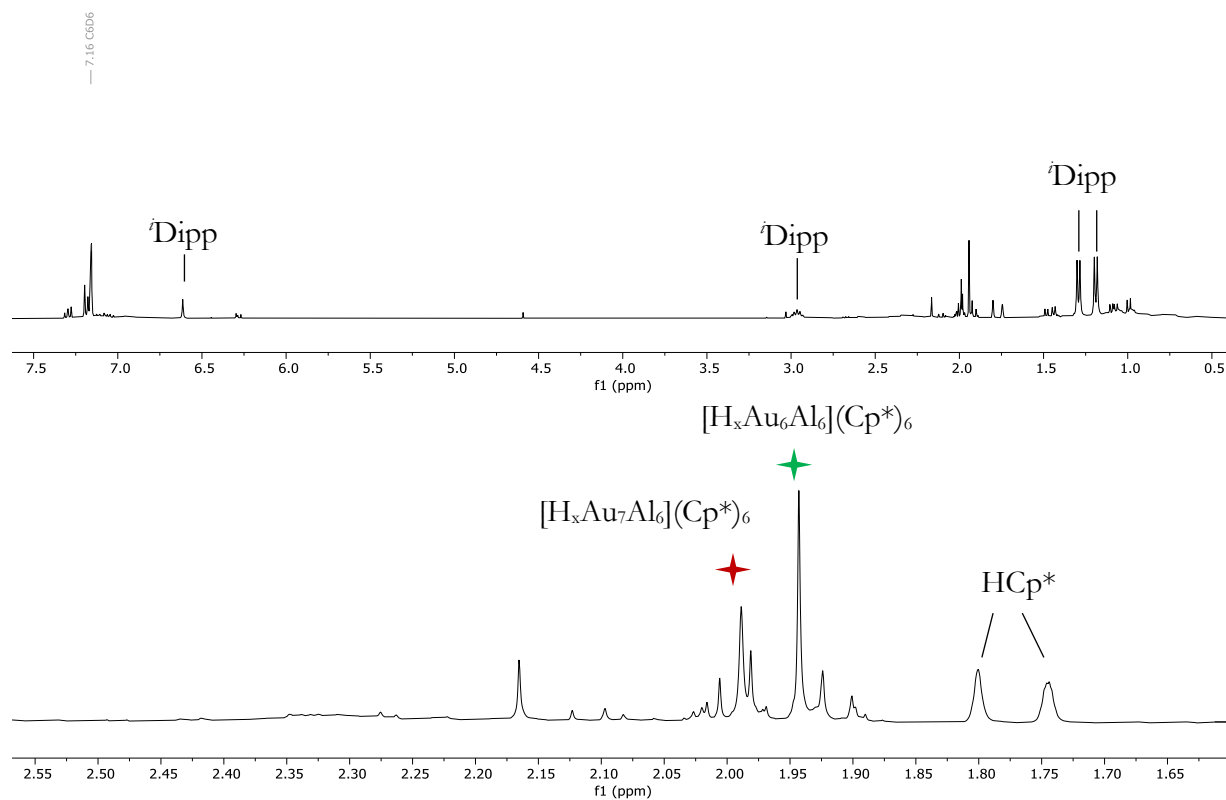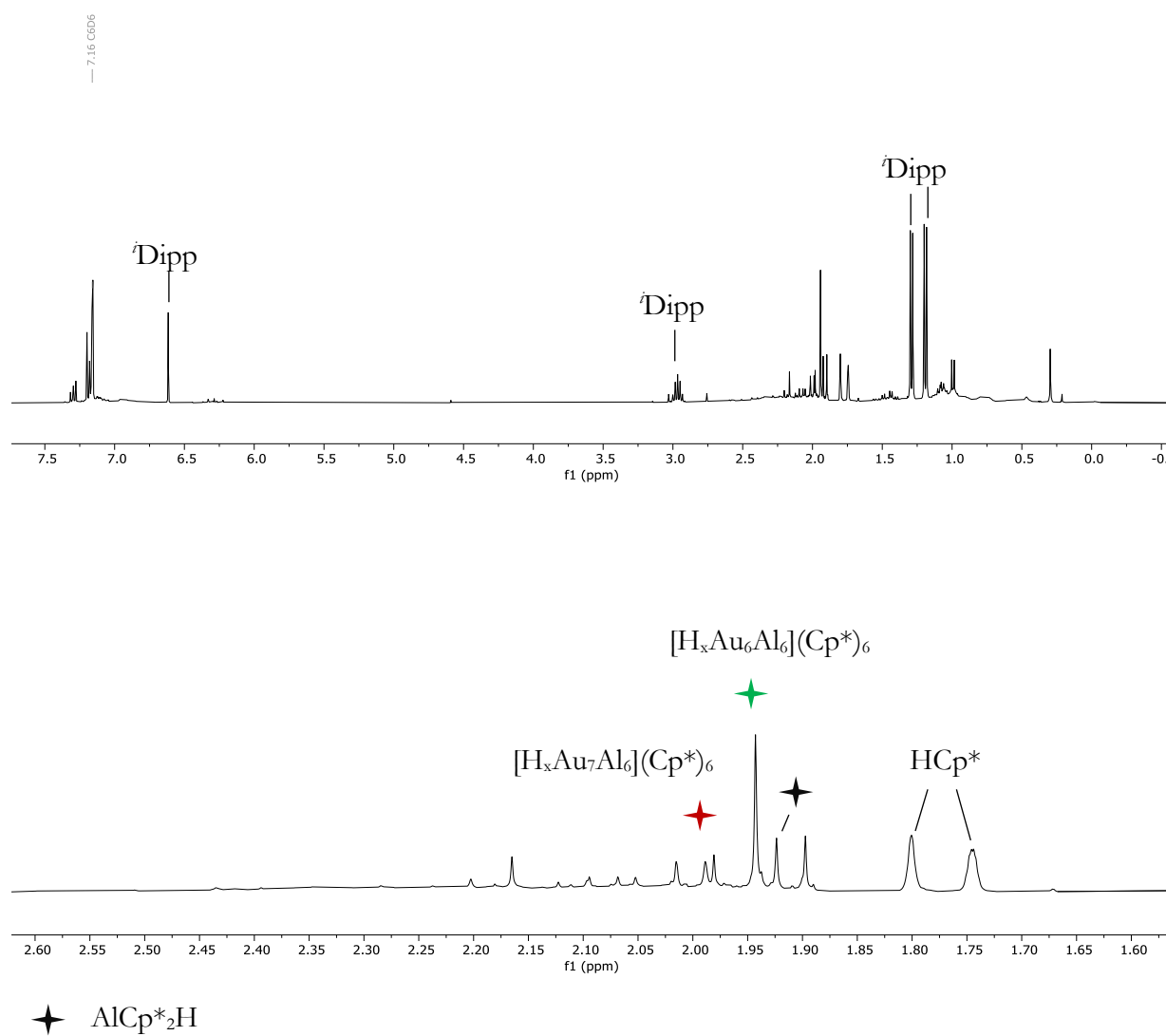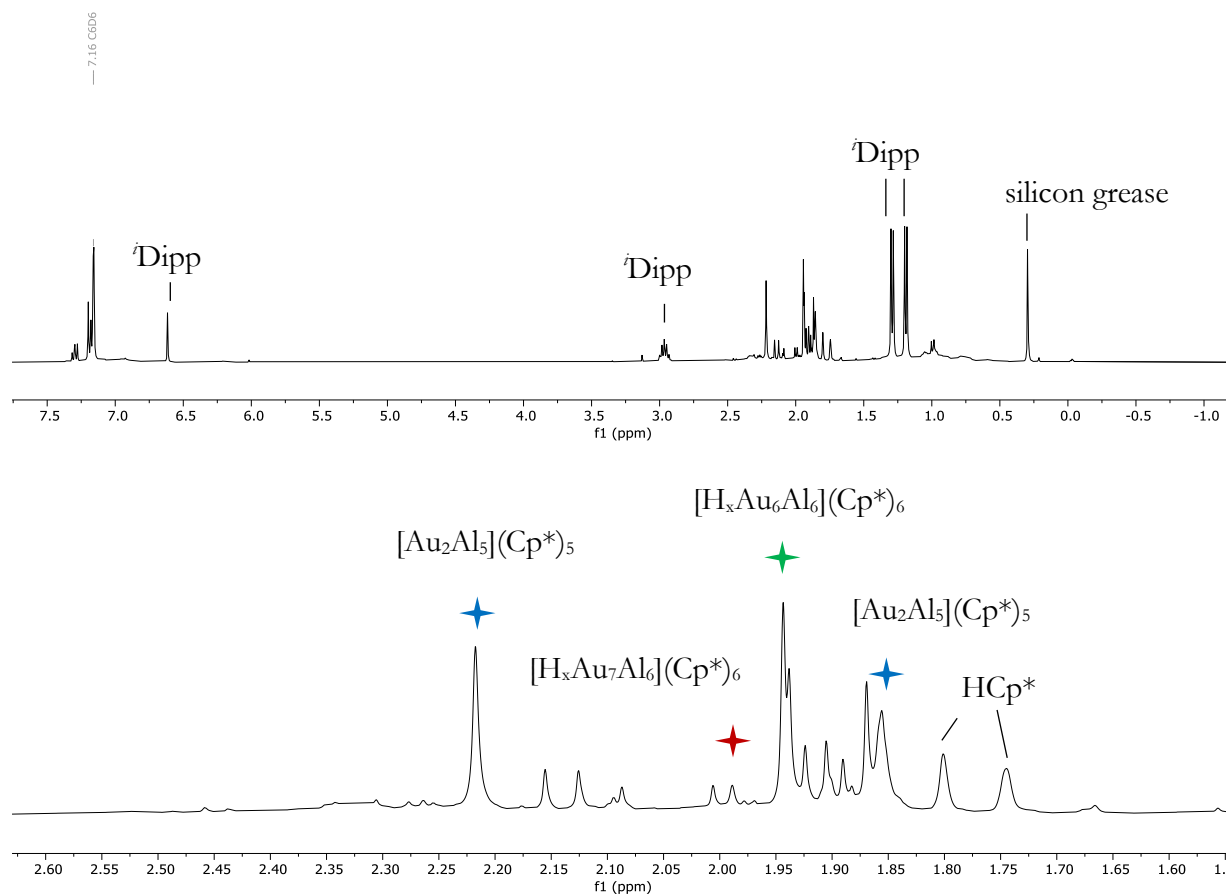
6.2 Supporting information for the chemical part
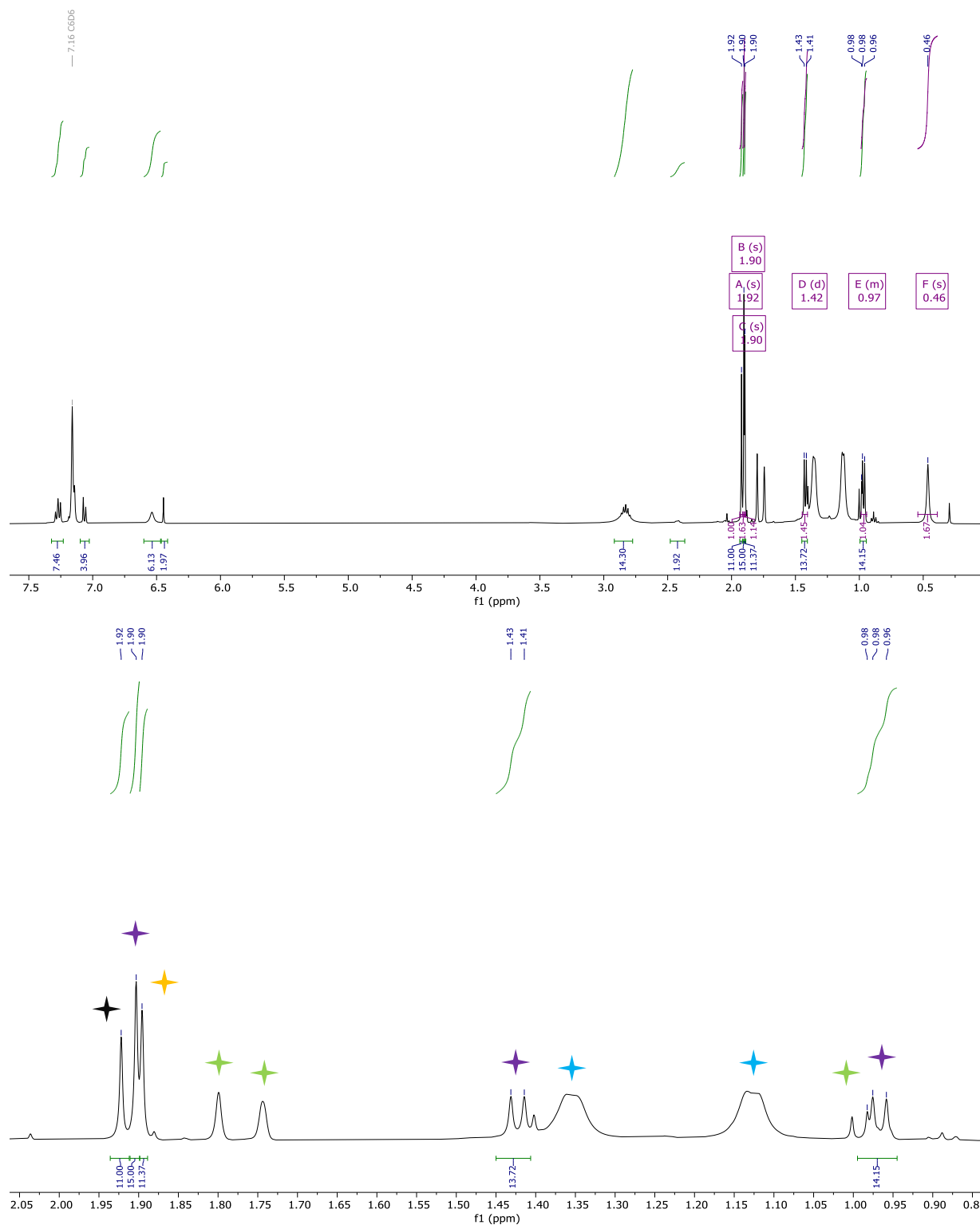
Figure S129: *In situ* ^{1}H-NMR spectrum (benzene-d$_6$) of the reaction Cp*$_2$AlH$_2$ + ^{i}Dipp (1:1.5, 75 °C, 2 h).

✦ HCp*   ✦ ^{i}DippAlCp*   ✦ AlCp*$_2$H   ✦ AlCp*   ✦ ^{i}Dipp (dynamically coordinated)

*Reaction of ^{i}Dipp with AlCp*H$_2$ in a 1:1 molar ratio leads to the adduct species ^{i}DippAlCp*H$_2$ as concluded from the integrals of the peaks in in situ ^{1}H-NMR analysis (Scheme S1a)). The*

corresponding reaction in a 0.5:1 ratio yields a product with Cp*:^{i}Dipp ratio of 2:1. A symmetric, dimeric compound with a bridging ^{i}Dipp ligand is suggested as structural motif for this adduct (Scheme S1 b)). Heating of AlCp*H$_2$ with an excess of ^{i}Dipp (1.5 eq.) in benzene-d$_6$ yields ^{1}H-NMR spectra with dynamically coordinated ^{i}Dipp ligand, ^{i}DippAlCp*H$_2$, AlCp*$_2$H, AlCp* and HCp* as organic side product. The results indicate that upon heating, ligand scrambling between two molecules of ^{i}DippAlCp*H$_2$ yields AlCp*$_2$H and Al$_x$(^{i}Dipp)$_y$H$_x$ aggregates (Scheme S1 c)). Indeed, [Al$_2$(^{i}Dipp)$_2$H$_5$]$^+$ is observed in LIFDI-MS of these solutions and the detected broad peak at 3.5-4 ppm in the ^{1}H-NMR spectrum might be attributed to the hydrides in such a species.[304] The observed broad peaks of dynamically coordinating ^{i}Dipp are consistent with literature data on coordination of ^{i}Dipp to AlH$_3$.[304] The species AlCp*$_2$H undergoes reductive elimination at elevated temperature to yield AlCp* and HCp*, just as observed in ^{1}H-NMR analysis (Scheme S1 c)).
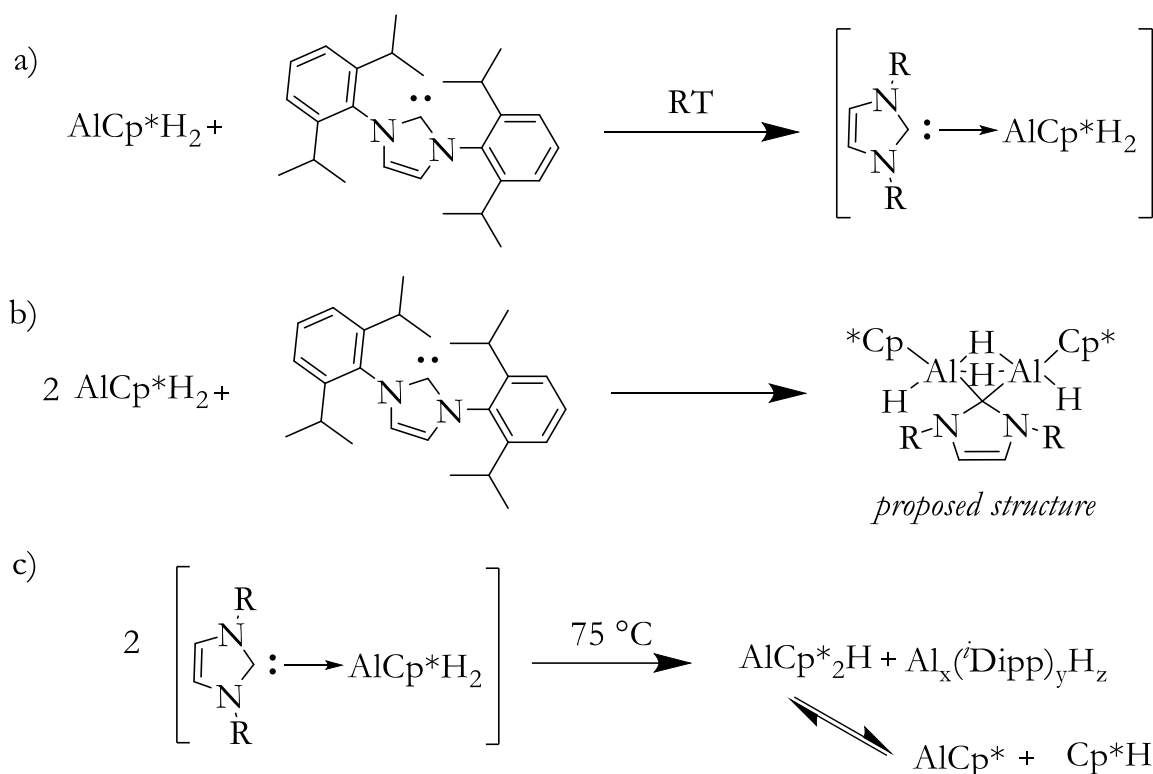
Scheme S1: Proposed reactions occurring in the ^{i}Dipp + Cp*AlH$_2$ system at the basis of *in situ* ^{1}H-NMR and LIFDI-MS data. a) 1:1 adduct formation between ^{i}Dipp and Cp*AlH$_2$. b) 1:2 adduct formation between ^{i}Dipp and Cp*AlH$_2$. c) Thermal degradation of the ^{i}DippAlCp*H$_2$ adduct leading to AlCp*H$_2$ and regeneration of AlCp*. R = 2,6-diisopropylphenyl.

6.2.18 Synthesis of trimetallic Cu/Au/Al clusters

The following supporting data documentation refers to pages 199-203.
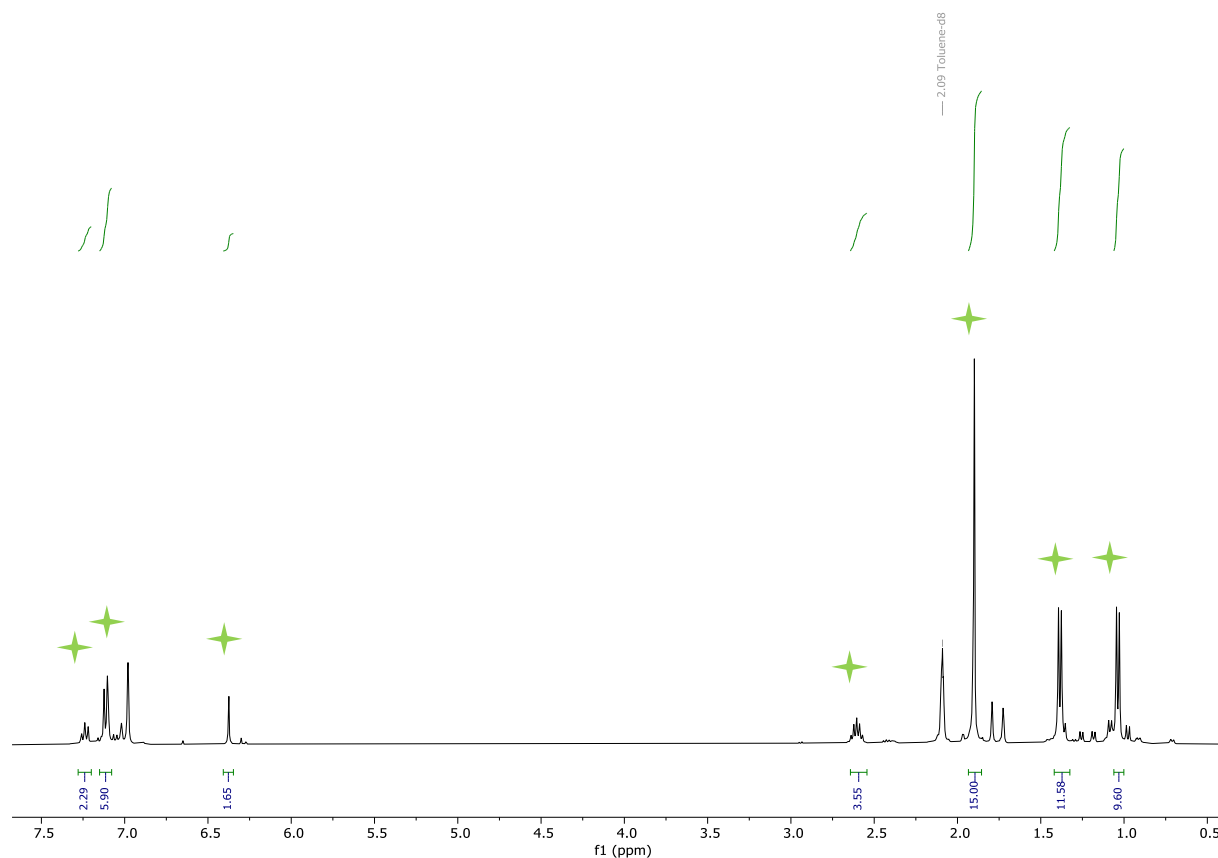
Figure S130: ^{1}H-NMR spectrum (toluene-d$_8$) of the reaction [Cu$_2$Al](Cp*)$_3$ + [^{t}DippAuH] (1:2) (75 °C, 2 h).

✦   [Cp*Cu^{t}Dipp]

The reaction between [Cu$_2$Al](Cp)$_3$ and [^{t}DippAuH] (1:2) results in cleavage of triangular [Cu$_2$Al](Cp*)$_3$ and formation of [Cp*Cu^{t}Dipp]. Unfortunately, no cluster species were identified in LIFDI-MS of the reaction solution, probably large nuclearity clusters are formed, which cannot be detected by LIFDI-MS at the current stage of methodical development.*

6.2 Supporting information for the chemical part
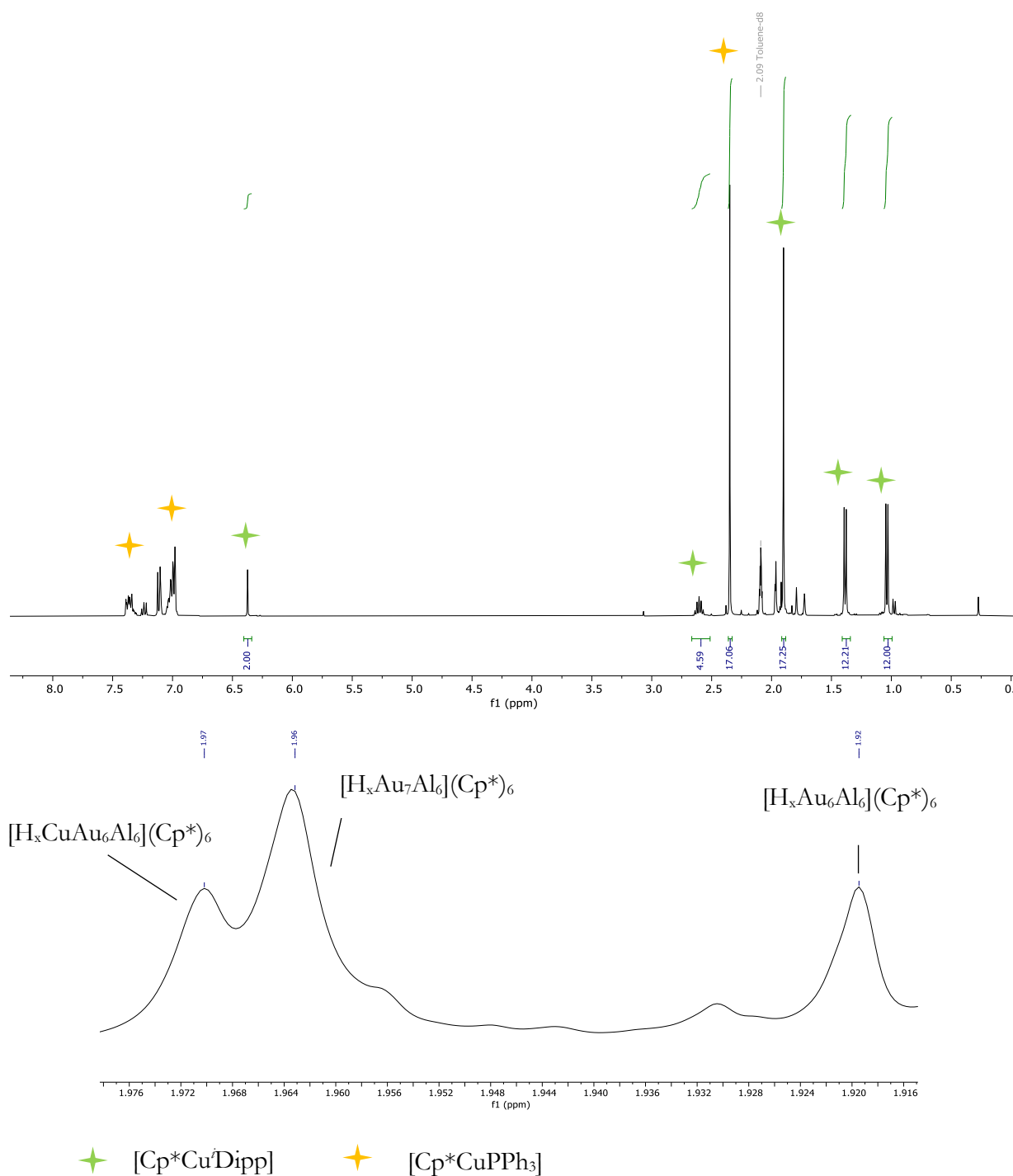
Figure S131: ^{1}H-NMR spectrum (toluene-d$_8$) of the reaction [Cu$_2$Al](Cp*)$_3$ + [^{i}DippAuH] + PPh$_3$ (1:1:1) (75 °C, 2 h, entry A in Table 7). Top: Full-range spectrum, bottom: enlarged region of the cluster attributed Cp* signals.
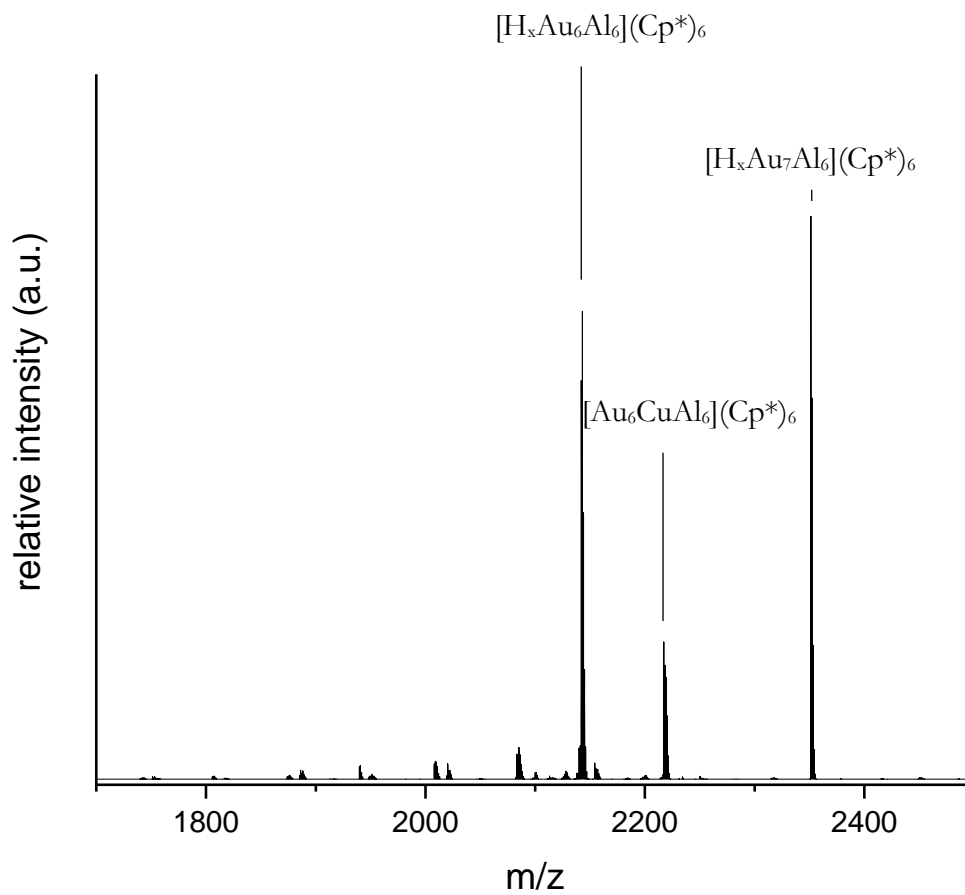
Figure S132: *In situ* LIFDI-MS spectrum of the reaction [Cu₂Al](Cp*)₃ + [^{i}DippAuH] + PPh₃ (1:1:1) (75 °C, 2 h, entry A in Table 7).

The reaction between [Cu₂Al](Cp)₃ and [^{i}DippAuH] (1:1) and 1 eq. of PPh₃ results in formation of [Cp*C(^{i}Dipp)] and [Cp*CuPPh₃]. Besides [H$_x$Au₆/₇Al₆](Cp*)₆, [Au₆CuAl₆](Cp*)₆ is detected in LIFDI-MS analysis and a signal in the corresponding in situ ¹H-NMR spectrum can be tentatively assigned to this species. Noteworthy, [Au₄CuAl₅](Cp*)₆ was isolated in single-crystalline form from the reaction solutions, but these results could not be reproduced so far.*

6. Appendix

6.2 Supporting information for the chemical part
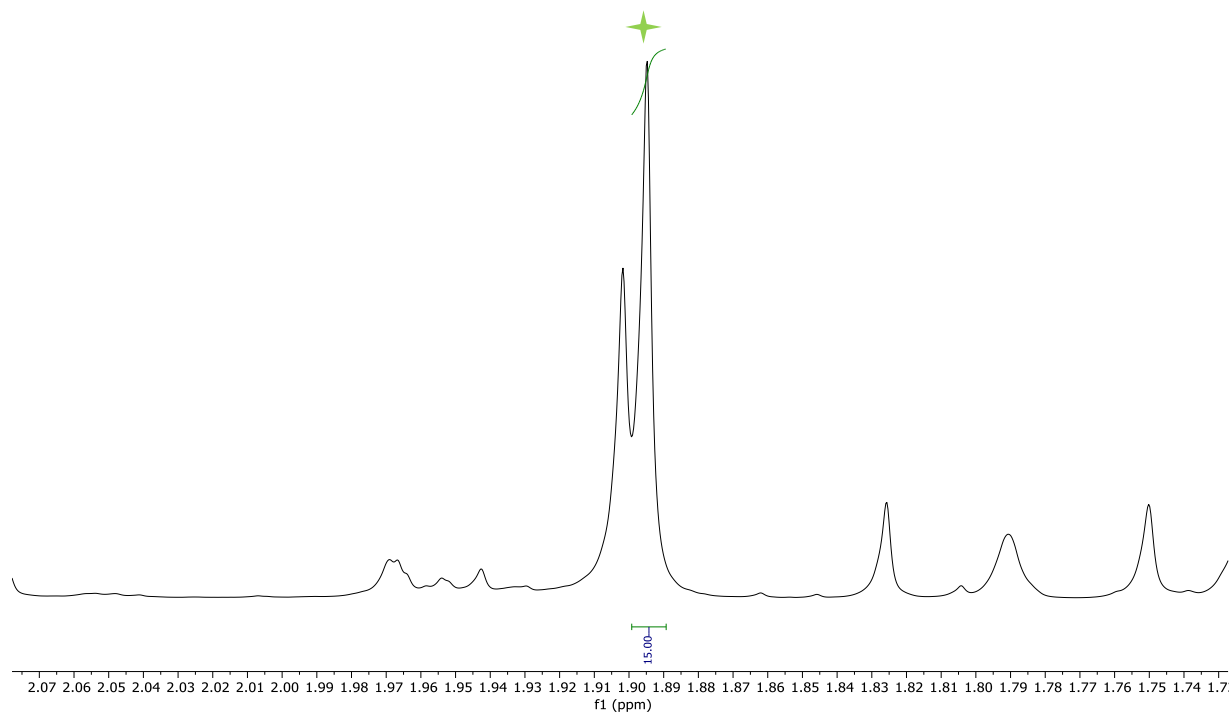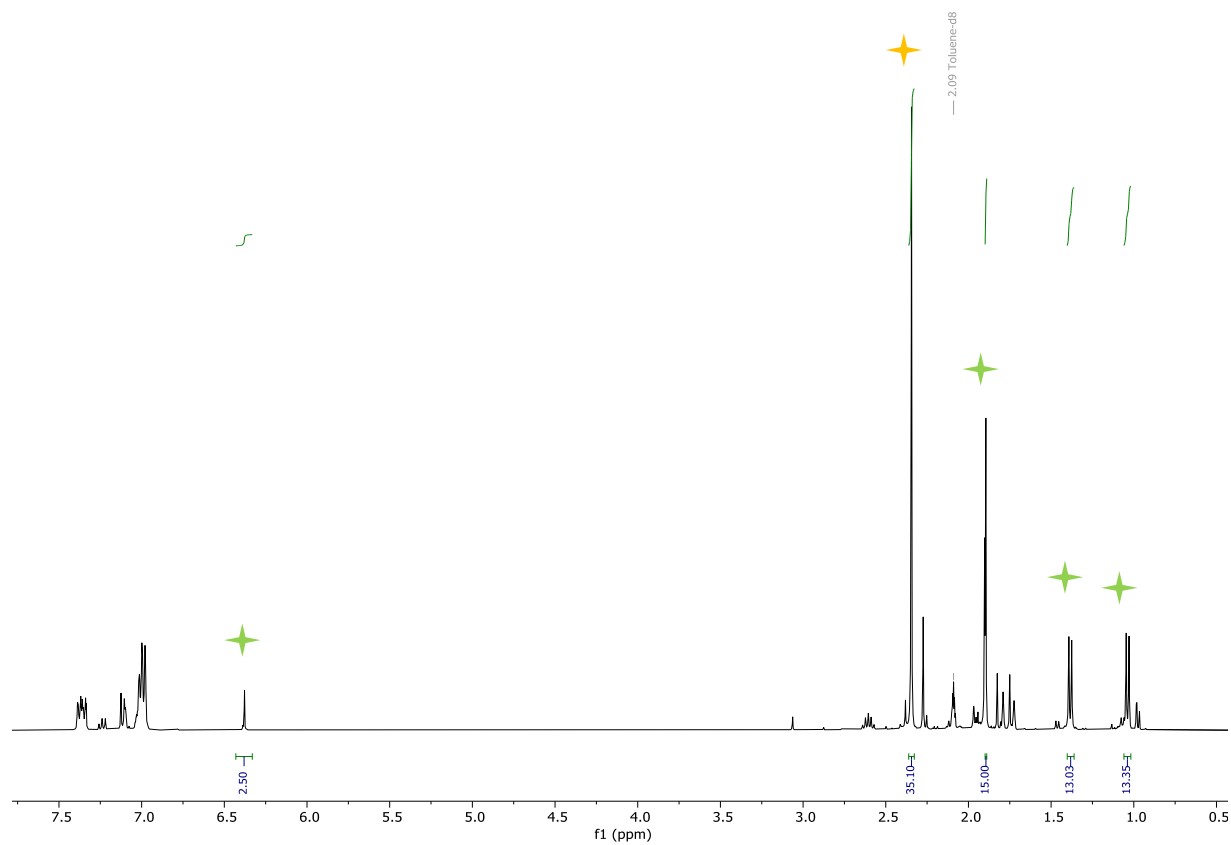
★ [Cp*Cu^{i}Dipp]   ★ [Cp*CuPPh$_3$]

Figure S133: ^{1}H-NMR spectrum (toluene-d$_8$) of the reaction [Cu$_2$Al](Cp*)$_3$ + [^{i}DippAuH] + PPh$_3$ (1.5:1:2) (75 °C, 2 h, entry B in Table 7). Top: Full-range spectrum, bottom: enlarged region of the

6. Appendix

6.2 Supporting information for the chemical part

Cp* attributed signals. The peak at 1.905 ppm is of unknown origin, but tentatively assigned to a Cu/Au/Al cluster compound.
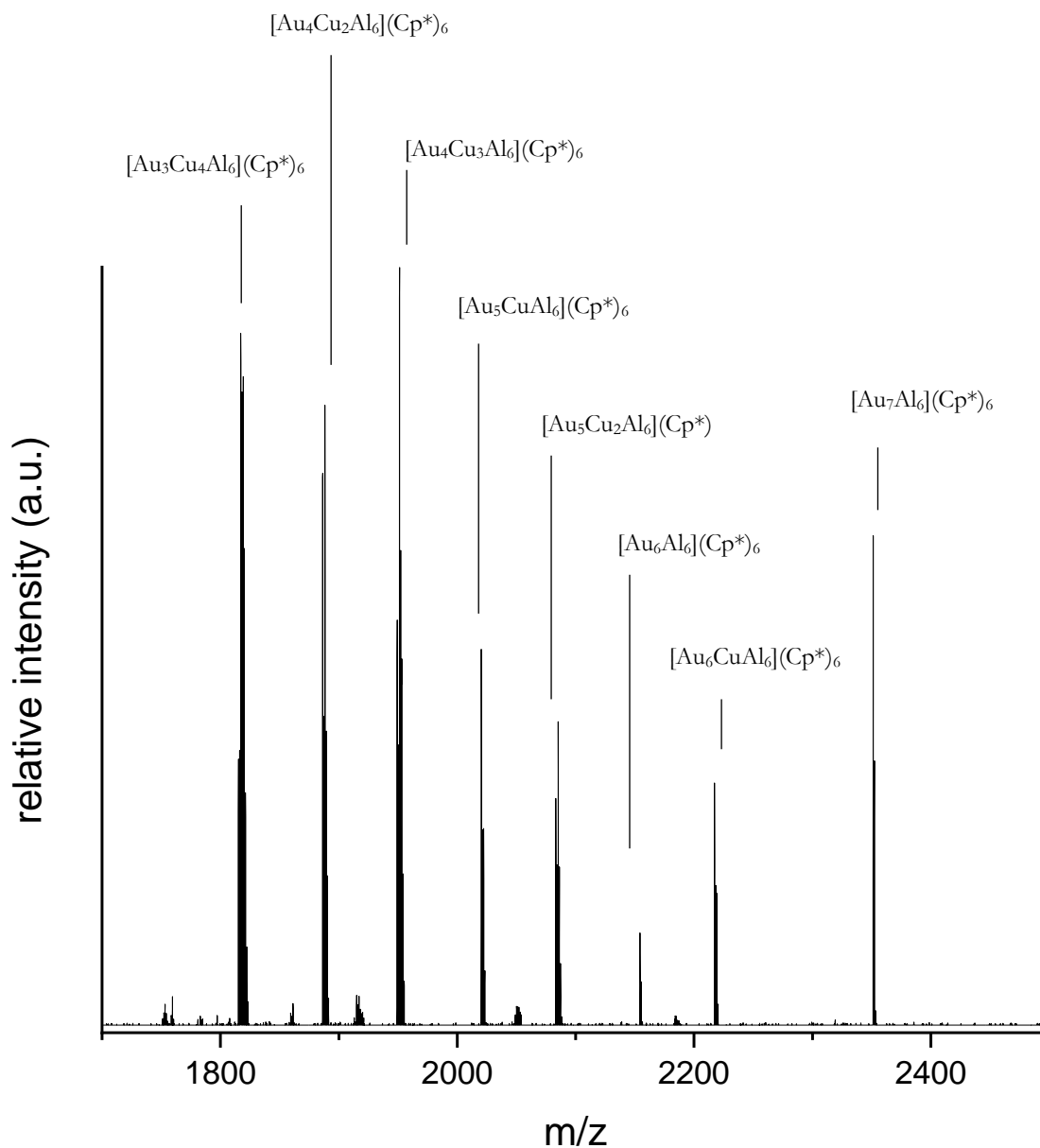
Figure S134: *In situ* LIFDI-MS spectrum of the reaction [Cu$_2$Al](Cp*)$_3$ + [^{i}DippAuH] + PPh$_3$ (1.5:1:2) (75 °C, 2 h, entry B in Table 7).

The reaction between [Cu$_2$Al](Cp)$_3$ and [^{i}DippAuH] (1.5:1) and 2 eq. of PPh$_3$ produces a ternary Cu/Au/Al cluster library as observed in LIFDI-MS analysis. In in situ ^{1}H-NMR analysis, formation of [Cp*CuPPh$_3$] and [Cp*Cu^{i}Dipp] is observed.*

6. Appendix

6.2 Supporting information for the chemical part
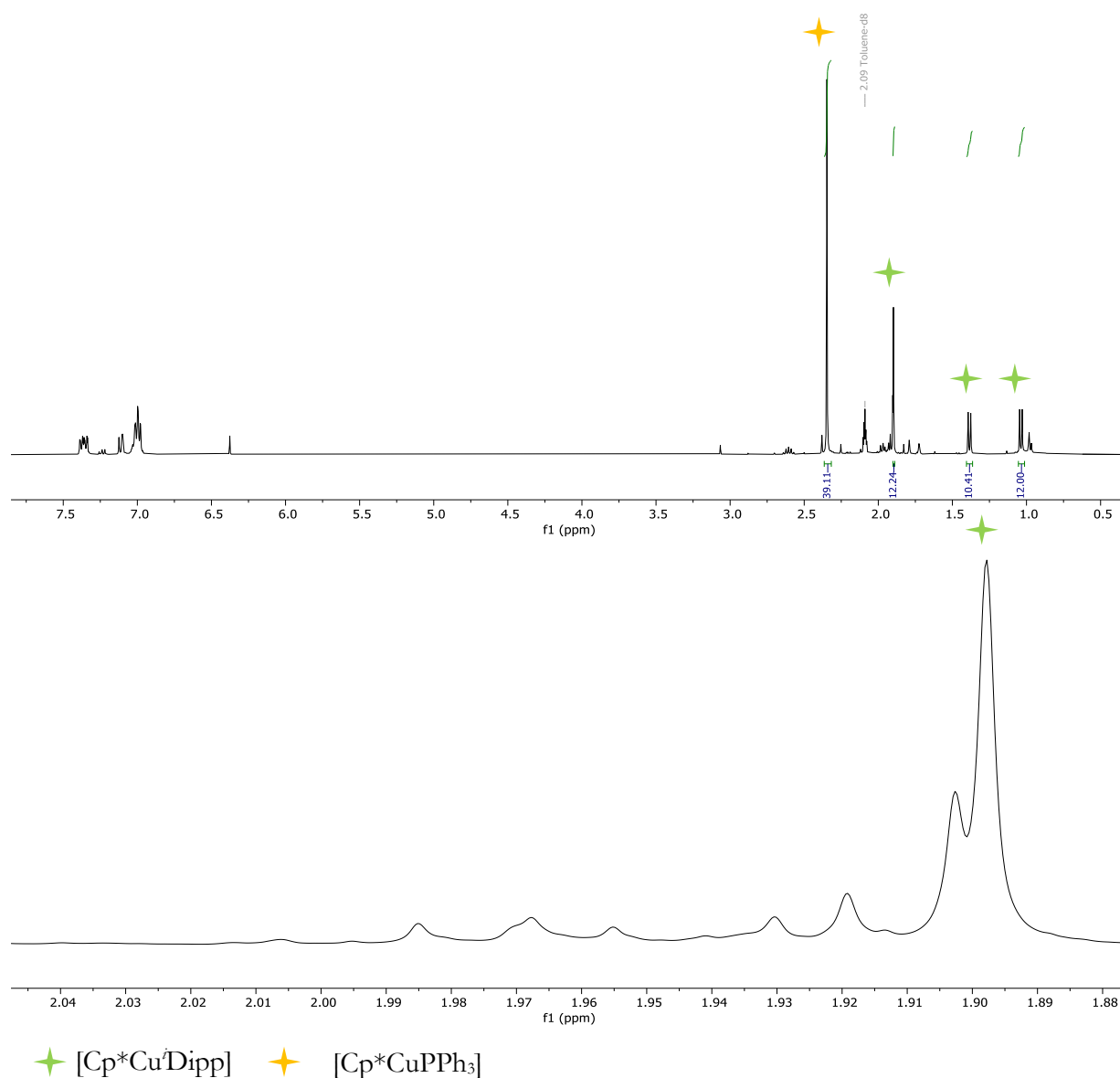
Figure S135: ^{1}H-NMR spectrum (toluene-d$_8$) of the reaction [Cu$_2$Al](Cp*)$_3$ + [^{i}DippAuH] + PPh$_3$ (5:4:5) (75 °C, 2 h, entry C in Table 7). Top: Full-range spectrum, bottom: Enlarged region of the Cp* attributed signals. The peak at 1.905 ppm is of unknown origin, but tentatively assigned to a Cu/Au/Al cluster compound. Corresponding LIFDI-MS data is found in Figure 82.

The reaction between [Cu$_2$Al](Cp)$_3$ and [^{i}DippAuH] (5:4) and 5 eq. of PPh$_3$ produces a ternary Cu/Au/Al cluster library as observed in LIFDI-MS analysis. In in situ ^{1}H-NMR analysis, formation of [Cp*CuPPh$_3$] and [Cp*Cu^{i}Dipp] is observed.*

7. References

Uncategorized References

1. Heiz, U.; Sanchez, A.; Abbet, S.; Schneider, W.-D., Catalytic oxidation of carbon monoxide on monodispersed platinum clusters: each atom counts. *J. Am. Chem. Soc.* **1999,** *121* (13), 3214-3217.
2. Sanchez, A.; Abbet, S.; Heiz, U.; Schneider, W.-D.; Häkkinen, H.; Barnett, R.; Landman, U., When gold is not noble: nanoscale gold catalysts. *J. Phys. Chem. A* **1999,** *103* (48), 9573-9578.
3. Lang, S. M.; Bernhardt, T. M., Gas phase metal cluster model systems for heterogeneous catalysis. *Phys. Chem. Chem. Phys.* **2012,** *14* (26), 9255-9269.
4. Wales, D. J.; Bogdan, T. V., Potential energy and free energy landscapes. *J. Phys. Chem. B* **2006,** *110* (42), 20765-20776.
5. Buchwalter, P.; Rosé, J.; Braunstein, P., Multimetallic catalysis based on heterometallic complexes and clusters. *Chem. Rev.* **2015,** *115* (1), 28-126.
6. Hollemann, A. F., Wiberg, Nils, Lehrbuch der Anorganischen Chemie. **2007,** (102nd edition), 1408.
7. Gourdon, O.; Gout, D.; Williams, D. J.; Proffen, T.; Hobbs, S.; Miller, G. J., Atomic distributions in the γ-brass structure of the Cu− Zn system: a structural and theoretical study. *Inorg. Chem.* **2007,** *46* (1),251-260.
8. Ponweiser, N.; Lengauer, C. L.; Richter, K. W., Re-investigation of phase equilibria in the system Al-Cu and structural analysis of the high-temperature phase η_1-Al$_{1-\delta}$Cu. *Intermetallics* **2011,** *19* (11), 1737-1746.
9. Hume-Rothery, W.; Raynor, G., The Structure of Metals and Alloys, *the Institute of Metals. London*, **1969**.
10. Grin, Y.; Wagner, F. R.; Armbrüster, M.; Kohout, M.; Leithe-Jasper, A.; Schwarz, U.; Wedig, U.; von Schnering, H. G., CuAl$_2$ revisited: Composition, crystal structure, chemical bonding, compressibility and Raman spectroscopy. *J. Solid State Chem.* **2006,** *179* (6), 1707-1719.
11. Arnberg, L.; Westman, S., Crystal perfection in a noncentrosymmetric alloy. Refinement and test of twinning of the γ-Cu$_9$Al$_4$ structure. *Acta Crystallogr. Sec. A* **1978,** *34* (3), 399-404.
12. Armbrüster, M.; Kovnir, K.; Friedrich, M.; Teschner, D.; Wowsnick, G.; Hahne, M.; Gille, P.; Szentmiklósi, L.; Feuerbacher, M.; Heggen, M., Al$_{13}$Fe$_4$ as a low-cost alternative for palladium in heterogeneous hydrogenation. *Nat. Mater.* **2012,** *11* (8), 690-693.
13. Armbrüster, M.; Kovnir, K.; Behrens, M.; Teschner, D.; Grin, Y.; Schlögl, R., Pd− Ga intermetallic compounds as highly selective semihydrogenation catalysts. *J. Am. Chem. Soc.* **2010,** *132* (42), 14745-14747.
14. Oroshnik, W. (**1978**). *U.S. Patent No. 4,092,366*. Washington, DC: U.S. Patent and Trademark Office.
15. Zhou, H.; Yang, X.; Li, L.; Liu, X.; Huang, Y.; Pan, X.; Wang, A.; Li, J.; Zhang, T., PdZn intermetallic nanostructure with Pd–Zn–Pd ensembles for highly active and chemoselective semi-hydrogenation of acetylene. *ACS Catal.* **2016,** *6* (2), 1054-1061.
16. Liu, Y.; Liu, X.; Feng, Q.; He, D.; Zhang, L.; Lian, C.; Shen, R.; Zhao, G.; Ji, Y.; Wang, D., Intermetallic Ni$_x$M$_y$ (M= Ga and Sn) Nanocrystals: A Non-precious Metal Catalyst for Semi-Hydrogenation of Alkynes. *Adv. Mater.* **2016,** *28* (23), 4747-4754.
17. Grin, J.; Burkhardt, U.; Ellner, M.; Peters, K., Refinement of the Fe$_4$Al$_{13}$ structure and its relationship to the quasihomological homeotypical structures. *Z. Kristallogr. Cryst. Mater.* **1994,** *209* (6), 479-487.
18. Armbrüster, M.; Borrmann, H.; Wedel, M.; Prots, Y.; Giedigkeit, R.; Gille, P., Refinement of the crystal structure of palladium gallium (1:1), PdGa. *Z. Kristallogr. NCS* **2010,** (4), 617-618.
19. Suzuki, N.; Ito, S., Synthesis and optical property of β-brass colloid. *J. Phys. Chem. B* **2006,** *110* (5), 2084-2086.
20. Chen, H.; Lin, L.; Li, H.; Li, J.; Lin, J.-M., Aggregation-induced structure transition of protein-stabilized zinc/copper nanoclusters for amplified chemiluminescence. *ACS nano* **2015,** *9* (2), 2173-2183.

7. References

21. Bhaskar, S. P.; Jagirdar, B. R., A journey from bulk brass to nanobrass: a comprehensive study showing structural evolution of various Cu/Zn bimetallic nanophases from the vaporization of brass. *J. Alloys Compd.* **2017,** *694*, 581-595.

22. Kattel, S.; Ramírez, P. J.; Chen, J. G.; Rodriguez, J. A.; Liu, P., Active sites for CO_2 hydrogenation to methanol on Cu/ZnO catalysts. *Science* **2017,** *355* (6331), 1296-1299.

23. Yang, Y.; Evans, J.; Rodriguez, J. A.; White, M. G.; Liu, P., Fundamental studies of methanol synthesis from CO_2 hydrogenation on Cu (111), Cu clusters, and Cu/ZnO $(000\bar{1})$. *Phys. Chem. Chem. Phys.* **2010,** *12* (33), 9909-9917.

24. Behrens, M.; Studt, F.; Kasatkin, I.; Kühl, S.; Hävecker, M.; Abild-Pedersen, F.; Zander, S.; Girgsdies, F.; Kurr, P.; Kniep, B.-L., The active site of methanol synthesis over $Cu/ZnO/Al_2O_3$ industrial catalysts. *Science* **2012,** *336* (6083), 893-897.

25. Hambrock, J.; Schröter, M. K.; Birkner, A.; Wöll, C.; Fischer, R. A., Nano-brass: Bimetallic copper/zinc colloids by a nonaqueous organometallic route using $[Cu(OCH(Me)CH_2NMe_2)_2]$ and Et_2Zn as precursors. *Chem. Mater.* **2003,** *15* (22), 4217-4222.

26. Cokoja, M.; Parala, H.; Schröter, M. K.; Birkner, A.; van den Berg, M. W.; Klementiev, K. V.; Grünert, W.; Fischer, R. A., Nano-brass colloids: synthesis by co-hydrogenolysis of $[CpCu(PMe_3)]$ with $[ZnCp*_2]$ and investigation of the oxidation behaviour of α/β-CuZn nanoparticles. *J. Mater. Chem.* **2006,** *16* (25), 2420-2428.

27. Schütte, K.; Meyer, H.; Gemel, C.; Barthel, J.; Fischer, R. A.; Janiak, C., Synthesis of Cu, Zn and Cu/Zn brass alloy nanoparticles from metal amidinate precursors in ionic liquids or propylene carbonate with relevance to methanol synthesis. *Nanoscale* **2014,** *6* (6), 3116-3126.

28. Vukojević, S.; Trapp, O.; Grunwaldt, J. D.; Kiener, C.; Schüth, F., Quasi-homogeneous methanol synthesis over highly active copper nanoparticles. *Angew. Chem. Int. Ed.* **2005,** *44* (48), 7978-7981.

29. Wales, D. J., Electronic structure of clusters. *Encycl. Inorg. Chem.* **2006**.

30. Scharfe, S.; Kraus, F.; Stegmaier, S.; Schier, A.; Faessler, T. F., Zintl ions, cage compounds, and intermetalloid clusters of group 14 and group 15 elements. *Angew. Chem. Int. Ed.* **2011,** *50* (16), 3630-3670.

31. Churchill, M. R.; Hutchinson, J. P., Crystal structure of tetrairidium dodecacarbonyl, $Ir_4(CO)_{12}$. An unpleasant case of disorder. *Inorg. Chem.* **1978,** *17* (12), 3528-3535.

32. Jena, P.; Sun, Q., Super atomic clusters: design rules and potential for building blocks of materials. *Chem. Rev.* **2018,** *118* (11), 5755-5870.

33. Khanna, S.; Jena, P., Atomic clusters: Building blocks for a class of solids. *Phys. Rev. B* **1995,** *51* (19), 13705.

34. Ekardt, W., The super-atom model: link between the metal atom and the infinite metal. *Z. Phys. B* **1996,** *103* (2), 305-312.

35. Bratsch, S. G., Standard electrode potentials and temperature coefficients in water at 298.15 K. *J. Phys. Chem. Ref. Data* **1989,** *18* (1), 1-21.

36. Cook, A. W.; Jones, Z. R.; Wu, G.; Scott, S. L.; Hayton, T. W., An organometallic Cu_{20} nanocluster: Synthesis, characterization, immobilization on silica, and "Click" chemistry. *J. Am. Chem. Soc.* **2018,** *140* (1), 394-400.

37. Chakrahari, K. K.; Liao, J. H.; Kahlal, S.; Liu, Y. C.; Chiang, M. H.; Saillard, J. Y.; Liu, C., $[Cu_{13}\{S_2CN^nBu_2\}_6(acetylide)_4]^+$: A Two-Electron Superatom. *Angew. Chem.* **2016,** *128* (47), 14924-14928.

38. Yuan, P.; Chen, R.; Zhang, X.; Chen, F.; Yan, J.; Sun, C.; Ou, D.; Peng, J.; Lin, S.; Tang, Z., Ether-Soluble Cu_{53} Nanoclusters as an Effective Precursor of High-Quality CuI Films for Optoelectronic Applications. *Angew. Chem.* **2019,** *131* (3), 845-849.

39. Qu, M.; Zhang, F. Q.; Wang, D. H.; Li, H.; Hou, J. J.; Zhang, X. M., Observation of Non-FCC Copper in Alkynyl-Protected Cu_{53} Nanoclusters. *Angew. Chem., Int. Ed.* **2020,** *59* (16), 6507-6512.

40. Nguyen, T.-A. D.; Jones, Z. R.; Goldsmith, B. R.; Buratto, W. R.; Wu, G.; Scott, S. L.; Hayton, T. W., A Cu_{25} nanocluster with partial Cu (0) character. *J. Am. Chem. Soc.* **2015,** *137* (41), 13319-13324.

41. Barik, S. K.; Huo, S.-C.; Wu, C.-Y.; Chiu, T.-H.; Liao, J.-H.; Wang, X.; Kahlal, S.; Saillard, J.-Y.; Liu, C.-W., Polyhydrido Copper Nanoclusters with a Hollow Icosahedral Core: $[Cu_{30}H_{18}\{E_2P(OR)_2\}_{12}]$(E= S or Se; R= n Pr, ^{i}Pr or ^{t}Bu). *Chem. Eur. J.* **2020,** *26* (46), 10471-10479.

42. Dhayal, R. S.; Liao, J.-H.; Kahlal, S.; Wang, X.; Liu, Y.-C.; Chiang, M.-H.; van Zyl, W. E.; Saillard, J.-Y.; Liu, C., $[Cu_{32}(H)_{20}\{S_2P(O^iPr)_2\}_{12}]$: The Largest Number of Hydrides Recorded in a Molecular Nanocluster by Neutron Diffraction. *Chem. Eur. J.* **2015,** *21* (23), 8369-8374.

7. References

43. Huang, R.-W.; Yin, J.; Dong, C.; Ghosh, A.; Alhilaly, M. J.; Dong, X.; Hedhili, M. N.; Abou-Hamad, E.; Alamer, B.; Nematulloev, S., $[Cu_{81}(PhS)_{46}(^tBuNH_2)_{10}(H)_{32}]^{3+}$ Reveals the Coexistence of Large Planar Cores and Hemispherical Shells in High-Nuclearity Copper Nanoclusters. *J. Am. Chem. Soc.* **2020,** *142* (19), 8696-8705.

44. Lee, S.; Bootharaju, M. S.; Deng, G.; Malola, S.; Baek, W.; Häkkinen, H.; Zheng, N.; Hyeon, T., $[Cu_{32}(PET)_{24}H_8Cl_2](PPh_4)_2$: A Copper Hydride Nanocluster with a Bisquare Antiprismatic Core. *J. Am. Chem. Soc.* **2020,** *142* (32), 13974-13981.

45. Li, Y. L.; Wang, J.; Luo, P.; Ma, X. H.; Dong, X. Y.; Wang, Z. Y.; Du, C. X.; Zang, S. Q.; Mak, T. C., Cu_{14} Cluster with Partial Cu(0) Character: Difference in Electronic Structure from Isostructural Silver Analog. *Adv. Sci.* **2019,** *6* (18), 1900833.

46. Vázquez-Vázquez, C.; Banobre-Lopez, M.; Mitra, A.; Lopez-Quintela, M. A.; Rivas, J., Synthesis of small atomic copper clusters in microemulsions. *Langmuir* **2009,** *25* (14), 8208-8216.

47. Vilar-Vidal, N.; Blanco, M. C.; Lopez-Quintela, M. A.; Rivas, J.; Serra, C., Electrochemical synthesis of very stable photoluminescent copper clusters. *J. Phys. Chem. C* **2010,** *114* (38), 15924-15930.

48. Wei, W.; Lu, Y.; Chen, W.; Chen, S., One-pot synthesis, photoluminescence, and electrocatalytic properties of subnanometer-sized copper clusters. *J. Am. Chem. Soc.* **2011,** *133* (7), 2060-2063.

49. Schmid, G., The relevance of shape and size of Au_{55} clusters. *Chem. Soc. Rev.* **2008,** *37* (9), 1909-1930.

50. Schmid, G.; Pfeil, R.; Boese, R.; Bandermann, F.; Meyer, S.; Calis, G.; Vandervelden, W., Au_{55} [P $(C_6H_5)_3]_{12}Cl_6$-a gold cluster of an exceptional size. *Chem. Ber./Recl.* **1981,** *114* (11), 3634-3642.

51. Yao, Q.; Chen, T.; Yuan, X.; Xie, J., Toward total synthesis of thiolate-protected metal nanoclusters. *Acc. Chem. Res.* **2018,** *51* (6), 1338-1348.

52. Yuan, X.; Zhang, B.; Luo, Z.; Yao, Q.; Leong, D. T.; Yan, N.; Xie, J., Balancing the rate of cluster growth and etching for gram-scale synthesis of thiolate-protected Au_{25} nanoclusters with atomic precision. *Angew. Chem.* **2014,** *126* (18), 4711-4715.

53. Luo, Z.; Nachammai, V.; Zhang, B.; Yan, N.; Leong, D. T.; Jiang, D.-e.; Xie, J., Toward understanding the growth mechanism: tracing all stable intermediate species from reduction of Au (I)–thiolate complexes to evolution of Au_{25} nanoclusters. *J. Am. Chem. Soc.* **2014,** *136* (30), 10577-10580.

54. Negishi, Y.; Nobusada, K.; Tsukuda, T., Glutathione-protected gold clusters revisited: bridging the gap between gold (I)− thiolate complexes and thiolate-protected gold nanocrystals. *J. Am. Chem. Soc.* **2005,** *127* (14), 5261-5270.

55. Heaven, M. W.; Dass, A.; White, P. S.; Holt, K. M.; Murray, R. W., Crystal structure of the gold nanoparticle $[N(C_8H_{17})_4][Au_{25}(SCH_2CH_2Ph)_{18}]$. *J. Am. Chem. Soc.* **2008,** *130* (12), 3754-3755.

56. Yan, N.; Xia, N.; Liao, L.; Zhu, M.; Jin, F.; Jin, R.; Wu, Z., Unraveling the long-pursued Au_{144} structure by x-ray crystallography. *Sci. Adv.* **2018,** *4* (10), eaat7259.

57. Zeng, C.; Li, T.; Das, A.; Rosi, N. L.; Jin, R., Chiral structure of thiolate-protected 28-gold-atom nanocluster determined by X-ray crystallography. *J. Am. Chem. Soc.* **2013,** *135* (27), 10011-10013.

58. Das, A.; Li, T.; Nobusada, K.; Zeng, C.; Rosi, N. L.; Jin, R., Nonsuperatomic $[Au_{23}(SC_6H_{11})_{16}]^-$ nanocluster featuring bipyramidal Au_{15} kernel and trimeric $Au_3(SR)_4$ motif. *J. Am. Chem. Soc.* **2013,** *135* (49), 18264-18267.

59. Song, Y.; Wang, S.; Zhang, J.; Kang, X.; Chen, S.; Li, P.; Sheng, H.; Zhu, M., Crystal structure of selenolate-protected $Au_{24}(SeR)_{20}$ nanocluster. *J. Am. Chem. Soc.* **2014,** *136* (8), 2963-2965.

60. Yang, H.; Wang, Y.; Edwards, A. J.; Yan, J.; Zheng, N., High-yield synthesis and crystal structure of a green Au_{30} cluster co-capped by thiolate and sulfide. *Chem. Commun.* **2014,** *50* (92), 14325-14327.

61. Jadzinsky, P. D.; Calero, G.; Ackerson, C. J.; Bushnell, D. A.; Kornberg, R. D., Structure of a thiol monolayer-protected gold nanoparticle at 1.1 Å resolution. *Science* **2007,** *318* (5849), 430-433.

62. Uhl, W., Tetrakis [bis(trimethylsilyl)methyl]dialan (4), eine Verbindung mit Aluminium— Aluminium-Bindung. *Z. Naturforsch. B.* **1988,** *43* (9), 1113-1118.

63. Schnöckel, H., Structures and properties of metalloid Al and Ga clusters open our eyes to the diversity and complexity of fundamental chemical and physical processes during formation and dissolution of metals. *Chem. Rev.* **2010,** *110* (7), 4125-4163.

64. Cui, C.; Roesky, H. W.; Schmidt, H. G.; Noltemeyer, M.; Hao, H.; Cimpoesu, F., Synthesis and structure of a monomeric aluminum (I) compound $[\{HC(CMeNAr)_2\}Al](Ar= 2,6–^iPr_2C_6H_3)$: A stable aluminum analogue of a carbene. *Angew. Chem.* **2000,** *112* (23), 4444-4446.

65. Arnold, J., Dalton Discussion 11: The renaissance of main group chemistry. *Dalton Trans.* **2008,** (33), 4334-4335.

7. References

66. Ecker, A.; Weckert, E.; Schnöckel, H., Synthesis and structural characterization of an Al$_{77}$ cluster. *Nature* **1997,** *387* (6631), 379-381.

67. Schnepf, A.; Schnöckel, H., Metalloid aluminum and gallium clusters: element modifications on the molecular scale? *Angew. Chem., Int. Ed.* **2002,** *41* (19), 3532-3554.

68. Dohmeier, C.; Loos, D.; Schnöckel, H., Aluminum (I) and gallium (I) compounds: syntheses, structures, and reactions. *Angew. Chem., Int. Ed. Engl.* **1996,** *35* (2), 129-149.

69. Gemel, C.; Steinke, T.; Cokoja, M.; Kempter, A.; Fischer, R. A., Transition metal chemistry of low valent group 13 organyls. *Eur. J. Inorg. Chem.* **2004,** *2004* (21), 4161-4176.

70. Vollet, J.; Hartig, J. R.; Schnöckel, H., Al$_{50}$C$_{120}$H$_{180}$: a pseudofullerene shell of 60 carbon atoms and 60 methyl groups protecting a cluster core of 50 aluminum atoms. *Angew. Chem., Int. Ed.* **2004,** *43* (24), 3186-3189.

71. Vollet, J.; Burgert, R.; Schnöckel, H., Al$_{20}$X$_{10}$ (X=Cl, Br): Snapshots of the Formation of Metalloid Clusters from Polyhedral Al$_n$X$_m$ Molecules. *Angew. Chem., Int. Ed.* **2005,** *44* (42), 6956-6960.

72. Purath, A.; Köppe, R.; Schnöckel, H., An Al$_{12}$R$_8^-$ cluster as an intermediate on the way from aluminium (I) compounds to aluminium metal. *Chem. Commun.* **1999,** (19), 1933-1934.

73. Flad, H.-J.; Schautz, F.; Wang, Y.; Dolg, M.; Savin, A., On the bonding of small group 12 clusters. *Eur. Phys. J. D* **1999,** *6* (2), 243-254.

74. Viklund, P.; Svensson, C.; Hull, S.; Simak, S. I.; Berastegui, P.; Häußermann, U., From V$_8$Ga$_{36.9}$Zn$_{4.1}$ and Cr$_8$Ga$_{29.8}$Zn$_{11.2}$ to Mn$_8$Ga$_{27.4}$Zn$_{13.6}$: A Remarkable Onset of Zn-Cluster Formation in an Intermetallic Framework. *Chem. Eur. J.* **2001,** *7* (23), 5143-5152.

75. Zhen, S.; Seff, K., Crystal Structure of a Zinc Sorption Complex of Cd^{2+}-Exchanged Zeolite X Containing Tetrahedral Cd$^{2+}_4$(μ_3-Zn^{0}Cd^{2+}Zn^0)$_4$ Clusters. *J. Phys. Chem. B* **1999,** *103* (31), 6493-6497.

76. Häussermann, U.; Viklund, P.; Svensson, C.; Eriksson, S.; Berastegui, P.; Lidin, S., The Hume–Rothery Compound Mn$_8$Ga$_{27.4}$Zn$_{13.6}$: Separated Zn$_{13}$-Clusters Interspersed in a Primitive Cubic Host Lattice. *Angew. Chem., Int. Ed.*, **1999,** 38 (4), 488-492.

77. Aguado, A.; Vega, A.; Lebon, A.; Von Issendorff, B., Insulating or metallic: Coexistence of different electronic phases in zinc clusters. *Angew. Chem.* **2015,** *127* (7), 2139-2143.

78. Vaida, M. E.; Marsh, B. M.; Leone, S. R., Nonmetal to metal transition and ultrafast charge carrier dynamics of Zn clusters on p-Si (100) by fs-XUV photoemission spectroscopy. *Nano Lett.* **2018,** *18* (7), 4107-4114.

79. Resa, I.; Carmona, E.; Gutierrez-Puebla, E.; Monge, A., Decamethyldizincocene, a stable compound of Zn (I) with a Zn-Zn bond. *Science* **2004,** *305* (5687), 1136-1138.

80. Hicks, J.; Underhill, E. J.; Kefalidis, C. E.; Maron, L.; Jones, C., A Mixed-Valence Tri-Zinc Complex, [LZnZnZnL](L= Bulky Amide), Bearing a Linear Chain of Two-Coordinate Zinc Atoms. *Angew. Chem., Int. Ed.* **2015,** *54* (34), 10000-10004.

81. Freitag, K.; Gemel, C.; Jerabek, P.; Oppel, I. M.; Seidel, R. W.; Frenking, G.; Banh, H.; Dilchert, K.; Fischer, R. A., The σ-Aromatic Clusters [Zn$_3$]$^+$ and [Zn$_2$Cu]: Embryonic Brass. *Angew. Chem., Int. Ed.* **2015,** *54* (14), 4370-4374.

82. Banh, H.; Dilchert, K.; Schulz, C.; Gemel, C.; Seidel, R. W.; Gautier, R.; Kahlal, S.; Saillard, J. Y.; Fischer, R. A., Atom-Precise Organometallic Zinc Clusters. *Angew. Chem., Int. Ed.* **2016,** *55* (10), 3285-3289.

83. Cui, P.; Hu, H.-S.; Zhao, B.; Miller, J. T.; Cheng, P.; Li, J., A multicentre-bonded [Zn(I)]$_8$ cluster with cubic aromaticity. *Nat. Commun.* **2015,** *6* (1), 1-5.

84. Eulenstein, A. R.; Franzke, Y. J.; Bügel, P.; Massa, W.; Weigend, F.; Dehnen, S., Stabilizing a metalloid {Zn$_{12}$} unit within a polymetallide environment in [K$_2$Zn$_{20}$Bi$_{16}$]$^{6-}$. *Nat. Commun.* **2020,** *11* (1), 1-8.

85. Mayer, K.; Weßing, J.; Fässler, T. F.; Fischer, R. A., Intermetalloid Clusters: Molecules and Solids in a Dialogue. *Angew. Chem., Int. Ed.* **2018,** *57* (44), 14372-14393.

86. Freitag, K.; Banh, H.; Gemel, C.; Seidel, R. W.; Kahlal, S.; Saillard, J.-Y.; Fischer, R. A., Molecular brass: Cu$_4$Zn$_4$, a ligand protected superatom cluster. *Chem. Commun.* **2014,** *50* (63), 8681-8684.

87. Robilotto, T. J.; Bacsa, J.; Gray, T. G.; Sadighi, J. P., Synthesis of a trigold monocation: an isolobal analogue of [H$_3$]$^+$. *Angew. Chem., Int. Ed.* **2012,** *51* (48), 12077-12080.

88. Banh, H.; Hornung, J.; Kratz, T.; Gemel, C.; Pöthig, A.; Gam, F.; Kahlal, S.; Saillard, J.-Y.; Fischer, R. A., Embryonic brass: pseudo two electron Cu/Zn clusters. *Chem. Sci.* **2018,** *9* (48), 8906-8913.

89. Steinke, T.; Gemel, C.; Winter, M.; Fischer, R. A., The Clusters [M$_a$(ECp*)$_b$](M= Pd, Pt; E= Al, Ga, In): Structures, Fluxionality, and Ligand Exchange Reactions. *Chem. Eur. J.* **2005,** *11* (5), 1636-1646.

7. References

90. Steinke, T.; Gemel, C.; Cokoja, M.; Winter, M.; Fischer, R. A., AlCp* as a Directing Ligand: C-H and Si-H Bond Activation at the Reactive Intermediate [Ni(AlCp*)₃]. *Angew. Chem., Int. Ed.* **2004,** *43* (17), 2299-2302.

91. Bollermann, T.; Puls, A.; Gemel, C.; Cadenbach, T.; Fischer, R. A., Reactions of cationic transition metal acetonitrile complexes [M(CH₃CN)ₙ]ᵐ⁺ with GaCp*: novel gallium complexes of iron, cobalt, copper and silver. *Dalton Trans.* **2009,** (8), 1372-1377.

92. Ganesamoorthy, C.; Weßing, J.; Kroll, C.; Seidel, R. W.; Gemel, C.; Fischer, R. A., The Intermetalloid Cluster [(Cp*AlCu)₆H₄], Embedding a Cu₆ Core Inside an Octahedral Al₆ Shell: Molecular Models of Hume–Rothery Nanophases. *Angew. Chem., Int. Ed.* **2014,** *53* (30), 7943-7947.

93. Weßing, J.; Ganesamoorthy, C.; Kahlal, S.; Marchal, R.; Gemel, C.; Cador, O.; Da Silva, A. C.; Da Silva, J. L.; Saillard, J. Y.; Fischer, R. A., The Mackay-Type Cluster [Cu₄₃Al₁₂](Cp*)₁₂: Open-Shell 67-Electron Superatom with Emerging Metal-Like Electronic Structure. *Angew. Chem., Int. Ed.* **2018,** *57* (44), 14630-14634.

94. Erickson, J. D.; Mednikov, E. G.; Ivanov, S. A.; Dahl, L. F., Isolation and Structural Characterization of a Mackay 55-Metal-Atom Two-Shell Icosahedron of Pseudo-Iₕ Symmetry, Pd₅₅L₁₂ (μ₃-CO)₂₀ (L= PR₃, R= Isopropyl): Comparative Analysis with Interior Two-Shell Icosahedral Geometries in Capped Three-Shell Pd₁₄₅, Pt-Centered Four-Shell Pd–Pt M₁₆₅, and Four-Shell Au₁₃₃ Nanoclusters. *J. Am. Chem. Soc.* **2016,** *138* (5), 1502-1505.

95. Kuo, K., Mackay, anti-Mackay, double-Mackay, pseudo-Mackay, and related icosahedral shell clusters. *Struct. Chem.* **2002,** *13* (3-4), 221-230.

96. Rollmann, G.; Gruner, M. E.; Hucht, A.; Meyer, R.; Entel, P.; Tiago, M. L.; Chelikowsky, J. R., Shellwise Mackay transformation in iron nanoclusters. *Phys. Rev. Lett.* **2007,** *99* (8), 083402.

97. Tran, N. T.; Powell, D. R.; Dahl, L. F., Nanosized Pd₁₄₅(CO)ₓ(PEt₃)₃₀ Containing a Capped Three-Shell 145-Atom Metal-Core Geometry of Pseudo Icosahedral Symmetry. *Angew. Chem., Int. Ed.* **2000,** *39* (22), 4121-4125.

98. Dass, A.; Theivendran, S.; Nimmala, P. R.; Kumara, C.; Jupally, V. R.; Fortunelli, A.; Sementa, L.; Barcaro, G.; Zuo, X.; Noll, B. C., Au₁₃₃(SPh-ᵗBu)₅₂ nanomolecules: X-ray crystallography, optical,electrochemical, and theoretical analysis. *J. Am. Chem. Soc.* **2015,** *137* (14), 4610-4613.

99. Muhr, M.; Hornung, J.; Weßing, J.; Jandl, C.; Gemel, C.; Fischer, R. A., Formation of a Propeller-Shaped Ni₄Ga₃ Cluster Supported by Transmetalation of Cp* from Ga to Ni. *Inorg. Chem.* **2020,** *59* (7), 5086-5092.

100. Weßing, J., From Intermetallics to Intermetalloid Clusters. *Dissertation* **2018,** Technische Universität München.

101. Lyon, J. T.; Gruene, P.; Fielicke, A.; Meijer, G.; Janssens, E.; Claes, P.; Lievens, P., Structures of silicon cluster cations in the gas phase. *J. Am. Chem. Soc.* **2009,** *131* (3), 1115-1121.

102. Schwarz, H., Chemistry with methane: concepts rather than recipes. *Angew. Chem., Int. Ed.* **2011,** *50* (43), 10096-10115.

103. Bouwen, W.; Thoen, P.; Vanhoutte, F.; Bouckaert, S.; Despa, F.; Weidele, H.; Silverans, R. E.; Lievens, P., Production of bimetallic clusters by a dual-target dual-laser vaporization source. *Rev. Sci. Intrum.* **2000,** *71* (1), 54-58.

104. Knight, W.; Clemenger, K.; de Heer, W. A.; Saunders, W. A.; Chou, M.; Cohen, M. L., Electronic shell structure and abundances of sodium clusters. *Phys. Rev. Lett.* **1984,** *52* (24), 2141.

105. Butcher, C. P.; Dinca, A.; Dyson, P. J.; Johnson, B. F.; Langridge-Smith, P. R.; McIndoe, J. S., A Strategy for Generating Naked-Metal Clusters for Gas-Phase Reactivity Studies by FTICR–MS. *Angew.Chem., Int. Ed.* **2003,** *42* (46), 5752-5755.

106. Chakraborty, P.; Pradeep, T., The emerging interface of mass spectrometry with materials. *NPG Asia Mater.* **2019,** *11* (1), 1-22.

107. Lechtken, A.; Neiss, C.; Kappes, M. M.; Schooss, D., Structure determination of gold clusters by trapped ion electron diffraction: Au₁₄⁻–Au₁₉⁻. *Phys. Chem. Chem. Phys.* **2009,** *11* (21), 4344-4350.

108. Fielicke, A.; Von Helden, G.; Meijer, G., Far-Infrared spectroscopy of isolated transition metal clusters. *Eur. Phys. J. D* **2005,** *34* (1), 83-88.

109. Passalacqua, R.; Parathoner, S.; Centi, G.; Halder, A.; Tyo, E. C.; Yang, B.; Seifert, S.; Vajda, S., Electrochemical behaviour of naked sub-nanometre sized copper clusters and effect of CO₂. *Catal. Sci.Technol.* **2016,** *6* (18), 6977-6985.

7. References

110. Katakuse, I.; Ichihara, T.; Fujita, Y.; Matsuo, T.; Sakurai, T.; Matsuda, H., Mass distributions of negative cluster ions of copper, silver, and gold. *Int. J. Mass Spectrom. Ion Processes* **1986,** *74* (1), 33-41.

111. Hirabayashi, S.; Ichihashi, M., Stability of Aluminum-Doped Copper Cluster Cations and Their Reactivity toward NO and O_2. *J. Phys. Chem. A* **2015,** *119* (32), 8557-8564.

112. Socaciu, L. D.; Hagen, J.; Le Roux, J.; Popolan, D.; Bernhardt, T. M.; Wöste, L.; Vajda, Š., Strongly cluster size dependent reaction behavior of CO with O_2 on free silver cluster anions. *J. Chem. Phys.* **2004,** *120* (5), 2078-2081.

113. Taketoshi, A.; Haruta, M., Size-and structure-specificity in catalysis by gold clusters. *Chem. Lett.* **2014,** *43* (4), 380-387.

114. Jena, N. K.; Chandrakumar, K.; Ghosh, S. K., Beyond the gold–hydrogen analogy: doping gold cluster with H-atom–O_2 activation and reduction of the reaction barrier for CO oxidation. *J. Phys. Chem. Lett.* **2011,** *2* (12), 1476-1480.

115. Cox, D.; Reichmann, K.; Trevor, D.; Kaldor, A., CO chemisorption on free gas phase metal clusters. *J. Chem. Phys.* **1988,** *88* (1), 111-119.

116. Bergeron, D.; Castleman Jr, A., Chemical formation of neutral complexes from charged metal clusters: reactions of pre-formed aluminum cluster anions with methyl iodide. *Chem. Phys. Lett.* **2003,** *371* (1-2), 189-193.

117. Zou, X. P.; Wang, L. N.; Li, X. N.; Liu, Q. Y.; Zhao, Y. X.; Ma, T. M.; He, S. G., Noble-Metal-Free Single-Atom Catalysts $CuAl_4O_{7-9}^-$ for CO Oxidation by O_2. *Angew. Chem.* **2018,** *130* (34), 11155-11159.

118. Li, X.-N.; Wang, L.-N.; Mou, L.-H.; He, S.-G., Catalytic CO oxidation by gas-phase metal oxide clusters. *J. Phys. Chem. A* **2019,** *123* (43), 9257-9267.

119. Day, V.; Day, R.; Kristoff, J.; Hirsekorn, F.; Muetterties, E., Fluxional, catalytically active metal cluster, heptakis (tert-butylisocyanide) tetranickel. *J. Am. Chem. Soc.* **1975,** *97* (9), 2571-2573.

120. Sappa, E., Reactions of ruthenium carbonyl clusters with alkynes. *J. Clust. Sci.* **1994,** *5* (2), 211-263.

121. Meister, G.; Rheinwald, G.; Stoeckli-Evans, H.; Süss-Fink, G., Hydrogen activation by arene ruthenium complexes in aqueous solution. Part 2. Build-up of cationic tri-and tetra-nuclear ruthenium clusters with hydrido ligands. *J. Am. Chem. Soc., Dalton Trans.* **1994,** (22), 3215-3223.

122. Beck, R.; Shoshani, M.; Johnson, S. A., Catalytic Hydrogen/Deuterium Exchange of Unactivated Carbon–Hydrogen Bonds by a Pentanuclear Electron-Deficient Nickel Hydride Cluster. *Angew. Chem.* **2012,** *124* (47), 11923-11926.

123. Mahoney, W. S.; Brestensky, D. M.; Stryker, J. M., Selective hydride-mediated conjugate reduction of. alpha.,. beta.-unsaturated carbonyl compounds using $[(Ph_3P)CuH]_6$. *J. Am. Chem. Soc.* **1988,** *110* (1), 291-293.

124. Ohki, Y.; Shimizu, Y.; Araake, R.; Tada, M.; Sameera, W.; Ito, J. I.; Nishiyama, H., $Co_6H_8(P^iPr_3)_6$: A Cobalt Octahedron with Face-Capping Hydrides. *Angew. Chem., Int. Ed.* **2016,** *55* (51), 15821-15825.

125. Weinert, B.; Mitzinger, S.; Dehnen, S., (Multi-) Metallic Cluster Growth. *Chem. Eur. J.* **2018,** *24* (34), 8470-8490.

126. Sun, Z.-M.; Zhao, Y.-F.; Li, J.; Wang, L.-S., Diversity of Functionalized Germanium Zintl Clusters: Syntheses and Theoretical Studies of $[Ge_9PdPPh_3]^{3-}$ and $[Ni@(Ge_9PdPPh_3)]^{2-}$. *J. Clust. Sci.* **2009,** *20* (3), 601-609.

127. Esenturk, E. N.; Fettinger, J.; Eichhorn, B., Synthesis and characterization of the $[Ni_6Ge_{13}(CO)_5]^{4-}$ and $[Ge_9Ni_2(PPh_3)]^{2-}$ Zintl ion clusters. *Polyhedron* **2006,** *25* (2), 521-529.

128. Benda, C. B.; Waibel, M.; Fässler, T. F., On the formation of intermetalloid clusters: titanocene (III) diammin as a versatile reactant toward nonastannide zintl clusters. *Angew. Chem.* **2015,** *127* (2), 532-536.

129. Wang, J. Q.; Stegmaier, S.; Wahl, B.; Fässler, T. F., Step-by-Step Synthesis of the Endohedral Stannaspherene $[Ir@Sn_{12}]^{3-}$ via the Capped Cluster Anion $[Sn_9Ir(cod)]^{3-}$. *Chem. Eur. J.* **2010,** *16* (6), 1793-1798.

130. Mayer, K.; Schiegerl, L. J.; Fässler, T. F., On the Reactivity of Silylated Ge_9 Clusters: Synthesis and Characterization of $[ZnCp^*(Ge_9\{Si(SiMe_3)_3\}_3)]$, $[CuP^iPr3(Ge_9\{Si (SiMe_3)_3\}_3)]$, and $[(CuP^iPr_3)_4 \{Ge_9 (SiPh_3)_2\}_2]$. *Chem. Eur. J* **2016,** *22* (52), 18794-18800.

7. References

131. He, H.; Klein, W.; Jantke, L. A.; Faessler, T. F., Metal-Centered Zintl Ions Isolated by Direct Extraction from Endohedral Intermetallic Precursor:$[Co_{1-x}@Sn_9]^{4-}$ ($x \approx 0.32$) and $[Co_2@Sn_{17}]^{5-}$. *Z. Anorg. Allg. Chem.* **2014,** *640* (14), 2864-2870.

132. Mitzinger, S.; Bandemehr, J.; Reiter, K.; McIndoe, J. S.; Xie, X.; Weigend, F.; Corrigan, J. F.; Dehnen, S., $(Ge_2P_2)^{2-}$: a binary analogue of 4 as a precursor to the ternary cluster anion $[Cd_3(Ge_3P)_3]^{3-}$. *Chem. Commun.* **2018,** *54* (12), 1421-1424.

133. Xu, L.; Sevov, S. C., Heteroatomic deltahedral clusters of main-group elements: synthesis and structure of the Zintl ions $[In_4Bi_5]^{3-}$, $[InBi_3]^{2-}$, and $[GaBi_3]^{2-}$. *Inorg. Chem.* **2000,** *39* (23), 5383-5389.

134. Mitzinger, S.; Broeckaert, L.; Massa, W.; Weigend, F.; Dehnen, S., Understanding of multimetallic cluster growth. *Nat. Commun.* **2016,** *7* (1), 1-10.

135. Toshima, N.; Yonezawa, T., Bimetallic nanoparticles—novel materials for chemical and physical applications. *New J. Chem.* **1998,** *22* (11), 1179-1201.

136. Schütte, K.; Doddi, A.; Kroll, C.; Meyer, H.; Wiktor, C.; Gemel, C.; van Tendeloo, G.; Fischer, R. A.; Janiak, C., Colloidal nickel/gallium nanoalloys obtained from organometallic precursors in conventional organic solvents and in ionic liquids: noble-metal-free alkyne semihydrogenation catalysts. *Nanoscale* **2014,** *6* (10), 5532-5544.

137. Cokoja, M.; Parala, H.; Schröter, M.-K.; Birkner, A.; van den Berg, M. W.; Grünert, W.; Fischer, R. A., Nanometallurgy of Colloidal Aluminides: Soft Chemical Synthesis of $CuAl_2$ and α/β-CuAl Colloids by Co-Hydrogenolysis of $(AlCp^*)_4$ with $[CpCu(PMe_3)]$. *Chem. Mater.* **2006,** *18* (6), 1634-1642.

138. Vitulli, G.; Bernini, M.; Bertozzi, S.; Pitzalis, E.; Salvadori, P.; Coluccia, S.; Martra, G., Nanoscale copper particles derived from solvated Cu atoms in the activation of molecular oxygen. *Chem. Mater.* **2002,** *14* (3), 1183-1186.

139. Ponce, A. A.; Klabunde, K. J., Chemical and catalytic activity of copper nanoparticles prepared via metal vapor synthesis. *J. Mol. Catal. A Chem.* **2005,** *225* (1), 1-6.

140. Deveson, A.; Dehnen, S.; Fenske, D., Syntheses and structures of four new copper (I)–selenium clusters: size dependence of the cluster on the reaction conditions. *J. Chem. Soc., Dalton Trans.* **1997,** (23), 4491-4498.

141. Zhang, L.; Li, Z.; Zhang, Y.; Paau, M. C.; Hu, Q.; Gong, X.; Shuang, S.; Dong, C.; Peng, X.; Choi, M. M., High-performance liquid chromatography coupled with mass spectrometry for analysis of ultrasmall palladium nanoparticles. *Talanta* **2015,** *131*, 632-639.

142. Black, D. M.; Robles, G.; Lopez, P.; Bach, S. B.; Alvarez, M.; Whetten, R. L., Liquid chromatography separation and mass spectrometry detection of silver-lipoate $Ag_{29}(LA)_{12}$ nanoclusters: Evidence of isomerism in the solution phase. *Anal. Chem.* **2018,** *90* (3), 2010-2017.

143. Hossain, S.; Niihori, Y.; Nair, L. V.; Kumar, B.; Kurashige, W.; Negishi, Y., Alloy clusters: Precise synthesis and mixing effects. *Acc. Chem. Res.* **2018,** *51* (12), 3114-3124.

144. Domon, B.; Aebersold, R., Mass spectrometry and protein analysis. *Science* **2006,** *312* (5771), 212-217.

145. Aebersold, R.; Mann, M., Mass spectrometry-based proteomics. *Nature* **2003,** *422* (6928), 198-207.

146. Lee, C. W.; Yang, K. D.; Nam, D. H.; Jang, J. H.; Cho, N. H.; Im, S. W.; Nam, K. T., Defining a materials database for the design of copper binary alloy catalysts for electrochemical CO_2 conversion. *Adv. Mater.* **2018,** *30* (42), 1704717.

147. Gross, J. H., From the discovery of field ionization to field desorption and liquid injection field desorption/ionization-mass spectrometry—A journey from principles and applications to a glimpse into the future. *Eur. J. Mass Spectrom.* **2020,** *26* (4), 241-273.

148. Gross, J. H.; Nieth, N.; Linden, H. B.; Blumbach, U.; Richter, F. J.; Tauchert, M. E.; Tompers, R.; Hofmann, P., Liquid injection field desorption/ionization of reactive transition metal complexes. *Anal. Bioanal. Chem.* **2006,** *386* (1), 52-58.

149. Hu, Q.; Noll, R. J.; Li, H.; Makarov, A.; Hardman, M.; Graham Cooks, R., The Orbitrap: a new mass spectrometer. *J. Mass Spectrom.* **2005,** *40* (4), 430-443.

150. Olsen, J. V.; Macek, B.; Lange, O.; Makarov, A.; Horning, S.; Mann, M., Higher-energy C-trap dissociation for peptide modification analysis. *Nat. Methods* **2007,** *4* (9), 709-712.

151. Geiger, T.; Cox, J.; Mann, M., Proteomics on an Orbitrap benchtop mass spectrometer using all-ion fragmentation. *Mol. Cell. Proteom.* **2010,** *9* (10), 2252-2261.

7. References

152. Wu, C. C.; MacCoss, M. J., Shotgun proteomics: tools for the analysis of complex biological systems. *Curr. Opin. Mol. Ther.* **2002,** *4* (3), 242-250.

153. Käll, L.; Canterbury, J. D.; Weston, J.; Noble, W. S.; MacCoss, M. J., Semi-supervised learning for peptide identification from shotgun proteomics datasets. *Nat. Methods* **2007,** *4* (11), 923-925.

154. Diedrich, J. K.; Pinto, A. F.; Yates III, J. R., Energy dependence of HCD on peptide fragmentation: stepped collisional energy finds the sweet spot. *J. Am. Chem. Soc. Mass Spectrom.* **2013,** *24* (11), 1690-1699.

155. Bantscheff, M.; Schirle, M.; Sweetman, G.; Rick, J.; Kuster, B., Quantitative mass spectrometry in proteomics: a critical review. *Anal. Bioanal. Chem.* **2007,** *389* (4), 1017-1031.

156. Thompson, A.; Schäfer, J.; Kuhn, K.; Kienle, S.; Schwarz, J.; Schmidt, G.; Neumann, T.; Hamon, C., Tandem mass tags: a novel quantification strategy for comparative analysis of complex protein mixtures by MS/MS. *Anal. Chem.* **2003,** *75* (8), 1895-1904.

157. Heumann, K. G., Isotope dilution mass spectrometry. *Int. J. Mass Spectrom. Ion Processes* **1992,** *118*, 575-592.

158. Chen, P., Electrospray ionization tandem mass spectrometry in high-throughput screening of homogeneous catalysts. *Angew. Chem., Int. Ed.* **2003,** *42* (25), 2832-2847.

159. McIndoe, S., Spectroscopic and mass spectrometric methods for the characterisation of metal clusters. *Coord. Chem. Rev.* **2000,** *200*, 901-932.

160. Feichtinger, D.; Plattner, D. A., Direkter Nachweis von Mnv-oxo-salen-Komplexen. *Angew. Chem.* **1997,** *109* (16), 1796-1798.

161. Spence, T. G.; Burns, T. D.; Posey, L. A., Controlled Synthesis of Transition-Metal Ion Complex/Solvent Clusters by Electrospray Ionization. *J. Phys. Chem. A* **1997,** *101* (2), 139-144.

162. Hinderling, C.; Feichtinger, D.; Plattner, D. A.; Chen, P., A Combined Gas-Phase, Solution-Phase, and Computational Study of C− H Activation by Cationic Iridium (III) Complexes. *J. Am. Chem. Soc.* **1997,** *119* (44), 10793-10804.

163. Hinderling, C.; Chen, P., Rasches Screening von Olefinpolymerisationskatalysator-Bibliotheken durch Elektrospray-Ionisations-Tandem-Massenspektrometrie. *Angew. Chem.* **1999,** *111* (15), 2393-2396.

164. Dyson, P. J.; Hearley, A. K.; Johnson, B. F.; Khimyak, T.; McIndoe, J. S.; Langridge-Smith, P. R., Mass spectrometric method for the rapid characterization of transition metal carbonyl cluster reaction mixtures. *Organometallics* **2001,** *20* (19), 3970-3974.

165. Dyson, P. J.; Johnson, B. F.; McIndoe, J. S.; Langridge-Smith, P. R., Energy-dependent electrospray ionisation mass spectrometry: applications in transition metal carbonyl chemistry. *Rapid Commun. Mass Spectrom.* **2000,** *14* (5), 311-313.

166. Yao, Q.; Yuan, X.; Fung, V.; Yu, Y.; Leong, D. T.; Jiang, D.-e.; Xie, J., Understanding seed-mediated growth of gold nanoclusters at molecular level. *Nat. Commun.* **2017,** *8* (1), 1-11.

167. Cao, Y.; Guo, J.; Shi, R.; Waterhouse, G. I.; Pan, J.; Du, Z.; Yao, Q.; Wu, L.-Z.; Tung, C.-H.; Xie, J., Evolution of thiolate-stabilized Ag nanoclusters from Ag-thiolate cluster intermediates. *Nat. Commun.* **2018,** *9* (1), 1-6.

168. Bootharaju, M. S.; Joshi, C. P.; Alhilaly, M. J.; Bakr, O. M., Switching a nanocluster core from hollow to nonhollow. *Chem. Mater.* **2016,** *28* (10), 3292-3297.

169. Niihori, Y.; Uchida, C.; Kurashige, W.; Negishi, Y., High-resolution separation of thiolate-protected gold clusters by reversed-phase high-performance liquid chromatography. *Phys. Chem. Chem. Phys.* **2016,** *18* (6), 4251-4265.

170. Balkenhohl, F.; von dem Bussche-Hünnefeld, C.; Lansky, A.; Zechel, C., Kombinatorische Synthese niedermolekularer organischer Verbindungen. *Angew. Chem.* **1996,** *108* (20), 2436-2488.

171. Ding, K.; Du, H.; Yuan, Y.; Long, J., Combinatorial chemistry approach to chiral catalyst engineering and screening: Rational design and serendipity. *Chem. Eur. J.* **2004,** *10* (12), 2872-2884.

172. Reetz, M. T., Combinatorial and evolution-based methods in the creation of enantioselective catalysts. *Angew. Chem., Int. Ed.* **2001,** *40* (2), 284-310.

173. Furka, Á., Combinatorial chemistry: 20 years on…. *Drug Discov. Today* **2002,** *7* (1), 1-4.

174. Wilson, S. R.; Czarnik, A. W., *Combinatorial chemistry: synthesis and application.* **1997,** John Wiley & Sons.

175. Reetz, M. T., Combinatorial transition-metal catalysis: mixing monodentate ligands to control enantio-, diastereo-, and regioselectivity. *Angew. Chem., Int. Ed.* **2008,** *47* (14), 2556-2588.

7. References

176. Früchtel, J. S.; Jung, G., Organic chemistry on solid supports. *Angew. Chem., Int. Ed. Engl.* **1996,** *35* (1), 17-42.

177. Brenner, S.; Lerner, R. A., Encoded combinatorial chemistry. *Proc. Natl. Acad. Sci.* **1992,** *89* (12), 5381-5383.

178. Koinuma, H.; Takeuchi, I., Combinatorial solid-state chemistry of inorganic materials. *Nat. Mater.* **2004,** *3* (7), 429-438.

179. Danielson, E.; Golden, J. H.; McFarland, E. W.; Reaves, C. M.; Weinberg, W. H.; Di Wu, X., A combinatorial approach to the discovery and optimization of luminescent materials. *Nature* **1997,** *389* (6654), 944-948.

180. Danielson, E.; Devenney, M.; Giaquinta, D. M.; Golden, J. H.; Haushalter, R. C.; McFarland, E. W.; Poojary, D. M.; Reaves, C. M.; Weinberg, W. H.; Di Wu, X., A rare-earth phosphor containing one-dimensional chains identified through combinatorial methods. *Science* **1998,** *279* (5352), 837-839.

181. Cohen-Adad, M. T.; Laversenne, L.; Goutaudier, C.; Boulon, G.; Cohen-Adad, R.; Gharbi, M., New combinatorial chemistry approach in material science. *J. Phase Equilibria* **2001,** *22* (4), 379-385.

182. Schlögl, R., Combinatorial Chemistry in Heterogeneous Catalysis: A New Scientific Approach or "the King's New Clothes"? *Angew. Chem., Int. Ed.* **1998,** *37* (17), 2333-2336.

183. Corbett, P. T.; Leclaire, J.; Vial, L.; West, K. R.; Wietor, J.-L.; Sanders, J. K.; Otto, S., Dynamic combinatorial chemistry. *Chem. Rev.* **2006,** *106* (9), 3652-3711.

184. Lehn, J.-M.; Eliseev, A. V., Dynamic combinatorial chemistry. *Science* **2001,** *291* (5512), 2331-2332.

185. Hunt, R. A.; Otto, S., Dynamic combinatorial libraries: new opportunities in systems chemistry. *Chem. Commun.* **2011,** *47* (3), 847-858.

186. Goral, V.; Nelen, M. I.; Eliseev, A. V.; Lehn, J.-M., Double-level "orthogonal" dynamic combinatorial libraries on transition metal template. *Proc. Natl. Acad. Sci.* **2001,** *98* (4), 1347-1352.

187. Hiraoka, S.; Kubota, Y.; Fujita, M., Self-and hetero-recognition in the guest-controlled assembly of Pd (II)-linked cages from two different ligands. *Chem. Commun.* **2000,** (16), 1509-1510.

188. Caturello, N. A.; Besse, R.; Da Silva, A. C.; Guedes-Sobrinho, D.; Lima, M. P.; Da Silva, J. L., Ab initio investigation of atomistic insights into the nanoflake formation of transition-metal dichalcogenides: The examples of MoS_2, $MoSe_2$, and $MoTe_2$. *J. Phys. Chem. C* **2018,** *122* (47), 27059-27069.

189. Zibordi-Besse, L.; Seminovski, Y.; Rosalino, I.; Guedes-Sobrinho, D.; Da Silva, J. L., Physical and chemical properties of unsupported $(MO_2)_n$ clusters for M= Ti, Zr, or Ce and n= 1–15: a density functional theory study combined with the tree-growth scheme and Euclidean similarity distance algorithm. *J. Phys. Chem. C* **2018,** *122* (48), 27702-27712.

190. Liu, Q.; Xu, C.; Cheng, L., Structural and Electronic Properties of Nano-brass: Cu_xZn_y (x+ y= 11− 13) Clusters. *J. Clust. Sci.* **2019,** 1-7.

191. Rondina, G. G.; Da Silva, J. L., Revised basin-hopping Monte Carlo algorithm for structure optimization of clusters and nanoparticles. *J. Chem. Inf. Model.* **2013,** *53* (9), 2282-2298.

192. Gehrke, R.; Reuter, K., Assessing the efficiency of first-principles basin-hopping sampling. *Phys. Rev. B* **2009,** *79* (8), 085412.

193. Chen, M.; Dixon, D. A., Tree Growth-Hybrid Genetic Algorithm for Predicting the Structure of Small $(TiO_2)_n$, n= 2–13, Nanoclusters. *J. Chem. Theory Comput.* **2013,** *9* (7), 3189-3200.

194. Cha, S.-H., Comprehensive survey on distance/similarity measures between probability density functions. *Math. Models Methods Appl. Sci.* **2007,** *4* (1), 300-307.

195. Goldberger, J.; Tassa, T., A hierarchical clustering algorithm based on the Hungarian method. *Pattern Recognit. Lett.* **2008,** *29* (11), 1632-1638.

196. Khanna, S.; Jena, P., Assembling crystals from clusters. *Phys. Rev. Lett.* **1992,** *69* (11), 1664.

197. Walter, M.; Akola, J.; Lopez-Acevedo, O.; Jadzinsky, P. D.; Calero, G.; Ackerson, C. J.; Whetten, R. L.; Grönbeck, H.; Häkkinen, H., A unified view of ligand-protected gold clusters as superatom complexes. *Proc. Natl. Acad. Sci.* **2008,** *105* (27), 9157-9162.

198. Arakawa, H.; Sayama, K., Methanol Synthesis from CO_2 and H_2 Over Supported Copper-Zinc Oxide Catalyst. Significant Influence of Support on Methanol Formation. *Stud. Surf. Sci. Catal.* **1993,** *75*, 2777-2780.

199. Jadhav, A. P.; Pawar, A.; Kim, C. W.; Cha, H. G.; Pal, U.; Kang, Y. S., Effect of different additives on the size control and emission properties of Y_2O_3: Eu^{3+} nanoparticles prepared through the coprecipitation method. *J. Phys. Chem. C* **2009,** *113* (38), 16652-16657.

7. References

200. Yin, L.; Wang, Y.; Pang, G.; Koltypin, Y.; Gedanken, A., Sonochemical synthesis of cerium oxide nanoparticles—effect of additives and quantum size effect. *J. Colloid Interface Sci.* **2002,** *246* (1), 78-84.
201. Rizzuti, A.; Dassisti, M.; Mastrorilli, P.; Sportelli, M. C.; Cioffi, N.; Picca, R. A.; Agostinelli, E.; Varvaro, G.; Caliandro, R., Shape-control by microwave-assisted hydrothermal method for the synthesis of magnetite nanoparticles using organic additives.*J. Nanopart. Res.* **2015,** *17* (10), 1-16.
202. Yang, Y.; Chen, H.; Zhao, B.; Bao, X., Size control of ZnO nanoparticles via thermal decomposition of zinc acetate coated on organic additives. *J. Cryst. Growth* **2004,** *263* (1-4), 447-453.
203. Qian, H.; Zhu, Y.; Jin, R., Size-focusing synthesis, optical and electrochemical properties of monodisperse $Au_{38}(SC_2H_4Ph)_{24}$ nanoclusters. *ACS nano* **2009,** *3* (11), 3795-3803.
204. Cadenbach, T.; Bollermann, T.; Gemel, C.; Tombul, M.; Fernandez, I.; Hopffgarten, M. v.; Frenking, G.; Fischer, R. A., Molecular Alloys, Linking Organometallics with Intermetallic Hume−Rothery Phases:The Highly Coordinated Transition Metal Compounds $[M(ZnR)_n](n \geq 8)$ Containing Organo−Zinc Ligands. *J. Am. Chem. Soc.* **2009,** *131* (44), 16063-16077.
205. Bollermann, T.; Freitag, K.; Gemel, C.; Seidel, R. W.; von Hopffgarten, M.; Frenking, G.; Fischer, R. A., The Reactivity of $[Zn_2Cp^*{}_2]$: Trapping Monovalent {·ZnZnCp*} in the Metal-Rich Compounds $[(Pd,Pt)(GaCp^*)_a(ZnCp^*)_{4-a}(ZnZnCp^*)_{4-a}](a= 0, 2)$. *Angew. Chem., Int. Ed.* **2011,** *50* (3), 772-776.
206. Grirrane, A.; Resa, I.; Rodriguez, A.; Carmona, E.; Alvarez, E.; Gutierrez-Puebla, E.; Monge, A.; Galindo, A.; del Río, D.; Andersen, R. A., Zinc−Zinc Bonded Zincocene Structures. Synthesis and Characterization of $Zn_2(\eta^5-C_5Me_5)_2$ and $Zn_2(\eta^5-C_5Me_4Et)_2$. *J. Am. Chem. Soc.* **2007,** *129* (3), 693-703.
207. Freitag, K.; Molon, M.; Jerabek, P.; Dilchert, K.; Rösler, C.; Seidel, R. W.; Gemel, C.; Frenking, G.; Fischer, R. A., Zn··· Zn interactions at nickel and palladium centers. *Chem. Sci.* **2016,** *7* (10), 6413-6421.
208. Blum, V.; Gehrke, R.; Hanke, F.; Havu, P.; Havu, V.; Ren, X.; Reuter, K.; Scheffler, M., Ab initio molecular simulations with numeric atom-centered orbitals. *Comput. Phys. Commun.* **2009,** *180* (11), 2175-2196.
209. Perdew, J. P.; Burke, K.; Ernzerhof, M., Generalized gradient approximation made simple. *Phys. Rev. Lett.* **1996,** *77* (18), 3865.
210. Te Velde, G. t.; Bickelhaupt, F. M.; Baerends, E. J.; Fonseca Guerra, C.; van Gisbergen, S. J.; Snijders, J. G.; Ziegler, T., Chemistry with ADF. *J. Comput. Chem.* **2001,** *22* (9), 931-967.
211. Baerends, E., ADF2016, SCM. 2016; Theoretical Chemistry, Vrije Universiteit, Amsterdam, The Netherlands.
212. Resa, I.; Álvarez, E.; Carmona, E., Synthesis and Structure of Half-Sandwich Zincocenes. *Z. Anorg. Allg. Chem.* **2007,** *633* (11-12), 1827-1831.
213. Dunsford, J. J.; Clark, E. R.; Ingleson, M. J., Direct C (sp^2)-C(sp^3) Cross-Coupling of Diaryl Zinc Reagents with Benzylic, Primary, Secondary, and Tertiary Alkyl Halides. *Angew. Chem.* **2015,** *127* (19),5780-5784.
214. Berry, R.; Raynor, G. V., The crystal chemistry of the Laves phases. *Acta Cryst.* **1953,** *6* (2), 178-186.
215. Jordan, A. J.; Wyss, C. M.; Bacsa, J.; Sadighi, J. P., Synthesis and reactivity of new copper(I) hydride dimers. *Organometallics* **2016,** *35* (5), 613-616.
216. Wei, Q.-H.; Yin, G.-Q.; Zhang, L.-Y.; Shi, L.-X.; Mao, Z.-W.; Chen, Z.-N., Luminescent Ag^I-Cu^I Heterometallic Hexa-, Octa-, and Hexadecanuclear Alkynyl Complexes. *Inorg. Chem.* **2004,** *43* (11), 3484-3491.
217. Beck, J.; Strähle, J., Komplexe von 1, 5-Di (p-tolyl)-1, 4-pentaazadien-3-id, Kristallstrukturen von $[Cu(tolylNNNNNtolyl)]_3$ und $[Ni(tolylNNNNNtolyl)_2]_2$. *Angew. Chem.* **1985,** *97* (5), 419-420.
218. Meyer, E. M.; Gambarotta, S.; Floriani, C.; Chiesi-Villa, A.; Guastini, C., Polynuclear aryl derivatives of Group 11 metals. Synthesis, solid state-solution structural relationship, and reactivity with phosphines. *Organometallics* **1989,** *8* (4), 1067-1079.
219. Häkkinen, H., Atomic and electronic structure of gold clusters: understanding flakes, cages and superatoms from simple concepts. *Chem. Soc. Rev.* **2008,** *37* (9), 1847-1859.

7. References

220. Sharma, S.; Chakrahari, K. K.; Saillard, J.-Y.; Liu, C., Structurally Precise Dichalcogenolate-Protected Copper and Silver Superatomic Nanoclusters and Their Alloys. *Acc. Chem. Res.* **2018,** *51* (10), 2475-2483.

221. Dhayal, R. S.; Liao, J. H.; Wang, X.; Liu, Y. C.; Chiang, M. H.; Kahlal, S.; Saillard, J. Y.; Liu, C., Diselenophosphate-Induced Conversion of an Achiral [$Cu_{20}H_{11}$ {S_2P (O^iPr)$_2$}$_9$] into a Chiral [$Cu_{20}H_{11}${Se_2P (O^iPr)$_2$}$_9$] Polyhydrido Nanocluster. *Angew. Chem., Int. Ed.* **2015,** *54* (46), 13604-13608.

222. Jutzi, P.; Wieland, W.; Neumann, B.; Stammler, H.-G., 'Slipped-sandwich'-strukturen in der cyclopentadienyl-Kupfer-chemie. *J. Organomet. Chem.* **1995,** *501* (1-2), 369-374.

223. Martínez-Espada, N.; Mena, M.; Mosquera, M. E.; Pérez-Redondo, A.; Yelamos, C., Cyclopentadienyl and Alkynyl Copper (I) Derivatives with the [{Ti(η^5-C_5Me_5)(μ-NH)}$_3$(μ_3-N)]Metalloligand. *Organometallics* **2010,** *29* (24), 6732-6738.

224. Yu, K. K.; Yeung, C. M.; Tsang, S. C., Carbon dioxide fixation into chemicals (methyl formate) at high yields by surface coupling over a Pd/Cu/ZnO nanocatalyst. *J. Am. Chem. Soc.* **2007,** *129* (20), 6360-6361.

225. Fisher, I. A.; Bell, A. T., In-situ infrared study of methanol synthesis from H_2/CO_2 over Cu/SiO_2 and Cu/ZrO_2/SiO_2. *J. Catal.* **1997,** *172* (1), 222-237.

226. Tang, Q.-L.; Hong, Q.-J.; Liu, Z.-P., CO_2 fixation into methanol at Cu/ZrO_2 interface from first principles kinetic Monte Carlo. *J. Catal.* **2009,** *263* (1), 114-122.

227. Saito, M.; Fujitani, T.; Takeuchi, M.; Watanabe, T., Development of copper/zinc oxide-based multicomponent catalysts for methanol synthesis from carbon dioxide and hydrogen. *Appl. Catal. A-Gen.* **1996,** *138* (2), 311-318.

228. Liu, J.; Shi, J.; He, D.; Zhang, Q.; Wu, X.; Liang, Y.; Zhu, Q., Surface active structure of ultra-fine Cu/ZrO_2 catalysts used for the CO_2+H_2 to methanol reaction. *Appl. Catal. A-Gen.* **2001,** *218* (1-2), 113-119.

229. Fu, S. S.; Somorjai, G. A., Zinc oxide and oxygen overlayers on Cu (110): a model for CuZnO catalysts. *Appl. Surf. Sci.* **1991,** *48*, 93-103.

230. Bando, K. K.; Sayama, K.; Kusama, H.; Okabe, K.; Arakawa, H., In-situ FT-IR study on CO_2 hydrogenation over Cu catalysts supported on SiO_2, Al_2O_3, and TiO_2. *Appl. Catal. A-Gen.* **1997,** *165* (1-2), 391-409.

231. Ito, K.; Bernstein, H. J., The vibrational spectra of the formate, acetate, and oxalate ions. *Can. J. Chem.* **1956,** *34* (2), 170-178.

232. Carter Iii, R.; Poindexter, B.; Weber, W., Vibrational spectra of copper formate tetrahydrate, copper formate dihydrate and three anhydrous forms of copper formate. *Vib. Spectrosc.* **1991,** *2* (2-3), 125-134.

233. Edwards, J. F.; Schrader, G. L., Methanol, formaldehyde, and formic acid adsorption on methanol synthesis catalysts. *J. Phys. Chem.* **1985,** *89* (5), 782-788.

234. Benn, R.; Janssen, E.; Lehmkuhl, H.; Rufínska, A., ^{27}Al-NMR-Spektroskopie zur Charakterisierung von Organoaluminium-Verbindungen. *J. Organomet. Chem.* **1987,** *333* (2), 155-168.

235. Reger, D. L.; Huff, M. F., Synthesis and characterization of copper (I) trifluoroacetate alkyne complexes of type Cu_4(μ-O_2CCF_3)$_4$(μ-alkyne)$_2$ and Cu_2(μ-O_2CCF_3)$_2$(alkyne)$_2$. *Organometallics* **1990,** *9* (10), 2807-2810.

236. Macomber, D. W.; Rausch, M. D., (η^5-Cyclopentadienyl)- and (η^5-pentamethylcyclopentadienyl) copper compounds containing phosphine, carbonyl, and η^2-acetylenic ligands. *J. Am. Chem. Soc.* **1983,** *105* (16), 5325-5329.

237. Drescher, R.; Lin, S.; Hofmann, A.; Lenczyk, C.; Kachel, S.; Krummenacher, I.; Lin, Z.; Braunschweig, H., Ring expansion of alumoles with organic azides: selective formation of six-membered aluminum–nitrogen heterocycles. *Chem. Sci.* **2020,** *11* (21), 5559-5564.

238. RW, G., Wyckoff," Crystal Structures,". Interscience Publishers, **1963,** NY.

239. Buchin, B.; Steinke, T.; Gemel, C.; Cadenbach, T.; Fischer, R. A., Synthesis and Characterization of the Novel Al^I Compound Al(C_5Me_4Ph): Comparison of the Coordination Chemistry of Al(C_5Me_5) and Al(C_5Me_4Ph) at d^{10} Metal Centers. *Z. Anorg. Allg. Chem.* **2005,** *631* (13-14), 2756-2762.

240. Jerius, J. J.; Hahn, J. M.; Rahman, A. M.; Mols, O.; Ilsley, W. H.; Oliver, J. P., Synthesis, molecular structure, and NMR spectra of trimesitylaluminum, a novel molecule with three coordinate aluminum. *Organometallics* **1986,** *5* (9), 1812-1814.

241. Fenske, D.; Steck, J. C., New Cu-Te Clusters. *Angew. Chem., Int. Ed. Engl.* **1993,** *32* (2), 238-242.

7. References

242. Fackler, J. P.; López, C. A.; Staples, R. J.; Wang, S.; Winpenny, R.; Lattimer, R. P., Self assembly of isostructural copper(I)-silver(I) butterfly clusters with 2-mercaptothiazoline; syntheses and structures of $(PPh_3)_2Cu_4(C_3H_4NS_2)_4,[(C_5H_5N)Cu_4(C_3H_4NS_2)_4]_n,(PPh_3)_2Ag_4(C_3H_4NS_2)_4$ and $(PPh_3)_2Ag_2Cu_2(C_3H_4NS_2)_4$. *J. Chem. Soc., Chem. Commun.* **1992,** (2), 146-148.

243. Himmel, H.-J.; Vollet, J., Probing the reactivity of aluminum (I) compounds: the reaction of pentamethylcyclopentadienyl-aluminum, $Al[C_5(CH_3)_5]$, monomers with dihydrogen in a solid Ar matrix to give the new aluminum hydride molecule $H_2Al[C_5(CH_3)_5]$. *Organometallics* **2002,** *21* (26), 5972-5977.

244. Albright, T. A.; Burdett, J. K.; Whangbo, M.-H., *Orbital interactions in chemistry*. John Wiley & Sons: 2013.

245. Gonzalez-Gallardo, S.; Bollermann, T.; Fischer, R. A.; Murugavel, R., Cyclopentadiene based low-valent group 13 metal compounds: ligands in coordination chemistry and link between metal rich molecules and intermetallic materials. *Chem. Rev.* **2012,** *112* (6), 3136-3170.

246. Zubarev, D. Y.; Averkiev, B. B.; Zhai, H.-J.; Wang, L.-S.; Boldyrev, A. I., Aromaticity and antiaromaticity in transition-metal systems. *Phys. Chem. Chem. Phys.* **2008,** *10* (2), 257-267.

247. von Ragué Schleyer, P.; Maerker, C.; Dransfeld, A.; Jiao, H.; van Eikema Hommes, N. J., Nucleus-Independent Chemical Shiftes: A Simple and Efficient Aromaticity Probe. *J. Am. Chem. Soc.* **1996,** *118*, 6317-6318.

248. Li, X.; Kuznetsov, A. E.; Zhang, H.-F.; Boldyrev, A. I.; Wang, L.-S., Observation of all-metal aromatic molecules. *Science* **2001,** *291* (5505), 859-861.

249. Islas, R.; Heine, T.; Merino, G., Structure and Electron Delocalization in Al_4^{2-} and Al_4^{4-}. *J. Chem. Theory Comput.* **2007,** *3* (3), 775-781.

250. Mühlecker-Knoepfler, A.; Ellmerer-Müller, E.; Konrat, R.; Ongania, K.-H.; Wurst, K.; Peringer, P., Synthesis and crystal structure of the subvalent mercury cluster [triangulo-$Hg_3(\mu-$ dmpm)$_4$] $[O_3SCF_3]_4$ (dmpm= $Me_2PCH_2PMe_2$). *J. Am. Chem. Soc., Dalton Trans.* **1997,** (9), 1607-1610.

251. Peltier, J. L.; Soleilhavoup, M.; Martin, D.; Jazzar, R.; Bertrand, G., Absolute Templating of M (111) Cluster Surrogates by Galvanic Exchange. *J. Am. Chem. Soc.* **2020,** *142* (38), 16479-16485.

252. Li, X.-W.; Xie, Y.; Schreiner, P. R.; Gripper, K. D.; Crittendon, R. C.; Campana, C. F.; Schaefer, H. F.; Robinson, G. H., Cyclogallanes and metalloaromaticity. Synthesis and molecular structure of dipotassium tris((2,6-dimesitylphenyl)cyclogallene), $K_2[(Mes_2C_6H_3)Ga]_3$ (Mes= $2,4,6-Me_3C_6H_2$): a structural and theoretical examination. *Organometallics* **1996,** *15* (18), 3798-3803.

253. Blanchard, S.; Fensterbank, L.; Gontard, G.; Lacôte, E.; Maestri, G.; Malacria, M., Synthesis of Triangular Tripalladium Cations as Noble-Metal Analogues of the Cyclopropenyl Cation. *Angew. Chem., Int. Ed.,* **2014,** *53* (7), 1987-1991.

254. Wang, Y.; Monfredini, A.; Deyris, P.-A.; Blanchard, F.; Derat, E.; Maestri, G.; Malacria, M., All-metal aromatic cationic palladium triangles can mimic aromatic donor ligands with Lewis acidic cations. *Chem. Sci.* **2017,** *8* (11), 7394-7402.

255. Latouche, C.; Kahlal, S.; Lin, Y.-R.; Liao, J.-H.; Furet, E.; Liu, C.; Saillard, J.-Y., Anion encapsulation and geometric changes in hepta-and hexanuclear copper (I) dichalcogeno clusters: a theoretical and experimental investigation. *Inorg. Chem.* **2013,** *52* (22), 13253-13262.

256. Liao, P.-K.; Fang, C.-S.; Edwards, A. J.; Kahlal, S.; Saillard, J.-Y.; Liu, C., Hydrido copper clusters supported by dithiocarbamates: Oxidative hydride removal and neutron diffraction analysis of $[Cu_7 (H)\{S_2C(aza-15-crown-5)\}_6]$. *Inorg. Chem.* **2012,** *51* (12), 6577-6591.

257. Ichimura, T.; Mori, Y.; Sumitani, M.; Yoshihara, K., Intramolecular hydrogen transfer in the o-tolyl radical studied by time resolved absorption measurements. *J. Chem. Phys.* **1986,** *84* (3), 1943-1944.

258. Dangi, B. B.; Parker, D. S.; Yang, T.; Kaiser, R. I.; Mebel, A. M., Gas-Phase Synthesis of the Benzyl Radical ($C_6H_5CH_2$). *Angew. Chem.* **2014,** *126* (18), 4696-4701.

259. Gardner, K. A.; Mayer, J. M., Understanding CH bond oxidations: H· and H-transfer in the oxidation of toluene by permanganate. *Science* **1995,** *269* (5232), 1849-1851.

260. Zhu, L.; Yempally, V.; Isrow, D.; Pellechia, P. J.; Captain, B., Selective benzylic C–H activation of solvent toluene and m-xylene by an iron–tin cluster complex: $Fe_2(\mu-SnBu_2^t)_2(CO)_8$. *J. Organomet. Chem.* **2010,** *695* (1), 1-5.

261. Chatgilialoglu, C., Structural and chemical properties of silyl radicals. *Chem. Rev.* **1995,** *95* (5), 1229-1251.

7. References

262. Davidson, I. M.; Barton, T. J.; Hughes, K. J.; Ijadi-Maghsoodi, S.; Revis, A.; Paul, G. C., Kinetics of radical-forming homolyses in alkenyl-and tert-butylsilanes. The stability of. alpha.-and. beta.-silicon-substituted alkyl radicals. *Organometallics* **1987,** *6* (3), 644-646.

263. Wilt, J. W.; Aznavoorian, P. M., Favored reduction of. alpha.-chlorosilanes vs.. alpha.-chloroalkanes with tri-n-butyltin hydride. *J. Org. Chem.* **1978,** *43* (6), 1285-1286.

264. Krusic, P. J.; Kochi, J. K., Electron spin resonance of group IV organometallic alkyl radicals in solution. *J. Am. Chem. Soc.* **1969,** *91* (22), 6161-6164.

265. Wang, X.; Andrews, L., Gold is noble but gold hydride anions are stable. *Angew. Chem.* **2003,** *115* (42), 5359-5364.

266. Tsui, E. Y.; Müller, P.; Sadighi, J. P., Reactions of a stable monomeric gold (I) hydride complex. *Angew. Chem.* **2008,** *120* (46), 9069-9072.

267. Hornung, J. Hume-Rothery inspired Complexes and Clusters as Molecular Models for Intermediates in Heterogeneous Catalysis. *Dissertation* **2019,** Technische Universität München.

268. Devillard, M.; Nicolas, E.; Ehlers, A. W.; Backs, J.; Mallet-Ladeira, S.; Bouhadir, G.; Slootweg, J. C.; Uhl, W.; Bourissou, D., Dative Au→ Al interactions: Crystallographic characterization and computational analysis. *Chem. Eur. J.* **2015,** *21* (1), 74-79.

269. Puls, A.; Jerabek, P.; Kurashige, W.; Förster, M.; Molon, M.; Bollermann, T.; Winter, M.; Gemel, C.; Negishi, Y.; Frenking, G., Ein neuartiges Konzept zur Synthese mehrfach dotierter Goldcluster [(M@ Au$_n$M'$_m$) L$_k$]q$^+$. *Angew. Chem.* **2014,** *126* (17), 4415-4419.

270. Hicks, J.; Mansikkamäki, A.; Vasko, P.; Goicoechea, J. M.; Aldridge, S., A nucleophilic gold complex. *Nat. Chem.* **2019,** *11* (3), 237-241.

271. Cordero, B.; Gómez, V.; Platero-Prats, A. E.; Revés, M.; Echeverría, J.; Cremades, E.; Barragán, F.; Alvarez, S., Covalent radii revisited. *Dalton Trans.* **2008,** (21), 2832-2838.

272. Hsu, L.-S.; Wang, Y.-K.; Tai, Y.-L.; Lee, J.-F., Experimental and theoretical study of the electronic structure of AuAl$_2$, AuGa$_2$, and AuIn$_2$. *Phys. Rev. B* **2005,** *72* (11), 115115.

273. Gabbai, F. P.; Schier, A.; Riede, J.; Schmidbaur, H., Different pathways of the reaction of InCl with Ph$_3$PAuCl: isolation of the first mixed-valent mixed-metal gold/indium cluster. *Inorg. Chem.* **1995,** *34* (15), 3855-3856.

274. Weinberger, D. S.; Melaimi, M.; Moore, C. E.; Rheingold, A. L.; Frenking, G.; Jerabek, P.; Bertrand, G., Isolation of neutral mono-and dinuclear gold complexes of cyclic (alkyl)(amino) carbenes. *Angew. Chem., Int. Ed.* **2013,** *52* (34), 8964-8967.

275. Pettibone, J. M.; Hudgens, J. W., Gold cluster formation with phosphine ligands: etching as a size-selective synthetic pathway for small clusters? *ACS nano* **2011,** *5* (4), 2989-3002.

276. Brown, L. O.; Hutchison, J. E., Convenient preparation of stable, narrow-dispersity, gold nanocrystals by ligand exchange reactions. *J. Am. Chem. Soc.* **1997,** *119* (50), 12384-12385.

277. Tolman, C. A., Steric effects of phosphorus ligands in organometallic chemistry and homogeneous catalysis. *Chem. Rev.* **1977,** *77* (3), 313-348.

278. Bruker, I., APEX3 v2015. 5-2. Madison: Bruker AXS Inc: 2015.

279. SAINT, Version 8.34A, Bruker AXS Inc., Madison, Wisconsin, USA, 2014.

280. SADABS, Version 2014/5, Bruker AXS Inc., Madison, Wisconsin, USA, 2012.

281. G. M. Sheldrick, *Acta Crystallogr. Sect. A* **2015,** *71*, 3–8.

282. G. M. Sheldrick, *Acta Crystallogr. Sect. C* **2015,** *71*, 3–8.

283. C. B. Hübschle, G. M. Sheldrick, B. Dittrich, *J. Appl. Cryst.* **2011**, 44, 1281–1284.

284. International Tables for Crystallography, Vol. C (Ed.: A. J. Wilson), Kluwer Academic Publishers, Dordrecht, The Netherlands, 1992, Tables 6.1.1.4 (pp. 500–502), 4.2.6.8 (pp. 219–222), and 4.2.4.2 (pp. 193–199).

285. A. L. Spek, *Acta Crystallogr. Sect. C* **2015,** *71*, 9–18.

286. A. L. Spek, *Acta Crystallogr. Sect. D* **2009,** *65*, 148–155.

287. C. F. Macrae, I. J. Bruno, J. A. Chisholm, P. R. Edgington, P. McCabe, E. Pidcock, L. Rodriguez-Monge, R. Taylor, J. van de Streek, P. A. Wood, *J. Appl. Cryst.* **2008,** *41*, 466–470.

288. Van Lenthe, E. v.; Snijders, J.; Baerends, E., The zero-order regular approximation for relativistic effects: The effect of spin–orbit coupling in closed shell molecules. *J. Chem. Phys.* **1996,** *105* (15), 6505-6516.

289. ADF2017, SCM, Theoretical Chemistry, Vrije Universiteit: Amsterdam, The Netherlands; http://www.scm.com.

7. References

290. Becke, A. D. Density-functional exchange-energy approximation with correct asymptotic behavior. *Phys. Rev. A* **1988**, 38, 3098-3100.

291. Perdew, J. P., Density-functional approximation for the correlation energy of the inhomogeneous electron gas. *Physical Review B* **1986,** *33* (12), 8822.

292. GUI 2017, SCM, Amsterdam, The Netherlands, http://www.scm.com.

293. Glendening, E. D.; Badenhoop, J. K.; Reed, A. E.; Carpenter, J. E.; Bohmann, J. A.; Morales, C. M.; Weinhold, F. NBO 6.0, Theoretical Chemistry Institute, University of Wisconsin (Madison, WI, 2001, http://nbo6.chem.wisc.edu).

294. Schreckenbach, G.; Ziegler, T., Calculation of NMR shielding tensors using gauge-including atomic orbitals and modern density functional theory. *J. Phys. Chem.* **1995,** *99* (2), 606-611.

295. Loos, M.; Gerber, C.; Corona, F.; Hollender, J.; Singer, H., Accelerated isotope fine structure calculation using pruned transition trees. *Anal. Chem.* **2015,** *87* (11), 5738-5744.

296. Ganesamoorthy, C.; Loerke, S.; Gemel, C.; Jerabek, P.; Winter, M.; Frenking, G.; Fischer, R. A., Reductive elimination: a pathway to low-valent aluminium species. *Chem. Commun.* **2013,** *49* (28), 2858-2860.

297. del Rio, D.; Resa, I.; Rodriguez, A.; Sánchez, L.; Köppe, R.; Downs, A. J.; Tang, C. Y.; Carmona, E., IR and Raman Characterization of the Zincocenes $(\eta^5\text{-}C_5Me_5)_2Zn_2$ and $(\eta^5\text{-}C_5Me_5)(\eta^1\text{-}C_5Me_5)Zn$. *J. Phys. Chem. A* **2008,** *112* (42), 10516-10525.

298. Eberhart, M. S.; Norton, J. R.; Zuzek, A.; Sattler, W.; Ruccolo, S., Electron transfer from hexameric copper hydrides. *J. Am. Chem. Soc.* **2013,** *135* (46), 17262-17265.

299. Gusel'nikov, L.; Polyakov, Y. P.; Volnina, E.; Nametkin, N., Silyl and silylmethyl radicals, silylenes, sila-alkenes, and small ring silacycles in reactions of organochlorosilanes with alkali metal vapours. *J. Organomet. Chem.* **1985,** *292* (1-2), 189-203.

300. Kashimura, S.; Ishifune, M.; Yamashita, N.; Bu, H.-B.; Takebayashi, M.; Kitajima, S.; Yoshiwara, D.; Kataoka, Y.; Nishida, R.; Kawasaki, S.-i., Electroreductive Synthesis of Polysilanes, Polygermanes, and Related Polymers with Magnesium Electrodes. *J. Org. Chem.* **1999,** *64* (18), 6615-6621.

301. Mohamed, M.; Brook, M. A., Photolysis of tris (trimethylsilyl)silane: trapping of sisyl radicals. *Can. J. Chem.* **2000,** *78* (11), 1357-1362.

302. Sanganee, M. J.; Steel, P. G.; Whelligan, D. K., Novel one-pot synthesis of aryltris (trimethylsilyl) silanes. *J. Org. Chem.* **2003,** *68* (8), 3337-3339.

303. Herzog, U.; Roewer, G., Base catalysed hydrogenation of methylbromooligosilanes with trialkylstannanes, identification of the first methylbromohydrogenoligosilanes. *J. Organomet. Chem.* **1997,** *527* (1-2), 117-124.

304. Schneider, H.; Hock, A.; Bertermann, R.; Radius, U., Reactivity of NHC Alane Adducts towards N-Heterocyclic Carbenes and Cyclic(Alkyl)(amino)carbenes: Ring Expansion, Ring Opening, and Al−H Bond Activation. *Chem. Eur. J.* **2017**, *23* (50), 12387-12398.

8. Reprint permissions

8. Reprint permissions

8. Reprint permissions

8. Reprint permissions

AAAS MATERIAL:
1 figure from Domon & Aebersold
Science 14 Apr 2006:
Vol. 312, Issue 5771, pp. 212-217
DOI: 10.1126/science.1124619

Dear Max Schütz:

Thank you very much for your interest in the AAAS material identified in your request.

We are pleased to have you include this material in your thesis or dissertation subject to the following guidelines. These guidelines also appear on our website: http://www.sciencemag.org/help/reprints-and-permissions under the heading 'Using AAAS material in a thesis or dissertation'.

REPRODUCING AAAS MATERIAL IN YOUR THESIS OR DISSERTATION

AAAS permits the use of content published in it's journals but only provided the following criteria are met:

1. If you are using figures/tables, permission is granted for use in print and electronic versions of your dissertation or thesis.

2. A full text article may be used only in print versions of a dissertation or thesis. AAAS does not permit the reproduction of full text articles in electronic versions of theses or dissertations.

3. The following credit line must be printed along with the AAAS material: "From [Insert Full Reference Citation]/ Reprinted with permission from AAAS".

4. All required credit lines and notices must be visible any time a user accesses any part of the AAAS material and must appear on any printed copies that an authorized user might make.

8. Reprint permissions
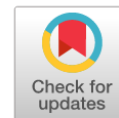
Exploring Cu/Al cluster growth and reactivity: from embryonic building blocks to intermetalloid, open-shell superatoms[†]

Max Schütz [ab], Christian Gemel [ab], Maximilian Muhr [ab], Christian Jandl [b], Samia Kahlal [c], Jean-Yves Saillard [c] and Roland A. Fischer [*ab]

[a]Department of Chemistry, Technical University Munich, Lichtenbergstrasse 4, D-85748 Garching, Germany. E-mail: roland.fischer@tum.de

[b]Catalysis Research Centre, Technical University Munich, Ernst-Otto-Fischer Strasse 1, D-85748 Garching, Germany

[c]Univ Rennes, CNRS, ISCR-UMR 6226, F-35000 Rennes, France

8. Reprint permissions

ELSEVIER LICENSE
TERMS AND CONDITIONS

Mar 25, 2021

This Agreement between Technical University of Munich -- Max Schütz ("You") and Elsevier ("Elsevier") consists of your license details and the terms and conditions provided by Elsevier and Copyright Clearance Center.

License Number	4973000236920
License date	Dec 20, 2020
Licensed Content Publisher	Elsevier
Licensed Content Publication	Intermetallics
Licensed Content Title	Re-investigation of phase equilibria in the system Al–Cu and structural analysis of the high-temperature phase η1-Al1−δCu
Licensed Content Author	Norbert Ponweiser,Christian L. Lengauer,Klaus W. Richter
Licensed Content Date	Nov 1, 2011
Licensed Content Volume	19
Licensed Content Issue	11
Licensed Content Pages	10
Start Page	1737
End Page	1746
Type of Use	reuse in a thesis/dissertation
Portion	figures/tables/illustrations
Number of figures/tables /illustrations	1
Format	both print and electronic
Are you the author of this Elsevier article?	No
Will you be translating?	No
Title	Fundamental Understanding of living cluster libraries in solution
Institution name	Technical University of Munich
Expected presentation date	Jun 2021
Order reference number	1
Portions	Figure 1 on page 2
Requestor Location	Technical University of Munich Lichtenbergstrasse 4
	Garching, 85748 Germany Attn: Technical University of Munich
Publisher Tax ID	GB 494 6272 12
Total	**0.00 EUR**
Terms and Conditions	

8. Reprint permissions

INTRODUCTION

1. The publisher for this copyrighted material is Elsevier. By clicking "accept" in connection with completing this licensing transaction, you agree that the following terms and conditions apply to this transaction (along with the Billing and Payment terms and conditions established by Copyright Clearance Center, Inc. ("CCC"), at the time that you opened your Rightslink account and that are available at any time at http://myaccount.copyright.com).

GENERAL TERMS

2. Elsevier hereby grants you permission to reproduce the aforementioned material subject to the terms and conditions indicated.

3. Acknowledgement: If any part of the material to be used (for example, figures) has appeared in our publication with credit or acknowledgement to another source, permission must also be sought from that source. If such permission is not obtained then that material may not be included in your publication/copies. Suitable acknowledgement to the source must be made, either as a footnote or in a reference list at the end of your publication, as follows:

"Reprinted from Publication title, Vol /edition number, Author(s), Title of article / title of chapter, Pages No., Copyright (Year), with permission from Elsevier [OR APPLICABLE SOCIETY COPYRIGHT OWNER]." Also Lancet special credit - "Reprinted from The Lancet, Vol. number, Author(s), Title of article, Pages No., Copyright (Year), with permission from Elsevier."

4. Reproduction of this material is confined to the purpose and/or media for which permission is hereby given.

5. Altering/Modifying Material: Not Permitted. However figures and illustrations may be altered/adapted minimally to serve your work. Any other abbreviations, additions, deletions and/or any other alterations shall be made only with prior written authorization of Elsevier Ltd. (Please contact Elsevier's permissions helpdesk here). No modifications can be made to any Lancet figures/tables and they must be reproduced in full.

6. If the permission fee for the requested use of our material is waived in this instance, please be advised that your future requests for Elsevier materials may attract a fee.

7. Reservation of Rights: Publisher reserves all rights not specifically granted in the combination of (i) the license details provided by you and accepted in the course of this licensing transaction, (ii) these terms and conditions and (iii) CCC's Billing and Payment terms and conditions.

8. License Contingent Upon Payment: While you may exercise the rights licensed immediately upon issuance of the license at the end of the licensing process for the transaction, provided that you have disclosed complete and accurate details of your proposed use, no license is finally effective unless and until full payment is received from you (either by publisher or by CCC) as provided in CCC's Billing and Payment terms and conditions. If full payment is not received on a timely basis, then any license preliminarily granted shall be deemed automatically revoked and shall be void as if never granted. Further, in the event that you breach any of these terms and conditions or any of CCC's Billing and Payment terms and conditions, the license is automatically revoked and shall be void as if never granted. Use of materials as described in a revoked license, as well as any use of the materials beyond the scope of an unrevoked license, may constitute copyright infringement and publisher reserves the right to take any and all action to protect its copyright in the materials.

9. Warranties: Publisher makes no representations or warranties with respect to the licensed material.

10. Indemnity: You hereby indemnify and agree to hold harmless publisher and CCC, and their respective officers, directors, employees and agents, from and against any and all claims arising out of your use of the licensed material other than as specifically authorized pursuant to this license.

11. No Transfer of License: This license is personal to you and may not be sublicensed, assigned, or transferred by you to any other person without publisher's written permission.

12. No Amendment Except in Writing: This license may not be amended except in a writing signed by both parties (or, in the case of publisher, by CCC on publisher's behalf).

13. Objection to Contrary Terms: Publisher hereby objects to any terms contained in any purchase order, acknowledgment, check endorsement or other writing prepared by you, which terms are inconsistent with these terms and conditions or CCC's Billing and Payment terms and conditions. These terms and conditions, together with CCC's Billing and Payment terms and conditions (which are incorporated herein), comprise the entire agreement between you and publisher (and CCC) concerning this licensing transaction. In the event of any conflict between your obligations established by these terms and conditions and those established by CCC's Billing and Payment terms and conditions, these terms and conditions shall control.

14. Revocation: Elsevier or Copyright Clearance Center may deny the permissions described in this License at their sole discretion, for any reason or no reason, with a full refund payable to you. Notice of such denial will be made using the contact information provided by you. Failure to receive such notice will not alter or invalidate the denial. In no event will Elsevier or Copyright Clearance Center be responsible or liable for any costs, expenses or damage incurred by you as a result of a denial of your permission request, other than a refund of the amount(s) paid by you to Elsevier and/or Copyright Clearance Center for denied permissions.

LIMITED LICENSE

The following terms and conditions apply only to specific license types:

15. **Translation**: This permission is granted for non-exclusive world **English** rights only unless your license was granted for translation rights. If you licensed translation rights you may only translate this content into the languages you requested. A professional translator must perform all translations and reproduce the content word for word preserving the integrity of the article.

8. Reprint permissions

16. **Posting licensed content on any Website**: The following terms and conditions apply as follows: Licensing material from an Elsevier journal: All content posted to the web site must maintain the copyright information line on the bottom of each image; A hyper-text must be included to the Homepage of the journal from which you are licensing at http://www.sciencedirect.com/science /journal/xxxxx or the Elsevier homepage for books at http://www.elsevier.com; Central Storage: This license does not include permission for a scanned version of the material to be stored in a central repository such as that provided by Heron/XanEdu. Licensing material from an Elsevier book: A hyper-text link must be included to the Elsevier homepage at http://www.elsevier.com . All content posted to the web site must maintain the copyright information line on the bottom of each image.

Posting licensed content on Electronic reserve: In addition to the above the following clauses are applicable: The web site must be password-protected and made available only to bona fide students registered on a relevant course. This permission is granted for 1 year only. You may obtain a new license for future website posting.

17. **For journal authors:** the following clauses are applicable in addition to the above:

Preprints:

A preprint is an author's own write-up of research results and analysis, it has not been peer-reviewed, nor has it had any other value added to it by a publisher (such as formatting, copyright, technical enhancement etc.).

Authors can share their preprints anywhere at any time. Preprints should not be added to or enhanced in any way in order to appear more like, or to substitute for, the final versions of articles however authors can update their preprints on arXiv or RePEc with their Accepted Author Manuscript (see below).

If accepted for publication, we encourage authors to link from the preprint to their formal publication via its DOI. Millions of researchers have access to the formal publications on ScienceDirect, and so links will help users to find, access, cite and use the best available version. Please note that Cell Press, The Lancet and some society-owned have different preprint policies. Information on these policies is available on the journal homepage.

Accepted Author Manuscripts: An accepted author manuscript is the manuscript of an article that has been accepted for publication and which typically includes author-incorporated changes suggested during submission, peer review and editor-author communications.

Authors can share their accepted author manuscript:

- immediately
  - via their non-commercial person homepage or blog
  - by updating a preprint in arXiv or RePEc with the accepted manuscript
  - via their research institute or institutional repository for internal institutional uses or as part of an invitation-only research collaboration work-group
  - directly by providing copies to their students or to research collaborators for their personal use
  - for private scholarly sharing as part of an invitation-only work group on commercial sites with which Elsevier has an agreement
- After the embargo period
  - via non-commercial hosting platforms such as their institutional repository
  - via commercial sites with which Elsevier has an agreement

In all cases accepted manuscripts should:

- link to the formal publication via its DOI
- bear a CC-BY-NC-ND license - this is easy to do
- if aggregated with other manuscripts, for example in a repository or other site, be shared in alignment with our hosting policy not be added to or enhanced in any way to appear more like, or to substitute for, the published journal article.

Published journal article (JPA): A published journal article (PJA) is the definitive final record of published research that appears or will appear in the journal and embodies all value-adding publishing activities including peer review co-ordination, copy-editing, formatting, (if relevant) pagination and online enrichment.

Policies for sharing publishing journal articles differ for subscription and gold open access articles:

Subscription Articles: If you are an author, please share a link to your article rather than the full-text. Millions of researchers have access to the formal publications on ScienceDirect, and so links will help your users to find, access, cite, and use the best available version.

Theses and dissertations which contain embedded PJAs as part of the formal submission can be posted publicly by the awarding institution with DOI links back to the formal publications on ScienceDirect.

If you are affiliated with a library that subscribes to ScienceDirect you have additional private sharing rights for others' research accessed under that agreement. This includes use for classroom teaching and internal training at the institution (including use in course packs and courseware programs), and inclusion of the article for grant funding purposes.

Gold Open Access Articles: May be shared according to the author-selected end-user license and should contain a CrossMark logo, the end user license, and a DOI link to the formal publication on ScienceDirect.

Please refer to Elsevier's posting policy for further information.

8. Reprint permissions

18. **For book authors** the following clauses are applicable in addition to the above: Authors are permitted to place a brief summary of their work online only. You are not allowed to download and post the published electronic version of your chapter, nor may you scan the printed edition to create an electronic version. **Posting to a repository:** Authors are permitted to post a summary of their chapter only in their institution's repository.

19. **Thesis/Dissertation**: If your license is for use in a thesis/dissertation your thesis may be submitted to your institution in either print or electronic form. Should your thesis be published commercially, please reapply for permission. These requirements include permission for the Library and Archives of Canada to supply single copies, on demand, of the complete thesis and include permission for Proquest/UMI to supply single copies, on demand, of the complete thesis. Should your thesis be published commercially, please reapply for permission. Theses and dissertations which contain embedded PJAs as part of the formal submission can be posted publicly by the awarding institution with DOI links back to the formal publications on ScienceDirect.

Elsevier Open Access Terms and Conditions

You can publish open access with Elsevier in hundreds of open access journals or in nearly 2000 established subscription journals that support open access publishing. Permitted third party re-use of these open access articles is defined by the author's choice of Creative Commons user license. See our open access license policy for more information.

Terms & Conditions applicable to all Open Access articles published with Elsevier:

Any reuse of the article must not represent the author as endorsing the adaptation of the article nor should the article be modified in such a way as to damage the author's honour or reputation. If any changes have been made, such changes must be clearly indicated.

The author(s) must be appropriately credited and we ask that you include the end user license and a DOI link to the formal publication on ScienceDirect.

If any part of the material to be used (for example, figures) has appeared in our publication with credit or acknowledgement to another source it is the responsibility of the user to ensure their reuse complies with the terms and conditions determined by the rights holder.

Additional Terms & Conditions applicable to each Creative Commons user license:

CC BY: The CC-BY license allows users to copy, to create extracts, abstracts and new works from the Article, to alter and revise the Article and to make commercial use of the Article (including reuse and/or resale of the Article by commercial entities), provided the user gives appropriate credit (with a link to the formal publication through the relevant DOI), provides a link to the license, indicates if changes were made and the licensor is not represented as endorsing the use made of the work. The full details of the license are available at http://creativecommons.org/licenses/by/4.0.

CC BY NC SA: The CC BY-NC-SA license allows users to copy, to create extracts, abstracts and new works from the Article, to alter and revise the Article, provided this is not done for commercial purposes, and that the user gives appropriate credit (with a link to the formal publication through the relevant DOI), provides a link to the license, indicates if changes were made and the licensor is not represented as endorsing the use made of the work. Further, any new works must be made available on the same conditions. The full details of the license are available at http://creativecommons.org/licenses/by-nc-sa/4.0.

CC BY NC ND: The CC BY-NC-ND license allows users to copy and distribute the Article, provided this is not done for commercial purposes and further does not permit distribution of the Article if it is changed or edited in any way, and provided the user gives appropriate credit (with a link to the formal publication through the relevant DOI), provides a link to the license, and that the licensor is not represented as endorsing the use made of the work. The full details of the license are available at http://creativecommons.org/licenses/by-nc-nd/4.0. Any commercial reuse of Open Access articles published with a CC BY NC SA or CC BY NC ND license requires permission from Elsevier and will be subject to a fee.

Commercial reuse includes:

- Associating advertising with the full text of the Article
- Charging fees for document delivery or access
- Article aggregation
- Systematic distribution via e-mail lists or share buttons

Posting or linking by commercial companies for use by customers of those companies.

20. **Other Conditions**:

v1.10

Questions? customercare@copyright.com or +1-855-239-3415 (toll free in the US) or +1-978-646-2777.

8. Reprint permissions

AIP PUBLISHING LICENSE
TERMS AND CONDITIONS

Mar 25, 2021

This Agreement between Technical University of Munich -- Max Schütz ("You") and AIP Publishing ("AIP Publishing") consists of your license details and the terms and conditions provided by AIP Publishing and Copyright Clearance Center.

License Number	4973070833334
License date	Dec 20, 2020
Licensed Content Publisher	AIP Publishing
Licensed Content Publication	Review of Scientific Instruments
Licensed Content Title	Production of bimetallic clusters by a dual-target dual-laser vaporization source
Licensed Content Author	Wim Bouwen, Peter Thoen, Frederik Vanhoutte, et al
Licensed Content Date	Jan 1, 2000
Licensed Content Volume	71
Licensed Content Issue	1
Type of Use	Thesis/Dissertation
Requestor type	Student
Format	Print and electronic
Portion	Figure/Table
Number of figures/tables	1
Title	Fundamental Understanding of living cluster libraries in solution
Institution name	Technical University of Munich
Expected presentation date	Jun 2021
Order reference number	2
Portions	Figure 1, page 2
Requestor Location	Technical University of Munich Lichtenbergstrasse 4
	Garching, 85748 Germany Attn: Technical University of Munich
Total	**0.00 EUR**

Terms and Conditions

AIP Publishing -- Terms and Conditions: Permissions Uses

AIP Publishing hereby grants to you the non-exclusive right and license to use and/or distribute the Material according to the use specified in your order, on a one-time basis, for the specified term, with a maximum distribution equal to the number that you have ordered. Any links or other content accompanying the Material are not the subject of this license.

1. You agree to include the following copyright and permission notice with the reproduction of the Material:"Reprinted from [FULL CITATION], with the permission of AIP Publishing." For an article, the credit line and permission notice must be printed on the first page of the article or book chapter. For photographs, covers, or tables, the notice may appear with the Material, in a footnote, or in the reference list.
2. If you have licensed reuse of a figure, photograph, cover, or table, it is your responsibility to ensure that the material is original to AIP Publishing and does not contain the copyright of another entity, and that the copyright notice of the figure,

8. Reprint permissions

photograph, cover, or table does not indicate that it was reprinted by AIP Publishing, with permission, from another source. Under no circumstances does AIP Publishing purport or intend to grant permission to reuse material to which it does not hold appropriate rights.
You may not alter or modify the Material in any manner. You may translate the Material into another language only if you have licensed translation rights. You may not use the Material for promotional purposes.

3. The foregoing license shall not take effect unless and until AIP Publishing or its agent, Copyright Clearance Center, receives the Payment in accordance with Copyright Clearance Center Billing and Payment Terms and Conditions, which are incorporated herein by reference.

4. AIP Publishing or Copyright Clearance Center may, within two business days of granting this license, revoke the license for any reason whatsoever, with a full refund payable to you. Should you violate the terms of this license at any time, AIP Publishing, or Copyright Clearance Center may revoke the license with no refund to you. Notice of such revocation will be made using the contact information provided by you. Failure to receive such notice will not nullify the revocation.

5. AIP Publishing makes no representations or warranties with respect to the Material. You agree to indemnify and hold harmless AIP Publishing, and their officers, directors, employees or agents from and against any and all claims arising out of your use of the Material other than as specifically authorized herein.

6. The permission granted herein is personal to you and is not transferable or assignable without the prior written permission of AIP Publishing. This license may not be amended except in a writing signed by the party to be charged.

7. If purchase orders, acknowledgments or check endorsements are issued on any forms containing terms and conditions which are inconsistent with these provisions, such inconsistent terms and conditions shall be of no force and effect. This document, including the CCC Billing and Payment Terms and Conditions, shall be the entire agreement between the parties relating to the subject matter hereof.

This Agreement shall be governed by and construed in accordance with the laws of the State of New York. Both parties hereby submit to the jurisdiction of the courts of New York County for purposes of resolving any disputes that may arise hereunder.

V1.2

Questions? customercare@copyright.com or +1-855-239-3415 (toll free in the US) or +1-978-646-2777.

8. Reprint permissions

SPRINGER NATURE LICENSE
TERMS AND CONDITIONS

Mar 25, 2021

This Agreement between Technical University of Munich -- Max Schütz ("You") and Springer Nature ("Springer Nature") consists of your license details and the terms and conditions provided by Springer Nature and Copyright Clearance Center.

License Number	4974250881468
License date	Dec 22, 2020
Licensed Content Publisher	Springer Nature
Licensed Content Publication	Nature Methods
Licensed Content Title	Higher-energy C-trap dissociation for peptide modification analysis
Licensed Content Author	Jesper V Olsen et al
Licensed Content Date	Aug 26, 2007
Type of Use	Thesis/Dissertation
Requestor type	academic/university or research institute
Format	print and electronic
Portion	figures/tables/illustrations
Number of figures/tables/illustrations	1
High-res required	no
Will you be translating?	no
Circulation/distribution	1 - 29
Author of this Springer Nature content	no
Title	Fundamental Understanding of living cluster libraries in solution
Institution name	Technical University of Munich
Expected presentation date	Jun 2021
Order reference number	4
Portions	Figure 1 b)
Requestor Location	Technical University of Munich Lichtenbergstrasse 4
	Garching, 85748 Germany Attn: Technical University of Munich
Total	**0.00 EUR**
Terms and Conditions	

Springer Nature Customer Service Centre GmbH
Terms and Conditions

This agreement sets out the terms and conditions of the licence (the **Licence**) between you and **Springer Nature Customer Service Centre GmbH** (the **Licensor**). By clicking 'accept' and completing the transaction for the material (**Licensed Material**), you also confirm your acceptance of these terms and conditions.

1. Grant of License

8. Reprint permissions

1. 1. The Licensor grants you a personal, non-exclusive, non-transferable, world-wide licence to reproduce the Licensed Material for the purpose specified in your order only. Licences are granted for the specific use requested in the order and for no other use, subject to the conditions below.

1. 2. The Licensor warrants that it has, to the best of its knowledge, the rights to license reuse of the Licensed Material. However, you should ensure that the material you are requesting is original to the Licensor and does not carry the copyright of another entity (as credited in the published version).

1. 3. If the credit line on any part of the material you have requested indicates that it was reprinted or adapted with permission from another source, then you should also seek permission from that source to reuse the material.

2. Scope of Licence

2. 1. You may only use the Licensed Content in the manner and to the extent permitted by these Ts&Cs and any applicable laws.

2. 2. A separate licence may be required for any additional use of the Licensed Material, e.g. where a licence has been purchased for print only use, separate permission must be obtained for electronic re-use. Similarly, a licence is only valid in the language selected and does not apply for editions in other languages unless additional translation rights have been granted separately in the licence. Any content owned by third parties are expressly excluded from the licence.

2. 3. Similarly, rights for additional components such as custom editions and derivatives require additional permission and may be subject to an additional fee. Please apply to Journalpermissions@springernature.com/bookpermissions@springernature.com for these rights.

2. 4. Where permission has been granted **free of charge** for material in print, permission may also be granted for any electronic version of that work, provided that the material is incidental to your work as a whole and that the electronic version is essentially equivalent to, or substitutes for, the print version.

2. 5. An alternative scope of licence may apply to signatories of the STM Permissions Guidelines, as amended from time to time.

3. Duration of Licence

3. 1. A licence for is valid from the date of purchase ('Licence Date') at the end of the relevant period in the below table:

Scope of Licence	Duration of Licence
Post on a website	12 months
Presentations	12 months
Books and journals	Lifetime of the edition in the language purchased

4. Acknowledgement

4. 1. The Licensor's permission must be acknowledged next to the Licenced Material in print. In electronic form, this acknowledgement must be visible at the same time as the figures/tables/illustrations or abstract, and must be hyperlinked to the journal/book's homepage. Our required acknowledgement format is in the Appendix below.

5. Restrictions on use

5. 1. Use of the Licensed Material may be permitted for incidental promotional use and minor editing privileges e.g. minor adaptations of single figures, changes of format, colour and/or style where the adaptation is credited as set out in Appendix 1 below. Any other changes including but not limited to, cropping, adapting, omitting material that affect the meaning, intention or moral rights of the author are strictly prohibited.

8. Reprint permissions

5. 2. You must not use any Licensed Material as part of any design or trademark.

5. 3. Licensed Material may be used in Open Access Publications (OAP) before publication by Springer Nature, but any Licensed Material must be removed from OAP sites prior to final publication.

6. Ownership of Rights

6. 1. Licensed Material remains the property of either Licensor or the relevant third party and any rights not explicitly granted herein are expressly reserved.

7. Warranty

IN NO EVENT SHALL LICENSOR BE LIABLE TO YOU OR ANY OTHER PARTY OR ANY OTHER PERSON OR FOR ANY SPECIAL, CONSEQUENTIAL, INCIDENTAL OR INDIRECT DAMAGES, HOWEVER CAUSED, ARISING OUT OF OR IN CONNECTION WITH THE DOWNLOADING, VIEWING OR USE OF THE MATERIALS REGARDLESS OF THE FORM OF ACTION, WHETHER FOR BREACH OF CONTRACT, BREACH OF WARRANTY, TORT, NEGLIGENCE, INFRINGEMENT OR OTHERWISE (INCLUDING, WITHOUT LIMITATION, DAMAGES BASED ON LOSS OF PROFITS, DATA, FILES, USE, BUSINESS OPPORTUNITY OR CLAIMS OF THIRD PARTIES), AND
WHETHER OR NOT THE PARTY HAS BEEN ADVISED OF THE POSSIBILITY OF SUCH DAMAGES. THIS LIMITATION SHALL APPLY NOTWITHSTANDING ANY FAILURE OF ESSENTIAL PURPOSE OF ANY LIMITED REMEDY PROVIDED HEREIN.

8. Limitations

8. 1. _BOOKS ONLY:_Where **'reuse in a dissertation/thesis'** has been selected the following terms apply: Print rights of the final author's accepted manuscript (for clarity, NOT the published version) for up to 100 copies, electronic rights for use only on a personal website or institutional repository as defined by the Sherpa guideline (www.sherpa.ac.uk/romeo/).

9. Termination and Cancellation

9. 1. Licences will expire after the period shown in Clause 3 (above).

9. 2. Licensee reserves the right to terminate the Licence in the event that payment is not received in full or if there has been a breach of this agreement by you.

<u>**Appendix 1 — Acknowledgements:**</u>

For Journal Content:
Reprinted by permission from [**the Licensor**]: [**Journal Publisher** (e.g. Nature/Springer/Palgrave)] [**JOURNAL NAME**] [**REFERENCE CITATION** (Article name, Author(s) Name), [**COPYRIGHT**] (year of publication)

For **Advance Online Publication papers:**
Reprinted by permission from [**the Licensor**]: [**Journal Publisher** (e.g. Nature/Springer/Palgrave)] [**JOURNAL NAME**] [**REFERENCE CITATION** (Article name, Author(s) Name), [**COPYRIGHT**] (year of publication), advance online publication, day month year (doi: 10.1038/sj.[JOURNAL ACRONYM].)

For Adaptations/Translations:
Adapted/Translated by permission from [**the Licensor**]: [**Journal Publisher** (e.g. Nature/Springer/Palgrave)] [**JOURNAL NAME**] [**REFERENCE CITATION** (Article name, Author(s) Name), [**COPYRIGHT**] (year of publication)

<u>**Note: For any republication from the British Journal of Cancer, the following credit line style applies:**</u>

Reprinted/adapted/translated by permission from [**the Licensor**]: on behalf of Cancer Research UK: : [**Journal Publisher**

376

8. Reprint permissions

(e.g. Nature/Springer/Palgrave)] [**JOURNAL NAME**] [**REFERENCE CITATION** (Article name, Author(s) Name), [**COPYRIGHT**] (year of publication)

For **Advance Online Publication** papers:
Reprinted by permission from The [**the Licensor**]: on behalf of Cancer Research UK: [**Journal Publisher** (e.g. Nature/Springer/Palgrave)] [**JOURNAL NAME**] [**REFERENCE CITATION** (Article name, Author(s) Name), [**COPYRIGHT**] (year of publication), advance online publication, day month year (doi: 10.1038/sj.[JOURNAL ACRONYM])

For Book content:
Reprinted/adapted by permission from [**the Licensor**]: [**Book Publisher** (e.g. Palgrave Macmillan, Springer etc) [**Book Title**] by [**Book author**(s)] [**COPYRIGHT**] (year of publication)

Other Conditions:

Version 1.2

Questions? customercare@copyright.com **or +1-855-239-3415 (toll free in the US) or +1-978-646-2777.**

8. Reprint permissions

SPRINGER NATURE LICENSE
TERMS AND CONDITIONS

Mar 25, 2021

This Agreement between Technical University of Munich -- Max Schütz ("You") and Springer Nature ("Springer Nature") consists of your license details and the terms and conditions provided by Springer Nature and Copyright Clearance Center.

License Number	4974720195201
License date	Dec 23, 2020
Licensed Content Publisher	Springer Nature
Licensed Content Publication	Nature
Licensed Content Title	Mass spectrometry-based proteomics
Licensed Content Author	Ruedi Aebersold et al
Licensed Content Date	Mar 13, 2003
Type of Use	Thesis/Dissertation
Requestor type	academic/university or research institute
Format	print and electronic
Portion	figures/tables/illustrations
Number of figures/tables /illustrations	1
High-res required	no
Will you be translating?	no
Circulation/distribution	1 - 29
Author of this Springer Nature content	no
Title	Fundamental Understanding of living cluster libraries in solution
Institution name	Technical University of Munich
Expected presentation date	Jun 2021
Order reference number	6
Portions	Figure 3, page 4
Requestor Location	Technical University of Munich Lichtenbergstrasse 4
	Garching, 85748 Germany Attn: Technical University of Munich
Total	**0.00 EUR**
Terms and Conditions	

Springer Nature Customer Service Centre GmbH
Terms and Conditions

This agreement sets out the terms and conditions of the licence (the **Licence**) between you and **Springer Nature Customer Service Centre GmbH** (the **Licensor**). By clicking 'accept' and completing the transaction for the material (**Licensed Material**), you also confirm your acceptance of these terms and conditions.

1. Grant of License

8. Reprint permissions

1. 1. The Licensor grants you a personal, non-exclusive, non-transferable, world-wide licence to reproduce the Licensed Material for the purpose specified in your order only. Licences are granted for the specific use requested in the order and for no other use, subject to the conditions below.

1. 2. The Licensor warrants that it has, to the best of its knowledge, the rights to license reuse of the Licensed Material. However, you should ensure that the material you are requesting is original to the Licensor and does not carry the copyright of another entity (as credited in the published version).

1. 3. If the credit line on any part of the material you have requested indicates that it was reprinted or adapted with permission from another source, then you should also seek permission from that source to reuse the material.

2. Scope of Licence

2. 1. You may only use the Licensed Content in the manner and to the extent permitted by these Ts&Cs and any applicable laws.

2. 2. A separate licence may be required for any additional use of the Licensed Material, e.g. where a licence has been purchased for print only use, separate permission must be obtained for electronic re-use. Similarly, a licence is only valid in the language selected and does not apply for editions in other languages unless additional translation rights have been granted separately in the licence. Any content owned by third parties are expressly excluded from the licence.

2. 3. Similarly, rights for additional components such as custom editions and derivatives require additional permission and may be subject to an additional fee. Please apply to
Journalpermissions@springernature.com/bookpermissions@springernature.com for these rights.

2. 4. Where permission has been granted **free of charge** for material in print, permission may also be granted for any electronic version of that work, provided that the material is incidental to your work as a whole and that the electronic version is essentially equivalent to, or substitutes for, the print version.

2. 5. An alternative scope of licence may apply to signatories of the STM Permissions Guidelines, as amended from time to time.

3. Duration of Licence

3. 1. A licence for is valid from the date of purchase ('Licence Date') at the end of the relevant period in the below table:

Scope of Licence	Duration of Licence
Post on a website	12 months
Presentations	12 months
Books and journals	Lifetime of the edition in the language purchased

4. Acknowledgement

4. 1. The Licensor's permission must be acknowledged next to the Licenced Material in print. In electronic form, this acknowledgement must be visible at the same time as the figures/tables/illustrations or abstract, and must be hyperlinked to the journal/book's homepage. Our required acknowledgement format is in the Appendix below.

5. Restrictions on use

5. 1. Use of the Licensed Material may be permitted for incidental promotional use and minor editing privileges e.g. minor adaptations of single figures, changes of format, colour and/or style where the adaptation is credited as set out in Appendix 1 below. Any other changes including but not limited to, cropping, adapting, omitting material that affect the meaning, intention or moral rights of the author are strictly prohibited.

8. Reprint permissions

5. 2. You must not use any Licensed Material as part of any design or trademark.

5. 3. Licensed Material may be used in Open Access Publications (OAP) before publication by Springer Nature, but any Licensed Material must be removed from OAP sites prior to final publication.

6. Ownership of Rights

6. 1. Licensed Material remains the property of either Licensor or the relevant third party and any rights not explicitly granted herein are expressly reserved.

7. Warranty

IN NO EVENT SHALL LICENSOR BE LIABLE TO YOU OR ANY OTHER PARTY OR ANY OTHER PERSON OR FOR ANY SPECIAL, CONSEQUENTIAL, INCIDENTAL OR INDIRECT DAMAGES, HOWEVER CAUSED, ARISING OUT OF OR IN CONNECTION WITH THE DOWNLOADING, VIEWING OR USE OF THE MATERIALS REGARDLESS OF THE FORM OF ACTION, WHETHER FOR BREACH OF CONTRACT, BREACH OF WARRANTY, TORT, NEGLIGENCE, INFRINGEMENT OR OTHERWISE (INCLUDING, WITHOUT LIMITATION, DAMAGES BASED ON LOSS OF PROFITS, DATA, FILES, USE, BUSINESS OPPORTUNITY OR CLAIMS OF THIRD PARTIES), AND
WHETHER OR NOT THE PARTY HAS BEEN ADVISED OF THE POSSIBILITY OF SUCH DAMAGES. THIS LIMITATION SHALL APPLY NOTWITHSTANDING ANY FAILURE OF ESSENTIAL PURPOSE OF ANY LIMITED REMEDY PROVIDED HEREIN.

8. Limitations

8. 1. _BOOKS ONLY:_Where **'reuse in a dissertation/thesis'** has been selected the following terms apply: Print rights of the final author's accepted manuscript (for clarity, NOT the published version) for up to 100 copies, electronic rights for use only on a personal website or institutional repository as defined by the Sherpa guideline (www.sherpa.ac.uk/romeo/).

9. Termination and Cancellation

9. 1. Licences will expire after the period shown in Clause 3 (above).

9. 2. Licensee reserves the right to terminate the Licence in the event that payment is not received in full or if there has been a breach of this agreement by you.

<u>Appendix 1 — Acknowledgements:</u>

For Journal Content:
Reprinted by permission from [**the Licensor**]: [**Journal Publisher** (e.g. Nature/Springer/Palgrave)] [**JOURNAL NAME**] [**REFERENCE CITATION** (Article name, Author(s) Name), [**COPYRIGHT**] (year of publication)

For **Advance Online Publication papers:**
Reprinted by permission from [**the Licensor**]: [**Journal Publisher** (e.g. Nature/Springer/Palgrave)] [**JOURNAL NAME**] [**REFERENCE CITATION** (Article name, Author(s) Name), [**COPYRIGHT**] (year of publication), advance online publication, day month year (doi: 10.1038/sj.[JOURNAL ACRONYM].)

For Adaptations/Translations:
Adapted/Translated by permission from [**the Licensor**]: [**Journal Publisher** (e.g. Nature/Springer/Palgrave)] [**JOURNAL NAME**] [**REFERENCE CITATION** (Article name, Author(s) Name), [**COPYRIGHT**] (year of publication)

<u>Note: For any republication from the British Journal of Cancer, the following credit line style applies:</u>

Reprinted/adapted/translated by permission from [**the Licensor**]: on behalf of Cancer Research UK: : [**Journal Publisher**

8. Reprint permissions

(e.g. Nature/Springer/Palgrave)] [**JOURNAL NAME**] [**REFERENCE CITATION** (Article name, Author(s) Name), [**COPYRIGHT**] (year of publication)

For **Advance Online Publication** papers:
Reprinted by permission from The [**the Licensor**]: on behalf of Cancer Research UK: [**Journal Publisher** (e.g. Nature/Springer/Palgrave)] [**JOURNAL NAME**] [**REFERENCE CITATION** (Article name, Author(s) Name), [**COPYRIGHT**] (year of publication), advance online publication, day month year (doi: 10.1038/sj.[JOURNAL ACRONYM])

For Book content:
Reprinted/adapted by permission from [**the Licensor**]: [**Book Publisher** (e.g. Palgrave Macmillan, Springer etc) [**Book Title**] by [**Book author**(s)] [**COPYRIGHT**] (year of publication)

Other Conditions:

Version 1.2

Questions? customercare@copyright.com or +1-855-239-3415 (toll free in the US) or +1-978-646-2777.

8. Reprint permissions

JOHN WILEY AND SONS LICENSE
TERMS AND CONDITIONS

Mar 25, 2021

This Agreement between Technical University of Munich -- Max Schütz ("You") and John Wiley and Sons ("John Wiley and Sons") consists of your license details and the terms and conditions provided by John Wiley and Sons and Copyright Clearance Center.

License Number	4974730044571
License date	Dec 23, 2020
Licensed Content Publisher	John Wiley and Sons
Licensed Content Publication	Angewandte Chemie International Edition
Licensed Content Title	Electrospray Ionization Tandem Mass Spectrometry in High-Throughput Screening of Homogeneous Catalysts
Licensed Content Author	Peter Chen
Licensed Content Date	Jun 24, 2003
Licensed Content Volume	42
Licensed Content Issue	25
Licensed Content Pages	16
Type of Use	Dissertation/Thesis
Requestor type	University/Academic
Format	Print and electronic
Portion	Figure/table
Number of figures/tables	1
Will you be translating?	No
Title	Fundamental Understanding of living cluster libraries in solution
Institution name	Technical University of Munich
Expected presentation date	Jun 2021
Order reference number	7
Portions	Figure 1, page 4
Requestor Location	Technical University of Munich Lichtenbergstrasse 4
	Garching, 85748 Germany Attn: Technical University of Munich
Publisher Tax ID	EU826007151
Total	**0.00 EUR**
Terms and Conditions	

TERMS AND CONDITIONS

This copyrighted material is owned by or exclusively licensed to John Wiley & Sons, Inc. or one of its group companies (each a"Wiley Company") or handled on behalf of a society with which a Wiley Company has exclusive publishing rights in relation to a particular work (collectively "WILEY"). By clicking "accept" in connection with completing this licensing transaction, you agree that the following terms and conditions apply to this transaction (along with the billing and payment terms and conditions established by the Copyright Clearance Center Inc., ("CCC's Billing and Payment terms and conditions"), at the time that you opened your RightsLink account (these are available at any time at http://myaccount.copyright.com).

8. Reprint permissions

Terms and Conditions

- The materials you have requested permission to reproduce or reuse (the "Wiley Materials") are protected by copyright.

- You are hereby granted a personal, non-exclusive, non-sub licensable (on a stand-alone basis), non-transferable, worldwide, limited license to reproduce the Wiley Materials for the purpose specified in the licensing process. This license, **and any CONTENT (PDF or image file) purchased as part of your order,** is for a one-time use only and limited to any maximum distribution number specified in the license. The first instance of republication or reuse granted by this license must be completed within two years of the date of the grant of this license (although copies prepared before the end date may be distributed thereafter). The Wiley Materials shall not be used in any other manner or for any other purpose, beyond what is granted in the license. Permission is granted subject to an appropriate acknowledgement given to the author, title of the material/book/journal and the publisher. You shall also duplicate the copyright notice that appears in the Wiley publication in your use of the Wiley Material. Permission is also granted on the understanding that nowhere in the text is a previously published source acknowledged for all or part of this Wiley Material. Any third party content is expressly excluded from this permission.

- With respect to the Wiley Materials, all rights are reserved. Except as expressly granted by the terms of the license, no part of the Wiley Materials may be copied, modified, adapted (except for minor reformatting required by the new Publication), translated, reproduced, transferred or distributed, in any form or by any means, and no derivative works may be made based on the Wiley Materials without the prior permission of the respective copyright owner.**For STM Signatory Publishers clearing permission under the terms of the** STM Permissions Guidelines **only, the terms of the license are extended to include subsequent editions and for editions in other languages, provided such editions are for the work as a whole in situ and does not involve the separate exploitation of the permitted figures or extracts,** You may not alter, remove or suppress in any manner any copyright, trademark or other notices displayed by the Wiley Materials. You may not license, rent, sell, loan, lease, pledge, offer as security, transfer or assign the Wiley Materials on a stand-alone basis, or any of the rights granted to you hereunder to any other person.

- The Wiley Materials and all of the intellectual property rights therein shall at all times remain the exclusive property of John Wiley & Sons Inc, the Wiley Companies, or their respective licensors, and your interest therein is only that of having possession of and the right to reproduce the Wiley Materials pursuant to Section 2 herein during the continuance of this Agreement. You agree that you own no right, title or interest in or to the Wiley Materials or any of the intellectual property rights therein. You shall have no rights hereunder other than the license as provided for above in Section 2. No right, license or interest to any trademark, trade name, service mark or other branding ("Marks") of WILEY or its licensors is granted hereunder, and you agree that you shall not assert any such right, license or interest with respect thereto

- NEITHER WILEY NOR ITS LICENSORS MAKES ANY WARRANTY OR REPRESENTATION OF ANY KIND TO YOU OR ANY THIRD PARTY, EXPRESS, IMPLIED OR STATUTORY, WITH RESPECT TO THE MATERIALS OR THE ACCURACY OF ANY INFORMATION CONTAINED IN THE MATERIALS, INCLUDING, WITHOUT LIMITATION, ANY IMPLIED WARRANTY OF MERCHANTABILITY, ACCURACY, SATISFACTORY QUALITY, FITNESS FOR A PARTICULAR PURPOSE, USABILITY, INTEGRATION OR NON-INFRINGEMENT AND ALL SUCH WARRANTIES ARE HEREBY EXCLUDED BY WILEY AND ITS LICENSORS AND WAIVED BY YOU.

- WILEY shall have the right to terminate this Agreement immediately upon breach of this Agreement by you.

- You shall indemnify, defend and hold harmless WILEY, its Licensors and their respective directors, officers, agents and employees, from and against any actual or threatened claims, demands, causes of action or proceedings arising from any breach of this Agreement by you.

- IN NO EVENT SHALL WILEY OR ITS LICENSORS BE LIABLE TO YOU OR ANY OTHER PARTY OR ANY OTHER PERSON OR ENTITY FOR ANY SPECIAL, CONSEQUENTIAL, INCIDENTAL, INDIRECT, EXEMPLARY OR PUNITIVE DAMAGES, HOWEVER CAUSED, ARISING OUT OF OR IN CONNECTION WITH THE DOWNLOADING, PROVISIONING, VIEWING OR USE OF THE MATERIALS REGARDLESS OF THE FORM OF ACTION, WHETHER FOR BREACH OF CONTRACT, BREACH OF WARRANTY, TORT, NEGLIGENCE, INFRINGEMENT OR OTHERWISE (INCLUDING, WITHOUT LIMITATION, DAMAGES BASED ON LOSS OF PROFITS, DATA, FILES, USE, BUSINESS OPPORTUNITY OR CLAIMS OF THIRD PARTIES), AND WHETHER OR NOT THE PARTY HAS BEEN ADVISED OF THE POSSIBILITY OF SUCH DAMAGES. THIS LIMITATION SHALL APPLY NOTWITHSTANDING ANY FAILURE OF ESSENTIAL PURPOSE OF ANY LIMITED REMEDY PROVIDED HEREIN.

- Should any provision of this Agreement be held by a court of competent jurisdiction to be illegal, invalid, or unenforceable,

8. Reprint permissions

that provision shall be deemed amended to achieve as nearly as possible the same economic effect as the original provision, and the legality, validity and enforceability of the remaining provisions of this Agreement shall not be affected or impaired thereby.

- The failure of either party to enforce any term or condition of this Agreement shall not constitute a waiver of either party's right to enforce each and every term and condition of this Agreement. No breach under this agreement shall be deemed waived or excused by either party unless such waiver or consent is in writing signed by the party granting such waiver or consent. The waiver by or consent of a party to a breach of any provision of this Agreement shall not operate or be construed as a waiver of or consent to any other or subsequent breach by such other party.

- This Agreement may not be assigned (including by operation of law or otherwise) by you without WILEY's prior written consent.

- Any fee required for this permission shall be non-refundable after thirty (30) days from receipt by the CCC.

- These terms and conditions together with CCC's Billing and Payment terms and conditions (which are incorporated herein) form the entire agreement between you and WILEY concerning this licensing transaction and (in the absence of fraud) supersedes all prior agreements and representations of the parties, oral or written. This Agreement may not be amended except in writing signed by both parties. This Agreement shall be binding upon and inure to the benefit of the parties' successors, legal representatives, and authorized assigns.

- In the event of any conflict between your obligations established by these terms and conditions and those established by CCC's Billing and Payment terms and conditions, these terms and conditions shall prevail.

- WILEY expressly reserves all rights not specifically granted in the combination of (i) the license details provided by you and accepted in the course of this licensing transaction, (ii) these terms and conditions and (iii) CCC's Billing and Payment terms and conditions.

- This Agreement will be void if the Type of Use, Format, Circulation, or Requestor Type was misrepresented during the licensing process.

- This Agreement shall be governed by and construed in accordance with the laws of the State of New York, USA, without regards to such state's conflict of law rules. Any legal action, suit or proceeding arising out of or relating to these Terms and Conditions or the breach thereof shall be instituted in a court of competent jurisdiction in New York County in the State of New York in the United States of America and each party hereby consents and submits to the personal jurisdiction of such court, waives any objection to venue in such court and consents to service of process by registered or certified mail, return receipt requested, at the last known address of such party.

WILEY OPEN ACCESS TERMS AND CONDITIONS
Wiley Publishes Open Access Articles in fully Open Access Journals and in Subscription journals offering Online Open. Although most of the fully Open Access journals publish open access articles under the terms of the Creative Commons Attribution (CC BY) License only, the subscription journals and a few of the Open Access Journals offer a choice of Creative Commons Licenses. The license type is clearly identified on the article.
The Creative Commons Attribution License
The Creative Commons Attribution License (CC-BY) allows users to copy, distribute and transmit an article, adapt the article and make commercial use of the article. The CC-BY license permits commercial and non-
Creative Commons Attribution Non-Commercial License
The Creative Commons Attribution Non-Commercial (CC-BY-NC)License permits use, distribution and reproduction in any medium, provided the original work is properly cited and is not used for commercial purposes.(see below)

Creative Commons Attribution-Non-Commercial-NoDerivs License
The Creative Commons Attribution Non-Commercial-NoDerivs License (CC-BY-NC-ND) permits use, distribution and reproduction in any medium, provided the original work is properly cited, is not used for commercial purposes and no modifications or adaptations are made. (see below)
Use by commercial "for-profit" organizations
Use of Wiley Open Access articles for commercial, promotional, or marketing purposes requires further explicit permission from Wiley and will be subject to a fee.
Further details can be found on Wiley Online Library http://olabout.wiley.com/WileyCDA/Section/id-410895.html

8. Reprint permissions

Other Terms and Conditions:

v1.10 Last updated September 2015

Questions? customercare@copyright.com or **+1-855-239-3415 (toll free in the US) or +1-978-646-2777.**

8. Reprint permissions

JOHN WILEY AND SONS LICENSE
TERMS AND CONDITIONS

Mar 25, 2021

This Agreement between Technical University of Munich -- Max Schütz ("You") and John Wiley and Sons ("John Wiley and Sons") consists of your license details and the terms and conditions provided by John Wiley and Sons and Copyright Clearance Center.

License Number	4974750628300
License date	Dec 23, 2020
Licensed Content Publisher	John Wiley and Sons
Licensed Content Publication	Angewandte Chemie International Edition
Licensed Content Title	Combinatorial Transition-Metal Catalysis: Mixing Monodentate Ligands to Control Enantio-, Diastereo-, and Regioselectivity
Licensed Content Author	Manfred T. Reetz
Licensed Content Date	Mar 18, 2008
Licensed Content Volume	47
Licensed Content Issue	14
Licensed Content Pages	33
Type of Use	Dissertation/Thesis
Requestor type	University/Academic
Format	Print and electronic
Portion	Figure/table
Number of figures/tables	1
Will you be translating?	No
Title	Fundamental Understanding of living cluster libraries in solution
Institution name	Technical University of Munich
Expected presentation date	Jun 2021
Order reference number	7
Portions	Scheme 4, page 3
Requestor Location	Technical University of Munich Lichtenbergstrasse 4
	Garching, 85748 Germany Attn: Technical University of Munich
Publisher Tax ID	EU826007151
Total	**0.00 EUR**
Terms and Conditions	

TERMS AND CONDITIONS

8. Reprint permissions

Terms and Conditions

- The materials you have requested permission to reproduce or reuse (the "Wiley Materials") are protected by copyright.

- You are hereby granted a personal, non-exclusive, non-sub licensable (on a stand-alone basis), non-transferable, worldwide, limited license to reproduce the Wiley Materials for the purpose specified in the licensing process. This license, **and any CONTENT (PDF or image file) purchased as part of your order,** is for a one-time use only and limited to any maximum distribution number specified in the license. The first instance of republication or reuse granted by this license must be completed within two years of the date of the grant of this license (although copies prepared before the end date may be distributed thereafter). The Wiley Materials shall not be used in any other manner or for any other purpose, beyond what is granted in the license. Permission is granted subject to an appropriate acknowledgement given to the author, title of the material/book/journal and the publisher. You shall also duplicate the copyright notice that appears in the Wiley publication in your use of the Wiley Material. Permission is also granted on the understanding that nowhere in the text is a previously published source acknowledged for all or part of this Wiley Material. Any third party content is expressly excluded from this permission.

- With respect to the Wiley Materials, all rights are reserved. Except as expressly granted by the terms of the license, no part of the Wiley Materials may be copied, modified, adapted (except for minor reformatting required by the new Publication), translated, reproduced, transferred or distributed, in any form or by any means, and no derivative works may be made based on the Wiley Materials without the prior permission of the respective copyright owner.**For STM Signatory Publishers clearing permission under the terms of the** STM Permissions Guidelines **only, the terms of the license are extended to include subsequent editions and for editions in other languages, provided such editions are for the work as a whole in situ and does not involve the separate exploitation of the permitted figures or extracts,** You may not alter, remove or suppress in any manner any copyright, trademark or other notices displayed by the Wiley Materials. You may not license, rent, sell, loan, lease, pledge, offer as security, transfer or assign the Wiley Materials on a stand-alone basis, or any of the rights granted to you hereunder to any other person.

- The Wiley Materials and all of the intellectual property rights therein shall at all times remain the exclusive property of John Wiley & Sons Inc, the Wiley Companies, or their respective licensors, and your interest therein is only that of having possession of and the right to reproduce the Wiley Materials pursuant to Section 2 herein during the continuance of this Agreement. You agree that you own no right, title or interest in or to the Wiley Materials or any of the intellectual property rights therein. You shall have no rights hereunder other than the license as provided for above in Section 2. No right, license or interest to any trademark, trade name, service mark or other branding ("Marks") of WILEY or its licensors is granted hereunder, and you agree that you shall not assert any such right, license or interest with respect thereto

- NEITHER WILEY NOR ITS LICENSORS MAKES ANY WARRANTY OR REPRESENTATION OF ANY KIND TO YOU OR ANY THIRD PARTY, EXPRESS, IMPLIED OR STATUTORY, WITH RESPECT TO THE MATERIALS OR THE ACCURACY OF ANY INFORMATION CONTAINED IN THE MATERIALS, INCLUDING, WITHOUT LIMITATION, ANY IMPLIED WARRANTY OF MERCHANTABILITY, ACCURACY, SATISFACTORY QUALITY, FITNESS FOR A PARTICULAR PURPOSE, USABILITY, INTEGRATION OR NON-INFRINGEMENT AND ALL SUCH WARRANTIES ARE HEREBY EXCLUDED BY WILEY AND ITS LICENSORS AND WAIVED BY YOU.

- WILEY shall have the right to terminate this Agreement immediately upon breach of this Agreement by you.

- You shall indemnify, defend and hold harmless WILEY, its Licensors and their respective directors, officers, agents and employees, from and against any actual or threatened claims, demands, causes of action or proceedings arising from any breach of this Agreement by you.

- IN NO EVENT SHALL WILEY OR ITS LICENSORS BE LIABLE TO YOU OR ANY OTHER PARTY OR ANY OTHER PERSON OR ENTITY FOR ANY SPECIAL, CONSEQUENTIAL, INCIDENTAL, INDIRECT, EXEMPLARY OR PUNITIVE DAMAGES, HOWEVER CAUSED, ARISING OUT OF OR IN CONNECTION WITH THE DOWNLOADING, PROVISIONING, VIEWING OR USE OF THE MATERIALS REGARDLESS OF THE FORM OF ACTION, WHETHER FOR BREACH OF CONTRACT, BREACH OF WARRANTY, TORT, NEGLIGENCE, INFRINGEMENT OR OTHERWISE (INCLUDING, WITHOUT LIMITATION, DAMAGES BASED ON LOSS OF PROFITS, DATA, FILES, USE, BUSINESS OPPORTUNITY OR CLAIMS OF THIRD PARTIES), AND WHETHER OR NOT THE PARTY HAS BEEN ADVISED OF THE POSSIBILITY OF SUCH DAMAGES. THIS LIMITATION SHALL APPLY NOTWITHSTANDING ANY FAILURE OF ESSENTIAL PURPOSE OF ANY LIMITED REMEDY PROVIDED HEREIN.

- Should any provision of this Agreement be held by a court of competent jurisdiction to be illegal, invalid, or unenforceable,

8. Reprint permissions

that provision shall be deemed amended to achieve as nearly as possible the same economic effect as the original provision, and the legality, validity and enforceability of the remaining provisions of this Agreement shall not be affected or impaired thereby.

- The failure of either party to enforce any term or condition of this Agreement shall not constitute a waiver of either party's right to enforce each and every term and condition of this Agreement. No breach under this agreement shall be deemed waived or excused by either party unless such waiver or consent is in writing signed by the party granting such waiver or consent. The waiver by or consent of a party to a breach of any provision of this Agreement shall not operate or be construed as a waiver of or consent to any other or subsequent breach by such other party.

- This Agreement may not be assigned (including by operation of law or otherwise) by you without WILEY's prior written consent.

- Any fee required for this permission shall be non-refundable after thirty (30) days from receipt by the CCC.

- These terms and conditions together with CCC's Billing and Payment terms and conditions (which are incorporated herein) form the entire agreement between you and WILEY concerning this licensing transaction and (in the absence of fraud) supersedes all prior agreements and representations of the parties, oral or written. This Agreement may not be amended except in writing signed by both parties. This Agreement shall be binding upon and inure to the benefit of the parties' successors, legal representatives, and authorized assigns.

- In the event of any conflict between your obligations established by these terms and conditions and those established by CCC's Billing and Payment terms and conditions, these terms and conditions shall prevail.

- WILEY expressly reserves all rights not specifically granted in the combination of (i) the license details provided by you and accepted in the course of this licensing transaction, (ii) these terms and conditions and (iii) CCC's Billing and Payment terms and conditions.

- This Agreement will be void if the Type of Use, Format, Circulation, or Requestor Type was misrepresented during the licensing process.

- This Agreement shall be governed by and construed in accordance with the laws of the State of New York, USA, without regards to such state's conflict of law rules. Any legal action, suit or proceeding arising out of or relating to these Terms and Conditions or the breach thereof shall be instituted in a court of competent jurisdiction in New York County in the State of New York in the United States of America and each party hereby consents and submits to the personal jurisdiction of such court, waives any objection to venue in such court and consents to service of process by registered or certified mail, return receipt requested, at the last known address of such party.

WILEY OPEN ACCESS TERMS AND CONDITIONS

Wiley Publishes Open Access Articles in fully Open Access Journals and in Subscription journals offering Online Open. Although most of the fully Open Access journals publish open access articles under the terms of the Creative Commons Attribution (CC BY) License only, the subscription journals and a few of the Open Access Journals offer a choice of Creative Commons Licenses. The license type is clearly identified on the article.

The Creative Commons Attribution License

The Creative Commons Attribution License (CC-BY) allows users to copy, distribute and transmit an article, adapt the article and make commercial use of the article. The CC-BY license permits commercial and non-

Creative Commons Attribution Non-Commercial License

The Creative Commons Attribution Non-Commercial (CC-BY-NC)License permits use, distribution and reproduction in any medium, provided the original work is properly cited and is not used for commercial purposes.(see below)

Creative Commons Attribution-Non-Commercial-NoDerivs License

The Creative Commons Attribution Non-Commercial-NoDerivs License (CC-BY-NC-ND) permits use, distribution and reproduction in any medium, provided the original work is properly cited, is not used for commercial purposes and no modifications or adaptations are made. (see below)

Use by commercial "for-profit" organizations

Use of Wiley Open Access articles for commercial, promotional, or marketing purposes requires further explicit permission from Wiley and will be subject to a fee.

Further details can be found on Wiley Online Library http://olabout.wiley.com/WileyCDA/Section/id-410895.html

8. Reprint permissions

Other Terms and Conditions:

v1.10 Last updated September 2015

Questions? customercare@copyright.com **or +1-855-239-3415 (toll free in the US) or +1-978-646-2777.**

8. Reprint permissions

<div align="center">

JOHN WILEY AND SONS LICENSE
TERMS AND CONDITIONS

</div>

Mar 25, 2021

This Agreement between Technical University of Munich -- Max Schütz ("You") and John Wiley and Sons ("John Wiley and Sons") consists of your license details and the terms and conditions provided by John Wiley and Sons and Copyright Clearance Center.

License Number	4973690925662
License date	Dec 21, 2020
Licensed Content Publisher	John Wiley and Sons
Licensed Content Publication	Angewandte Chemie
Licensed Content Title	Der intermetalloide Cluster [(Cp*AlCu)6H4], Stabilisierung eines Cu6-Kerns in einer oktaedrischen Al6-Hülle: molekulare Modellverbindungen für Hume-Rothery-Nanophasen
Licensed Content Author	Chelladurai Ganesamoorthy, Jana Weßing, Clarissa Kroll, et al
Licensed Content Date	Jun 24, 2014
Licensed Content Volume	126
Licensed Content Issue	30
Licensed Content Pages	5
Type of Use	Dissertation/Thesis
Requestor type	University/Academic
Format	Print and electronic
Portion	Figure/table
Number of figures/tables	1
Will you be translating?	Yes, including English rights
Number of languages	2
Title	Fundamental Understanding of living cluster libraries in solution
Institution name	Technical University of Munich
Expected presentation date	Jun 2021
Order reference number	3
Portions	TOC Scheme
Specific Languages	English, German
Requestor Location	Technical University of Munich Lichtenbergstrasse 4
	Garching, 85748 Germany Attn: Technical University of Munich
Publisher Tax ID	EU826007151
Total	**0.00 EUR**
Terms and Conditions	

TERMS AND CONDITIONS

This copyrighted material is owned by or exclusively licensed to John Wiley & Sons, Inc. or one of its group companies (each a"Wiley Company") or handled on behalf of a society with which a Wiley Company has exclusive publishing rights in relation to a particular work (collectively "WILEY"). By clicking "accept" in connection with completing this licensing transaction, you agree that

8. Reprint permissions

8. Reprint permissions

ESSENTIAL PURPOSE OF ANY LIMITED REMEDY PROVIDED HEREIN.

- Should any provision of this Agreement be held by a court of competent jurisdiction to be illegal, invalid, or unenforceable, that provision shall be deemed amended to achieve as nearly as possible the same economic effect as the original provision, and the legality, validity and enforceability of the remaining provisions of this Agreement shall not be affected or impaired thereby.

- The failure of either party to enforce any term or condition of this Agreement shall not constitute a waiver of either party's right to enforce each and every term and condition of this Agreement. No breach under this agreement shall be deemed waived or excused by either party unless such waiver or consent is in writing signed by the party granting such waiver or consent. The waiver by or consent of a party to a breach of any provision of this Agreement shall not operate or be construed as a waiver of or consent to any other or subsequent breach by such other party.

- This Agreement may not be assigned (including by operation of law or otherwise) by you without WILEY's prior written consent.

- Any fee required for this permission shall be non-refundable after thirty (30) days from receipt by the CCC.

- These terms and conditions together with CCC's Billing and Payment terms and conditions (which are incorporated herein) form the entire agreement between you and WILEY concerning this licensing transaction and (in the absence of fraud) supersedes all prior agreements and representations of the parties, oral or written. This Agreement may not be amended except in writing signed by both parties. This Agreement shall be binding upon and inure to the benefit of the parties' successors, legal representatives, and authorized assigns.

- In the event of any conflict between your obligations established by these terms and conditions and those established by CCC's Billing and Payment terms and conditions, these terms and conditions shall prevail.

- WILEY expressly reserves all rights not specifically granted in the combination of (i) the license details provided by you and accepted in the course of this licensing transaction, (ii) these terms and conditions and (iii) CCC's Billing and Payment terms and conditions.

- This Agreement will be void if the Type of Use, Format, Circulation, or Requestor Type was misrepresented during the licensing process.

- This Agreement shall be governed by and construed in accordance with the laws of the State of New York, USA, without regards to such state's conflict of law rules. Any legal action, suit or proceeding arising out of or relating to these Terms and Conditions or the breach thereof shall be instituted in a court of competent jurisdiction in New York County in the State of New York in the United States of America and each party hereby consents and submits to the personal jurisdiction of such court, waives any objection to venue in such court and consents to service of process by registered or certified mail, return receipt requested, at the last known address of such party.

WILEY OPEN ACCESS TERMS AND CONDITIONS
Wiley Publishes Open Access Articles in fully Open Access Journals and in Subscription journals offering Online Open. Although most of the fully Open Access journals publish open access articles under the terms of the Creative Commons Attribution (CC BY) License only, the subscription journals and a few of the Open Access Journals offer a choice of Creative Commons Licenses. The license type is clearly identified on the article.
The Creative Commons Attribution License
The Creative Commons Attribution License (CC-BY) allows users to copy, distribute and transmit an article, adapt the article and make commercial use of the article. The CC-BY license permits commercial and non-
Creative Commons Attribution Non-Commercial License
The Creative Commons Attribution Non-Commercial (CC-BY-NC)License permits use, distribution and reproduction in any medium, provided the original work is properly cited and is not used for commercial purposes.(see below)

Creative Commons Attribution-Non-Commercial-NoDerivs License
The Creative Commons Attribution Non-Commercial-NoDerivs License (CC-BY-NC-ND) permits use, distribution and reproduction in any medium, provided the original work is properly cited, is not used for commercial purposes and no modifications or adaptations are made. (see below)
Use by commercial "for-profit" organizations
Use of Wiley Open Access articles for commercial, promotional, or marketing purposes requires further explicit permission from

8. Reprint permissions

Wiley and will be subject to a fee.
Further details can be found on Wiley Online Library http://olabout.wiley.com/WileyCDA/Section/id-410895.html

Other Terms and Conditions:

v1.10 Last updated September 2015

Questions? customercare@copyright.com or +1-855-239-3415 (toll free in the US) or +1-978-646-2777.

8. Reprint permissions

1. Dalton transactions

0,00 EUR

Article: Enabling LIFDI-MS measurements of highly air sensitive organometallic compounds: A combined MS/glovebox technique

ISSN	1477-9234	**Publisher**	ROYAL SOCIETY OF CHEMISTRY	Publisher Terms and Conditions
Type of Use	Republish in a thesis/dissertation	**Portion**	Chapter/article	Special Terms Apply

Hide Details

LICENSED CONTENT

Publication Title	Dalton transactions	**Rightsholder**	Royal Society of Chemistry
Article Title	Enabling LIFDI-MS measurements of highly air sensitive organometallic compounds: A combined MS/glovebox technique	**Publication Type**	e-Journal
		Start Page	9031
		End Page	9036
Author/Editor	Royal Society of Chemistry (Great Britain)	**Issue**	26
		Volume	50
Date	01/01/2003		
Language	English		
Country	United Kingdom of Great Britain and Northern Ireland		

REQUEST DETAILS

Portion Type	Chapter/article	**Rights Requested**	Main product
Page range(s)	9031-9036	**Distribution**	Worldwide
Total number of pages	5	**Translation**	Original language of publication
Format (select all that apply)	Print, Electronic	**Copies for the disabled?**	No
Who will republish the content?	Author of requested content	**Minor editing privileges?**	Yes
Duration of Use	Life of current edition	**Incidental promotional use?**	No
Lifetime Unit Quantity	Up to 499	**Currency**	EUR

NEW WORK DETAILS

Title	Fundamental understanding of living cluster libraries in solution	**Institution name**	Technical University of Munich
		Expected presentation date	2021-09-01
Instructor name	Max Schütz		

ADDITIONAL DETAILS

Order reference number	N/A	**The requesting person / organization to appear on the license**	Max Schütz

REUSE CONTENT DETAILS

Title, description or numeric reference of the portion(s)	pages 9031-9036	**Title of the article/chapter the portion is from**	Enabling LIFDI-MS measurements of highly air sensitive organometallic compounds: A combined MS/glovebox technique
Editor of portion(s)	Fischer, Roland A.; Muhr, Maximilian; Heiß, Patricia; Schütz, Max; Bühler, Raphael; Gemel, Christian; Linden, H. Bernhard; Linden, Mathias	**Author of portion(s)**	Fischer, Roland A.; Muhr, Maximilian; Heiß, Patricia; Schütz, Max; Bühler, Raphael; Gemel, Christian; Linden, H. Bernhard; Linden, Mathias
Volume of serial or monograph	50		
Page or page range of portion	9031-9036	**Issue, if republishing an article from a serial**	26
		Publication date of portion	2021-07-06

If changes are required, remove the item from your cart and visit Special Requests within Manage Account

Remove

Total Items: 1

Cart Total: 0,00 EUR

Apply Promotional Code   CHECKOUT

8. Reprint permissions

☑ **2. Chemical Society reviews** ✎   0,00 EUR

Article: Intermetallic phases meet intermetalloid clusters

⊟ Hide Details

LICENSED CONTENT

Publication Title	Chemical Society reviews	**Publication Type**	e-Journal
Article Title	Intermetallic phases meet intermetalloid clusters	**Start Page**	8496
		End Page	8510
Author/Editor	Royal Society of Chemistry (Great Britain)	**Issue**	15
		Volume	50
Date	01/01/1972	**URL**	http://www.rsc.org/csr
Language	English		
Country	United Kingdom of Great Britain and Northern Ireland		
Rightsholder	Royal Society of Chemistry		

REQUEST DETAILS

Portion Type	Chapter/article	**Rights Requested**	Main product
Page range(s)	8496-8510	**Distribution**	Worldwide
Total number of pages	4	**Translation**	Original language of publication
Format (select all that apply)	Print, Electronic	**Copies for the disabled?**	No
Who will republish the content?	Author of requested content	**Minor editing privileges?**	Yes
Duration of Use	Life of current edition	**Incidental promotional use?**	No
Lifetime Unit Quantity	Up to 499	**Currency**	EUR

NEW WORK DETAILS

Title	Fundamental understanding of living cluster libraries in solution	**Institution name**	Technical University of Munich
		Expected presentation date	2021-09-01
Instructor name	Max Schütz		

ADDITIONAL DETAILS

Order reference number	N/A	**The requesting person / organization to appear on the license**	Max Schütz

REUSE CONTENT DETAILS

Title, description or numeric reference of the portion(s)	pages 8496-8510	**Title of the article/chapter the portion is from**	Intermetallic phases meet intermetalloid clusters
Editor of portion(s)	Schütz, Max; Gemel, Christian; Klein, Wilhelm; Fischer, Roland A.; Fässler, Thomas F.	**Author of portion(s)**	Schütz, Max; Gemel, Christian; Klein, Wilhelm; Fischer, Roland A.; Fässler, Thomas F.
Volume of serial or monograph	50	**Issue, if republishing an article from a serial**	15
Page or page range of portion	8496-8510	**Publication date of portion**	2021-08-02

If changes are required, remove the item from your cart and visit Special Requests within Manage Account   🗑 Remove

---

Total Items: 2   **Cart Total: 0,00 EUR**

Apply Promotional Code   **CHECKOUT**

395